Interior Decoration of Metal-Organic Frameworks through a Thermolabile Protecting Group Strategy

A thesis presented in partial fulfilment of the requirements of the degree of

Doctor of Philosophy

in

Chemistry

at Massey University, Manawatū, New Zealand

Heather Taylor Jameson

2019

For My Parents

(with apologies to my liver)

Abstract

Metal-organic frameworks are porous nanomaterials of modular construction that have shown themselves amenable to different modes of functionalization. Thermolytic deprotection (thermolysis) of incorporated thermolabile protecting groups (TPGs) has been one of these methods applied to tune the chemistry of MOFs and their material properties, accessing otherwise unattainable MOF topologies with enhanced porosity and reactive functionalities of particular interest in gas storage and separation and catalytic applications. In this thesis the TPG post-synthetic modification (PSM) technique is expanded upon in two ways. Firstly, through investigation of mono-and dual-functionalization within a flexible pillar-layer MOF family: localization of the TPG, influence on framework topology and gas sorption characteristics. Secondly, in synthesis of a set of novel ketene-protecting TPG ligands: ligand characterization, and endeavours at MOF incorporation.

Contributions

All the work in this thesis was completed by Heather Jameson

Except:

- Synthesis of functionalized 4,4`-bipyridine ligands and a mono-substituted MOF (including single crystal and NMR characterization) by Dr. Sebastian Blackwood.
- Some of the Meldrum's acid ligand synthetic routes presented in Chapter 4 were initially established by Mr. David Lun.

Acknowledgements

I had planned my life's endeavour –

But my life had plans for me.

I am lost

but not forever.

I am where I'm meant to be

~ Poem_for_your_sprog

I need to thank the large number of people who have contributed to this PhD. Firstly, thank you to my supervisor Professor Shane Telfer for introducing me to the marvellous MOF world and providing me with countless opportunities to develop during my PhD through conferences, symposiums, and workshops. Your patient support has made this possible.

Thank you to my Telfer group colleagues and interns, past and present who have guided, supported, and illuminated this PhD. Especially, Dr. Sebastian Blackwood, Dr. Lujia Liu, Dr. Tian Zhou, Dr. Adil Alkas, Dr. Omid Taheri, and David Perl for scientific discussions and technical assistance. And most importantly, their smiling faces. Nisansala Bandera, Subo Lee, and Joel Cornelio, your lovely presence made every day easier. A big thanks to David Lun for his generous assistance and guidance in the lab.

I also thank Dr. Pat Edwards for assisting with general and specialized NMR experiments and Professor Geoff Jameson for a thorough x-ray crystallography review. Professor Kathryn Stowell, Associate Professor Tracey Riley, IFS administration and technical staff and Massey counselling services have provided crucial aid during my PhD and thesis writing, and I thank them for helping keep me on track towards thesis submission.

I would like to acknowledge the financial support from Massey University through a much-appreciated Doctoral Scholarship and the MacDiarmid Institute for Advanced Materials and Nanotechnology for covering my doctoral fees. Thank you to the IFS postgraduate travel fund for supporting me to attend the MOF 2016 conference in Los Angeles. And thank you to NZIC for financial support to travel to their annual conferences and learn the local flavour of New Zealand Chemistry.

For the AMN-7 conference in Nelson I thank Professor Shane Telfer for the excellent organization and the MacDiarmid Institute. The latter I also thank for organizing annual student and postdoc symposiums which are top-quality and reinvigorating to research.

I thank the NZ Synchrotron Group Limited for enabling me to attend Cheiron School in 2015. The experience and learning was both timely and life-changing.

On a personal level…I have met many wonderful people during this journey. I cannot thank enough Prof. Kathryn Stowell for stepping up to an uncomfortable place when I most needed it.

To Hadee Thompson-Morrison, thanks for altering my life course for the better and in a completely unexpected direction.

To David Perl and our sustaining friendship, no backsies (like never)! You have been and continue to be a treasured companion on many past and future trips. Thanks for bringing goodness and more good people into my life.

To Lukas Hunziker, Cat Power, Zoë Erridge, Esther Anderson, Sara Hewson, Kersty Trainor, Lois Edwards, Tegan Owen – friends I could ask for help and who never failed to deliver.

To my sister, Kimberley, and brother, Andrew, you are my inspiration always. And for my parents, and your unwavering support (emotional, financial, ongoing) my gratitude is unending. Thank you, Mom for helping me stay grounded.

I would not be here and who I am today without any of you and I am eternally happy to have answered the question, "What if I try to finish this PhD?"

Try, try, try again. Fail again. Try better. Fail better.

Thanks to all who read this.

Publications and thesis structure

Publications relevant to this thesis

1. **H.Jameson**, Postsynthetic methods in metal-organic framework (MOF) chemistry, C*hemistry in New Zealand*, **2017**, 81, 112-114.

Additional publications

1. Saghatforoush, L., Moeini, K., Hosseini-Yazdi, S. A., Mardani, Z., Hajabbas-Farshchi, A., **Jameson, H. T**., Telfer, S. G., Woollins, J. D., Theoretical and experimental investigation of anticancer activities of an acyclic and symmetrical compartmental Schiff base ligand and its Co(II), Cu(II) and Zn(II) complexes, *RSC Advances*, **2018**, 62, 35625-35639.

Abbreviations

ACN	Acetonitrile
AIBN	Azobisisobutyronitrile
ASU	Asymmetric unit
Bbc	4,4`,4``-(Benzene-1,3,5-triyl-tris(benzene-4,1-diyl))tribenzoic acid
BET	Brunauer-Emmett-Teller
Bdc	1,4-Benzenedicarboxylic acid
Bpdc	Biphenyl-4,4`-dicarboxylic acid
Bpee	1,2-bipyridylethene
Bpy	4,4`-Bipyridine
Boc_2O	Di-*tert*-butyl dicarbonate (Boc anhydride)
Btc	Benzene-1,3,5-tricarboxylic acid
DABCO	1,4-Diazabicyclo[2.2.2]octane
DBF	*N*,*N*-dibutylformamide
DCC	*N*,*N*`-dicyclohexylcarbodiimide
DEF	*N*,*N*-diethylformamide
DMAP	4-Dimethylaminopyridine
DMF	*N*,*N*-dimethylformamide
Dobpdc	4,4′-dioxidobiphenyl-3,3′-dicarboxylic acid
DUT	Dresden University of Technology
Et_3N	Triethylamine
EtOAc	Ethyl acetate
GS	Gas sorption
HKUST	Hong Kong University of Science and Technology
IRMOF	Isoreticular metal-organic framework
IUPAC	International Union of Pure and Applied Chemistry
MIL	Matérial Institut Lavoisier

MOF	Metal-organic framework
MUF	Massey University framework
NBS	N-bromosuccinimide
NMR	Nuclear magnetic resonance
PCN	Porous coordination network
PCP	Porous coordination polymer
PSD	Postsynthetic deprotection
PSE	Postsynthetic exchange
PSI	Postsynthetic insertion
PSM	Postsynthetic modification
PXRD	Powder x-ray diffraction
SALE	Solvent-assisted ligand exchange
SALI	Solvent-assisted ligand insertion
SBU	Secondary building unit
STP	Standard temperature and pressure
SCXRD	Single crystal x-ray diffraction
TFA	Trifluoroacetic acid
TGA	Thermogravimetric analysis
THF	Tetrahydrofuran
TPG	Thermolabile protecting group
UiO	University of Oslo
UMCM	University of Michigan crystalline material
XRD	X-ray diffraction
ZIF	Zeolitic imidazolate framework

Table of Contents

Chapter 1 - Introduction

1.1. Metal-organic frameworks (MOFs)

Material adjectives applied to metal-organic frameworks are exceeded only by the explosive growth in published members of this novel subset of porous coordination polymers (PCPs) (Figure 1.1).[1] These PCPs can be rigid, flexible, responsive, inert, insulating, conductive, chiral, and have lent themselves to applications as diverse. As of 2013, the International Union of Pure and Applied Chemistry (IUPAC) defines a MOF as "a coordination network with organic ligands containing potential voids."[1]

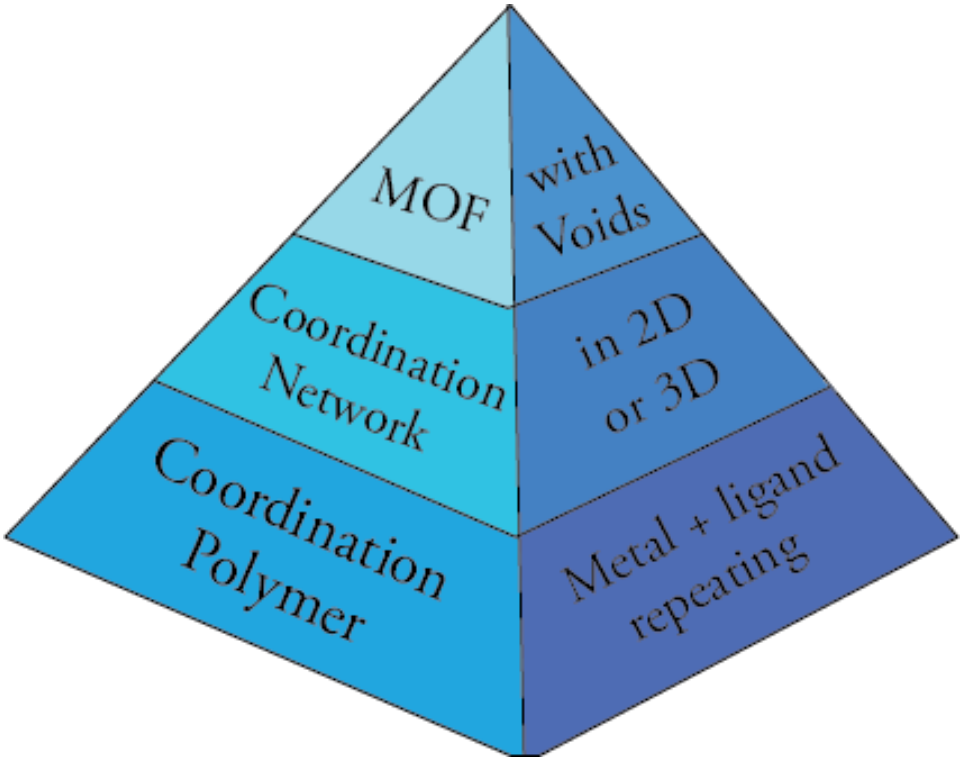

Figure 1.1: MOFs defined as a subset of coordination networks according to IUPAC.[1]

From a polymer perspective, the fundamental units (monomers) repeated in a metal-organic framework are the struts: organic molecules with divergently positioned coordinating moieties, and the nodes: metal ions or metal-ion clusters termed the secondary building unit or SBU. These elements are sufficient to replicate the entire framework, typically in three dimensions (Figure 1.2).

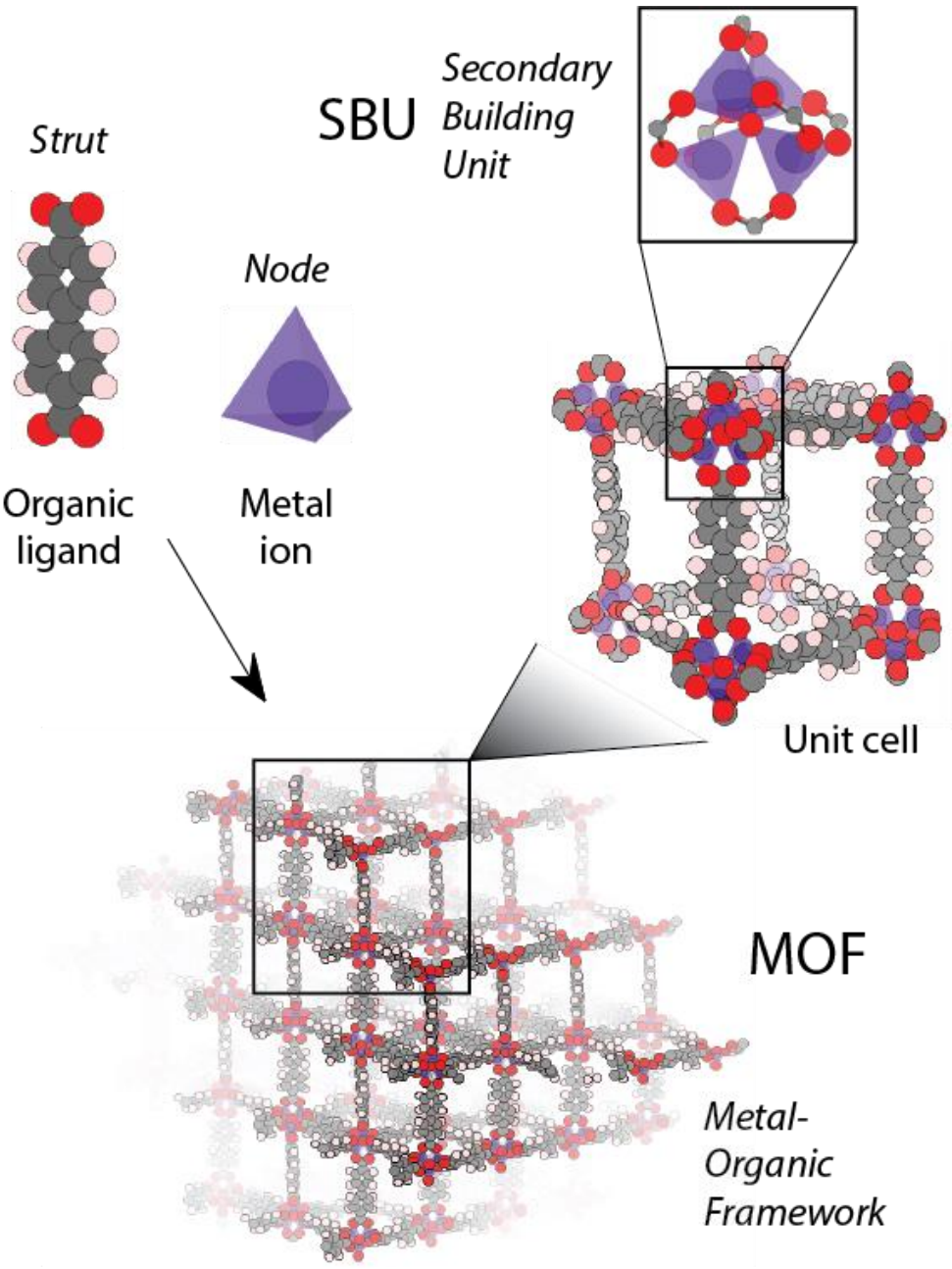

Figure 1.2: General MOF construction.

Due to the interchangeable nature of the substituents and the almost infinite variety of combinations therefore, the 'tuneable' or 'tailorable' MOF to a desired function is described often in literature with exemplary applications in areas as diverse as intracellular enzyme stabilization,[2] industrial separation of important mixtures,[3] and breakdown of toxic warfare agents (Figure 1.3).[4]

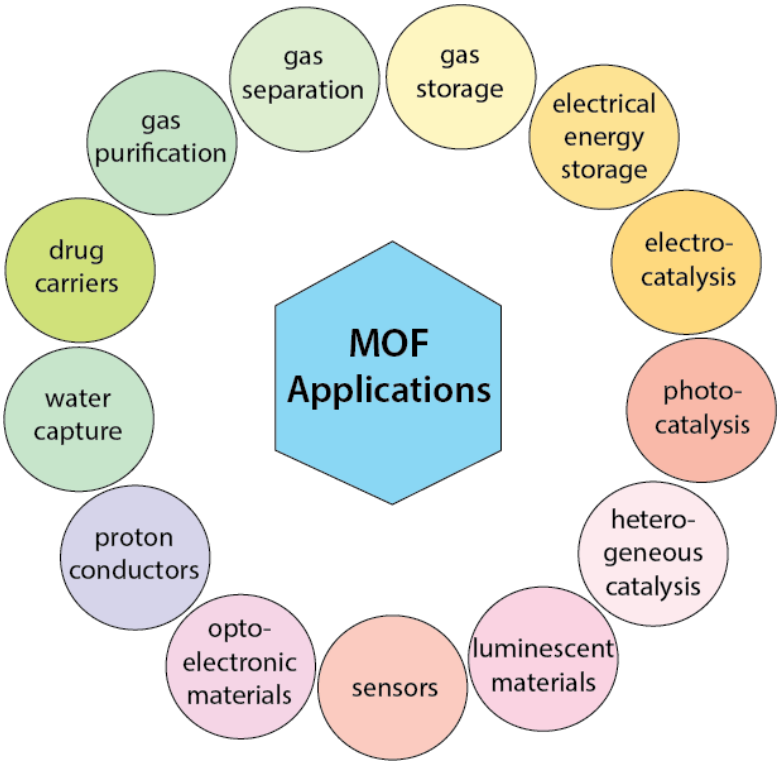

Figure 1.3: General MOF applications.

From a materials perspective, commonly MOFs are understood to have the minimal properties of crystallinity, (potential) permanent porosity and optionally high thermal stability (many zirconium-based MOFs retain the former two properties up to temperatures exceeding 500 ^{o}C).[5] These two main features: high crystallinity and impressive internal surface areas (7140 m^2/g for NU-110 MOF material in 2012)[6] are the key properties that have stimulated research further into this novel class of porous nanomaterials, fulfilling within three decades the visionary predictions made upon first discovery by Hoskins and Robson.[7-8] In 1990 Robson, remarking upon the spontaneous self-assembly of four-coordinate tetrahedral or six-coordinate octahedral metal nodes with divergently coordinating linear organic ligands, insightfully predicted materials with the following features:

1) Low density in combination with high crystallinity, porosity, chemical, mechanical, and thermal stability;
2) Pores allowing the diffusion, inclusion and separation of guest molecules, which enable;
3) Post-synthetic modification of the organic linkers, i.e. chemical transformation of ligands post incorporation into the metal-organic framework,
4) Active catalytic sites for heterogeneous catalytic applications, and
5) Cooperative catalytic activity through interaction between multiple sites.

One of the advantages of MOFs is the traceable influence of their interchangeable parts on the final properties of the material formed. Structure-function relationships can be readily drawn and thus the resultant self-assembled material can be "programmed".[9] The predicted MOF topology and material properties can be roughly coded by judicious choice of metal-organic complexes formed by metal ions or metal-containing clusters, nature of coordinating functionalities and the geometry of the divergent organic linkers, combined with a growing knowledge base of experimental MOF-guest interactions (Figure 1.4).

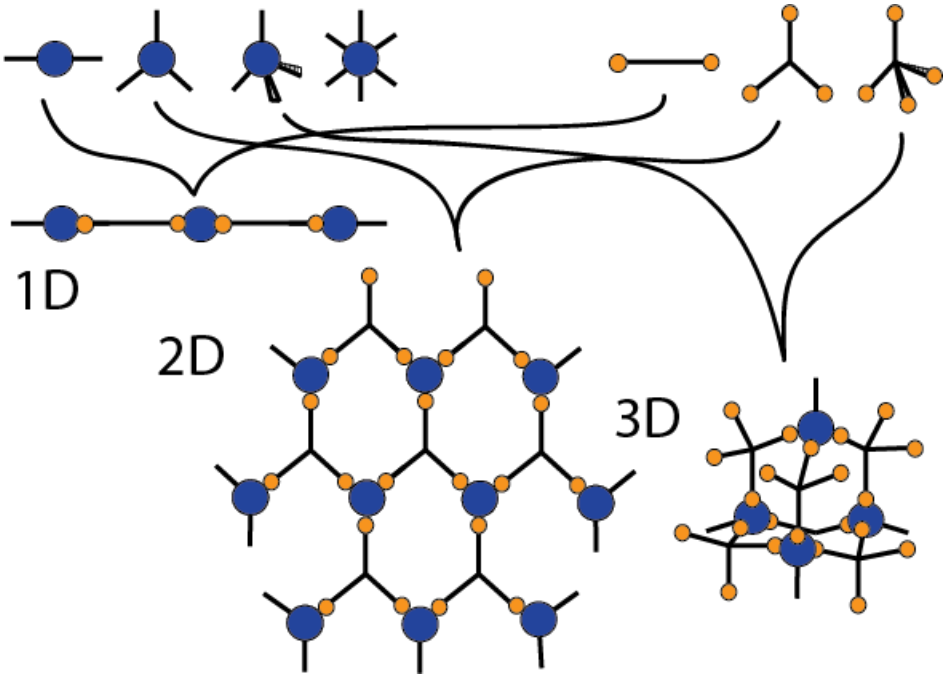

Figure 1.4: Schematic depiction of MOF topological construction.

Based on Pearson's hard/soft acid/base (HSAB) theory, the strength of the metal-ligand bonding of the materials can largely determine if the MOF is relatively robust –i.e., stable to moderate heating and removal of guest solvent molecules from the pores of the framework.

Alongside HKUST-1 (copper paddlewheel, $Cu_2(OH)_2(CO_2)_4$ metal cluster node or SBU) and MIL- 101 ($Cr_3O(OH)_3(CO_2)_6$), one of the first SBUs to be recognized as forming robust frameworks with high chemical stability was the $Zr_6O_4(OH)_4(CO_2)_{12}$ cluster building 'brick' of the UiO-66 isoreticular series (Figure 1.5).[10] Both chromium and zirconium MOFs with high charge cations - Cr^{3+} and Zr^{4+} respectively - feature a hard-hard pairing with carboxylate ligands. An example of a robust MOF formed from a soft-soft metal-ligand binding motif are zinc imidazolate frameworks.

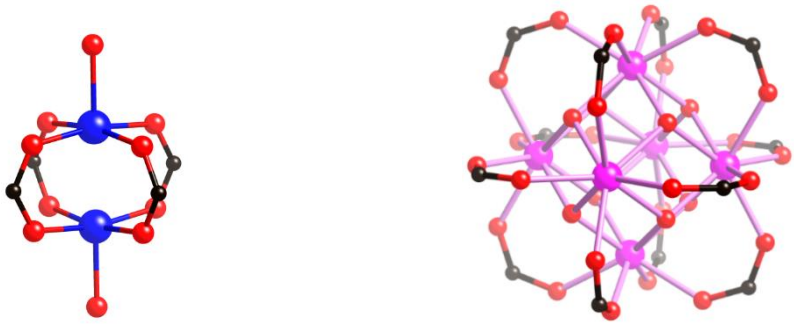

Figure 1.5: The $Zr_6O_4(OH)_4(CO_2)_{12}$ secondary building unit (SBU) of the UiO-MOF series (right) alongside the copper paddlewheel $Cu_2(OH)_2(CO_2)_4$ SBU (left).

Additionally, the reversibility of the metal-ligand binding is key to the synthesis of highly crystalline MOFs and is related to the size of the crystallites formed. Zirconium UiO MOFs frequently form microcrystalline powders instead of large single crystals; this can have important implications for processing of MOF materials on an industrial scale.

Regarding ligands, larger ligands of appropriate geometry for choice of MOF topology can lead to mesoporous (>2 nm) materials and impressive internal surface areas. Topologies including mesopores but precluding interpenetration (formation of another lattice within the pores of the first) have been of great interest in bio-applications for drug delivery and biomolecule sensing. An example is the honeycomb structure of MOF-74[11] (Figure 1.6). MOF-74 also contains unsaturated metal coordination spheres, termed open metal sites (OMS), by removal of the exchangeable axial ligand pointing into the pores. The presence of OMS or decoration by polar functionalities can determine host-guest interactions and location of guest molecules within the MOF structure.

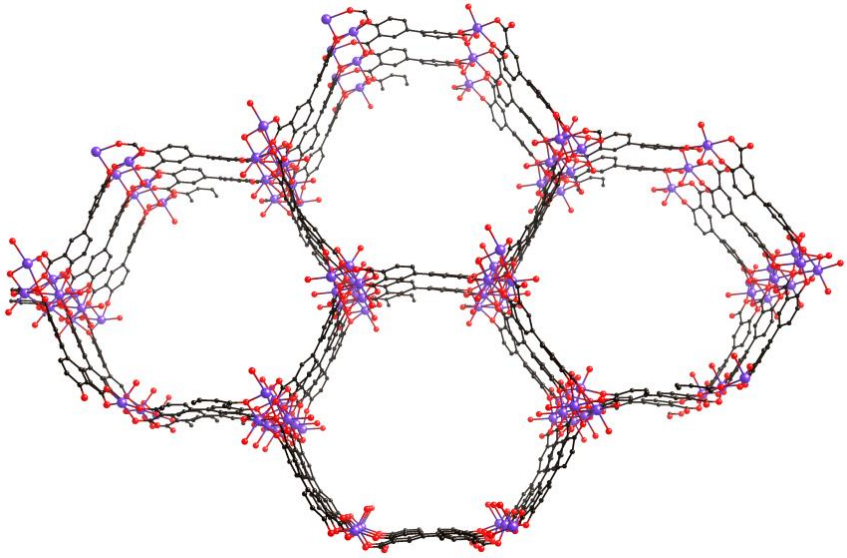

Figure 1.6: The honeycomb structure of MOF-74 resists interpenetration maintaining open 1D channels that can be systematically expanded well into the 2-50 nanometre (mesoporous) size range through simply increasing the organic ligand length.[12]

The MOF field is wide and daily expanding so in this chapter I will introduce the main concepts of imbuing functionality in MOFs, relevant characterization techniques, and a short history of thermolabile protecting groups and their use in polymeric materials.

1.1.1. Definitions and terminology

MOFs primarily use strongly bonding carboxylates, imidazolates as well as phosphates and sulfonates, to coordinate metal ions or metal ion clusters (inorganic secondary building units (SBUs)), but weaker neutral ligands based on pyridines have also been widely used. Interesting materials with bifunctional linkers incorporating hard and soft coordinating moieties – such as pyridine carboxylates[13] - have also been formed.

Alternate names for MOFs exist from historic and stubborn use; metal organic materials (MOMs),[14] porous coordination polymers (PCPs),[15] microporous coordination polymers, (MCPs) and porous coordination networks (PCNs).[16] In this thesis the term MOF will be used according to IUPAC definition (vide supra).

Exploration of the MOF field has necessarily led to the development of further concepts to aid in the definition and characterization of MOF materials. Among these key theoretical advancements have been the recognition of 1) the role of inorganic secondary building units (SBUs) in determining - and so also potentially predicting - the net topology of the final framework and 2) the consistency of the strength of bonds formed in a MOF material. Combined, these ideas fall under reticular synthesis: "the process of assembling judiciously designed rigid molecular building blocks into predetermined ordered structures (networks), which are held together by strong bonding".[17]

As with molecular formulae versus skeletal, there is structural information missing when describing MOFs by unit cell formulae alone. MOFs with different material properties can be described by the same unit cell formulae, such as in the case of interpenetration where a second identical lattice forms within the pores of the first. Thus, often the original name is used to unambiguously describe the composition and phase of the material with a number or affix being used for derivatives from the parent MOF. The original MOF name is most commonly that of the discovering institution, e.g. UiO = University of Oslo (UiO).[10] NU-110 = MOF 110 of Northwestern University (NU), HKUST = Hong Kong University of Science and Technology (HKUST),[18] and MIL = Matérial Institut Lavoisier.[19] However, the originating name of the material can refer to a broader aspect as in the case of isoreticular metal-organic frameworks (IRMOFs)[20] or zeolitic imidazolate frameworks (ZIFs).[21-22]

1.1.2. A brief history of MOFs and key milestones

Widely regarded as the first MOF is a popular art pigment dating back to 1706. Prussian blue or ($Fe_4[Fe(CN)_6]_3.xH_2O$)[23] is a compound first noted in coordination chemistry, a fundamental field upon which MOF research is built.

Shortly after Robson's seminal 1990 predictions of the field's future research,[8] Makoto Fujita and colleagues explored the first catalytic applications of MOFs in 1994.[24] Five years later, two further milestone MOFs were synthesised: HKUST-1, by Ian Williams and colleagues, illustrating the first incidence of post-synthetic modification (PSM) by removal of coordinated water molecules and subsequent binding by pyridine,[18] and MOF-5, in Omar Yaghi's group, demonstrating the first instance of permanent porosity of MOF materials.[25]

Of significance also in 1996, was the synthesis of the first pillar-layer type MOF, an extension of Hoffman clathrates.[26] Also in 1997, the first measurements of high pressure isotherms for MOF materials found that the Co-bpy MOF synthesized had a volumetric methane uptake of 77 v/v STP at 30 bar (i.e. 77 mL of methane was taken up per mL of MOF).[27]

Yaghi and co-workers (who first coined the term MOF in 1995)[28] undertook synthesis where $Zn_4O(CO_2)_6$ octahedral SBUs and 1,4-benzenedicarboxylate (bdc) linkers were combined to form the cubic MOF-5 (Figure 1.7), a single crystal structure was obtained, and permanent porosity confirmed through N_2 gas sorption isotherms in 1999.[25]

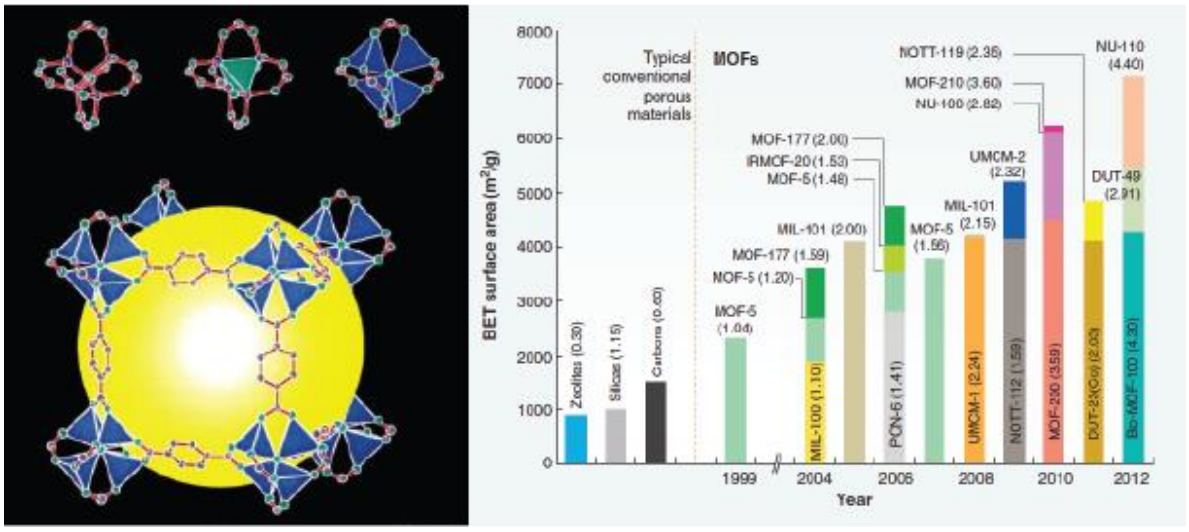

Figure 1.7: MOF-5 (left), the yellow sphere represents the internal void volume. (right) MOF BET surface area and year released with pore volume in cm^3/g in parentheses. Figure adapted from references ([25]) and ([29]) respectively.

This highly porous material was a breakthrough in gas sorption with a calculated Brunauer-Emmett-Teller (BET) surface area of 2,320 m^2g^{-1}, doubling the average zeolite surface area and on-par with benchmark industrial gas sorbents.[30]

The isoreticular MOF (IRMOF) series published in 2002 - of which MOF-5 corresponds to IRMOF-1 - broke new ground at the time, being the first study to thoroughly demonstrate the robust and tuneable nature of MOFs by expansion and decoration of the basic MOF-5 framework.[20] Gradual expansion of the network was achieved by simple substitution of a longer dicarboxylate linker in the MOF synthesis, increasing the pore size from 3.8 to 28.8 Å without affecting the overall primitive cubic (pcu) net topology (Figure 1.8a).[20]

In 2010, this study was carried further to demonstrate that chemical modification of the linkers was also possible while still retaining the original crystalline framework.[31] In the highly decorated multivariate (MTV) MOF, eight different modified linkers were simultaneously incorporated into the MOF-5 framework (Figure 1.8b). Thus, the IRMOF isoreticular series illustrates the great tuneability of MOF materials: that basic pore architecture can be expanded and decorated while the framework topology is maintained.

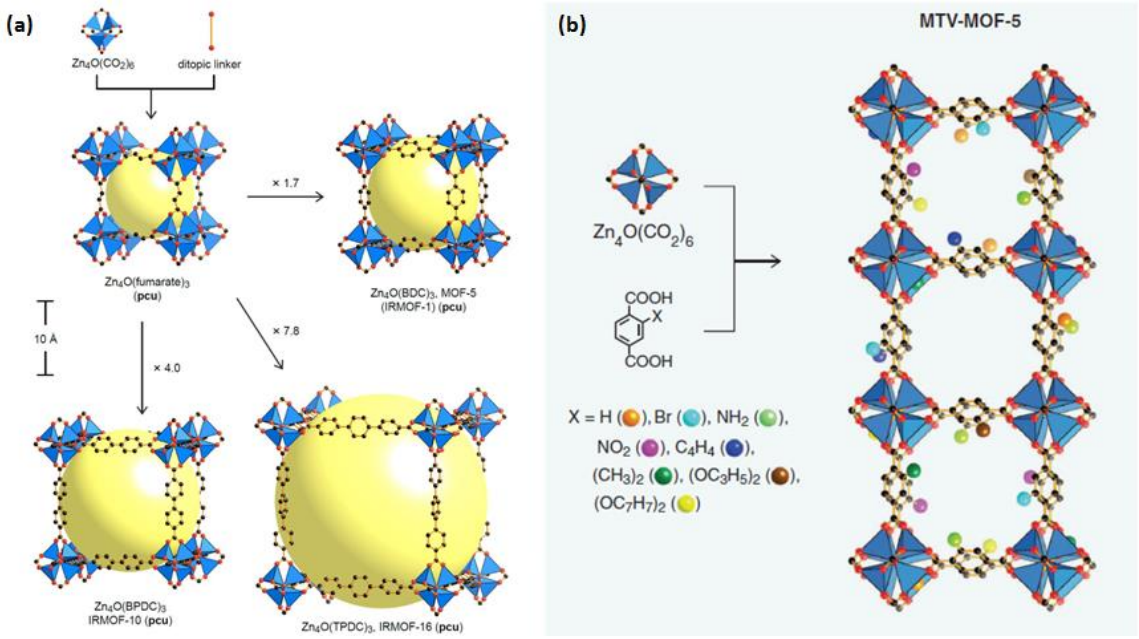

Figure 1.8: Summary of (a) the IRMOF series and (b) MTV-MOF-5. Figures 1.8a and 1.8b were adapted from reference ([29]).

Another zinc-based MOF, but with exceptional stability, was published by Chen's group in 2006 - the zeolitic imidazolate framework (ZIF-8).[21] Solvothermally synthesized in DMF or water from 2-methylimadazole and zinc nitrate, ZIF-8 is stable in neutral to very basic pH, surviving boiling in aqueous 8 M NaOH.[32] This framework is of particular interest in overlapping with the existent zeolite field through framework topology. While ZIFs have compromised stability relative to zeolites the organic linker enables immediate control over functionalization, a more challenging goal with aluminosilicates.

Around this time additional high stability MOFs were also discovered:

- 2005 - MIL-101[33-35] was first reported by the Férey group. Initially synthesized by mixing chromium(III) nitrate and bdc in presence of hydrofluoric acid, HF-free conditions were quickly developed.[36] MIL-101 was among the first MOFs reported to be resistant to hydrolytic and chemical treatment as well as possessing large mesopores with guest encapsulation up to 13.1 Å in diameter.[37] Among many published applications since, sulfonic acid modified MIL-101-Cr-SO_3H can be used as a solid Brønsted acid catalyst and the structure's open metal sites can be functionalized for enantioselective catalysis and selective gas sorption. Synthesis with iron as a metal source yields biodegradable MOF MIL-101-Fe with acceptably low biotoxicity and so potential applications in biomedical imaging and drug release.
- 2008 - the aforementioned zirconium UiO-66 MOF was synthesized in Lillerud's group, another MOF of stunning stability and extensive research.[10] Initial solvothermal synthesis was in DMF at 120 ^oC from bdc and $ZrCl_4$, although a wide range of synthetic conditions for tailoring size, crystallinity, defect concentration, and environmental impact have since been developed.

Related to the discovery of UiO-66 was the development of modulators for single crystal growth with benzoic acid grown single-crystals published in 2011. Subsequent understanding of the role of modulators in defect concentration of UiO MOFs[38] has driven research into "defect by design" materials[39] and the growing understanding of how defects in materials can impart flexibility in traditionally rigid MOFs.[40]

As there is a high energy penalty (38.2 kcal/mol)[41] associated with hydrolysis of the first carboxylate of the SBU of UiO-66, the $Zr_6O_4(OH)_4(CO_2)_{12}$ cluster has gone on to be used in construction of additional highly stable and porous MOFs using alternate ligands.[42-44]

Other zirconium-based MOFs are notably:

- 2007 - PCN-14, which has demonstrated the highest excess CH_4 uptake to date
- 2010 - NU-100 and NU-110.[45] NU-110 held the record for highest accessible pore volume (of 4.40 cm^3/g) until passed last year by DUT-60 (5.02 cm^3/g).
- 2013 - NU-1000,[46] which has found diverse industrial applications such as a catalyst for o-xylene isomerization at 523 K[47] and highly selective separation of toxic furanics, even in several hundred-fold excess sugar-furanics mixtures in bioethanol production.[48]

DUT-60 (2018)[49] is a modern MOF having been designed computationally using Zn_4O^{6+} nodes, ditopic and tritopic linkers to explore the stability limits of framework architectures with

ultrahigh porosity. Additionally, an unusual cluster precursor approach, resulting in minimal side product formation in the solvothermal synthesis, was used to produce the new crystalline framework. Despite the highest recorded accessible pore volume (5.02 cm^3/g) to date, the robust ith-d topology of DUT-60 provides an average bulk and shear modulus (4.97 GPa and 0.50 GPa, respectively) that suppresses pore collapse during desolvation.

From Dresden University also came the MOF, DUT-49.[50] DUT-49 demonstrated the unheard of and counter-intuitive phenomenon of decreasing gas volume uptake upon increasing pressure, termed negative gas adsorption.[51]

Many of these existing MOFs went on to application-ready developments such as HKUST-1 in 2013 meeting the Department of Energy (DoE) requirements for methane uptake - 227 v/v STP at 35 bar, 267 v/v STP at 65 bar, and 190 v/v STP working capacity.[52-53]

Or MOF-74, which went on to take up proteins in 2012, undergo cooperative CO_2 insertion in 2015, and incorporate a peptide into the MOF pores through seven post-synthetic reactions.

In 2009, SURMOF-1 study was carried out demonstrating the potential of surface functionalization with MOFs to form hierarchical nanomaterials of distinct properties.[54]

Further highlights are summarized in Figure 1.9.

From this auspicious beginning, a plethora of MOF papers has since been published, pushing further the boundaries of surface area and pore volume.[29] Still, the field continues to rapidly grow with progress made into many other research areas such as catalysis,[55-58] sensing,[59-62] and conductivity.[63-65]

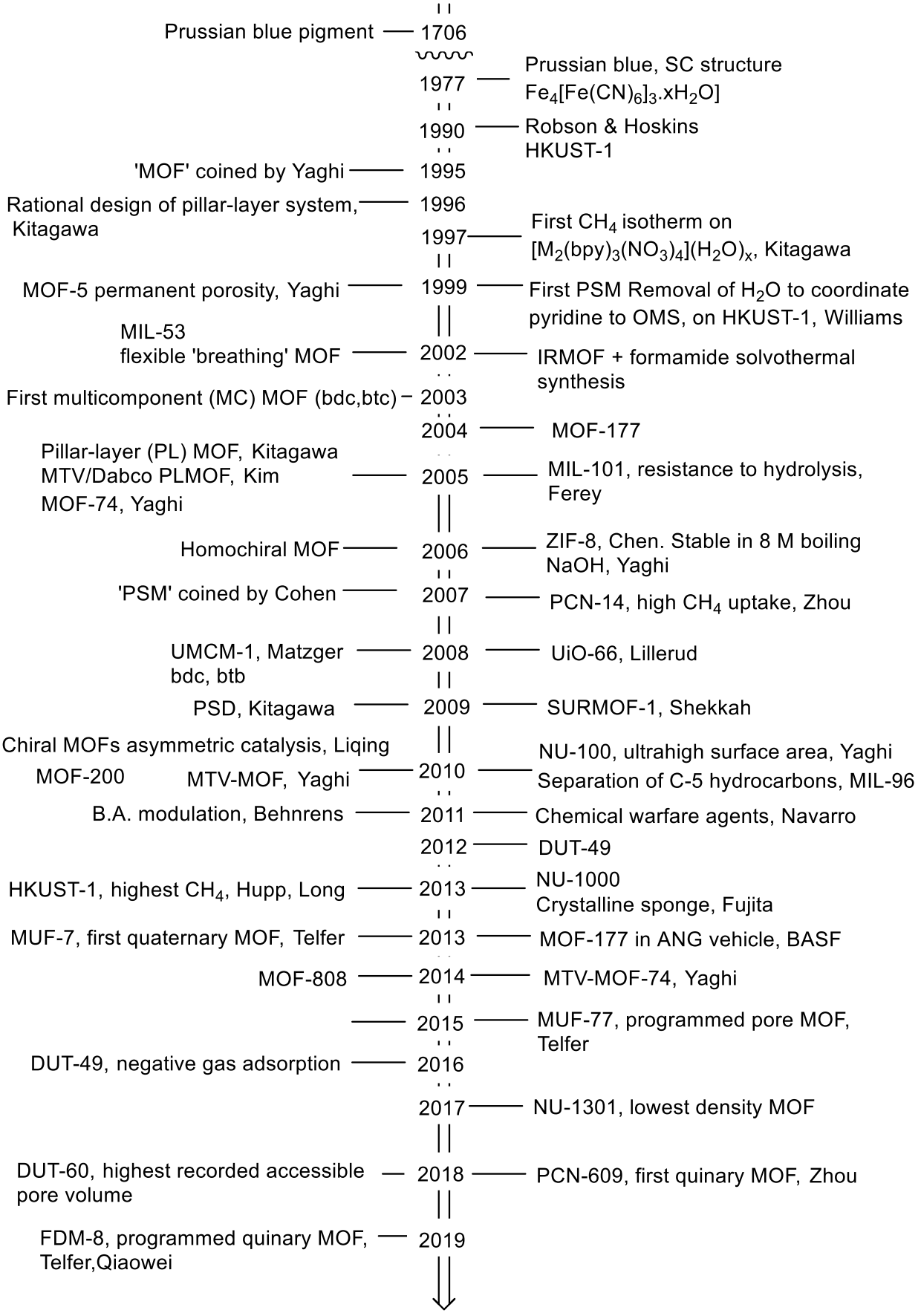

Figure 1.9: MOF annotated timeline.

1.2. Notable applications

1.2.1. Gas storage and separation

The most immediate application of MOFs is use of their high stability and porosity for CO_2 capture from industrial flue gas and for hydrogen and methane fuel storage. In this area MOFs are leading the way with a number of highly stable materials with high porosity and excess gas uptake available (Table 1.1).[29] For practical translation, in carbon dioxide storage a pressurised (35 bar) tank of MOF-200 would hold 17 times as much CO_2 as an empty one.[29] In hydrogen and methane storage it is important to distinguish the total uptake of a material from the volume of fuel delivered (working capacity). The working capacity is determined by the uptake of MOFs at high pressure where the larger the volume of gas adsorbed the better, to delivery of the fuel at low pressure where minimum adsorption of the gas on the framework is desirable. Although much progress has been made in tailoring gas uptake through polar decoration of MOF pores by open metal sites and added amino functionalities there is still further research needed[66] to achieve the 2017 U.S. Department of Energy (DOE) system targets for hydrogen adsorption (5.5 wt%, and 40 g/L at -40 ^{o}C to 60 ^{o}C below 60 bar). However, progress is sufficiently promising for Mercedes-Benz to deploy a fuel cell-powered demonstration model (F125) showcasing MOF hydrogen fuel tanks[67] and current tests by BASF on a natural gas powered vehicle using MOF tanks are also underway.[68]

Table 1.1: Leading MOFs in gas-uptake related properties.[29]

Property or application	Compound	Value achieved	
Lowest reported value			
Density	NU-1301	0.124 g/cm^3	69
Highest reported value			
Pore aperture	IRMOF-74-XI	98 Å	12
BET surface area	NU-110	7140 m^2/g	6
Pore volume	DUT-60	5.02 cm^3/g	49
Excess H_2 uptake	NU-100	9.0 wt%	70
Excess CH_4 uptake (290 K, 35 bar)	PCN-14	212 mg/g	71
Excess CO_2 uptake (298 K, 50 bar)	MOF-200	2347 g	72

1.2.2. Other separations and notable applications

Other separations have also been undertaken in efforts to find more energy efficient alternatives to industrial separations using cryogenic distillation, such as in petroleum enrichment or CO_2 separation from steel manufacturing where high temperatures are required to operate or regenerate absorbents. Break through experiments with gas mixtures are vital to determining practical MOFs for applications and computational screening of structures is now doing the heavy-lifting of discovery.[73]

Toxic gas storage

MOFs are now commercially available as adsorbents for toxic gases such as arsine.[74] These materials enable the use of negative pressure gas canisters which, upon perforation, cause atmosphere to enter as opposed to the expulsion of toxic gas, avoiding the current hazard involved in using the pressurized canisters which are standard in the field. Additionally, they are finding use in ammonia storage, a key chemical in the food supply chain.[75]

MOFs as heating/cooling system adsorbents

A significant contributor to the recent increase in global energy demand was the reliance on heating/cooling systems in the face of extreme weather patterns (harsh winters and heat waves). This energy consumption is only going to rise as climate change disruption deepens. Therefore, more energy efficient systems must be developed to face this growing demand and MOFs have become well-placed to meet this need with water-sorption-driven systems already underway.[76-78]

Explosive materials

Nitrogen rich materials have long been used for their violent expulsion of gas and heat upon oxidation. MOF materials have been designed to similarly react upon sudden impact. Given the range of stimuli available for triggering reactions in MOFs a new class of selectively inert and safe to handle explosives could be designed.[79]

1.2.3. Catalysis

Similarly to copper[80] and MIL-101 (aluminium,[81] chromium and iron[82]) structures, UiO-MOFs also show inherent catalytic activity offered by open metal sites through missing ligand defects.[83] Additionally this porous, non-interpenetrating framework has been extensively modified by post-synthetic modification (PSM) to produce a range of heterogeneous catalysts

resistant to degradation under many different reaction conditions.[84-88] A simple but clear example of modified MOF catalysis is the use of an amino functionalized linker for the cycloaddition of CO_2 to styrene epoxide where the catalytic activity of UiO-66-NH_2 was shown alongside comparably robust frameworks (Table 1.2).[89]

Table 1.2: Textural properties of MOFs and their catalytic activities for cycloaddition of CO_2 to styrene oxide.

Sample	Textural Property		Conversion (%)[a]	
	S_{BET} (m^2/g)[b]	V_{PORE} (cm^3/g)[c]	1h	4h
UiO-66-NH_2	970	0.31	70	95
UiO-66	1121	0.43	48	94
Mg-MOF-74	1525	0.62	59	94
MIL-101	3098	1.57	-	63
$Cu_3(btc)_2$/HKUST-1	1737	0.72	-	48

[a] Reaction conditions: 30 mL of solvent (chlorobenzene) and 5 mmol of styrene oxide at 373 K and 2.0 MPa of CO_2 pressure using 20 mg of catalyst. [b] S_{BET} = BET surface area. [c] V_{Pore} = Total pore volume.

Even after three cycles, no change was observed in the yield obtained using the UiO66-NH_2 catalyst.[89]

As demonstrated, even with a humble amino group introduced to the pore environment novel catalytic materials can be developed. This only scratches the surface of possibilities within MOF catalysis. As earlier introduced with the multivariate MOFs, multiple different functionalities can be introduced into one material, giving rise to synergistic effects and the building of domains. Core-shell or similar stepwise hierarchical structures could isolate these domains allowing for a production line of reactions within one material.

Another exciting direction lies within enzyme-like materials. Either enabling cooperative effects to occur from guest-responsive frameworks or construction of a highly ordered and conserved activation site. Multicomponent MOFs with two or more distinct ligands have shown ordering of functional groups on these ligands within the MOF pores. In particular, programmed pores introduced by Telfer *et al*. demonstrate how a homogenously distributed ordered catalytic site can be tuned to control reaction substrate and chirality.[90]

1.3. MOF structural diversity

Already from a short history and overview of key MOFs the structural diversity of these materials can be clearly shown (Figure 1.10). As of 2017, the total number of MOFs structures deposited in the CCD according to a targeted search was 69,999,[91] although a high duplicate rate has been found even in the MOF CoRe database of computational-ready structures.[92]

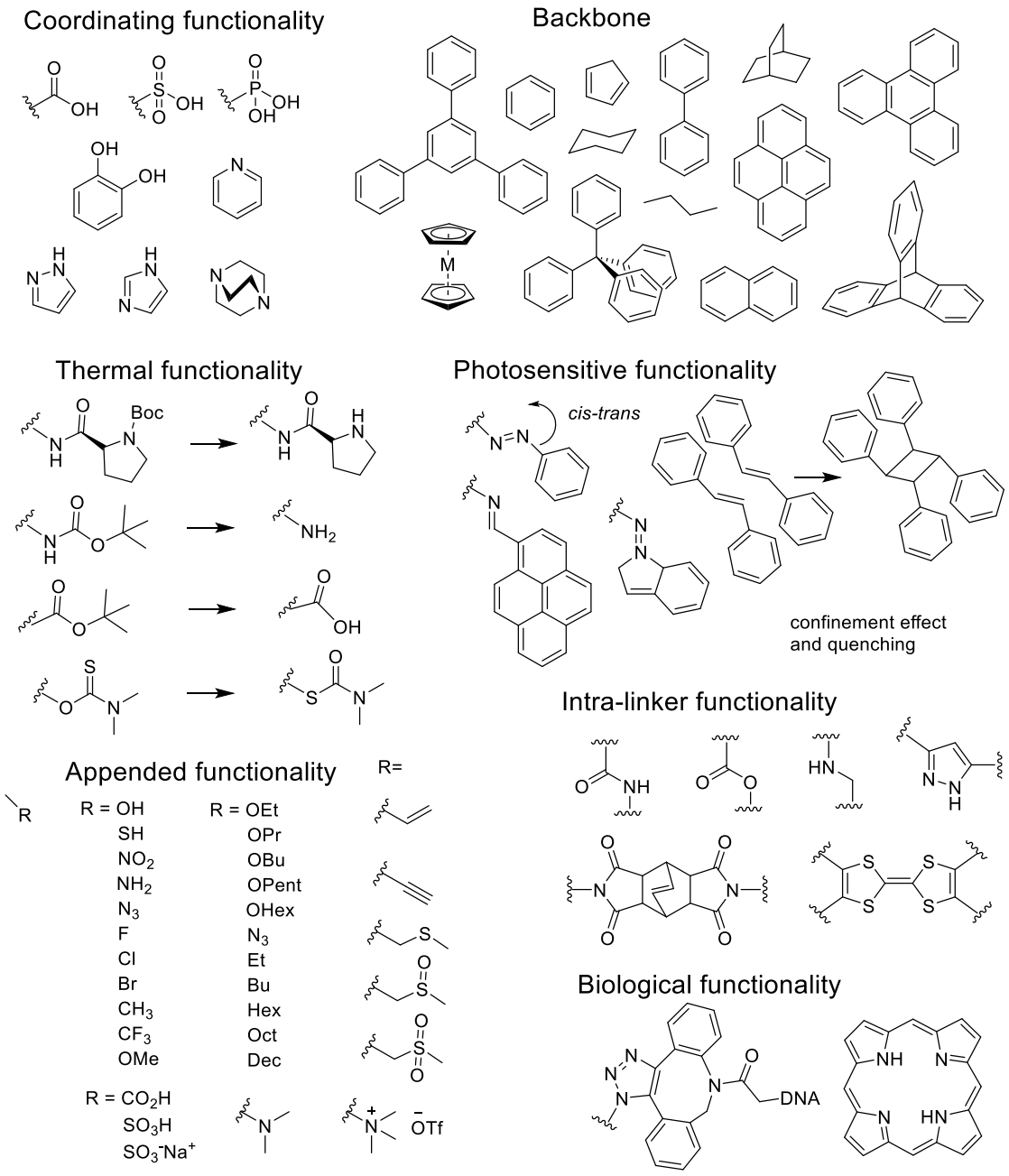

Figure 1.10: Overview of the diversity of MOF organic linkers illustrating (top) key ligand coordinating moieties and backbones and (bottom) types and modes of backbone functionalization such as intra-linker or appended functional groups which can be biological, charged, or reactive to stimuli such as heat and light.

1.4. MOF synthesis and introduction of functionality into MOFs

1.4.1. MOF synthesis methods and direct incorporation of functionality

The first MOF-5 synthesis used traditional vapour diffusion to form MOF crystals, as established within other crystallography-centric fields. In this synthesis, triethylamine was allowed to diffuse into a solution (DMF/chlorobenzene) of zinc nitrate, 1,4-benzenedicarboxylic acid (bdc) and a small volume of hydrogen peroxide at room temperature.[25] Triethylamine deprotonated the carboxylic acid groups and it was thought that hydrogen peroxide contributed oxygen to form the Zn_4O metal nodes. Shortly after, it was found the same MOF could be formed by heating in amide solvent alone. In this case, acid-catalyzed decomposition of diethylformamide (or other formamide), occurs in the presence of water at elevated temperature[93] to generate diethylamine which then gradually deprotonates the ligand[94-95] removing the need for the separate addition of a base (Figure 1.11).[96]

This is termed solvothermal synthesis and is the most general method used for MOF synthesis today.

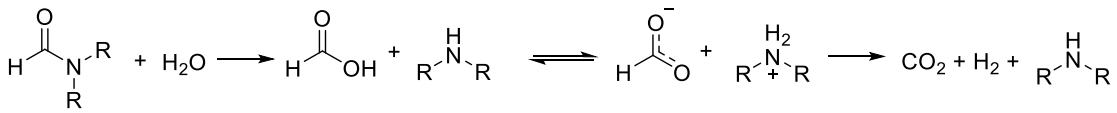

Figure 1.11: Formamide solvents in the presence of water generate base. R = Me, Et, ^{i}Pr, ^{n}Bu.

Apart from participating in the above reaction, water is also thought to contribute oxygen to the metal node cluster in some MOFs. Additionally, water has an important role to play in MOF phase or morphology in favouring a more stable MOF over one less resistant to hydrolysis and in promoting larger crystal formation through increasing the reversibility of ligand metal coordination and thus slowing the growth of the MOF material. In this last respect water is a classic example of a modulator where at high concentrations, degradation of the MOF and formation of multiple or amorphous phases[93, 97-98] can occur but in small volume percentages, crystal size and quality are enhanced.[99-100]

Modulators

Modulators are a class of compounds added to a MOF synthesis mixture (metal plus ligand plus solvent) specifically to control the phase or morphology of the resultant MOF without themselves being involved in the final construction (Figure 1.12). Modulators have been employed in the synthesis of MOFs of desired properties such as single crystal quality and size,[101] defect-free structure,[102] enhanced gas uptake[103] and catalytic activity.[104-105]

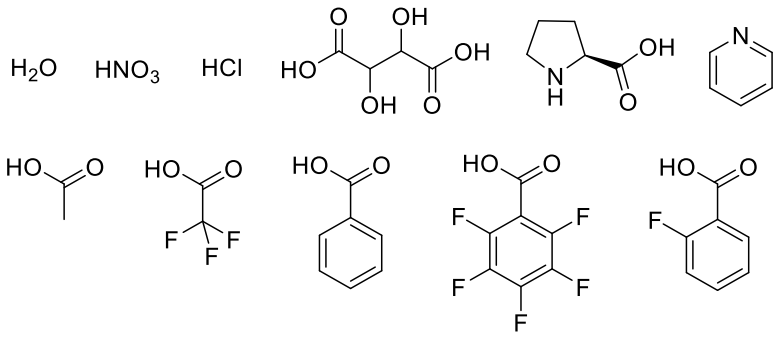

Figure 1.12: Examples of modulators used to tune pH and SBU node formation during MOF synthesis.

Often modulators are simple monotopic versions of the coordinating ligand, e.g., benzoic acid in the synthesis of UiO-66 using zirconium and benzene-dicarboxylic acid. The coordinating moiety of the modulator competes with the ligand during MOF synthesis, slowing the formation of the MOF. In the case of UiO-66, a high ratio of modulator to ligand is required for single crystal growth given the strong and rapid hard-hard metal ligand binding. By tuning the formation of multiple phases, modulators can also be used in synthesis of kinetically disfavoured products.[106]

Altering of the pH, through HCl or HNO_3, and reversible coordination, by non-divergent coordinating species, slows down MOF synthesis to favour node formation first – thus directing the final MOF topology and reducing amorphous phase formation.[107] Modulators can also manipulate the morphology of the MOF crystal formed,[105] additionally controlling catalytic properties of the bulk material.

Precursor nodes

Based on the concept of reticular chemistry/topological construction of MOFs there has been success in using precursor desired SBUs made in a separate step to solvothermal synthesis. This approach was used to synthesize DUT-60, whereby the SBU is designed, pre-formed, then reacted with ligand(s) of appropriate geometry to obtain the targeted topology. This can be desirable in cases where the SBU is difficult to form *in situ* or where multiple phases compete as is common in multicomponent MOF synthesis.

Alternative MOF synthesis methods

As the MOF field has grown so too has the number of MOF synthesis methods, ones that promote smaller crystals (microwave),[108-109] are solvent free (sonochemical,[110-111] electrochemical,[112] or mechanochemical)[113-114] or using green solvents such as water (hydrothermal)[115-117] have all taken their place batting for expansion of knowledge.

Caveats to direct synthesis

For a range of applications such as sensing,[118-119] catalysis,[120-121] and gas storage and separation,[122-124] a key factor is tailored chemical functionalization of the pores of the material. This can be challenging due to the limitations of traditional MOF synthesis.

Apart from targeting a particular choice of topology through choice of SBU and diverging linker, introduction of functionality into MOFs can take some general forms:

1) Organic linker functionalization through
- intrinsic linker functionality (presence of non-carbon atoms in backbone or a flexible link)
- attached functionality (polar, non-polar, asymmetric, chiral, metallic, dynamic (thermal, photo, conductive, reactive), biological)
- a combination of intrinsic and attached functionality (such as a chelating backbone with an open metal site (OMS))

2) Inorganic functionalization
- Post-synthetic metal exchange (PSME)
- Change in oxidation state
- Coordinated functionality

3) Surface functionalization
- coating
- attached functionality
- core-shell growth

While the IRMOF series illustrates many of the strengths of MOF materials – modular construction with high tuneability and retained crystallinity – some of the weaknesses of MOFs are also revealed. Zinc-carboxylate MOFs are now widely recognised as being among the more moisture sensitive MOF materials,[125-127] often decomposing through ligand displacement by water molecules absorbed from the atmosphere alone. Additionally, interpenetration – the formation of a second framework within the first – commonly occurs with the pcu topology MOF structures with larger pore apertures, as shown in the IRMOF series in Figure 1.13.

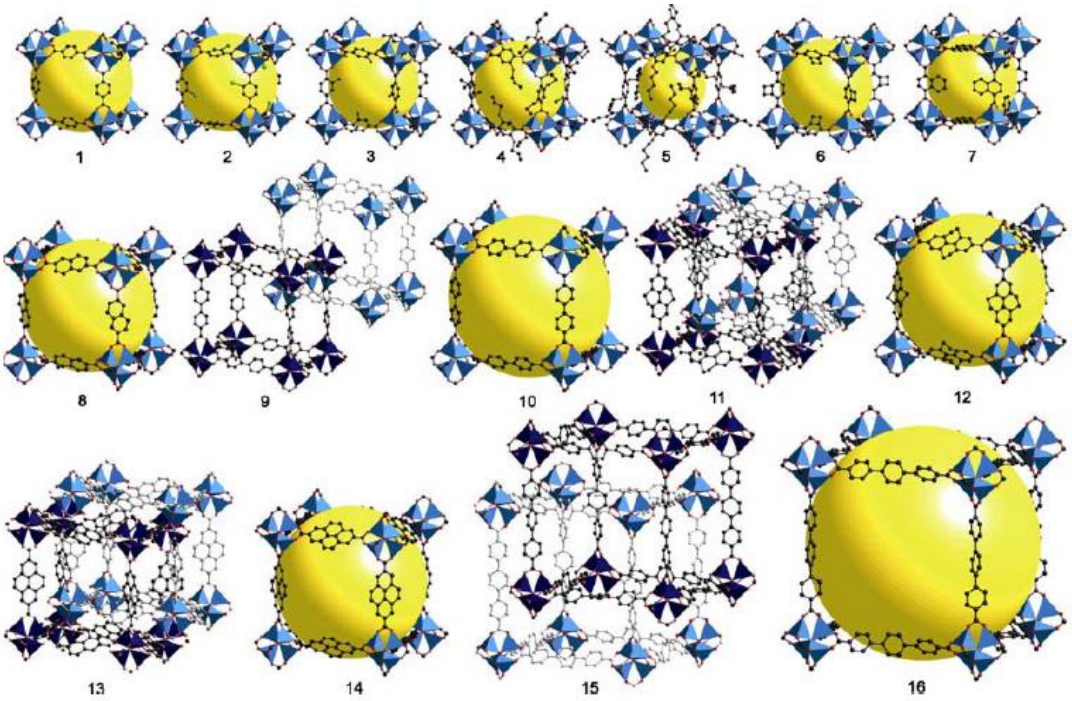

Figure 1.13: The iso-reticular metal-organic framework (IRMOF) series (1 to 16) showing interpenetration in the large pore structures. Yellow spheres represent pore volume. Figure was taken from reference ([128]).

Interpenetration is thermodynamically favoured due to increased van der Waals interactions between the two frameworks. As the second net obstructs the pores, reducing material porosity, the control of interpenetration is a significant area of MOF research.[129]

Finally, the omission of more chemically interesting functionalities such as carboxylic acids, nitriles, azides, alkylamines, thiols (thiophenols) and phosphines from the MTV-MOF (Figure 1.8) hints at a further limitation of MOF materials – the restrictive nature of the synthesis conditions on what functional groups are compatible with MOF formation. Many desirably reactive functional groups can be too sensitive to survive the common solvothermal conditions of MOF synthesis or direct competition by the functional group for metal coordination can occur (as with carboxylic acids and catechols). Additionally, tweaking of reaction conditions for each new functionality may be required.

1.4.2. Post-synthetic modification (PSM)

Post-synthetic modification (PSM) overcomes these difficulties in *de novo* synthesis, enabling the synthesis of materials otherwise not accessible whilst additionally purposing one MOF material into many variants possessing selected properties. The interchangeable nature of MOF components makes PSM a general machinery for the production of porous materials

of custom complexity. Consequently, PSM has been the subject of energetic research over the past decade and there are excellent recent perspectives published on this subject.[130-131]

The most general post-synthetic methods are post-synthetic (covalent) modification (PSM), exchange (PSE), insertion (PSI), deprotection (PSD), and polymerization (PSP), (Figure 1.14).

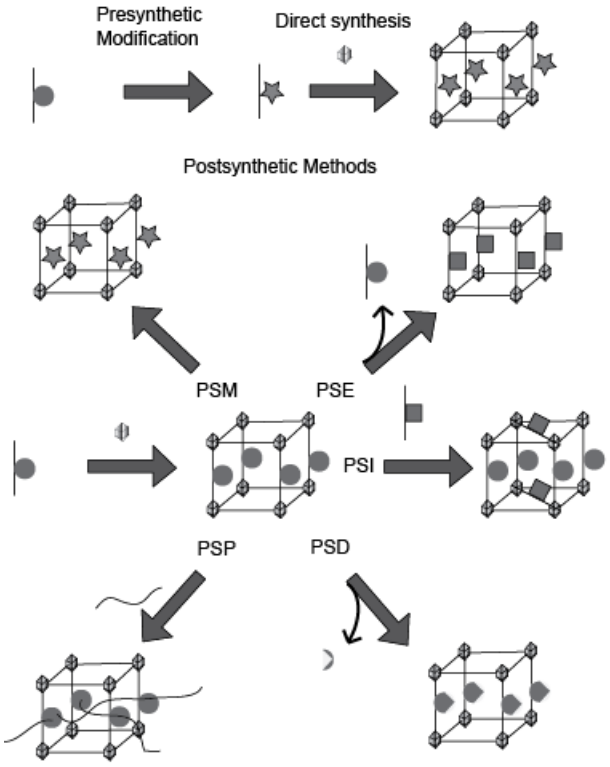

Figure 1.14: Post-synthetic methods.[132]

Post-synthetic modification (PSM) addresses many of these limitations. Recent strides in research have seen the development of a toolbox of techniques centred on increasing robustness or functionality through chemical treatment or making use of inherent framework robustness to introduce sensitive and thus interestingly reactive moieties into MOFs. The broad field of PSM can be roughly divided into three categories: covalent, dative and postsynthetic deprotection (PSD).[133]

1.4.3. Covalent PSM

Covalent PSM, involving the use of a (generally) chemical reagent to form a new covalent bond is among the most thoroughly investigated, successfully introducing reactive and thus interesting functionalities into frameworks. As with the post-synthetic techniques themselves, orthogonal chemistry can also play a role in this modification technique allowing parallel or sequential reactions to take place in the same material for the controlled introduction of

otherwise incompatible functionalities. This was shown early in the field by Cohen *et al*. where a UiO-66 framework containing two different ligands carrying a bromine or amine group (UiO-66-(Br)(NH_2)) underwent cyanation and acylation respectively in an orthogonal manner to generate the dual-functionalized UiO-66-(CN)(AM1) MOF (Figure 1.15).[89, 134]

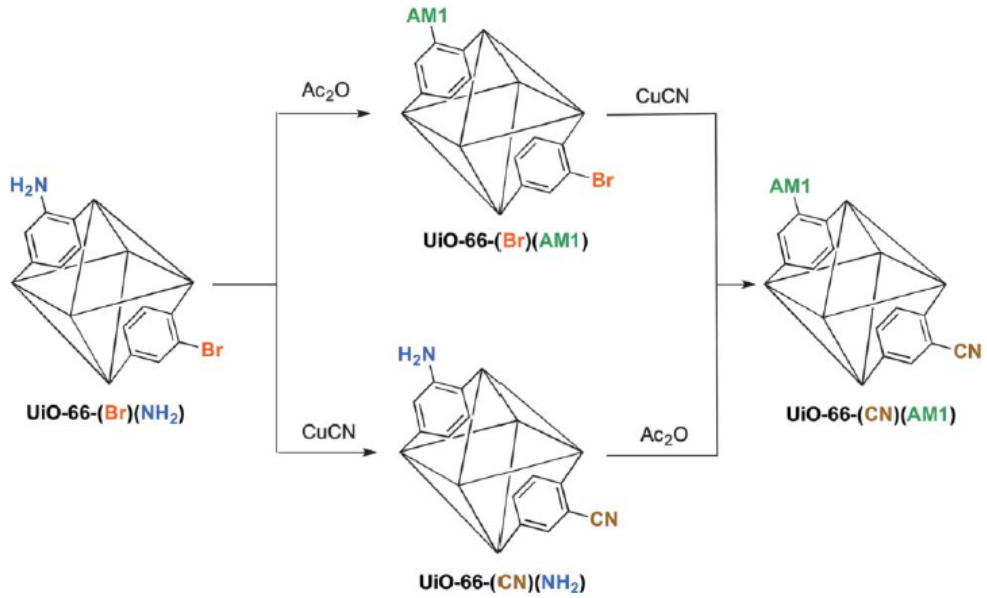

Figure 1.15: Tandem covalent PSM in the UiO-66-(Br)(NH_2) MOF. Figure reproduced from reference ([86]).

With establishment of ever more chemically robust MOFs covalent PSM has become among the most thoroughly investigated PSM methods, successfully introducing an array of reactive and thus interesting functionalities into frameworks.[131, 135]

PSM on a MOF has recently been extended up to seven separate steps. In a process reminiscent of the industrial assembly line, the robust MOF-74 framework was selected and subjected to a series of PSM and PSD steps to install a tripeptide functionality within the pores which was then shown to mimic the activity and spatial selectivity of the enzyme inspiration.[136]

Post-synthetic polymerization

The brittle nature of most MOF materials is a limiting factor in their application. Synthesis of hybrid MOF-polymer mixed-matrix membranes (MMMs) is thus an area of explosive research subject to its own reviews.[137-138] Post-synthetic polymerization (PSP) is carried out through three main modes; (1) using polymerizable guest molecules, (2) self-polymerization of functionalized organic ligands in a MOF in the absence of guest molecules, and (3) direct synthesis of MOFs from polymeric organic ligands, although the last is not truly post-synthetic.

Flexible photo-induced MOF-polymer stand-alone films were achieved in a facile synthesis from an amine-functionalized UiO MOF.[139] First PSM was carried out on the organic linker to form methylacrylamide groups. The modified MOF was then mixed with guest acrylate monomers and a photoinitiator before undergoing copolymerization in the presence of UV irradiation. This PSP method allowed moldable membranes to be made which were then shown to separate Cr^{VI} ions from solution with improved performance over the bare constituents alone.

Limitations of covalent PSM and PSP;

1. Precursor functional group limited to compatibility with MOF synthesis
2. Reaction of functional group can require harsh conditions which may lead to framework degradation.
3. Diffusion limitations can be severe depending on MOF pore size aperture thus functional group conversion may be significantly <100% and chemical species may become trapped within the material.

1.4.4. Post-synthetic insertion (PSI) and post-synthetic exchange (PSE)

Historically, dative PSM first involved the removal of coordinated solvent molecules from inorganic SBUs to reveal open metal sites for additional guest coordination, increasing gas uptake or water resistance.[140-141] However, the lability of the metal-ligand bond and porosity of MOFs also allows post-synthetic exchange (PSE) or insertion (PSI) of complete organic linker struts or metal nodes. This is sometimes termed solvent-assisted ligand exchange (SALE) or insertion (SALI) due to the use of solvents to diffuse ligands in and out of the pores.

Within the Telfer group, a quaternary MOFs (constructed from three different ligands and a metal) underwent PSE of two of the three ligands from crystallographically determined positions to introduce defects which could then be 'healed' in a second step while the primary, 'load-bearing' ligand and metal ion maintained the crystalline structure, even up to vacancies of 80%.[142] Defect manipulation such as this is an active area of research due to potential enhancement of gas uptake, selectivity, phase transformations or catalytic capabilities from open metal sites (OMS).[38, 40, 120, 143-144]

Figure 1.16 illustrates how PSE combined with PSI can be exploited to install chemical handles or catalytic groups within MOFs. Using PSE, installation of a ligand bearing a chelating catechol moiety into a robust Zr^{IV}-carboxylate MOF, UiO-67, was achieved. Subsequent dative PSI of Fe^{III} or Cr^{III} into this site then generates a catalytically active MOF that was unattainable through direct synthesis.[145] In a zeolitic imidazolate framework (ZIF) the

Zn^{II} ions and 4,5-dichloro-imidazole ligand were exchanged for Mn^{II} and 4-bromo-imidazole respectively in the same ZIF-71 MOF.[146]

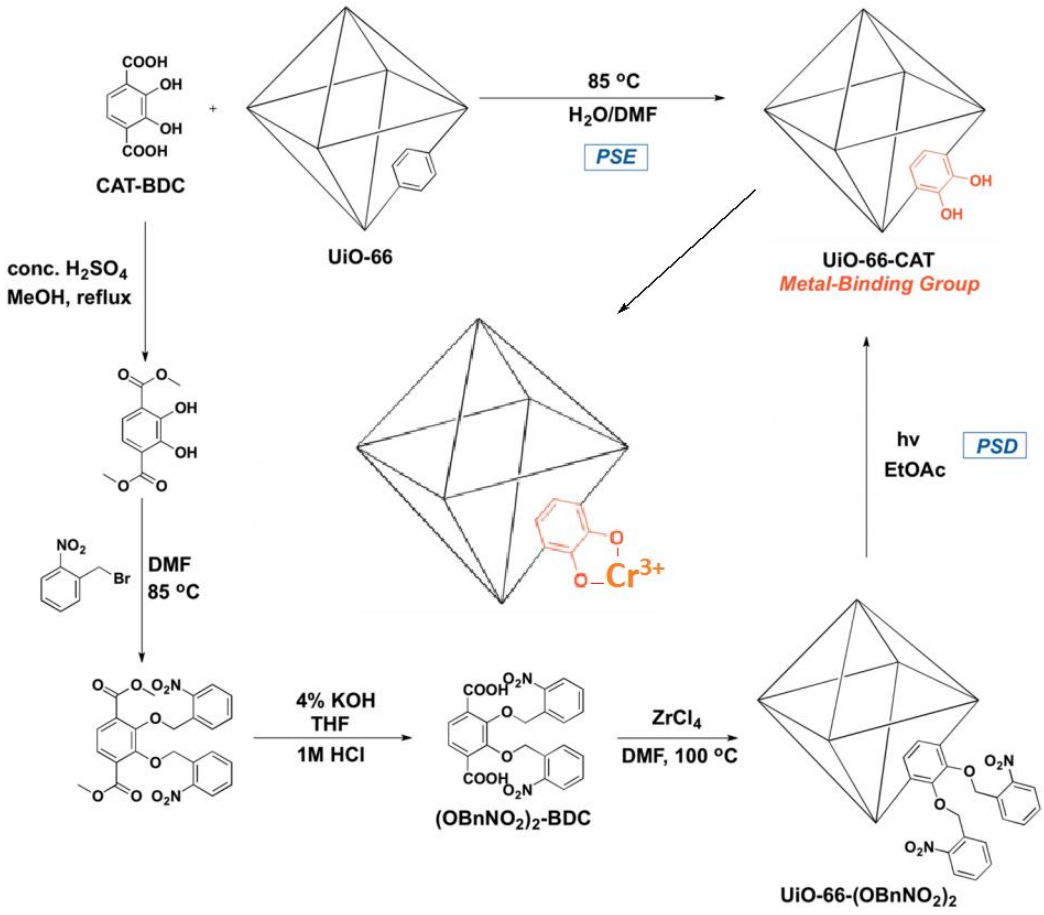

Figure 1.16: A catechol ligand is introduced into the UiO-66 framework by post-synthetic ligand exchange or by post-synthetic deprotection (PSD) using photolytic treatment.

Post-synthetic insertion has been used to increase the dimensionality of an as-synthesised MOF from a 2D polymer sheet to 3D framework through pillaring of Cu^{II}-carboxylate sheets by 1,4-diazabicyclo[2.2.2]octane in a single-crystal transformation.[147]

In bMOF-100 lattice, PSE was implemented to systematically expand the MOF pore aperture, increasing the pore size from ~2 to 2.84 nm.[148] This sequential expansion could then also be halted at intermediate stages to introduce porosity gradients in the material[149] or carried out quantitatively to syntheses a new topology with double the pore volume.[150]

Rationalized by the application of hard−soft acid−base theory, PSE of a Zn^{II} or Mg^{II} ion in the nodes of a MOF for a kinetically labile low valence Ti^{III} metal ion and subsequent oxidation (post-synthetic metathesis and oxidation (PSMO)) was used to obtain a Ti^{IV} MOF, the resulting material both otherwise not obtainable through direct synthesis and of greater robustness than the parent framework.[151]

Drawbacks:

1. Not all MOF topologies have open metal sites suitable for ligand insertion or possess sufficiently labile ligands for exchange.
2. As with PSM and PSP, this method is diffusion and equilibrium driven, so incomplete exchange is likely, reducing MOF functional group loading.
3. Dependence on a concentration gradient to drive ligand exchange makes this method costly due to amount of functionalized ligand required and potential time-delay to allow multiple refreshes of solution.
4. No guaranteed capability of recycling of exchange solvent and ligands presents a significant hurdle for industrial applications requiring scaling.

1.4.5. Post-synthetic deprotection (PSD)

Post-synthetic deprotection (PSD), involving the cleavage of a chemical bond within the MOF framework, has been of particular interest to the Telfer research group with seminal work published on the use of photo and thermolabile protecting groups in MOFs to prevent interpenetration and incorporate otherwise MOF-incompatible chemical functionalities.[152-153] In Figure 1.16 a photolabile nitrobenzyl protecting group was used in a PSD route whereby the protected catechol ligand is introduced during MOF synthesis then the metal coordinating functionality revealed by post-synthetic photolytic treatment.

In addition to serving as a trigger for cleavage of thermolabile protecting groups, heating of the thermally robust MOF materials (generally stable to above 300 ^{o}C) with an appropriately functionalized organic ligand can accomplish post-synthetic rearrangement (PSR) in a reagent-less transformation on the linker itself.[154]

1.5. Thermolabile protecting groups (TPGs)

1.5.1. Overview

There are some challenges to searching for TPGs, in light of the variable nature of their composition, action, broad area of application and naming. In this thesis they are defined as involving a thermally-triggered chemical change, this can be within a set number of atoms, as in a rearrangement or cyclization to reveal a novel configuration, or loss of atoms, as in expulsion of a fragment to uncover another chemical functionality.

Thermal additions are not considered, nor are thermal processes requiring catalysts or chemical additives occurring at elevated temperatures considered under TPG. Within the thermal deprotection reactions defined there are some historic areas of interest. The application of TPGs within the MOF field draws on the organic chemistry, DNA, and polymer synthesis fields and these are briefly mentioned first.

1.5.2. Use of TPGs in organic compounds

Thermolabile protecting groups have an important place in organic synthesis and a variety of groups are known, including carbamates, 2-pyridinyl, *tert*-butyl esters, Meldrum's acid and blocked isocyanates (Figure 1.17).

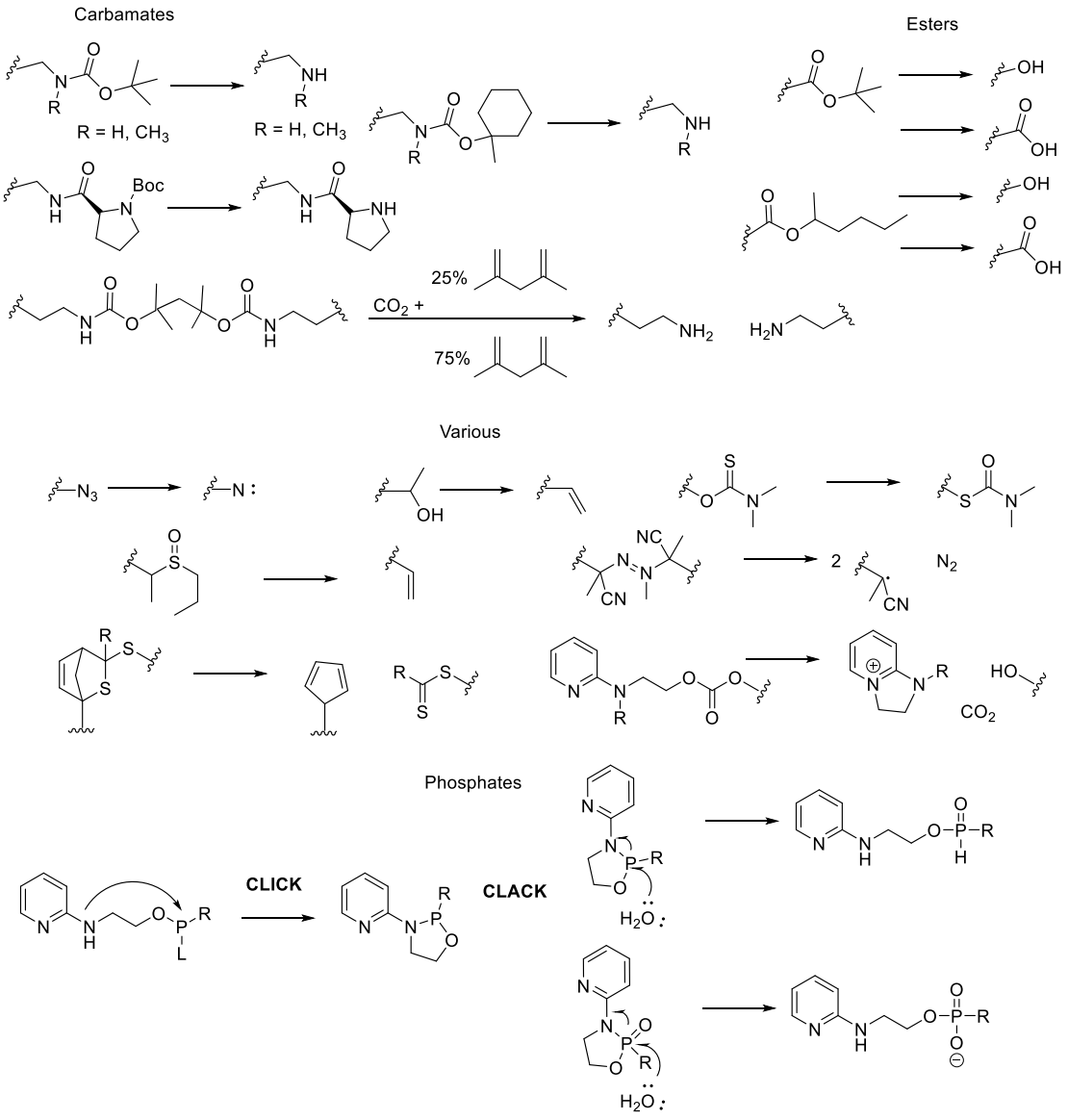

Figure 1.17: Overview of select TPGs in organic synthesis.

Among these thermolabile protecting groups is a subset that does not so much reveal the required functionality but an intermediate en route to the desired product. This is done by generating a reactive intermediate species *in situ*.

A key molecule in the total synthesis of complex organic molecules is Meldrum's acid.

First discovered in 1908 (structure correctly assigned 1948)[155] this species was found to generate a reactive ketene species upon thermolysis (>200 ^{o}C) which could then react with a broad range of nucleophiles to form multiple different functional groups. The ketene can also undergo intramolecular reactions useful in building challenging ring systems in natural product synthesis or other total organic synthesis efforts (Figure 1.18).

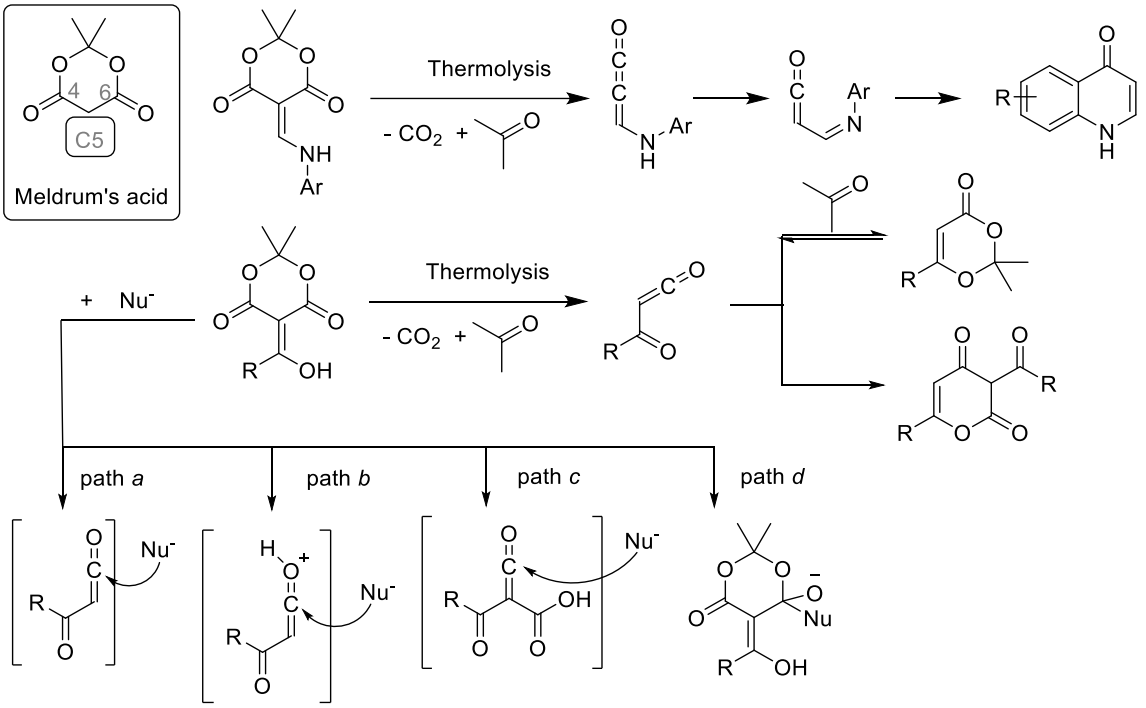

Figure 1.18: Examples of useful organic synthesis pathways through reactive ketene intermediates formed *in situ* upon thermolysis of Meldrum's acid derivatives.[155-157]

As not all reaction substrates are compatible with harsh thermolytic conditions, tuning of the thermolysis temperature of Meldrum's acid has been the subject of research,[158] and computational efforts into understanding the special reactivity of this molecule are ongoing.

1.5.3. Use of TPGs in DNA synthesis

N-(2-pyridyl) TPGs (Figure 1.19) are used in oligonucleotides as part of the polymerase chain reaction (PCR). By using TPGs the level of undesired primer-dimers and mis-primed products are substantially reduced because PCR amplification can only start after heat-

triggered activation has removed the 3'-protecting group to produce the unprotected 3`-hydroxyl that is the typical substrate for the *Taq* DNA polymerase. At the higher temperatures at which deprotection occurs primer-template specificity is optimal.[159]

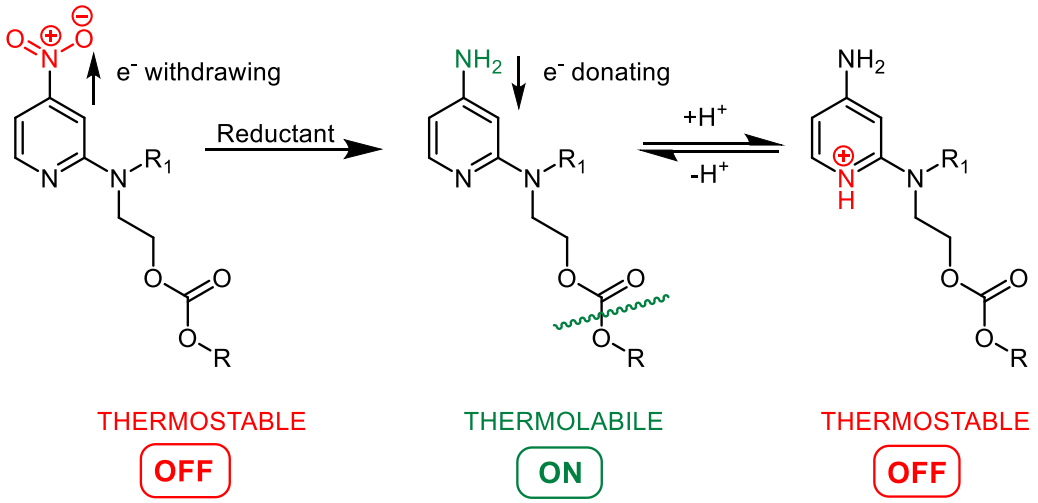

Figure 1.19: Thermostability of 2-pyridyl TPGs.

Tuning of the thermolability of the N-(2-pyridyl) TPGs is achieved by changing the nucleophilic character of the pyridyl ring through three main factors:

1) Pyridine nitrogen hydrogen-bonding
2) Electron-donating/withdrawing substituents
3) Steric and structural factors

Despite the nucleophilicity of the pyridyl ring driving the reaction, conformational factors were the most influential on thermal properties with the ability of the molecule to adopt a favourable conformation (minimizing the N1-C8 distance) for thermocyclization dominating observed thermolysis. In particular, two torsion angles were identified as key indicators of thermolability.

Nucleophilic properties of a molecule and their hydrogen-bonding interactions are also important factors in thermocyclization. Hydrogen bonds control the properties of nucleophilic centers in solution and in solid-state and results show intra- and intermolecular bonding to be highly relevant to engineering practical TPGs that are both stable at ambient temperatures and labile upon heating.[160]

1.5.4. Use of TPGs in polymers

Polymer chemistry background to PGs

Thermolyzable polymers or polymerization upon thermolysis have both been widely applied in the polymer field. Many thermoresponsive polymers incorporate thermally-triggered functionalities to change the bulk properties of the polymer such as density and hydrophobicity upon heating.

Cross-linking of polymers – Meldrum's acid

Besides reacting with a nucleophile, the thermolytically formed ketene of Meldrum's acid can dimerize with a neighbouring ketene. When this reaction is appended to a polymer backbone the dimerization results in crosslinking (Figure 1.20).

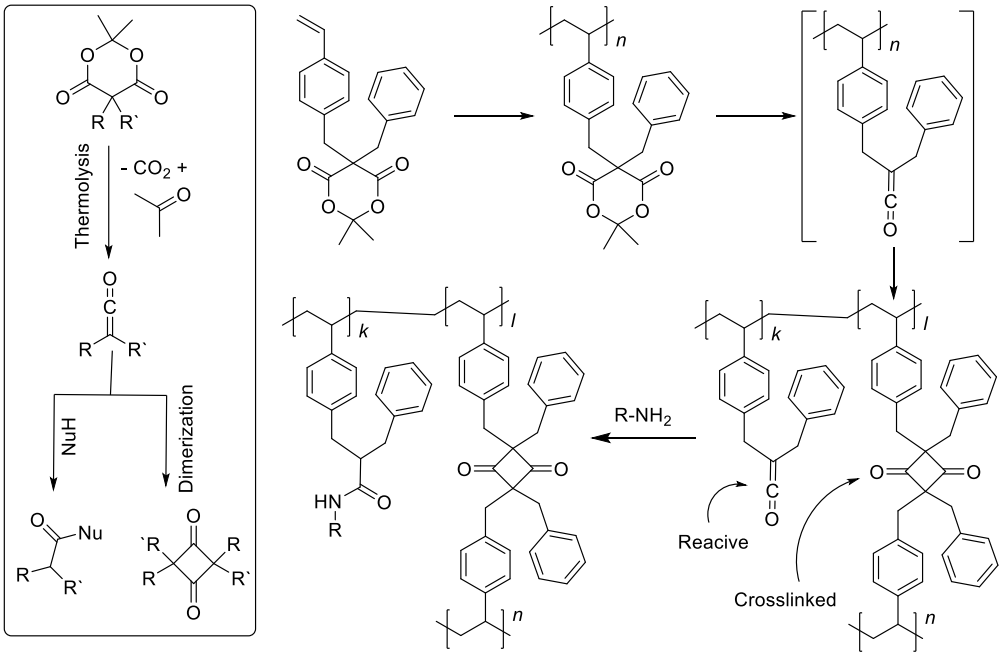

Figure 1.20: Cross-linking of polymers through *in situ* generation of reactive ketene upon thermolysis of Meldrum's acid. Adapted from reference.[161]

Truly a multipurpose moiety, Meldrum's acid has also been incorporated into the silicon anode of a lithium battery where the revealed ketene not only participates in crosslinking through dimerization but also covalently binds to the anode. Additionally, by hydrolysis of some Meldrum's acid groups to a malonate moiety in the presence of lithium hydroxide, self-healing properties are imbued to the material through generation of supramolecular bonding interactions.[162]

1.6. Introduction to selected experimental techniques

1.6.1. TGA technique

Thermogravimetric analysis (TGA) measures the weight loss of a sample over time at constant or varying temperature, allowing for the percentage of thermolabile groups present to be estimated and the thermal stability of a material determined (Figure 1.21).

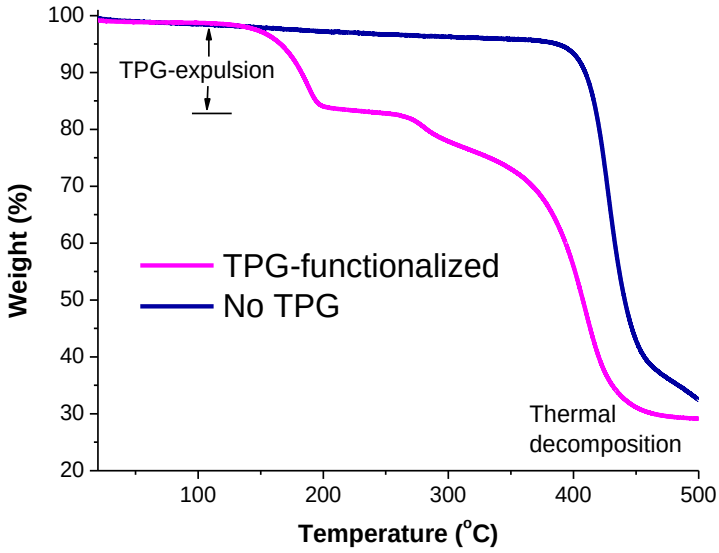

Figure 1.21: Process of thermogravimetric analysis (TGA).

Additionally, guest solvent volume or loading capacity in MOFs may be approximated while coordinated solvent molecules in the MOF formula can be calculated.

1.6.2. Gas adsorption

1.6.2.1. Adsorption process

Key concepts in the diffusion of a gas molecule through a porous material are the surface area available and the nature of the adsorbate-surface interaction. Diffusion is assumed to be a mixture of Knudsen and molecular diffusion (Figure 1.22) in a regular porous material with a mixed pore size regime.

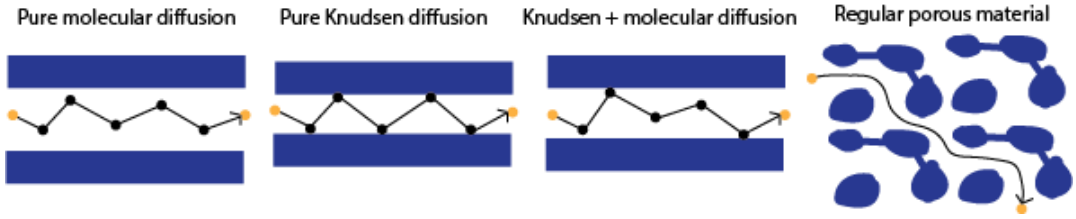

Figure 1.22: Diffusion processes in a porous solid.

Increasing the surface area a molecule can interact with increases the volume of gas adsorbed (Figure 1.23a). Where the adsorbing molecule interacts with the surface a monolayer can form. Members of this monolayer may be chemisorbed or physisorbed (Figure 1.23b and c). At pressure ranges where a monolayer of physisorbed molecules occurs a probe-accessible surface area can be calculated. Measuring gas sorption in a porous solid at a constant temperature by dosing with a known volume of gas to an equilibrated pressure gives rise to a gas sorption isotherm. Figure 1.23d and e illustrates the key points during a gas sorption isotherm and relevant isotherm phenomenon related to pore-filling by the guest gas molecules.

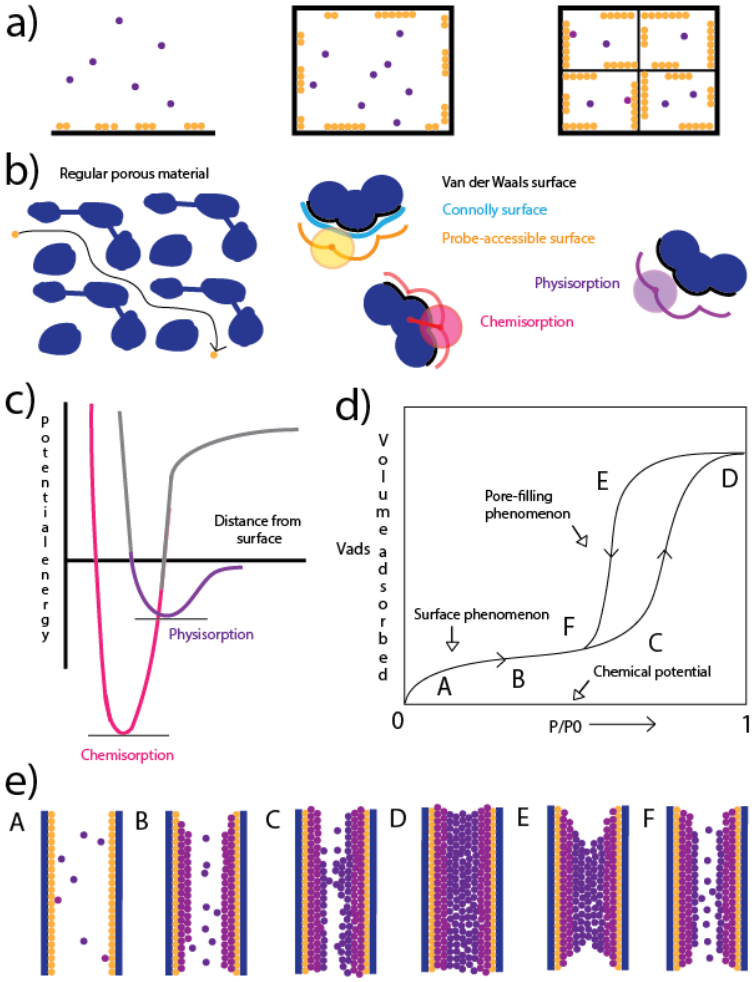

Figure 1.23: Different diffusion processes during gas adsorption as a function of surface area and physisorption versus chemisorption.[163] a) The amount of gas molecules adsorbed (gold) vs free (purple) increases with surface area, enabling a larger gas storage volume. From left to right can be viewed as going from a surface, to a typical gas cylinder, to a porous nanomaterial. b) In a regular porous material, if the probe molecule forms a chemical bond with the pore surface, chemisorption occurs. However, if the probe molecule only interacts with the van der Waals surface of the pore walls then physisorption occurs. At pressure ranges where a monolayer of physisorbed molecules occurs a probe accessible surface area can be calculated. c) The two main interactions the diffusing gas molecule can undergo with the pore walls - physisorption and chemisorption - depend on the intermolecular distance. d) A gas sorption isotherm illustrating key points during measurement and relevant phenomenon related to e) pore-filling by the guest gas molecules.

Gas adsorption isotherms can take on various shapes depending on the nature of the adsorbate surface and pore size distribution (Figure 1.24). Within the MOF field, Type II isotherms and IV/V isotherms are associated with rigid and flexible MOF structures respectively.

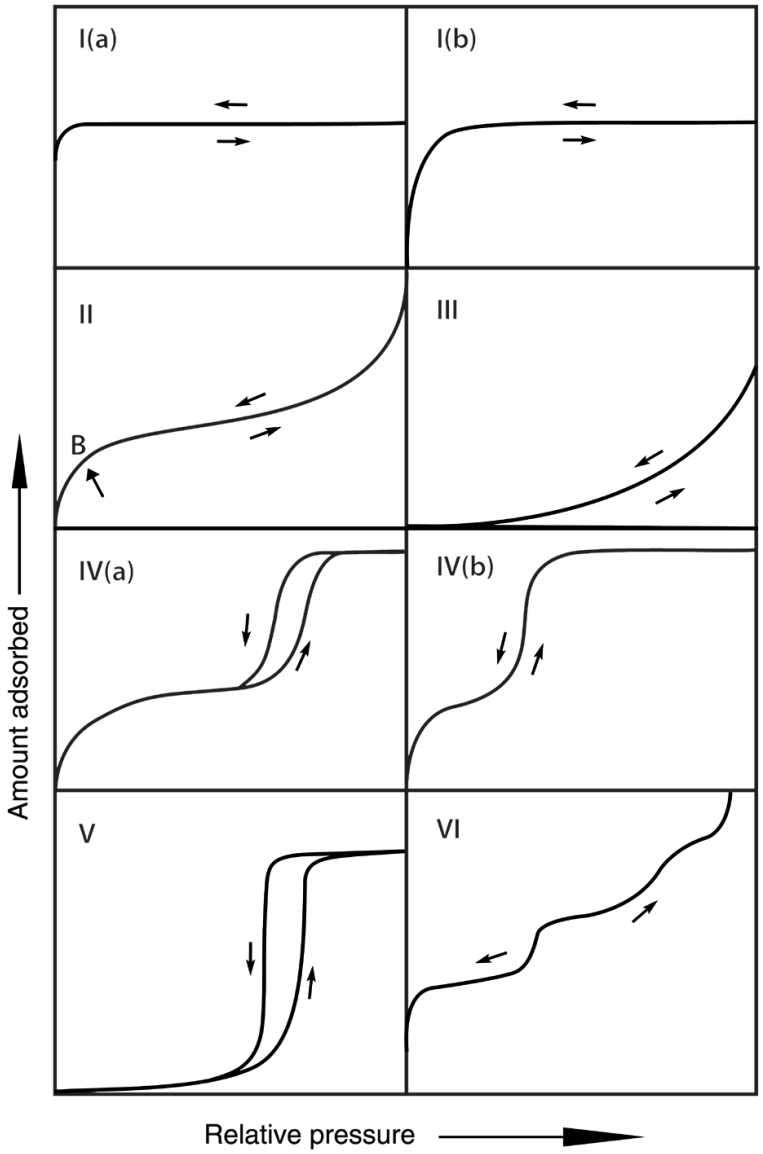

Figure 1.24: Definition of gas sorption isotherm shapes, updated by IUPAC in 2015.[164]

These different isotherm shapes yield themselves to different analysis, such as Henry, Langmuir, and Brunauer-Emmet-Teller (BET) models.

1.6.2.2. Gas adsorption apparatus

To record these isotherms there are two main approaches: gravimetric and manometric; both rely on accurate measurement of change in sample weight or volume respectively during gas dosing. Although manometric is considered more suitable for physisorption measurements with N_2, Ar, and Kr at cryogenic temperatures, gravimetric analysis is popular due to accessibility of highly accurate scales and excellent high vacuum turbo pumps (Figure 1.25).

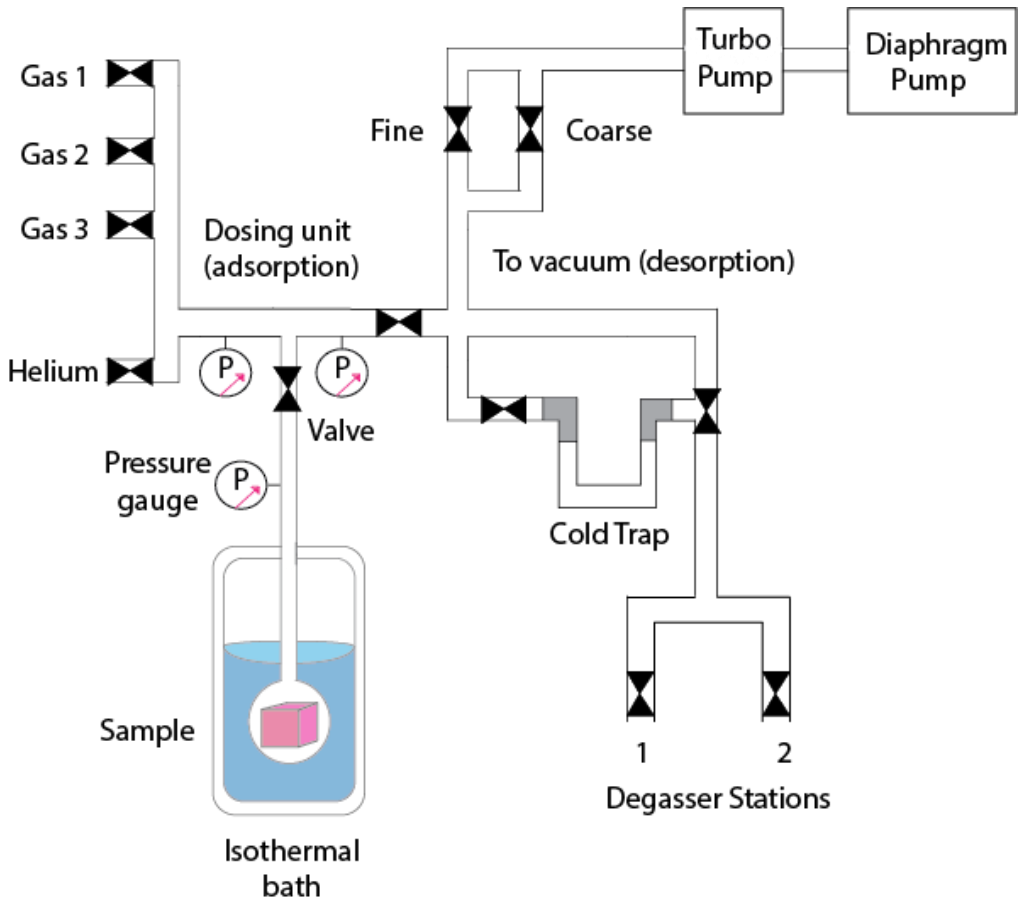

Figure 1.25: Gas sorption general apparatus showing degassing stations for sample activation and sample port within an isothermal bath. Different gas sorption isotherms can be collected on the same sample by changing the gas selected in the dosing unit. Fine and coarse vacuum enables both rapid and accurate gas sorption characterization.

In a typical gas sorption isotherm measurement, the sample is first loaded onto a degasser station with a cold trap to capture the removed solvent upon activation before placing onto the sample port (Figure 1.25). During isotherm collection the sample is kept at a constant temperature in an isothermal bath and the pressure monitored for equilibrium post dosing with a known volume of gas (adsorption). A desorption isotherm is then measured by removing gas by vacuum pump, allowing pressure to equilibrate at each point.

1.6.2.3. BET surface area calculations

Measurement and reporting of a Brunauer-Emmett-Teller (BET) surface area is the current standard in the MOF field. BET surface areas are commonly calculated using N_2 isotherms at 77 K and given in m^2/g.

There are several considerations when examining BET surface areas in literature:

1) they are still not consistently reported for measured isotherms[165]

2) they are more accurately described as an "apparent surface area which may be regarded as an adsorbent "fingerprint"" due to the following caveats:

– N_2 interacts with adsorbates due to the presence of a significant quadrupole moment and thus the cross-sectional area of a N_2 gas molecule probe based on a densely-packed monolayer could be inaccurate by as much as 20 %

– Due to this adsorbate-gas interaction and slow diffusion limitations at low temperature, pore-blocking by adsorbed N_2 can occur, thereby excluding narrow and or micropore surfaces from the calculation

For these reasons, IUPAC has recommended the use of Ar(g) isotherms at 87 K for more accurate surface area determination. Argon lacks a quadrupole moment, has lower reactivity than the diatomic nitrogen and has advantages for micropore and mesopore analysis of materials with narrow pores.[164]

Finally, with increasing interest and research into flexible MOF materials, the following factors are relevant when regarding BET surface areas:

3) Cooperativity is not accounted for in BET calculations. IUPAC recommends computational insight into flexible or structure-changing materials be sought alongside experimental measurements to more accurately reflect reality of gas/liquid gas-sorbate phase and interactions. Computational studies sampling unit cell size and calculation of free energy profiles are beginning to answer this need.[166-167]

To improve consistency in the application and reporting of BET methods, guidelines were developed by Walton and Snurr for identifying an appropriate BET linear region:[168]

1) Isotherm shape should be appropriately considered.
   That is, a plot of volume of N_2 adsorbed vs P/P_0, where P/P_0 is the ratio of P, the pressure of the system at each point in the measurement, and P_0, the condensation

pressure of the adsorbent at the temperature of the measurement, gives curves suitable for Langmuir or Henry fitting.

2) Volume of gas adsorbed must be continuously increasing with P/P_0 in area fitted. That is, the isotherm region selected has $v(1 - P/P_0)$ increasing with respect to P/P_0 (where v is amount of N_2 adsorbed,).
3) Intercept of the fitted plot must be positive.

   That is, $\frac{P/P_0}{v(1-P/P_0)}$ plotted against P/P_0 using sequential data points must yield a positive intercept b and a slope a, where $\frac{1}{a+b}$ is equal to the number of gas molecules adsorbed in the initial monolayer (v_m). Thus the BET surface area can then be calculated using:

$$A_{BET} = v_m \left(\frac{cm^3}{g}\right) * \frac{1\,(mol)}{22400\,(cm^3)} * \sigma_0 \left(\text{Å}^2\right) * N_A \left(mol^{-1}\right) * 10^{-20} \left(\frac{m^2}{\text{Å}^2}\right)$$

where N_A is Avogadro's constant and σ_0 is the cross-sectional area of a N_2 molecule (16.2 $Å^2$).

Reliability of measurements and calculations

Sources of error are cumulative for gas dosing/pressure measurements and a correction for the dead space in the sample tube is applied. However, instrumental error is nominal and major sources of error in gas sorption isotherms measured are invariably due to dependence on sample preparation and absence of proven reproducibility of MOF isotherms from repeated measurements on the same or multiple samples.

Chapter 2 –Mono-functionalized pillar-layer MOFs (PLMOFs)

2.1. Introduction

A flexible MOF framework series was chosen to study the impact of thermolabile protecting groups (TPGs) in MOFs. Specifically, a zinc-based pillar-layer MOF structure was selected. These mixed-linker MOFs comprise two-dimensional Zn-dicarboxylate layers connected into three dimensions through a second 'pillar' ligand, commonly coordinating through a nitrogen containing functionality such as 4,4`-bipyridine or a diamine species (Figure 2.1).

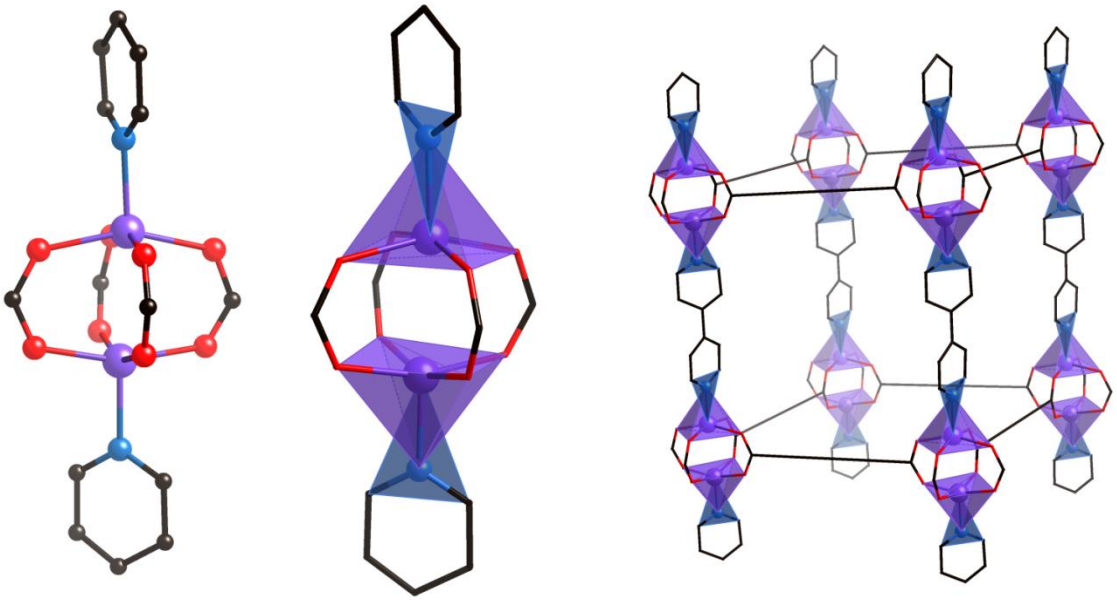

Figure 2.1: The zinc secondary building unit (SBU) of a pillar-layer MOF with coordinating 4,4`-bipyridines in ball-and-stick and stylized representation. The stylised net shows simplified 4,4`-biphenyl dicarboxylic acid linkers in 2D sheets. Atom colour code is: C-black, N-blue, O-red, Zn-purple.

Pillar-layer MOFs are an interesting subset of MOFs. Their flexible construction means both the pillar and layer components can angle and twist - whilst maintaining the coordination nodes and material crystallinity - in response to stimuli such as pressure and host-guest interactions. This has obvious potential in sensor applications but they are also of particular relevance to the issue of delivering a practical working capacity in natural gas storage vehicles. This is through the frequently stepwise nature of their isotherms where a 'gate effect' is observed at a pressure great enough to alter the metal-organic framework, opening the pores to guest gas molecules, whereupon the material's gas uptake sharply increases. In release of the

gas, following along the desorption curve, the reverse is observed where the narrowing of the framework pores results in a rapid expulsion of guest molecules to resume the 'closed' structure at the initial low pressure. This allows a larger volume of gas to be delivered over a smaller pressure range than a more gradually sloped gas sorption isotherm (Figure 2.2).

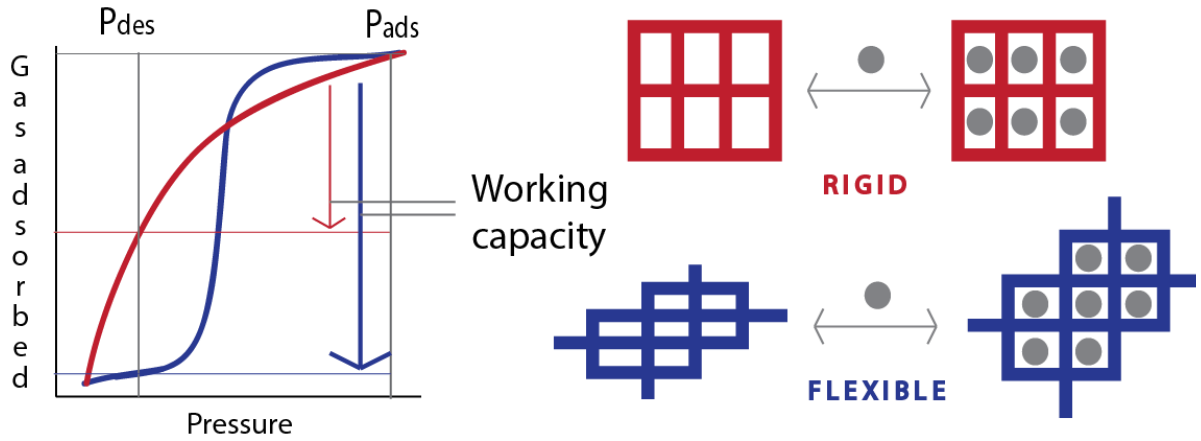

Figure 2.2: Deliverable capacity isotherm. Figure adapted from reference.[169]

A key component to the surface area in larger pore or flexible MOF structures is the presence, and extent, of interpenetration. With the capacity to allow the bulk of another lattice within the first, through large pores or flexibility, formation of a second (or more) lattice interpenetrating the first is favoured due to increased van der Waals interactions. While this results in a reduction of gravimetric pore volume, the surface area available for adsorption of gas molecules greatly increases and stability of the material improves.

Further fine tuning within the pores can also be seen to dramatically affect the observed gas uptake, especially if the interaction with the gas can be enhanced or optimised. This strength of the interaction between an adsorbate and a solid adsorbent is called the heat (enthalpy) of adsorption and for MOFs specifically refers to the isosteric heat of adsorption, determined from the analysis of gas adsorption isotherms at different temperatures. The greater the isosteric heat of adsorption the stronger the interaction of the gas with the framework and so the higher the expected volumetric gas uptake at low gas pressures.

Although open metal sites (OMS) have also been established as having a beneficial effect on gas uptake from their high enthalpy of adsorption with most gases, due to the consequently larger energy penalty in removing gas molecules from these sites, the more limited options for coordinating to OMS, and their susceptibility to water, the organic linker presents a more promising target for modification to deliver an effective working capacity.

The functionalization of the organic struts can in this way be seen as an ideal platform for optimizing gas uptake through improved gas sorption dynamics and has been heavily pursued in literature.

Thermolabile protecting groups (TPGs) in flexible MOFs offer tuning of the stepwise isotherm, interpenetration control and functionalization for optimizing gas storage and separation properties. Further applications range towards heterogeneous catalysis, as with the mixed linker MOFs localization of the functional groups and synergistic effects from two different oriented moieties is possible.

These were some of the goals targeted in introducing TPG ligands into a flexible pillar-layer MOF. In this chapter, either the 4,4`-bipyridine (bpy) or 4,4`-biphenyldicarboxylic acid (bpdc) ligand backbone was modified with a *tert*-butyl ester (-TBE) or carbamate (-NHBoc) TPG to create a family of mono-functionalized pillar-layer MOFs. Their synthesis, properties, comparison to synthesis of unprotected MOFs, and partial thermolysis and gas sorption characterization are presented herein.

2.2. Results and discussion

The Telfer group previously established the synthesis of a carbamate TPG group (referred to as -NHBoc) introduced onto a 4,4`-biphenyldicarboxylic acid (bpdc) and 4,4`-bipyridine (bpy) backbone. A protected carboxylic acid functionality using a *tert*-butyl ester (-TBE) was also installed on a bpy backbone. In prior work presented in the thesis of Dr. Sebastian Blackwood,[170] I combined these two novel bpy ligands with unmodified bpdc and zinc nitrate to form mono-functionalized materials analogous to known MOF BMOF-1-bpdc.[171] The analysis of these materials will be included here for completeness in exploring the mono-functionalization of the pillar-layer framework, BMOF-1-bpdc, hereafter referred to as MUF20-Aα. MUF stands for Massey University Framework and has been used by this group previously for naming new materials.[142, 172-173] MUF is used here as we were initially unaware of BMOF-1-bpdc in literature.[171, 174] The two suffix letters designate the ligands incorporated; an uppercase Roman alphabet (A, B, C) and lower case Greek alphabet (α, β, γ) to signify the bpdc and bpy ligands used respectively. For ease of reference a fold-out at the back of this thesis is included with a list of ligands, assigned letters and combinations installed in MOFs in this work.

For full comparative study of the influence of the nature and placement of TPGs in mono-functionalization of the MUF20-Aα framework, the synthesis of the requisite bpdc-TBE ligand was targeted and achieved in a relatively straightforward manner (see Figure 2.3).

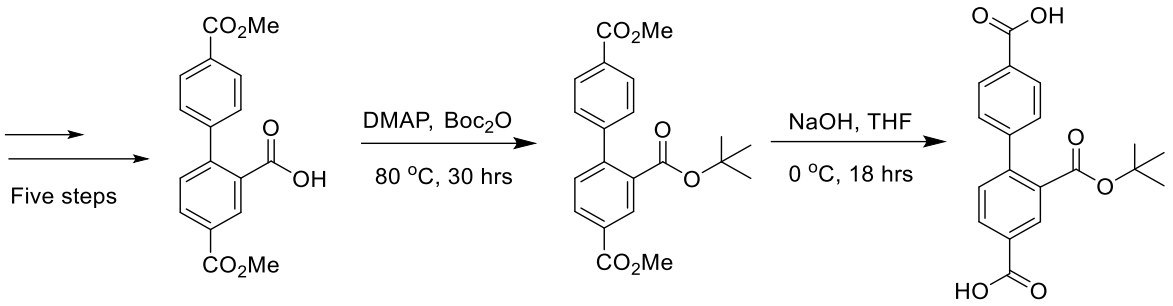

Figure 2.3: Synthesis of the bpdc-TBE ligand.

The bpdc-TBE ligand was obtained in good yield and its purity was confirmed by ^{1}H NMR analysis (see Figure 2.4). Further synthesis details are included at the end of this Chapter and in the Appendix.

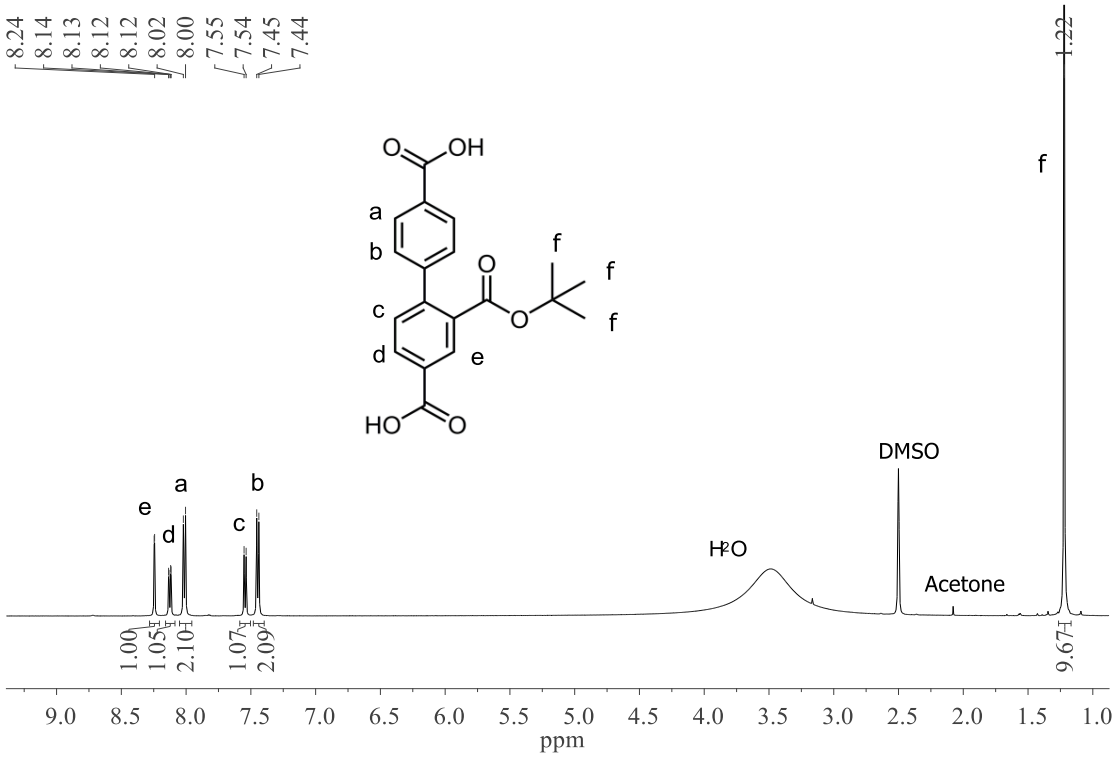

Figure 2.4: ^{1}H NMR spectrum of bpdc-TBE in DMSO-d_6. Trace acetone from the NMR tube is flagged.

The complete TPG-ligand set is shown below in Figure 2.5:

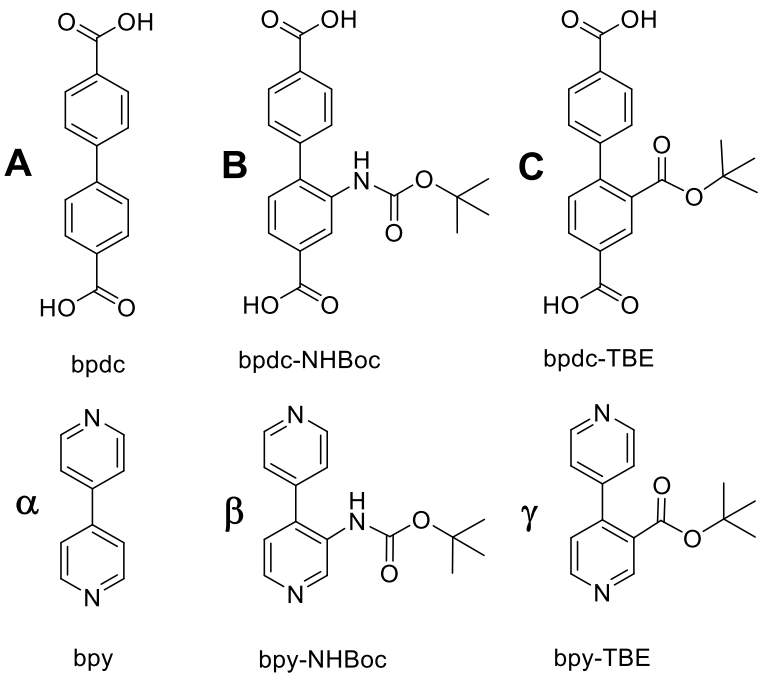

Figure 2.5: TPG ligands installed into the MUF20-Aα framework and their designated letters for shorthand annotation.

Ligand thermal properties were explored through thermogravimetric analysis (TGA) where the sample was heated at a rate of 5 ^{o}C/min in an aluminum pan under N_2(g) flow and the sample weight change recorded. Percentage weight loss versus temperature was then plotted to give the following TGA traces (Figure 2.6). A comparison TGA plot including unprotected and unfunctionalized ligands is included in the experimental section at the end of this chapter.

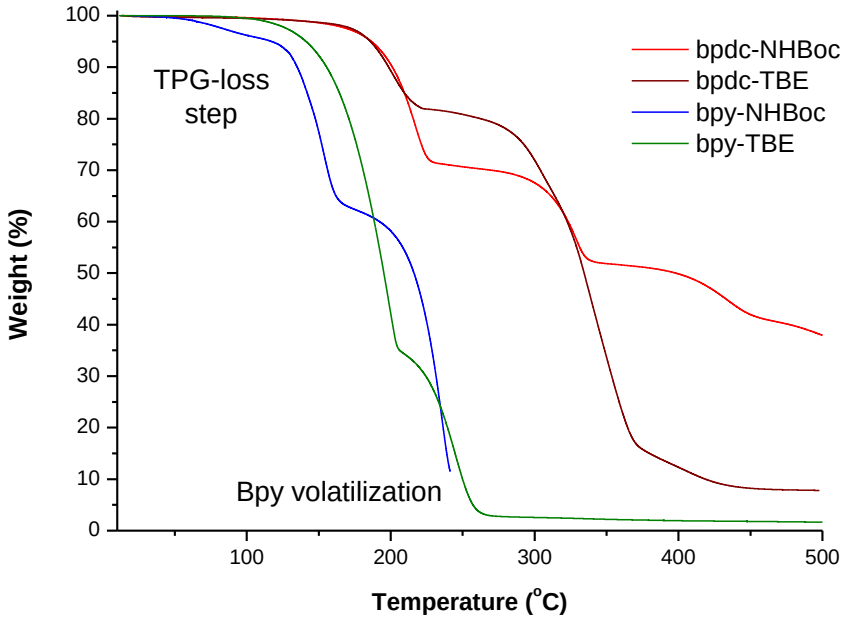

Figure 2.6: Thermogravimetric analysis (TGA) traces for TPG-functionalized ligands.

The TGA curves have characteristic steps associated with triggered decomposition of the TPG functionality and subsequent release of volatile fragments isobutylene and CO_2 (Figure 2.7).

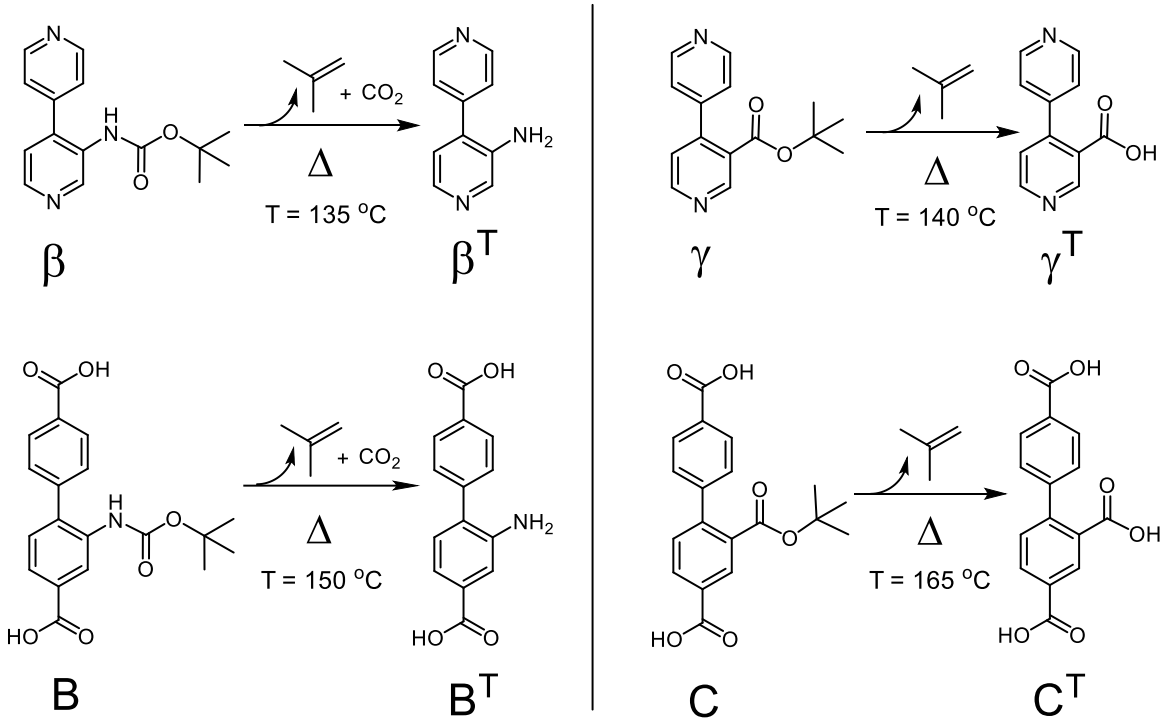

Figure 2.7: Thermolysis of TPG-functionalized ligands to reveal amine and carboxylic acid species with approximate starting temperature of thermolysis as indicated by TGA.

Additional ligand decomposition pathways at higher temperatures can also be identified such as decarboxylation at ~300 °C for the bpdc backbone ligands. The dramatic low temperature weight loss of the bpy was determined to be due to the high volatility of the bpy itself (bare bpy was observed to begin weight loss at 69 °C) and thus is not a feature of the TPG functionality. The ligand percentage weight loss steps can be measured and compared against the expected weight loss of the theoretical TPG fragments.

Due to the gradual nature of weight loss as local thermal energy approaches the required threshold for bond cleavage there is ambiguity in determining start and end points of the thermolytic process. This results in the slight differences noted between experimental and calculated (see Table 2.1). Precise curve coordinates used to calculate weight percentages can be found in the Appendix.

Table 2.1: Experimental and calculated weight losses for TPG-ligands.

Ligand	$T_{1/2\Delta}$ (°C)*	Experimental Weight loss (%)	Calculated Weight Loss (%)
bpdc-NHBoc	150	29.0	28.0
bpdc-TBE	165	17.8	16.4
bpy-NHBoc	135	33.7	36.9
bpy-TBE	140	65.9	21.9

* $T_{1/2\Delta}$ is defined as the midpoint of the temperature range over which weight loss associated with thermolysis occurs and is rounded to the nearest 5 °C.

Experimental and calculated weight losses match well for all ligands save bpy-TBE where the thermolytic release of isobutylene coincides with evaporation of the relatively volatile bpy backbone from the TGA pan. This happens to a lesser extent with bpy-NHBoc but low temperature weight loss is still observed. ^{1}H NMR analysis of the thermolyzed material MUF20-Aγ^T indicates clean bpy-CO_2H (γ^T) is formed.

To investigate the effect of steric bulk and protecting group in controlling interpenetration and suppressing unwanted phases, the synthesis of the unprotected mono-functionalized MOF analogues was undertaken in parallel using ligands carrying the bare functionalities: bpdc-NH_2 (B`), bpdc-$CO_2$H (C`), bpy-NH_2 (β`), and bpy-$CO_2$H (γ`), designated as the unprotected analogues to the TPG ligands by a dash (`) as shown in Figure 2.8.

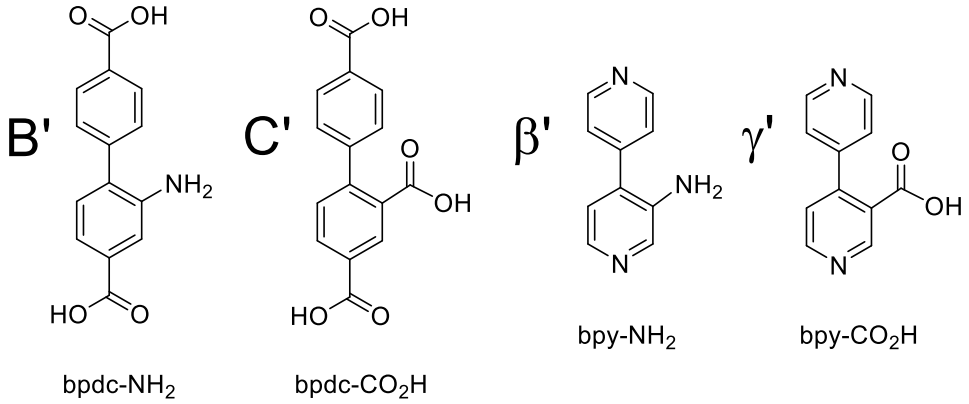

Figure 2.8: Unprotected ligands utilized.

During MOF synthesis attempts and ligand purification, the single crystal structure of a potassium coordination polymer (bpy-CO_2K) was collected and is included in the Appendix.

2.2.1. Synthesis and characterization of MUF20 analogues

MOF synthesis

Achieving the targeted family of mono-functionalized MOFs (Figure 2.9) required optimization of synthesis conditions.

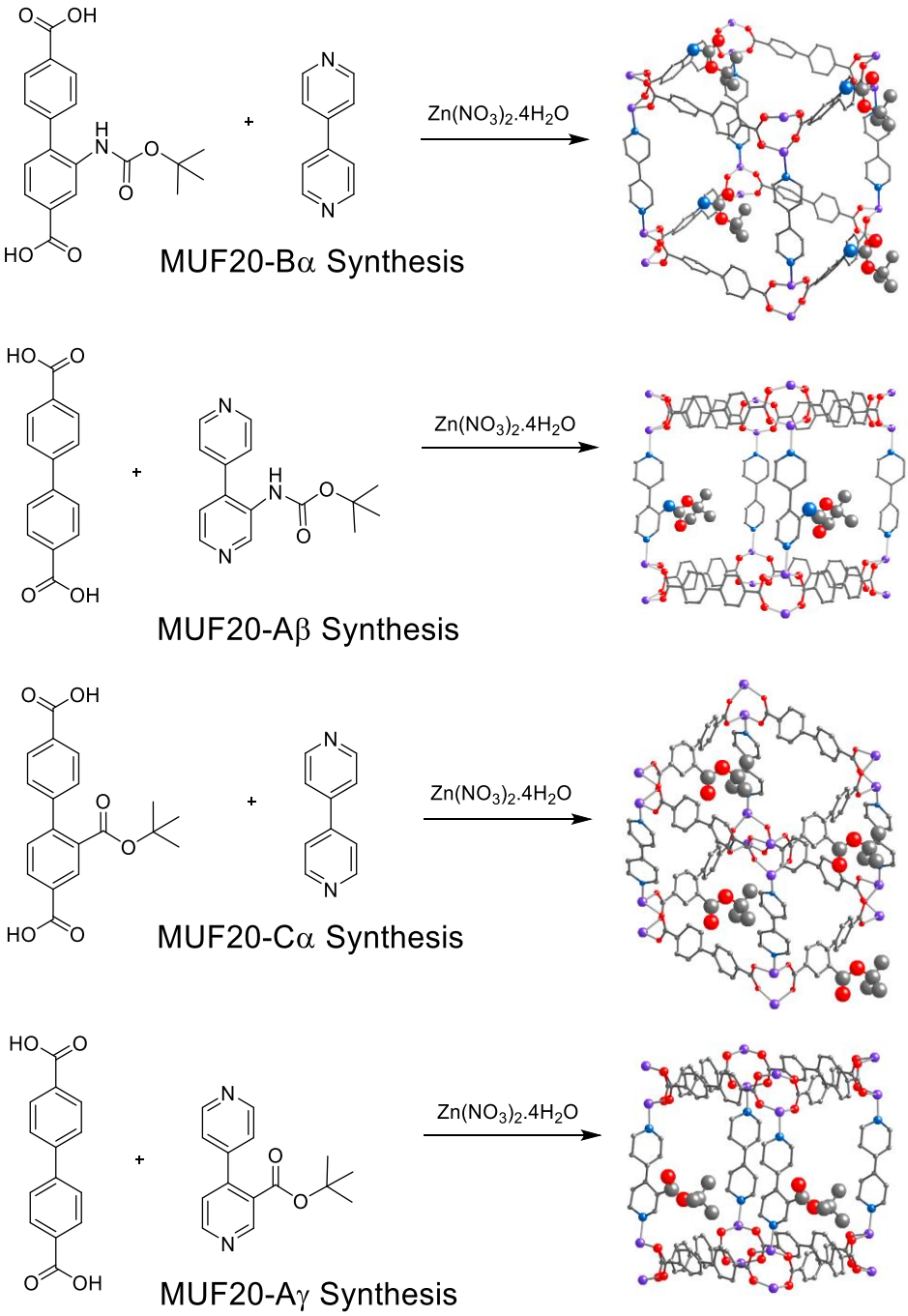

Figure 2.9: TPG ligands installed into MUF20-Aα. For clarity only selected TPGs are shown (presented in larger radii). MOFs are viewed along the layers of the bpdc to show the bpy functional group in MUF20-Aβ and MUF20-Aγ and are tilted to look down along the bpy axis in MUF20-Bα and MUF20-Cα to show bpdc-functionalization. Atom colour code is; C-grey, O-red, N-blue, Zn-purple.

Due to the steric influence of the bulky TPG ligands, bpy ligands were excluded and bpdc-only [$Zn_4O(bpdc)_3$] (IRMOF-9/10) MOFs formed as competing phases during MUF20 MOF synthesis. This was especially the case when the larger carbamate (-NHBoc) TPG group was involved, as in synthesis of MUF20-Bα and MUF20-Aβ (top of Figure 2.9).

To favour forming the pillar-layer MUF20 over the bpdc-only MOF, methanol was introduced into the reaction solvent mixture (1:4, DMF:methanol) and the ratio of bpy-NHBoc:bpdc or bpy:bpdc-NHBoc increased from 1.0:1 to 1.6:1. Alongside these two variables, concentration of the reaction mixture was also found to be significant as large surface areas for nucleation of MOF crystals favoured an IRMOF film in larger vials. Therefore, all upscaled MUF20 syntheses used multiple vials in parallel with optimized surface area to volume to concentration conditions (see experimental section at end of chapter for specific conditions for each MOF).

Lower quality crystals were commonly encountered due to known framework weaknesses – particularly regarding the weaker soft-hard zinc-oxygen bonds of the paddle-wheel [$M_2(COO)_4$]-based secondary building unit (SBU) - and sensitivity of the flexible framework to external stimuli. Desolvating the material – the optimum way to observe the functional group sidechains crystallographically - changed the structure dramatically in some of this pillar-layer family, as observed by powder x-ray diffraction analysis (PXRD) in the case of MUF20-Dα and MUF20-Bα materials (Figure 2.10).

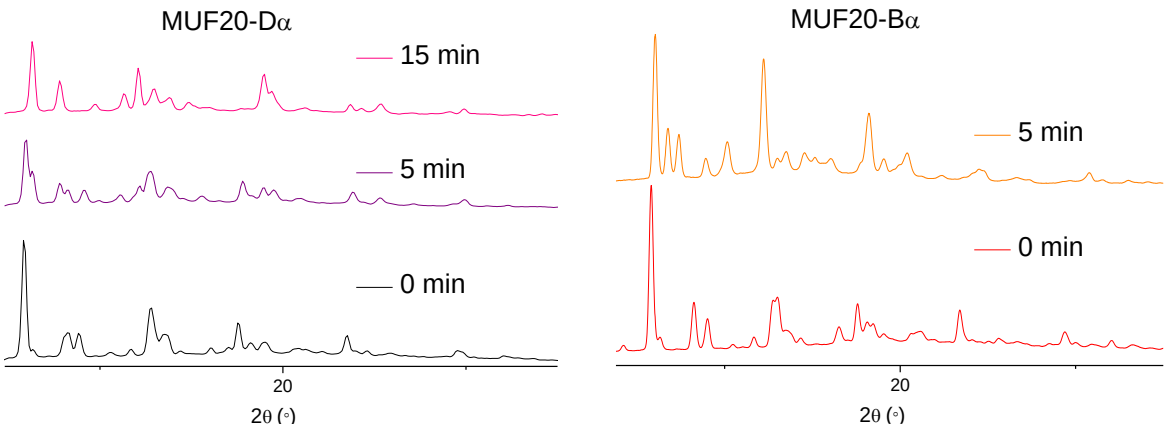

Figure 2.10: Solvated state dependent PXRD changes. MOF samples in DMF were allowed to dry under atmosphere while analyzing in 5 minute intervals until no further phase change observed.

Due to the dynamic nature of pillar-layer frameworks in response to external stimuli, PXRD patterns served mainly as a guideline in this MOF study, in contrast to the incredibly reliable

fingerprint nature of more rigid MOFs, which show little structural change upon host-guest interaction. However, despite differing state of solvation and small-scale structural changes, a clear pattern for the main family of functionalized MUF20 analogues can be observed (Figure 2.11). Particularly of note is that the distorted (MUF20-B`α-dis) and diamondoid topology (MUF20-B`α-dia) structures, formed by the bare ligand, bpdc-NH_2, show a distinct PXRD pattern compared to the MUF20 analogues - corresponding to their different MOF topology as confirmed by single-crystal, PXRD and NMR analysis, and elaborated on later in this thesis.

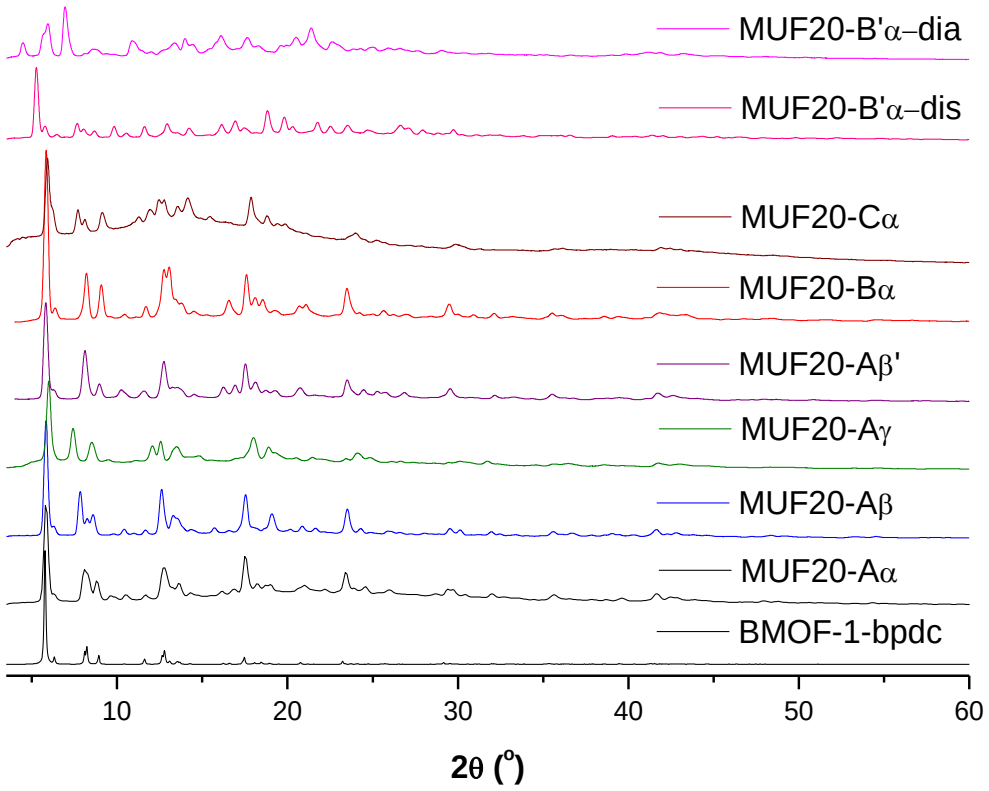

Figure 2.11: Experimental PXRD patterns for the parent and mono-functionalized materials. From bottom; MUF20-Aα (calculated from literature (BMOF-1-bpdc) single crystal structure)[171] and experimental PXRD pattern for the same material synthesized under conditions used in this study followed by the novel materials MUF20-Aβ, MUF20-Aγ, MUF20-Aβ`, MUF20-Bα, MUF20-Cα, MUF20-B`α-dis, MUF20-B`α-dia.

Despite the aforementioned limitations of PXRD analysis, the single crystal structures obtained are reliable and supported by ^{1}H NMR analysis. The latter technique involves digestion (acid or base disruption of metal-oxygen bonding and subsequent dissolution of ligands) of the washed and dried MOF material. The characteristic 2:1 bpdc:bpy ligand ratio of the pillar-layer (MUF20-Aα, $[Zn_2(bpdc)_2(bpy)]$) MOF structure is observed in the NMR spectra (see end of chapter).

The TPG moieties were unusually highly ordered within the pores of the MOF (Figure 2.9). This can be attributed to interactions between lattice and functional groups within the narrowed pores confining the TPG in a preferred configuration as detailed later. Contrastingly, the free amine functionalized MUF20 analogue, MUF20-Aβ`, showed the bpy-NH_2 functional group to be disordered over the possible ligand substituent sites in typical fashion.

Synthesis with unprotected ligands

Synthesis of MOF frameworks containing unprotected amine or carboxylic acid functionalities was undertaken using the bare ligands: bpdc-NH_2 (B`), bpdc-$CO_2H$ (C`), bpy-NH_2 (β`), and bpy-$CO_2H$ (γ`) (Figure 2.8).

At this point it became clear that the protected functionalities, despite the issue of steric bulk introducing a competing IRMOF phase, formed the desired MUF20 materials infinitely more easily than the unprotected amine or carboxylic acids, with one exception. Both bare carboxylic acid ligands formed unknown phases that could not be characterized and the unprotected bpdc-NH_2 ligand formed two distinct new phases, neither of which were MUF20-Aa. However, bpy-NH_2 cleanly formed MUF20-Aβ` and was able to be completely characterized. Chapter 3 expands on these results to draw clear trends, while in this chapter it is sufficient to note that MUF20-Aβ` formed the identical phase to the other MUF20 TPG-functionalized MOFs and could thus be included in comparison and interpretation of the gas sorption and thermolysis results for the mono-functionalized MUF20 family.

2.2.2. Effect of TPG functionalization on MOF structure

One of the goals in this study of flexible MOFs was controlling interpenetration during MOF formation through incorporation of bulky thermolabile protecting groups (TPGs). Subsequent thermolytic cleavage of the TPG could then trigger additional porosity as well as reveal useful functional groups in the pores, as has been successfully achieved previously by the Telfer group in the quintessential IRMOF structure using a Boc-protected proline.[153, 175]

However, despite the steric bulk of the TPG groups, MUF20-Bα, MUF20-Cα, MUF20-Aβ, and MUF20-Aγ analogues all retained the 2-fold interpenetrated structure of the parent framework (Figure 2.12).

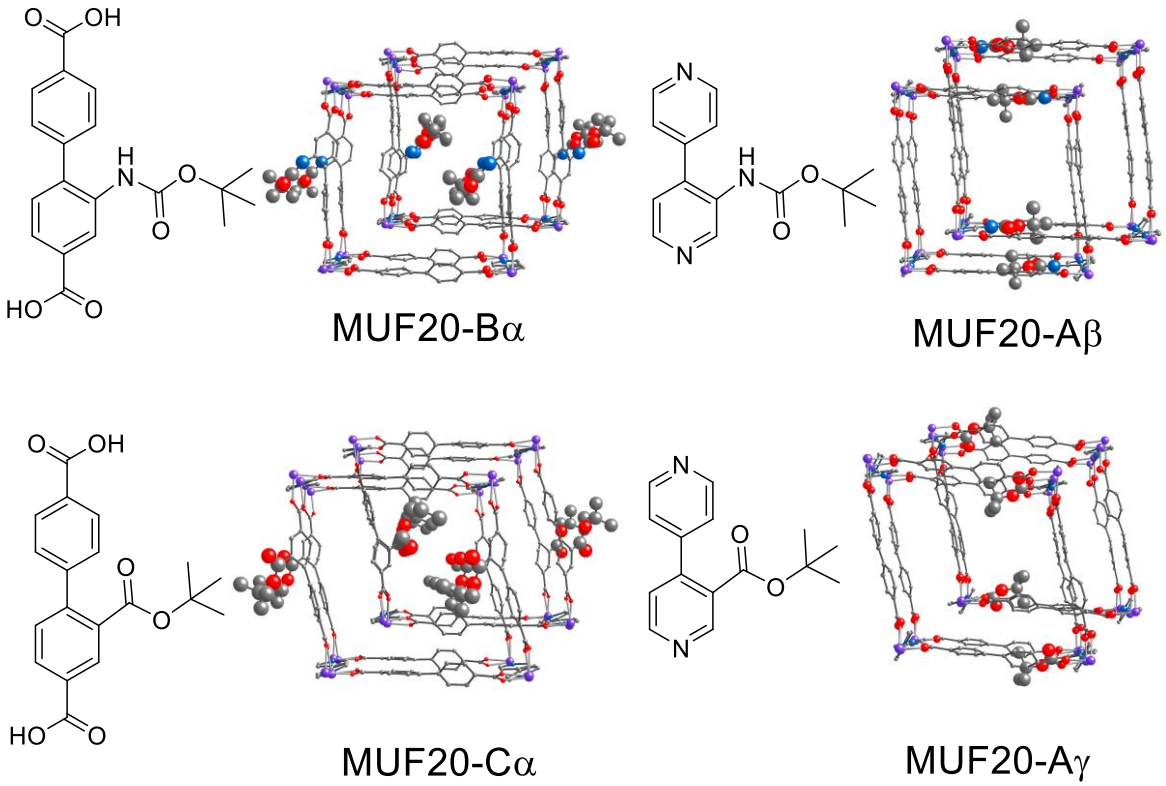

Figure 2.12: Observed 2-fold interpenetration in the TPG mono-functionalized materials as viewed along the bpy axis. Localization of the TPGs within the layers (left) and 'walls' (right) of the pillar-layer structure is linked to position of the group on the bpdc or bpy ligand respectively.

As with the parent material, the presence of an interpenetrating second framework greatly increases the MOF stability by reducing access to the inorganic SBU by water, resisting framework collapse.[176]

This interpenetration result contrasts with the ready exclusion of a second lattice in the more rigid IRMOF framework where a proline-Boc group of similar bulk and polarity successfully formed the non-interpenetrated IRMOF-10 phase. However, within the flexible pillar-layer MOF framework there is precedent with bulky functionalities on the bpdc ligand not only allowing but promoting formation of a second lattice within the first lattice pores. In the elegant study by Cohen et al. nitro functionalization of the bpdc-ligand (bpdc-NO_2) was shown to have an intermediate point where the bulk prevented secondary lattice formation.[174] However, upon doubly functionalizing the bpdc to form the asymmetrically substituted bpdc-$(NO_2)_2$ ligand, the MOF reverted to a doubly interpenetrated structure. This was attributed through modelling and crystallographic analysis to inter-lattice interactions set up between the two nitro groups of the bpdc-$(NO_2)_2$ of neighbouring lattices.

Similarly, in the synthesis of the bulky TPG-functionalized analogues the structure remains interpenetrated and shows high ordering of the substituents from favourable interactions set up with the second lattice. The stability gained by increased van der Waals interactions sufficient to overcome the energetic penalty of significant bpdc ligand distortion and SBU coordination angle changes in the case of the TBE functionalized MOFs (Fig 2.12). This result led to the following question: "Does a doubly functionalized MOF have sufficient steric bulk to prevent interpenetration in a pillar-layer MOF structure?" the answer is explored in Chapter 3.

Crystallographic analysis of these MOFs indicates that the substitution placement can have greater impact than the type. This echoes studies carried out by Fischer and Henke et al.[177] into the milestone pillar-layer MOF DMOF-1, where instead of bpy, 1,4-diazabicyclo[2.2.2]octane (DABCO) is used to pillar the Zn^{2+} carboxylate layers which consist of the shortened linear dicarboxylate ligand, 1,4-benzenedicarboxylate (bdc). Using alkoxyether substituents they investigated the effect of position of functionality on the bdc backbone on the material finding that an opposing (symmetric) configuration of the substituents - as opposed to a cis (same-side) substitution pattern - gave the strongest influence on the bulk. However, in their study only the bdc was functionalized and the difference in influence was explained through a more uniform pore environment created in the flexible framework when the substituents were positioned on opposing sides which enables larger bulk changes upon exposure to stimuli. In this research the location of the TPG within the layer or pillar of the MOF is controlled exploring the interplay of both nature and position of functionalization on the material properties.

2.2.3. Thermolysis of mono-functionalized MUF20 materials

The thermal properties of the mono-functionalized MUF20 analogues were explored through TGA (Figure 2.13).

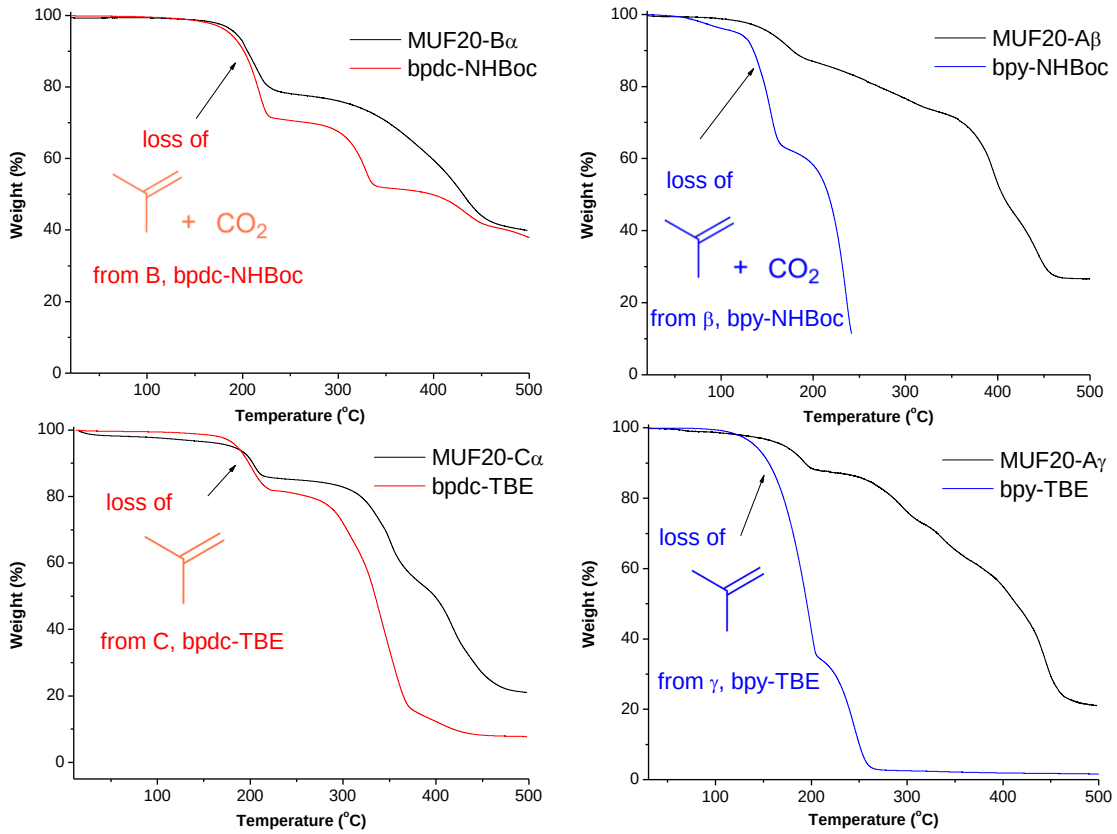

Figure 2.13: Thermogravimetric analysis (TGA) traces for MUF20-Bα, MUF20-Cα, MUF20-Aβ, and MUF20-Aγ, compared to relevant TPG-functionalized ligand.

These weight losses were then tabulated (Table 2.2) and compared against the expected weight losses of the leaving theoretical TPG fragments (see Figure 2.14).

Table 2.2: Experimental and calculated percentage weight losses of TPG-MOFs.

MOF	$T_{1/2\Delta}$ (°C)*	Experimental Weight loss (%)	Calculated Weight Loss (%)
MUF20-Bα	180	21.2	20.1
MUF20-Cα	160	12.3	11.6
MUF20-Aβ	140	12.0	11.3
MUF20-Aγ	150	7.0	6.5

* $T_{1/2\Delta}$ is defined as the midpoint of the temperature range over which weight loss associated with thermolysis occurs and is rounded to the nearest 5 °C.

The experimental weight losses correlated well to the calculated values for all MOFs, including MUF20-Aβ and MUF20-Aγ, where it can be observed that the bpy-NHBoc and bpy-

TBE ligands are stabilized by the MOF framework and unable to evaporate at lower temperatures.

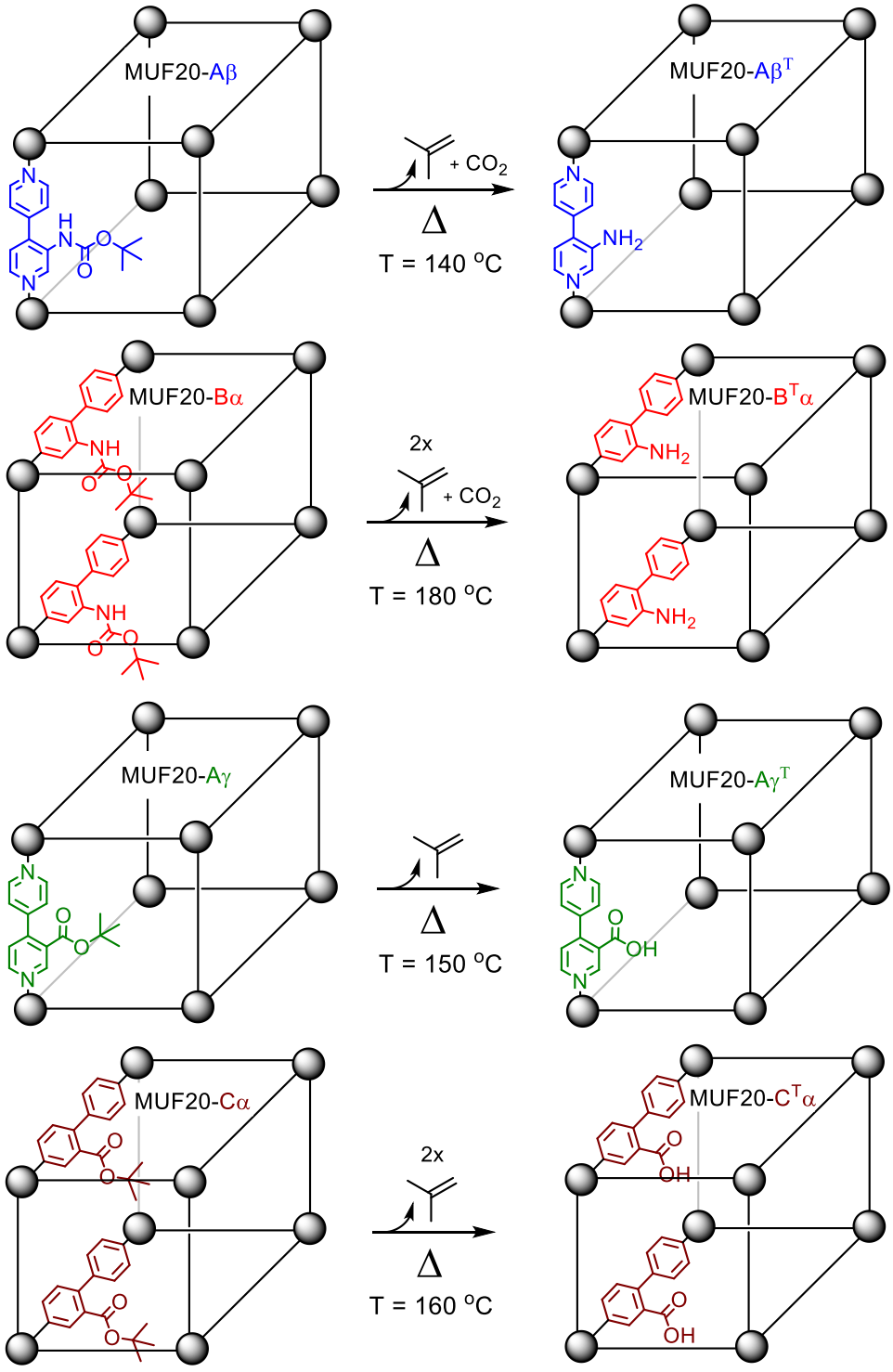

Figure 2.14: Thermolysis of TPG ligands in MOF illustrating the loss of thermolytic fragments isobutylene and CO_2 for MUF20-Aβ and MUF20-Bα (with carbamate TPG –NHBoc) and isobutylene for MUF20-Aγ and MUF20-Cα (with *tert*-butyl ester TPG –TBE) respectively.

Now that the bpy ligands are no longer evaporating off the pan, a trend can be tentatively drawn on the tuning of MOF thermal properties by backbone influence on TPG-functionalization. Moving from a bpdc to bpy-based backbone decreased the thermolytic temperature required for 50 % thermolysis (approximate midpoint of TPG loss step) from ~170 ^{o}C to less than 155 ^{o}C. This observation on the backbone influence on the TPG stability ties in with literature on the 2-pyridinyl thermolabile groups commented on in the introduction.[178]

Comparing the MOFs alongside each other (Figure 2.15) shows the fine-tuning of thermal properties possible within the same framework using TPGs and their position on a bpy (pillar) or bpdc (layer) ligand in the MOF. Due to the 2:1 bpdc:bpy ligand stoichiometry in [Zn_2(bpdc)$_2$(bpy)] MOF structure the percentage weight loss step associated with the bpdc-TPG is roughly double that of the bpy-TPG. This result is most obvious in the case of the carbamate (–NHBoc) TPG installed in MUF20-Bα and MUF20-Aβ.

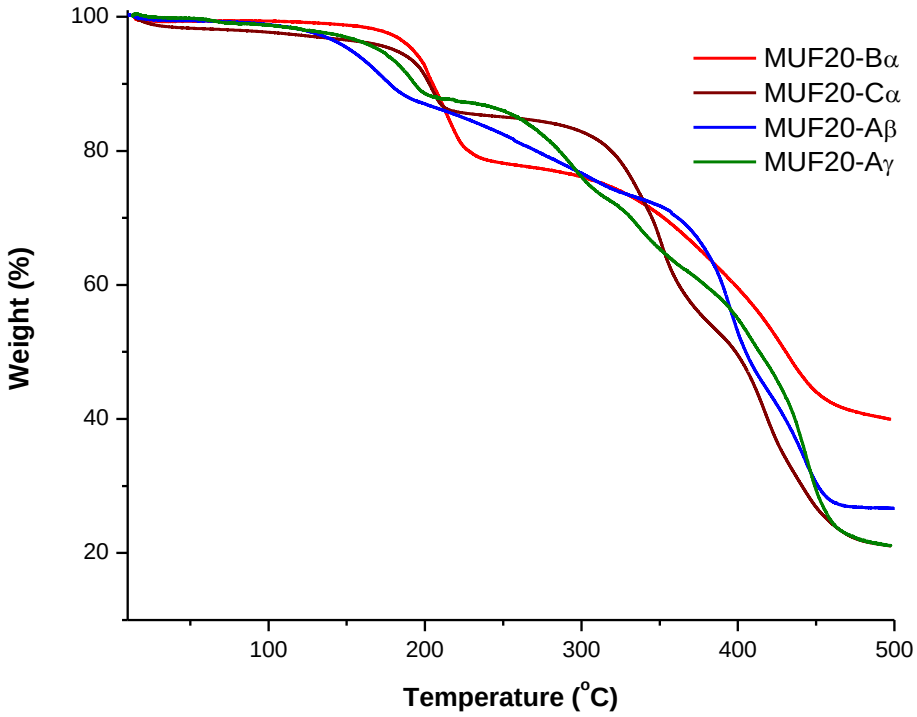

Figure 2.15: Thermogravimetric analysis (TGA) traces for TPG-functionalized MUF20 MOFs. Bpy-TPG materials show a lower thermolysis temperature compared to bpdc-TPG MOFs while bpdc-TPG functionalized materials give a larger percentage weight loss overall.

As shown in the TGA traces, each of the MOFs has a plateau post loss of the TPG group. So-called loop TGAs - where the material is heated past thermolysis, cooled and then reheated - show that the remaining material was completely thermolyzed (no further TPG loss step

observed in TGA) and stable to further degradation until high temperature (no weight loss of material until post 200 °C), illustrating the triggered nature of the thermal properties of TPG-functionalized MOF materials (Figure 2.16).

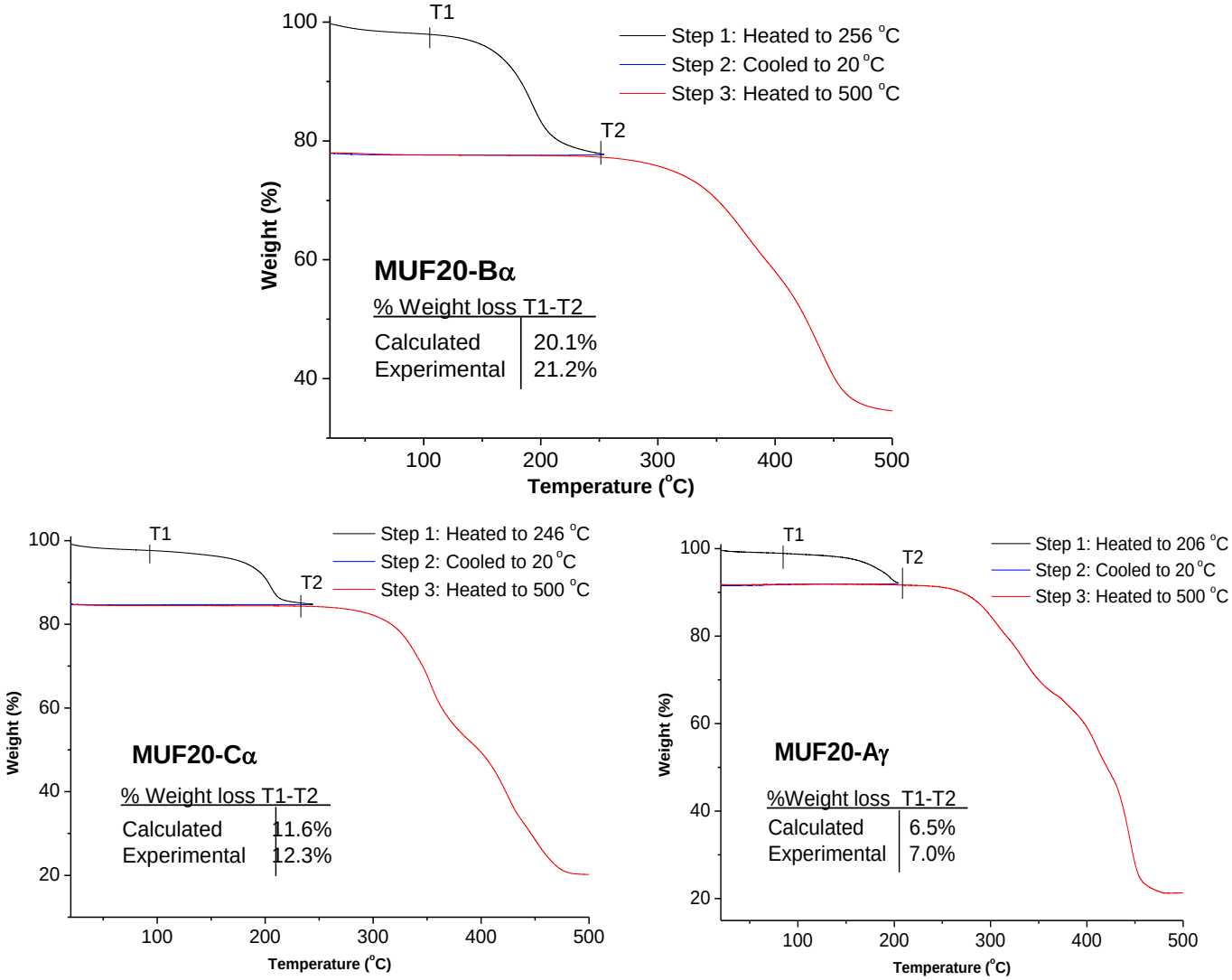

Figure 2.16: Thermogravimetric analysis (TGA) traces, looped to illustrate triggered loss of the thermolabile protecting group (TPG), for MUF20-Bα**,** MUF20-Cα**,** and MUF20-Aγ. Due to insufficient bpy-NHBoc ligand, MUF20-Aβ was not analyzed in this manner within the time of this study.

In the third step of the loop TGA the material heated can be described as the thermolyzed analogue to the parent material. Ligands carrying the thermolytically revealed functionalities are labelled accordingly: bpdc-NH_2 (B^T), bpdc-CO_2H (C^T), bpy-NH_2 (β^T), and bpy-CO_2H (γ^T), the thermolyzed analogues to the TPG ligands designated by superscript (^{T}) immediately following the MOF organic component thermolyzed to distinguish them from the bare or unprotected ligands used in direct MOF synthesis, see example below (Figure 2.17).

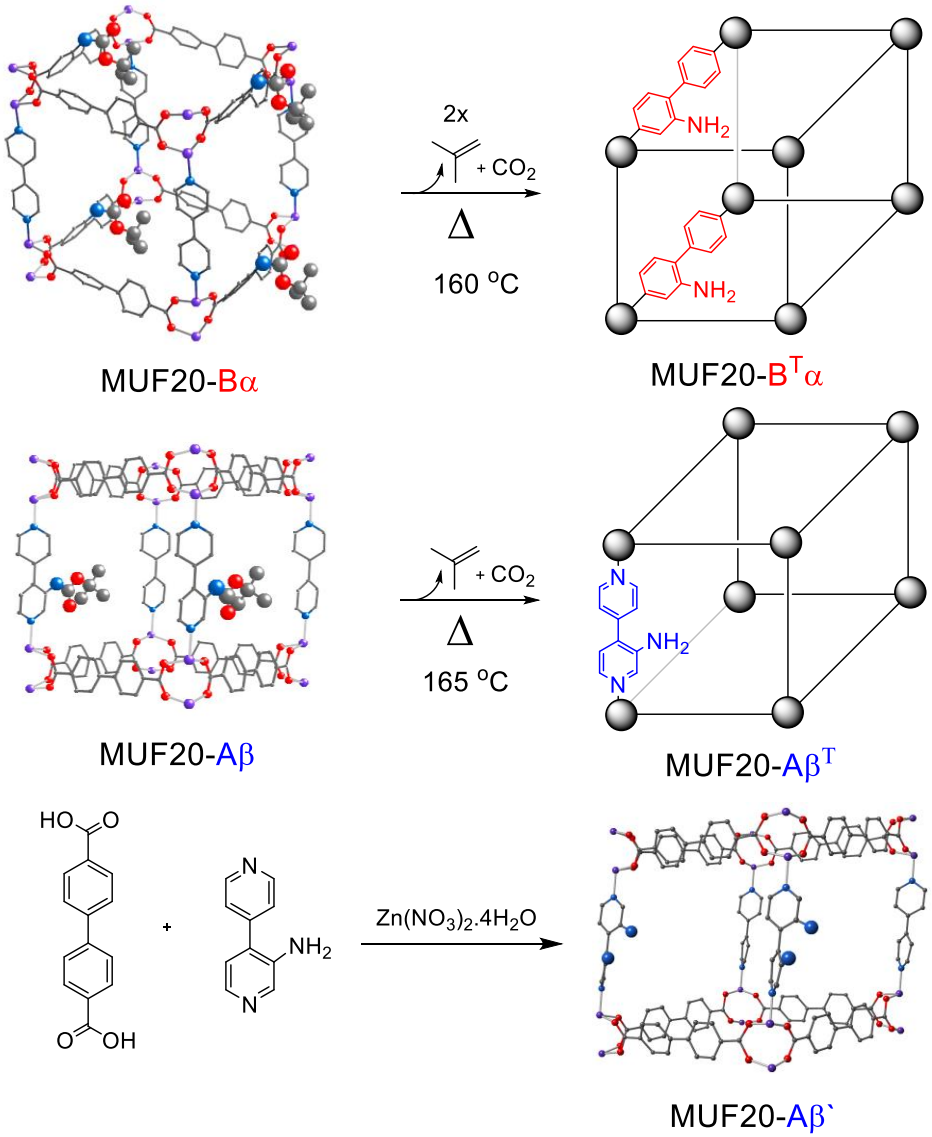

Figure 2.17: Amine-functionalized materials formed through thermolytic deprotection (MUF20-Bα and MUF20-Aβ thermolyzed to MUF20-B^{T}α and MUF20-Aβ^{T}) versus unprotected synthesis (MUF20-Aβ`). The materials MUF20-Aβ$^{T}$ and MUF20-Aβ` are functionally different (by single-crystal and powder x-ray diffraction) with the free amine of the unprotected synthesis analogue crystallographically disordered. Atom colour code; C-grey, O-red, N-blue, Zn-purple.

At this point it is important to draw the distinction between thermal integrity and material crystallinity. The TGA clearly shows the MUF20 materials to be thermally stable until onset of organic ligand decomposition at ~300 °C. This indicates solely that no further loss of material from the MOF occurs upon heating above thermolysis temperature but gives no insight into structural integrity. When undertaking trials for optimal thermolysis conditions of sensitive materials the temperature at which approximately 30 to 50% of the material is thermolyzed (first third to half of the recorded TGA percentage weight loss step) served as a starting thermolysis temperature.

To determine if the periodic nature of the MOF structure was maintained post thermolysis PXRD analysis of the thermolyzed materials was carried out. The MOFs were carefully solvent exchanged multiple times to remove any impurities that might catalyse framework degradation and a range of thermolysis conditions undertaken. Of particular interest was solvent free thermolysis due to the green nature of this method and ability to carry out gas sorption (GS) analysis upon the sample post *in situ* thermolysis on the activation port.

However, under a wide range of temperatures, times, solvent free and solvated, vacuum, microwave, etc (see Appendix) only limited crystallinity was maintained upon thermolysis in all members of the MUF20 family synthesized with the exception of MUF20-Dα, elaborated on later in this chapter. Optimal thermolysis conditions achieved at time of gas sorption analysis were used and PXRD analysis of these materials is shown in Figure 2.18. Sample degradation is clear in the loss of high 2Θ peaks and increased amorphous background in the PXRD analysis of the thermolyzed materials (designated with '^{T}'). A shift of the highest intensity peak to higher 2Θ upon thermolysis suggests a narrowing of the pore structure. In some materials this shift already occurs upon drying. Where activation (complete solvent guest removal, conditions detailed hereafter) of the MOF materials affected the PXRD both analysis (dried and post-activation) are included.

Of note is that in flexible pillar-layer MOF structures the importance of examining the effects of activation conditions on the material has been highlighted in literature in the isolation of an intermediate phase in the closely related system of $[Co_2(ndc)_2(bpy)]$ (ndc = 2,6-napthalene dicarboxylic acid) by alteration of activation conditions. The material is known to transform in a single crystal to single crystal fashion from the as-synthesized 2-fold interpenetrated material to a less porous triply interpenetrated form upon solvent removal at room temperature (1 week) or 120 ^{o}C (12 hrs). Further activation trials revealed that under intermediate activation conditions (80 ^{o}C for 12 hrs) a doubly-interpenetrated structure with distorted metal-ligand bonding was observed.[179] In this literature study a significant change in major PXRD peaks was observed (2Θ shifts of 2^{o} or more). This magnitude change was only observed in MUF20-Aγ^{T} which also showed significant degradation therefore PXRD analysis suggests that the activation conditions used effected relatively minor structural changes in the materials in this thesis.

Due to constraints on ligand amount (notably the 4,4'-bipyridine TPG ligands with an overall synthesis yield below 10 %) parallel thermolysis trials were restricted and more trials

were not undertaken. Therefore this study does not conclude that the MUF20 framework is incompatible with a TPG strategy.

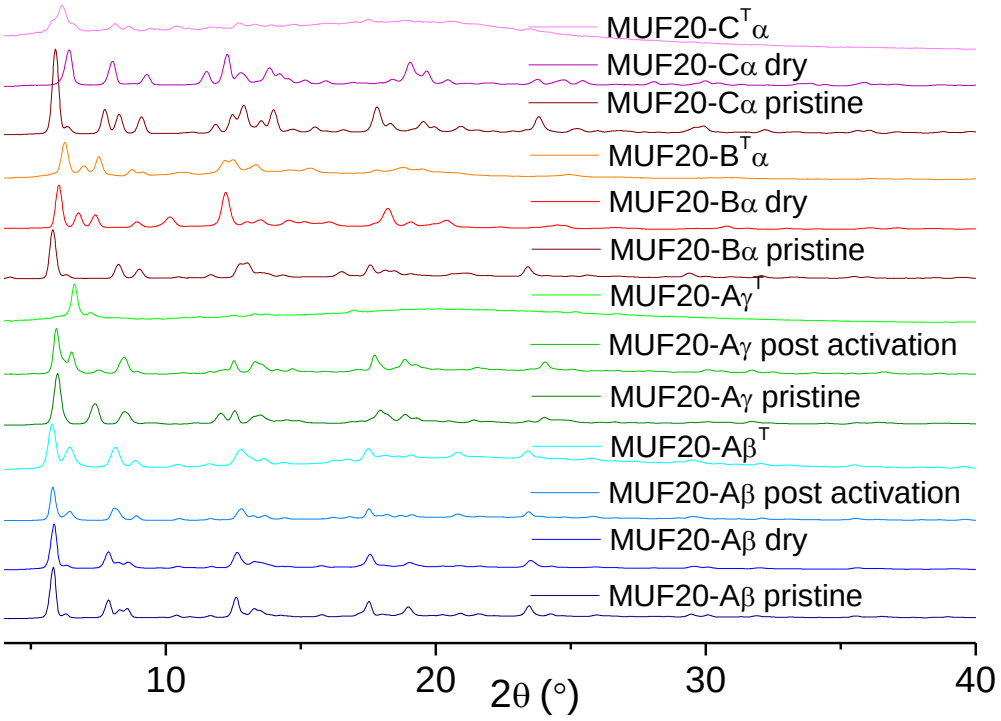

Figure 2.18: PXRD patterns of thermally deprotected materials MUF20-B^{T}α, MUF20-Aβ^{T}, and MUF20-Aγ^{T}. PXRD patterns of pristine and activated MOFs are included for comparison of structure changes upon desolvation and activation.

The PXRD analysis of the samples used in gas sorption indicate that for MUF20-B^{T}α and MUF20-Aβ^{T} material crystallinity is maintained with some amorphization but MUF20-Aγ^{T} is clearly substantially degraded post thermolysis. When compared with ^{1}H NMR analysis the differences can be attributed in part to extent of thermolysis with MUF20-B^{T}α showing only 25% deprotection, MUF20-Aβ^{T} 88% and MUF20-Aγ^{T} 96%, suggesting that for the thermolysis conditions trialled framework decomposition is concurrent with TPG deprotection.

MUF20-C^{T}α showed even greater propensity than MUF20-Aγ^{T} to degrade upon thermolytic deprotection and was therefore not characterized at the time by gas sorption. However, further trials showed promise in obtaining a crystalline MUF20 carrying a carboxylic acid functionalized bpdc ligand obtained through thermolytic deprotection of a TBE TPG.

The exception to the observed rule of degradation of material crystallinity accompanying full thermolysis will also be explored at the end of this chapter and distinguishing features examined to highlight factors that may contribute to thermolytic resilience.

However, of note is that MUF20-$B^T\alpha$ is the only route to a bpdc-NH_2 functionalized MUF20 analogue as all attempts with the bare bpdc-NH_2 ligand under direct synthesis conditions yielded non-MUF20 phase materials. Similarly, MUF20-$A\gamma^T$, despite marginal crystallinity, is the only carboxylic acid functionalized bpy pillar-layer MOF due to the extent of MOF synthesis disruption by an unprotected carboxylic acid functionality. Thus, both these materials illustrate the success of a thermolabile protecting group strategy in accessing functionalized MOFs otherwise inaccessible through direct synthesis.

2.2.4. Gas adsorption analysis of mono-functionalized MOFs

Despite this lack of crystallinity upon partial thermolysis there remained the possibility of the material being porous, therefore gas adsorption analysis was undertaken for certain materials within study time constraints.

As mentioned earlier, phase issues upon scaling of MOF synthesis for gas sorption meant that samples were primarily synthesized through parallel 4 mg vials and the material then combined.

Materials were thoroughly solvent exchanged from the reaction mixture DMF:MeOH through DMF thrice (to remove residual ligands and zinc salts that might block pores) and into dry CH_2Cl_2 (on sieves) at least thrice to remove any guest DMF molecules that can increase the gas uptake through increased interaction with gas molecules in the pores. Samples were taken to confirm crystallinity and purity through PXRD and ^1H NMR analysis. The bulk sample was then transferred under CH_2Cl_2 and inert atmosphere into a pre-weighed gas sorption tube. The tube was then back-flushed thrice with Ar(g), and the sample under a small amount of solvent was placed onto the gas sorption activation port. Multiple activation trials determined that a heating rate of 1 ^oC/min up to 80 ^oC and holding for 12 hours activated, i.e., removed solvent from, the sample while maintaining crystallinity. For the bpy-functionalized MOFs a gentler activation procedure of 30 ^oC for 10 hours was required to yield higher gas uptakes.

After determining the weight of the activated sample gas sorption analysis was carried out where the sample was dosed with known volume of the chosen gas into the sample tube and the pressure recorded frequently until a constant value repeated, reflecting that the adsorbed and non-adsorbed gas have reached equilibrium. As detailed in Chapter 1, the amount of gas adsorbed by the material can then be calculated using the ideal gas equation to find the difference between the expected pressure and equilibrium pressure measured. This is repeated for subsequent pressure points so that a plot of known volume of gas (cc/g) is plotted against

equilibrium pressure at constant temperature to form a gas isotherm. The endpoint of the isotherm at the highest pressure is termed the total gas uptake of the material and is understood to be when the pore volume is completely occupied by gas molecules.

Worth noting is that, as the MOF field has grown, knowledge surrounding the importance and range of activation conditions has also deepened[180-181] and been shown to be critical in accurately and reproducibly recording the gas sorption isotherms of a material.[165] Judicious choice of solvent is required as the violent removal of large volumes of guest molecules can degrade MOF structure[182] and recent studies post this data collection have shed light in this area for optimization of activation procedures.[183] Further trials of different activation conditions could therefore improve upon the results presented herein.

Challenges in flexible MOF gas sorption measurements

A remaining challenge in gas sorption measurements, specifically of flexible framework materials, is the presence of hysteresis. In rigid frameworks hysteresis can largely be attributed to mesopore filling and inadequate equilibration time. However, in measuring flexible frameworks the hysteresis arising from an overly short equilibration time must be separated from hysteresis arising from phase changes in the materials upon reaching a gate-opening pressure. Therefore, trials were undertaken to investigate equilibration times (Figure 2.19).

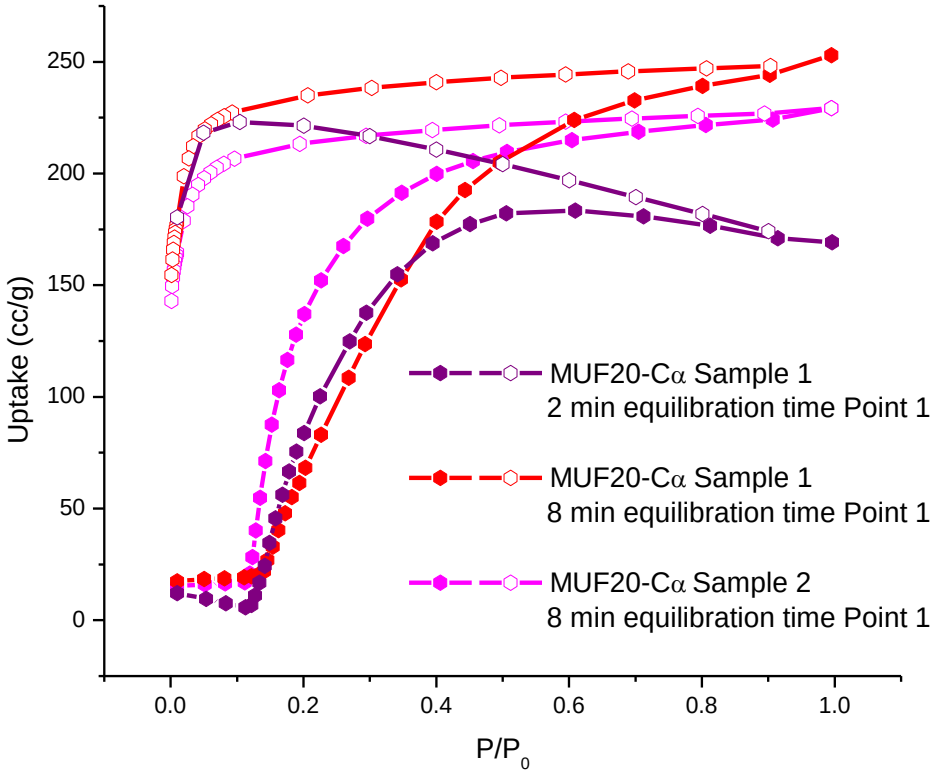

Figure 2.19: Volumetric N_2 adsorption (filled) and desorption (open) isotherms measured at 77 K on one sample under different conditions (2 versus 8 min equilibration time) and two samples under the same conditions (8 min equilibration time). Point 1 is the first measurement point collected of the gas sorption isotherm. Lines are a guide to the eye only.

Huge variation in the isotherm shape occurred upon changing the equilibration time of the first measurement (Point 1) from 2 to 8 min. Inadequate equilibration time at the start of gas adsorption leads to an initial negative slope, i.e. decreasing gas uptake at higher pressures and upon desorption causes a positive slope to be recorded, i.e. increasing gas uptake at lower pressures, due to the slow kinetics of gas diffusion in the adsorbent. This is reminiscent of both soft porous crystals with shape memory effects where initial measurement conditions affect later values and of observed dependence of isotherm shape and uptake on the allowed time at each data point and *cumulative* exposure to gas prior to that point.[184] In this case insufficient equilibration time at point one caused the recorded isotherm to lag behind true values for the rest of the collection. Further increase in the initial point equilibration time or increasing the first 10 measurement equilibration times did not significantly affect the isotherm.

Increasing the equilibration time across the collection flattened the hysteresis loop and increased the total gas uptake slightly but this difference was within observed sample variation and made collections prohibitively time costly. Therefore, an equilibration time of 8 min for

the initial point and 2 min for each point after was used as standard for N_2 at 77 K gas sorption measurements on these materials and in other low temperature measurements.

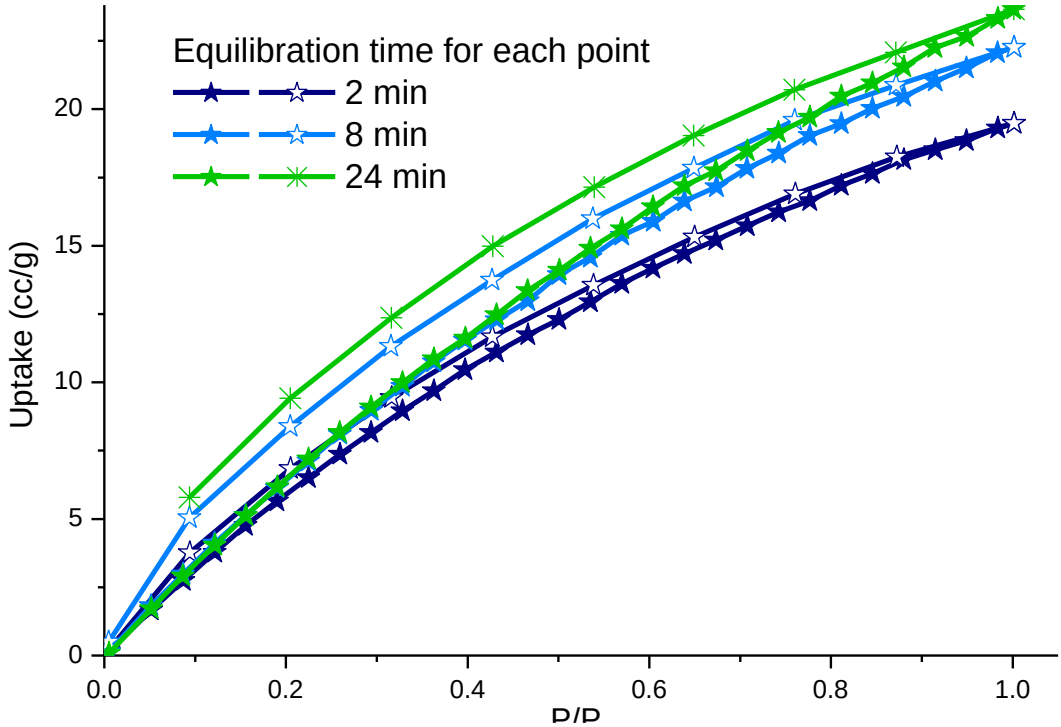

Figure 2.20: Volumetric CO_2 adsorption (filled) and desorption (open) isotherms measured at 298 K with increasing equilibration times for point collection on material MUF20-Aβ`. Lines are a guide to the eye only.

Unlike low temperature measurements where increasing the equilibration time flattened the hysteresis loop, for CO_2 at 298 K an increase in hysteresis was observed (Figure 2.20). This has been shown in literature to be a kinetic barrier related phenomenon where the true isotherm is approached post initial hysteresis increase (Figure 2.21). However, even increasing the equilibration time by 12-fold did not show a narrowing of the hysteresis loop. Thus, the non-reversible isotherms at 2 min equilibration time were measured for convenience and it is simply noted that the observed total gas uptakes for hysteretic materials upon gas sorption of CO_2 at 298 K are lower than true values due to insufficient equilibration time.

An excellent resource[184] examining the effect of time, temperature, and kinetics on hysteresis in the related framework $[Zn_2(bpdc)_2(bpee)]$ (bpee = 1,2-bipyridylethene) concludes that both "the degree of hysteresis between adsorption and desorption as well as the inflection point in the S-shaped isotherm were heavily dependent on the allowed time at each data point and also on the cumulative gas exposure time" due to mass-transfer limitations. Additionally, they noted that even under optimized conditions the observed gas uptake may still not be the real capacity at true equilibrium.

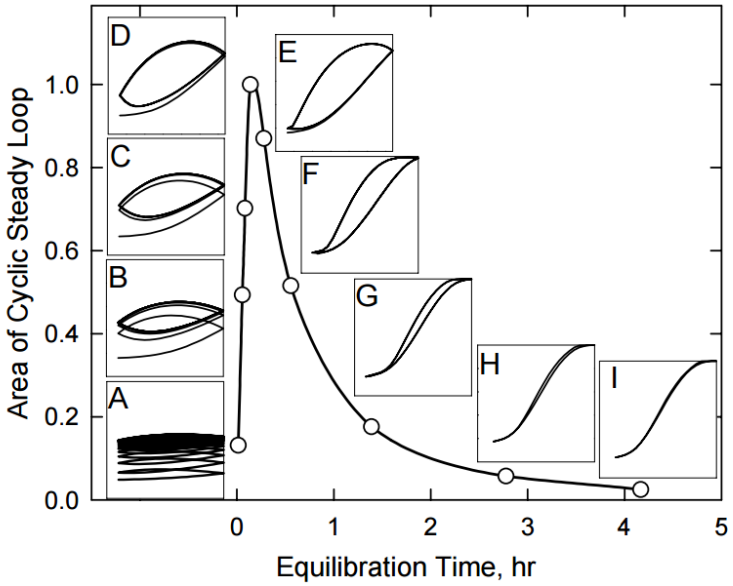

Figure 2.21: Plot of area of cyclic steady loop vs equilibration time. Reproduced from Illam Park's 2001 conference paper.[185]

During initial gas sorption trials, non-ideal MUF20-Aβ and MUF20-Aγ materials were analyzed twice; firstly, containing DMF (~27%) and secondly, containing ~10% of a bdc impurity. Even in the presence of a high concentration of DMF, insufficient sample treatment overestimated total gas uptake by only 1.1 - 2.4%. This is less than in literature with carbon dioxide uptake greatly increased in the presence of residual DMF.[186] More significantly in this PLMOF study, DMF was shown to cause multiple side species to form during thermolysis of the carbamate TPG, -NHBoc (although not in the case of the *tert*-butyl ester, -TBE).

The bdc impurity more interestingly was shown to greatly increase the gas uptake of MUF20-Aβ and MUF20-Aγ to approximately that of the bpdc functionalized MOFs (a greater than 200 % increase in total gas uptake). Thermolytic resilience and general sample robustness was also improved upon the pure MUF20-Aβ and MUF20-Aγ materials and hysteresis behaviour was distinct. A possible explanation is the introduction of defects into the MOF enabled inter-lattice interactions otherwise not possible that both maintained a more open pore structure and enhanced thermal stability. Notably, the impurity was shown to slightly decrease (-3.1 %) the total uptake of the free amine functionalized MUF20-Aβ`, likely due to stronger interaction of the free amine with the free carboxylic acid of the bdc impurity doped MOF. Full gas sorption isotherms on these defect materials are included in the Appendix but are not fully discussed here. This illustrates the importance of material purity and careful treatment in collecting accurate and reproducible gas sorption isotherms for MOF materials as well as an

interesting note into potential doping of pillar-layer MOFs to increase stability and control material properties by an inbuilt defect approach as an alternative to linker functionalization,[187] solvent-assisted linker exchange (SALE)[188] or post-synthetic metal exchange (PSME).[189]

Gas sorption isotherms (N_2, H_2, CO_2 and CH_4) were collected for the pillar-layer MOF materials: MUF20-Bα, MUF20-Cα, MUF20-Aβ, MUF20-Aγ, unprotected analogue MUF20-Aβ`, and thermolysis analogues MUF20-B^Tα, MUF20-Aβ^T, and MUF20-Aγ^T. Only N_2 isotherms at 77 K were found in literature for comparison to the parent MOF material (BMOF-1-bpdc) at the time of writing.

Within the GS analysis undertaken, insights can be gained into the effect of:

1) TPG position, by comparing the bpdc- *versus* bpy-monofunctionalized MOFs
2) TPG steric factors and polarity, by comparing the carbamate, *tert*-butyl ester, and amine ligands
3) partial thermolysis to full thermolysis in the framework with percentage of revealed free amines balanced against pore collapse, by comparison of MUF20-Bα, MUF20-B^Tα, MUF20-Aβ^T, MUF20-Aγ^T, and MUF20-Aβ`

MUF20 materials with TPGs occluding the pores are expected to have initially a lower total gas uptake than the parent unfunctionalized material which could then be increased upon thermolysis due to the larger pore volume formed and increased heat of adsorption from the polar functionalities revealed. In the event of framework integrity being maintained, this increase in gas uptake would balance against decrease in London/dispersion interactions by polar gases with the highly polarizable *tert*-butyl groups post decomposition and expulsion of isobutylene. In reality, the degradation of framework structure upon full thermolysis dominates.

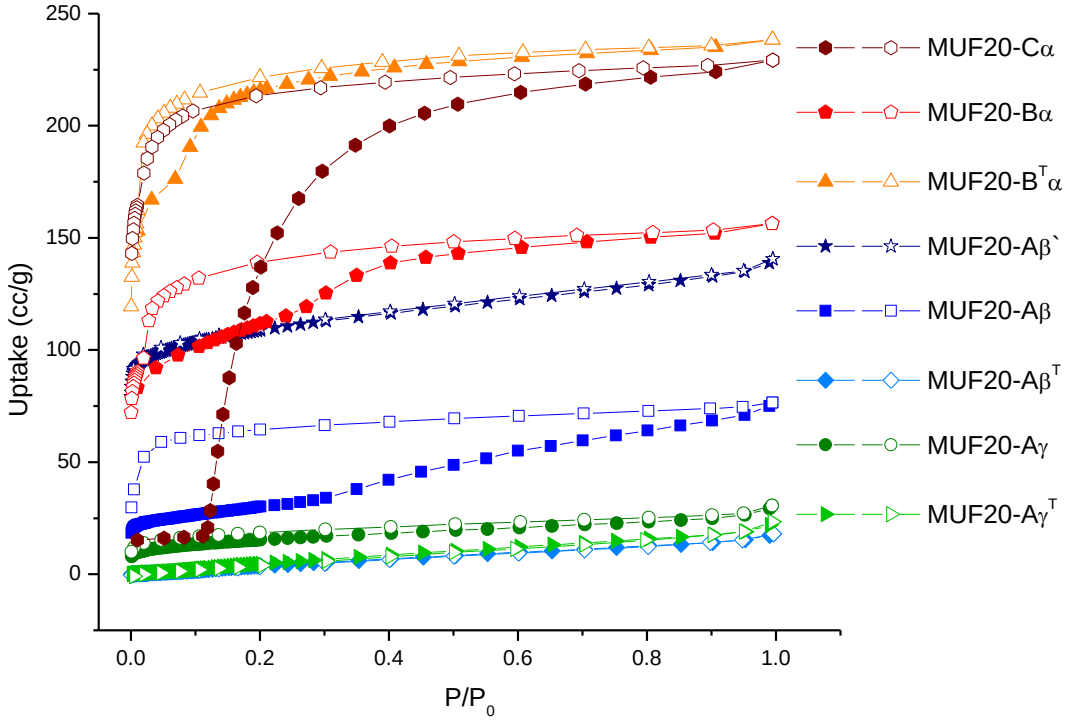

Figure 2.22: Volumetric N_2 adsorption (filled) and desorption (open) isotherms measured at 77 K. Lines are a guide to the eye only.

The N_2 at 77 K gas sorption isotherms (Figure 2.22) show a mixture of hysteretic behaviours. Notably upon thermolysis the hysteresis is either decreased or eliminated; this is to be expected if thermolytic deprotection is accompanied by framework degradation with partial pore collapse restricting the movement in the pillar-layer framework material. Alternatively, in the partially deprotected crystalline MUF20-B^{T}α material, the revealed amines could take part in increased inter-lattice interactions and thus constrain the framework.

Clearly there is partial pore collapse occurring in the 88 and 96 % deprotected MUF20-Aβ^T and MUF-20 Aγ^T versus the only 25 % deprotected MUF20-B^{T}α thermolyzed material as despite an increase in pore volume from expulsion of isobutylene and CO_2 (carbamate themolysis) or isobutylene (*tert*-butyl thermolysis) there is a decrease in the total gas uptake of the material corresponding to pore collapse.

Looking at the thermolyzed materials alone (Figure 2.23) shows a marked change in behaviour upon partial thermolysis with maintained crystallinity versus almost complete thermolysis with marginal crystallinity.

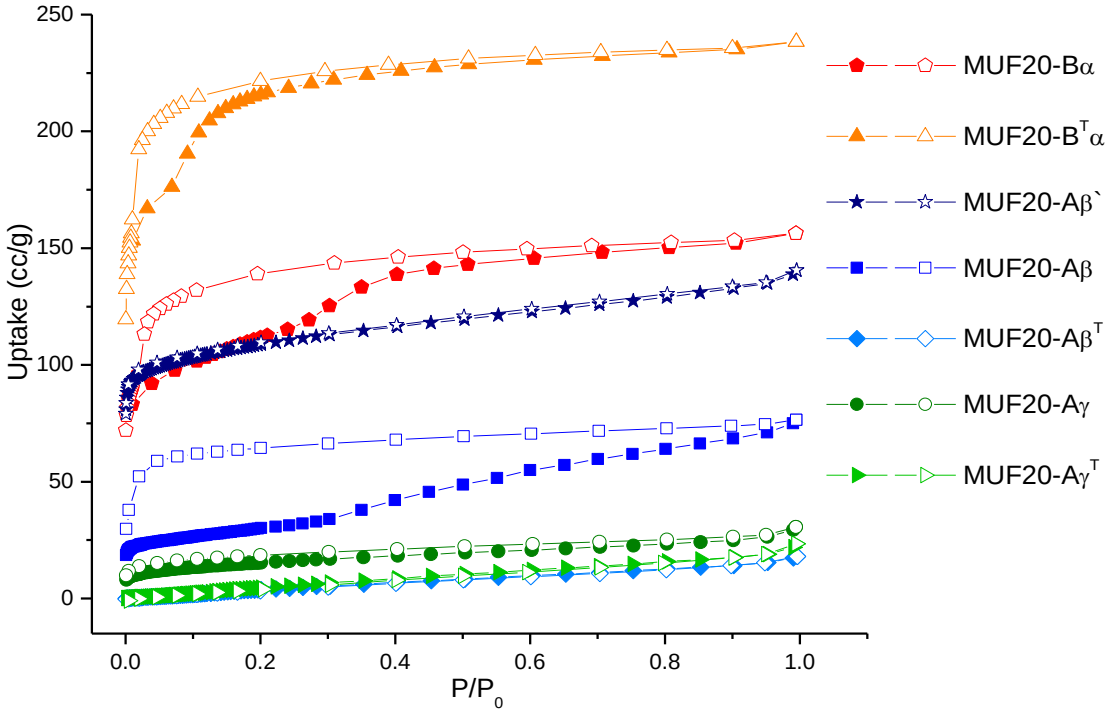

Figure 2.23: Volumetric N_2 adsorption (filled) and desorption (open) isotherms measured at 77 K. Lines are a guide to the eye only.

Unlike the example of MUF20-Aβ^T where MUF20-Aβ` readily formed, MUF20-B`α - with free amine located on the bpdc ligand - cannot be formed directly and only MUF20-B^{T}α gives access to this bpdc-NH_2 functionalized pillar-layer MOF. However, given the increased total volume uptake of MUF20-Aβ`, it is reasonable to assume that, given appropriate thermolysis conditions which maintained crystallinity, the gas uptake of MUF20-Aβ would be increased upon thermolytic deprotection as in MUF20-Bα.

Noted is that the more polar-functionalized materials all have decreased (MUF20-B^{T}α) or absent (MUF20-Aβ^T, MUF20-Aγ^T, MUF20-Aβ`) hysteresis. As observed with the bdc-impurity gas sorption isotherms, this could be related to increased interactions between frameworks from the free amines or carboxylic acids present restricting inter-lattice motion in response to guest molecules. Alternatively, as initial hysteresis is reduced in the bpy-functionalized MOFs, a closing of the hysteresis loops could indicate an absence of pore-blocking due to removal of the bulky TPG substituents.

The mono-functionalized family total gas uptake can be compared showing the marked change in pore volume and hysteresis upon location of the TPG in the bpdc layer versus bpy backbone of the pillar-layer MOF structure (Figure 2.24). Functionalization by the –NHBoc

TPG doubles the total gas uptake (76 to 156 cm^3/g) going from the bpy to bpdc backbone in line with the TPG concentration doubling due the MUF20 ligand ratio, $[Zn_2(bpdc)_2(bpy)]$. However, the -TBE group shows the most drastic effect, going from the lowest gas uptake of N_2 at 77 K to the highest (30 to 229 cm^3/g). By doubling the concentration of TBE groups through placement in the carboxylate layer the total gas uptake of the MOF is increased 8-fold, indicating that there is more than just a concentration effect at play.

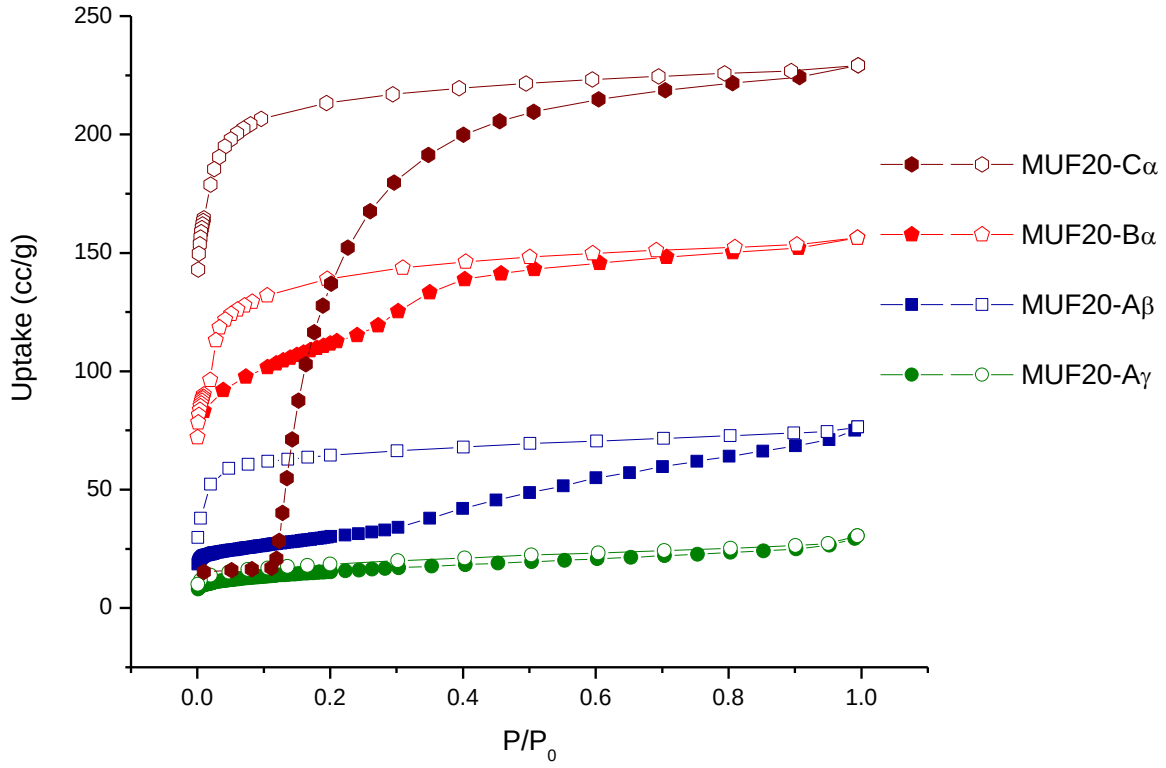

Figure 2.24: Volumetric N_2 adsorption (filled) and desorption (open) isotherms measured at 77 K. Lines are a guide to the eye only.

Modification of the bpdc backbone by the -TBE group surprisingly changes the pore shape and framework to dramatically increase the total pore volume. This effect occurs despite doubling the number of TBE groups present in the MOF with an expected occlusion of pores, reduction of pore volume, and decrease in volumetric gas uptake. This implies that a TPG on the bpdc backbone is in fact opening the pores of the framework to a greater extent than the bpy or non-functionalized MOFs.

However, as all functionalized materials have a total gas uptake greater than that of the parent material at 77 K (> 15 cc/g reported by Cohen et al), this suggests that the bulk does in fact open the pores of the pillar-layer framework to guest molecules.[171] A narrower pore

structure is to be expected in an evacuated material that is dynamic enough to maximise van der Waals interactions by shifting of the lattice structure and has been observed in other flexible MOF systems.[190] Placement of a TPG group in pillar or layer may maintain a more open pore structure upon solvent evacuation and thus allow a greater volume of gas uptake in general in flexible frameworks that might otherwise adopt denser forms.

2.2.5. BET surface area calculations

The BET surface areas for MUF20-Aβ, MUF20-Aγ, and MUF20-Aβ` were then calculated from the N_2 isotherms at 77 K as elaborated on in Chapter 1 and illustrated in Figures 2.25. Remaining BET calculation figures are included in Appendix.

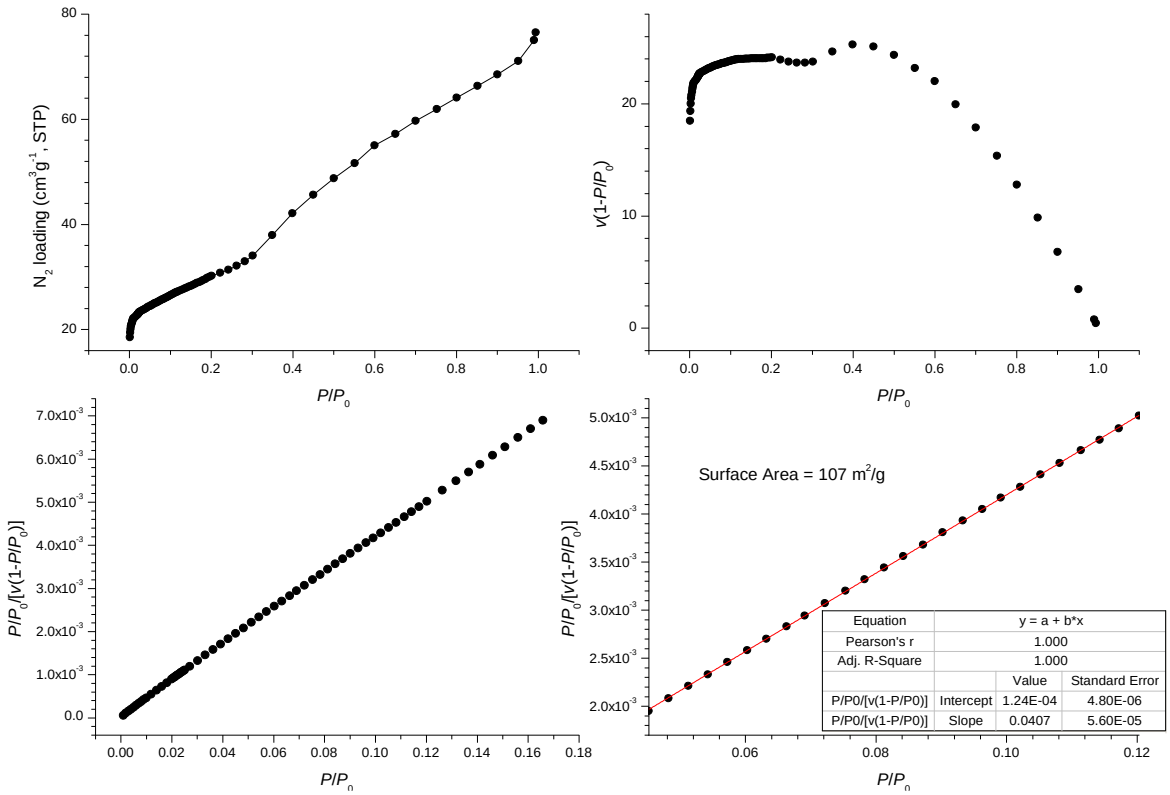

Figure 2.25: BET calculation for MUF20-Aβ from the N_2 isotherms at 77 K.

BET surface area calculations for MUF20-Aβ^T and MUF20-Aγ^T were unreliably low (surface areas of 2 g/m^2 for both materials calculated, see Appendix) due to insufficient gas uptake at low pressure related to partial pore collapse of the material.

The areas obtained (107, 56, and 413 m^2/g for MUF20-Aβ, MUF20-Aγ, and MUF20-Aβ` respectively) show that TPG-functionalization of the MUF20 framework increased the surface area of the MOF in the case of carbamate but not *tert*-butyl ester over the parent framework of 60 m^2/g reported for BMOF-1-bpdc reported by Cohen et al.[174] As the installed group adds surface area for gas molecules to adsorb onto, the decrease observed in MUF20-Aγ is likely due to a change in the MOF structure upon desolvation to exclude N_2 guest molecules. This is further supported by a solvent loss single crystal study presented later in Chapter 3. As expected, introduction of a free amine into the pillar-layer framework significantly increases apparent surface area as the polar functionality can interact with the quadrupole moment of N_2.

Unlike with the bpy-functionalized materials, MUF20-Bα and MUF20-Cα showed little to no uptake at low pressure under N_2 at 77 K related to a gate-opening pressure effect. More than 16 hrs were required to collect the first pressure point at 0.005 P/P$_0$ and attempts to collect lower P points were abandoned after 24 hrs. This is in contrast to MUF20-Aβ and MUF20-Aγ collections starting at 0.001 P/P$_0$ within 2 hrs. A preliminary run of Ar at 77 K for the bpdc-functionalized MUF20 MOFs showed similar large hysteresis and high P/P$_0$ initial gas uptake behaviour (see Appendix). The pore-blocking effect of bpdc functionalization vs bpy functionalization can be clearly seen in Figure 2.26.

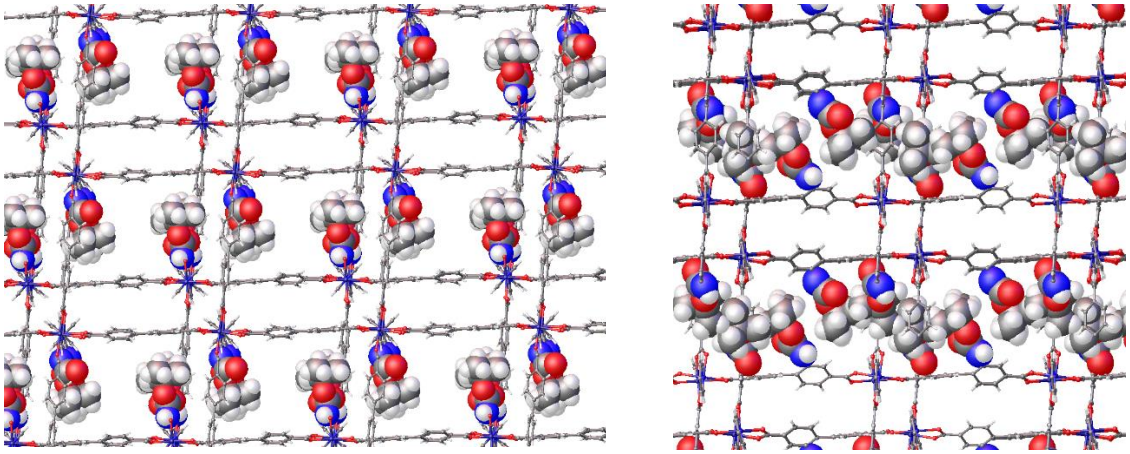

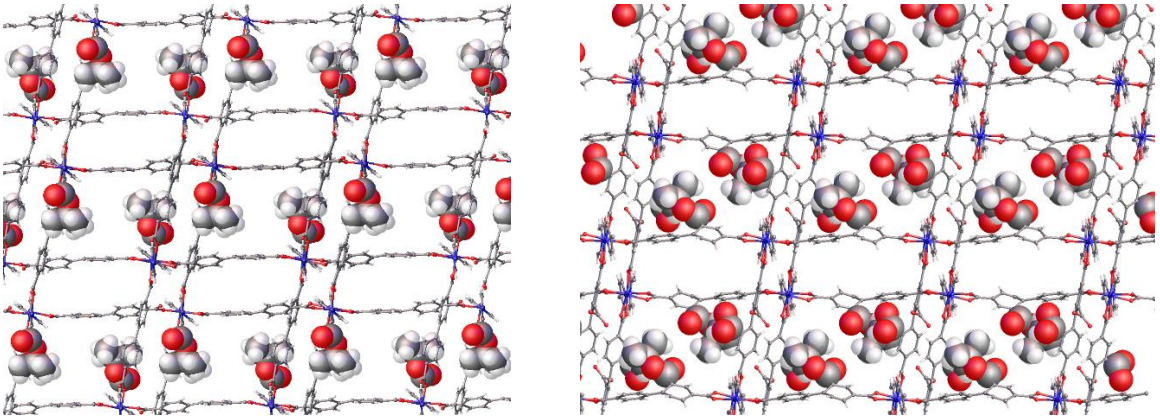

Figure 2.26: Filling of pores by TPGs placed on bpy (left) vs bpdc (right) by -NHBoc (top) and -TBE (bottom) functional groups. Atom colour code; C-grey, H-white, O-red, N-blue, Zn-purple.

Given above limitations, N_2 isotherms at 77 K yield extremely approximate BET surface area calculations for MUF20-Bα, MUF20-Cα, and MUF20-B^{T}α tabulated in Table 2.3. As an illustrative example, in the parent material BMOF-1-bpdc, the BET surface area calculated from the measurement of three independent samples ranges from 34 – 86 m^2/g.

MUF20-Cα (Figure 2.27) was least amenable to BET surface area calculation due to the sharply sigmoidal shape of the isotherm. Two different BET plots were used to illustrate the change in apparent surface area upon transitioning past the gate-opening pressure. At the typically low P/P_0 values used to calculate BET, MUF20-Cα has an apparent surface area of 64 m^2/g but when a second higher P/P_0 linear region of the BET plot is used post gate-opening pressure, a BET surface area of 754 m^2/g is obtained. As the former yields a slightly negative intercept and the latter is at high P/P_0, these are illustrative values only for comparison to MUF20-Aβ, MUF20-Aγ, and MUF20-Aβ^T.

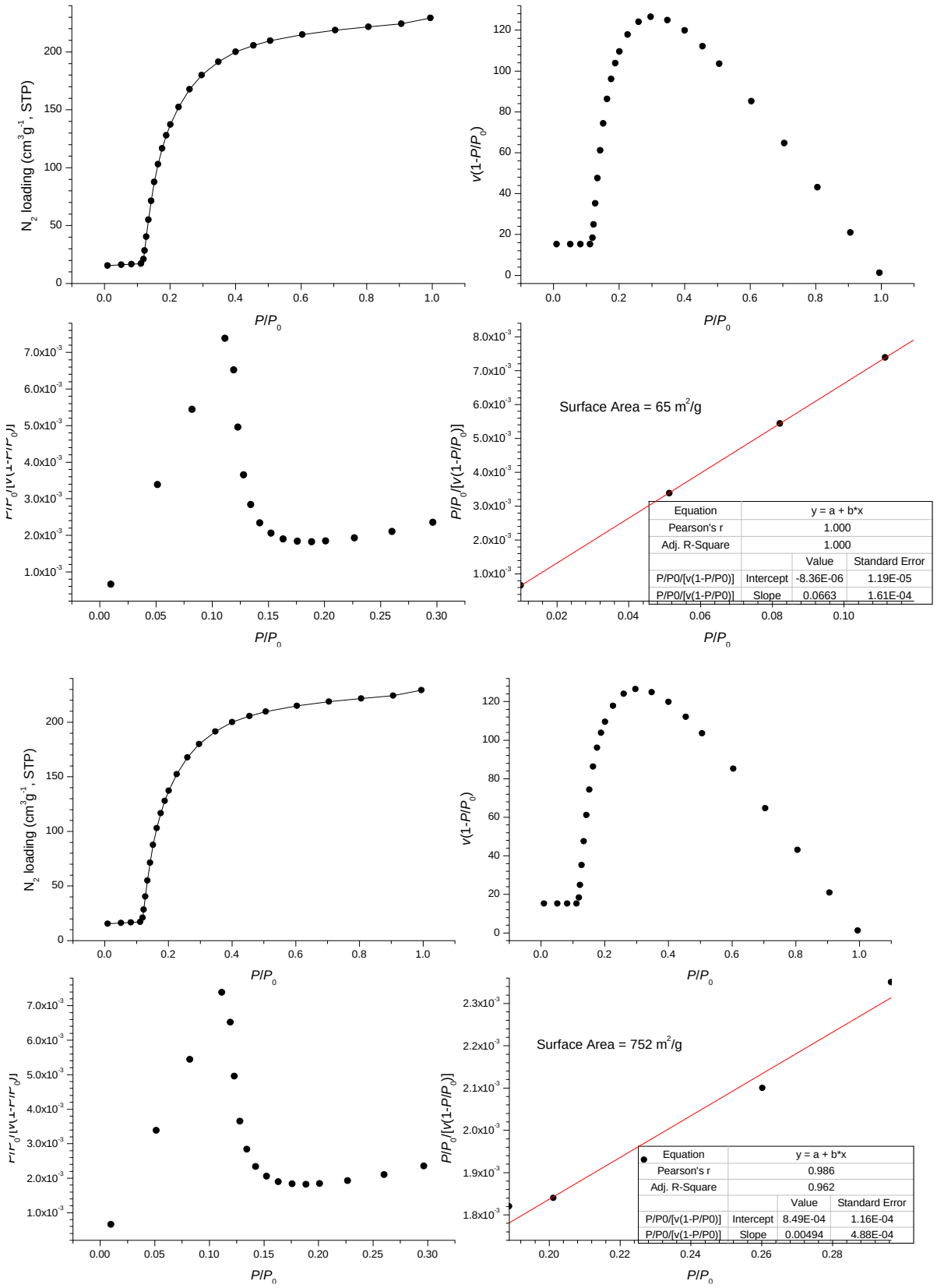

Figure 2.27: BET calculation for MUF20-Cα from the N_2 isotherms at 77 K using low (top) and higher (bottom) P/P_0 BET plot regions.

CO_2 is a more polarizable molecule than N_2 and so inaccuracy in surface area calculations arise. The interaction of the more polarizable CO_2 molecule probing the pore surface and greater influence of CO_2-CO_2 interactions result in an underestimation of the surface area, because assumptions of purely physisorption sorbate-gas interactions and negligible gas-gas interactions dictating monolayer formation become suspect.

However, there is some validity to this analysis with an investigation by Kim et al.[191] showing that for MOF materials of different pore size regimes one can obtain approximate BET surface areas matching within 30% to their geometric surface areas calculated from the single crystal structures. In an ultra-microporous only MOF with pore diameters < 7 Å, the BET areas became more accurate, approaching 10%. Additionally, they showed computationally that increasing the CO_2-adsorbate interaction strength increased the accuracy of the BET calculation by shifting the isotherm type closer to Type 1, enabling an improved determination of the linear region used for the BET plot as the impact of CO_2-CO_2 interactions was reduced. Approximate BET surface areas using CO_2 were calculated for the MUF-20 materials. An example is shown in Figure 2.28. These results are tabulated below (Table 2.3) along with full calculations in the Appendix.

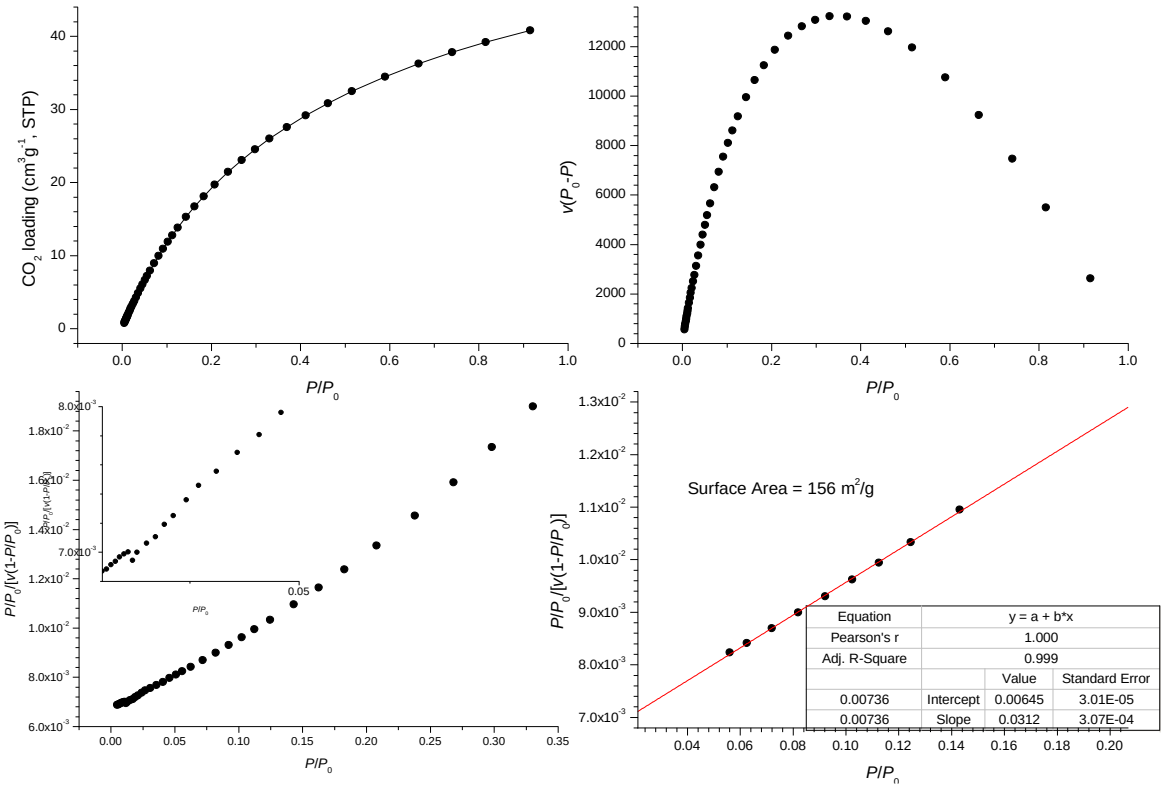

Figure 2.28: BET calculation for MUF20-Cα calculated from CO_2 isotherms at 273 K.

Table 2.3: Experimental and calculated* surface areas

MOF	Surface area (m^2/g)			
	BET (N_2)	Geometric (N_2)	BET(CO_2)	Geometric (CO_2)
MUF20-Aβ	107	848	40	980
MUF20-Aγ	56	793	55	958
MUF20-Aβ^T	2	-	86	-
MUF20-Aγ^T	2	-	35	-
MUF20-Aβ`	413	1197	135	1370
MUF20-Bα	413	522	111	623
MUF20-Cα	752	440	156	532
MUF20-B^{T}α	852	-	154	-

*calculated from solvent void volumes generated in Mercury v4.10. Details in Appendix.

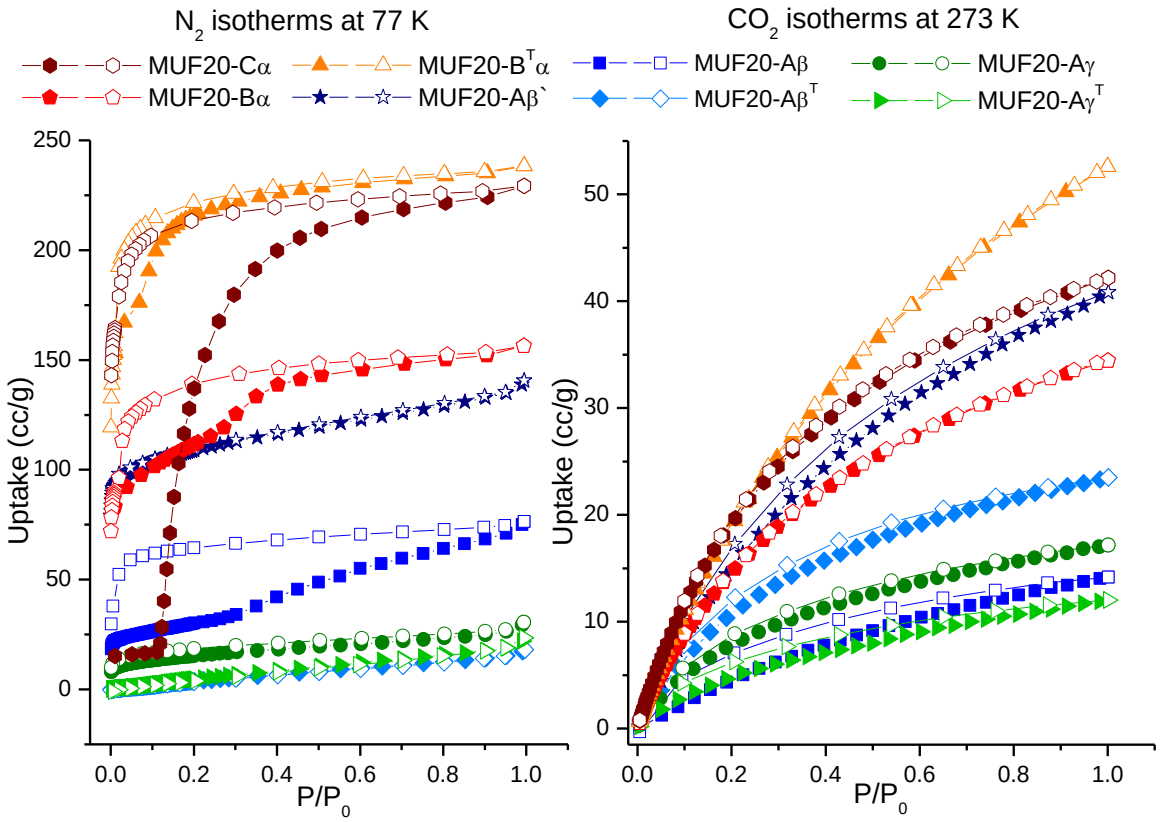

Figure 2.29: Volumetric N_2 (left) and CO_2 (right) adsorption (filled) and desorption (open) isotherms measured at 77 K and 273 K respectively. Lines are a guide to the eye only.

CO_2 isotherms were shown to give severely underestimated BET surface areas in all cases except in MUF20-Aγ and the partially collapsed materials, MUF20-Aβ^T and MUF20-Aγ^T. This is consistent with the likely solvent-evacuated structure of MUF20-Aγ having majority of pores within the ultramicroporous region (< 7 Å) and more suitable for CO_2 BET surface area analysis. For the thermally treated bpy-functionalized materials a carbon dioxide accessible surface area greater than the N_2 accessible surface area indicates that while the structure is degraded during thermolysis conditions, some porosity is maintained.

As mentioned in Chapter 1, caution in consideration of all BET surface areas must be taken as this is not strictly a probe accessible surface area so much as an apparent surface area that can be used as a rough estimate and fingerprint characterization of the material porosity. In comparison to the geometric surface areas calculated from the single crystal structure and probes of different sizes (see Appendix for full calculation details) there is clearly a huge difference between a static porous crystal model and the real structure undergoing dynamic change with guests, heat and pressure changes. However, the calculated surface areas are not outside the realm of possibility with the 1,4-diazabicyclo[2.2.2]octane (DABCO) and 1,4-benzenedicarboxylic acid (bdc)-based pillar-layer MOF, DMOF-1, having BET surface area of 1450 m^2/g[192] and nitro-functionalized DABCO and bpdc structure, DMOF-1-bpdc-NO_2, a BET surface area of 708 m^2/g. Given the low BET surface areas commonly encountered with the [Zn_2(bpdc)$_2$(bpy)] pillar-layer structures, functionalization of the bpdc ligand with an appropriate group should be considered as a route to increase porosity in this subset of MOFs.

As temperature increases the total gas uptake and observed hysteresis decrease as barrier to diffusion is lowered and any gate-opening structural changes are shifted to lower pressure.[184] This leads to the decreased gas uptake and lack of hysteresis observed in the N_2 isotherms collected at 273 K (Appendix).

At 273 K for N_2 and CH_4, MUF20-Aβ` has similar volumetric uptake as MUF20-Cα and MUF20-B^{T}α with MUF20-Aβ yielding the lowest uptake - even less than the partially degraded MUF20-Aβ^T and MUF20-Aγ^T materials. It is unclear what caused these results but as the uptake is low in general - giving rise to poor data quality artefacts such as negative gas sorption upon desorption - this was not investigated further. N_2 at 298 K was negligible/negative for all materials and so is attached in Appendix.

At higher temperatures, MUF20-Aγ^T shows a stronger effect of pore collapse on gas uptake than MUF20-Aβ^T. MUF20-Aβ^T contains free amino groups which can form strong interactions with incoming gases thus, with sufficient ambient energy for gas molecules to diffuse into the

partially collapsed structure, this increased enthalpy of interaction will yield a higher uptake. Additionally, the isotherm suggests potential mesopore formation upon thermolysis with larger total gas uptake due to increased volume of large pores formed in the hierarchical structure.

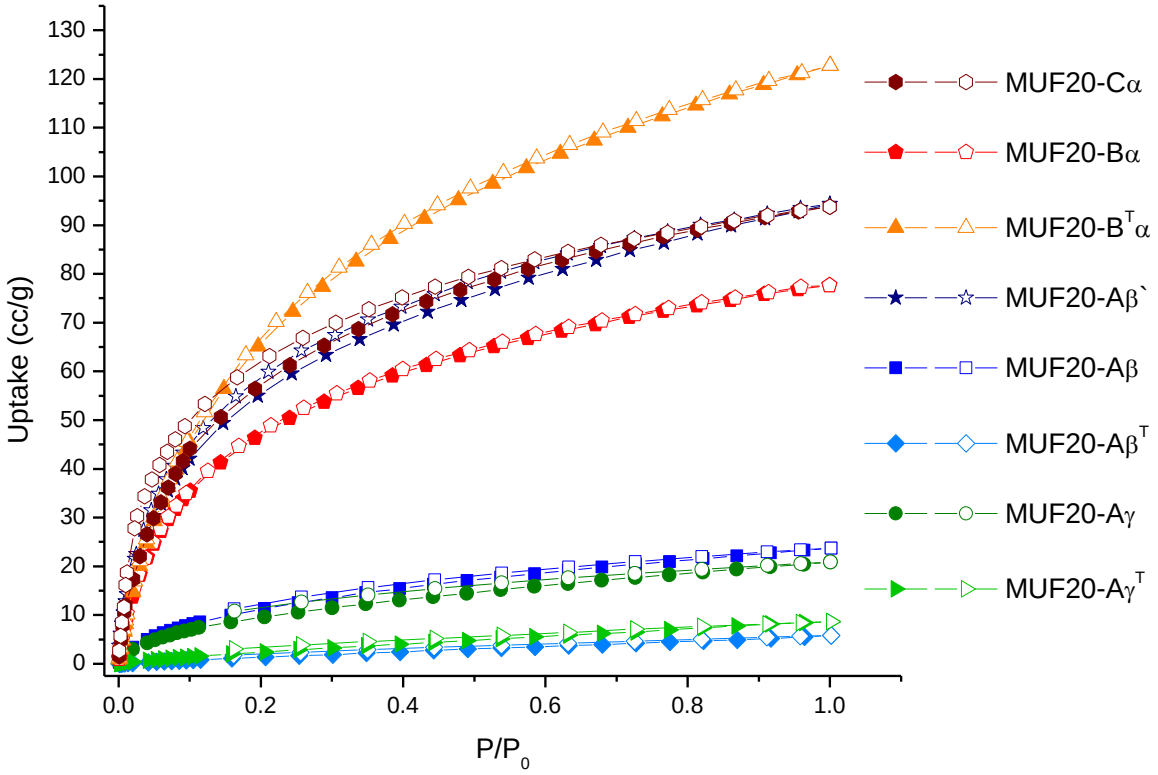

Figure 2.30: Volumetric H_2 adsorption (filled) and desorption (open) isotherms measured at 77 K. Lines are a guide to the eye only.

H_2 isotherms at 77 K (Figure 2.30) repeat the observation of N_2 where, despite increased bulk to occlude the pores, the bpdc-functionalized MOFs in fact show greater volumetric uptakes with the exception of MUF20-Aβ`. However, there is some shifting of the highest volumetric uptake due to changes in the pore size regime of the materials. The presence of narrower pores more accessible to the smaller $H_2$ molecule in MUF20B$^T$α and MUF20-Aβ` causes the former to now significantly exceed and the latter to match MUF20-Cα total gas uptake.

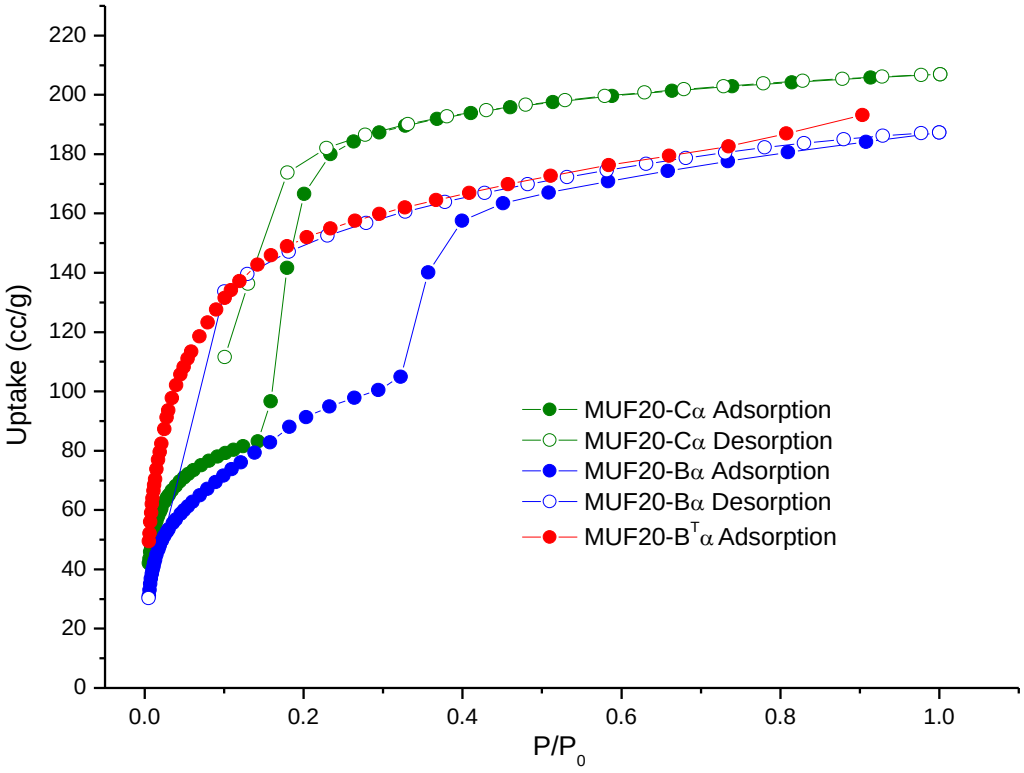

Figure 2.31: Volumetric CO_2 adsorption (filled) and desorption (open) isotherms measured at 195 K. Lines are a guide to the eye only.

To investigate the significant hysteresis observed in the N_2 isotherms at 77 K, low temperature isotherms for MUF20-Bα, MUF20-Cα, and MUF20-B^{T}α for CO_2 at 195 K were collected (Figure 2.31). A dramatic isotherm shape change is observed upon partial thermolysis of MUF20-Bα, with a shift from isotherm Type IV to an apparent Type I in the low pressure region of the adsorption curve. MUF20-B^{T}α illustrates that even revealing a quarter of the potential amine sites in MUF20-Bα can significantly affect material properties. Unfortunately, the desorption curve of MUF20-B^{T}α was not recorded due to condensation of CO_2 in the pores of the MOF at the same P/P_0 (with uptake suddenly increasing to 22,000 cc/g) most likely due to error in the temperature of the bath during data collection. The nature of the TPG substituent to tune hysteresis and uptake is observed, as installing a *tert*-butyl vs carbamate group shifts the required pressure for second uptake step lower from 0.33 to 0.18 P/P_0 and a narrower hysteresis is observed in the isotherm of MUF20-Cα compared to MUF20-Bα.

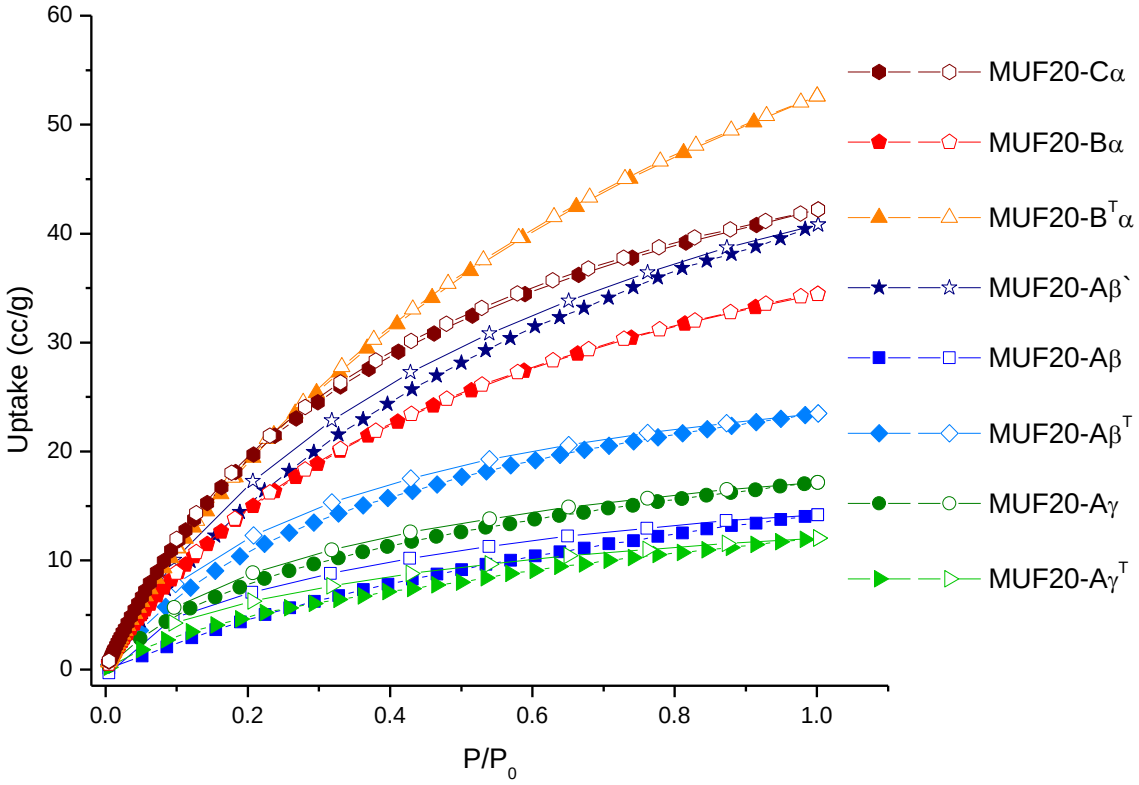

Figure 2.32: Volumetric CO_2 adsorption (filled) and desorption (open) isotherms measured at 273 K. Lines are a guide to the eye only.

Upon increasing the temperature to 273 K, the low temperature hysteresis behaviour in the more pore-occluding bpdc-functionalized MOFs disappears and selective presence of slight hysteresis in the functionalized bpy analogues is observed (Figure 2.32).

Free amines in both MUF20B^{T}α and MUF20-Aβ^T yielded an increase in total CO_2 uptake. In the case of MUF20-B^{T}α this correlates with the shown increase in pore volume upon thermolysis with maintained crystallinity. However, in the case of MUF20-Aβ^T, where the total volumetric uptake was markedly decreased upon thermolysis due to partial pore collapse (as indicated by decreased crystallinity by PXRD), this result must be explained in terms of the kinetic barrier to diffusion into the material being reduced at higher temperatures. Thus, the gas molecules are able to access otherwise blocked areas of the material where the free amine functionalities have higher enthalpy of interaction with CO_2 and so increase the gas uptake over the non-thermolyzed material. This also is observed at 298 K with CO_2 (Figure 2.33).

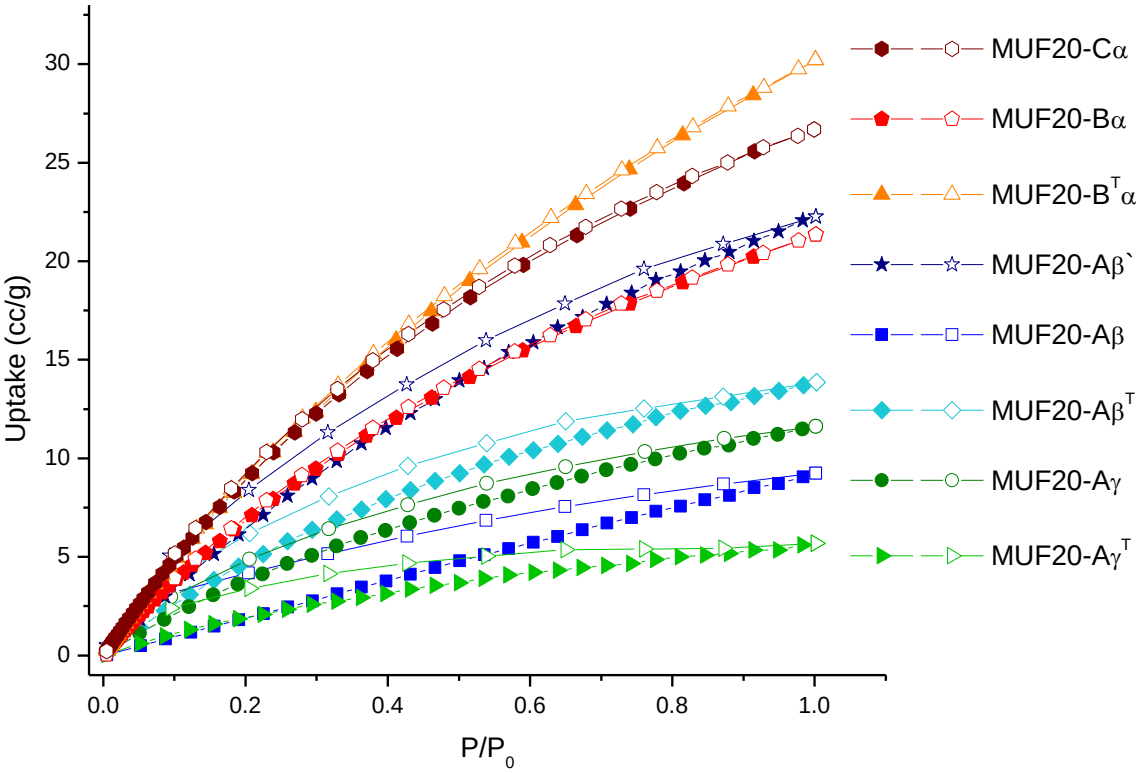

Figure 2.33: Volumetric CO_2 adsorption (filled) and desorption (open) isotherms measured at 298 K. Lines are a guide to the eye only.

MUF20-Aγ^T, with far more significant degradation of the framework upon thermolysis does not show this temperature dependent uptake as the barrier to diffusion is much greater than any enhancement upon access to the exposed carboxylic acid functional groups.

As with CO_2, CH_4 shows higher gas uptake by MUF20-Aβ^T despite decreased volume as the kinetic barrier to diffusion into the MOF is overcome (Figures 2.32, 2.33).

In absence of *in situ* PXRD-GS analysis or other guest-free solvent structures it is difficult to exclude the possibility that the hysteresis observed is solely an artefact of diffusion/insufficient equilibrium time. Thus, structure-gas sorption relationships can only be lightly inferred.

As shown by PXRD and GS results, the mono-functionalized MOFs presented were insufficiently stable under all thermolysis conditions trialled to date for fully thermolyzed materials to maintain crystallinity. However, this can be seen from the example detailed below to be more likely a feature of the limitation of this study than a characteristic of all TPG-functionalized pillar-layer MOFs.

2.2.6. Addressing thermal instability

Within the synthesis scheme for bpdc-TBE (see experimental section) is included that for another novel bpdc-TPG ligand, bpdc-2mh, carrying a carboxylic acid protected by a 2-methylhexyl ester group (see Figure 2.34). Although bpdc-2mh could not be resynthesized at the time despite trialling multiple conditions - and so is not included in the gas sorption comparison of mono-functionalized MUF20 frameworks – this MOF analogue yielded single crystal quality material post thermolysis. Due to the unique thermal stability of the bpdc-2mh MOF it is included in this work for single crystallographic comparison and as an indicator of the tuneability of this MOF platform for achieving, within the same framework, materials of differing properties - especially enhanced thermolytic robustness.

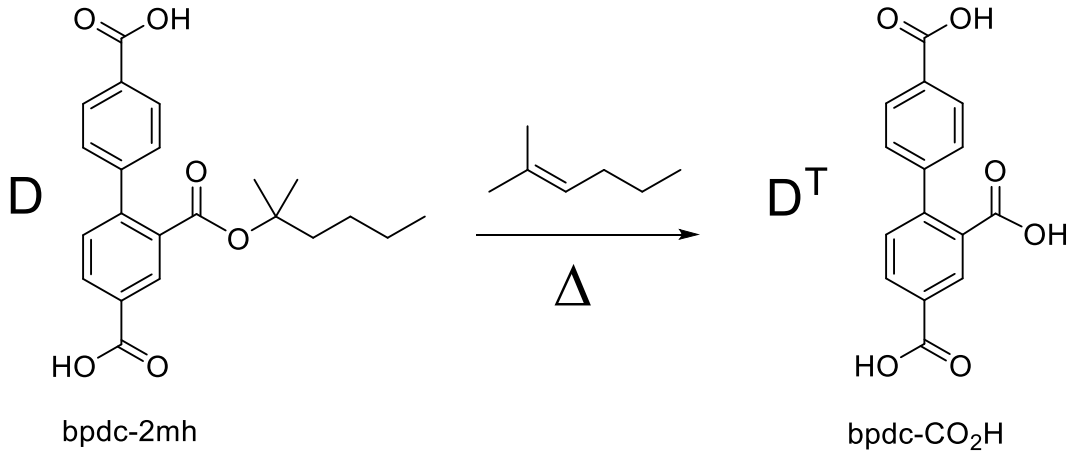

Figure 2.34: 2-methyl-2-hexylester bpdc (bpdc-2mh) ligand and thermolysis product.

Thermolytically stable [Zn_2(bpdc-2mh)$_2$(bpy)] (MUF20-Dα)

A slightly bulkier thermolabile protecting group than -NHBoc or -TBE, 2-methylhexyl ester (-2mh) was installed in the MUF20 framework under similar conditions - DMF:MeOH (1:4) with $Zn(NO_3)_2.4H_2O$, 1.6:1 bpy:bpdc-2mh – as for the rest of the TPG family. MUF20-Dα is interpenetrated and ^{1}H NMR spectroscopy of the digested MOF in DCl/DMSO-d_6 showed that the thermolabile protecting group, 2-methylhexyl ester, survived MOF synthesis (peaks between 0.5 and 1.5 ppm in Figure 2.35) and confirmed the presence of bpy in the MOF in the 1:2 bpy:bpdc linker ratio expected in a pillar-layer structure. TGA traces of the MOF and ligand are included in experimental at the end of this chapter.

MUF20-Dα was exceedingly stable upon exposure to atmosphere and, remarkably, single-crystal quality thermolyzed MOF samples were obtained best when solvent guests were

completely evacuated and the framework heated under $Ar_{(g)}$ in a microwave vessel at 160 ^{o}C for 3 hours. The deprotected MOF MUF20-D^{T}α [Zn_2(bpdc-$CO_2H)_2$(bpy)] was digested in DCl/DMSO-d_6 and the 2-methylhexyl ester peaks (between 0.5 and 1.5 ppm) were shown through ^{1}H NMR spectroscopy to have disappeared, indicating the release of 2-methylhex-2-ene to reveal a carboxylic acid functionality in the framework (Figure 2.35).

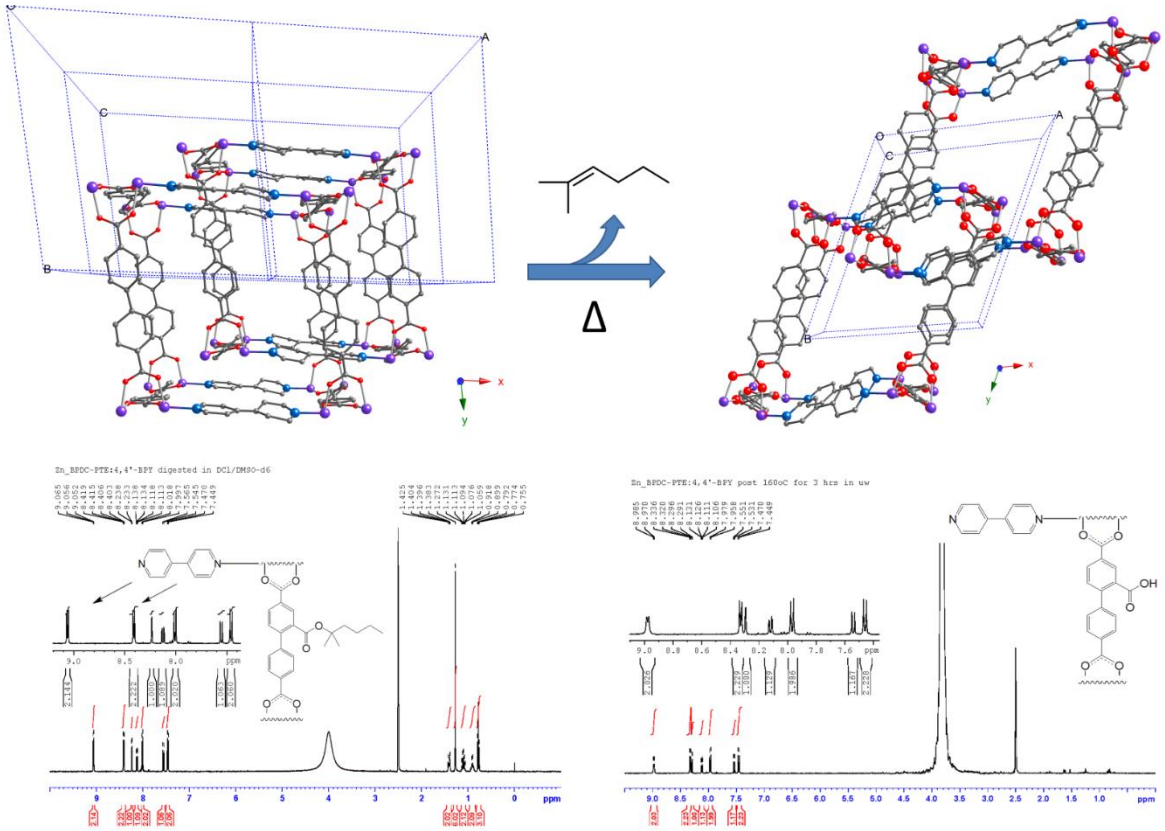

Figure 2.35: Single-crystal x-ray structures of MUF20-Dα pre- and post- thermolysis and corresponding ^{1}H NMR spectra. For clarity the atoms of the introduced functional group are omitted. Atom colour code is as follows: C-grey, O-red, N-blue, Zn-purple.

Single-crystal X-ray analysis showed a drastic change in the unit cell of the thermolyzed framework (Figure 2.36, Table 2.4).

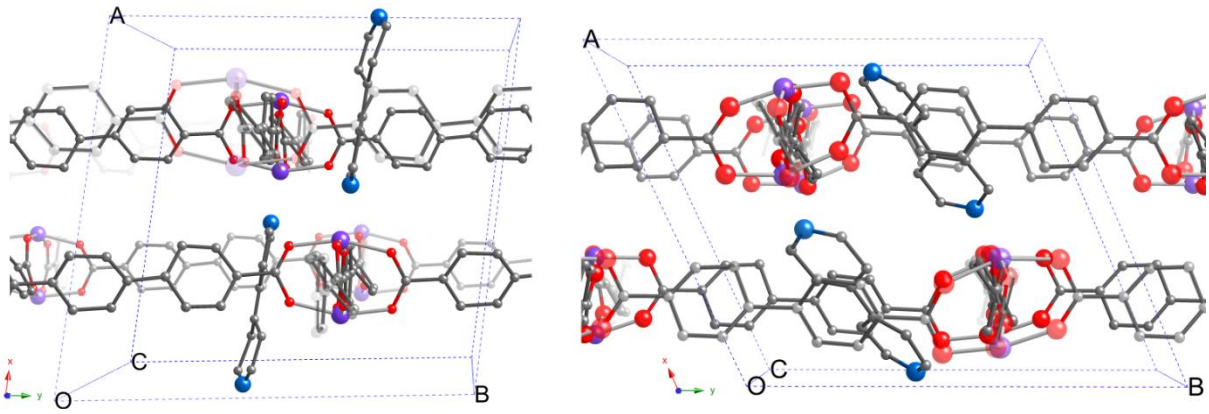

Figure 2.36: Position of the bpy ligands in unit cell of MUF20-Dα pre (left) and post (right) thermolysis. Atom colour code; C-grey, O-red, N-blue, Zn-purple.

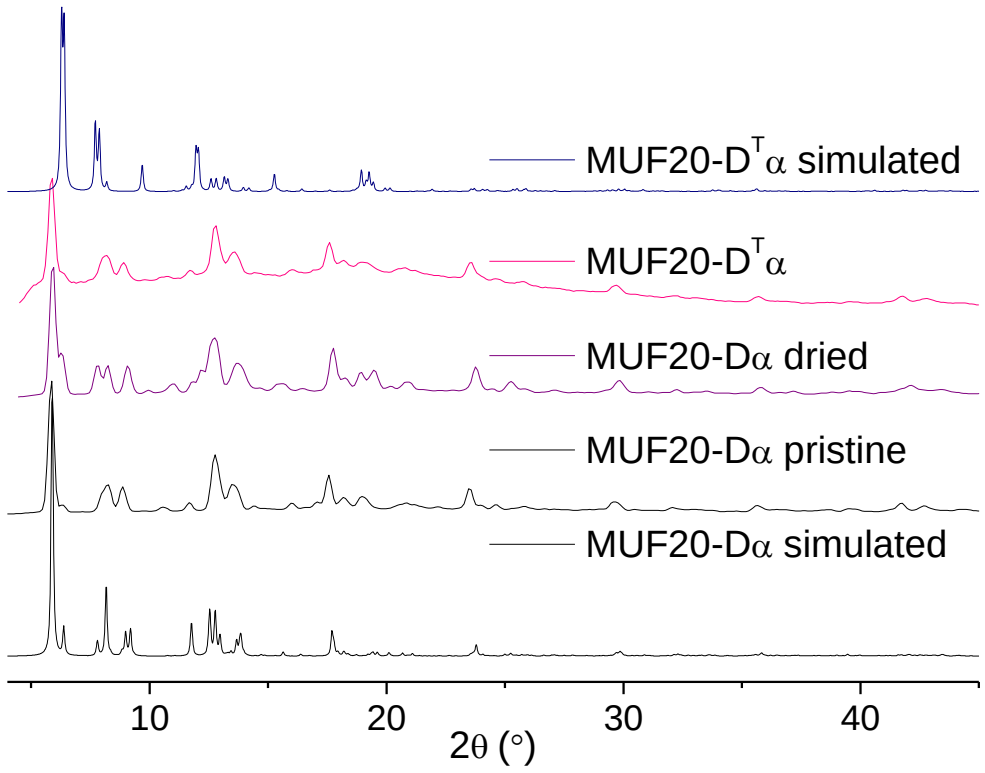

Figure 2.37: PXRD analysis of MUF20-Dα pristine, dried, pre and post thermolysis and the PXRD diffractogram simulated from the thermolyzed single crystal structure.

The cell decreased in length in all directions, although most (>0.5 Å) along the *a* axis. Subsequently, the unit cell volume was also greatly decreased (3169 to 2649 Å^3). Most drastic is the change in the unit cell angles, visually obvious above in the distortion of the thermolyzed crystal structure, due to the slanting of the bpy pillars from approximately perpendicular to lie more within the plane of the zinc-carboxylate layers (Figure 2.36). This brings the ligands of

the two interpenetrated frameworks closer along the *a* axis, explaining the larger decrease in this unit cell length relative to the *b* and *c* axis.

Measurement of the thermal expansion of related materials with insight from variable temperature single crystal diffraction (VT-SCD), indicates a combined stretching-tilting mechanism can be involved.[193]

Table 2.4: The unit cell parameters of MUF20-Dα pre- and post-thermolysis.

	MUF20-Dα	MUF20-D^{T}α
	$[Zn_2(bpdc\text{-}2mh)_2(bpy)]$	$[Zn_2(bpdc\text{-}CO_2H)_2(bpy)]$
Space group	*P*-1	*P*-1
Unit cell	**a** 13.999(5)	**a** 13.469(3)
Dimensions	**b** 15.191(5)	**b** 15.103(3)
Å / º	**c** 15.204(5)	**c** 15.126(3)
	α 82.288(5)	α 91.063(6)
	β 84.860(5)	β 109.658(8)
	γ 82.624(5)	γ 112.036(8)
Unit cell volume (Å^3)	3168.9(19)	2648.9(9)

Notably, the unit cell volume is decreased upon thermolysis as the lattice shift to increase van der Waals interactions and orientate the carboxylic acid groups towards each other (Figure 2.38). This suggest that some decrease in volume of a material upon thermolysis may result from a crystalline transition to a more densely packed material.

Thus, similar to MUF20-Aγ^{T}, MUF20-Dα demonstrated the success of the thermolabile protecting group strategy in incorporating into a MOF framework a carboxylic acid functionality which was otherwise incompatible with MOF direct synthesis due to the tendency for the free carboxyl group to also coordinate zinc. Additionally, despite changing the MOF unit cell structure, crystallinity is sufficiently maintained through thermolysis for single-crystal x-ray analysis and this crystallinity is confirmed in the bulk material through PXRD. NMR analysis confirms that the ligands are in expected ratio and material largely clean post thermolytic treatment.

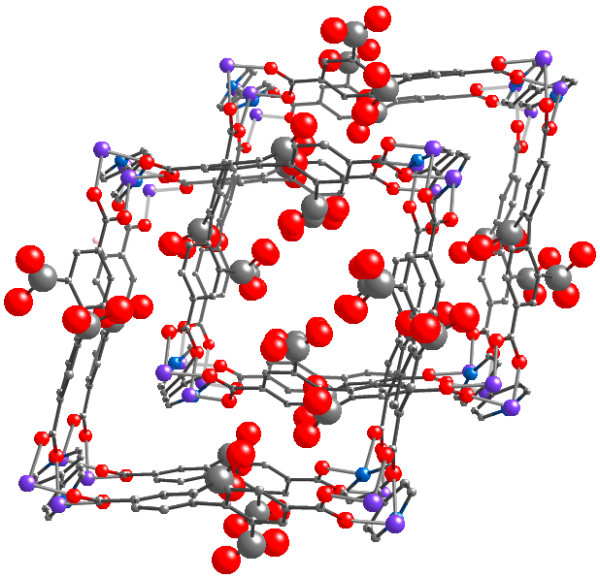

Figure 2.38: Thermolyzed single crystal structure of MUF20-D^{T}α showing free carboxylic acid groups (hydrogens are omitted for clarity). Atom colour code; C-grey, O-red, N-blue, Zn-purple.

The distinguishing characteristics most likely to lie behind this thermolytic resilience is the presence of long alkyl chains within the MOF pores. Unlike the case of -TBE or -NHBoc, these long alkyl chains allow interaction with the phenyl group of the second lattice without distortion of the framework (Figure 2.39). Upon thermolysis the alkyl chains can maintain this interaction as they slowly diffuse through the pores and there is no sudden collapse of structure to maximise van der Waals interactions.

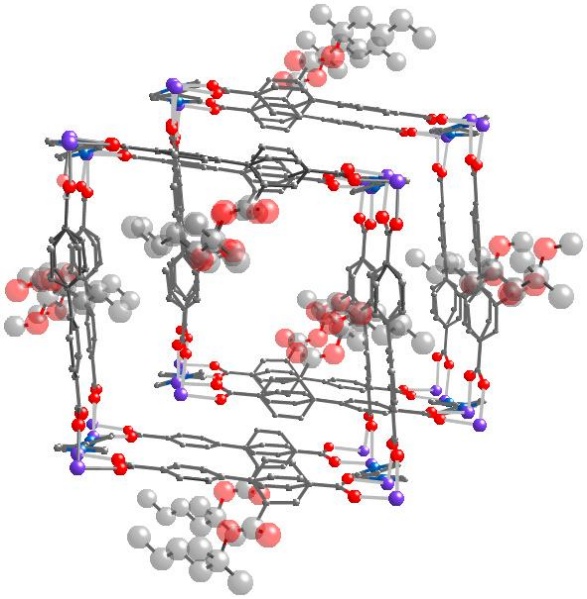

Figure 2.39: MUF20-Dα single crystal structure, the TPGs are presented as partially transparent larger radii and some disordered sidechains omitted for clarity. Atom colour code; C-grey, O-red, N-blue, Zn-purple.

During thermolysis it is probable that these alkyl chains act like solvent guests as in Henke et al.[177] These substituents interact with themselves and the framework and so may act as a support for the framework during thermolysis, as in the related structure examined by Henke, increased stability of the material was observed.

2-Methylhex-2-ene is also different in shape and polarity to the isobutylene and CO_2 fragments which are roughly more spherical and polar. As with the low polarity solvents now recommended for use in activation procedures for optimal surface area,[183] the lower polarity, slow diffusing 2-methylhex-2-ene fragments may optimally undergo thermolytic expulsion from the flexible pillar-layer MOF without triggering abrupt pore collapse.

Recent literature on optimizing activation procedures for MOF materials has recommended the use of low polarity alkyl solvents such as pentane, which has passing similarity to the 2-Methylhex-2-ene fragment released during thermolytic formation of MUF20-$D^T\alpha$, further supporting this hypothesis and future area of research. These insights will lead to more targeted development of TPGs for flexible MOF structures.

2.3. Conclusion

In this work, a novel TPG ligand carrying a carboxylic acid functionality protected by a *tert*-butyl ester group was synthesized and successfully incorporated into a pillar-layer framework. The family of mono-functionalized MUF20-Aα MOFs was completed, characterized by XRD, ^{1}H NMR spectroscopy, GS, and thermolysis undertaken. The material properties at each stage were compared and conclusions drawn as to the effect of substituent type and position on the MOF structure and bulk properties. Insights for further studies were gained such as improving thermal stability of flexible pillar-layer MOFs containing TPGs by appending a pore-filling alkyl chain to the thermolabile protecting groups to support against pore collapse during thermolysis.

2.4. Experimental section

2.4.1. General procedures

All starting compounds and solvents were used as received from commercial sources without further purification unless otherwise noted. NMR spectra were recorded at room temperature

on a Bruker-500 Avance instrument, with the use of the solvent proton as an internal standard. Thermogravimetric analysis (TGA) was performed on a TA Instruments Q50 instrument.

2.4.2. Ligand synthesis and characterization

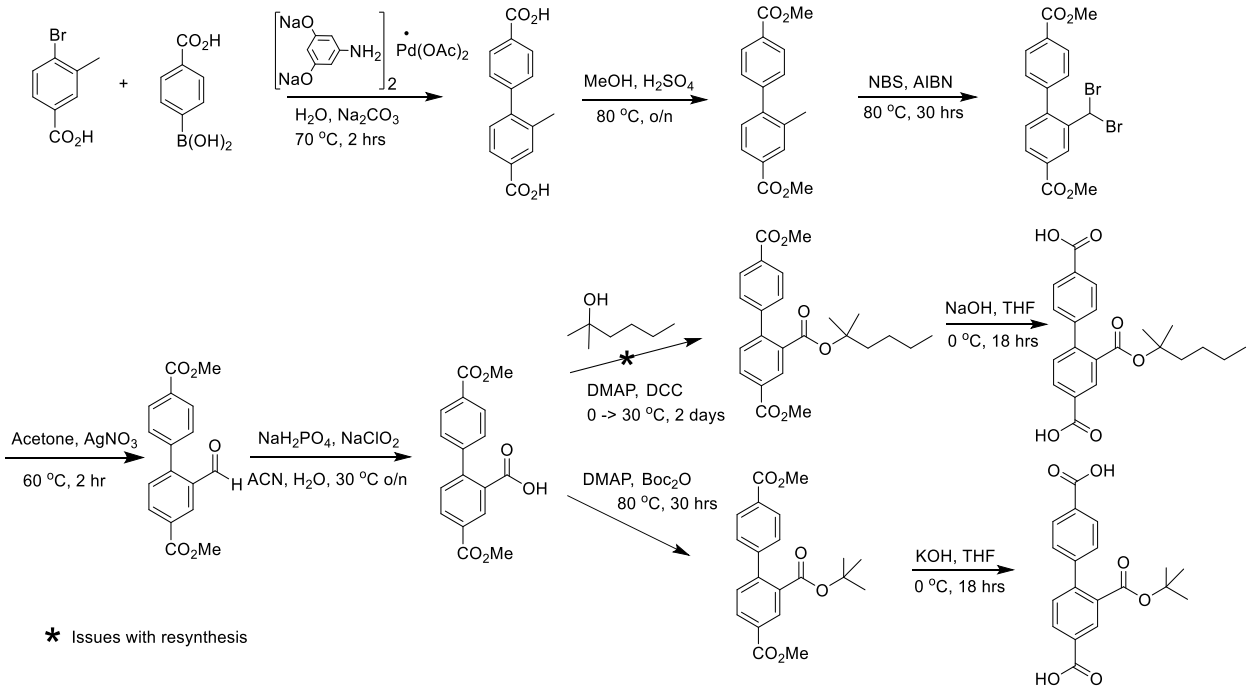

Only the final steps are shown below, full bpdc-TBE ligand synthesis is included in Appendix.

2-*tert*-Butyl 4,4`-dimethyl biphenyl-2,4,4`-tricarboxylate

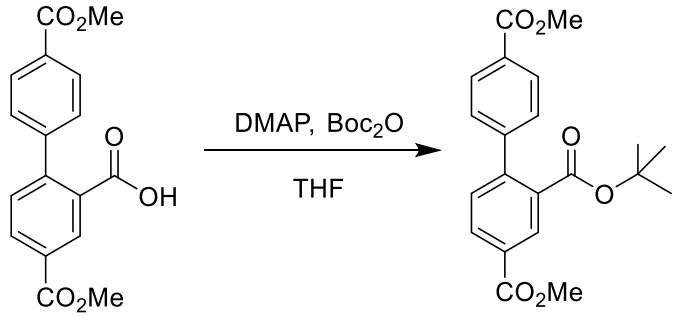

Dimethyl 2-carboxylic acid biphenyl-4,4`-dicarboxylate (1.50 g, 4.78 mmol) and DMAP (518 mg, 4.24 mmol) were suspended in dry THF (30 mL) and placed under Ar(g) before refluxing at 88 °C for 15 minutes. Di-*tert*-butyl dicarbonate (7.61 g, 34.9 mmol) in dry THF (5 mL) was then added dropwise over 25 minutes *via* syringe during which time the opaque suspension formed a clear yellow solution, gradually darkening to a dark brown. The brown/black solution was refluxed for 15 hours. After cooling to room temperature, additional 4-dimethylaminopyridine (DMAP) (512 mg, 4.19 mmol) was added before returning to reflux followed by dropwise addition of di-*tert*-butyl dicarbonate (6.01 g, 27.5 mmol) in dry THF (5

mL). After 2 hours the solvent was then removed *in vacuo* and the dark brown/black fluid cooled on ice before extracting with 1 M KOH and CH_2Cl_2 (5 x 20 mL). The organic layer was dried over Na_2SO_4, filtered and solvent removed. The dark brown solid was then dissolved in minimum CH_2Cl_2 and purified *via* silica flash column chromatography (CH_2Cl_2) to afford a colourless oil and white solid (1.48 g, 84%). ^{1}H NMR (400 MHz, $CDCl_3$) δ 8.46 (d, *J* = 1.5 Hz, 1H), 8.16 (dd, *J* = 8.0, 1.8 Hz, 1H), 8.09 (d, *J* = 8.6 Hz, 2H), 7.40 (d, *J* = 8.4 Hz, 3H), 3.96 (s, 3H), 3.95 (s, 3H), 1.27 (s, 9H).

2-(*tert*-Butoxycarbonyl)biphenyl-4,4`-dicarboxylic acid

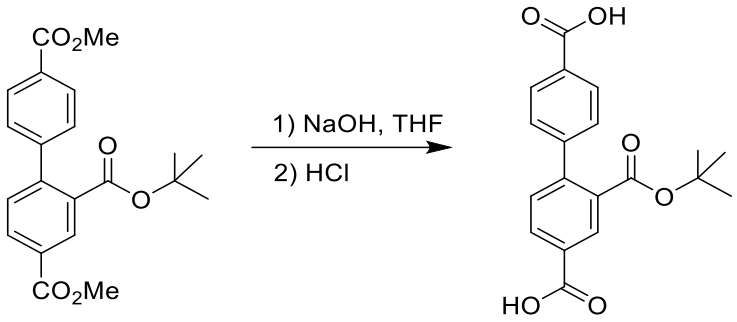

Dimethyl 2-carboxylic acid biphenyl-4,4`-dicarboxylate (1.20 g, 3.22 mmol) was dissolved in dry THF (18 mL), placed under Ar(g) and cooled on ice before the addition of 1 M NaOH (28.5 mL, 28.5 mmol). The opaque suspension was stirred on ice, allowing to gradually warm to room temperature and stirred for 3 hrs. THF was then removed *in vacuo* before cooling the aqueous layer on ice and gradually acidifying with 1 M HCl to pH 2.0. The fine white solid was then collected via suction filtration, washing thoroughly with H_2O before drying overnight under high vacuum to yield a fine white powder (1.04 g, 94%). ^{1}H NMR (500 MHz, DMSO-d_6) δ 13.20 (s, 2H), 8.25 (s, 1H), 8.13 (d, *J* = 8.0 Hz, 1H), 8.02 (d, *J* = 8.1 Hz, 2H), 7.56 (d, *J* = 8.0 Hz, 1H), 7.45 (d, *J* = 8.1 Hz, 2H), 1.23 (s, 9H).

TGA of all bpy and bpdc ligands used

The unprotected and unfunctionalized bpy and bpdc ligands were analyzed by TGA for comparison against the thermal properties of the TPG ligands, bpy-NHBoc, bpy-TBE, bpdc-NHBoc and bpdc-TBE. The bpy-CO_2H TGA trace is noticeably shifted to a higher temperature for first weight loss step and this is explained by the isolation of a bpy-CO_2K polymer that persisted post Sephadex purification of the ligand batch.

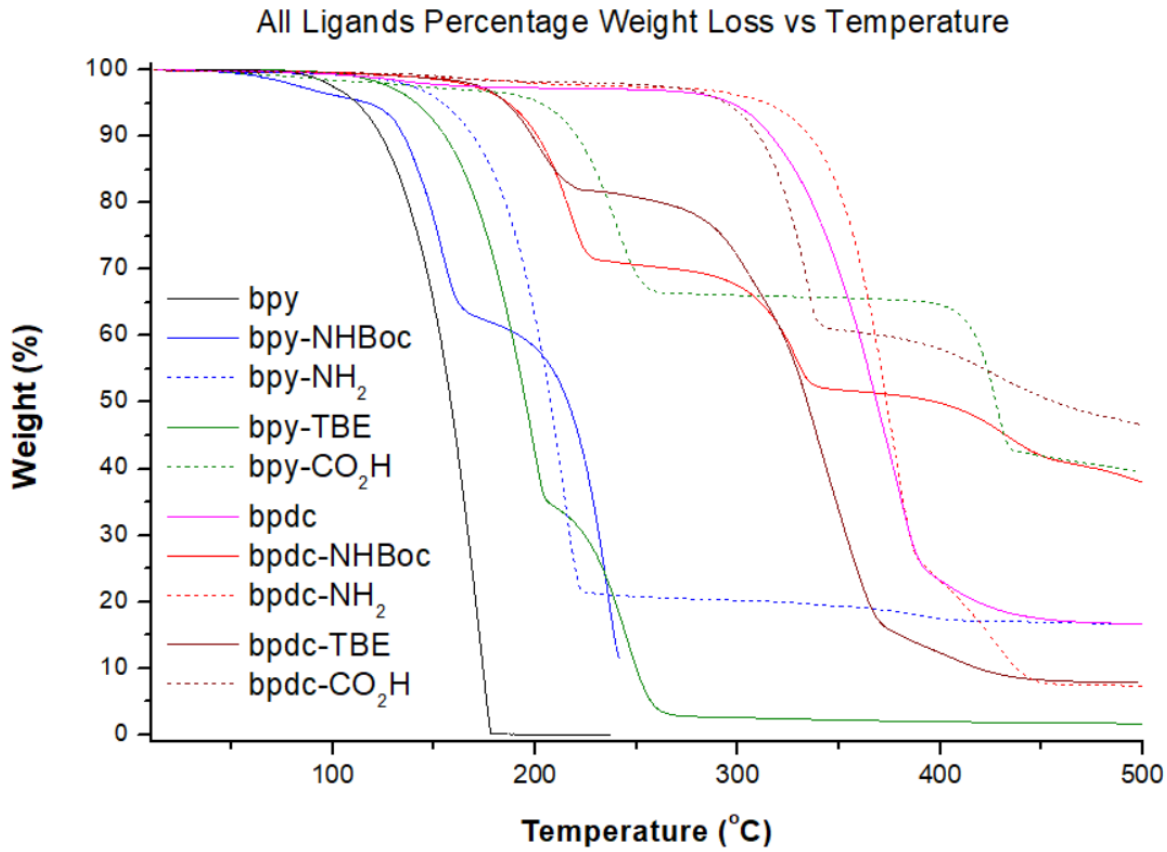

Figure 2.40: Thermogravimetric analysis (TGA) traces of unfunctionalized, unprotected and TPG-protected bpy and bpdc ligands.

2.4.3. MOF synthesis and characterization

^{1}H NMR analysis of digested MUF20 MOF samples

For ^{1}H NMR spectroscopy, the mother liquor of the as-synthesized MOF crystals was replaced with fresh dry DMF multiple times, followed by repeated washing (>3) and subsequent soaking in dry CH_2Cl_2 for several hours. The excess CH_2Cl_2 was then decanted and the samples placed under vacuum overnight to remove residual solvent from the pores. The crystals were then digested using the following protocol: 23 µL of a 35% DCl solution in D_2O was mixed with 1 mL of DMSO-d_6 to give a DCl/DMSO-d_6 stock solution. Around 5 mg of MOF was digested in 150 µL of this stock solution together with 480 µL of DMSO-d_6. Samples were briefly sonicated as needed and spectra were acquired immediately following dissolution.

Thermogravimetric Analysis (TGA)

Thermogravimetric analyses were performed on a TA Instruments Q50 instrument. Fresh MOF samples were prepared as for NMR analysis except that samples were placed under high

vacuum for a minimum of 24 hours. Samples were then transferred to an aluminum sample pan and measurements taken under an N_2 flow with a heating rate of 5 °C /min.

Powder X-ray diffraction patterns

All powder X-ray diffraction experiments were carried out on a Rigaku Spider X-ray diffractometer with Cu K_α radiation (Rigaku MM007 microfocus rotating-anode generator), monochromated and focused with high-flux Osmic multilayer mirror optics; diffraction peaks were recorded on a curved image plate detector. The data were obtained from freshly prepared MOF samples that had been minimally ground into slurry in a small amount of DMF, DEF or DBF (solvent dried on molecular sieves) and kept damp with solvent throughout the measurement. The two-dimensional images of the Debye rings were integrated with 2DP[194] (Version 1.0.3.4) to give *I versus* 2θ diffractograms. The predicted powder patterns were generated from their single-crystal structures using Mercury v4.10.

Single crystal X-ray diffraction

MOF crystals were mounted on a MiTaGen mylar loop, placed into dry DEF or DBF before coating in Fomblin oil and placed under cold stream at stated temperature in crystallography table. Diffraction data was collected on a Rigaku Spider diffractometer equipped with a MicroMax MM007 rotating-anode generator (Cu K_α radiation, 1.54180 Å), high-flux Osmic multilayer mirror optics; diffraction peaks were recorded on a curved image-plate detector. Data were collected at the temperatures listed and were integrated, scaled, and averaged with FS_Process.[195] XPREP was used to determine the space group and the structures were solved using SHELXS or SHELXT and refined with SHELXL.[196] Platon was employed to determine the solvent accessible volume.[197] All non-hydrogen atoms were found in the electron density difference map. All hydrogen atoms were calculated using the appropriate restraints. All non-hydrogen atoms were refined anisotropically except in cases justified in CIF.

Table 2.5: Crystallography data of MUF20-Aβ and MUF20-Aβ`

MOF	**MUF20-Aβ**	**MUF20-Aβ`**
Formula	$C_{21.5}H_{16.5}N_{1.5}O_5Zn$	$C_{19}H_{12}N_{1.5}O_4Zn$
Formula weight	441.23	390.67
Crystal size (mm)	0.081 × 0.075 × 0.063	0.445 × 0.278 × 0.159
Temperature (K)	126	119
Wavelength (Å)	1.54187	1.54187
Crystal system	Triclinic	Triclinic
Space group	*P*-1	*P*-1
Unit cell lengths (Å)	a = 13.984(5) b = 15.193(6) c = 15.195(6)	a = 14.012(3) b = 15.210(3) c = 15.232(3)
Unit cell angles (°)	α = 79.737(17) β = 87.915(18) γ = 82.984(16)	α = 79.972(8) β = 85.371(7) γ = 82.836(6)
Unit cell volume ($Å^3$)	3153(2)	3166.1(11)
Z	4	4
D_{calc} (g cm^{-3})	0.930	0.820
μ (mm^{-1})	1.270	1.198
F(000)	904.0	794
Reflns coll./unique, R_{int}	44553 / 11800, 0.0961	39715 / 11777, 0.1782
Data range	8.0 Å > *d* > 0.81 Å	8.0 Å > *d* > 0.81 Å
Index ranges	-17≤*h*≤16, -18≤*k*≤18, -16≤*l*≤18	-16≤*h*≤17, -18≤*k*≤18, -17≤*l*≤13
Completeness	95.2 %	94.4%
T_{min}, T_{max}	0.508, 1.00	0.564, 1.00
R indices for data with $I>2\sigma(I)$	R_1 = 0.1082; wR_2 = 0.3032	R_1 = 0.1189; wR_2 = 0.3006
R indices for all data	R_1 = 0.1504; wR_2 = 0.3379	R_1 = 0.2426; wR_2 = 0.3456
Largest difference peak and hole (e $Å^{-3}$)	1.13/-1.78	0.83/-0.75

Table 2.6: Crystallography data of MUF20-Aγ, and MUF20-Aγ-MeOH Loss

MOF	**MUF20-Aγ**	**MUF20-Ay-MeOH Loss**
Formula	$C_{21.5}H_{16}NO_5Zn$	$C_{43}H_{32}N_2O_{10}Zn_2$
Formula weight	433.72	867.44
Crystal size (mm)	0.223 × 0.212 × 0.198	0.47 × 0.30 × 0.15
Temperature (K)	173	153
Wavelength (Å)	1.54187	1.54187
Crystal system	Triclinic	Monoclinic
Space group	*P*-1	$P2_1/c$
Unit cell lengths (Å)	a = 14.1684(16) b = 15.2099(15) c = 15.226(2)	a = 14.1030(3) b = 15.2176(4) c = 29.468(2)
Unit cell angles (°)	α = 103.443(8) β = 91.726(7) γ = 92.642(7)	α = 90 β = 92.409(7) γ = 90
Unit cell volume ($Å^3$)	3185.0(7)	6318.6(5)
Z	4	4
D_{calc} (g cm^{-3})	0.905	0.912
μ (mm^{-1})	1.247	1.257
F(000)	888.0	1776
Reflns coll./unique, R_{int}	31785 / 11305, 0.1447	54266 / 12177, 0.0608
Data range	8.0 Å > *d* > 0.81 Å	8.0 Å > *d* > 0.81 Å
Index ranges	-12≤*h*≤16, -17≤*k*≤18, -18≤*l*≤18	-17≤*h*≤12, -17≤*k*≤18, -32≤*l*≤36
Completeness	90.2 %	98.0 %
T_{min}, T_{max}	0.564, 1.00	0.443, 1.00
R indices for data with $I>2\sigma(I)$	R_1 = 0.2290; wR_2 = 0.5075	R_1 = 0.0963; wR_2 = 0.3188
R indices for all data	R_1 = 0.2909; wR_2 = 0.5541	R_1 = 0.1143; wR_2 = 0.3413
Largest difference peak and hole (e $Å^{-3}$)	1.92/-1.18	1.03/-1.13

Table 2.7: Crystallography data of MUF20-Bα, MUF20-Cα, and MUF20-Dα

MOF	**MUF20-Bα**	**MUF20-Cα**	**MUF20-Dα**
Formula	$C_{31.88}H_{27.1}N_{2.54}O_8Zn_{1.33}$	$C_{28.67}H_{19.33}N_{1.33}O_8Zn_{1.33}$	$C_{47}H_{38}N_2O_{12}Zn_2$
Formula weight	660.94	597.61	953.12
Crystal size (mm)	0.537 × 0.451 × 0.445	0.07 × 0.30 × 0.10	0.41 × 0.17 × 0.19
Temperature (K)	153	163	163
Wavelength (Å)	1.54187	1.54187	1.54187
Crystal system	Triclinic	Triclinic	Triclinic
Space group	*P*-1	*P*-1	*P*-1
Unit cell lengths (Å)	a = 13.9887(4) b = 15.1934(11) c = 15.2045(11)	a = 13.9898(5) b = 15.1487(4) c = 15.1715(11)	a = 13.999(5) b = 15.191(5) c = 15.204(5)
Unit cell angles (°)	α = 87.058(6) β = 81.071(6) γ = 83.746(6)	α = 79.013(6) β = 83.067(6) γ = 82.204(6)	α = 82.288(5) β = 84.860(5) γ = 82.624(5)
Unit cell volume (Å^3)	3171.4(3)	3112.2(3)	3168.9(19)
Z	3	3	2
D_{calc} (g cm^{-3})	1.038	0.957	0.999
μ (mm^{-1})	1.338	1.315	0.802
F(000)	1020.0	914.0	979.0
Reflns coll./unique, R_{int}	42028 / 11741, 0.0627	40445 / 11443, 0.1264	45523 / 11880, 0.1005
Data range	8.0 Å > *d* > 0.81 Å	8.0 Å > *d* > 0.81 Å	8.0 Å > *d* > 0.81 Å
Index ranges	-16≤*h*≤17, -13≤*k*≤18, -18≤*l*≤18	-15≤*h*≤10, -18≤*k*≤18, -18≤*l*≤18	-16≤*h*≤11, -18≤*k*≤18, -18≤*l*≤18
Completeness	94.3 %	98.0 %	95.4 %
T_{min}, T_{max}	0.443, 1.00	0.548, 1.00	0.521, 1.00
R indices for data with *I*>2σ(*I*)	R_1 = 0.1140; wR_2 = 0.3409	R_1 = 0.1248; wR_2 = 0.3221	R_1 = 0.1655; wR_2 = 0.4114
R indices for all data	R_1 = 0.1274; wR_2 = 0.3691	R_1 = 0.2228; wR_2 = 0.3842	R_1 = 0.2112; wR_2 = 0.4532
Largest difference peak and hole (e Å^{-3})	1.82/-1.68	0.71/-0.70	1.53 / −1.01

Table 2.8: Crystallography data of MUF20-$D^T\alpha$

MOF	**MUF20-$D^T\alpha$**
Formula	$C_{20}H_{12}NO_6Zn$
Formula weight	427.68
Crystal size (mm)	0.21 x 0.25 x 0.15
Temperature (K)	163
Wavelength (Å)	1.54187
Crystal system	Triclinic
Space group	*P*-1
Unit cell lengths (Å)	a = 13.469(3) b = 15.103(3) c = 15.126(3)
Unit cell angles (°)	α = 91.063(6) β = 109.658(8) γ = 112.036(8)
Unit cell volume ($Å^3$)	2648.9(9)
Z	4
D_{calc} (g cm^{-3})	1.072
μ (mm^{-1})	1.524
F(000)	868.0
Reflns coll./unique, R_{int}	35251 / 3203, 0.1603
Data range	8.0 Å > *d* > 0.81 Å
Index ranges	$-15 \le h \le 15$, $-17 \le k \le 17$, $-17 \le l \le 13$
Completeness	100.0 %
T_{min}, T_{max}	0.430, 1.000
R indices for data with $I>2\sigma(I)$	R_1 = 0.1595, wR_2 = 0.3955
R indices for all data	R_1 = 0.1876, wR_2 = 0.4174
Largest difference peak and hole (e $Å^{-3}$)	1.06/-0.84

MUF20-Aβ **[$Zn_2(bpdc)_2(bpy\text{-}NHBoc)$]**

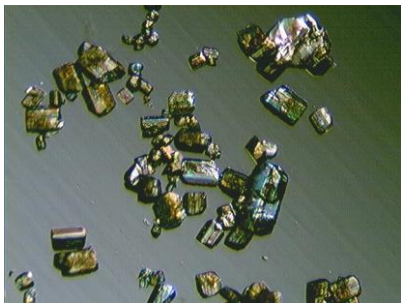

Bpdc (2.4 mg, 0.010 mmol), bpy-NHBoc (4.7 mg, 0.017 mmol), and $Zn(NO_3)_2.4H_2O$ (2.4 mg, 9.2 μmol) were combined in a 4 mL scintillation vial. MeOH (1.0 mL) was then added and the mixture briefly sonicated before addition of DMF (0.25 mL). After sonicating a second time the vial was placed in an oven at 85 °C for 15 hours. Colourless block clusters formed. Yield: 16.1 mg. Anal. calcd. for $[C_{86}H_{66}N_6O_{20}Zn_4]$: C, 58.52; H, 3.77; N, 4.76; Found: C, 58.31; H, 3.41; N, 4.59. To scale up the synthesis, a parallel synthetic method was adopted (multiple vials using the scale described above).

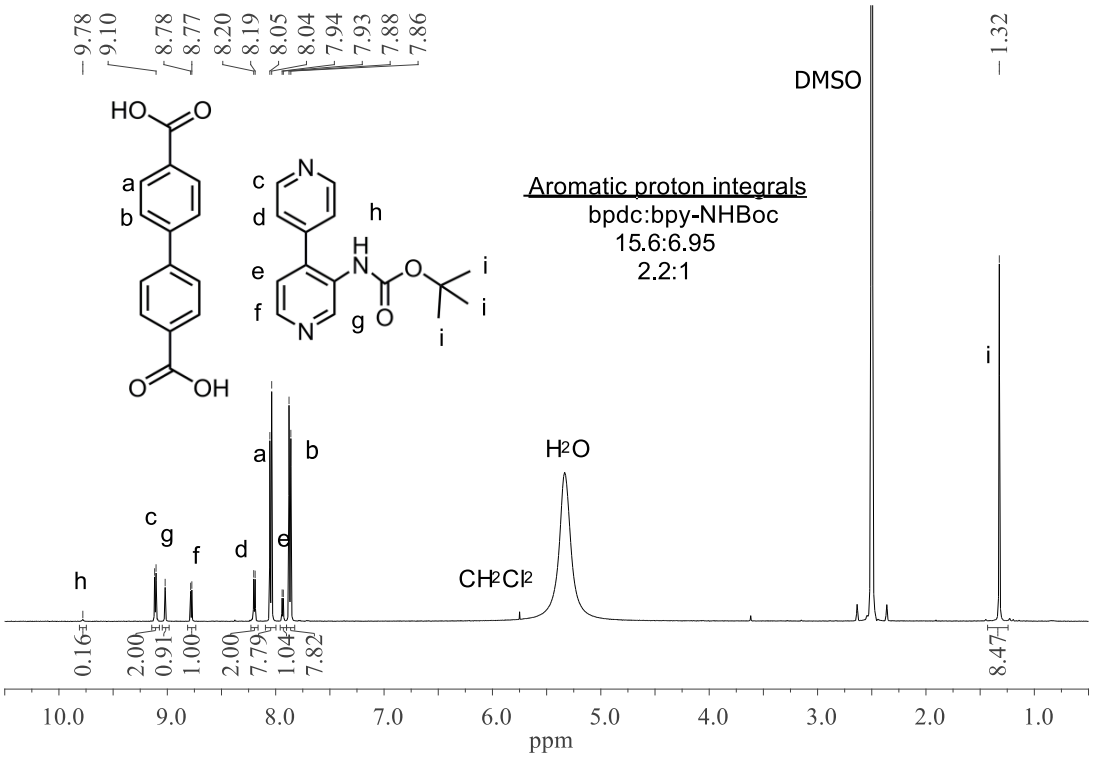

Figure 2.41: ^{1}H NMR spectrum of digested MUF20-Aβ in DMSO-d_6/DCl.

MUF20-$Aβ^T$

MUF20-Aβ was thermolyzed on the activation port of the gas sorption instrument. The dried and activated sample was placed under vacuum and then heated to 165 °C for 10 hours. The sample was then backfilled with N_2 before being transferred to the gas sorption measurement port.

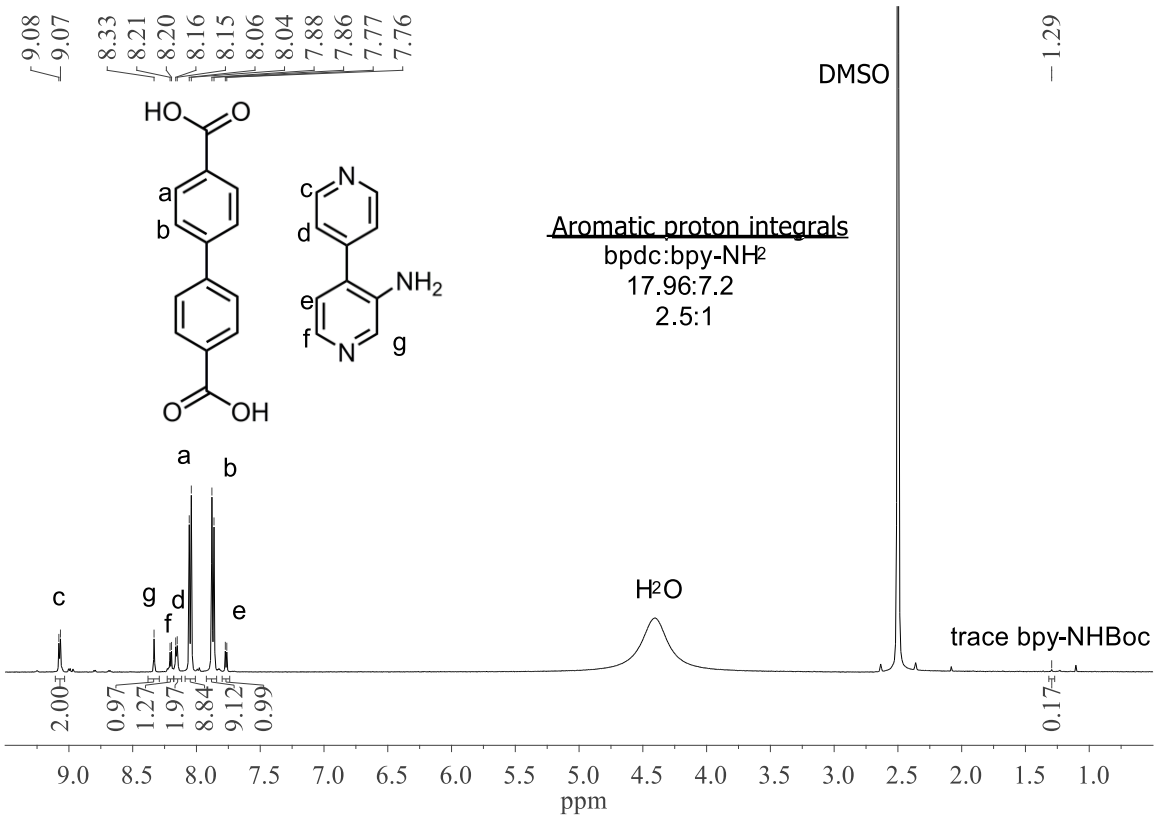

Figure 2.42: ^{1}H NMR spectrum of digested MUF20-Aβ^{T} in DMSO-d_6/DCl.

MUF20-Aβ` **$[Zn_2(bpdc)_2(bpy\text{-}NH_2)]$**

Bpdc (12.5 mg, 0.052 mmol), bpy-NH_2 (14.4 mg, 0.084 mmol), and $Zn(NO_3)_2.4H_20$ (11.6 mg, 0.044 mmol) were combined in a 25 mL Schott bottle pre-treated with Sigmacote. MeOH (5.0 mL) was then added, and the suspension briefly sonicated before the addition of DMF (1.25 mL) and re-subjection to brief sonication before placing in an oven at 85 °C for 18 hours. After 10 mins in the oven, the lid of the Schott bottle was re-tightened and Teflon tape placed around the join of the lid and bottle. Yield: 13.4 mg. Anal. calcd. for $[C_{38}H_{24}N_2O_8Zn_2]$: C, 59.48; H, 3.15; N, 3.65; Found: C, 59.26; H, 3.53; N, 3.58.

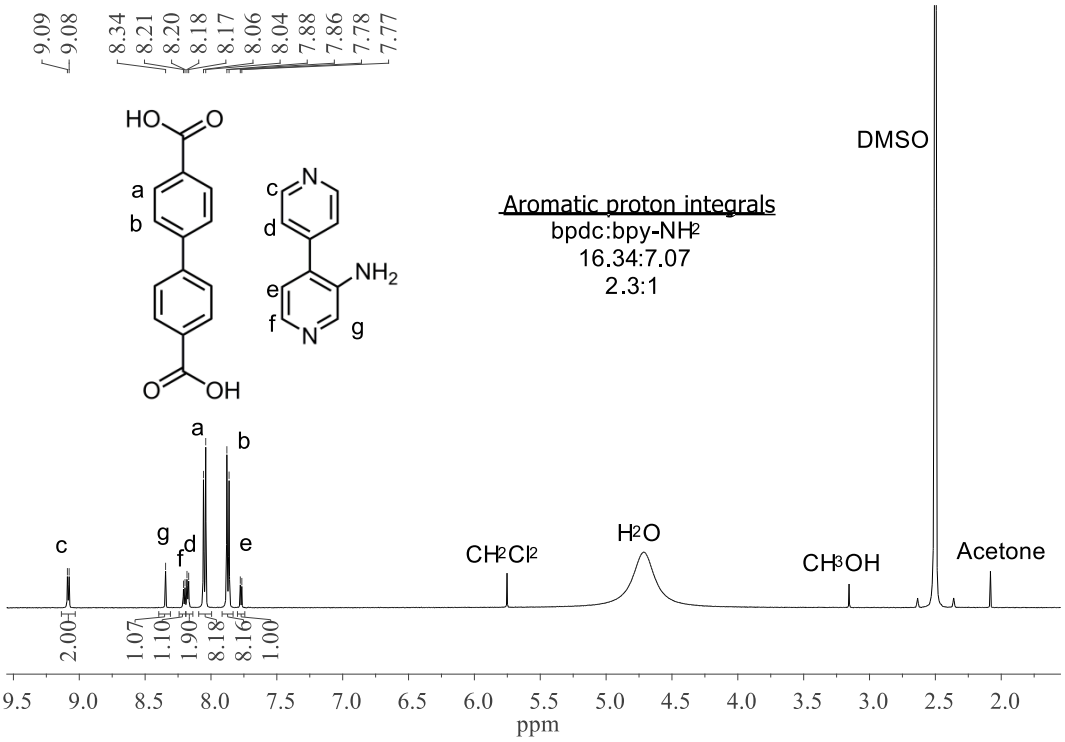

Figure 2.43: ^{1}H NMR spectrum of digested MUF20-Aβ` in DMSO-d_6/DCl.

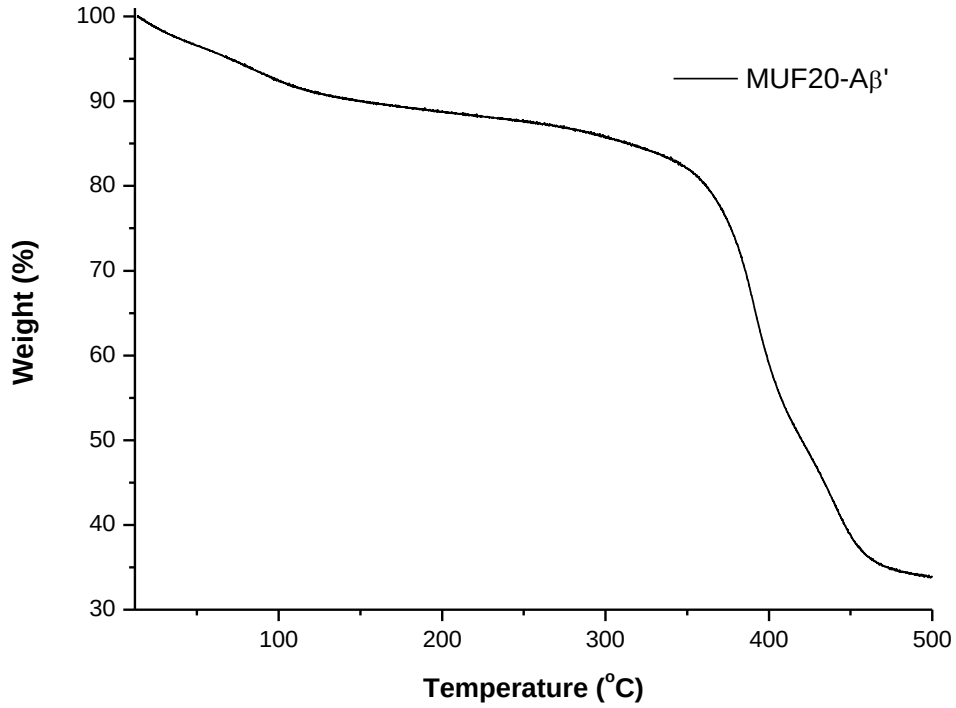

Figure 2.44: Thermogravimetric analysis (TGA) trace for MUF20-Aβ`.

MUF20-Aγ **[$Zn_2(bpdc)_2(bpy\text{-}TBE)$]**

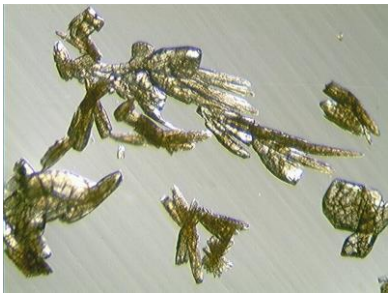

Bpdc (5.0 mg, 0.021 mmol), bpy-TBE (8.8 mg, 0.034 mmol), and $Zn(NO_3)_2.4H_2O$ (5.1 mg, 0.020 mmol) were combined in a 4 mL scintillation vial. MeOH (1.0 mL) was then added and the mixture briefly sonicated before addition of DMF (0.25 mL). After sonicating a second time the vial was placed in an oven at 85 °C overnight. Colourless needle clusters formed. Yield: 13.2 mg. Anal. calcd. for [$C_{43}H_{32}N_2O_{10}Zn_2$]: C, 59.53; H, 3.72; N, 3.23; Found: C, 58.97; H, 3.93; N, 3.23. To scale up the synthesis, a parallel synthetic method was adopted (multiple vials using the scale described above).

Single crystal methanol-loss synthesis

Bpdc (5.0 mg, 0.021 mmol), bpy-TBE (8.8 mg, 0.034 mmol), and $Zn(NO_3)_2.4H_2O$ (5.1 mg, 0.020 mmol) were combined in a 20 mL scintillation vial. MeOH (4.0 mL) was then added and the mixture briefly sonicated before addition of DMF (1.0 mL). After sonicating a second time the vial was placed in an oven at 85 °C overnight. Approximately 80% of the solvent volume was lost during the synthesis. Although appearing cracked on the surface, the colourless flat needles diffracted intensely to the edge of the detector and a good SCXRD data set was obtained.

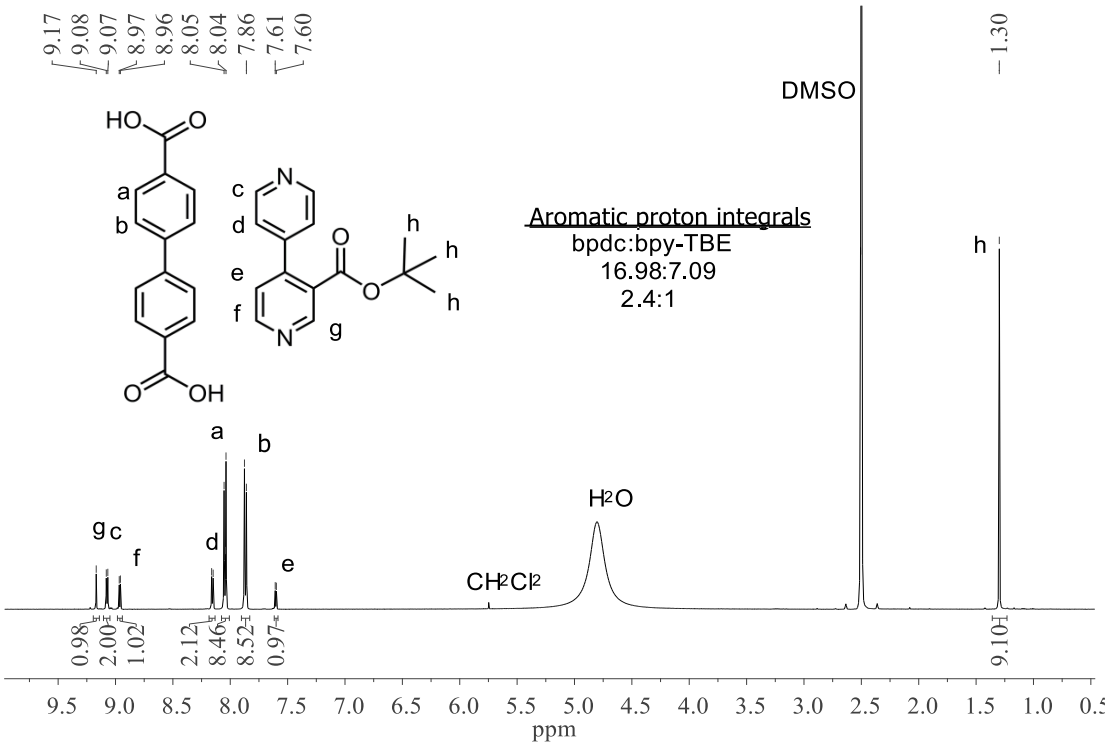

Figure 2.45: ^{1}H NMR spectrum of digested MUF20-Aγ in DMSO-d_6/DCl

MUF20-Aγ^{T}

MUF20-Aγ was thermolyzed on the activation port of the gas sorption instrument. The sample was placed under vacuum and then heated to 165 °C for 10 hours. The sample was then backfilled with N_2 before being transferred to the gas sorption measurement port.

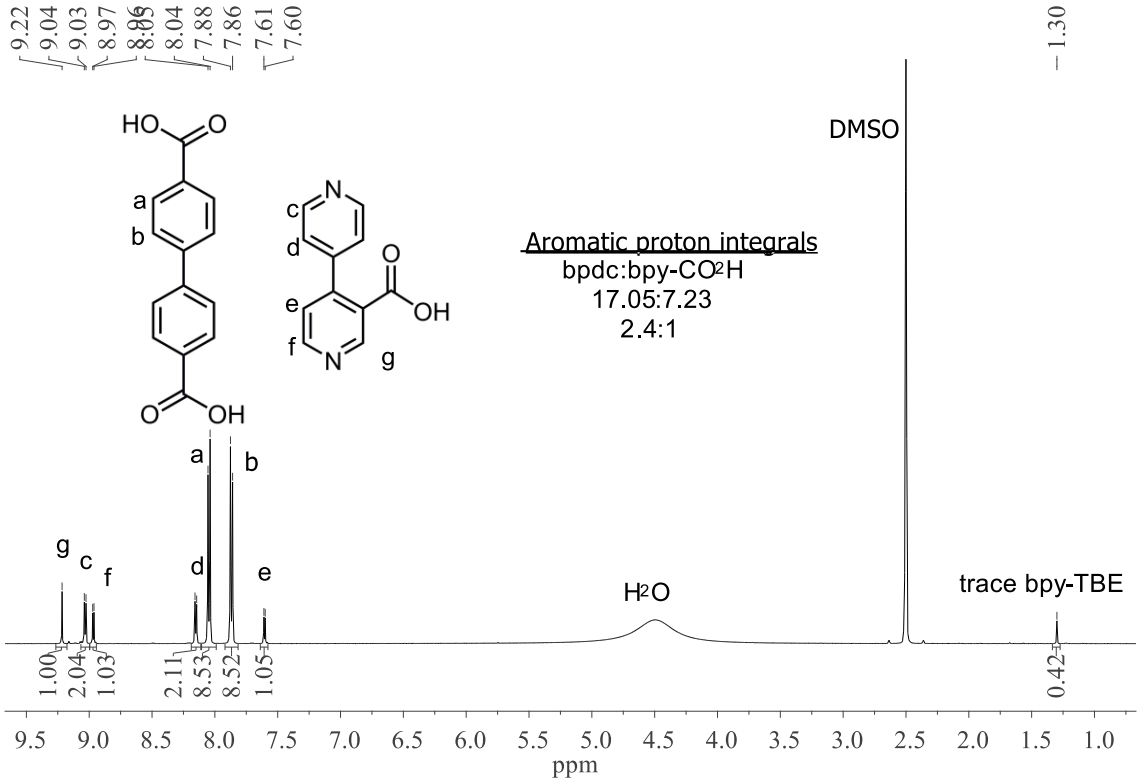

Figure 2.46: ^{1}H NMR spectrum of digested MUF20-Aγ^{T} in DMSO-d_6/DCl.

MUF20-Bα [Zn_2(bpdc-NHBoc)$_2$(bpy)]

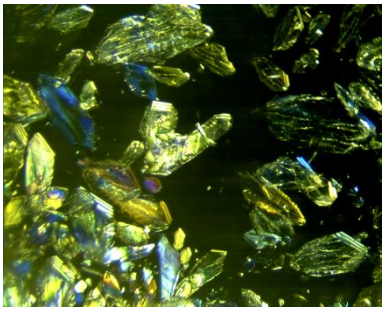

Bpdc-NHBoc (5.0 mg, 0.014 mmol), 4,4`-bipyridine (5.0 mg, 0.032 mmol), and $Zn(NO_3)_2.4H_2O$ (4.3 mg, 0.016 mmol) were combined in a 4 mL scintillation vial. MeOH:DMF (1.0:0.25 mL) was then added and the mixture briefly sonicated before placing in an oven at 85 °C for 12 hours. After 10 min in the oven, the lid of the vial was re-tightened and Teflon tape placed around the join of the lid. Pale yellow needle clusters and chunks formed. To scale up the synthesis, a parallel synthetic method was adopted (multiple vials using the scale described above).

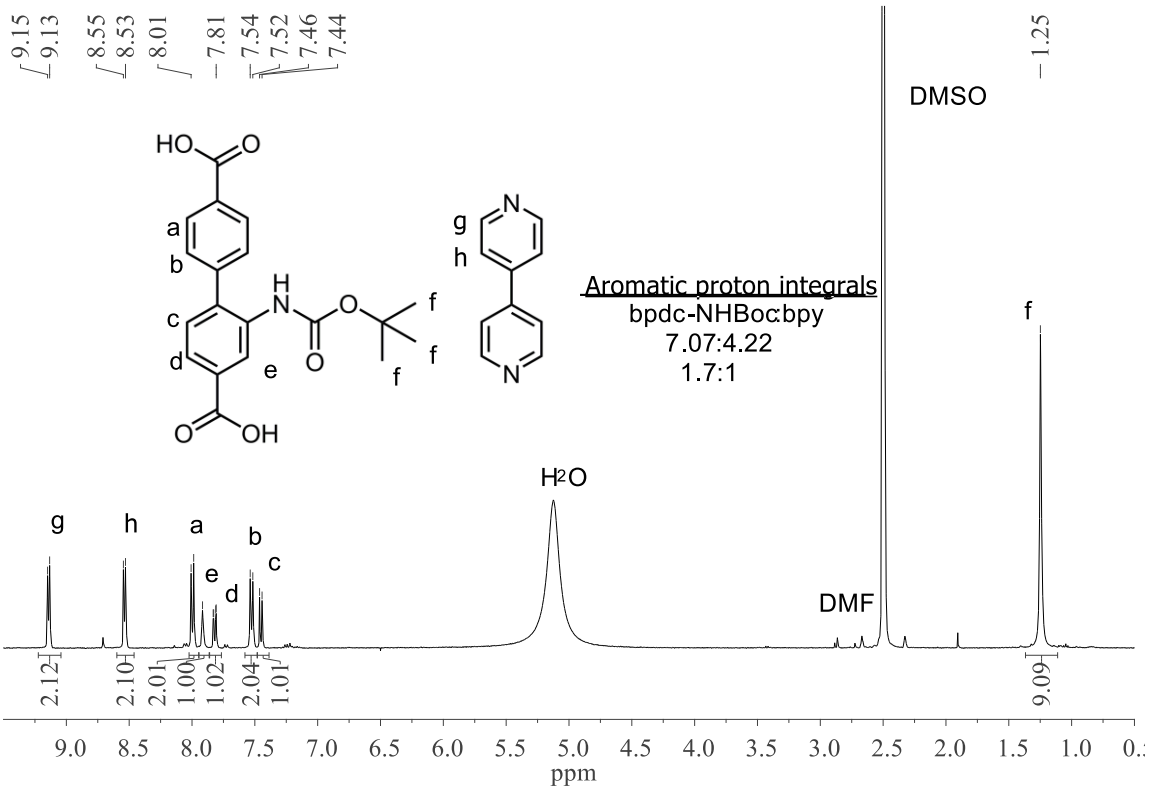

Figure 2.47: ^{1}H NMR spectrum of digested MUF20-Bα in DMSO-d_6/DCl.

MUF20-B^{T}α

Despite multiple trials no condition was found whereupon crystallinity of the MOF was retained alongside total thermolytic deprotection.

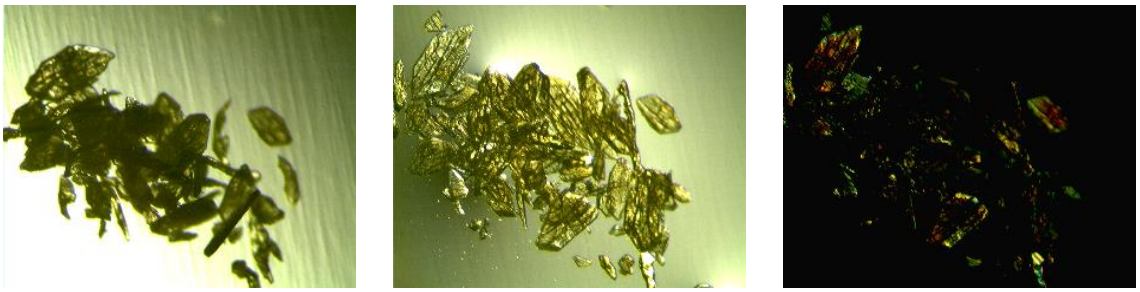

Figure 2.48: MUF20-B^{T}α post thermolysis dry, resolvated in DEF, and in DEF under polarized light showing crystallinity preserved.

Partial thermolysis was shown to retain a high level of crystallinity. Sample was partially thermolyzed by heating at 160 ^{o}C for 3 hrs under inert atmosphere.

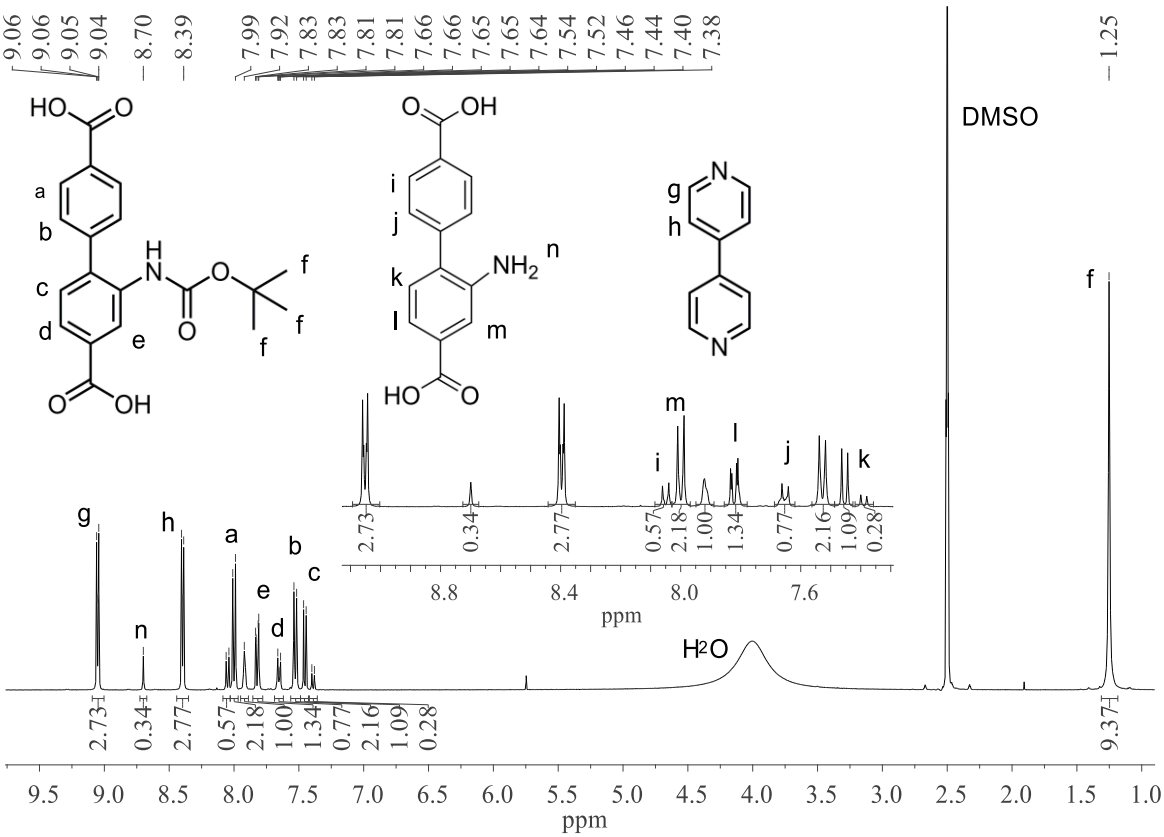

Figure 2.49: ^{1}H NMR spectrum of digested MUF20-B^{T}α in DMSO-d_6/DCl.

MUF20-Cα **[Zn_2(bpdc-TBE)$_2$(bpy)]**

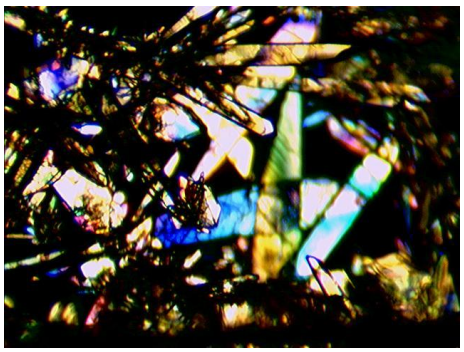

Bpdc-TBE (50.0 mg, 0.146 mmol), 4,4`-bipyridine (24.0 mg, 0.154 mmol), and $Zn(NO_3)_2.4H_2O$ (37.0 mg, 0.142 mmol) were combined in a 50 mL Schott bottle. MeOH (10 mL) was then added and the mixture briefly sonicated before addition of DMF (2.5 mL). After sonicating a second time the vial was placed in an oven at 85 °C for 20 hours. After 10 mins in the oven, the lid of the vial was re-tightened and Teflon tape placed around the join of the lid. Clear colourless narrow plates were formed. Yield: 57.5 mg.

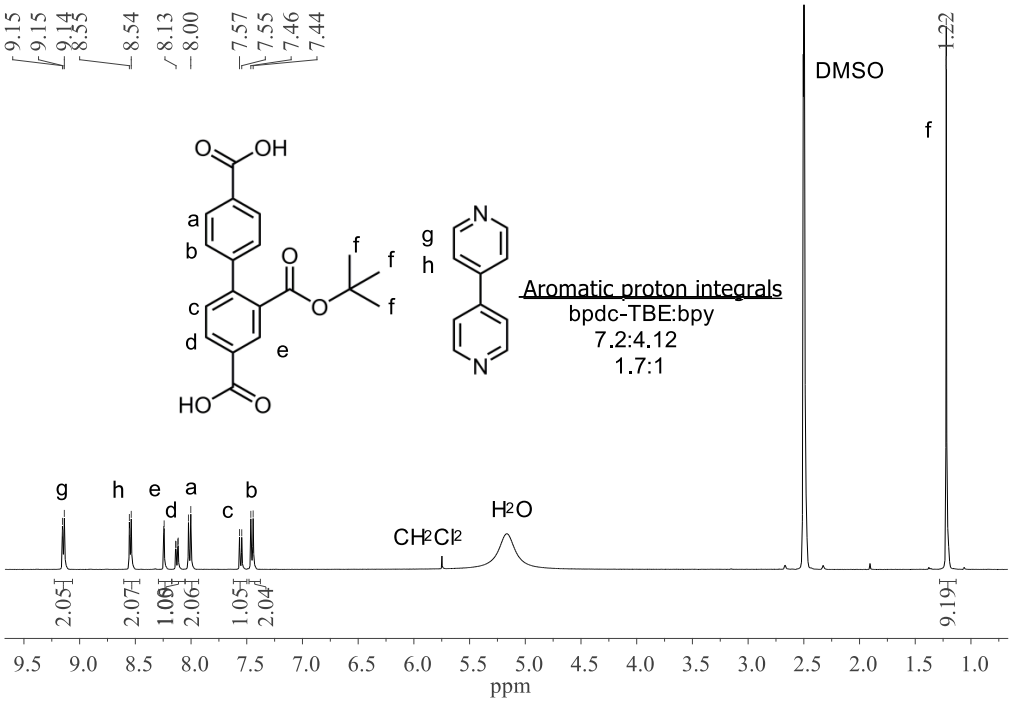

Figure 2.50: ^{1}H NMR spectrum of digested MUF20-Cα in DMSO-d_6/DCl.

MUF20-C^{T}α

Freshly synthesised MUF-20-Cα was washed twice with dry DMF, twice with DBF before placing in fresh DBF and microwave heating at 160 ^{o}C for 3.5 hours. The product was marginally crystalline (see Figure 2.51 PXRD inset).

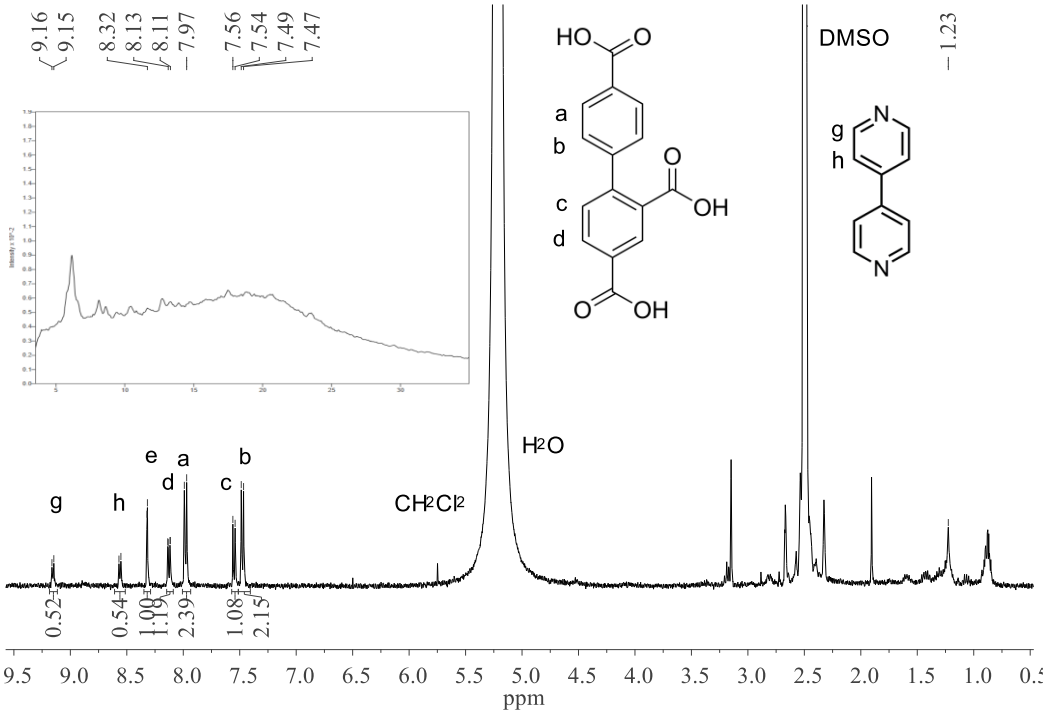

Figure 2.51: ^{1}H NMR spectrum of digested MUF20-C^{T}α in DMSO-d_6/DCl post microwaving in DBF at 160 ^{o}C for 3.5 hrs. Inset shows PXRD diffractogram.

MUF20-Dα **[Zn_2(bpdc-2mh)$_2$(bpy)]**

Bpdc-2mh (10.0 mg, 0.026 mmol), 4,4`-bipyridine (4.2 mg, 0.027 mmol), and $Zn(NO_3)_2.4H_2O$ (5.6 mg, 0.022 mmol) were combined in a 5 mL vial. MeOH (0.5 mL) was then added and the mixture briefly sonicated before addition of DMF (2.0 mL). After sonicating a second time the vial was placed in an oven at 85 °C for 20 hours. After 10 mins in the oven, the lid of the vial was re-tightened and Teflon tape placed around the join of the lid. Clear colourless narrow plates were formed.

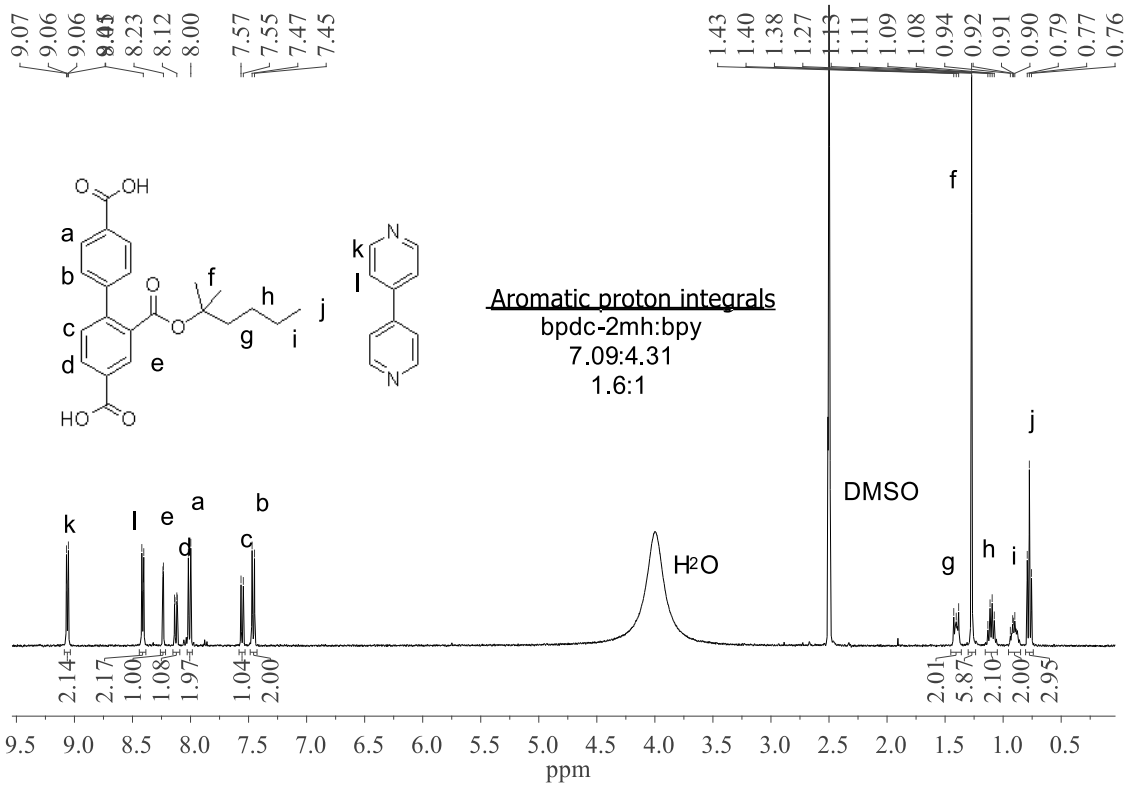

Figure 2.52: ^{1}H NMR spectrum of digested MUF20-Dα in DMSO-d_6/DCl.

MUF20-D^Tα

Freshly synthesised MUF-20-Dα was washed twice with dry DMF, several times with dry CH_2Cl_2 before removing solvent under vacuum. The sample was then placed in a microwave vessel, flushed with Ar and heated at 160 ^oC for 3 hours.

Table 2.9: Experimental and calculated weight losses of bpdc-2mh and MUF20-Dα.

MOF	$T_{1/2\Delta}$ (^oC)*	Experimental Weight loss (%)	Calculated Weight Loss (%)
Bpdc-2mh	160	25.5	27.5
MUF20-Dα	165	17.4	18.7

* $T_{1/2\Delta}$ is defined as the midpoint of the temperature range over which weight loss associated with thermolysis occurs and is rounded to the nearest 5 ^oC.

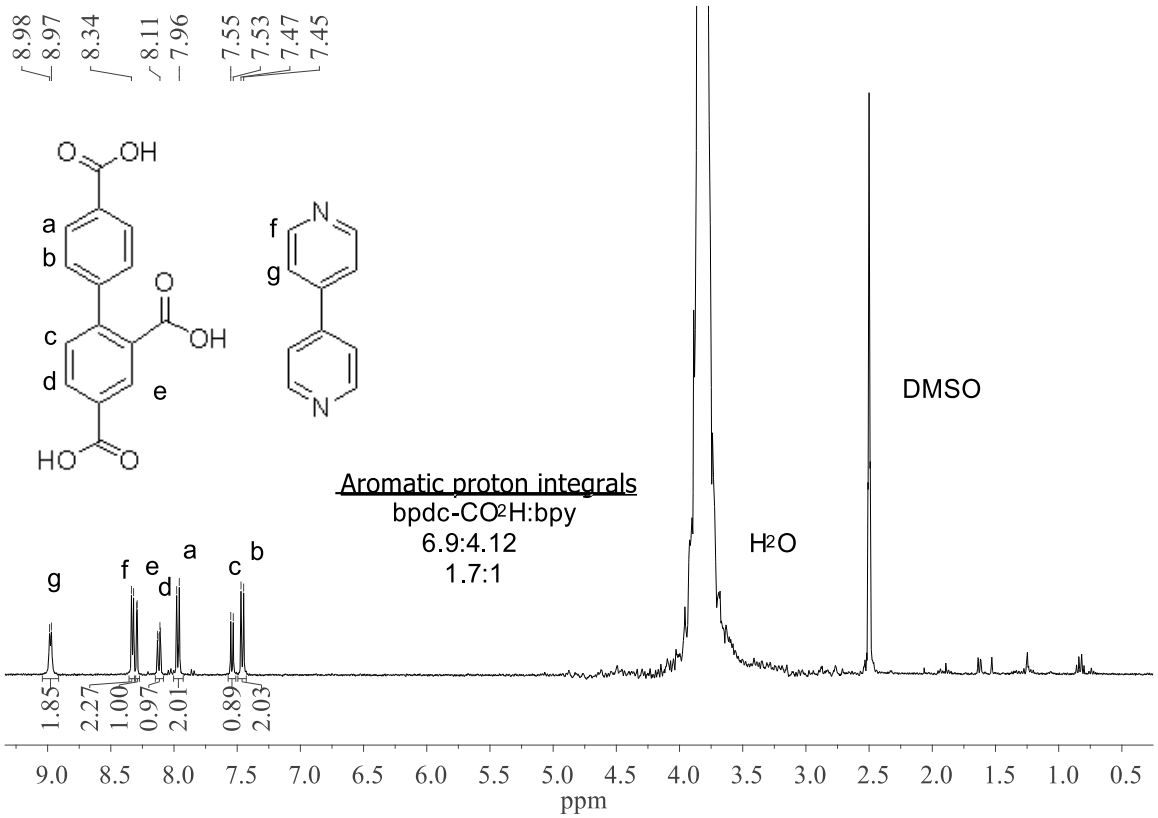

Figure 2.53: ^{1}H NMR spectrum of digested MUF20-D^{T}α in DMSO-d_6/DCl post microwaving at 160 ^{o}C for 3 hrs.

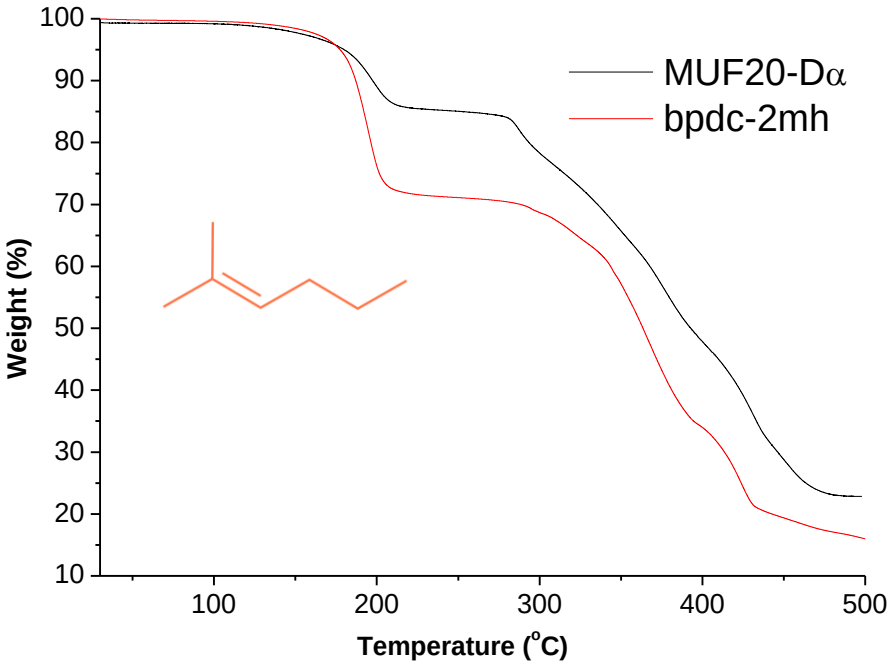

Figure 2.54: Thermogravimetric analysis (TGA) trace for MUF20-Dα and ligand bpdc-2mh with thermolytic fragment 2-methylhex-2-ene illustrated.

Chapter 3 –Dual-functionalized pillar-layer MOFs (PLMOFs)

3.1. Introduction

Completing the picture framed with mono-functionalized MOFs in Chapter 2, a family of dual-functionalized MOFs was identified and synthesis undertaken to explore the effect on material properties such as framework topology, including interpenetration control. As in Chapter 2, to more fully determine the effect of the TPGs used, direct MOF synthesis utilizing the unprotected amine and carboxylic acid functionalized 4,4`-bipyridine (bpy) and 4,4`-biphenyldicarboxylic acid (bpdc) ligands was also attempted. The MOF structures examined in this study are summarized in the fold out at back and Table 3.1.

3.2. Results and discussion

3.2.1. Dual-functionalized TPG MOFs

Dual-functionalized PLMOFs were targeted from combinations of the below ligand set (Figure 3.1) and their themolyzed analogues pursued where possible.

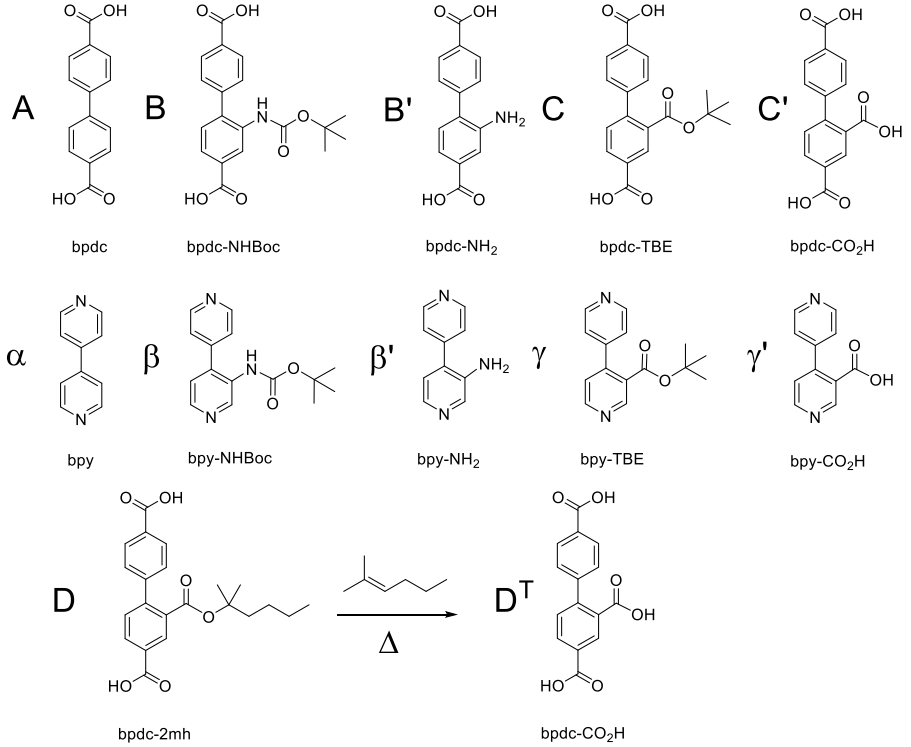

Figure 3.1: Ligand set explored in the MUF20 framework, their designated shorthand letter and example of thermolytic analogues synthesized.

The main threads in this chapter are to firstly answer the question, "Will dual-functionalization prevent interpenetration in the flexible pillar-layer framework, given that one

TPG is insufficient to prevent secondary lattice formation?" Secondly, to examine the effect of type and location of TPG on the structure and framework properties and thirdly, explore the inter-lattice interactions that contribute to maximal interpenetration control and suppression of unwanted phases. Finally, thermal properties of the materials are investigated and preliminary thermolysis results discussed.

3.2.2. Synthesis of MOF family

MOFs were primarily synthesised from 1.25 to 2 mL of 1:4 DMF:MeOH, 1:1.6 bpdc:bpy TPG ligands, 0.84-1.3 equivalents $Zn(NO_3)_2.4H_2O$ in an oven at 85 ^oC for 9-18 hrs. Some MOFs required an increase from 1:4 to 1:9 DMF:MeOH to increase single crystal size and phase purity and are noted in the experimental section of this chapter. Most MOF synthesis optimization was straightforward and unremarkable. However, one MOF in this family, MUF20-B`γ, was of particular interest due to an initial synthesis of an unknown phase at 85 $^oC$ that transitioned overnight at room temperature to form phase-pure MUF20-B`γ.

Initially the unknown and air-sensitive phase was thought to be IRMOF-9/10, as it had been encountered as a competing phase with bulky bpdc-NHBoc and bpy-TPG ligands. However, the PXRD diffractogram, when carefully collected in DEF - a lower-volatility solvent – and in sleeve did not match IRMOF-9/10. A more rigid MOF such as IRMOF can be expected to be less solvent-state dependent in its powder diffractogram than PLMOFs thus this made IRMOF-9/10 unlikely. As the material was not single-crystal suitable and PXRD analysis did not match literature the identity of the unwanted phase was not pursued further.

MUF20-B`γ yielded insight into the mechanics of formation of this pillar-layer MOF as different synthesis conditions showed that the unstable phase was disfavoured only at lower temperatures over a longer timeframe. With respect to changing MOF phase the energy barrier was very low, occurring at < 18 ^oC over the course of 24 hours. In the case of MOF formation, a lower temperature decreases decomposition of the dimethylformamide solvent to dimethylamine and so slows the starting reaction rate while higher temperature accelerates base formation, subsequent bpdc deprotonation and so increases initial rate of MOF formation. The lower stability of the unknown phase relative to MUF20 phase then allows for gradual shift to the MUF20 product, particularly favourable in the presence of water. Placing the unknown MOF phase into fresh solvent stopped any phase transformation. This observation in part contributed to mistakenly identifying the unknown as IRMOF-9/10 since without residual bpy MUF20 would not be able to form and exposure to trace water in the mother liquor would

favour a phase change to doubly-interpenetrated pillar-layer MOF due to the sensitivity of the zinc-carboxylate framework to hydrolytic collapse. Phase-pure synthesis of this material was achieved by lowering of the reaction temperature to 75 ^{o}C and extending the reaction time to three days.

The related MOF, MUF20-Cβ`, also benefited from the lower temperature synthesis at 75 ^{o}C to achieve phase-purity. These results suggest that in this MOF framework the combination of a free H-bonding amine functionality with the strong inter-lattice interactions of the *tert*-butyl ester group places the flexible pillar-layer MOFs in a more complex energy landscape of potential reaction products than well-known MOF phases such as UMCM-1 that act as thermodynamic sinks with rapid and irreversible formation.

In stark contrast to the bpdc-TBE ligand MOF synthesis, where no competing IRMOF or amorphous phases were observed and both dual-functionalized pillar-layer frameworks formed with high crystallinity and yield, in the case of the MUF20-Bβ and MUF20-Bγ phases the localization of the TPG prevents inclusion of a second bulky substituent in either a non or interpenetrated way to the point of excluding MUF20 phase formation entirely (Figure 3.2).

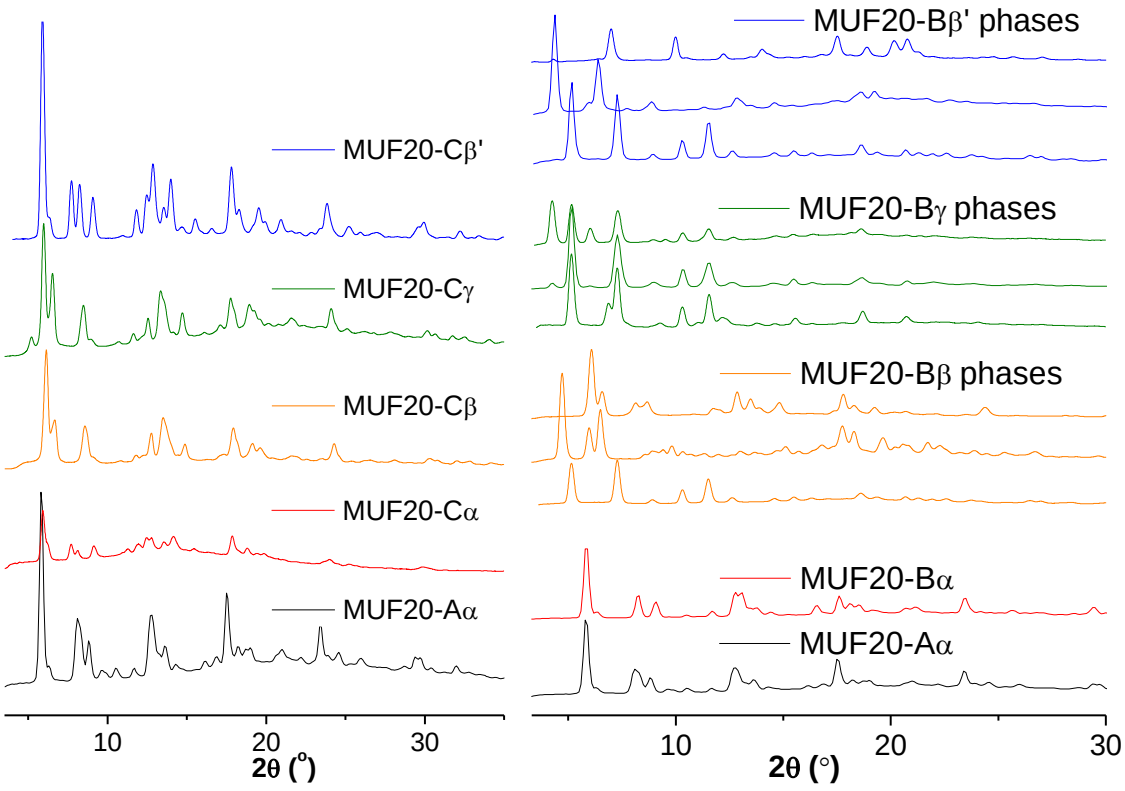

Figure 3.2: Comparison of the PXRD patterns for the parent material MUF20-Aα and the synthesis attempts of novel materials left: MUF20-Cα, MUF20-Cβ, MUF20-Cγ, and MUF20-Cβ`, right: MUF20-Bα, MUF20-Bβ, MUF20-Bγ, and MUF20-Bβ`.

Upon synthesis of the initial pair using bpdc-NHBoc the results indicated that there is an orientation dependent threshold bulk tolerance of the framework whereupon the pillar-layer phase is no longer energetically favoured and instead an IRMOF phase competes, composed of the bulky TPG carrying bpdc ligand alone. In all conditions trialled, MUF20-Bβ could not be formed cleanly, yielding mixed phases or, in the event of a phase-pure synthesis of MUF20-Bβ (from PXRD and NMR ratios), consistently showing at least 20% deprotection of both bpy-NHBoc and bpdc-NHBoc with crystals showing great sensitivity to handling and single crystal data collection. This segregation of ligands and multiplication of phases is attributable to the previously observed localization within the pores of the MOF of the steric bulk of the carbamate-functionalized bpdc ligand, inhibiting inclusion of another bulky functional group on the shorter bpy pillar and thus disfavouring the inclusion of the bpy ligand in preference to forming its own lattice. In MUF20-Bγ, both IRMOF-9 (non-interpenetrated) and IRMOF-10 (2-fold interpenetrated) bpdc-only phases were shown to compete. In neither MUF20-Bγ nor MUF20-Bβ' was a MUF20 phase observed (Figure 3.2).

However, these results with the bpdc-NHBoc (B) ligand should be held in contrast to bpdc-TBE (C) and bpdc-2mh (D) based MOFs MUF20-Cβ, MUF20-Cγ, and MUF20-Dβ, all of which readily accommodated two TPGs within the MUF20 framework in phase-pure synthesis with no ligand deprotection.

The complete TPG-functionalized MUF20 MOF family achieved is below (Figure 3.3)

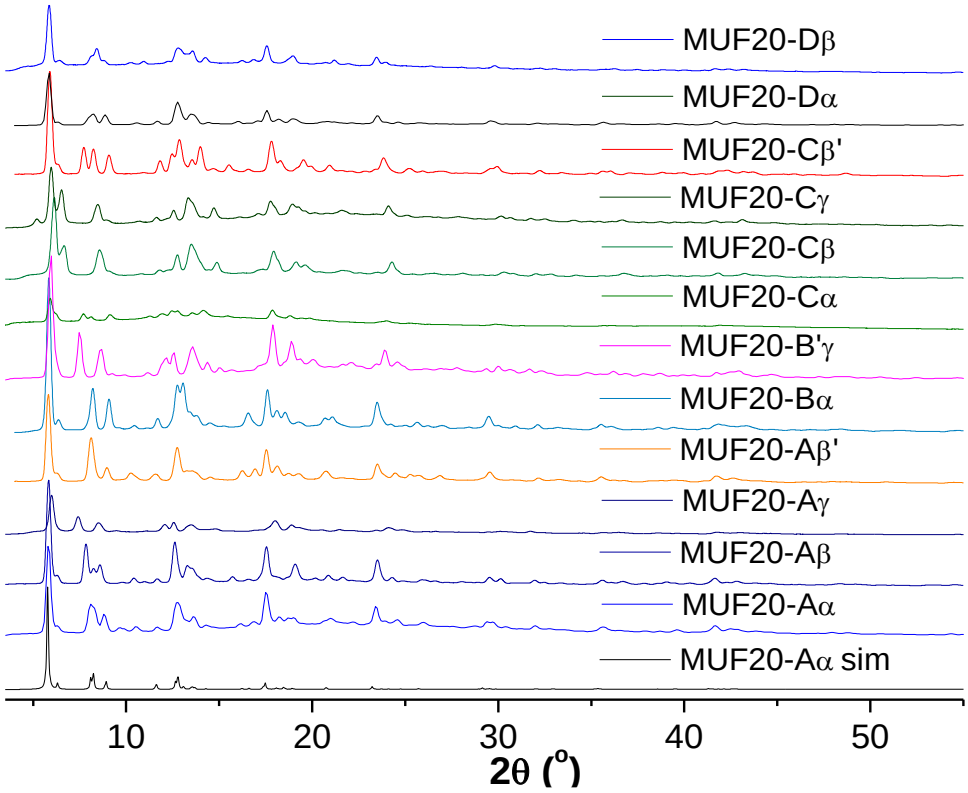

Figure 3.3: PXRD diffractograms for the parent material MUF20-Aα and the TPG-functionalized novel material analogues successfully synthesized; MUF20-Aβ, MUF20-Aγ, MUF20-Aβ`, MUF20-Bα, MUF20-B`γ, MUF20-Cα, MUF20-Cβ, MUF20-Cγ, MUF20-Cβ`, MUF20-Dα, and MUF20-Dβ.

The PXRD patterns all match well with the parent simulated and experimental MOF structure, MUF20-Aα, and ^{1}H NMR ratios of the materials yielded the expected 2:1 ratio of bpdc:bpy ligands (see experimental section end of chapter). Single-crystal analysis was carried out on all materials and confirmed the pillar-layer MOF structure was formed.

To answer the question: would bulky interpenetrating groups on both the linker and pillar ligands prevent interpenetration? The first MOF synthesized in this dual functionalized family was MUF20-Dβ.

3.2.3. $[Zn_2(bpdc\text{-}2mh)_2(bpy\text{-}NHBoc)]$ MUF20-Dβ

Bpdc-2mh and bpy-NHBoc were combined in DMF:MeOH with zinc nitrate at 85 ^{o}C for 12 hours and MUF20-Dβ obtained. Given the demonstrated post-thermolysis crystallinity of MUF20-Dα this MOF has the potential to form a novel and otherwise unattainable amphoteric crystalline MOF post thermolysis. As shown in Figure 3.4, despite the presence of two protecting groups in the MOF the additional steric bulk was still insufficient to discourage the

growth of a second net in the flexible pillar-layer structure. Upon functionalization of the pillar bpy ligand by -NHBoc the MOF lost the sensitivity to solvated state observed in MUF20-Dα (noted in Chapter 2). Single-crystal x-ray analysis of the MUF20-Dβ structure revealed the thermolabile protecting groups to be highly ordered with the *tert*-butyl atoms of the NHBoc and 2-methylhexyl ester clearly visible in the electron density maps. As the functional groups of both interpenetrating net ligands lie closely alongside each other steric restrictions may be restraining ligand movement resulting in crystallographic ordering.

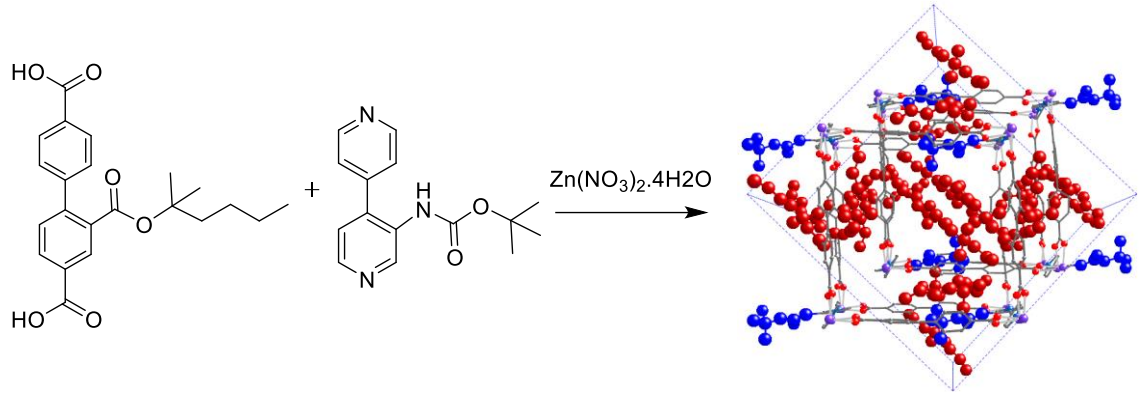

Figure 3.4: Interpenetrated structure of MUF20-Dβ. The 2-methylhexyl-ester groups of the biphenyl linker are shown in red while the Boc-protected amine groups of the bpy pillars are in blue. Some TPGs are omitted for clarity. Other atom colour coding is: C-grey, O-red, N-blue, Zn-purple.

As part of the family of TPG protected pillar-layer MOFs synthesized in the Telfer group, MUF20-Dβ was the first doubly functionalized member. The two-fold interpenetrated result of MUF20-Dβ was then replicated with bpdc-TBE, in the related MOF, MUF20-Cβ. The third doubly TPG-functionalized member of the bpdc-TBE column, MUF20-Cγ containing a *tert*-butyl ester TPG on both the bpy and bpdc, also cleanly formed the doubly interpenetrated MUF20 pillar-layer MOF.

3.2.4. Examination of type and location of TPG on structure and framework properties

An early example in the different behaviour of these materials upon exposure to similar stimuli was found within the materials MUF20-Aγ and MUF20-Bα upon methanol loss during synthesis at 85 ^{o}C. The obtained crystal structures for MUF20-Bα showed little to no difference (see Figure 3.5a). However, MUF20-Aγ revealed a drastic change from the expected triclinic *P*-1 cell and square grid-like lattice stacking to a higher symmetry *P* $2_1/c$ group with a sharply angled wave-like pattern to the two interpenetrating lattices (Figure 3.5b). This methanol-loss structure was synthesized and data collected by Dr. Sebastian Blackwood.

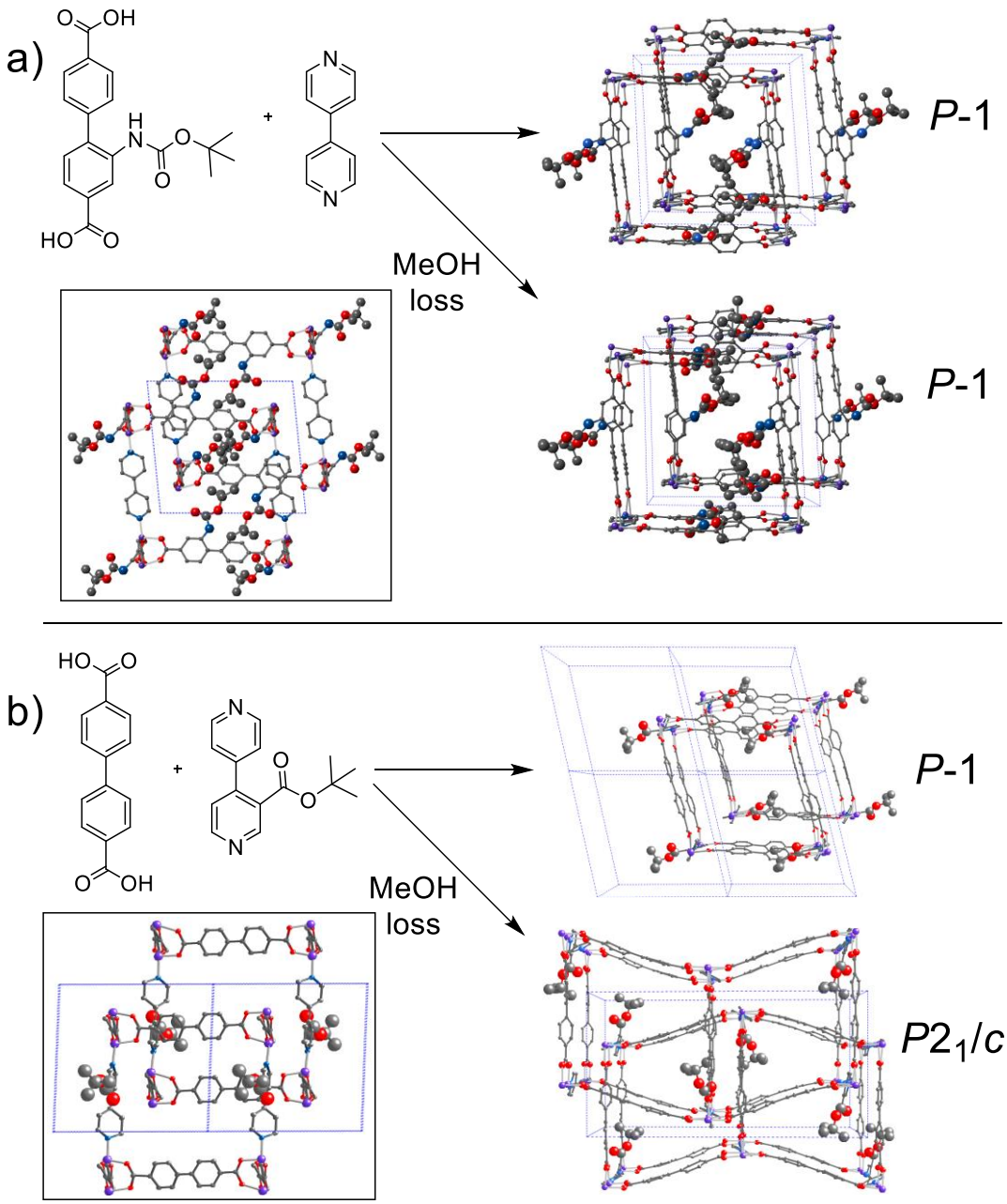

Figure 3.5: MUF20-Bα (top) and MUF20-Aβ (bottom) react differently to environmental stressors such as methanol loss at 85 °C during MOF synthesis. Pore blocking behaviour with bpdc-TPGs (top inset) maintains structure while bpy-TPGs allow significant lattice distortion. Atom colour code is; C-grey, O-red, N-blue, Zn-purple.

This difference in stimuli response can be traced back to the TPG-functionalization of the material where positioning of the bpdc-TPG in the pores of the MOF maintains structure. The increased concentration of bulky functionalities appears less important than the location of the steric hindrance both within the layer and angling between the lattices. This may contribute to supporting the bpy pillar from the sharp slanting observed within the thermolyzed MOF MUF20-D^{T}α where the bpy ligands shifted substantially to lie closer within the zinc-

carboxylate planes of the pillar-layer MOF structure. This solvent-loss study builds on the gas sorption results in Chapter 2 where the bpdc functionalized materials MUF20-Bα and MUF20-Cα showed a much greater guest-dependent behaviour in the higher P/P_0 gate-opening pressure and significant hysteresis. Additionally, both MUF20-Bα and MUF20-Dα showed shifts in their PXRD diffractograms upon drying whilst maintaining crystallinity. The thermolytic resilience of MUF20-Dα draws on this pore-blocking behaviour to support the framework from collapse and in the case of MUF20-Bα during methanol solvent-loss, TPG pore occupation can be shown to prevent the distortion of the lattice stacking. Reasons for the relatively low thermolytic stability of MUF20-Cα, MUF20-Cβ, MUF20-Cγ, and MUF20-Cβ` in comparison to MUF20-Bα, and MUF20-Dα can be drawn from the very different lattice interactions set up by the shorter length *tert*-butyl ester TPG.

Distortion of pillar-layer MOFs in response to changes in methanol concentration has recently been studied in the $Cu(DE\text{-}bdc)_2(dabco)$ system layered on a substrate.[198] Methanol dependent changes from narrow to large pore structures were shown to be additionally controlled through layer thickness. Further understanding of the flexibility of MOF systems is key in the rational design of MOFs for applications.

The MUF20-Aα analogues (Figure 3.6) display interesting changes in symmetry and structure upon both ligand functionalization and thermolysis. As can be seen the lattice distortion observed in MUF20-Aγ upon methanol loss was later replicated upon introduction of specific steric bulk to the framework in the materials MUF20-Cβ and MUF20-Cγ. The unit cell parameters of the functionalized MUF20 family presented in Figure 3.6 are summarized in Table 3.1.

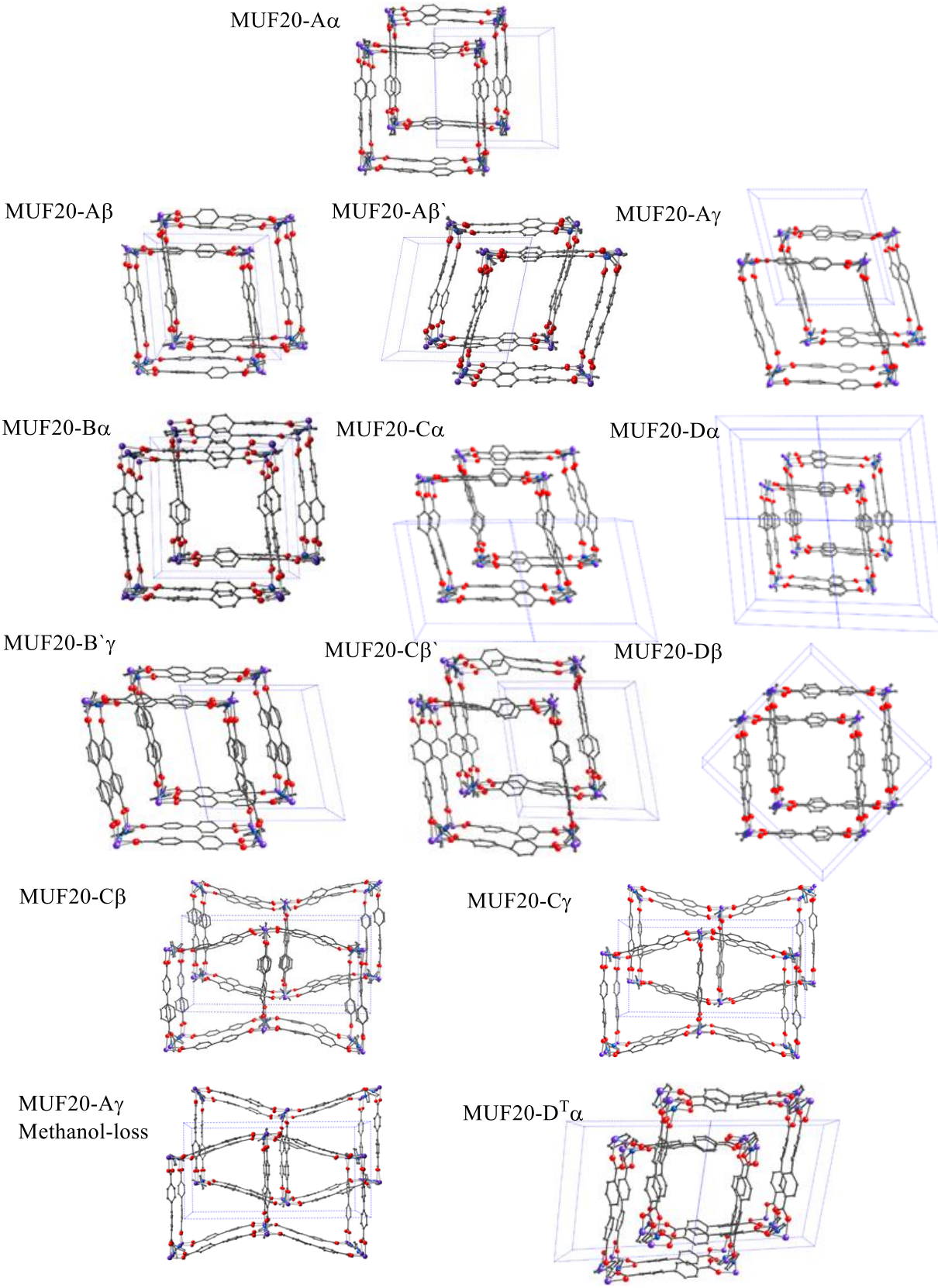

Figure 3.6: Family of functionalized pillar-layer frameworks with unit cell shown.

Table 3.1: Key unit cell parameters of functionalized MUF20-Aα pillar-layer MOFs*

MUF20-Aα (from *literature*[171] and own synthesis)					
Space group: *P*-1		***a*** *14.071(5)*	***b*** *15.265(5)*	***c*** *15.351(6)*	
Cell volume: *3275.98*		**a** 13.9884(9)	**b** 15.2071(9)	**c** 15.2268(6)	
3159.2		***α*** *88.337(13)*	***β*** *85.779(14)*	***γ*** *85.205(11)*	
		α 80.375(6)	**β** 86.347(6)	**γ** 81.932(4)	
MUF20-Aβ		**MUF20-Aβ`**		**MUF20-Aγ**	
Space group:	**a** 13.984(5)	**Space group:**	**a** 14.012(3)	**Space group:**	**a**14.1684(16)
P-1	**b** 15.193(6)	*P*-1	**b** 15.210(3)	*P*-1	**b**15.2099(15)
Cell volume:	**c** 15.195(6)	**Cell volume**:	**c** 15.232(3)	**Cell volume**:	**c** 15.226(2)
3153(2)	**α** 79.737(17)	3166.1(11)	**α** 79.972(8)	3185.0(7)	**α** 103.443(8)
	β 87.915(18)		**β** 85.371(7)		**β** 91.726(7)
	γ 82.984(16)		**γ** 82.836(6)		**γ** 92.642(7)
MUF20-Bα		**MUF20-Cα**		**MUF20-Dα**	
Space group:	**a** 13.9887(4)	**Space group:**	**a** 13.9898(5)	**Space group:**	**a** 13.999(5)
P-1	**b** 15.1934(11)	*P*-1	**b** 15.1487(4)	*P*-1	**b** 15.191(5)
Cell volume:	**c** 15.2045(11)	**Cell volume**:	**c**15.1715(11)	**Cell volume**:	**c** 15.204(5)
3171.4(3)	**α** 87.058(6)	3112.2(3)	**α** 79.013(6)	3168.9(19)	**α** 82.288(5)
	β 81.071(6)		**β** 83.067(6)		**β** 84.860(5)
	γ 83.746(6)		**γ** 82.204(6)		**γ** 82.624(5)
MUF20-B`γ		**MUF20-Cβ`**		**MUF20-Dβ**	
Space group:	**a** 14.127(2)	**Space group:**	**a** 14.0092(5)	**Space group:**	**a** 21.0550(4)
P-1	**b** 15.199(2)	*P*-1	**b** 15.1569(5)	*C* 2/*c*	**b** 21.9947(4)
Cell volume:	**c** 15.2211(19)	**Cell volume**:	**c** 15.1729(11)	**Cell volume**:	**c** 28.029(2)
3196.5(8)	**α** 78.132(5)	3132.8(3)	**α** 79.813(6)	12938.1(10)	**α** 90
	β 88.961(6)		**β** 83.549(6)		**β** 94.615(7)
	γ 88.251(6)		**γ** 82.851(6)		**γ** 90

MUF20-Cβ		MUF20-Cγ	
Space group:	**a** 14.046(5)	**Space group:**	**a** 14.041
P $2_1/c$	**b** 15.200(5)	*P* $2_1/c$	**b** 15.182
Cell volume:	**c** 29.517(5)	**Cell volume**:	**c** 29.470
6294(3)	**α** 90	6274.5	**α** 90
	β 92.914(5)		**β** 92.87
	γ 90		**γ** 90
MUF20-Aγ methanol-loss		**MUF20-D^{T}α**	
Space group:	**a** 14.1030(3)	**Space group:**	**a** 13.469(3)
P $2_1/c$	**b** 15.2176(4)	*P*-1	**b** 15.103(3)
Cell volume:	**c** 29.468(2)	**Cell volume**:	**c** 15.126(3)
6318.6(5)	**α** 90	2648.9(9)	**α** 91.063(6)
	β 92.409(7)		**β** 109.658(8)
	γ 90		**γ** 112.036(8)
Unit cell dimensions in: Å / º		**Unit cell volume in:** $Å^3$	

***** solvated and disordered (modelled) crystal structures

All mono-functionalized analogues have similar unit cell volumes although distances and angles vary slightly. Functionalization generally slightly decreases cell volume except upon double-functionalization with TPGs, doubling the volume in MUF20-Cβ and MUF20-Cγ, and quadrupling the parent cell volume of 3275.98 to 12,938.1 $Å^3$ in MUF20-Dβ. The methanol-loss form of MUF20-Aγ, sharing the same wave-like lattice pattern of MUF20-Cβ and MUF20-Cγ, also doubled over the volume of the parent and standard MUF20-Aγ material to 6318.65 $Å^3$, accompanied by an increase in symmetry from *P*-1 to *P* $2_1/c$.

While these MOFs were not analyzed by gas sorption due to initial synthesis challenges, ligand limitations and poor initial thermolysis results, their crystal structure volume, density and calculated volume and geometric surface areas can be compared for their desolvated and non-disordered structures (Table 3.2).

Table 3.2: Crystal structure properties and calculated solvent accessible voids of MUF20 MOFs*

MOF MUF20- (space group)	Cell Vol** (Å^3)	Density (g/cm^3)**	Pore Volume (Å^3)		% Unit Cell Volume		Surface area (m^2/g)	
			N_2	CO_2	N_2	CO_2	N_2	CO_2
Aα	3159.2	0.805	636	736	20.1	23.3	1407	1551
Aβ	3152.5	0.93	369	458	11.7	14.5	848	980
Aβ`	3165.9	0.821	516	632	16.3	20	1197	1370
Aγ	3185.1	0.905	325	432	10.2	13.6	794	958
Bα	3137.5	0.912	214	279	6.8	8.9	522	623
Cα	3112.2	1.004	152	201	4.9	6.5	440	532
Dα	3168.9	1.102	66	99	2.1	3.1	226	296
D^Tα	2648.8	1.072	189	243	7.1	9.2	562	663
B`γ	3196.6	0.932	249	333	7.8	10.4	643	780
Cβ`	3132.8	0.935	292	377	9.3	12	727	861
Dβ	12938.1	1.198	419	529	3.2	4.1	175	204
Cβ	6293.7	1.143	297	382	4.7	6.1	299	354
Cγ	6274.3	1.024	390	530	6.2	8.4	402	493
Aγ-MeOH-loss	6318.7	0.912	641	795	10.1	12.6	624	720

*Surface areas calculated from solvent void volumes generated in Mercury v4.10. **Desolvated and non-disordered structures were used. Details in Appendix.

3.2.5. Suppression of unwanted phases

Alongside the TPG-functionalized pillar-layer MOFs some highly interpenetrated phases were also isolated from syntheses trialling the unprotected bpdc and bpy ligands, especially from the freely H-bonding unprotected amine of the bpdc-NH_2 ligand, B`. The dominant phases

isolated were variants on a diamondoid net topology with large pores that are then multiply interpenetrated by 3 to 4 additional lattices arranged in distinct configurations.

3.2.6. MUF20-Aα-dia: a diamondoid 5-fold interpenetrated structure

Under the conditions used for MUF20 synthesis another phase was formed for the parent MOF that illustrates the flexible nature of pillar-layer MOFs and their sensitivity to synthesis conditions. In the case of MUF20 methanol served as a useful suppressant of the IRMOF phase, allowing phase pure 2:1 bpdc:bpy pillar-layer MOFs to be synthesized despite the bulkiness of the thermolabile protecting groups favouring the larger pores of an IRMOF cubic structure. In this instance by altering the solvent mixture and feed ratio of bpy ligand as necessary for TPG-functionalized MUF20 formation (increased concentration of methanol and bpy ligand), the parent MUF20-Aα 2-fold interpenetrated pillar-layer MOF could be completely disfavoured and phase-pure synthesis of a 5-fold interpenetrated diamondoid type framework occurs (Figure 3.7 and also in fold-out at back).

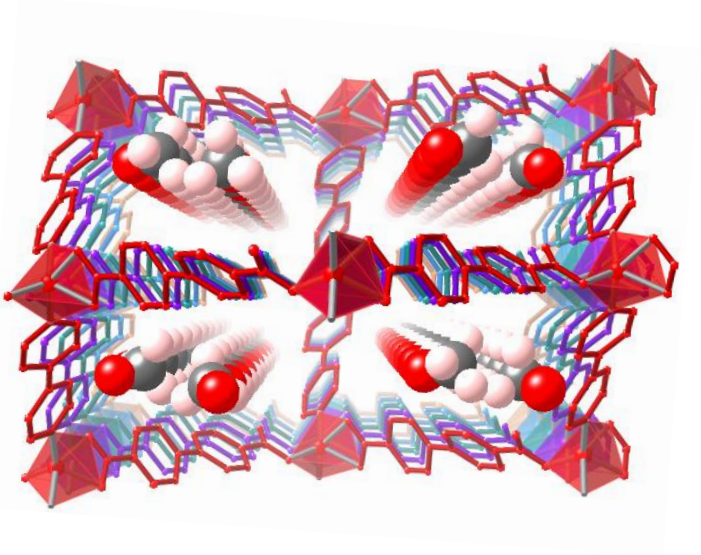

Figure 3.7: MUF20-Aa-dia phase with hydrogen-bonding methanol in pores. The zinc(II) SBUs are presented as polyhedra and organic linkers as sticks, each net is coloured distinctly and methanol is shown as van der Waals radii coloured; C-grey, O-red, H-white.

A potential explanation lies within the chains of methanol molecules crystallographically ordered within the pores, acting as a template for the dia-net topology to form but absent in the TPG-occluded pores of the functionalized MUF20 lattices (Figure 3.8).

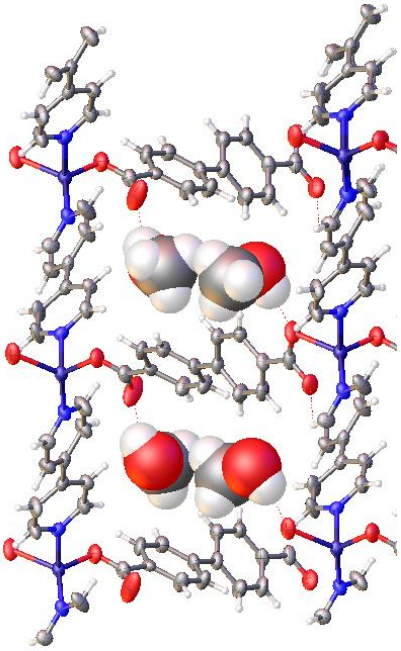

Figure 3.8: MUF20-Aa-dia phase lattice methanol hydrogen-bonding interactions.

In a fumarate and azobipyridine zinc MOF of 5-fold interpenetrated diamondoid topology, strong hydrogen bonding with lattice associated water molecules was observed to aid in MOF stabilization.[199] Thermolabile protecting groups can be shown to suppress this highly interpenetrated phase as in all MOFs synthesised with TPGs on the bpdc backbone the 5-fold interpenetrated dia phase was absent. With the MUF20-B` series it can be seen that the favoured interactions set up by the *directing hydrogen-bonding* free amine group on the bpdc causes the MUF20-Aα-dia phase to compete.

3.2.7. MUF20-B`α-dis and MUF20-B`α-dia

In Chapter 2, the free amine was noted to have a strongly directing influence on the phase only when placed on the bpdc ligand (B`) with incorporation on the bpy (β`) pillar showing little effect on MUF20-Aβ` formation. In MUF20-B`α, two different phases were isolated: MUF20-B`α-dis; a pseudo MUF20 phase that shows significant SBU distortion, and MUF20-B`α-dia with the same diamondoid topology as found above with MUF20-Aα-dia. With the exception of MUF20-B`γ and MUF20-B`α-dis, use of the unprotected ligand B` formed almost exclusively diamondoid frameworks containing a 1:1 ratio of bpdc:bpy and tetrahedrally coordinated zinc nodes (Figure 3.9).

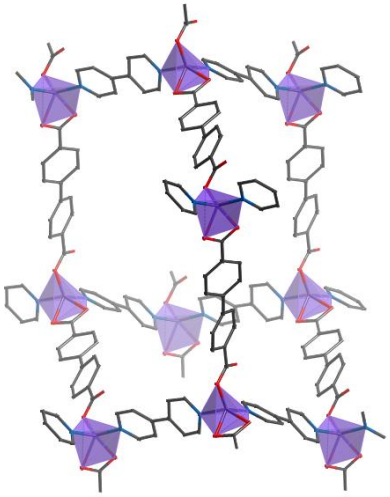

Figure 3.9: The diamondoid topology base cell. Each Zn^{2+} (shown as purple polyhedra) is coordinated by two bpdc and bpy ligands. This unit repeats to form the lattice in three dimensions with the large open space remaining in the pore allowing multiple lattices to interpenetrate.

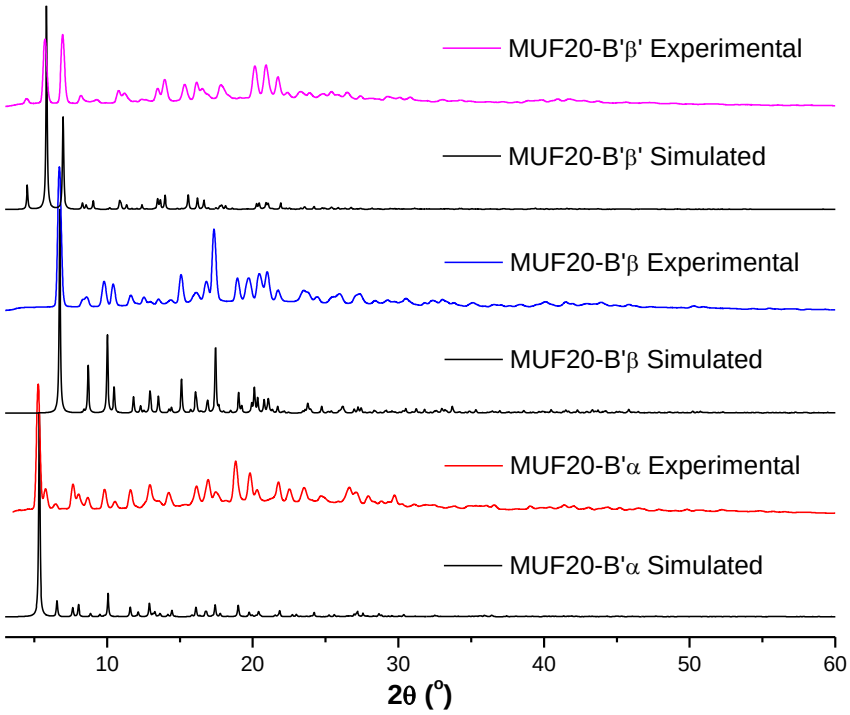

Figure 3.10: Simulated (calculated from single crystal structure) and experimental PXRD patterns for the materials MUF20-B`α-dis, MUF20-B`β, and MUF20-B`β` MOFs.

The single crystal structures of these phases were isolated and the materials shown to be phase pure from comparison of their simulated powder patterns to bulk experimental PXRD (Figure 3.10) as well as ^{1}H NMR digest ligand ratios closely matching to the predicted 1:1 (see experimental section end of chapter).

A similar phase with tetrahedrally coordinated Zn^{2+} was observed in DMOF synthesis using a sterically hindered bpdc-$(NO_2)_2$ ligand.[174] However, DMF molecules acted as capping terminal ligands to the coordination spheres and a 2D polymer structure was formed. In MUF20-B`α-dia the bipyridine ligands pillar the coordination polymer into a 3D network.

Functionalizing the bpy pillar with either another amine or carbamate functionality did not alter the dia net formation but introduction of the strongly directing *tert*-butyl ester group caused an immediate switch back to an IRMOF/MUF20 equilibrium where lowering of the temperature yielded purely the 2-fold interpenetrated MUF20 structure.

In dual-functionalized MOF synthesis attempts with the unprotected carboxylic acid ligands bpdc-CO_2H (C`) and bpy-$CO_2H$ (γ`), as with the mono-functionalized MOFs, MUF20-C`α and MUF20-Aγ`, all conditions trialled produced only multiple phases, amorphous materials or in the event of a consistent PXRD material, apparently pure phases did not yield single crystals suitable for structure analysis and were inconsistent in their NMR ligand ratios, varying as greatly as from 1:0.5 to 1:16 bpy:bpdc species, despite thorough washing of the material in each case (see Appendix). MUF20-$A\gamma^T$ and MUF20-$D^T\alpha$ are thus the only phase pure MUF20 MOFs formed containing free carboxylic acid ligands and the only known literature pillar-layer MOFs functionalized with carboxylic acids through a TPG approach.

3.2.8. Examination of inter-lattice interactions in MOF structure

Previously in Chapter 2, framework flexibility was found to be more responsive to the nature of the bpdc substituent. This trend continues in the remaining members of this functionalized family and is non-explicable through sole concentration of TPG groups in MOF but is most strongly related to lattice interactions possible from bpdc specific substitution. Although the -NHBoc group interfered with pillar-layer MOF formation when on the bpdc, there were no issues upon shifting the group to the bpy or pillar ligand. Likewise, a free amine on the bpdc directs the formation of multiple non-MUF20 phases but when located on the bpy pillar-layer MOFs MUF20-Aβ`and MUF20-Cβ` form without issue.

As we will see as we explore the single crystal analysis results, TPG functionalization within a pillar-layer framework affects topology through some main roles by localization of the TPGs:

1) Directing into the central pore to promote inter-lattice interactions (i.e., driving interpenetration)

2) Directing within the plane of the layer to exclude formation of the flexible pillar layer MOF and promote formation of bpdc or bpy only phases due to the steric bulk
3) Preventing formation of unwanted highly interpenetrated phases through cloaking of coordinating or H-accepting/donating functionalities.

The results presented herein suggest that approaching the knotty problem of interpenetration control in a flexible framework requires a less simplistic approach than considering steric bulk alone. Instead, designing of the functionality-lattice interaction alongside pore occlusion would be a fruitful direction of research. Such an approach is consistent with the manipulation of known interactions in the supramolecular chemistry of catenanes and rotaxanes and this approach is increasingly established in the use of mechanisms of MOF formation and research into the origins of breathing behaviour within the MOF field.

Indeed, within the Telfer group this interaction-specific approach was beautifully established within the more rigid IRMOF-9/10 framework. Using inter-lattice specific interactions enabled a high degree of interpenetration control and the synthesis of hybrid materials composed of two different lattices with partial interpenetration percentages.[200]

In flexible frameworks of diamondoid net topology the dynamic nature of the inter-lattice bonding has been explored to the extent of synthesizing a solvent-switchable phase change with continuous or stepped breathing and tuneable selectivity of CO_2 vs CH_4.[201] Investigation of the specific bonding[202] in these entangled supramolecular networks is an expanding area of research due to novel catenation modes such as helical molecular braiding[203] and rare net connectivities[204] leading to a large range in diverse properties such as thermal expansion behaviour[205], xenon/krypton selectivity,[206] and triggerable methane uptake at industrial storage pressures.[207]

In research carried out by Barbour et al, twisting of the bpy and carboxylate ligands out of plane and distortion of metal-ligand bonding were shown to be key in the deformation and transition into a more highly interpenetrated phase of a related pillar-layer MOF structure (Figure 3.11).[179, 208]

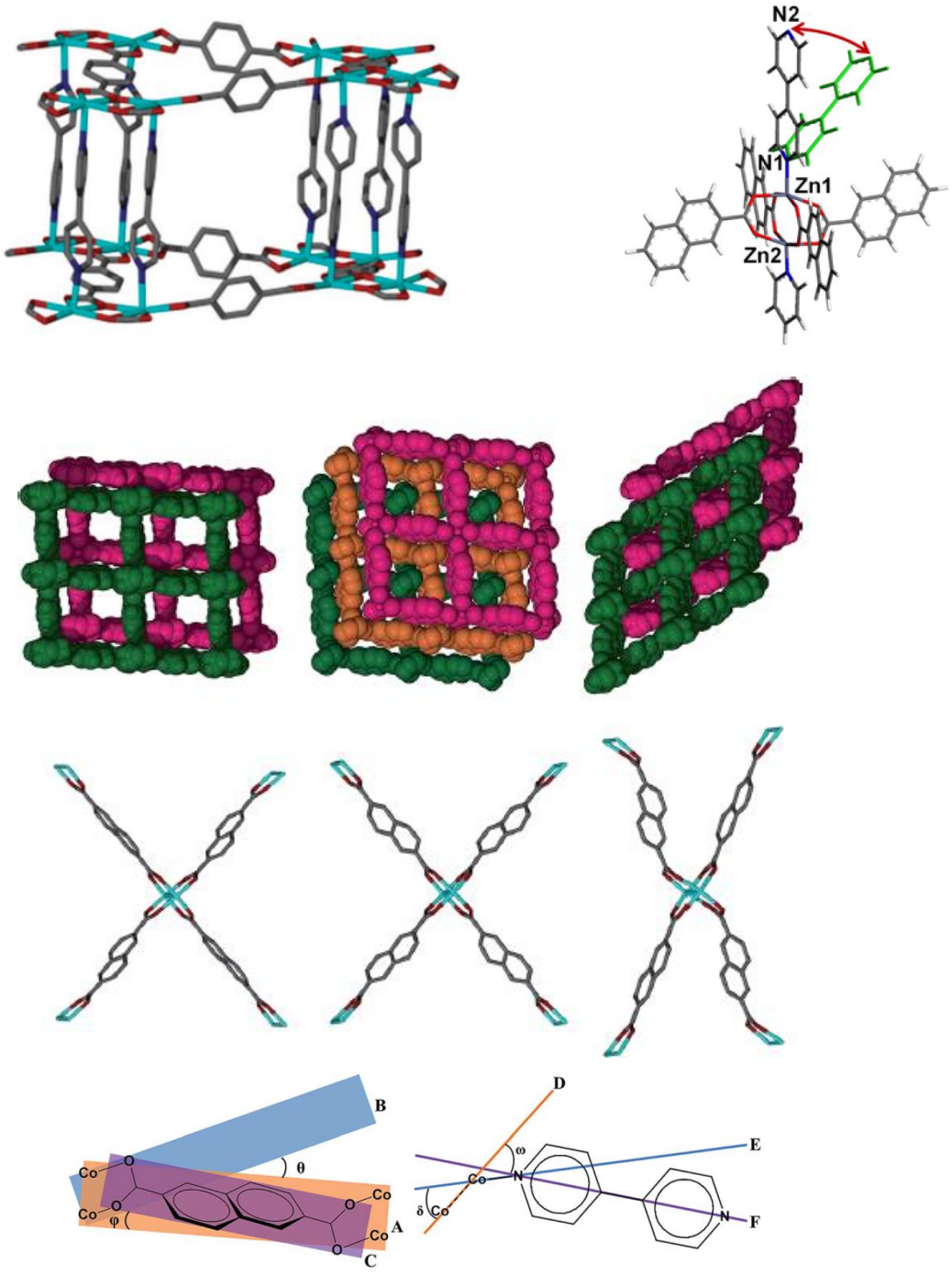

Figure 3.11: Key modes of MOF distortion involved in interpenetration changes in pillar-layer MOFs. Top left, rotation of terephthalate aromatic ring, one of the pillaring bpy rings out of plane (dihedral angle of 38.7(8)°) and distortion of metal-carboxylate bonding upon occurs upon activation of a [Cd(bdc)(bpy)] MOF at 150 °C. Top right illustrates tilting of bpy ligand upon conversion to a triply interpenetrated phase of $[Zn_2(ndc)_2(bpy)]$. Middle and bottom are the single crystal structures of the doubly and triply interpenetrated MOF $[Co_2(ndc)_2(bpy)]$ and an isolated intermediate between the two with highly distorted structure. An analysis of a naphthalene unit of the intermediate shows key angle properties affected: A: Co_2-Co_2 metal atom plane; B: Co_2–carboxylate oxygen plane; C: aromatic plane of ndc; D: Co_2 cluster metal–metal axis; E: metal–nitrogen; F: N-N axis of bpy. Figures adapted from references.[179, 208-209]

This was echoed in the previously mentioned BMOF-1-bpdc$(NO_2)_2$ with a measured dihedral angle between phenyl rings of bpdc-$(NO_2)_2$ being greater than that of bpdc-NO_2 (φ >110^o) thus setting up the interactions between NO_2 groups of neighbouring lattices to favour a return to a doubly-interpenetrated form.[174]

3.2.9. Effect of functionalization on MOF structure

How does functionalization, instead of sterically hindering interpenetration, favour it by distorting the framework to set up inter-lattice interactions?

3.2.10. MUF20-Bα and MUF20-B`α

This is best illustrated first with the simplest case comparing MUF20-Bα and MUF20-B`α:

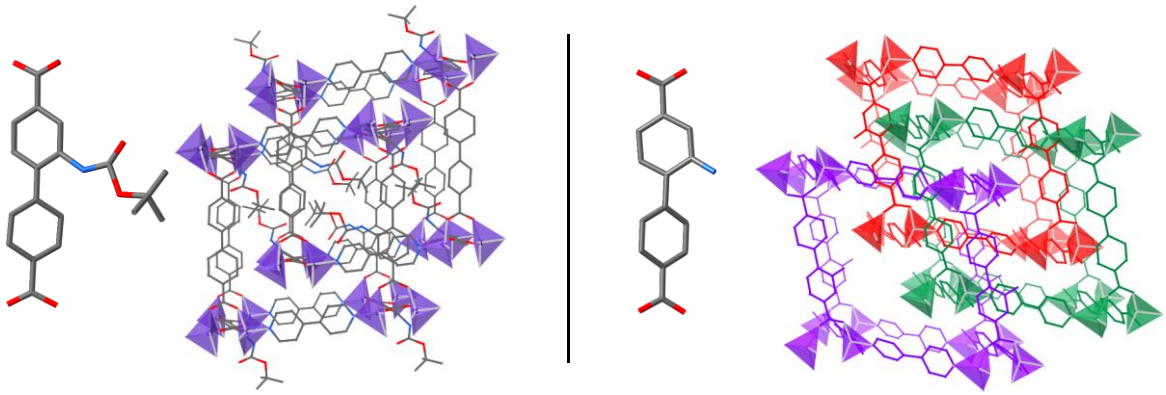

Figure 3.12: MUF20-Bα and MUF20-B`α ligand configuration and interpenetration.

Comparing (Figure 3.12) the MUF20 traditional pillar-layer SBU with the distorted MUF20-B`α-dis SBU the effect of the hydrogen bond-forming ability of the free amine on the biphenyl backbone becomes obvious. The coordination of the amine to a neighbouring freed carboxylate oxygen causes the biphenyl ligand to twist out of the 'layer' plane, pulling the Zn^{2+} ions ligand binding angles into a more tetrahedral coordination environment. The MUF20 pillar-layer MOF SBU has a ratio of 2:1 bpdc to bpy ligands from four bpdc ligands and two bpy ligands coordinating two Zn^{2+} ions to form a mirrored square pyramidal environment. Instead of this SBU, in MUF20-B`α the two Zn^{2+} ions are tetrahedrally coordinated. Two of the carboxylates bridge the two Zn^{2+} ions as in the pillar-layer SBU but the remaining two are twisted out of this layer to coordinate only singly through one oxygen. This is to favour hydrogen bond formation between the remaining freed carboxylate oxygens and the free amines of the bpdc-NH_2 ligands in adjacent interpenetrating lattices (Figure 3.13).

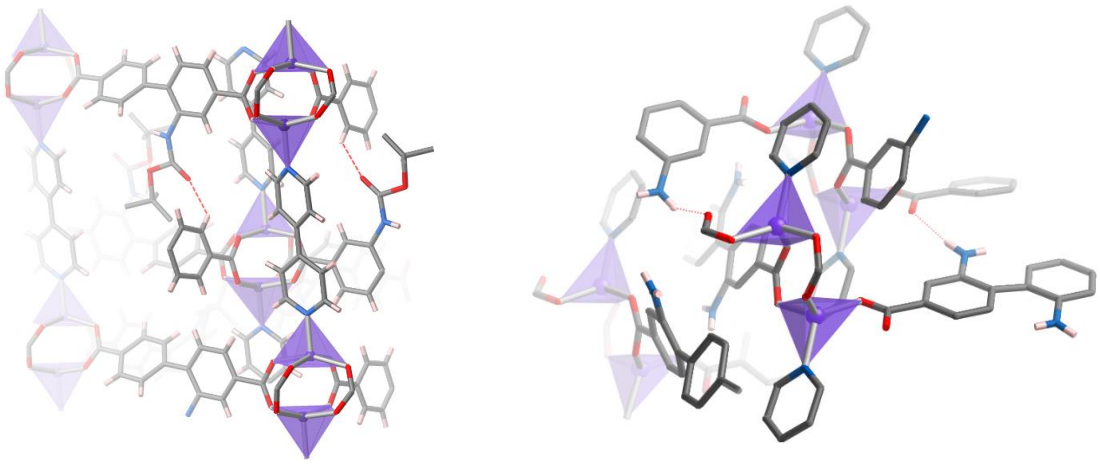

Figure 3.13: MUF20-Bα and MUF20-B`α materials showing the hydrogen bonding between the free amine of the bpdc-$NH_2$ ligand and freed carboxylate oxygen of the distorted SBU in MUF20-B`α.

This distorted environment of the SBU and reduced steric bulk allows the inclusion of a second lattice within the pores of the first two, yielding a 3-fold interpenetrated structure (Figure 3.14).

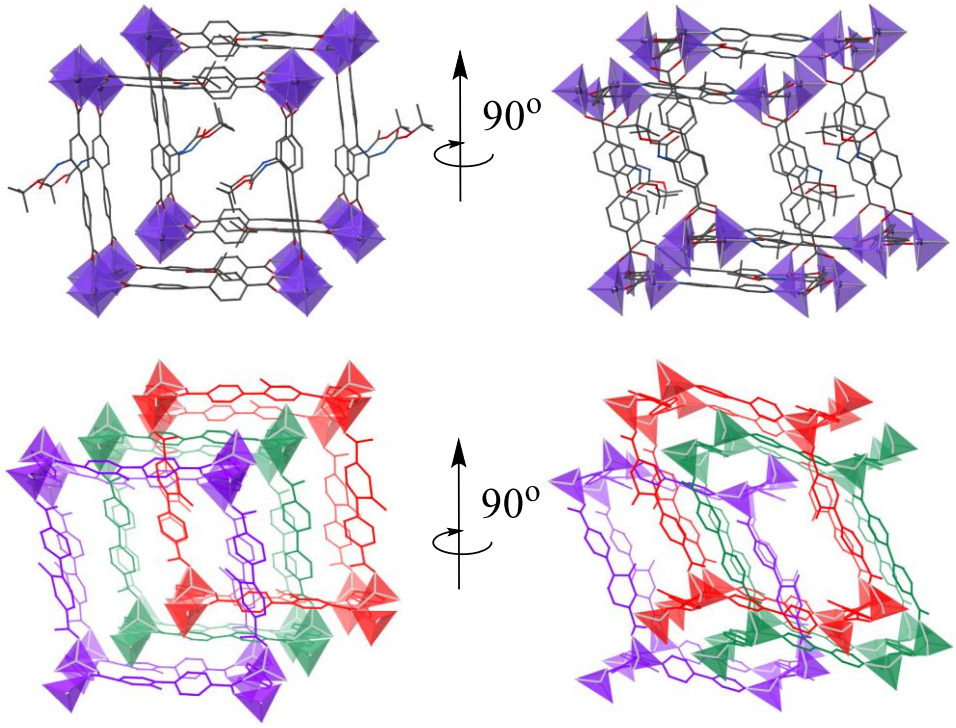

Figure 3.14: MUF20-Bα (top) and MUF20-B`α (bottom).

Competing with this 3-fold phase is another non-MUF20 phase that was isolated. Unlike the 3-fold phases that retain a pillar-layer structure, albeit heavily distorted, this secondary phase is of the same diamondoid asymmetric unit cell as MUF20-Aα-dia. However, MUF20-B`α-dia adopts a different lattice arrangement and a 4-fold instead of 5-fold degree of interpenetration.

During trialling of synthesis conditions, it was found that a 10% doping of the MUF20-B`α synthesis with bpdc allowed clean formation of the distorted pillar-layer framework over the dia net phase. Even such a small reduction in the percentage of inter-lattice promoting interactions can yield great selectivity in the final phase formed.

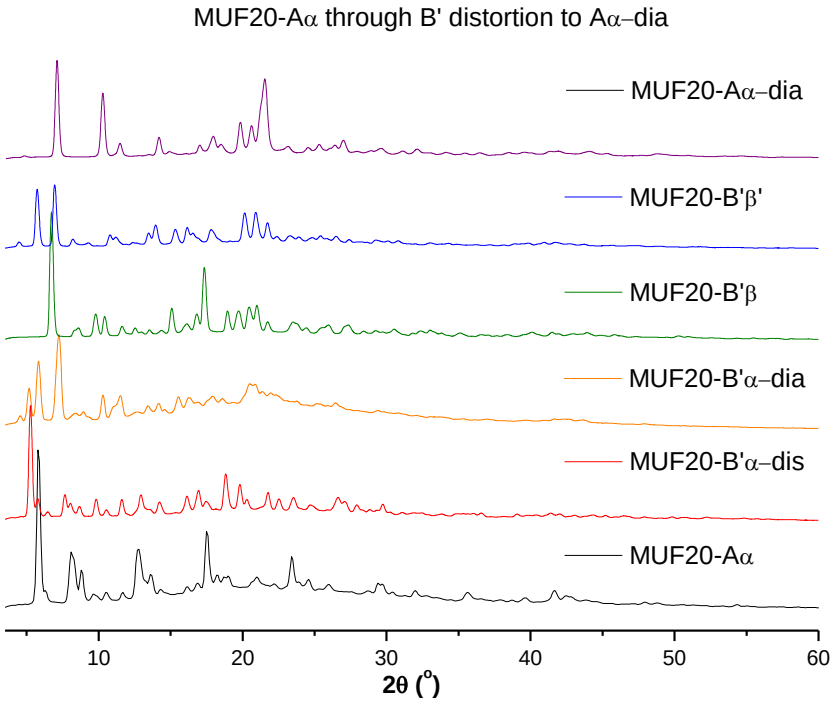

Figure 3.15: Experimental PXRD patterns for MUF20-Aα, MUF20-B`α-dis, MUF20-B`α-dia, MUF20-B`β, MUF20-B`β` phase with MUF20-Aα-dia illustrating the interplay of phases among these flexible MOF materials.

In literature, isolation of these intermediate configurations between dominant phases is still relatively rare. In an napthalenedicarboxylate (ndc) and bpy cobalt pillar-layer MOF structure a doubly-interpenetrated structure intermediate between two main phases was isolated.[179] Such studies are important in determining the make-up of MOFs both from reaction mixtures where multiple phases are possible, and during activation and other treatment conditions when structural changes in soft materials are probable.

3.2.11. MUF20-B`β and MUF20-B`β`

From this 3-fold H-bonding distorted pillar-layer framework a reasonable explanation would be that inclusion of a thermolabile protecting group on the bpy might allow the degree of interpenetration to be reduced back to 2-fold.

But this is not straightforwardly the case. Introduction of a hydrogen-donating functional group, even appended by a bulky *tert*-butoxy group, still allows for increased interpenetration

and completes the distortion of the twisted SBU observed in MUF20-B`α-dis to form a completely independent tetrahedral Zn(bpdc)(bpy) SBU. The reason for this is due to the amine of the -NHBoc group on the bpy being a hydrogen bond donator to the freed carboxylate oxygen of a neighbouring lattice bpdc (Figure 3.16).

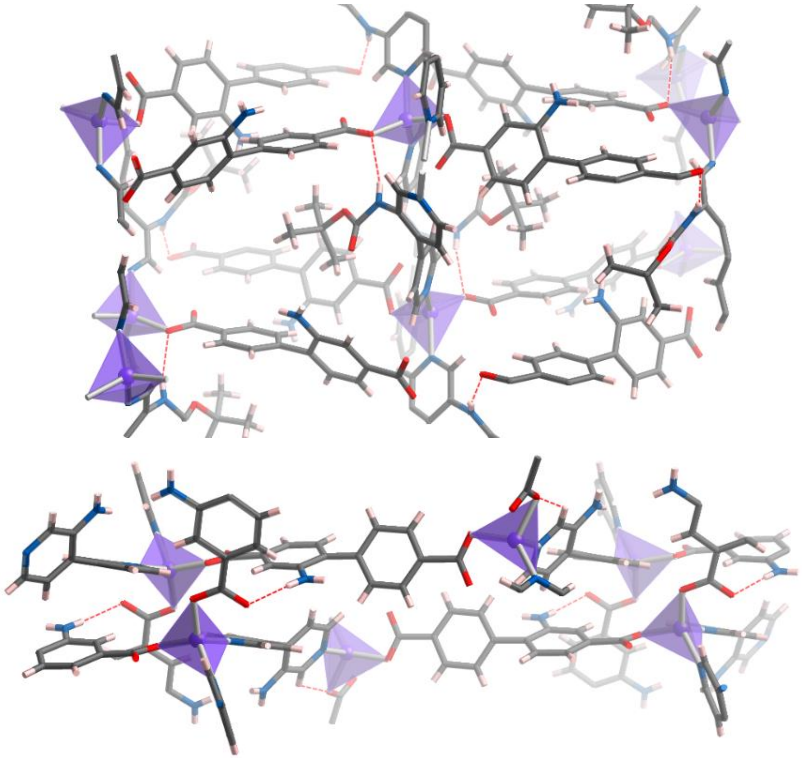

Figure 3.16: MUF20-B`β (top) and MUF20-B`β` (bottom) illustrating the similar hydrogen-bonding motif between the carbamate nitrogen of the former and the free amine of the latter.

Thus, despite the presence of a bulky group on the bpy, there is no reduction in interpenetration and instead, due to the additional H-bonding amine lattice interactions, a fourth net is added as the SBU is completely switched to the tetrahedral node of a large pore diamondoid topology. The H-bond donating -NHBoc moiety substituting for the freed amine on the biphenyl in twisting the biphenyl ligands away from the paddle-wheel based SBU coordination mode.

As determined from synthesis of the succeeding MOFs, MUF20-B`α and MUF20-B`β, the presence of the NHBoc thermolabile protecting group on the bipyridine has limited interference with the hydrogen bond between the bpdc carboxylate oxygens and the free bpdc-NH_2 group of a neighbouring lattice.

However, the increased concentration of hydrogen donating free amines in MUF20-B`β` does result in a more densely packed configuration than MUF20-Aα-dia or MUF20-B`β as the amines of each lattice form tight networks with the carboxylate oxygens of a neighbour lattice (Figure 3.17).

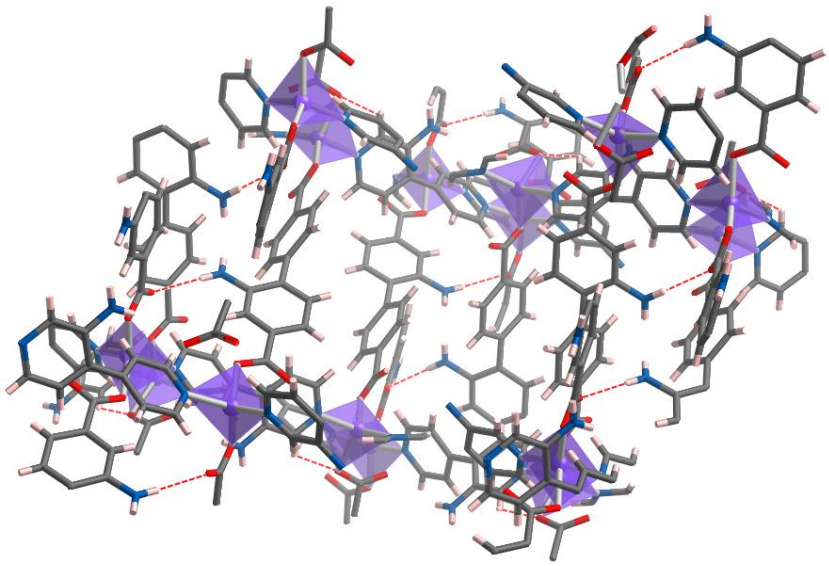

Figure 3.17: MUF20-B`β`single crystal structure illustrating the phase-directing hydrogen-bonding between neighbouring lattices through free amines that is suppressed in the bpy-NHBoc functionalized framework, MUF20-B`β. Pairing of these nets through the interactions drives a distinct 2 + 2 interpenetration topology.

Additionally, while both MUF20-B`α-dia and MUF20-B`β` form a quadruply interpenetrated structure, due to both reduced steric bulk and involvement of the free amines of the bpy-NH_2 ligand, a more complex autocatenation occurs with the four nets split into two sets of two stacked next to each other and then interpenetrating the remaining two lattices from opposite direction. So that, as opposed to all the struts lying parallel along the walls of the pores, they crisscross (Figure 3.18).

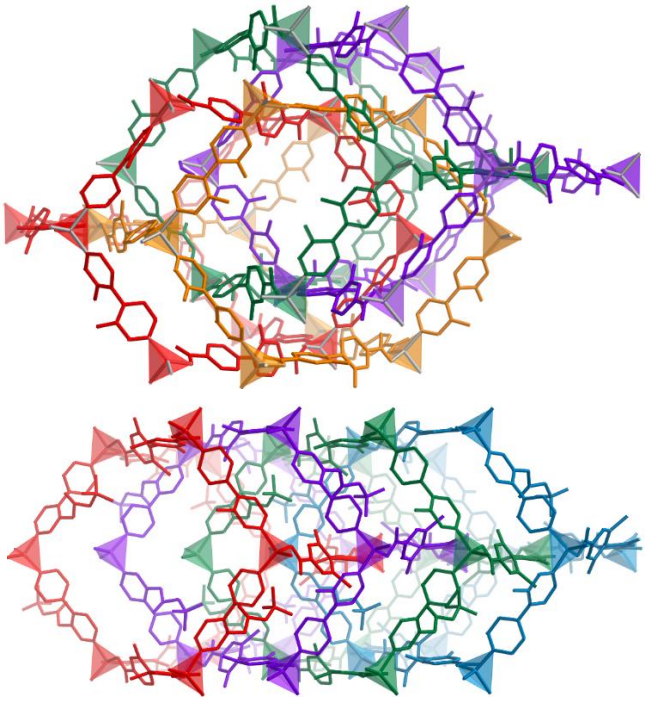

Figure 3.18: MUF20-B`β` (top) versus MUF20-B`β (bottom) illustrating the struts of independent lattices crossing each other or lying in parallel configuration respectively.

Alternatively, the interpenetration pattern can be viewed as, instead of the four nets identically interpenetrating, the set is divided into two offset interpenetrating nets (Figure 3.19).

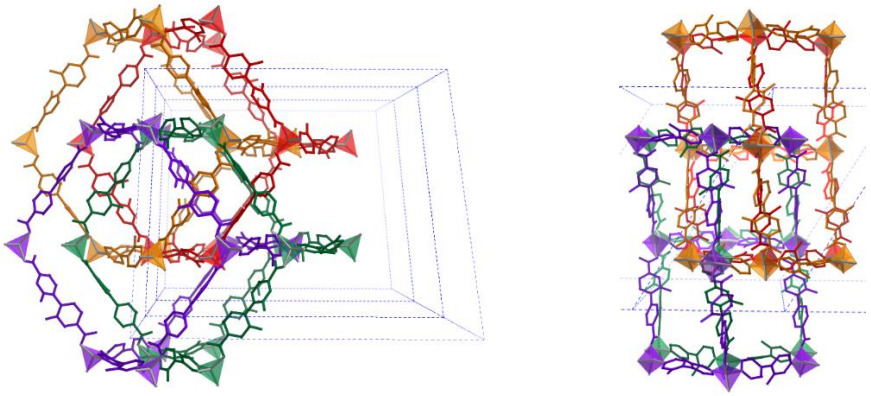

Figure 3.19: MUF20-B`β` showing pair-wise interpenetration and offset net spacing.

Even when TPGs are absent, functionalized linkers decrease interpenetration of diamondoid MUF20-Aα-dia phase from 5 to 4-fold. In the use of the unprotected ligands bpdc-NH_2 and bpy-NH_2, a material heavily doped with free amines is created. These free –NH_2 functionalities line walls of this porous material and create pockets suitable for hydrogen bonding of guest molecules such as methanol (Figure 3.20).

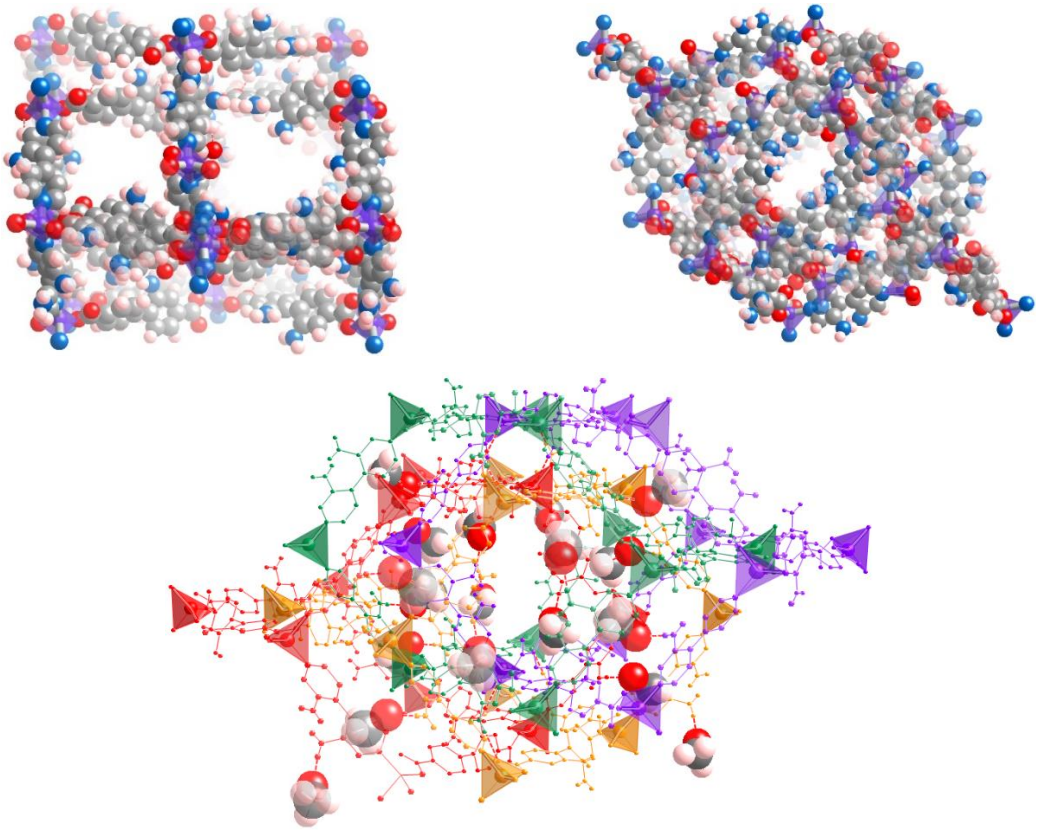

Figure 3.20: Free amine-lined pores in MUF20-B`β` (top) and methanol hydrogen-bonding in pockets of pore (bottom). Methanol are shown with van der Waals radii and are coloured: C-grey, O-red, H-pink.

However, through steric bulk and prevention of additional H-bonding interactions from the bpy-NHBoc a return to the MUF20-Aα-dia topology occurs upon introduction of a carbamate TPG on the bpy ligand, with MUF20-B`β showing 4-fold interpenetration with stacking of one net next to another (Figures 3.21, 3.22).

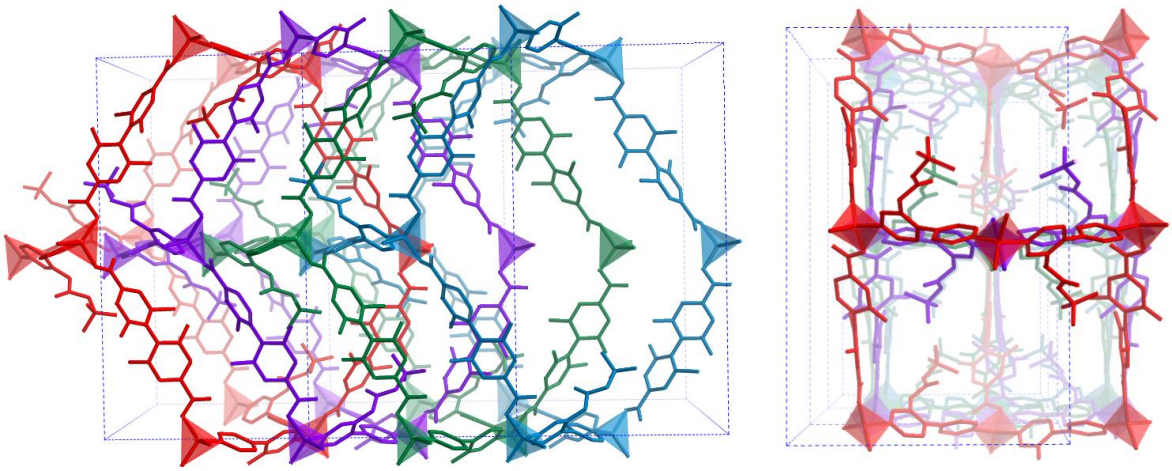

Figure 3.21: Interpenetration in MUF20-B`β and return to one dimensional pore structure observed in MUF20-Aα-dia. Unit cell shown in dotted lines.

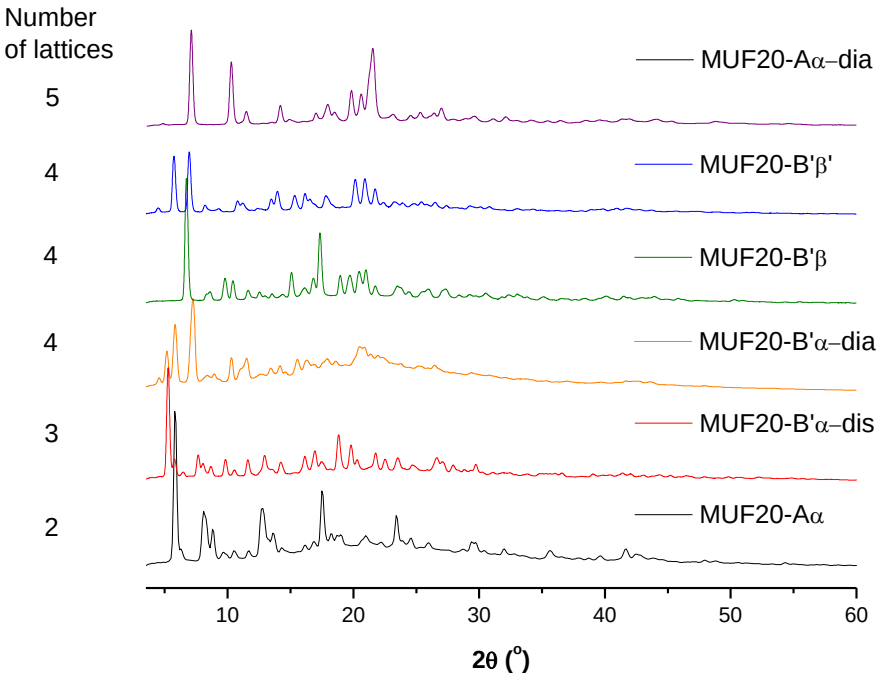

Figure 3.22: Experimental PXRD diffractograms for MUF20-Aα, MUF20-B`α-dis, MUF20-B`α-dia, MUF20-B`β, MUF20-B`β` and MUF20-Aα-dia with number of lattices noted on left, illustrating the interplay of phases among these flexible MOF materials.

This echoes the gas sorption results in Chapter 2 where the presence of bulky TPG groups in fact increases the porosity of the materials formed through favouring a more open pore phase.

In MUF20-B`β the TPG forces the MOF into a 1D channel material where the bulk of the TPGs occupy the inside of the channel, potentially acting as temperature activated gates to guest molecule diffusion (Figure 3.23).

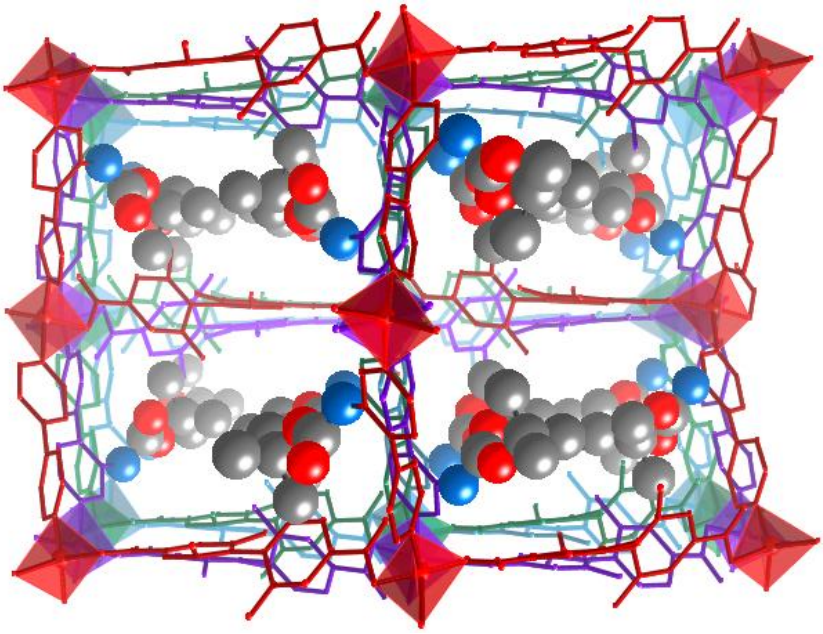

Figure 3.23: MUF20-B`β with –NHBoc sidechains presented in large radii, coloured: C-grey, O-red, N-blue. Hydrogens are omitted for clarity.

Related to this topology are the synthesis of MUF20-Bβ` and MUF20-Aβ`. Both ligand sets formed the MUF20-B`β phase (as identified through PXRD analysis, Figure 3.24) upon methanol-loss during synthesis. In the case of MUF20-Bβ`, using a lower temperature synthesis of 70 ^{o}C also yielded the diamondoid based 1D channel topology. No single crystals of suitable quality were present and phase-pure synthesis of MUF20 was prioritized. All of the diamondoid-based phases in Figure 3.22 were also encountered during the numerous MUF20-Bβ synthesis trials indicating that the proton-donating NH of the carbamate group was a significant factor in determining resultant phase.

The material MUF20-B`β is of particular interest for future gas sorption analysis and thermolysis due to the lining of the inner pores by amines and subsequent removal of the pore-occluding TPGs upon heating. Due to the high interpenetration of this material it is likely to be robust to thermolysis. A caveat of this increased support is the greater rigidity that may impact any breathing or gate-opening characteristics of the MOF. However, literature research into non-TPG functionalized, highly interpenetrated diamondoid MOFs indicate that the materials still exhibit significant flexibility and intriguing stepped isotherms specific to guest-host interactions.[210]

Table 3.3: Crystal structure properties of non-MUF20 phase MOFs.*

MOF MUF20-	Space group	Cell Volume ($Å^3$)	Density	Pore Volume ($Å^3$)		Unit Cell Volume (%)		Surface area (m^2/g)	
				N_2	CO_2	N_2	CO_2	N_2	CO_2
Aα-dia	*Cc*	2428.3	1.263	0.1	9.76	2.79	0.4	31	72
B`α-dis	*P*-1	3232.1	1.335	180.2	231.5	5.6	7.2	388	459
B`α-dia	*P*-1	6570.0	0.964	676.8	844.9	10.3	12.9	589	682
B`β	*Pbca*	6514.7	1.207	20.1	59.7	0.3	0.9	45	94
B`β`	*C*2/*c*	13529	1.027	1268.8	1613.8	9.4	11.9	441	517

*Surface areas calculated from solvent void volumes generated in Mercury v4.10. Details in Appendix, section.

3.2.12. MUF20-B`γ and MUF20-Cβ`

Despite the presence of a directing free amine on the bpdc ligand, upon changing the nature of the thermolabile protecting group on the bpy to the less sterically bulky but more rigid and non-H-bonding *tert*-butyl group, there is a drastic reduction in interpenetration and presence of competing phases, with only the MUF20 2-fold interpenetrated PLMOF formed (Figure 3.24).

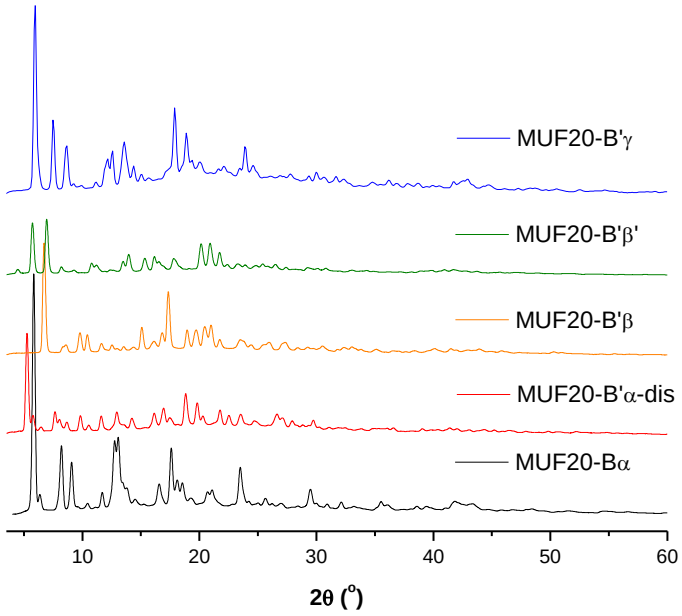

Figure 3.24: PXRD patterns showing deviance from MUF20-Aα phase (exemplified in MUF20-Bα) through the B`-ligand-based materials; MUF20-B`α, MUF20-B`β, MUF20-B`β` and resumption of original phase through introduction of TBE group on bpy ligand in MUF20-B`γ.

This illustrates the importance of the nature of the TPG group as the absence of the hydrogen donating moiety of the carbamate is more significant than the decreased bulk going from the carbamate to the *tert*-butyl ester group in preventing highly interpenetrated phases forming. The directing influence of the –TBE TPG can be seen in the non-classical hydrogen bonding set up within the structure which favours the formation of the paddle-wheel based SBU as opposed to the tetrahedral zinc node of the dominating bpdc-NH_2 phases (Figure 3.25).

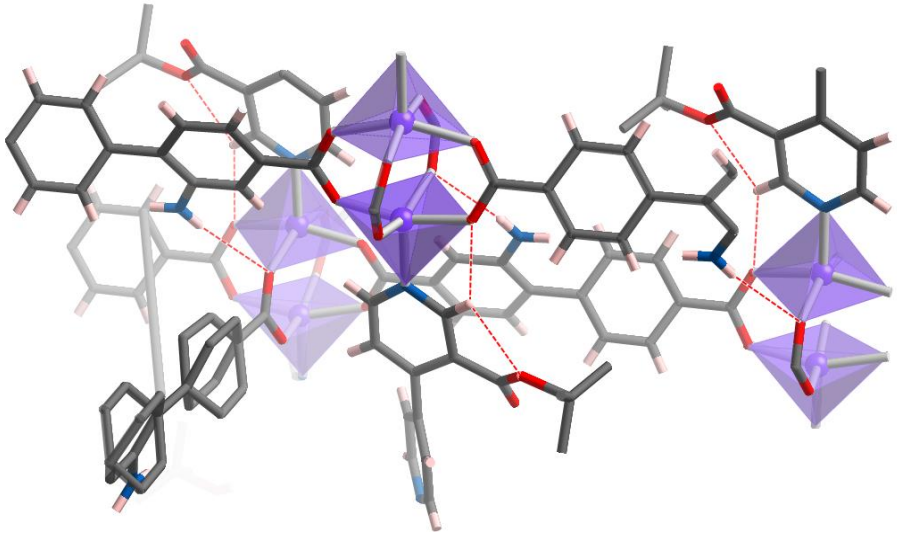

Figure 3.25: Single crystal structure of MUF20-B`γ showing classical and non-classical hydrogen bonding. Atom colour code: C-grey, H-pink, O-red, N-blue, Zn-purple.

From MUF20-B`γ there is good opportunity to compare the effect of positioning of the thermolabile groups by contrast against MUF20-Cβ` where the amine versus TBE groups have been switched from bpdc to a bpy backbone (Figure 3.26).

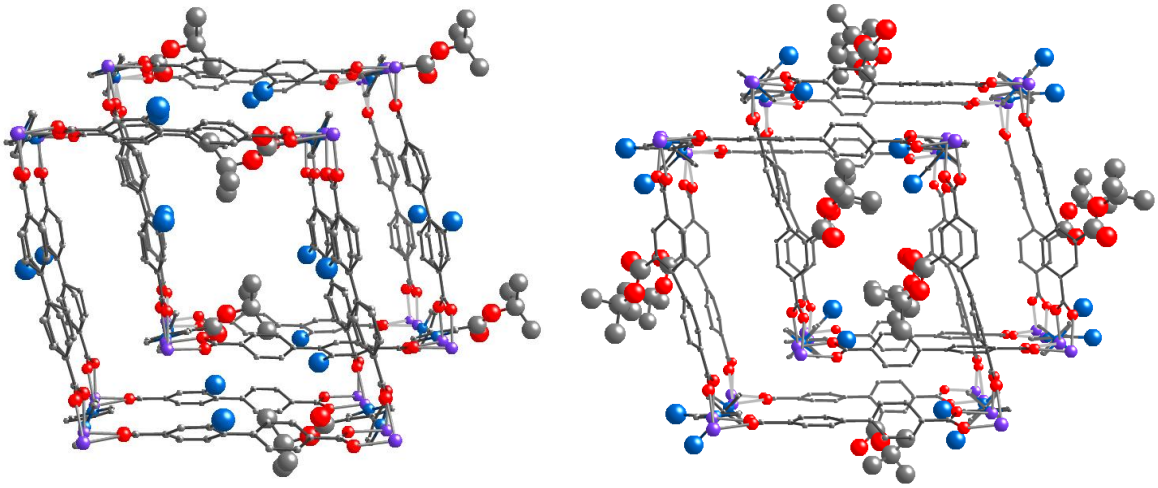

Figure 3.26: MUF20-B`γ (left) versus MUF20-Cβ` (right). TPGs are presented in larger atomic radii. Some TPGs and hydrogens have been omitted for clarity. Atom colour code: C-grey, O-red, N-blue, Zn-purple.

It can be clearly seen that much the same structure is obtained. This is due to the similar molecular interactions set up by the *directing tert*-butyl group with the second lattice regardless of location of the TPG on bpy or bpdc ligand.

In both cases the *tert*-butyl ester groups can be seen to project into the pores of the MOF, looking along the bpy axis (Figure 3.27). The non-polar *tert*-butyl CH_3 hydrogens reach across the pore space to interact with the face of the bpy or biphenyl ligand of the second lattice in MUF20-B'γ and MUF20-Cβ` respectively.

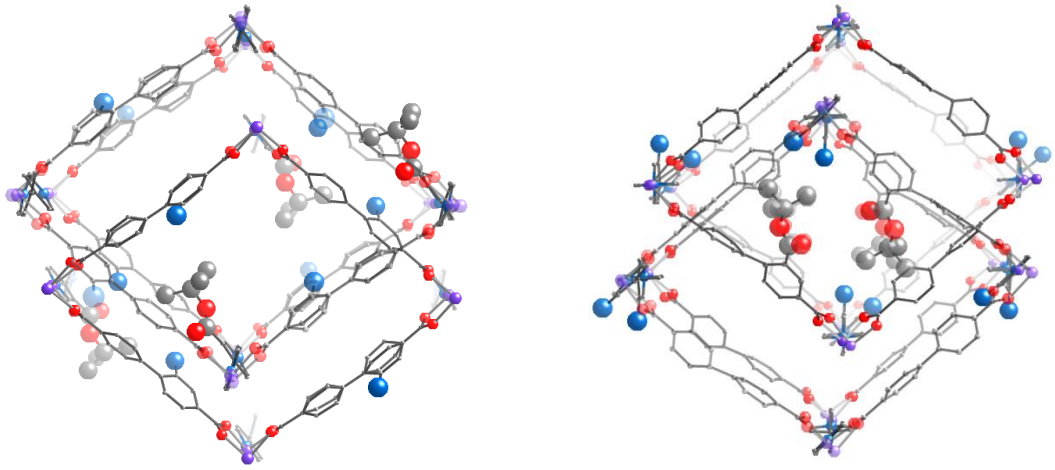

Figure 3.27: MUF20-B`γ (left) versus MUF20-Cβ` (right). Both MOFs show the TBE projecting into the pore of the MOF even when present on the bpy (left). Hydrogens and some functional groups are omitted for clarity. Atom colour code: C-grey, O-red, N-blue, Zn-purple.

The reverse switch, with the free amine located on the bpy versus the bpdc again shows, as with MUF20-B`α vs MUF20-Aβ`, the amine on the bpy has little influence on the resultant MUF20 clean phase formation with MUF20-Cβ` much the same as MUF20-Cα.

3.2.13. MUF20-Cα, MUF20-Cβ, and MUF20-Cγ

Throughout the MUF20-C series (Figure 3.28), the *tert*-butyl ester to phenyl interaction dominates and only the doubly-interpenetrated MUF20 phase is observed despite growing distortion of the lattices from the parent grid form.

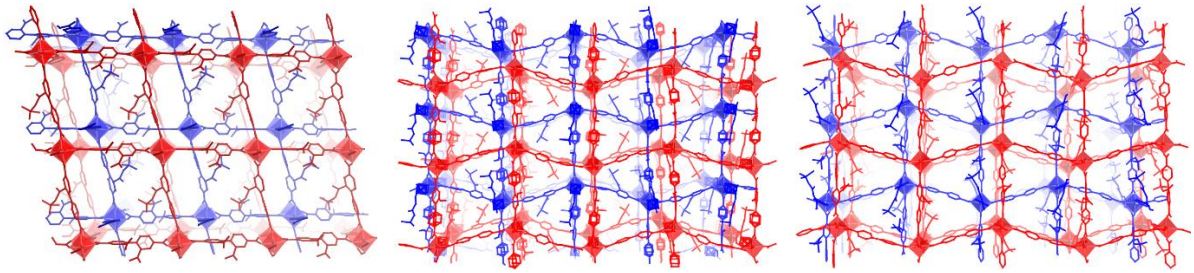

Figure 3.28: MUF20-Cα, MUF20-Cβ, and MUF20-Cγ (left to right). The two lattices in each MOF are uniformly coloured for clarity.

Although the overall MOF structure remains the same pillar-layer throughout the series, the increasing steric bulk of dual functionalization with TPG groups can be observed in the distortion of the lattices with the coordination angle of the biphenyl dicarboxylate deviating increasingly from the ideal 180°. Observable again is that the most notable distortion is not present in the more sterically bulky β ligand but in the the γ ligand due to the favoured van der Waals interaction with the phenyl rings of the second lattice. In this case the presence of the TBE ester on the bpy layer also distorts the lattice to promote this interaction.

3.2.14. MUF20-Aγ

In the absence of the TBE group on the bpdc ligand this sharp angling was still oberved in MUF20-Aγ upon MeOH-loss during synthesis as noted previously.

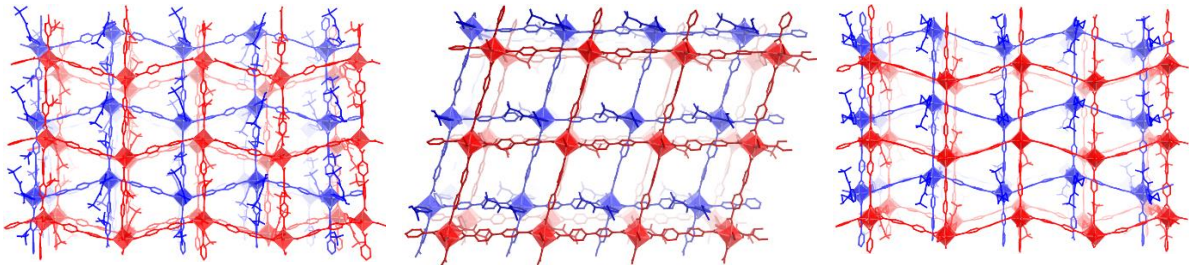

Figure 3.29: MUF20-Cγ (left) versus MUF20-Aγ without and with MeOH loss during synthesis (middle and right respectively). The two lattices in each MOF are uniformly coloured for clarity.

The –TBE groups in the distorted wave structures in MUF20-Cγ and MUF20-Aγ can be seen to occupy near identical positions in the lattices.

While the single crystal structures were obtained from crystals straight from the reaction mixture and placed in oil, experimental PXRD diffractograms are collected after gentle grinding of the crystalline material in DMF. As both the methanol-loss and regular materials have almost identical powder diffraction patterns this indicates that the change in structure is reversible. While the presence of TPG bulk in the pores of MUF20-Cγ seemingly locks the structure into the wave form irreversibly, for MUF20-Aγ conversion between the distorted wave and square grid form can be achieved at room temperature with solvent (Figure 3.30).

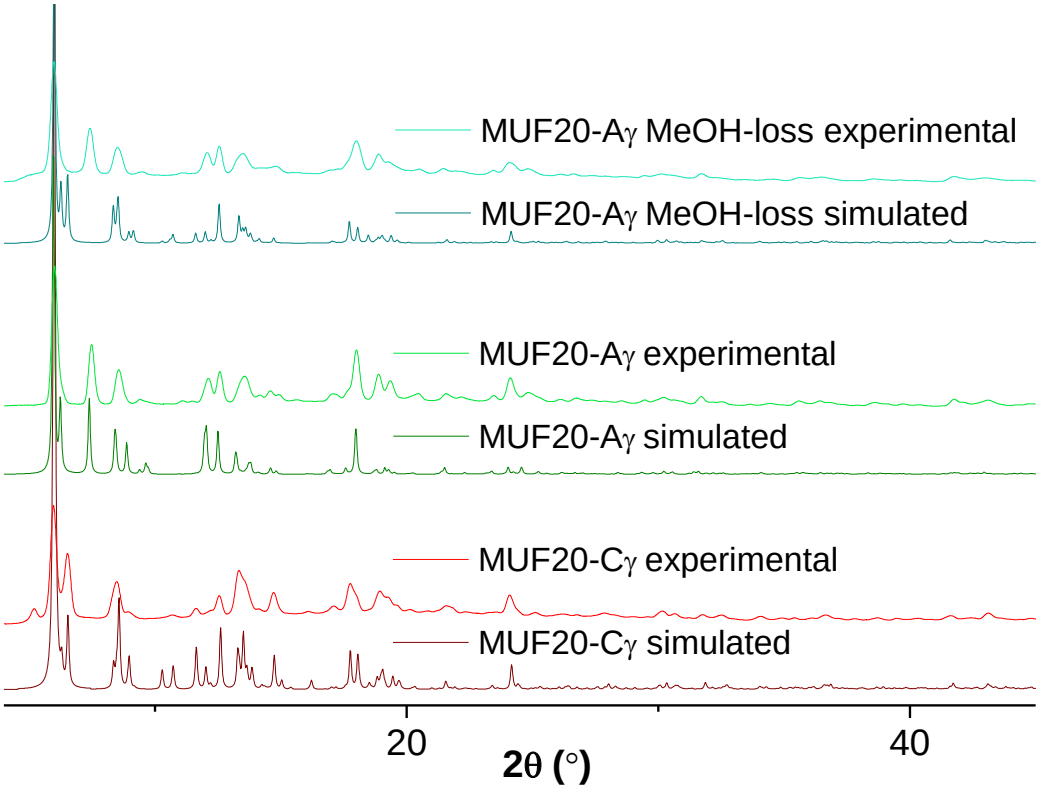

Figure 3.30: Simulated and experimental PXRD diffractograms for MUF20-Cγ versus MUF20-Aγ without and with MeOH loss during synthesis.

As noted earlier, a similar synthesis that underwent methanol loss yielded no difference in material form when the TPG ligand involved was bpdc-NHBoc in MUF20-Bα.

This is not to say that the steric bulk of the TPG on the bpy ligand is still not a significant factor in distorting the lattice as can be seen in the slanting of the second lattice going from MUF20-Cα, MUF20-Cβ` to MUF20-Cβ (Figure 3.31).

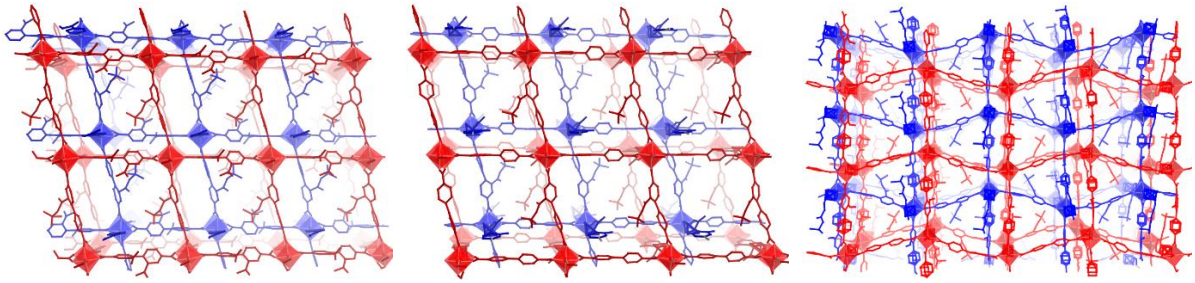

Figure 3.31: MUF20-Cα, MUF20-Cβ` to MUF20-Cβ (left to right). The two lattices in each MOF are uniformly coloured for clarity.

This wave-like effect occurrs as the lattices distort to both accommodate the TBE-phenyl interaction and the greater steric bulk on the bpy pillar. Notably MUF20-Dβ retains the parent MOF square-grid form (Figure 3.32).

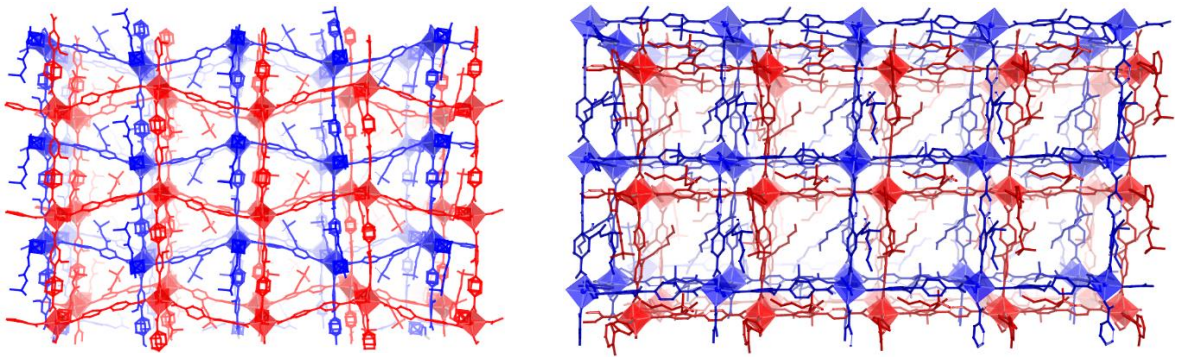

Figure 3.32: MUF20-Cβ (left) versus MUF20-Dβ (right). Only one of each disordered alkyl chain is shown. The two lattices in each MOF are uniformly coloured for clarity.

Clearly the MUF20-Dβ SBU maintains the square angles of the carboxylate layers and excludes the extreme angling and resultant wave-form observed for MUF20-Cβ. Similar to MUF20-Bα the additional steric bulk is accommodated within the MOF pores but unlike bpdc-NHBoc and bpdc-TBE, the -2mh alkyl chain is disordered and maintains the most open pore form where the chains localize.

Interestingly, crystallographic ordering of the TBE group on the second bpdc ligand of the asymmetric unit cell varied through the series. Being most strongly ordered on one site only in MUF20-Cβ and lacking even residual electron density peaks in MUF20-Cγ (NMR ratio supports no bpdc present). This result suggests that the bpdc sidechain is both highly ordered (on the first bpdc of the ASU) and highly disordered (on the second bpdc) throughout the crystal with no preferred orientation/interactions set up constraining position in the latter case.

In MUF20-Cα and MUF20-Cβ` the TBE on the second bpdc can be observed through disordered electron density on a single side of the ligand backbone but was only modelled to the carboxyl group due to high disorder (disordered over two sites on one side) still present.

In MUF20-Cβ, the second bpdc TBE can be seen to be located on the side away from the proximal bpy-NHBoc pyridine ring of own lattice so as to interact with the methyl hydrogens of the -NHBoc group of the ring furthest from the shared SBU. Given that there is space available to point into the pore away from this –NHBoc group, this is likely the favoured orientation due to specific interactions (Figure 3.33).

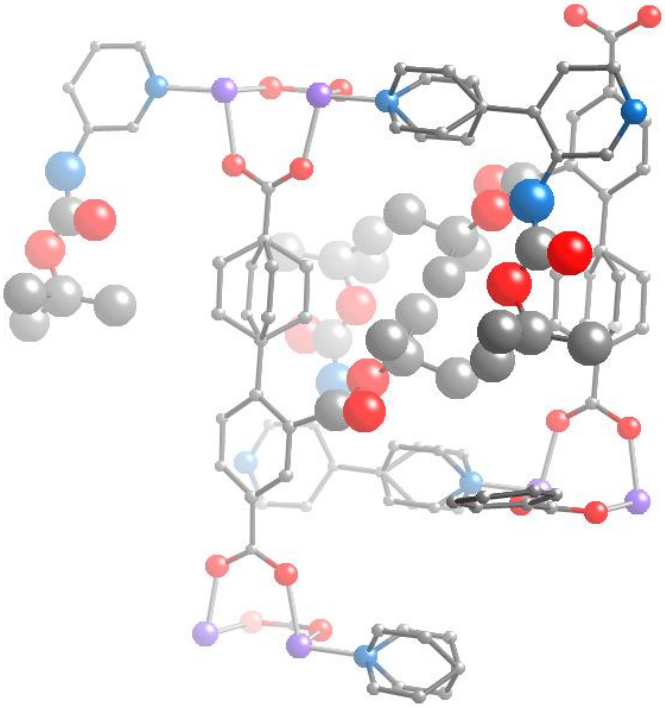

Figure 3.33: In the single crystal structure of MUF20-Cβ, the -TBE TPG is ordered through inter-lattice interactions with a neighbouring lattice -TBE and intra-lattice interactions with NHBoc. Proximity of the functionalized pyridine ring of the bipyridine ligand on one side inhibits disordering of the -TBE group. Atom colour code: C-grey, O-red, N-blue, Zn-purple.

This crystallographic analysis explores the factors influencing phase in pillar-layer MOF formation with bulky substituents. Bulk properties are affected by the stability of the phase formed, and thermolytic release of fragments may be tuned by these interactions.

3.2.15. Thermal properties of functionalized MOFs

The thermal properties of all the TPG-functionalized pillar-layer MOFs were explored through TGA and are presented as a cohesive family of thermoresponsive materials with mono-functionalized materials included from Chapter 2 for completeness and analysis of trends (Figure 3.34).

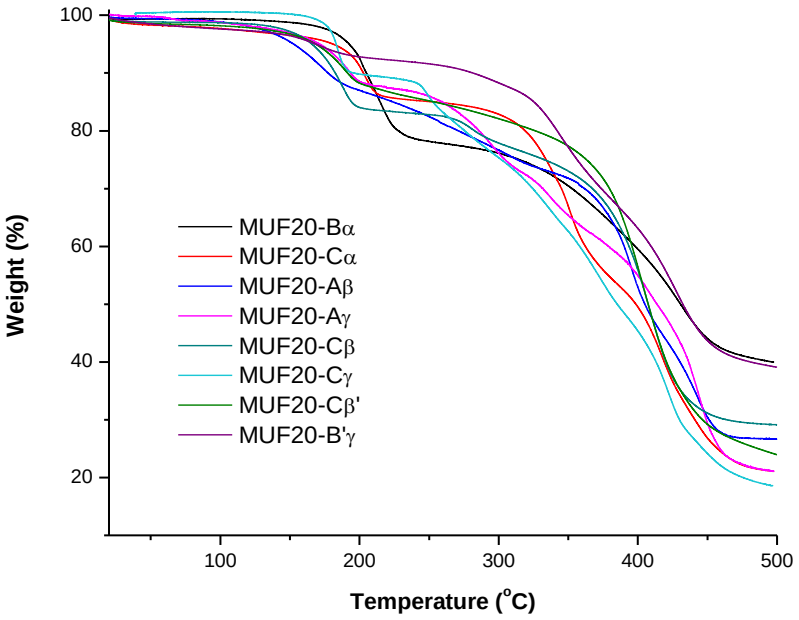

Figure 3.34: Thermogravimetric analysis (TGA) trace for all TPG-functionalized BMOF-1-bpdc analogues indicating the tuning of MOF thermal properties through this PSM strategy.

As shown above, inclusion of a TPG allows a range of thermal curves to be accessed. These curves can be broken down into related TPG ligand threads, beginning with the bpdc-TBE (C) ligand series (Figure 3.35).

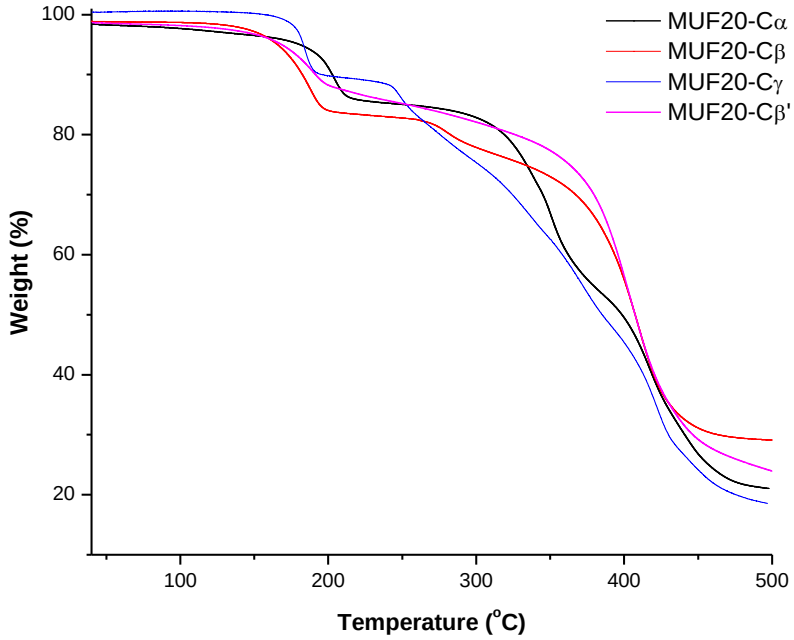

Figure 3.35: Thermogravimetric analysis (TGA) trace for MUF20-Cα, MUF20-Cβ, MUF20-Cγ, and MUF20-Cβ` MOFs.

Table 3.4: Experimental and calculated percentage weight losses of bpdc-TBE (C) MOFs.

MOF	$T_{1/2\Delta}$ (°C)	Experimental Weight loss (%)	Calculated Weight Loss (%)
MUF20-Cα	160	12.3	11.6
MUF20-Cβ	145, 240	21.3	19.6
MUF20-Cγ	170, 225	16.3	15.8
MUF20-Cβ`	155	11.5	11.4

* $T_{1/2\Delta}$ is defined as the midpoint of the temperature range over which weight loss associated with thermolysis occurs and is rounded to the nearest 5 °C.

The experimental weight losses (Table 3.4) correlated well to the calculated values for all MOFs with some slight deviation. These deviations can be attributed to difficulty in determining start and end points of thermolysis (Figure 3.35) and sample preparation where trace solvent may reside within the MOF pores and be lost at low temperatures at the beginning of the TGA traces. As before in Chapter 2, above 300 °C, degradation of the organic ligands occurs, culminating in ZnO and carbonaceous residue remaining on the pan. The precise points used in calculations are in the Appendix.

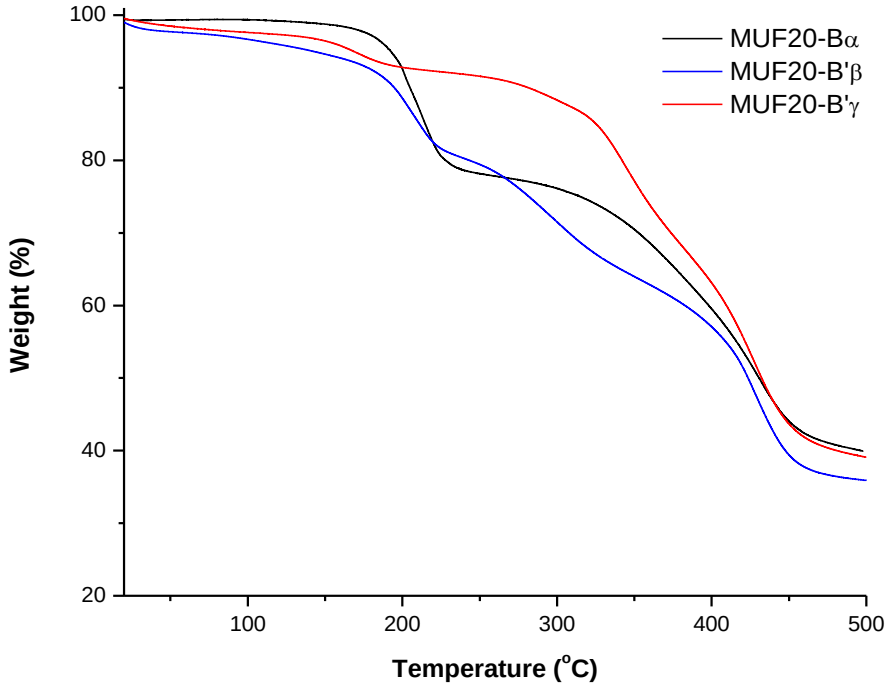

Figure 3.36: Thermogravimetric analysis (TGA) trace for MUF20-Bα, MUF20-B`γ and MUF20-B`β.

Table 3.5: Experimental and calculated percentage weight losses of TPG-functionalized bpdc-NHBoc and bpdc-NH_2 (B and B`) MOFs.

MOF	$T_{1/2\Delta}$ (^oC)	Experimental Weight loss (%)	Calculated Weight Loss (%)
MUF20-Bα	180	21.2	20.1
MUF20-B`γ	145	5.5	6.3
MUF20-B`β*	145	17.2	17.9

*Note: Non-MUF20-Aα phase

The TPG-functionalized members of the B and B' ligand combinations were limited to singly-functionalized MOFs. From the TGA (Figure 3.36), the experimental weight losses match well with the calculated weight losses (Table 3.5). The MOFs bearing free amines all share a tendency to show a slightly sloping initial weight loss despite extensive solvent exchanging and drying under high vacuum. This could be attributable to coordinated solvent molecules associated with the lattice. However, no trace of DMF is found in NMR analysis of these activated materials (see experimental section). Insight from polymer chemistry suggests increased residual mass of nitrogen-containing MOFs post TGA heating to 550 ^oC may be related to a higher degree of thermal cross-linking in decomposition residue due to higher free amine content.[211]

The Table 3.4 neatly summarises the importance of topology and ligand backbone functionalization choice in determining the height of the thermolysis step. The bpdc ligand is present in a 2:1 ratio in MUF20-Bα and thus has a significant effect in the TGA with a 20 % weight loss step. The bpy-TBE ligand in MUF20-B`γ, on the other hand, has a much smaller impact on the weight loss (5-7%) of the material upon heating due to releasing only isobutylene and being present at half the concentration to the bpdc-NH ligand. In the non-pillar-layer material, MUF20-B'β, both ligands are present in a 1:1 ratio and thus the bpy-NHBoc has a greater impact of 17-18% on the % weight loss of the material than the related MUF20-Aβ MOF at 11-12%.

The MOFs were then put through loop TGAs to confirm loss of TPG group in steps analysed and contributions of ligands to MOF percentage weight loss (Figures 3.37-3.46).

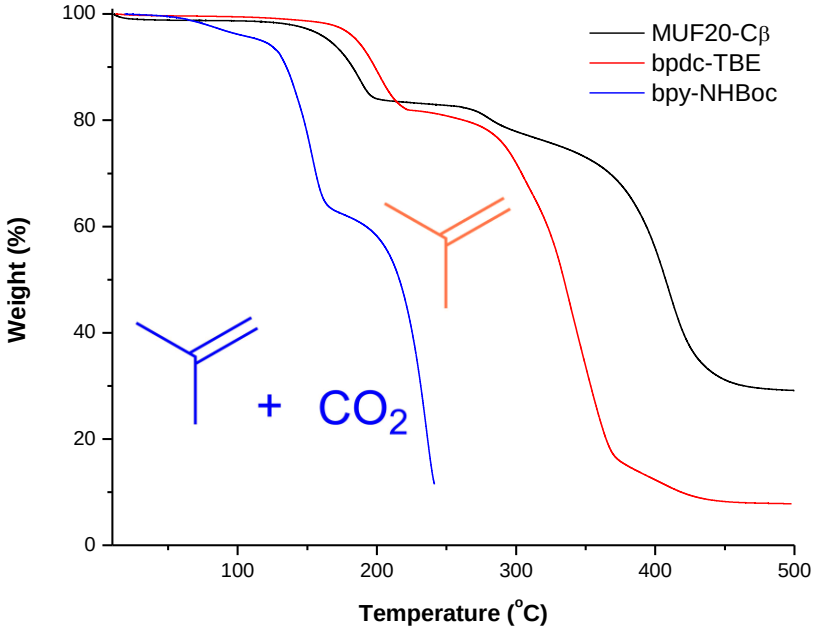

Figure 3.37: Thermogravimetric analysis (TGA) trace for MUF20-Cβ and TPG-ligands bpdc-TBE and bpy-NHBoc illustrating the expected thermolytic losses in final MOF TGA trace and individual loop TGA steps (below).

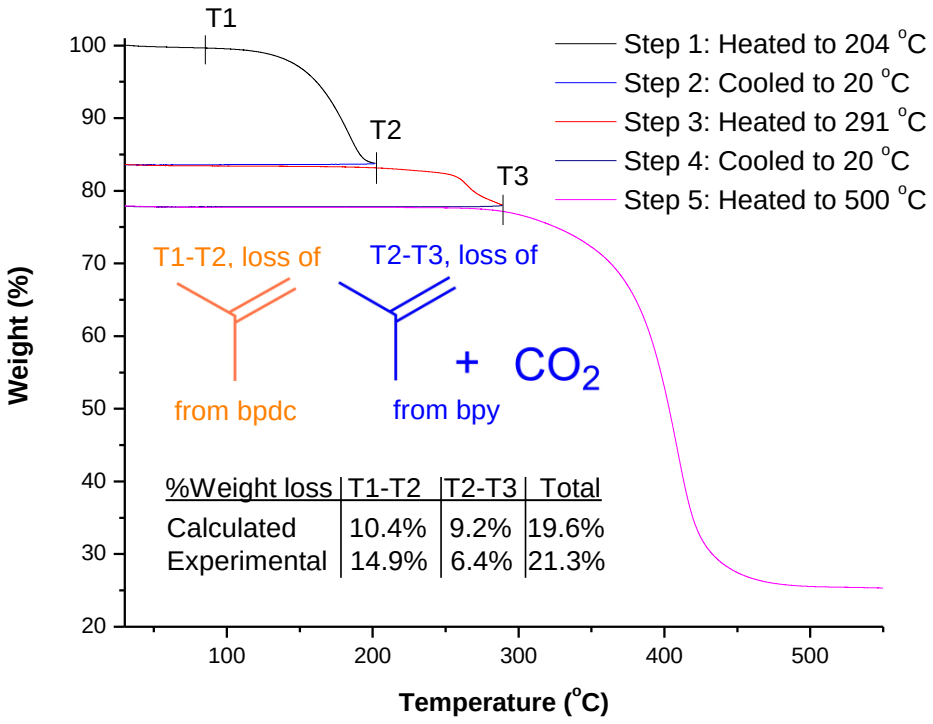

Figure 3.38: Thermogravimetric analysis (TGA) trace for MUF20-Cβ, looped to illustrate triggered loss of thermolabile protecting group (TPG).

From the loop TGA (Figure 3.38), the percentage weight losses indicate that the thermolysis deprotecting steps for bpdc-TBE and bpy-NHBoc overlap to some degree within MUF20-Cβ material. However, the total percentage weight loss of 21.3% is in good agreement with the total calculated of 19.6% for complete thermolysis of both bpdc and bpy TPG ligands to reveal a carboxylic acid and amino group respectively. The experimental percentage weight loss is no doubt slightly higher also due to the difficulty in determining point T3 at border of degradation temperatures for the organic ligands at ~300 ^{o}C.

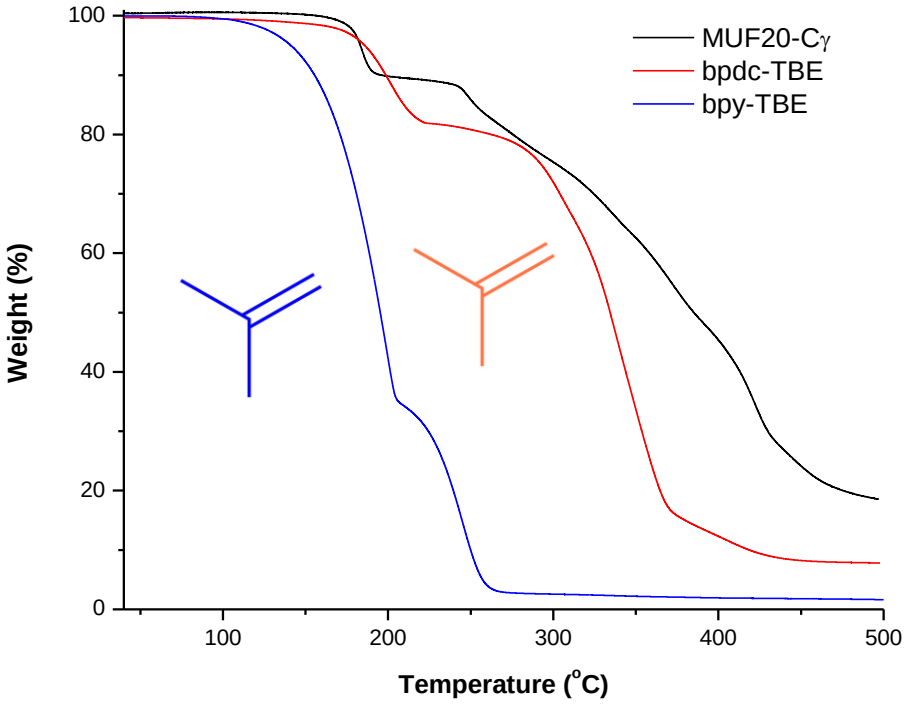

Figure 3.39: Thermogravimetric analysis (TGA) trace for MUF20-Cγ and TPG-ligands bpdc-TBE and bpy-TBE illustrating the expected thermolytic losses in final MOF TGA trace and individual loop TGA steps (below).

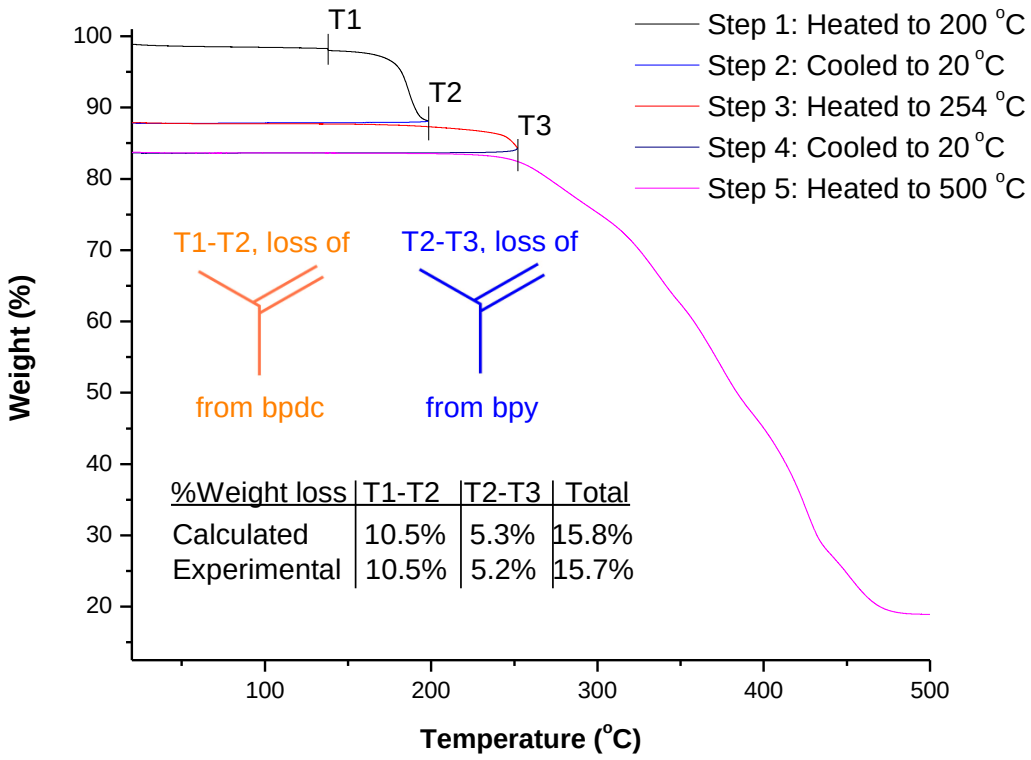

Figure 3.40: Thermogravimetric analysis (TGA) trace for MUF20-Cγ, looped to illustrate triggered loss of thermolabile protecting groups (TPGs).

In Figure 3.40, each step clearly shows a loss of isobutylene mass corresponding to the expected number of fragments per ligand in the MOF structure. As the bpdc:bpy ratio is 2:1 in MUF20 the percentage weight loss is expected to be 10% and 5% for bpdc-TBE and bpy-TBE thermolysis in MOF respectively. This experimentally is closer to 3:1 due to the difficulty in separating closely related steps. However, the cumulative percentage weight loss of 16.3% matches the calculated percentage weight loss of 16.3%. The accuracy of the T3 point is affected by overlap with the organic decomposition temperature of the bpdc-CO_2H and bpy-CO_2H even when stabilized within the metal-organic framework.

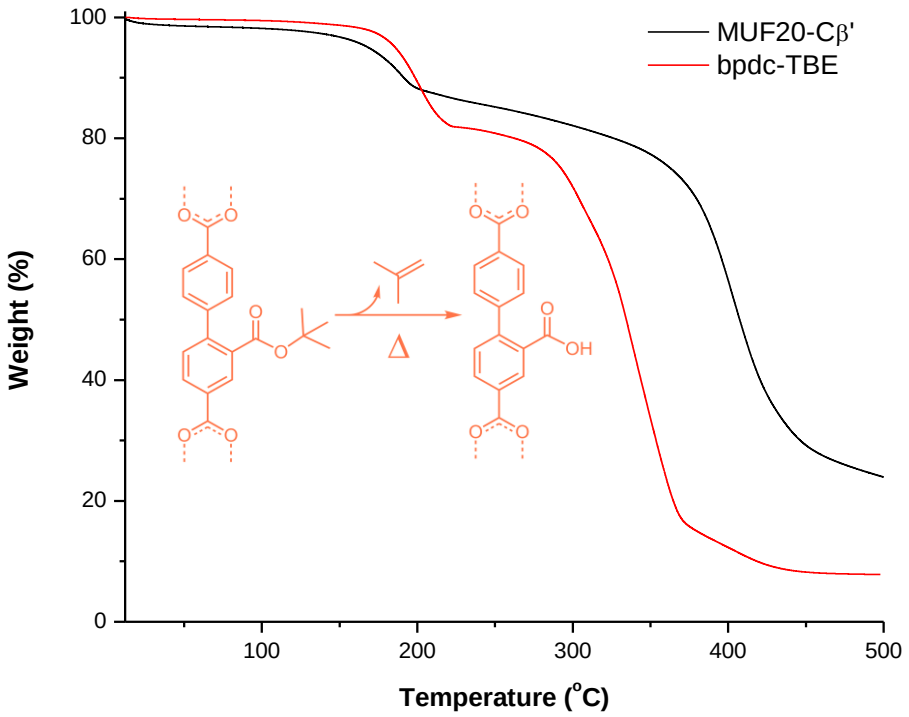

Figure 3.41: Thermogravimetric analysis (TGA) trace for MUF20-Cβ` and TPG-ligand bpdc-TBE illustrating the expected thermolytic loss in final MOF TGA trace and individual loop TGA step (below).

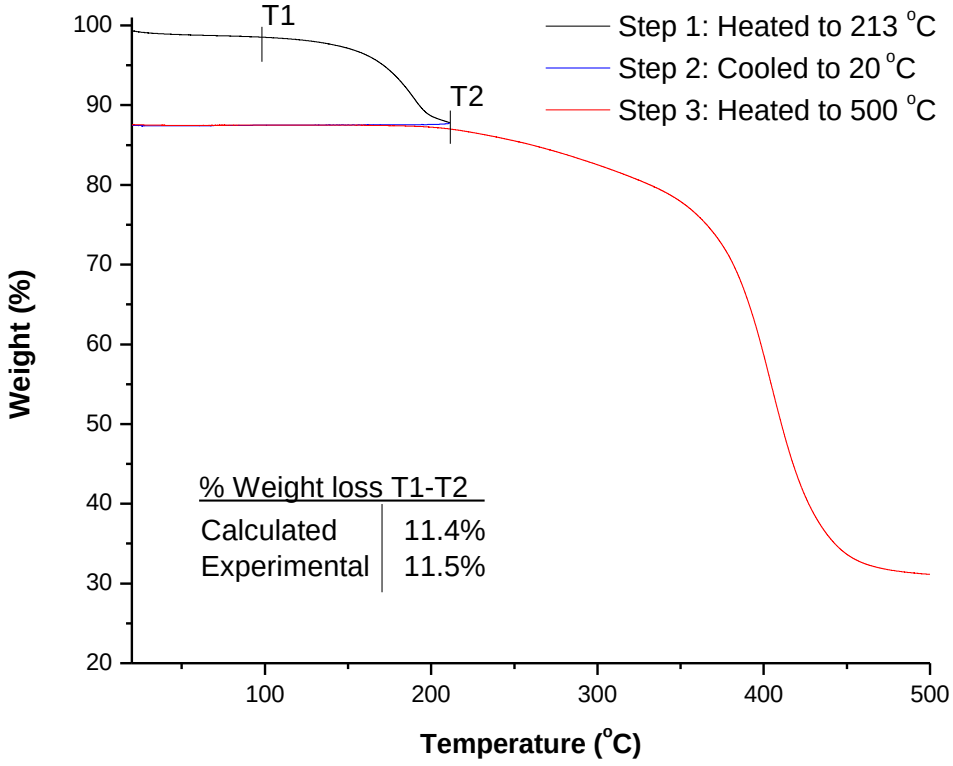

Figure 3.42: Thermogravimetric analysis (TGA) trace for MUF20-Cβ`, looped to illustrate triggered loss of thermolabile protecting group (TPG).

The MUF20-Cβ` material (Figure 3.41) also shares the initial slope noted in the MUF20-B` MOF materials earlier. Again, no DMF is observable in the pores from NMR analysis (see experimental section). The experimental and calculated percentage weight losses (Figure 3.42) match well for the expulsion of isobutylene from the bpdc-TBE ligands of the pillar-layer framework to reveal a bpdc-CO_2H functionality. Similarly, as with thermolyzed bpy-TBE in MUF20-Aγ^T in Chapter 2, incorporation of such a strongly coordinating group is challenging through direct synthesis and was not possible to achieve under the multiple conditions trialled in this thesis. Thus, the TPG strategy successfully attained an otherwise inaccessible functionalized material. Thermolyzed MUF20-C^{T}β` is also an amphoteric MOF containing both free carboxylic acids and amines.

Despite the similarities in crystal structure, MUF20-B`γ shows a very different TGA trace to MUF20-Cβ` (Figure 3.43). A very low experimental percentage weight loss was measured on this material (Figure 3.44). Most likely this is due to residual DMF found in the material occluding the thermolysis step below 200 °C as DMF boils at 153 °C.

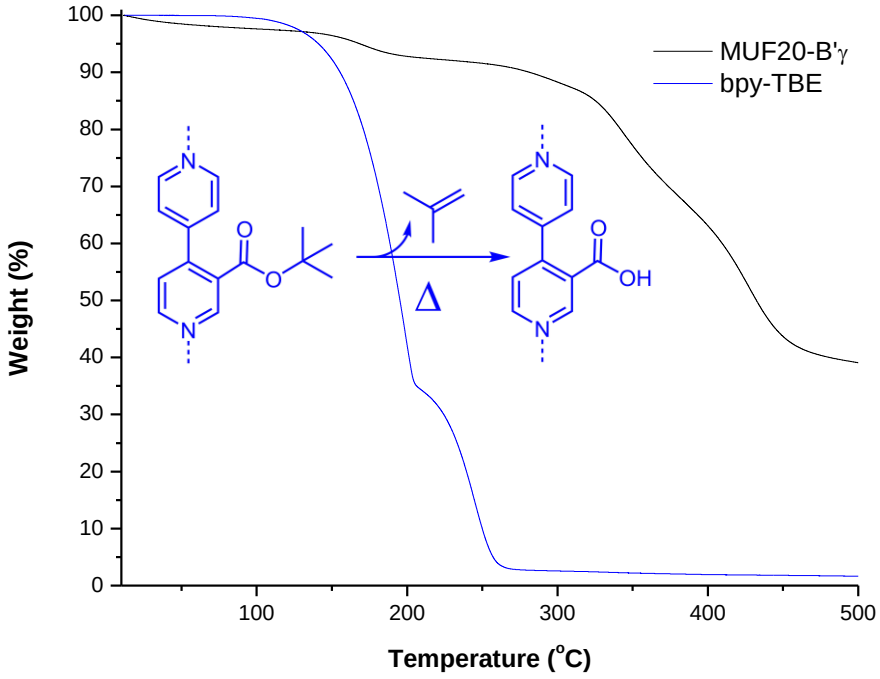

Figure 3.43: Thermogravimetric analysis (TGA) trace for MUF20-B`γ and TPG-ligand bpy-TBE illustrating the expected thermolytic loss in final MOF TGA trace and individual loop TGA step (below).

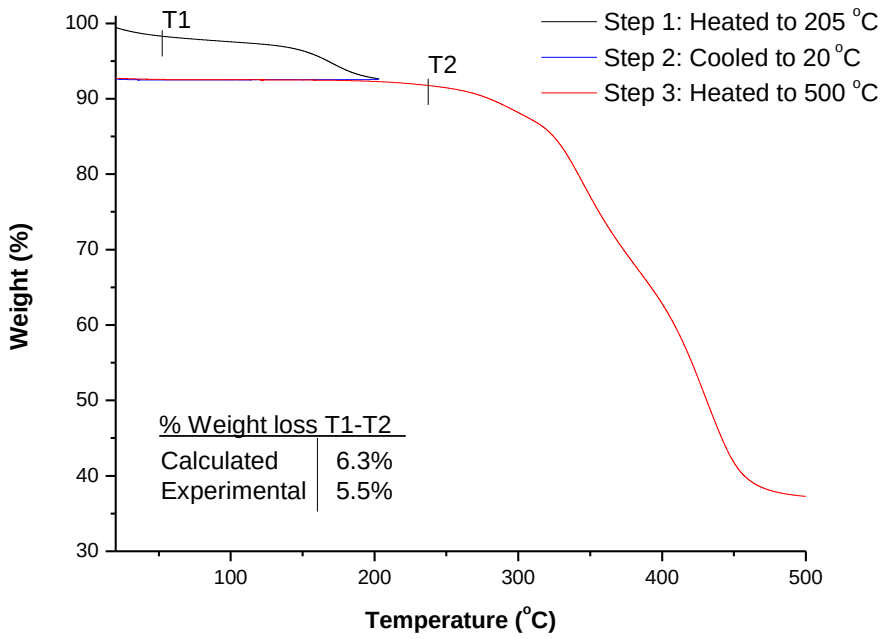

Figure 3.44: Thermogravimetric analysis (TGA) trace for MUF20-B`γ, looped to illustrate triggered loss of thermolabile protecting group (TPG).

The experimental and calculated percentage weight loses (Figure 3.44) are in good agreement for loss of isobutylene and CO_2 from the bpy-NHBoc ligand in a 1:1 ratio with the bpdc-NH_2 ligand in the diamondoid phase MOF. This thermolysis step should reveal a central amine-lined one-dimensional pore that may show unique gas sorption or guest properties.

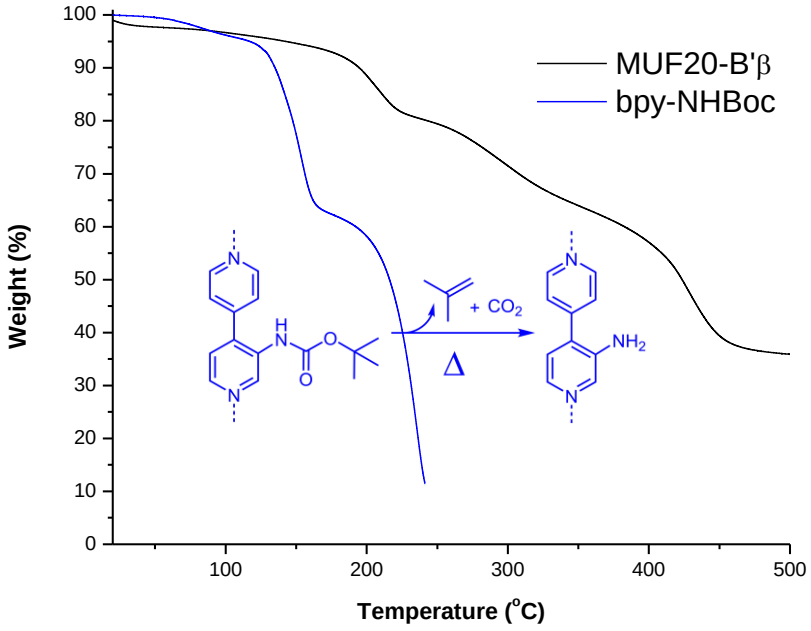

Figure 3.45: Thermogravimetric analysis (TGA) trace for MUF20-B`β and TPG-ligand bpy-NHBoc illustrating the expected thermolytic loss in final MOF TGA trace and individual loop TGA step (below).

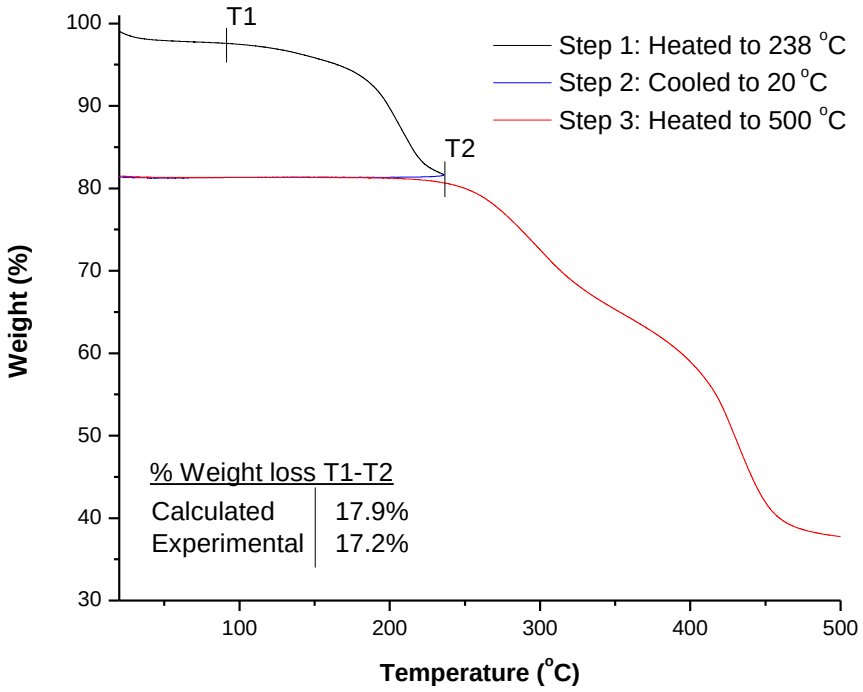

Figure 3.46: Thermogravimetric analysis (TGA) trace for MUF20-B`β, looped to illustrate triggered loss of thermolabile protecting group (TPG).

The loop TGAs suggest TPG loss in the above steps due to the agreement of the measured weight losses and subsequent absence of weight loss steps of the post-thermolytic material. However, NMR analysis of the material at the T2 and T3 (for doubly-functionalized materials) would further support this conclusion. These experiments were not done during this thesis due to time and material constraints but are an important part of characterizing these materials and their thermolytic properties.

Another important characterization of these materials would be establishing thermolysis conditions that maintain framework crystallinity. These are most likely to be distinct from TGA thermolysis as under N_2 flow the dried materials are more susceptible to pore collapse as is supported by preliminary thermolysis studies on the dual-functionalized MUF20 MOF family. Multiple thermolysis conditions have been trialled (see Appendix) but this study has not been exhaustive. Already there are some promising leads with bulky polar solvents under microwave irradiation. Additionally, literature has made great strides forward and sideways during the course of this thesis. There is greater understanding of the mechanisms of decomposition as well as improved methods in maintaining crystallinity upon activation. Alternative solvents and thermolysis conditions may yet yield crystalline structures of these thermolyszed materials.

If total thermolytic deprotection is confirmed to be concurrent with framework collapse in the combination of -TBE and -NHBoc functionalized materials, the amorphous materials may still have high gas uptakes or other functionality. Also as shown with the MUF20-Bα MOF in Chapter 2 partial thermolytic deprotection may yield crystalline materials of novel hybrid properties otherwise unattainable directly, providing an alternative way to how the TPG strategy can tailor MOF form to function through doping of the material with heterogenous functionality as opposed to a uniform change.

3.3. Conclusion

A family of doubly-functionalized pillar-layer MOFs was pursued and their non-thermolabile protected functionalities similarly targeted for comparative direct synthesis.

Overall

This research contributes to the body of knowledge developing on the structural relevance of multicomponent MOF functionalization in the choice of ligand backbone to modify, as well as insights into the interactions formed during MOF synthesis itself, which is still very much a 'black box' area in MOF chemistry. Both of these factors – the positional relevance and phase-directing interactions of functional groups during synthesis – form an important part in designing catalytic MOF pores.

In Chapter 3, this analysis was expanded through a full range of MOF syntheses including comparison to the directly functionalized ligand backbone analogues. This work elaborated on the directing influence of the more strongly coordinating carboxylate ligand in the formation of pillar-layer MOFs as well as the importance of the functional group utilized. Bpdc-TBE groups were shown to localise within the layers of the MOF, allowing for the steric bulk of an additional -TBE or -NHBoc TPG on the pillar bpy as well as readily forming the half-protected MUF20-Cβ`. The bpdc-NHBoc functionalized MOF did not allow for this. Due to the positioning of the functionality within the pores of the MOF, not even the presence of an amine moiety proved compatible. This is compounded by the presence of a hydrogen donor in the amine of the carbamate moiety which can interact with a freed carboxylate oxygen of a neighbouring lattice. In all synthesis conditions trialled, competing phases were either persistently present or dominating. In particular, an IRMOF phase was favoured where the steric bulk of the -NHBoc group on the bpdc ligand directly prohibited inclusion of any modified bpy ligand.

The validity of controlling material properties by TPG strategy was shown in the ability to completely reverse the directing effect of the bpdc-NH_2 ligand when combined with a specifically modified bpy ligand. While bpy-NH_2 and bpy-NHBoc still favoured formation of the MUF20-B`α-dia or diamondoid MOF, bpy-TBE completely disfavoured these competing phases, forming purely MUF20-B`γ.

Limitations

While gas sorption and thermolysis was carried out on the mono-functionalized bpy analogues an obvious limitation in the research presented in this thesis is the absence of full characterisation for the remainder of the family. Conditions yet may be found where these MOFs may be thermolyzed whilst maintaining crystallinity and porosity, such as use of microwave heating and bulky guest molecules, either gaseous or liquid, to support the framework during thermolysis. The anomalous stability of the bpdc-2mh based MOF MUF20-Dα to thermolysis intriguingly hints at a tuneable barrier to pore collapse.

However, as the MOF analogues in this work proved insufficiently stable to survive the thermolysis conditions without discernible effect on the crystallinity of the material, this exhaustive undertaking was not pursued at this time. With the development of a more rapid and high-yielding synthesis of the bpy-NHBoc ligand this work may be more feasible in future.

3.4. Experimental section

3.4.1. General procedures

All starting compounds and solvents were used as received from commercial sources without further purification unless otherwise noted. NMR spectra were recorded at room temperature on a Bruker-500 Avance instrument, with the use of the solvent proton as an internal standard. Thermogravimetric analysis (TGA) was performed on a TA Instruments Q50 instrument.

3.4.2. MOF synthesis and characterization

^{1}H NMR analysis of digested MUF20 MOF samples

For ^{1}H NMR spectroscopy, the mother liquor of the as-synthesized MOF crystals was replaced with fresh dry DMF multiple times, followed by repeated washing and subsequent soaking in dry CH_2Cl_2 for several hours. The excess CH_2Cl_2 was then decanted and the samples placed under vacuum overnight to remove residual solvent from the pores. The crystals were then digested using the following protocol: 23 µL of a 35% DCl solution in D_2O was mixed

with 1 mL of DMSO-d_6 to give a DCl/DMSO-d_6 stock solution. Around 5 mg of MOF was digested in 150 µL of this stock solution together with 480 µL of DMSO-d_6. Spectra were acquired immediately following dissolution.

Thermogravimetric Analysis (TGA)

Freshly prepared MOF samples were prepared as for NMR analysis except that samples were placed under vacuum for a minimum of 24 hours. Samples were then transferred to an aluminum sample pan and then measurements were commenced under an N_2 flow with a heating rate of 5 °C /min.

Powder X-ray diffraction patterns

All powder X-ray diffraction experiments were carried out on a Rigaku Spider X-ray diffractometer with Cu K_α radiation (Rigaku MM007 microfocus rotating-anode generator), monochromated and focused with high-flux Osmic multilayer mirror optics; diffraction patterns were recorded on a curved image plate detector. The data were obtained from freshly prepared MOF samples that had been ground into slurry in a small amount of DMF, DEF or DBF and kept damp with solvent throughout the measurement. The two-dimensional images of the Debye rings were integrated with 2DP[194] (Version 1.0.3.4) to give *I versus* 2θ diffractograms. The predicted powder patterns were generated from their single-crystal structures using Mercury v3.8.

Single crystal X-ray diffraction

MOF crystals were mounted on a MiTeGen mylar loop, placed into dry DEF or DBF (except for MUF20-B`γ which was kept in mother liquor) before coating in Fomblin oil and placed under cold stream at stated temperature in crystallography table. Diffraction data was collected on a Rigaku Spider diffractometer equipped with a MicroMax MM007 rotating-anode generator (Cu K_α radiation, 1.54180 Å), high-flux Osmic multilayer mirror optics; diffraction data were recorded on a curved image-plate detector. Data were collected at the temperatures listed in crystallography tables and were integrated, scaled, and averaged with FS_Process.[195] XPREP was used to determine the space group and the structures were solved using SHELXS or SHELXT and refined with SHELXL.[196] Platon was employed to determine the solvent accessible volume.[197] All non-hydrogen atoms were found in the electron density difference map. All hydrogen atoms were calculated using the appropriate restraints. All non-hydrogen atoms were refined anisotropically.

Table 3.6: Crystallography data of MUF20-Aα-dia, MUF20-B`α-dis, and MUF20-B`α-dia

MOF	**MUF20-Aα-dia**	**MUF20-B`α-dis**	**MUF20-B`α-dia**
Formula	$C_{52}H_{48}N_4O_{12}Zn_2$	$C_{40.67}H_{32}N_{4.67}O_{9.33}Zn_2$	$C_{24}H_{17}N_3O_4Zn$
Formula weight	1051.68	866.11	476.77
Crystal size (mm)	0.27 × 0.24 × 0.08	0.47 × 0.30 × 0.15	0.9 × 0.35 × 0.16
Temperature (K)	173.15	153	293
Wavelength (Å)	1.54187	1.54187	1.54187
Crystal system	Monoclinic	Triclinic	Triclinic
Space group	*Cc*	*P*-1	*P*-1
Unit cell lengths (Å)	a = 25.1053(17) b = 7.5079(4) c = 15.0724(14)	a = 13.8284(6) b = 14.4675(6) c = 16.7482(12)	a = 16.691(2) b = 21.174(2) c = 21.372(3)
Unit cell angles (°)	α = 90 β = 121.270(9) γ = 90	α = 97.527(7) β = 94.081(7) γ = 102.029(7)	α = 95.636(7) β = 110.287(8) γ = 107.734(8)
Unit cell volume (Å^3)	2428.3(4)	3232.1(3)	6570.3(14)
Z	2	3	8
D_{calc} (g cm^{-3})	1.438	1.335	0.964
μ (mm^{-1})	1.781	1.847	1.241
F(000)	1088.0	1330.0	1952.0
Reflns coll./unique, R_{int}	15984 / 4051, 0.0580	43516 / 12046, 0.0690	70756 / 7951, 0.1050
Data range	8.0 Å > *d* > 0.81 Å	8.0 Å > *d* > 0.81 Å	8.0 Å > *d* > 1.20 Å
Index ranges	-30≤*h*≤29, -9≤*k*≤13, -13≤*l*≤17	-17≤*h*≤15, -16≤*k*≤17, -20≤*l*≤20	-20≤*h*≤20, -25≤*k*≤25, -24≤*l*≤26
Completeness	84.6 %	95.0 %	99.9 %
T_{min}, T_{max}	0.768, 1.00	0.495, 1.00	0.297, 1.00
R indices for data with *I*>2σ(*I*)	R_1 = 0.0490; wR_2 = 0.1127	R_1 = 0.1439; wR_2 = 0.3951	R_1 = 0.1481; wR_2 = 0.4319
R indices for all data	R_1 = 0.0552; wR_2 = 0.1293	R_1 = 0.1794; wR_2 = 0.4393	R_1 = 0.1744; wR_2 = 0.4613
Largest difference peak and hole (e Å^{-3})	0.89/-1.28	2.26/-1.42	0.75/-0.58

Table 3.7: Crystallography data of MUF20-Cβ, MUF20-Cγ, and MUF20-Cβ`

MOF	**MUF20-Cβ**	**MUF20-Cγ**	**MUF20-Cβ`**
Formula	$C_{53}H_{49}N_3O_{14}Zn_2$	$C_{188.45}H_{156.21}N_{7.53}O_{47.53}Zn_8$	$C_{28.67}H_{21.48}N_2O_{6.67}Zn_{1.33}$
Formula weight	1082.69	3797.66	587.78
Crystal size (mm)	0.61 x 0.25 x 0.15	0.46 × 0.11 × 0.07	0.41 × 0.17 × 0.19
Temperature (K)	120	153	153
Wavelength (Å)	1.54187	1.54187	1.54187
Crystal system	Monoclinic	Monoclinic	Triclinic
Space group	$P2_1/c$	$P2_1/c$	P-1
Unit cell lengths (Å)	a = 14.046(5) b = 15.200(5) c = 29.517(5)	a = 14.041 b = 15.182 c = 29.470	a = 14.0092(5) b = 15.1569(5) c = 15.1729(11)
Unit cell angles (°)	α = 90 β = 92.914(5) γ = 90	α = 90 β = 92.87 γ = 90	α = 79.813(6) β = 83.549(6) γ = 82.851(6)
Unit cell volume (Å^3)	6294(3)	6274.5	3132.8(3)
Z	4	1	3
D_{calc} (g cm^{-3})	1.143	1.005	0.935
μ (mm^{-1})	0.818	0.811	1.278
F(000)	2240.0	1920.0	902.0
Reflns coll./unique, R_{int}	62617 / 11948, 0.1052	53471 / 11905, 0.0732	38986 / 11590, 0.0722
Data range	8.0 Å > d > 0.81 Å	8.0 Å > d > 0.81 Å	8.0 Å > d > 1.15 Å
Index ranges	-15≤h≤17, -12≤k≤17, -36≤l≤36	-16≤h≤11, -18≤k≤18, -36≤l≤33	-13≤h≤17, -18≤k≤18, -18≤l≤18
Completeness	96.4 %	96.4 %	94.1 %
T_{min}, T_{max}	0.422, 1.00	0.430, 1.00	0.498, 1.00
R indices for data with I>2σ(I)	R_1 = 0.1600; wR_2 = 0.4327	R_1 = 0.2446; wR_2 = 0.5846	R_1 = 0.2051; wR_2 = 0.5008
R indices for all data	R_1 = 0.1899; wR_2 = 0.4602	R_1 = 0.2812; wR_2 = 0.6126	R_1 = 0.2326; wR_2 = 0.5342
Largest difference peak and hole (e Å^{-3})	2.14/-1.43	5.54/-2.24	2.58/-1.46

Table 3.8: Crystallography data of MUF20-B`β, MUF20-B`β`, and MUF20-B`γ

MOF	**MUF20-B`β**	**MUF20-B`β`**	**MUF20-B`γ**
Formula	$C_{38.67}H_{34.67}N_{5.33}O_8Zn_{1.33}$	$C_{28.57}H_{24}N_{4.57}O_{5.71}Zn_{1.14}$	$C_{21.5}H_{16.77}N_{1.77}O_5Zn$
Formula weight	789.21	597.52	445.32
Crystal size (mm)	0.61 x 0.25 x 0.15	0.47 × 0.30 × 0.15	0.41 × 0.17 × 0.19
Temperature (K)	175	175	120
Wavelength (Å)	1.54187	1.54187	1.54187
Crystal system	Orthorhombic	Monoclinic	Triclinic
Space group	*Pbca*	*C*2/*c*	*P*-1
Unit cell lengths (Å)	a = 17.6454(4) b = 14.1096(3) c = 26.1666(18)	a = 29.866(2) b = 30.724(2) c = 17.3945(12)	a = 14.127(2) b = 15.199(2) c = 15.2211(19)
Unit cell angles (°)	α = 90 β = 90 γ = 90	α = 90 β = 122.047(9) γ = 90	α = 78.132(5) β = 88.961(6) γ = 88.251(6)
Unit cell volume ($Å^3$)	6514.7(5)	13529(2)	3196.5(8)
Z	6	14	4
D_{calc} (g cm^{-3})	1.207	1.027	0.925
μ (mm^{-1})	1.404	1.273	1.259
F(000)	2448.0	4304.0	913.0
Reflns coll./unique, R_{int}	83501 / 6380, 0.0986	74399 / 6107, 0.1129	28249 / 9927, 0.0884
Data range	8.0 Å > *d* > 0.81 Å	8.0 Å > *d* > 1.05 Å	8.0 Å > *d* > 0.81 Å
Index ranges	-21≤*h*≤16, -16≤*k*≤17, -31≤*l*≤32	-36≤*h*≤33, -37≤*k*≤37, -21≤*l*≤21	-17≤*h*≤13, -18≤*k*≤16, -18≤*l*≤17
Completeness	99.7%	100 %	78.9 %
T_{min}, T_{max}	0.597, 1.00	0.457, 1.00	0.363, 1.00
R indices for data with $I>2\sigma(I)$	R_1 = 0.1453; wR_2 = 0.3668	R_1 = 0.1087; wR_2 = 0.3369	R_1 = 0.1213; wR_2 = 0.3458
R indices for all data	R_1 = 0.2195; wR_2 = 0.4282	R_1 = 0.1244; wR_2 = 0.3611	R_1 = 0.1396; wR_2 = 0.3701
Largest difference peak and hole (e $Å^{-3}$)	1.12/-1.02	0.94/-0.88	1.52/-1.41

Table 3.9: Crystallography data of MUF20-Dβ

Compound	**MUF20-Dβ**
Formula	$C_{39.17}H_{38.83}N_2O_{9.33}Zn_{1.33}$
Formula weight	774.05
Crystal size (mm)	0.61 x 0.25 x 0.15
Temperature (K)	163
Wavelength (Å)	1.54187
Crystal system	Monoclinic
Space group	*C*2/*c*
Unit cell lengths (Å)	a = 21.0550(4) b = 21.9947(4) c = 28.029(2)
Unit cell angles (°)	α = 90 β = 94.615(7) γ = 90
Unit cell volume ($Å^3$)	12938.1(10)
Z	12
D_{calc} (g cm^{-3})	1.192
μ (mm^{-1})	1.402
F(000)	4830.0
Reflns coll./unique, R_{int}	72488 / 12525, 0.0796
Data range	8.0 Å > *d* > 0.81 Å
Index ranges	-25≤*h*≤25, -26≤*k*≤25, -34≤*l*≤32
Completeness	98.4%
T_{min}, T_{max}	0. 760, 1.000
R indices for data with $I>2\sigma(I)$	R_1 = 0.1176, wR_2 = 0.3251
R indices for all data	R_1 = 0.1677, wR_2 = 0.3934
Largest difference peak and hole (e $Å^{-3}$)	1.79/-2.26

MOF synthesis

MUF20-Aα **$[Zn_2(bpdc)_2(bpy)]$**

Phase 1: 2-fold interpenetrated pillar-layer framework

Bpdc (2.6 mg, 0.011 mmol), 4,4'-bipyridine (2.6 mg, 0.017 mmol), and $Zn(NO_3)_2.4H_2O$ (2.8 mg, 0.011 mmol) were combined in a 4 mL scintillation vial. MeOH:DMF (1.0:0.25 mL) was

then added and the mixture briefly sonicated before placing in an oven at 85 °C for 12 hours. After 10 mins in the oven, the lid of the vial was re-tightened and Teflon tape placed around the join of the lid. Slightly yellow needle clusters and chunks formed.

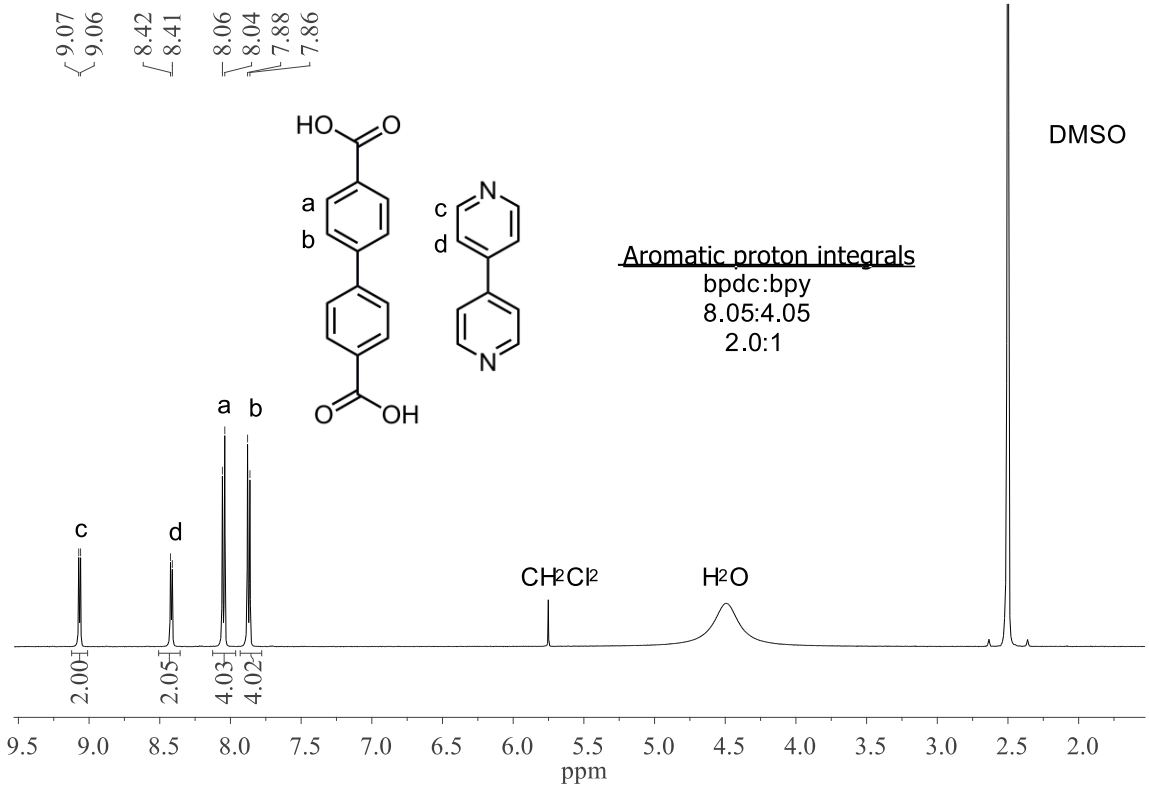

Figure 3.47: ^{1}H NMR spectroscopic analysis of digested MUF20-Aα in DMSO-d_6/DCl.

MUF20-Aα-dia diamondoid phase [Zn(bpdc)(bpy)]

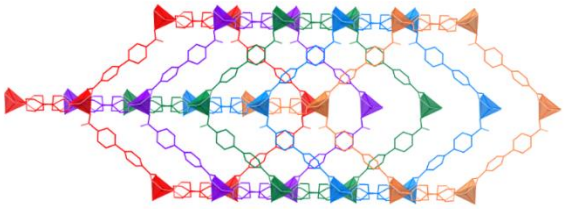

Phase 2: 5-fold interpenetrated diamondoid structure

Bpdc (2.6 mg, 0.011 mmol), 4,4'-bipyridine (2.6 mg, 0.017 mmol), and $Zn(NO_3)_2.4H_2O$ (2.8 mg, 0.011 mmol) were combined in a 4 mL scintillation vial. MeOH : DMF (1.0:0.25 mL) was then added and the mixture briefly sonicated before placing in an oven at 85 °C for 12 hours. After 10 mins in the oven, the lid of the vial was re-tightened and Teflon tape placed around the join of the lid. Slightly yellow needle clusters and chunks formed.

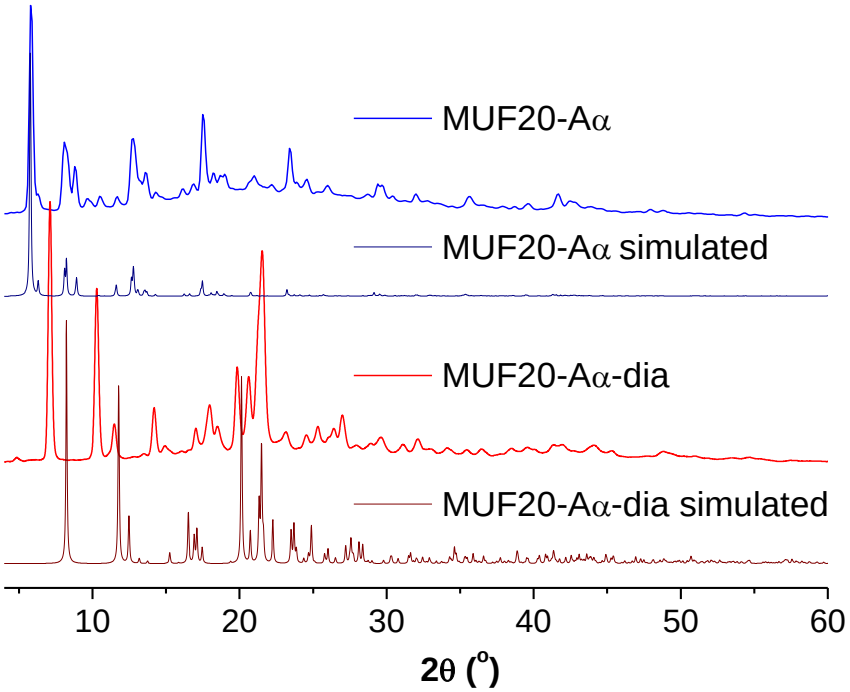

Figure 3.48: Experimental PXRD patterns for the MUF20-Aα-dia diamondoid phase and the MUF20-Aα phase.

The observed difference between the simulated and experimental PXRD of MUF20-Aα is indicative of a potential breathing interaction with the different solvent molecules present (MeOH:DMF for single-crystal structure and DEF for bulk PXRD analysis).

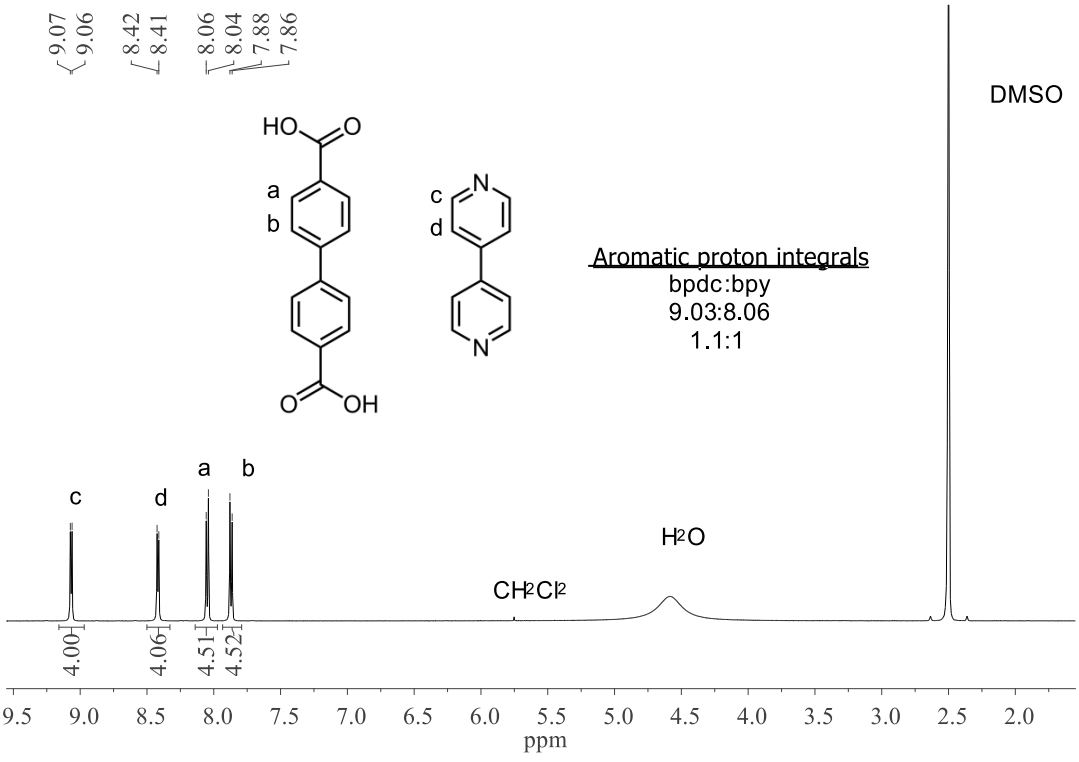

Figure 3.49: ^{1}H NMR spectroscopic analysis of digested MUF20-Aα-dia in DMSO-d_6/DCl.

MUF20-B`α-dis [Zn_2(bpdc-NH_2)$_2$(bpy)]

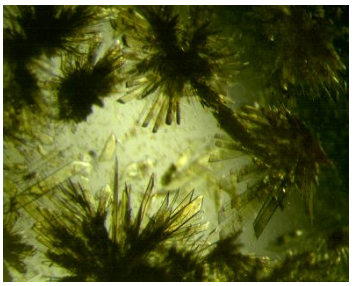

Bpdc-NH_2 (5.0 mg, 0.020 mmol), 4,4`-bipyridine (3.3 mg, 0.021 mmol), benzoic acid (2.3 mg, 0.020 mmol), and $Zn(NO_3)_2.4H_2O$ (4.3 mg, 0.016 mmol) were combined in a 4 mL scintillation vial. 4:1 MeOH:DMF (1.25 mL) was then added and the mixture briefly sonicated before placing in an oven at 85 °C for 22 hours. Large and clustered bright yellow flat needle crystals formed.

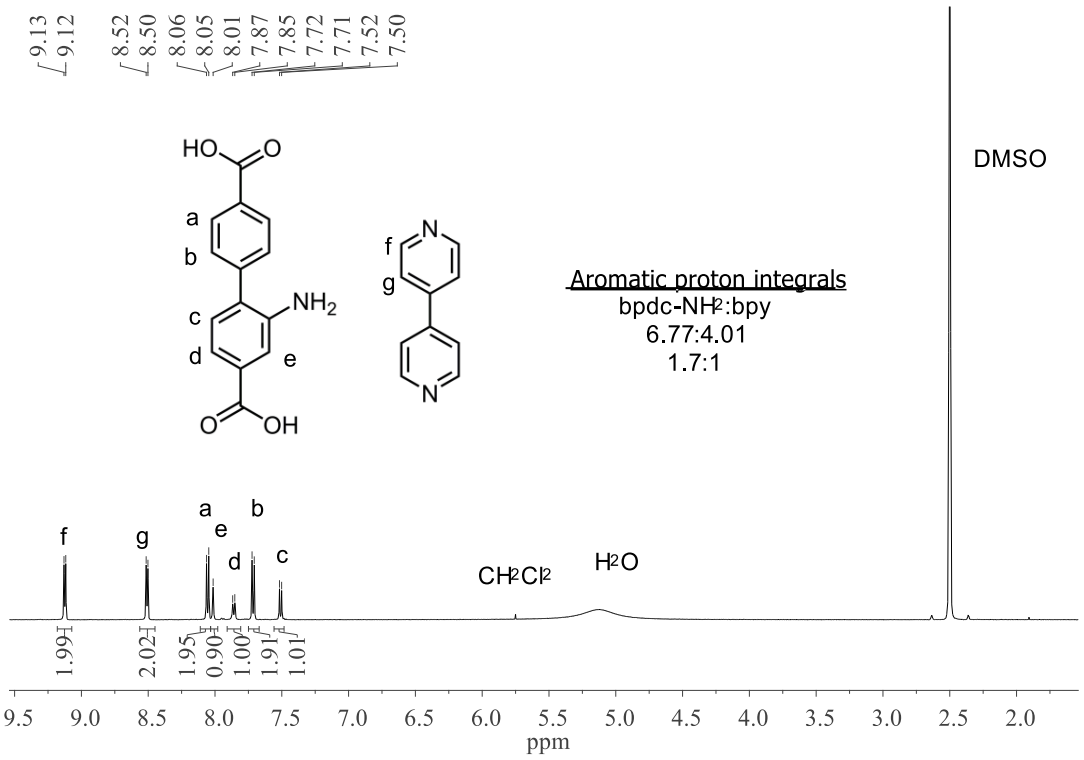

Figure 3.50: ^{1}H NMR spectrum of digested MUF20-B`α-dis in DMSO-d_6/DCl.

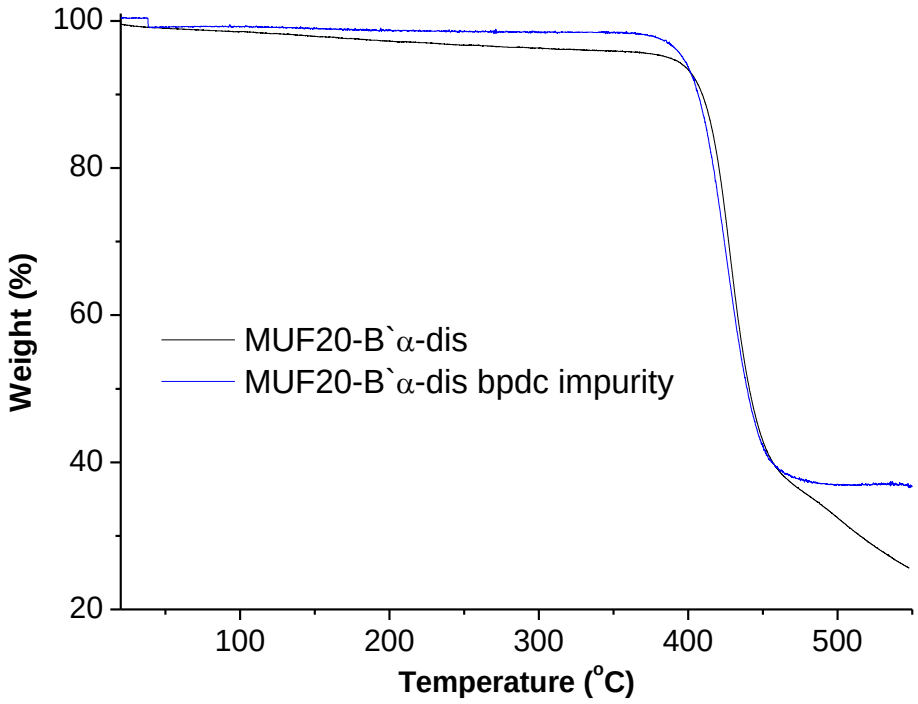

Figure 3.51: Thermogravimetric analysis (TGA) trace for MUF20-B`α-dis (pure and 10% bpdc impurity materials).

The high thermal stability of the MUF20-B`α is surprising given the distorted coordination environment of the SBU and is in stark contrast to the steady decomposition of MUF20-B`β`.

MUF20-B`α-dia [Zn(bpdc-NH_2)(bpy)]

Phase 2: 4-fold interpenetrated diamondoid structure (experimental PXRD and NMR ligand ratio matches MUF20-B`β`)

Bpdc-NH_2 (5.0 mg, 0.020 mmol), 4,4`-bipyridine (3.3 mg, 0.021 mmol), and $Zn(NO_3)_2.4H_2O$ (4.5 mg, 0.017 mmol) were combined in a 4 mL scintillation vial. 4:1 MeOH:DMF (1.25 mL) was then added and the mixture briefly sonicated before placing in an oven at 75 °C for 2 days. Blocky pale yellow crystals formed.

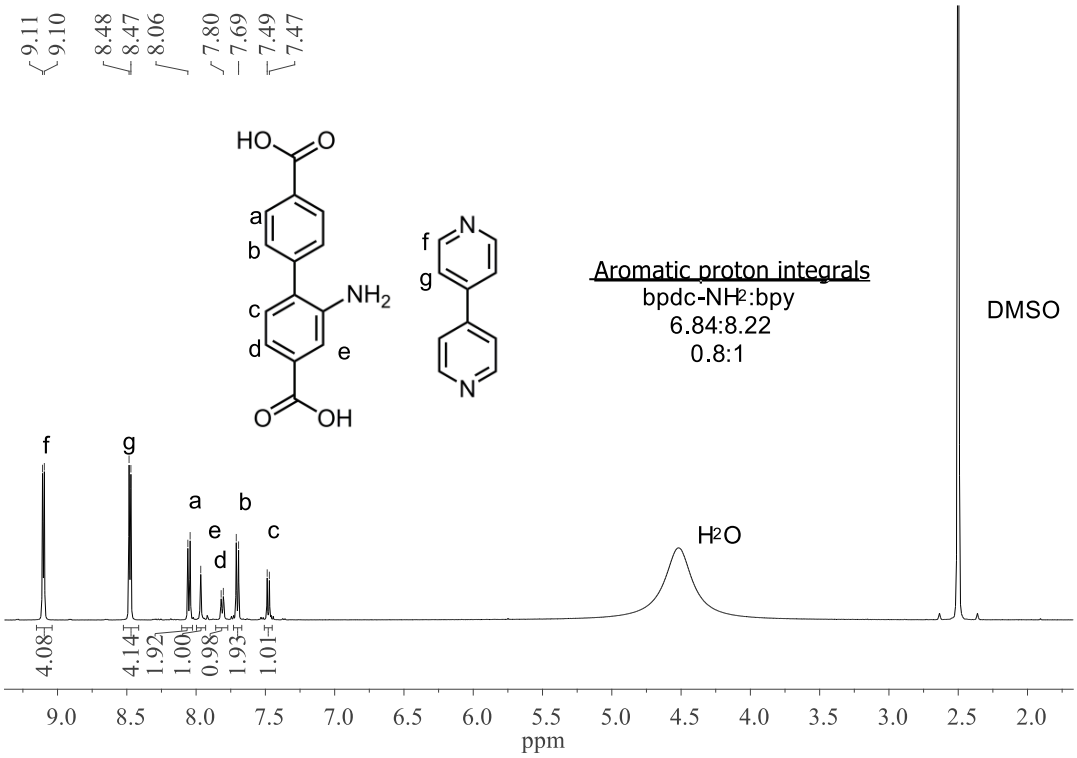

Figure 3.52: ^{1}H NMR spectroscopic analysis of digested MUF20-B`α-dia in DMSO-d_6/DCl.

MUF20-B`β [Zn(bpdc-NH_2)(bpy-NHBoc)]

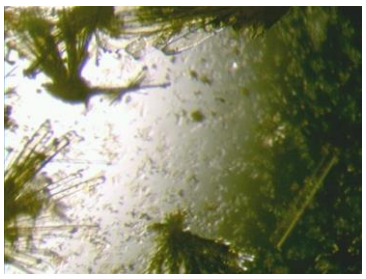

Bpdc-NH_2 (4.9 mg, 0.0190 mmol), bpy-NHBoc (8.4 mg, 0.0310 mmol), and $Zn(NO_3)_2.4H_2O$ (4.6 mg, 0.0176 mmol) were combined in a 4 mL scintillation vial. MeOH:DMF (1.0:0.25 mL) was then added and the mixture briefly sonicated before placing in an oven at 85 °C for 9 hours. After 10 min in the oven, the lid of the vial was re-tightened and Teflon tape placed around the join of the lid. Pale yellow needle clusters and chunks formed.

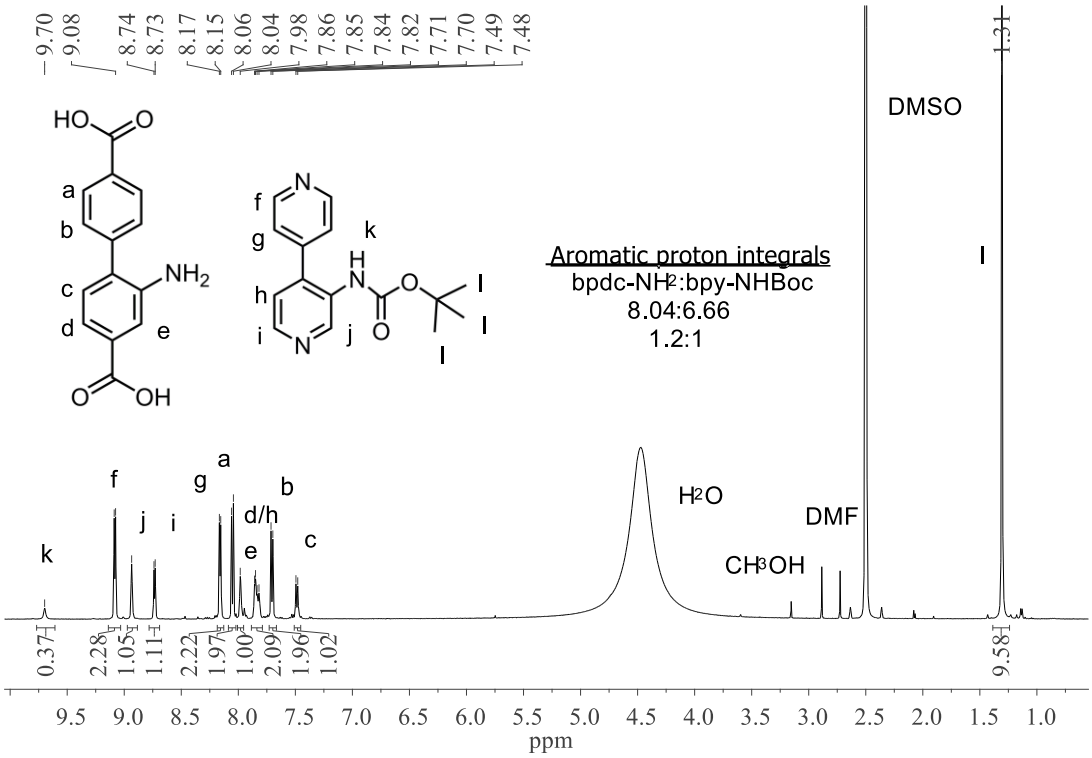

Figure 3.53: ^{1}H NMR spectrum of digested MUF20-B`β in DMSO-d_6/DCl.

MUF20-B`β` **[Zn(bpdc-NH_2)(bpy-NH_2)]**

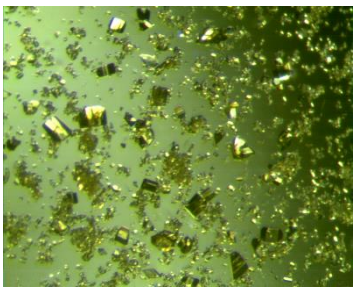

Bpdc-NH_2 (5.1 mg, 0.0198 mmol), bpy-NH_2 (5.3 mg, 0.0310 mmol) and $Zn(NO_3)_2.4H_2O$ (4.5 mg, 0.0172 mmol) were combined in a 4 mL scintillation vial. MeOH:DMF (1.0:0.25 mL) was then added and the mixture briefly sonicated before placing in an oven at 85 °C for 9 hours. After 10 min in the oven, the lid of the vial was re-tightened and Teflon tape placed around the join of the lid. Pale yellow needle clusters and chunks formed.

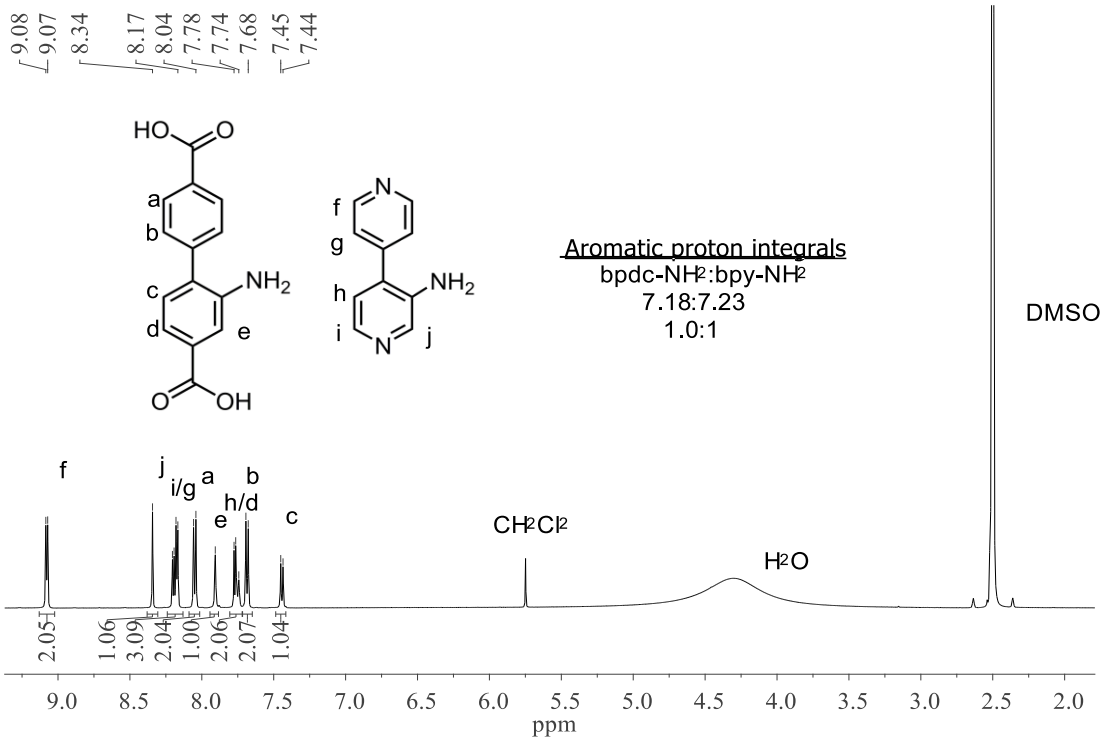

Figure 3.54: ^{1}H NMR spectrum of digested MUF20-B`β` in DMSO-d_6/DCl.

MUF20-B`γ **[Zn_2(bpdc-NH_2)$_2$(bpy-TBE)]**

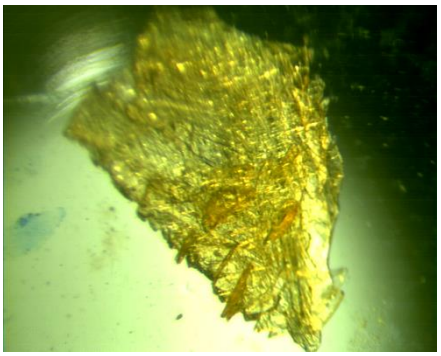

Bpdc-NH_2 (5.0 mg, 0.0194 mmol), bpy-TBE (8.1 mg, 0.0316 mmol), and $Zn(NO_3)_2.4H_2O$ (4.3 mg, 0.0164 mmol) were combined in a 4 mL scintillation vial. MeOH:DMF (1.0:0.25 mL) was then added and the mixture briefly sonicated before placing in an oven at 75 °C for 3 days. After 10 min in the oven, the lid of the vial was re-tightened and Teflon tape placed around the join of the lid. Large, clear yellow crystal plates formed.

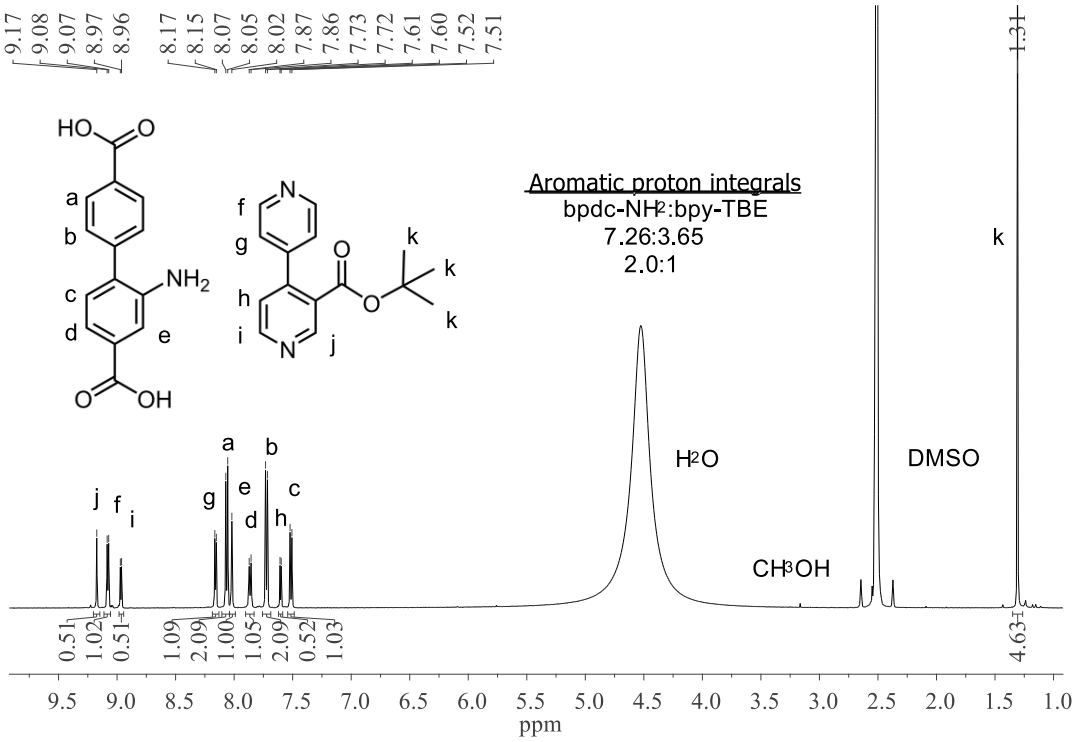

Figure 3.55: ^{1}H NMR spectrum of digested MUF20-B`γ in DMSO-d_6/DCl.

MUF20-B`γ^{T}

Despite multiple trials no condition was found whereupon reasonable crystallinity of the MOF framework was retained alongside total thermolytic deprotection.

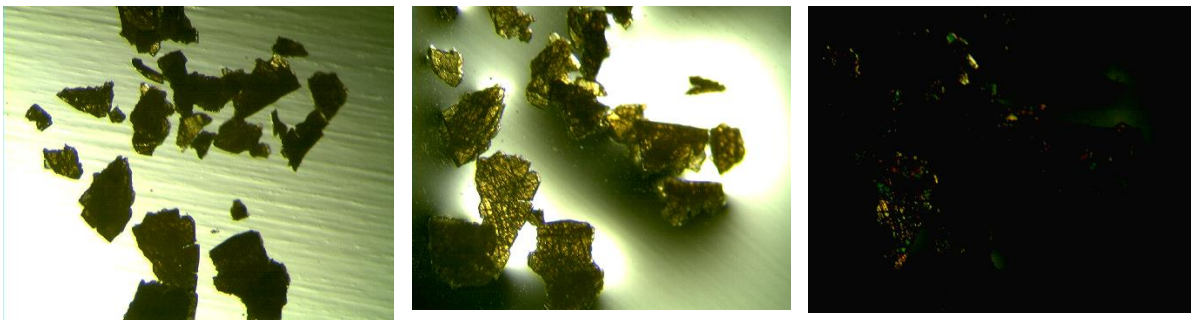

Figure 3.56: MUF20-B`γ^{T} post thermolysis dry, in DEF, and in DEF under polarized light.

At best a partial retention of crystallinity, as indicated by transparency and polarized light was retained. Full details in Appendix.

MUF20-Cβ [Zn_2(bpdc-TBE)$_2$(bpy-NHBoc)]

Bpdc-TBE (10.6 mg, 0.0310 mmol), bpy-NHBoc (8.5 mg, 0.031 mmol), and $Zn(NO_3)_2.4H_2O$ (7.9 mg, 0.030 mmol) were combined in a 4 mL scintillation vial. MeOH (2.0 mL) was then added and the mixture briefly sonicated before addition of DMF (0.5 mL). After

sonicating a second time the vial was placed in an oven at 85 °C for 18 hrs. After 10 min in the oven, the lid of the vial was re-tightened and Teflon tape placed around the join of the lid. Clear pale yellow needle clusters formed.

Upscale:

Bpdc-TBE (15.0 mg, 0.0438 mmol), bpy-NHBoc (12.5 mg, 0.0461 mmol), and $Zn(NO_3)_2.4H_2O$ (11.4 mg, 0.0436 mmol) were combined in a 4 mL scintillation vial. MeOH (2.0 mL) was then added and the mixture briefly sonicated before addition of DMF (0.5 mL). After sonicating a second time the vial was placed in an oven at 85 °C for 20 hrs. After 10 min in the oven, the lid of the vial was re-tightened and Teflon tape placed around the join of the lid. Pale brown large crystal shards formed.

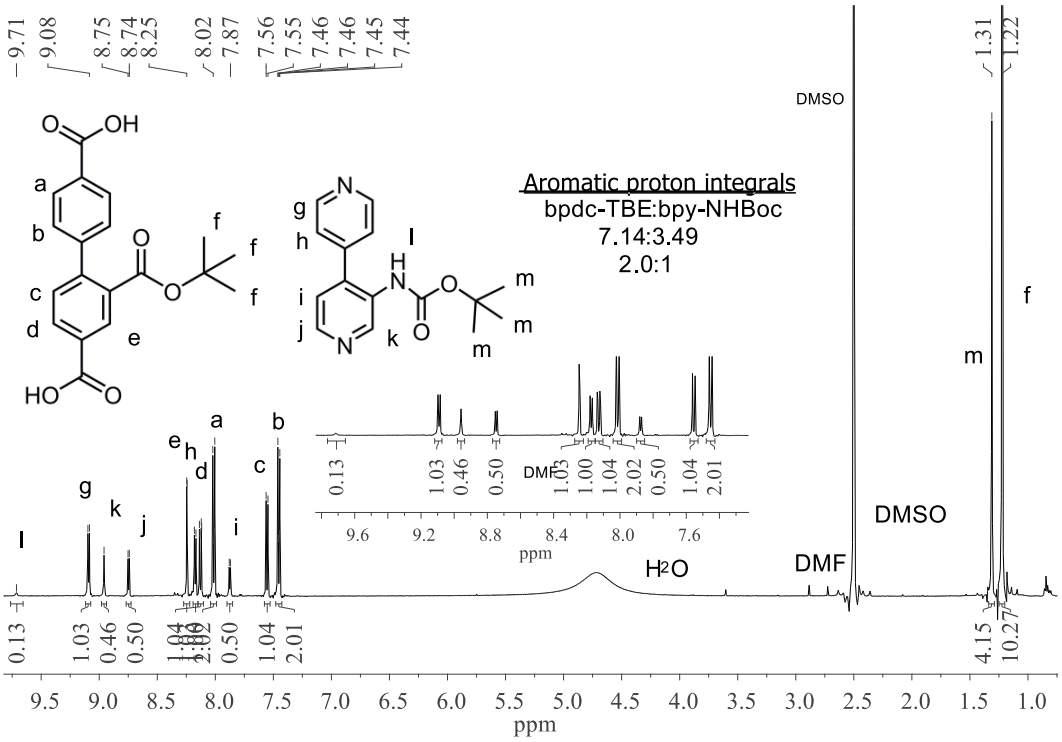

Figure 3.57: ^{1}H NMR spectrum of digested MUF20-Cβ in DMSO-d_6/DCl

MUF20-$C^T\beta^T$

Freshly synthesized MUF-20-Cβ was washed twice with dry DMF, twice with DBF before placing in fresh DBF and heating at 160 ^oC for 3.5 hours. Amorphous MOF consisting of the deprotected ligands, bpdc-CO_2H, bpy-NHBoc was obtained.

MUF20-Cβ` **[Zn_2(bpdc-TBE)$_2$(bpy-NH_2)]**

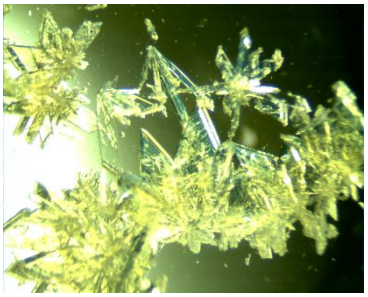

Bpdc-TBE (5.1 mg, 0.015 mmol), bpy-NH_2 (2.2 mg, 0.013 mmol), and $Zn(NO_3)_2.4H_2O$ (3.4 mg, 0.013 mmol) were combined in a 4 mL scintillation vial. MeOH:DMF (1.0:0.25 mL) was then added and the mixture briefly sonicated before placing in an oven at 75 °C for 18 hrs. After 10 min in the oven, the lid of the vial was re-tightened and Teflon tape placed around the join of the lid. Clear pale yellow needle clusters formed.

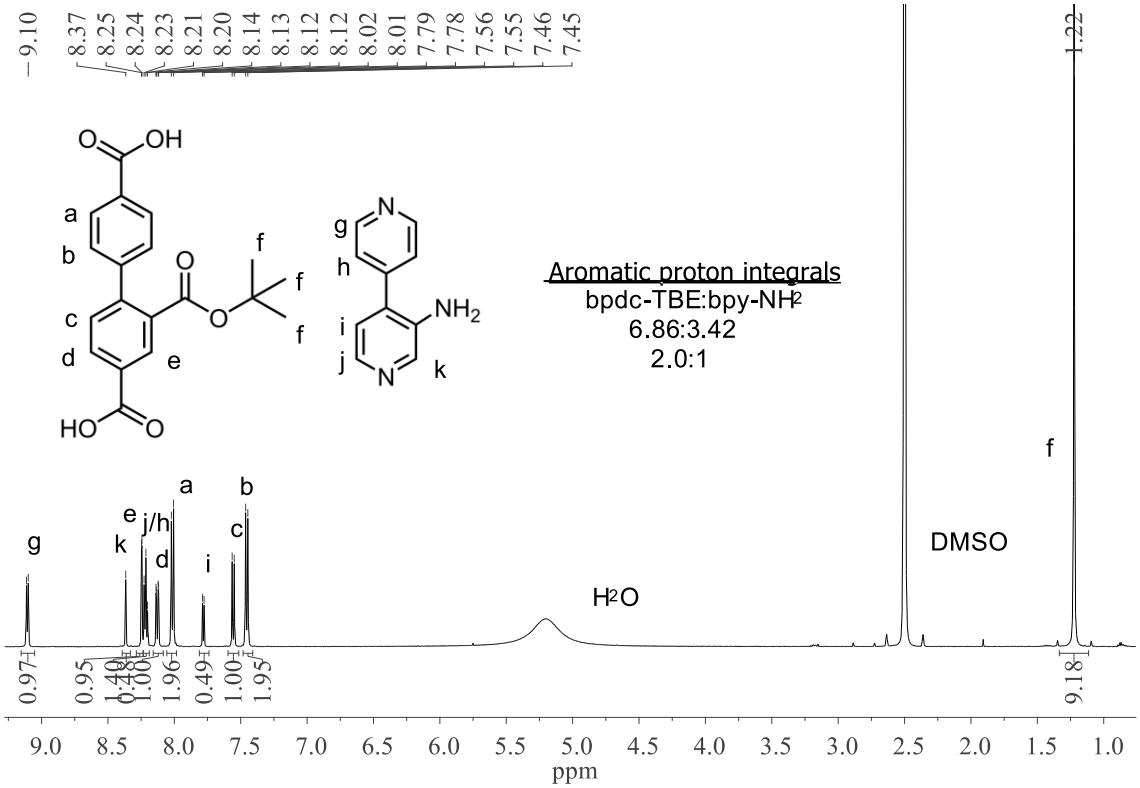

Figure 3.58: ^{1}H NMR spectrum of digested MUF20-Cβ` in DMSO-d_6/DCl.

MUF20-Cγ **[Zn_2(bpdc-TBE)$_2$(bpy-TBE)]**

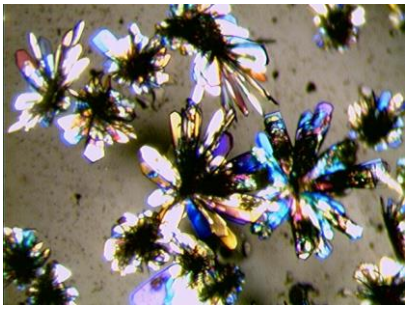

Bpdc-TBE (10.0 mg, 0.0292 mmol), bpy-TBE (12.0 mg, 0.0468 mmol), and $Zn(NO_3)_2.4H_2O$ (7.7 mg, 0.0295 mmol) were combined in a 4 mL scintillation vial. MeOH (2.0 mL) was then added and the mixture briefly sonicated before addition of DMF (0.5 mL). After sonicating a second time the vial was placed in an oven at 85 °C for 18 hrs. After 10 min in the oven, the lid of the vial was re-tightened and Teflon tape placed around the join of the

lid. Small, clear needle clusters formed. Yield: 13.8 mg. To scale up the synthesis, a parallel synthetic method was adopted (multiple vials using the scale described above).

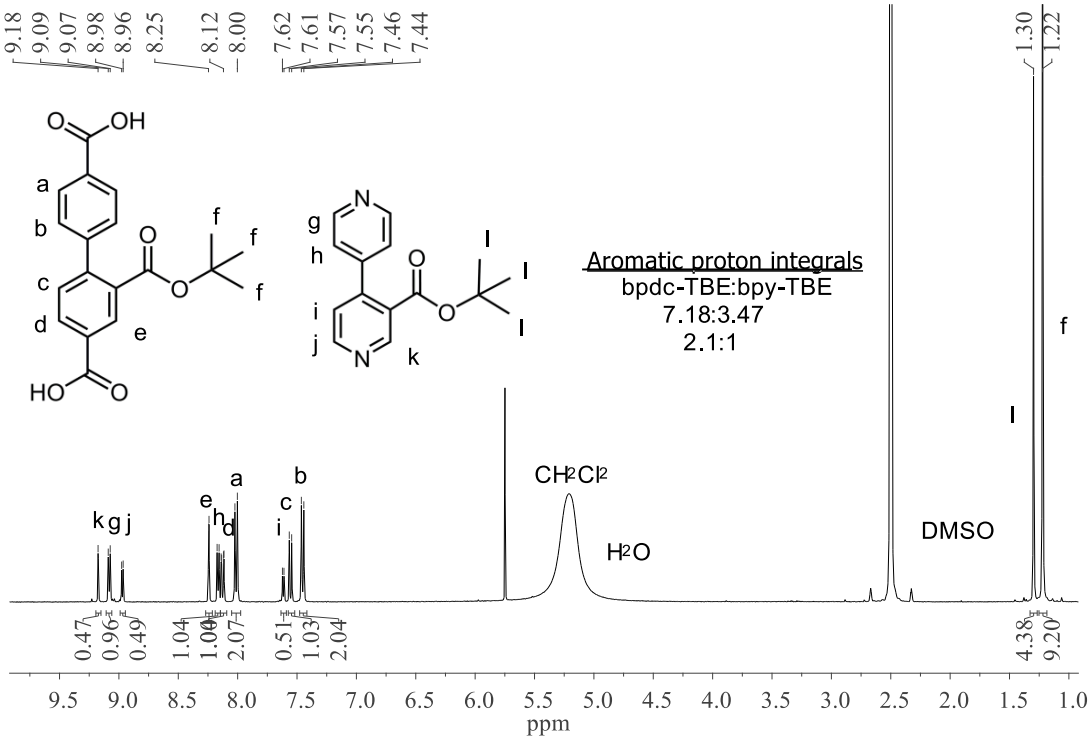

Figure 3.59: ^{1}H NMR spectrum of digested MUF20-Cγ in DMSO-d_6/DCl.

MUF20-$C^{T}\gamma^{T}$

Freshly synthesised MUF-20-Cγ was washed twice with dry DMF, twice with DBF before placing in fresh DBF and heating at 160 ^{o}C for 3.5 hours. Amorphous MOF consisting of the deprotected ligands, bpdc-CO_2H and bpy-CO_2H, was obtained.

MUF20-Dβ [Zn_2(bpdc-2mh)$_2$(bpy-NHBoc)]

Bpdc-2mh (10.6 mg, 0.0310 mmol), bpy-NHBoc (8.5 mg, 0.031 mmol), and $Zn(NO_3)_2.4H_2O$ (7.9 mg, 0.030 mmol) were combined in a 4 mL scintillation vial. MeOH (2.0 mL) was then added and the mixture briefly sonicated before addition of DMF (0.5 mL). After sonicating a second time the vial was placed in an oven at 85 °C for 18 hrs. After 10 min in the oven, the lid of the vial was re-tightened and Teflon tape placed around the join of the lid. Clear pale yellow needle clusters formed. Yield: 15.5 mg.

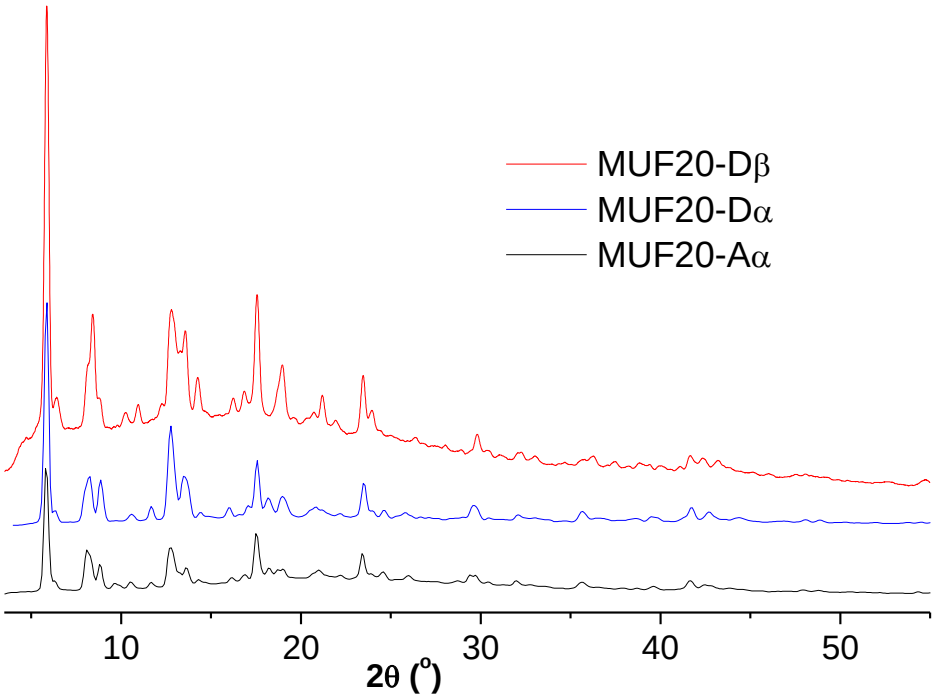

Figure 3.60: PXRD analysis of MUF20 MOFs containing the ligand bpdc-2mh (D).

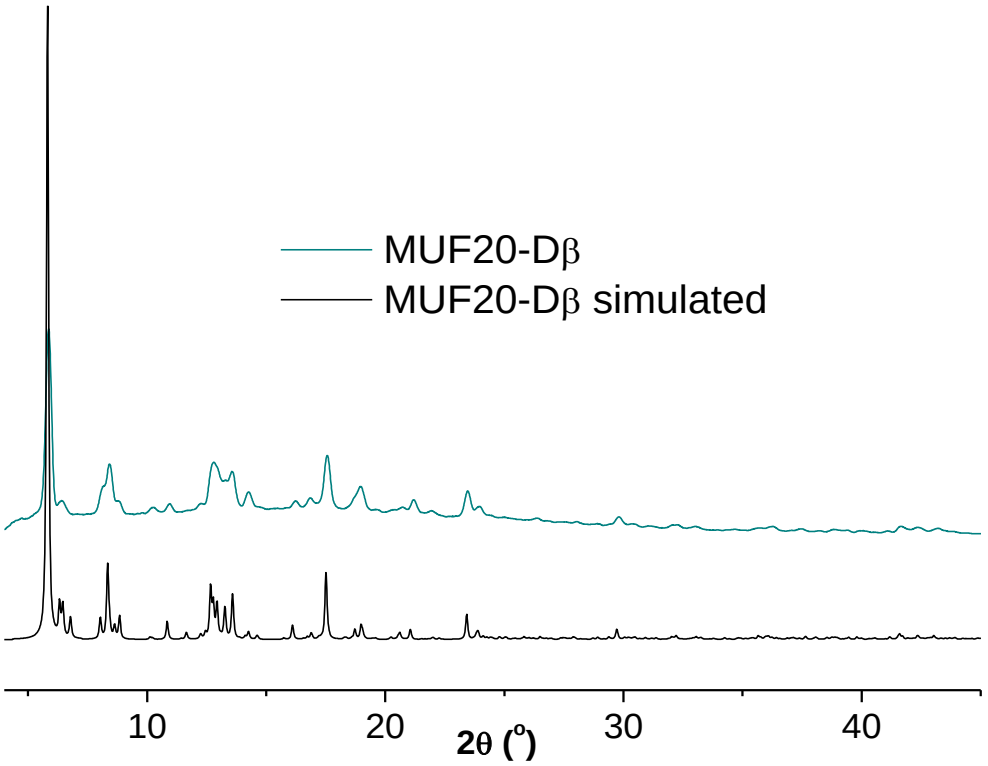

Figure 3.61: Simulated PXRD from single crystal and experimental PXRD of MUF20-Dβ.

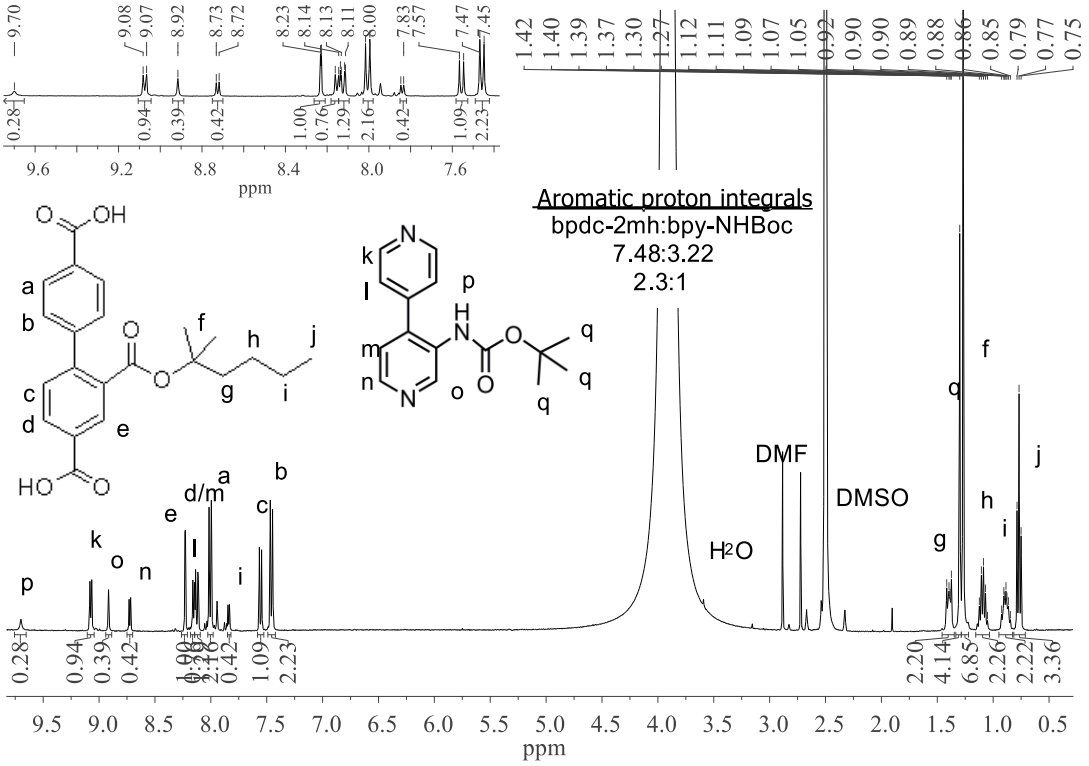

Figure 3.62: ^{1}H NMR spectrum of digested MUF20-Dβ in DMSO-d_6/DCl

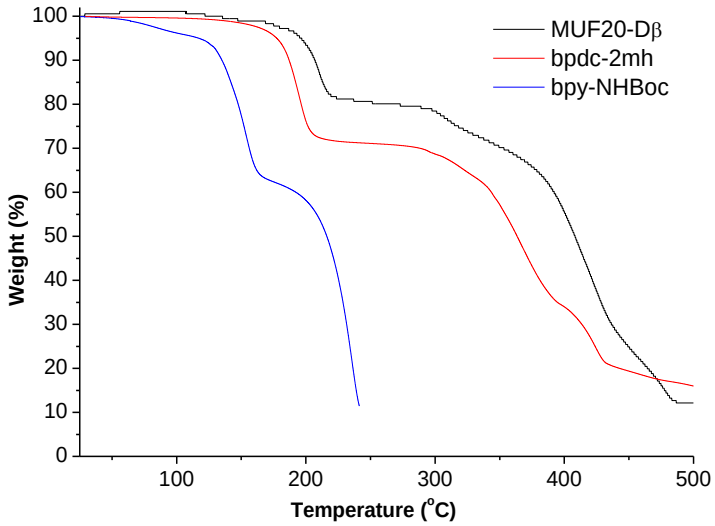

Figure 3.63: Thermogravimetric analysis (TGA) trace for MUF20-Dβ.

Table 3.8: Experimental and calculated percentage weight losses for MUF20-Dβ.

MOF	$T_{1/2\Delta}$ (^{o} C)	Experimental Weight loss (%)	Calculated Weight Loss (%)
MUF20-Dβ	195	21.0	25.4

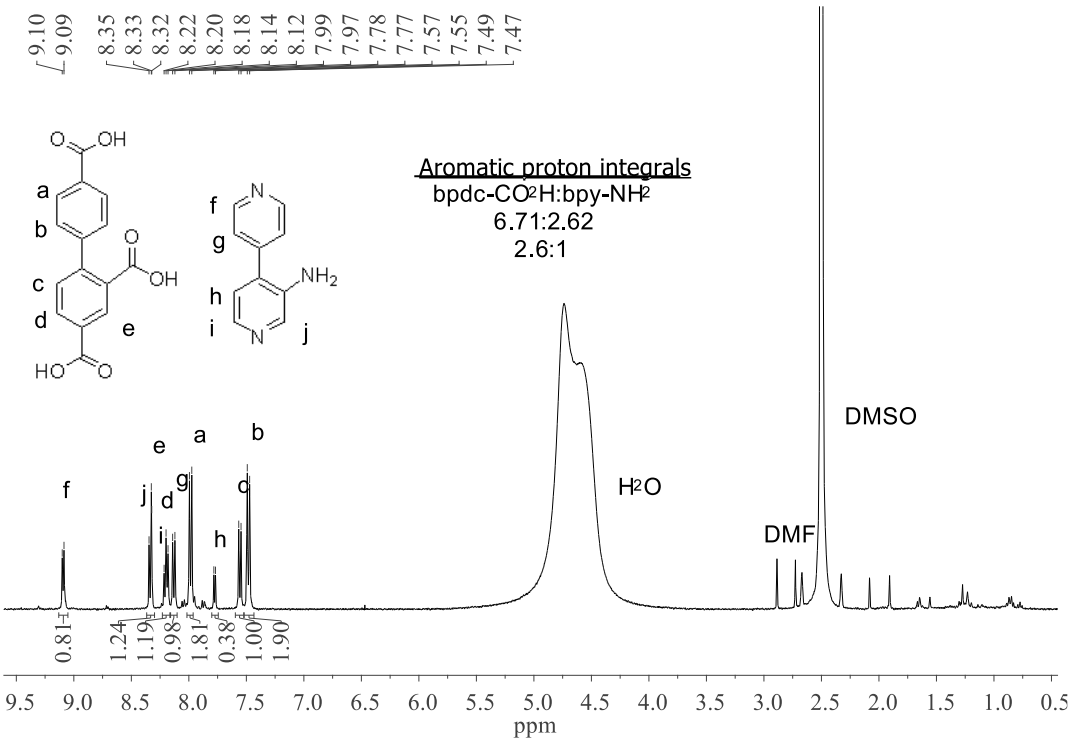

Figure 3.64: ^{1}H NMR spectrum of digested MUF20-Dβ post heating in microwave at 160 ^{o}C for 3 hrs in DMSO-d_6/DCl.

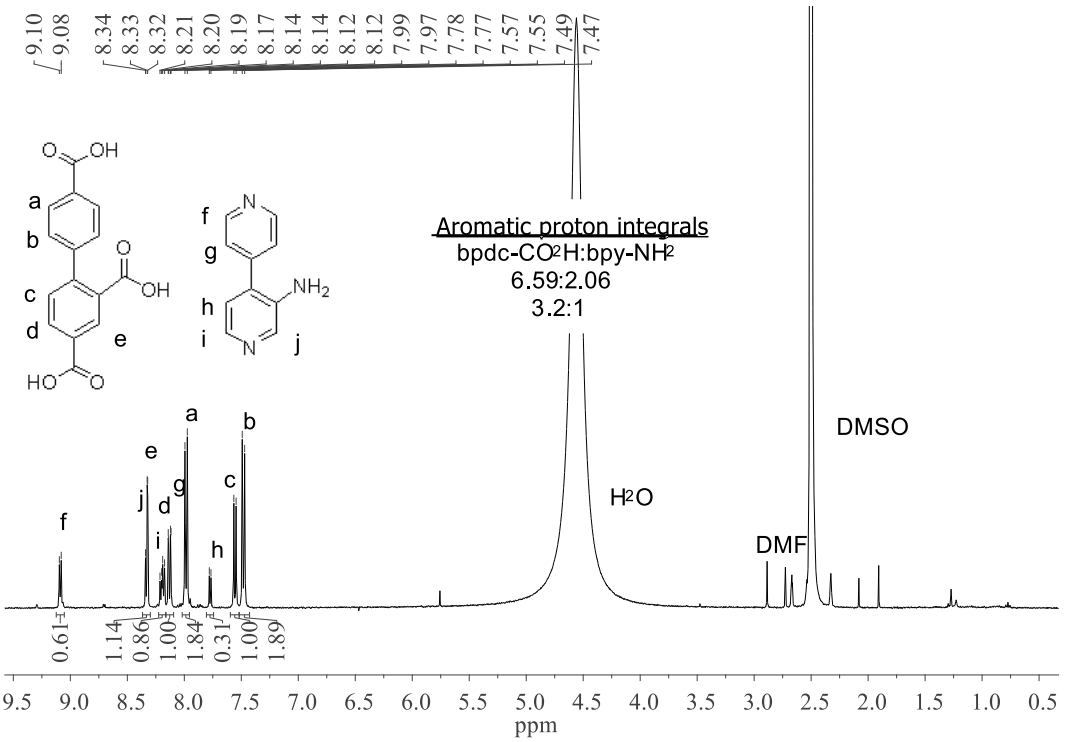

Figure 3.65: ^{1}H NMR spectrum of digested MUF20-Dβ in DMSO-d_6/DCl post heating in microwave at 160 ^{o}C for 3hrs, post washing with DMF then CH_2Cl_2.

Chapter 4 –Meldrum's acid ligands; synthesis of a ketene TPG

4.1.Introduction

The catalytic activity of MOFs has already demonstrated some unique characteristics of the MOF pore environment: inherent size-selectivity due to pore size restrictions,[212] regio- and chemoselectivity in some reaction/topology combinations,[213] enantioselectivity in homochiral MOFs[214] and stabilization of enzymes while maintaining high turnover rates.[2] However, beyond the introduction of known active species, the chemical functionalities in many of these MOFs either have been intrinsic to the structure or have been simpler functional groups such as the amine in UiO-66 described in the Introduction. Whilst there have been some more adventurous functional groups such as alkynes, azides, nitro,[215] sulfoxides,[175, 216] thiols,[217] porphyrins[218-219] and prolines[220] incorporated into MOFs, the options are still limited and at times require additional metals, such as in copper click chemistry,[221-222] or harsh chemical conditions raising the possibility of metal metathesis[151, 223-224] or structural MOF decomposition. Meldrum's acid is thus of particular interest as a MOF functional group as it readily forms a ketene upon thermolysis (releasing CO_2 and acetone).[161] Ketenes are known to be highly reactive, especially towards nucleophiles, giving access to a raft of functional groups such as amides, acid chlorides, esters and more exotic chiral functionalities[225-226] that would otherwise be difficult to introduce directly (e.g. carboxylic acid groups as shown in Chapters 2 and 3).

Introduction of this novel protected ketene group into MOF materials has a multi-fold goal: expanding the current library of MOF thermolabile protecting groups and establishing easy access to many different potential chemical functionalities through the incorporation of a reactive intermediate. This method offers many advantages over traditional covalent modification of MOFs, with the use of a TPG bypassing the limitations of solvothermal synthesis explored in Chapters 1-3 and the broad reactivity of the ketene eliminating the necessity of optimizing MOF synthesis conditions for each new functionalized ligand as well as reducing both the harshness and number of covalent post-synthetic modification steps required when starting from a more basic chemical handle, such as amine.[135] The ubiquitous benzene-1,4-dicarboxylic acid (bdc), biphenyl-4,4`-dicarboxylic acid (bpdc) ligand backbones functionalised with Meldrum's acid TPG would be compatible with many of the known MOF frameworks based on linear ditopic carboxylate ligands as linkers. Therefore, the synthesis of

four novel Meldrum's acid TPG MOF ligands; bdc-Meldrums, bpdc-Meldrums, bpdc-CHMeldrums and bpdc-symMeldrums is elaborated on in this chapter (Figure 4.1).

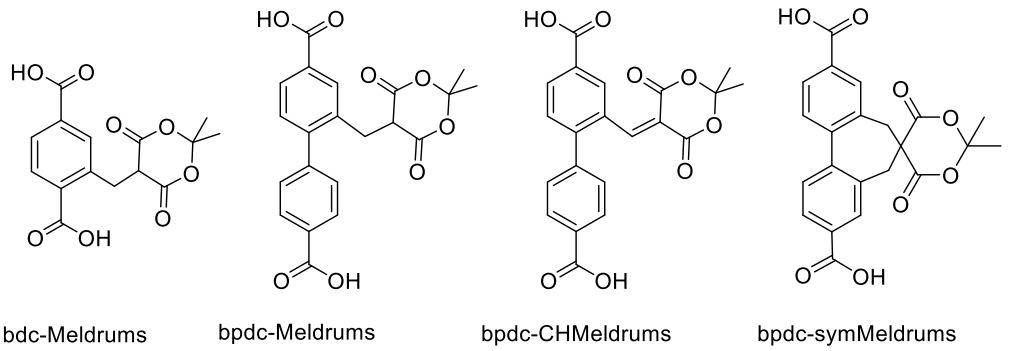

Figure 4.1: Meldrum's acid TPG MOF ligands.

4.2. Results and discussion

Synthetic routes to the MOF ligands, bdc-Meldrums and bpdc-Meldrums, had previously been established in the Telfer research group by Mr. David Lun (Figure 4.2).

1.)

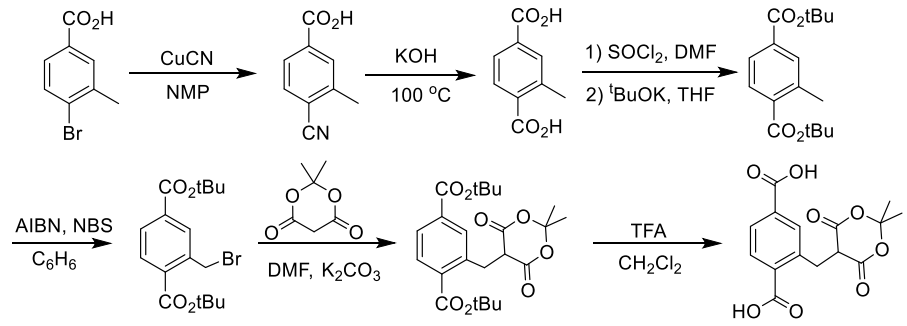

2.)

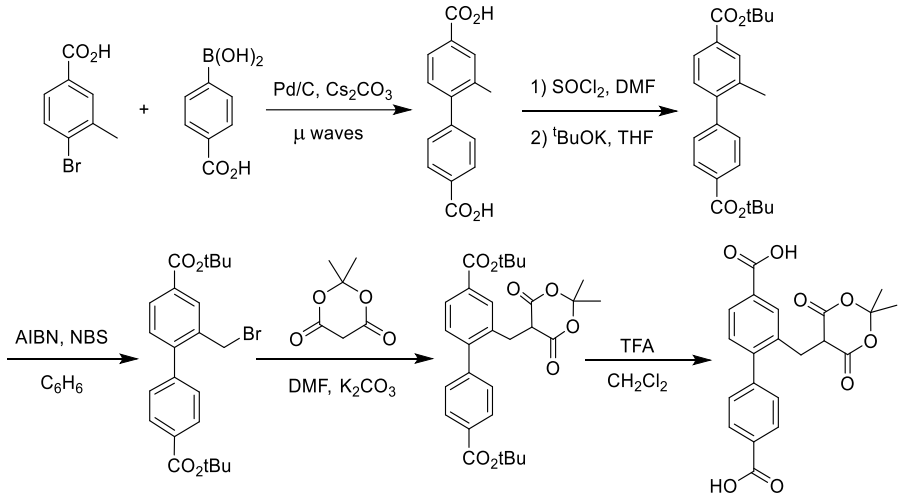

Figure 4.2: Synthetic routes for 1) bdc-Meldrums and 2) bpdc-Meldrums established by Mr. David Lun.

Unfortunately, this synthesis scheme challenged at key steps. During the course of resynthesis of these ligands a competing side-product was analyzed and identified as the bis-substituted product (Figure 4.3 and Appendix).

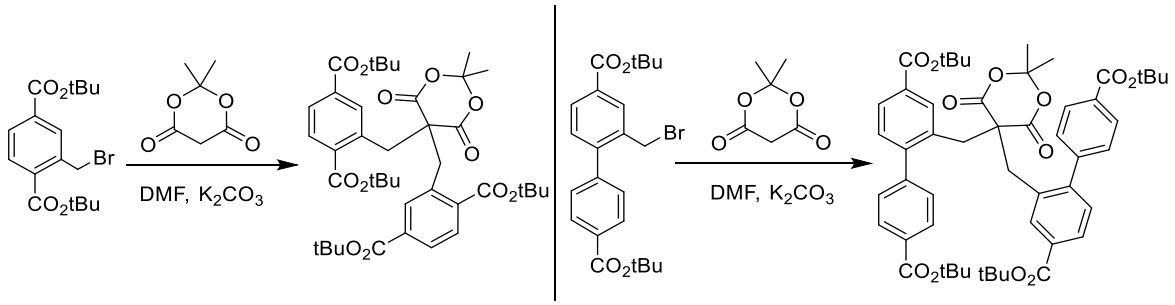

Figure 4.3: Bis-substituted side-products of Meldrum's addition reaction using alkyl bromides.

This side product, formed from double addition of the brominated starting material to Meldrum's acid, is more favoured at lower ratios of Meldrum's acid which had enabled the easier recrystallization work up in the optimized synthesis. However, this compound is also still present at higher concentrations of Meldrum's acid used and has been observed to be a common problem in the synthesis of substituted Meldrum's acid species.[155] By lowering the ratios used and developing a recrystallization method, a greater than 53% yield of the *tert*-butyl ester derivative of the desired mono-substituted bdc-Meldrum's ligand can be isolated as a crystalline solid from an effectively 1:1 mixture of the mono-:di-substituted species. The di-substituted species then crystallizes from the filtrate (see experimental section).

However, synthesis of the bpdc-Meldrums species proved even more challenging as, in the case of the chemistry of the biphenyl dicarboxylic acid backbone, yields of the *tert*-butyl esterification procedure were limited to 65%. More grievously, the Meldrum's acid addition step persistently produced a mixture of products difficult to purify with yields pre-column commonly < 30% and post-column as low as 8%.

Despite numerous conditions trialled with different temperatures, bases and solvents this could not be improved upon and in fact seemed to increase the proportion of the side-product. The double addition bis-substituted product noted to form in the bdc-Meldrums acid ligand synthesis appeared to be a dominating reaction in the biphenyl backbone to the point of being the main product, especially over longer reaction times.

Upon consideration of the literature, the struggles with double addition to Meldrum's acid can be largely avoided by approach from an alternate synthetic angle that offers not only the Meldrum's acid group but also an equally chemically versatile and potentially more robust alkylidene Meldrum's acid functionality. Removal of the highly acidic proton of the Meldrum's acid moiety may increase resistance of the ligand to hydrolytic attack and also yield an alternate cumulenone species, a methylene ketene, upon thermolysis. A simple reduction of the double bond accesses the original Meldrum's acid group. Although this adds an additional step to the original synthesis it bypasses the persistently low-yielding Meldrum's acid addition step in favour of a robust Knoevenagel condensation reaction with ready purification of the product through crystallization from boiling methanol/water.

This synthetic route also combines with the more reliable methyl esterified bpdc-TBE ligand synthesis in Chapter 2 allowing for better efficiency as multiple ligands can be accessed from one starting material instead of using two separate parallel synthesis. The aldehyde starting material for oxidation to carboxylic acid and subsequent *tert*-butyl esterification in the synthesis of bpdc-TBE can instead be reacted with Meldrum's acid in the presence of pyrrolidinium acetate to yield an alkylidene Meldrum's acid (bpdc-CHMeldrums) species. This ligand can then undergo reduction via $NaBH_4$ to form the desired Meldrum's acid (bpdc-Meldrums) cleanly and in good yield (see Figure 4.4).

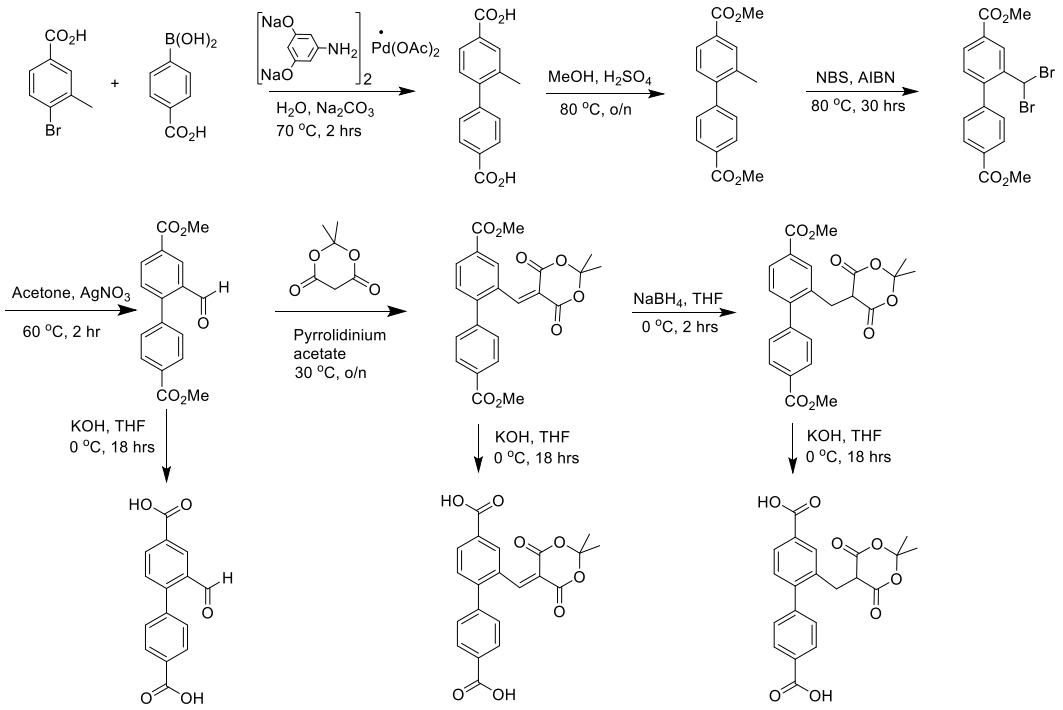

Figure 4.4: Combined ligand synthesis scheme.

Given the robustness of the Meldrum's acid on the biphenyl backbone to the methyl-ester removal conditions, a methyl ester–based synthetic route was then developed by Mr. David Lun to make the symmetric Meldrum's acid ligand (bpdc-symMeldrums).

In the case of this symmetrically disubstituted species the Meldrum's acid group did not survive the final reaction step (Figure 4.5).

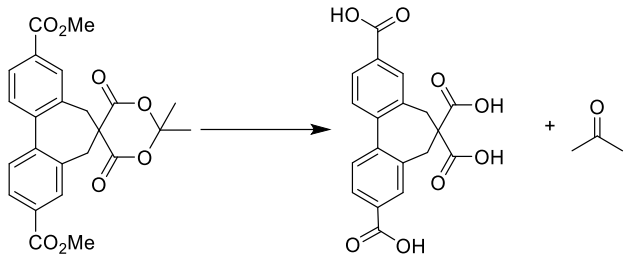

Figure 4.5: The ester of the symmetrically substituted Meldrum's acid decomposes preferentially over those of the biphenyl backbone, forming malonic acid and acetone, even under gentle methyl ester removal conditions.

Despite trialling a range of methyl-ester removal conditions, in each case the Meldrum's acid functionality was preferentially hydrolyzed. In light of the relatively increased stability of the bis-substituted side products over their mono-substituted analogues it is surprising that the symmetrically disubstituted Meldrum's acid functionality was so susceptible to hydrolysis.

Subsequently, in synthesizing this ligand for MOFs a *tert*-butyl ester protecting group for the carboxylic acids was utilized and the Meldrum's acid functionality, as in the original *tert*-butyl ester-based route, survived ester removal under TFA/dry CH_2Cl_2 conditions (Figure 4.6).

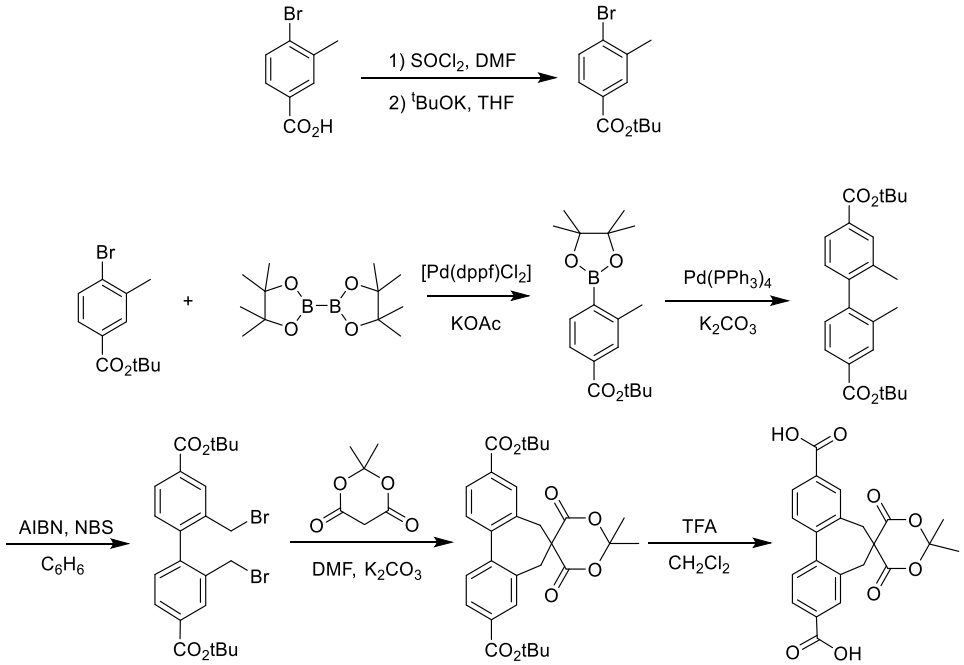

Figure 4.6: bpdc-Meldrums ligand synthesis

The Meldrum's acid addition reaction step on the dibrominated ligand proceeded smoothly and in good yield with no side products observed.

4.2.1. Thermolysis of Meldrum's acid ligands

Meldrum's acid functionality is known to undergo thermolysis to reveal a ketene or methyleneketene (Figure 4.7).[158, 227-229]

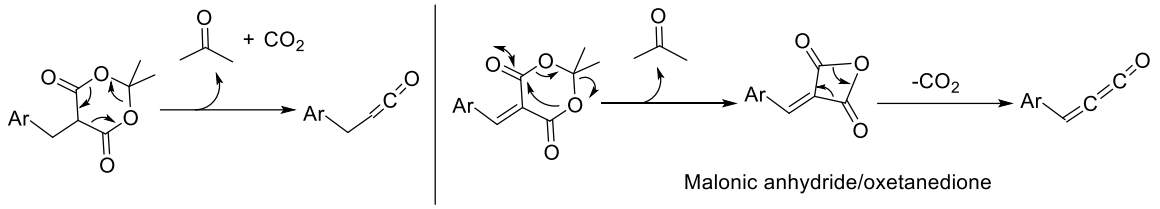

Figure 4.7: Mechanisms of thermolysis of Meldrum's and alkylidene Meldrum's acid attached to an aromatic backbone.

The expected species formed upon thermolysis of the Meldrum's acid ligands are illustrated in Figure 4.8.

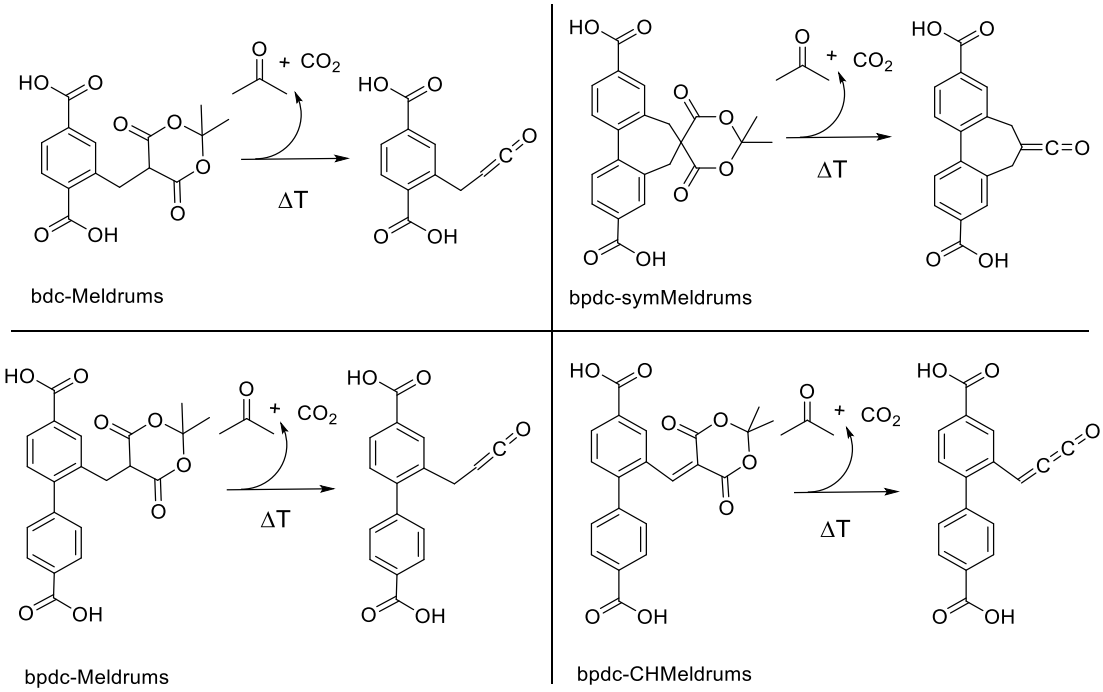

Figure 4.8: Proposed thermolysis of Meldrum's acid ligands to reveal a ketene functional group. In the case of bpdc-CHMeldrums a methylene ketene group is formed.

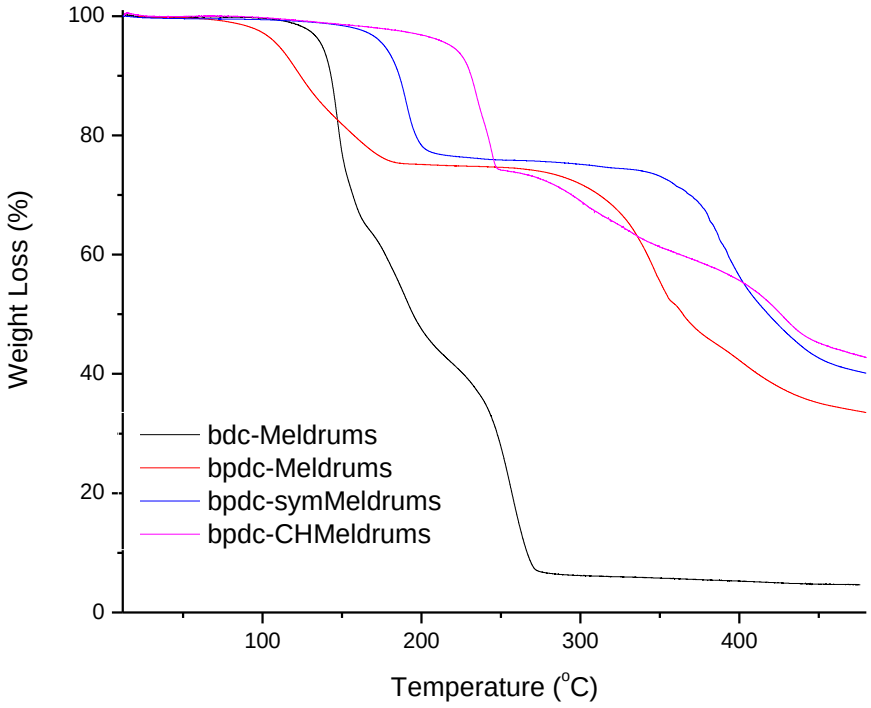

Figure 4.9: Thermogravimetric analysis (TGA) trace for Meldrum's acid ligands.

Analysis of the TGA curves (Figure 4.8) yields the following weight losses (Table 4.1) as compared to calculated weight losses expected for formation of ketene species (expelled CO_2 and acetone).

Table 4.1: Experimental and calculated weight losses for Meldrum's acid TPG ligands.

Ligand	T_{kf} (°C)*	Experimental Weight loss (%)	Calculated Weight Loss (%)
bdc-Meldrums	124	32.6	31.7
bpdc-Meldrums	129	24.6	25.6
bpdc-CHMeldrums	170	25.9	25.8
bpdc-symMeldrums	177	23.6	24.9

* T_{kf} is defined as the temperature at which 5 mol% of CO_2 and acetone has been generated.[158]

As can be seen, the values are in good agreement for loss of acetone and CO_2 from the parent Meldrum's acid functionalized ligand. Due to the gradual nature of the weight loss as thermal energy approaches the required threshold for bond cleavage there is some ambiguity in determining start and end points of the thermolytic process. This results in the slight differences noted between experimental and calculated. Precise curve coordinates used to calculate weight percentages can be found in the experimental section.

The temperature of ketene formation (T_{kf}) can be defined as the temperature at which 5 mol% of CO_2 and acetone has been generated.[158] Notably, shifting to a biphenyl dicarboxylic acid backbone initially lowers T_{kf} but, in the absence of the acidic hydrogen atom of the Meldrum's acid moiety in bpdc-CHMeldrums or bpdc-symMeldrums, the onset temperature of ketene formation significantly increases. The dramatic drop from most to least stable ligand in this set hinges on a simple reduction from an alkylidene Meldrum's acid to a monoalkyl substituted Meldrum's acid, suggesting the key role the hydrogen atom at this position plays in determining thermal stability. T_{kf} dependence on hydrogen bonding and ring strain influence is elaborated on later in this chapter.

Additional partial characterization by gas chromatography (GC) of the headspace of sealed thermolyzed samples also indicated the presence of acetone – an expected product in ketene formation (Figure 4.10).

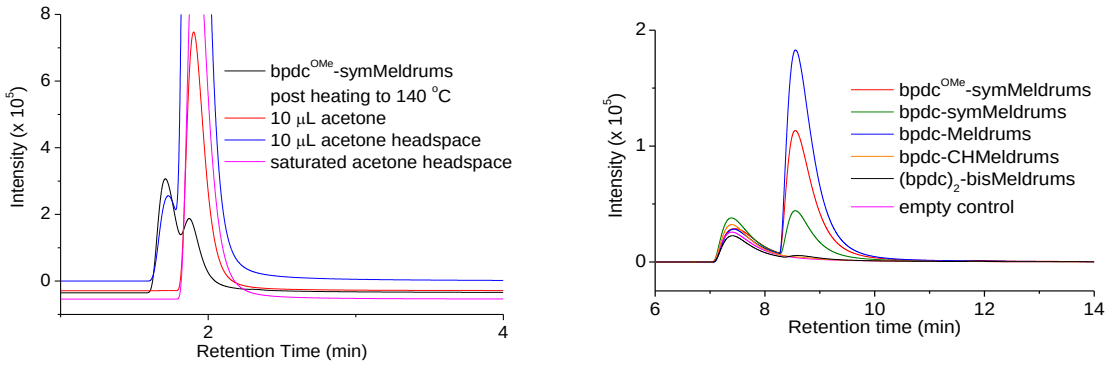

Figure 4.10: GC analysis of headspace of selected heated Meldrum's acid ligands. Leading peak is an artefact of low concentration headspace sampling as indicated by 10 μL headspace sample (left) and empty vial sample (right). When the ligand sample concentration is very low (samples bpdc-CHMeldrums and $(bpdc)_2$-bisMeldrums (right)) there is still a visible peak corresponding to acetone. When a high concentration of sample is present as in the methylated ester version ($bpdc^{OMe}$-symMeldrums) the peak corresponding to released acetone is increased as expected. All Meldrum's acid ligands were thermolyzed at temperatures derived from their TGA traces.

A more conclusive related characterization method would be GC-MS of the headspace of thermolyzed Meldrum's acid ligand samples or alternatively TGA-MS. This latter experiment could also be conducted in two steps to further support ketene formation. Step 1 would involve heating samples of the dried ligands under vacuum to the individual thermolysis temperatures indicated by TGA and then Step 2 would trap the reactive possible ketene formed by addition of a nucleophile such as a simple alcohol to produce a more readily characterized species. Use of deuterated methanol would enable same sample analysis by both NMR and ESI-MS.

Fourier transform infrared spectroscopy is commonly used to identify ketenes due to the characteristic stretch at 2,103 cm^{-1}. While this has most commonly been done *in situ* under

flash vacuum pyrolysis,[226] when appropriately stabilized in a polymer this C=O stretch has been observed at room temperature.[161] Some preliminary characterization indicated changes upon thermolysis but no ketene stretch was observed at 2,103 cm^{-1} (Figure 4.11). This is to be expected for such a reactive species in absence of any stabilizing matrix.

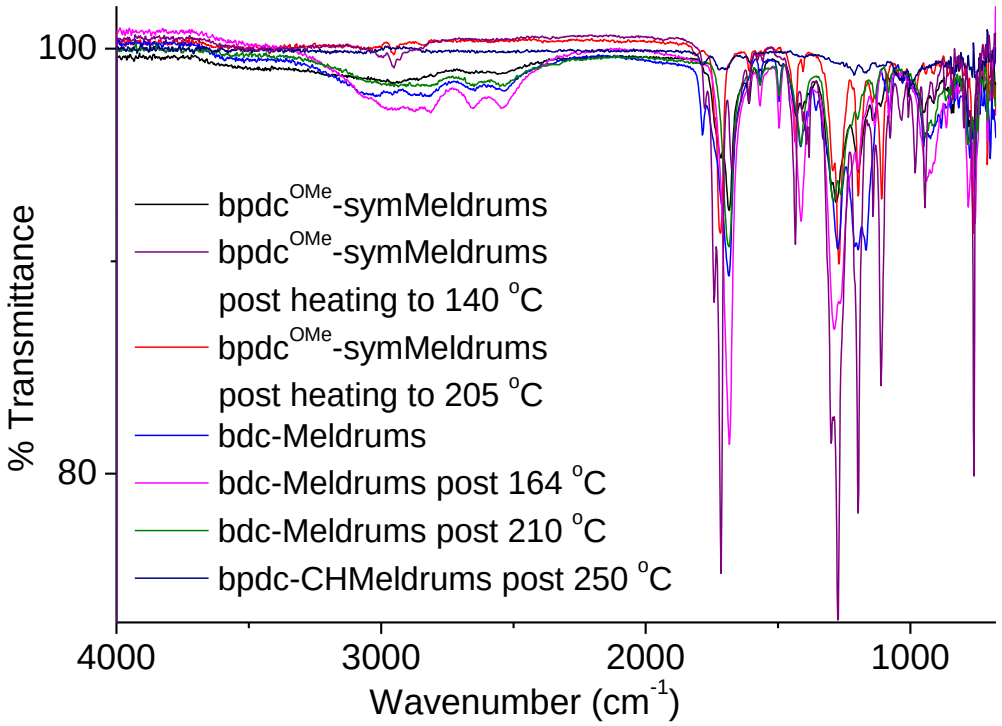

Figure 4.11: IR spectra of selected Meldrum's acid ligands pre and post range of thermolysis conditions, none show ketene carbonyl stretch between 2000 and 2300 cm^{-1}.

However, of primary consideration for the purposes of this study was the characterization of ligand stability under typical MOF solvothermal synthesis conditions so this was prioritized over further ketene characterization.

4.2.2. Ligand stability trials

To investigate the stability of the ligands for traditional solvothermal MOF synthesis the bdc-Meldrum's and bpdc-Meldrum's ligands were separately dissolved in DMF-d_7 and heated in approximate 10 °C steps over the range 70 – 150 °C. The ^{1}H NMR spectrum was recorded after 10 minutes at each temperature. Both bdc-Meldrum's and bpdc-Meldrum's decomposed at relatively low temperatures, as marked by the disappearance of the CH proton peak of the Meldrum's acid moiety at ~4.9 ppm (Figures 4.12, 4.13).

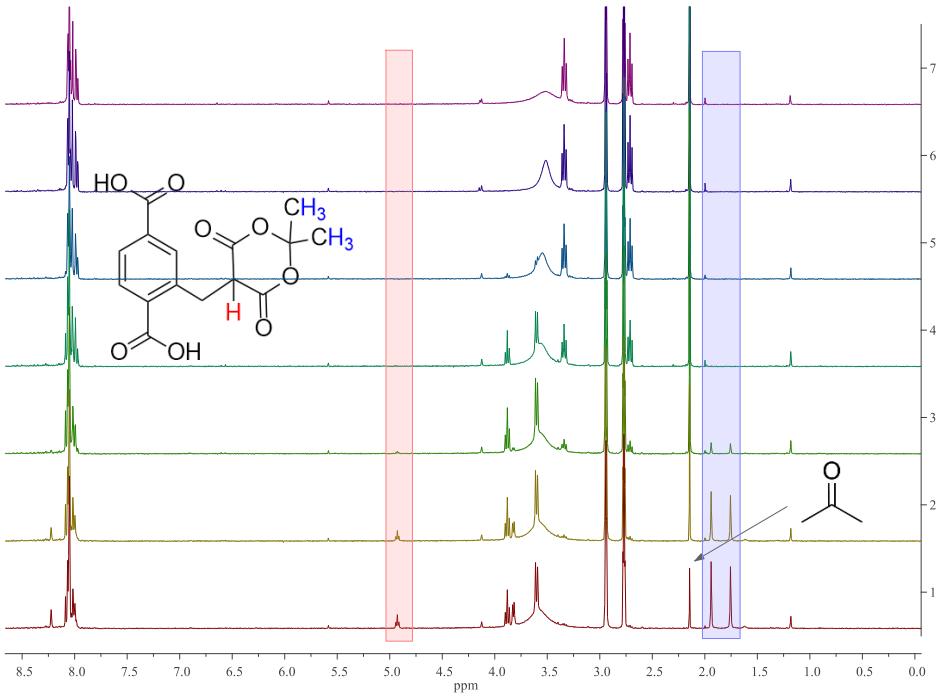

Figure 4.12: Stability of Meldrum's acid group in MOF synthesis conditions on bdc. In DMF-d_7, free ligand, bdc-Meldrums, was heated in an oil bath for 10 minutes at each temperature before recording the ^{1}H NMR spectrum at 20 (red), 70 (dark yellow), 80 (green), 90 (dark green), 100 (blue), 110 (purple), and 120 ^{o}C (pink).

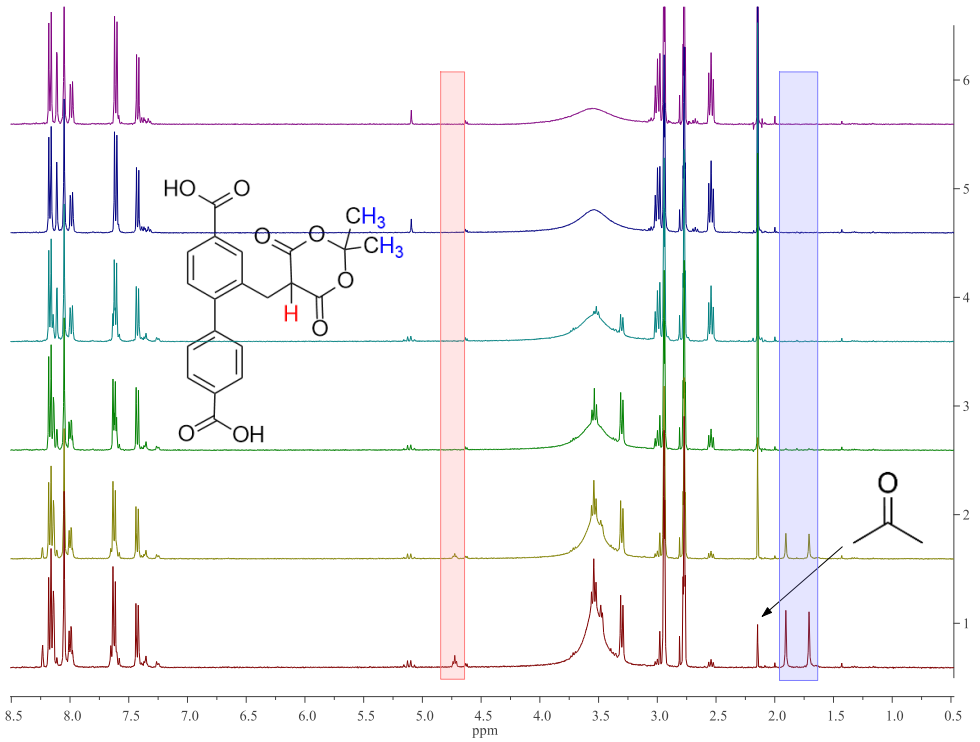

Figure 4.13: Stability of Meldrum's acid group in MOF synthesis conditions on a bpdc backbone. In DMF-d_7, free ligand, bpdc-Meldrums, was heated in an oil bath for 10 minutes at each temperature before recording the ^{1}H NMR spectrum at 20 (red), 70 (yellow), 80 (green), 90 (dark green), 100 (purple), and 110 ^{o}C (pink).

These ligands were also found to be unstable in DMF at room temperature as acetone, a decomposition product of the Meldrum's acid group, was found to be present in all of the starting (20 °C) spectra of the above stability trials (peak at ~2.1 ppm). To exclude the acetone being contributed from another source fresh dried bdc-Meldrum's was placed in a new NMR tube in fresh DMF-d_7 and monitored at room temperature over the course of a week. As seen below (Figure 4.14), after 20 minutes in DMF at room temperature the Meldrum's acid group is already partially degraded, forming acetone at 2.1 ppm. This increases alongside decrease of the CH (~4.9 ppm) and methyl peaks (~1.7 and 1.9 ppm) of the Meldrum's acid moiety until almost complete disappearance post 1 week.

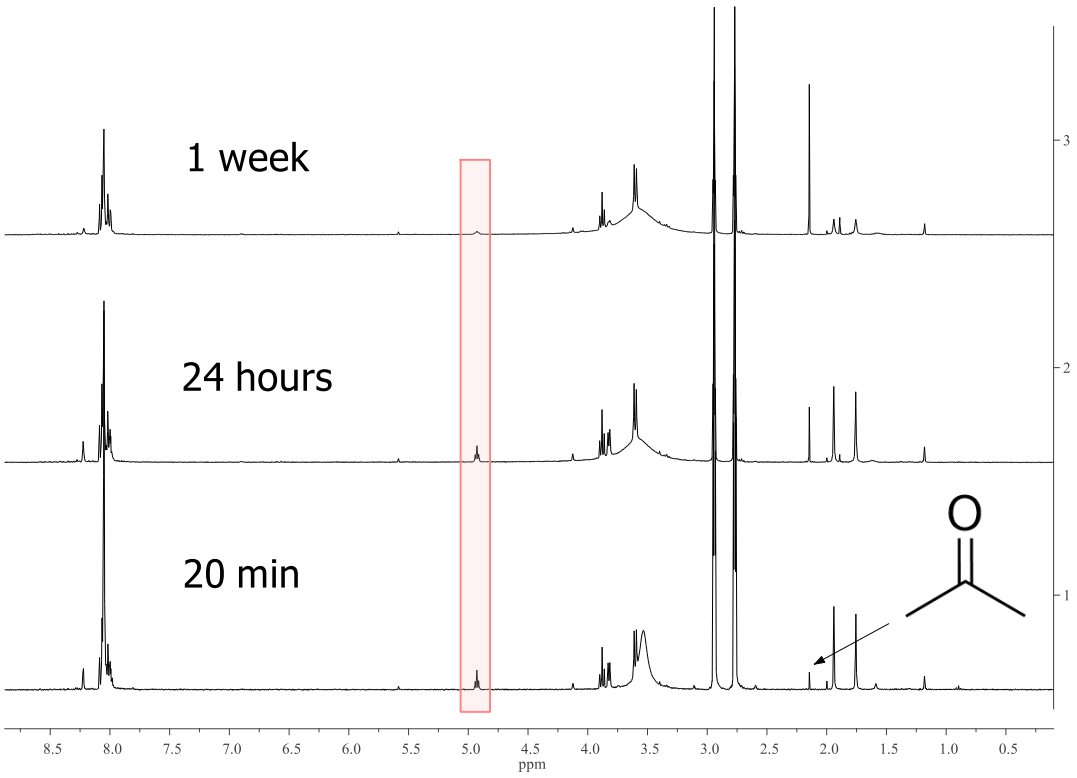

Figure 4.14: Stability of Meldrum's acid group on a bdc backbone in DMF-d_7 at room temperature from bottom; post 20 min, 24 hrs, and 1 week.

Unfortunately, despite the careful use of high vacuum over days, fresh solvent and new NMR tube there is water present in the sample. It is unclear where the water is from but is most likely present in the commercial solvent source, DMF-*d*7. Surprisingly, in literature investigating scandium triflate-catalyzed intramolecular acylation mechanism with Meldrum's acid, despite use of gloveboxes and utmost care, water was also found to be a persistent contaminant.[228] Presence of water in this case does not seriously affect the ligand stability implications for traditional solvothermal MOF synthesis conditions which usually use metal

salt hydrates and the practical reality of trace water in the amide-based solvents no matter how thoroughly distilled and dried.

Some methods could be further trialled to remove water from the reaction mixture such as triethylorthoformate or proton sponges but the amide solvents alone with decomposition to dimethylamine may be expected to also catalyze the decomposition to malonic acid and acetone of these sensitive Meldrum's acid species. Acetic acid anhydride addition to act as an additive to reform any decomposed Meldrum's in situ during MOF synthesis is another possibility that was not trialled but a related experiment using the alkylidene Meldrum's acid ligand and Meldrum's acid in MOF reaction mixture was unsuccessful.

The bdc-Meldrum's acid ligand was found to be similarly unstable in other solvents (DMSO-d_6 and CD_3OD) but was more stable in acetone-d_6 at room temperature with no change in ^1H NMR peak patterns over one week at room temperature. This is due to inhibition of the equilibrium set up between the Meldrum's acid and the corresponding hydrolytic decomposition products of malonic acid and acetone as illustrated below (Figure 4.15).

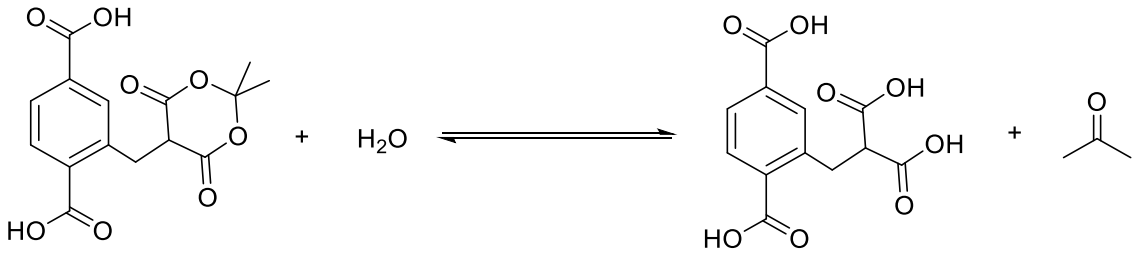

Figure 4.15: Equilibrium set up between Meldrum's acid ligand and the corresponding hydrolytic decomposition products of malonic acid and acetone.

This decomposition process was supported by undertaking the historic reverse reaction - synthesis of Meldrum's acid from a malonic acid and acetone in the presence of acetic anhydride and an acid catalyst – on the decomposed ligand (Figure 4.16).

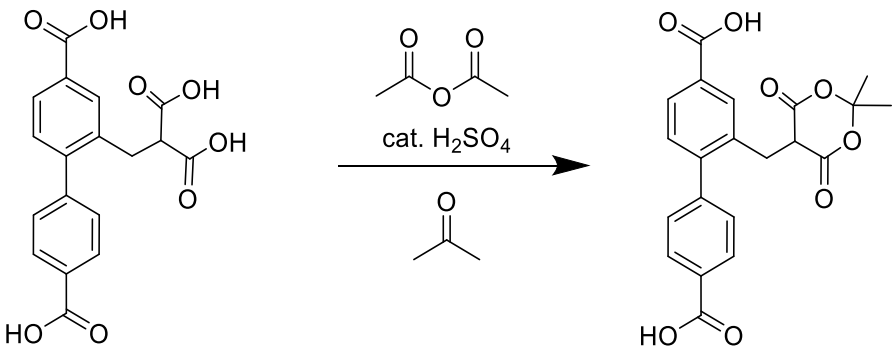

Figure 4.16: Synthesis of a Meldrum's acid moiety from malonic acid.

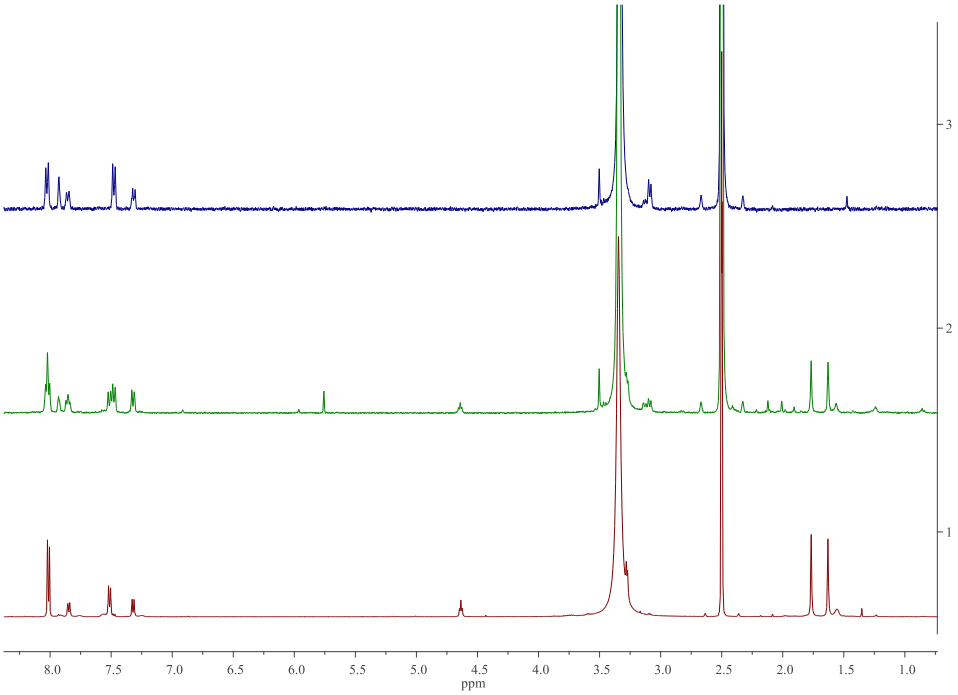

Figure 4.17: ^{1}H NMR spectrum showing starting material decomposition product (blue), bpdc-Meldrums ligand (red), and mixed malonic acid to Meldrum's acid reaction product (green) in DMSO-d_6.

However, as the product could not be isolated cleanly from the reaction mixture this is simply presented as evidence supporting a malonic acid decomposition product (see experimental section).

Additionally, the Meldrum's acid functionalized ligands were found to be sufficiently reactive that, once malonic acid product was present even at trace levels within the mixture, the equilibrium set up highly favours complete conversion to the malonic acid decomposition product, occurring as a dry solid under inert atmosphere or vacuum at room temperature over a week and readily going to completion within days under air atmosphere.

During synthesis, the esterified ligands and bis-substituted side products were crystallized and analyzed by single crystal x-ray diffraction.

4.2.3. Solid-state bonding and experimental stability of ligands

Crystal structures represent some energy minimum. Precise characterization of molecular structure in solution is challenging. However, many structural characteristics, especially inter and intramolecular interactions, also occur at the equilibrium of molecular conformations in solution. [160]

Literature investigations of substituted benzyl Meldrum's acid species suggest that conformational considerations dominate over electrostatic factors in dictating the structure observed in solid-state and solution. Specifically, in absence or presence of intramolecular bonding, a common boat conformation was most encountered with the acidic hydrogen of the Meldrum's acid moiety occupying the pseudoaxial position and the benzylic group in a pseudoequatorial position. The conformation of the aromatic groups that minimizes the $A^{1,3}$-allylic strain is adopted. Significantly, upon sufficiently large increase of this $A^{1,3}$-allylic strain – as with benzyl *ortho* substituent bulk - the chair conformation of Meldrum's acid is adopted.

The stability of the substituted Meldrum's acid species varies greatly. In the above study the substituted species were stable across a wide temperature range (-55 to 55 ^{o}C) and in multiple solvents including DMSO-*d*6. XRD and NMR data established that the conformational properties of benzyl Meldrum's derivatives were correlated to their solid state except in the case of DMSO where an equilibrium of intra- and inter-molecular bonding interactions was observed.[230]

Thermal stability of Meldrum's acid species has been investigated under TGA thermolysis conditions and tuning of ketene formation explored through control of three main factors:

1) Carbonyl carbon atom electron acceptance from an intramolecular Lewis base
2) Electron withdrawal by a Brønsted acid
3) Spiro-ring strain at the C-5 position

Literature studies indicate that lowering of ketene formation temperature (T_{kf}) of Meldrum's acid derivatives occurs upon formation of intermolecular hydrogen bonding and interaction with electron donating/withdrawing groups by the carbonyls. As with neighbouring group participation (NGP) in organic chemistry using Lewis bases and carbonyls to accelerate and/or determine reaction stereochemistry, the "structure and energetics of Meldrum's acid derivatives dictates their reactivity." [158]

Hydrogen-bonding in the solid state - such as through Brønsted-acid activation of Meldrum's acid carbonyl groups – has been shown to lower thermal stability of the derivative.

Within the four main Meldrum's acid species examined (bdc-Meldrums, bpdc-Meldrums, bpdc-symMeldrums, and bpdc-CHMeldrums) a wide range of T_{kf} exists with full thermolysis occurring as low as ~150 ^{o}C for bdc-Meldrums and as high as ~ 250 ^{o}C for bpdc-CHMeldrums (Figure 4.8). For the bis-substituted Meldrum's acid side products, unique thermolysis behaviour is also shown in their TGA traces relative to the mono-substituted Meldrum analogues (Figure 4.18).

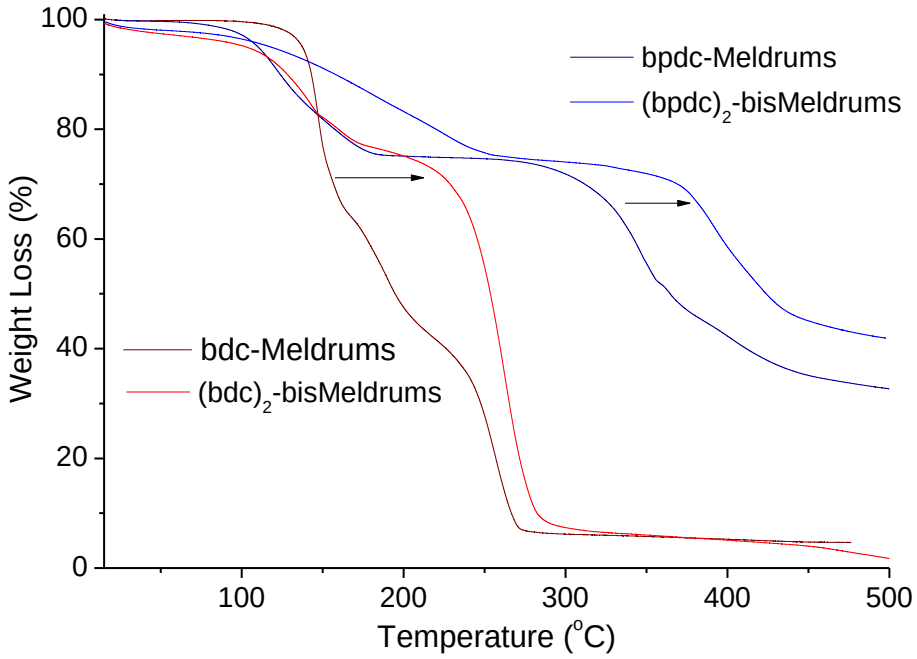

Figure 4.18: Thermogravimetric analysis (TGA) traces for the mono-substituted bdc- and bpdc-Meldrums ligands and their bis-substituted analogues bdc- and bpdc-bisMeldrums.

For bdc-Meldrum and bpdc-Meldrums, both exhibit the favoured boat formation with the Meldrum's acid moiety involved in intermolecular non-classical hydrogen bonding (Figures 4.19, 4.20). In bdc-Meldrums an additional intramolecular hydrogen-bonding interaction between the carbonyl oxygen and benzyl hydrogen is present (Figure 4.19). Bdc-Meldrums exhibits the lowest thermal stability of the substituted Meldrum's species synthesized in this thesis.

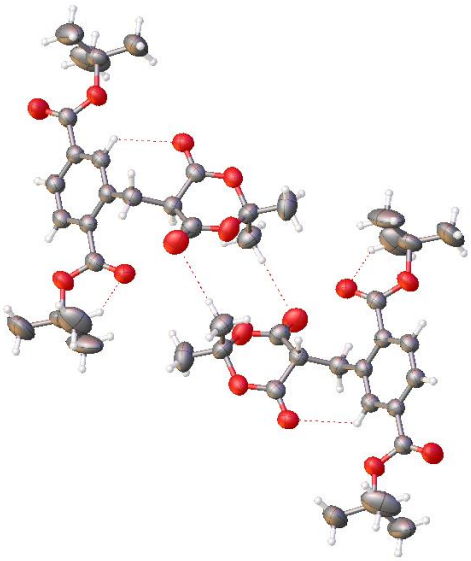

Figure 4.19: Single crystal structure for esterified bdc-Meldrums showing non-classical hydrogen-bonding interactions.

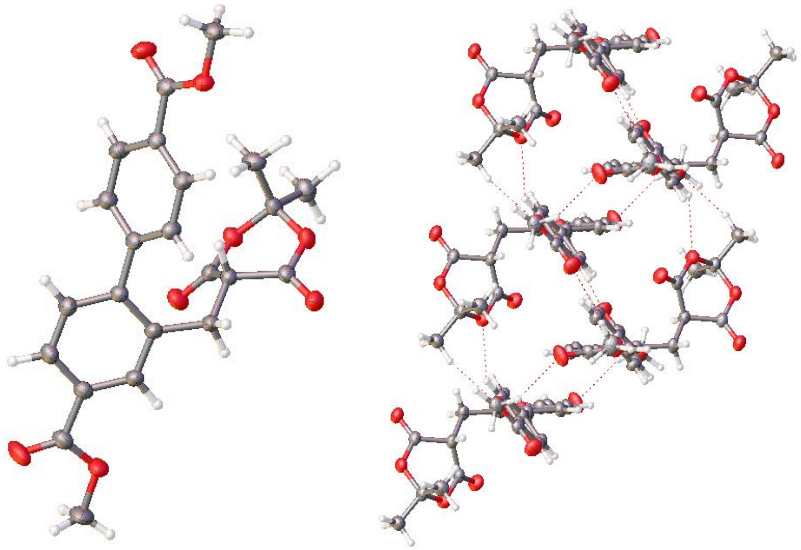

Figure 4.20: Single crystal structure for esterified bpdc-Meldrums showing non-classical hydrogen-bonding interactions.

In contrast to the mono-substituted Meldrum's acid ligands, both bpdc-CHMeldrums and the symmetrically di-substituted bpdc-symMeldrums constrain the Meldrum's acid moiety in a flattened boat conformation (Figures 4.21, 4.22).

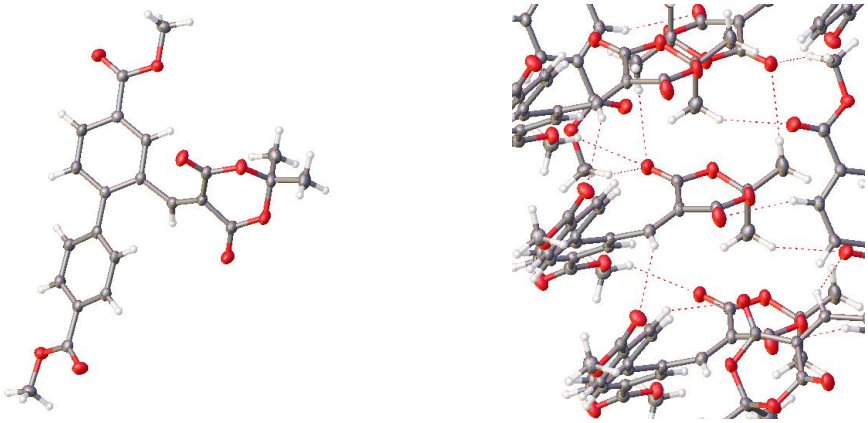

Figure 4.21: Single crystal structure for esterified bpdc-CHMeldrums showing non-classical hydrogen-bonding interactions.

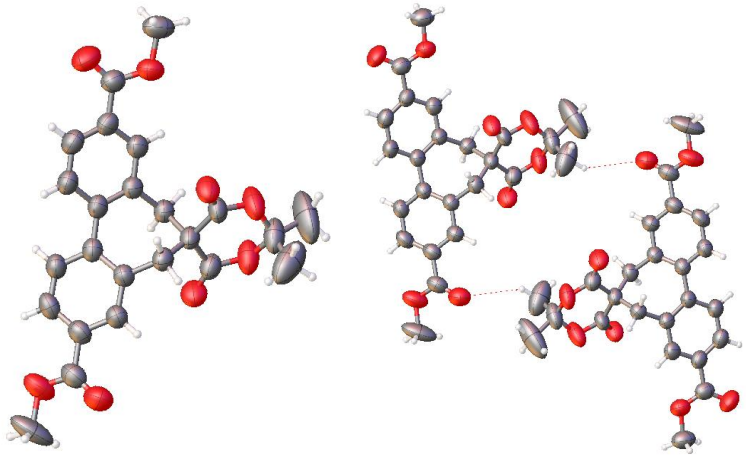

Figure 4.22: Single crystal structure for esterified bpdc-symMeldrums showing non-classical hydrogen-bonding interactions.

Contrasting the structures of bpdc-CHMeldrums versus bpdc-symMeldrums, the observed susceptibility of the latter to degradation under methyl ester hydrolysis conditions may be explained by the substantially diminished presence of hydrogen-bonding interactions in the solid state as both ligand species lack the acidic hydrogen of the parent Meldrum's acid (bpdc-CHMeldrums through formation of an alkylidene species and bpdc-symMeldrums through dialkyl substitution) but of the two methyl-esterified ligands, only the alkylidene Meldrum's acid species shows strong intermolecular hydrogen-bonding interactions in the solid state.

This would have been predicted to lower thermal stability of the Meldrum's acid but instead a much higher temperature for ketene formation is observed. This suggests that the 7-membered ring formed from disubstitution of Meldrum's acid onto the same biphenyl backbone may be straining the attached 6-membered Meldrum's acid ring to favour hydrolytic decomposition to the malonic acid species which would then possess much greater degrees of freedom.

This is supported by the experimentally observed stability of the bis-substituted Meldrum's acid species at room temperature or in humid atmosphere. These bis-substituted species push the required temperature for thermolysis slightly higher than their mono-substituted analogues (Figure 4.18). This is in opposition to the increased presence of non-classical intramolecular bonding in single crystal structures of the esterified ligands (Figures 4.23, 4.24).

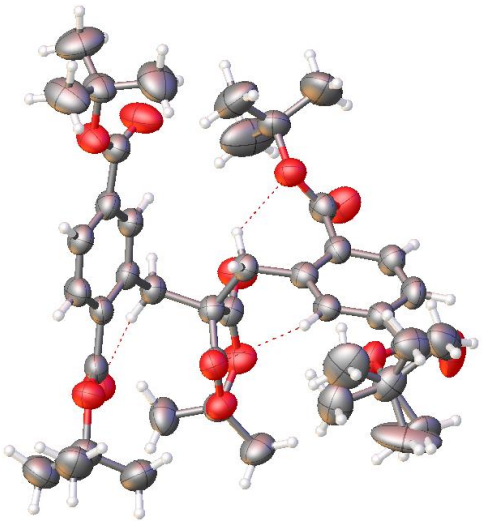

Figure 4.23: Single crystal structure for esterified $(bdc)_2$-bisMeldrums showing non-classical intramolecular hydrogen-bonding interactions.

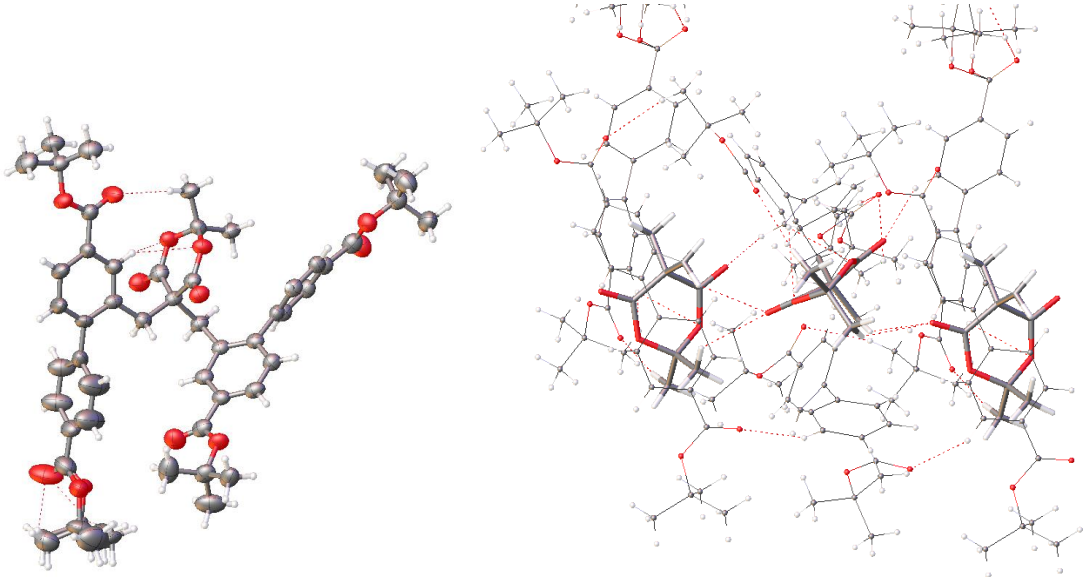

Figure 4.24: Single crystal structure for esterified $(bpdc)_2$-bisMeldrums showing intra (left) and intermolecular (right) non-classical hydrogen-bonding interactions. Meldrum's acid moiety is presented as stick to illustrate the severe flattening of the 6-membered ring and interactions between Meldrum's acids on different molecules.

A flattening of the Meldrum's acid moiety (and thus an increase in ring strain) can be observed along the series of Meldrum's acid ligands (Figure 4.25).

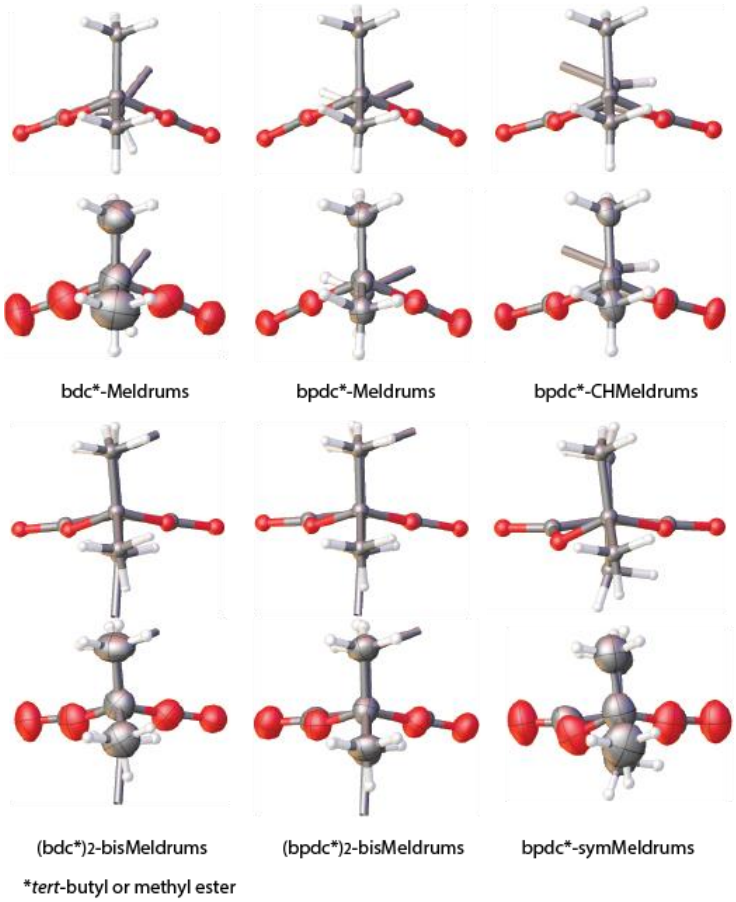

Figure 4.25: Flattening of the Meldrum's acid moiety in the ligands from left to right through the esterified bdc-Meldrums, bpdc-Meldrums, bpdc-CHMeldrums, bpdc-symMeldrums, $(bdc)_2$-bisMeldrums, and $(bpdc)_2$-bisMeldrums.

A few general trends:

- Di-substituted derivatives are both hydrolytically and thermally more stable than the mono-substituted Meldrum's acid ligands
- The alkylidene Meldrum's acid is more stable than the corresponding reduced Meldrum's acid form or mayhap more accurately no α-C-H atom > α-C H atom present (see bpdc-symMeldrums)
- Presence of two aromatic rings attached to the Meldrum's acid moiety is more stable than if attached symmetrically to same biphenyl backbone.
- The mono-substituted terephthalic acid-based derivative is more stable than the extended biphenyl ligand.

Computational investigations into the reason behind the unexpected reactivity of the Meldrum's acid may be of interest. Single-crystal structures collected on the esterified ligands demonstrate some notable structural differences around the Meldrum's acid group.

- Presence of α-carbon hydrogen atom

- Tetrahedral nature of α-carbon conformation
- Sheltering of β-carbon atom hydrogen(s)
- 'Planarity' of 6-membered ring/emphasis of boat conformation
- Angle of ketone oxygens relative to ring
- Angle of CH/CH_2 groups to α-carbon in 6-membered ring plane (also CH_3 group angles)

Studies have been conducted as to the effect of the substituent on the acidity of the remaining proton. These have implied that intramolecular bonding plays a key role in the acidity of the proton and stability of the Meldrum's acid group to nucleophilic attack. Malonic acid formation results in autocatalysis under neutral hydrolysis conditions as formation of the acid releases protons.

4.2.4. Formation of a spirocyclic Meldrum's acid compound

In the presence of trace amounts of methanol and pyrrolidinium acetate the methylated bpdc-CHMeldrum's ligand undergoes double addition reaction at room temperature to form the spirocyclic product (Figure 4.26).

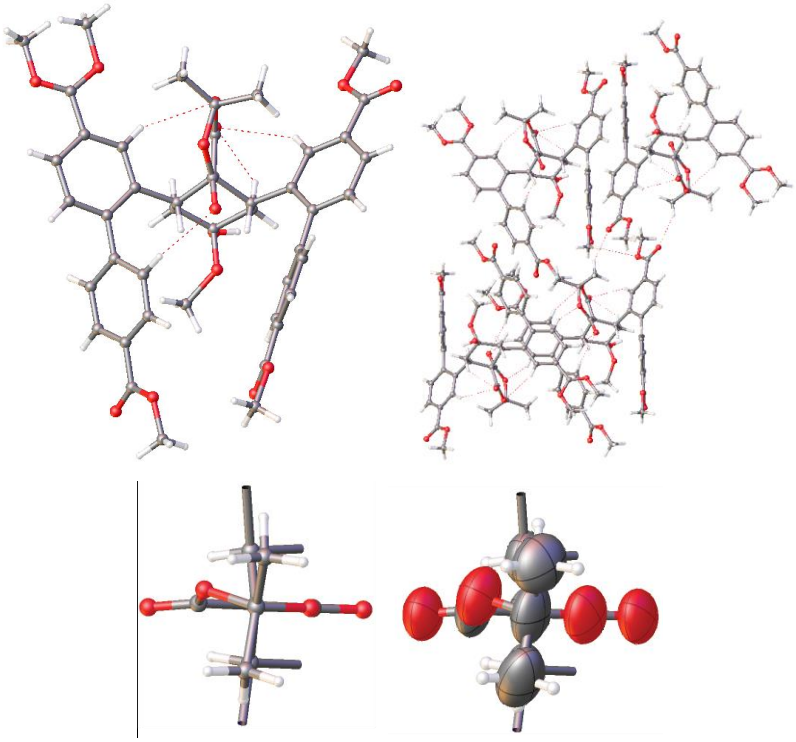

Figure 4.26: Single crystal structure for spirocyclic Meldrum's acid ligand showing intra (left) and intermolecular (right) non-classical hydrogen-bonding. As data quality for this structure was poor the figure is presented in ball and stick style for clarity. The planarity of the Meldrum's acid ring (bottom) is shown in stick and ellipsoid (plotted at 50% probability).

A closely related prochiral spirocyclic Meldrum's acid was formed under similar conditions.[231] In the literature study, the symmetric triketone species formed from an asymmetric domino Knoevenagel/Diels–Alder reaction contained a cyclohexanone ring, although a dimethoxy substituted cyclohexane ring was also observed.

Similar to the disubstituted symmetric Meldrum's acid ligand, the spirocyclic compound was found to decompose under mild methyl ester removal conditions. However, in this case the molecule undergoes an apparent polymerization process as supported by physical changes in the collected product transitioning from a white powder to an elastic sticky solid under vacuum at room temperature and the subsequently broadened spectra in $CDCl_3$ and DMSO-d6.

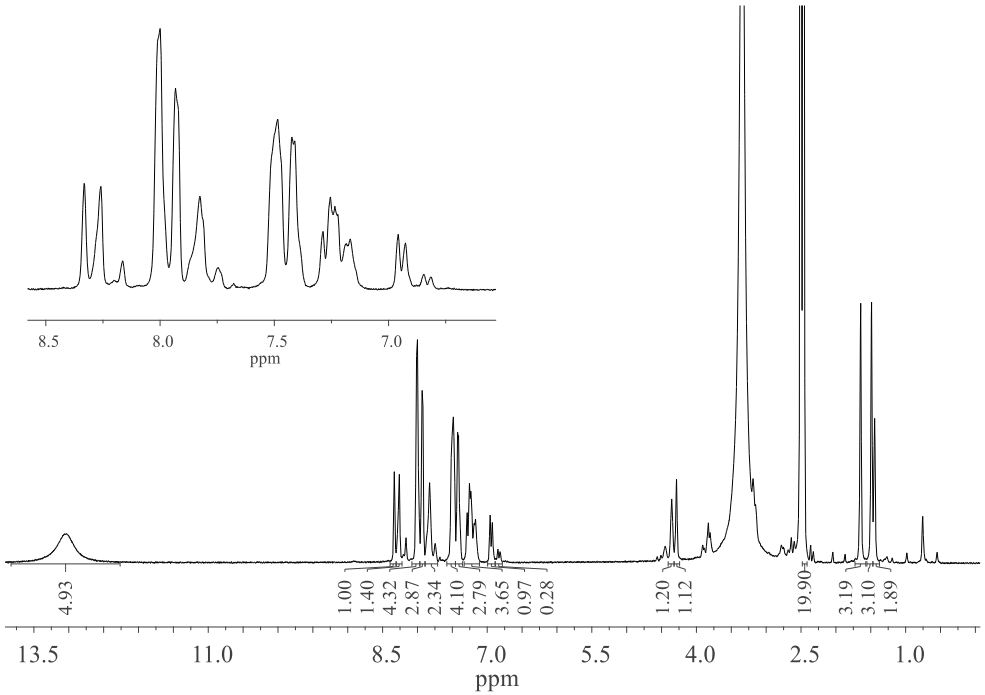

Figure 4.27: ^{1}H NMR spectrum of digested spirocyclic Meldrum's acid ligand showing peak broadening attributed to polymer formation

4.2.5. Synthesis of an extended symmetric bpdc-based Meldrum's acid ligand

Using the above insight into the improved stability of a disubstituted species and the apparent detrimental impact of a biphenyldicarboxylic acid substituent on Meldrum's acid relative to other, more robust, literature derivatives, an attempt to isolate the Meldrum's acid moiety from the aromatic backbone was undertaken. In brief, a di-alkylether separated dibromo ligand was synthesized and addition of Meldrum's acid attempted (see Appendix). Due to the separation of the aromatic ring, the alkyl bromide was significantly deactivated and did not undergo reaction with Meldrum's acid even upon heating or addition of stronger base.

Given the ready reaction of the aldehyde species in a Knoevenagel condensation this would be an improved substrate for synthesis of a less unstable Meldrum's acid ligand through separation from the aromatic backbone and reduction of ring strain. Also reaction of mono-substituted Meldrum's acid ligands with a range of electron-donating and electron-withdrawing substituents may give rise to tuneable sensitivity of the group as observed with the 2-pyridinyl thermolabile protecting groups commented on in the Introduction. Placement of the Meldrum's ligand on a bipyridine backbone may also prove successful in forming a more robust Meldrum's acid ligand for MOF solvothermal MOF synthesis.

4.3. Conclusion

Synthetic routes were established to four new potential MOF ligands containing precursors to a ketene or methylene ketene using novel Meldrum's acid thermolabile protecting groups. TGA analysis of the free ligands show weight losses corresponding well to the calculated loss of acetone and CO_2(g) upon thermal decomposition of the Meldrum's acid group and ketene formation. GC analysis of the headspace of dried heated samples indicates presence of acetone. Solvent stability studies of selected ligands, bdc-Meldrums and bpdc-Meldrums showed decomposition at room temperature to a malonic acid species within a day in all solvents excepting acetone, which inhibits the formation of the decomposition product by establishing an equilibrium with the starting material. The decomposition is accelerated upon even mild (20 ^{o}C) heating in amide solvents and will tend to completion in presence of trace water or malonic acid species even when stored under vacuum.

Despite the synthetic challenges, the Meldrum's acid ligands were successfully made and subsequently found to undergo thermolysis to form the desired ketene and methylene ketene species. The challenge remained to incorporate them into a MOF before they hydrolysis to unwanted species. Therefore, alternative MOF synthesis routes with the existent ligands were pursued.

4.4. Experimental section

4.4.1. General procedures

All starting compounds and solvents were used as received from commercial sources without further purification unless otherwise noted. NMR spectra were recorded at room temperature (unless otherwise specified) on a Bruker-400 or -500 Avance instrument, with the use of the

solvent proton as an internal standard. Thermogravimetric analysis (TGA) was performed on a TA Instruments Q50 instrument. Single crystals were mounted on a MiTaGen mylar loop, put into Fomblin oil and placed under cold stream at stated temperature in crystallography table. Diffraction data was collected on a Rigaku Spider diffractometer equipped with a MicroMax MM007 rotating-anode generator (Cu K_α radiation, 1.54180 Å), high-flux Osmic multilayer mirror optics; diffraction data were recorded on a curved image-plate detector. Data were collected at the temperatures listed in crystallography tables and were integrated, scaled, and averaged with FS_Process.[195] XPREP was used to determine the space group and the structures were solved using SHELXS or SHELXT and refined with SHELXL.[196] Platon was employed to determine the solvent accessible volume.[197] All non-hydrogen atoms were found in the electron density difference map. All hydrogen atoms were calculated using the appropriate restraints. All non-hydrogen atoms were refined anisotropically.

4.4.2. Ligand synthesis and characterization

a) Di-*tert*-butyl 2-((2,2-dimethyl-4,6-dioxo-1,3-dioxan-5-yl)methyl)terephthalate

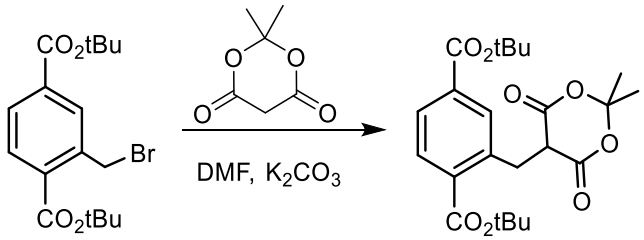

Di-*tert*-butyl 2-(bromomethyl)terephthalate (1.04 g, 2.70 mmol) was dissolved in dry DMF (5.7 mL) and cooled on ice for 10 min before the addition of 2,2-dimethyl-1,3-dioxane-4,6-dione (426 mg, 2.95 mmol), and potassium carbonate (403 mg, 2.92 mmol). The pale yellow suspension was then stirred for 7 hours on ice. The reaction was quenched by pouring over ice/H_2O before gradually acidifying to pH 1.5 with 1 M HCl. The white solid was then collected via suction filtration, washing copiously with cold H_2O before drying under suction and further drying overnight under high vacuum. The solid was recrystallized from minimum hot CH_2Cl_2 and hexane, washing the crystalline solid thoroughly with cold hexane. White crystalline solid (692 mg, 1.59 mmol, 59%). ^{1}H NMR (500 MHz, $CDCl_3$) δ 8.16 (d, *J* = 1.1 Hz, 1H), 7.88 (dd, *J* = 8.1, 1.5 Hz, 1H), 7.79 (d, *J* = 8.1 Hz, 1H), 4.39 (t, *J* = 6.2 Hz, 1H), 3.63 (d, *J* = 6.2 Hz, 2H), 1.78 (d, *J* = 14.4 Hz, 6H), 1.59 (d, *J* = 8.0 Hz, 18H).

b) 2-((2,2-Dimethyl-4,6-dioxo-1,3-dioxan-5-yl)methyl)terephthalic acid

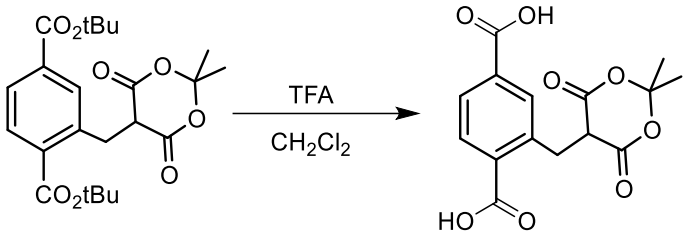

Di-*tert*-butyl 2-((2,2-dimethyl-4,6-dioxo-1,3-dioxan-5-yl)methyl)terephthalate (299 mg, 0.689 mmol) was dissolved in dry CH_2Cl_2 (60 mL) and cooled on ice before the addition of TFA (5.31 mL, 68.9 mmol). The reaction was then left to slowly warm to room temperature with stirring over 16 hours. The solvent was removed *in vacuo*, and the resulting white residue further dried under high vacuum, yielding a white solid (215 mg, 0.667 mmol, 97%). ^{1}H NMR (500 MHz, DMSO-d_6) δ 13.21 (s, 2H), 7.98 (s, 1H), 7.90 (d, J = 8.0 Hz, 1H), 7.85 (d, J = 8.0 Hz, 1H), 4.78 (t, J = 5.7 Hz, 1H), 3.64 (d, J = 5.6 Hz, 2H), 1.80 (s, 3H), 1.68 (s, 3H).

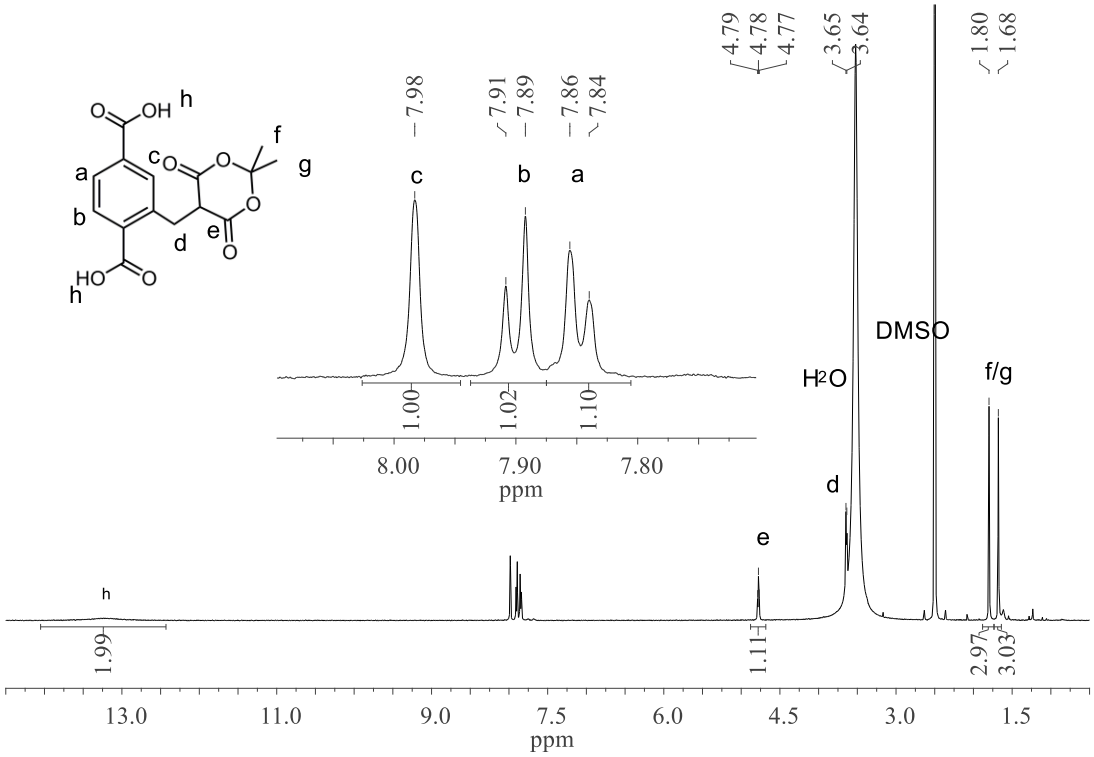

Figure 4.28: Ligand bdc-Meldrums in DMSO-d_6.

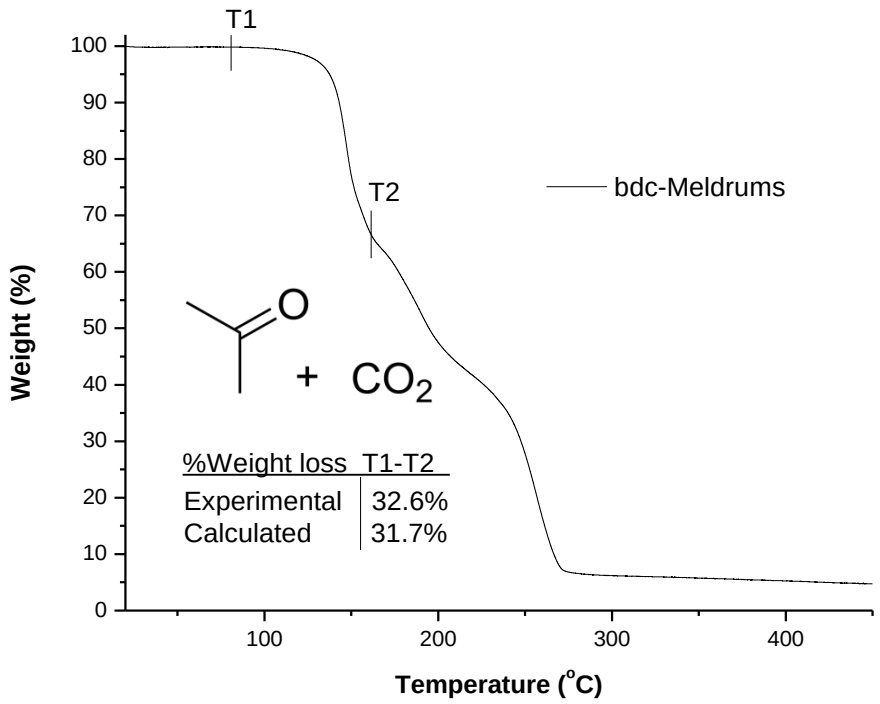

Figure 4.29: Thermogravimetric analysis (TGA) trace for bdc-Meldrums.

Dimethyl 2-formylbiphenyl-4,4'-dicarboxylate starting material made as during synthesis of bpdc-TBE (Chapter 2) used in reaction below.

c) Dimethyl 2-((2,2-dimethyl-4,6-dioxo-1,3-dioxan-5-ylidene)methyl)biphenyl-4,4'-dicarboxylate

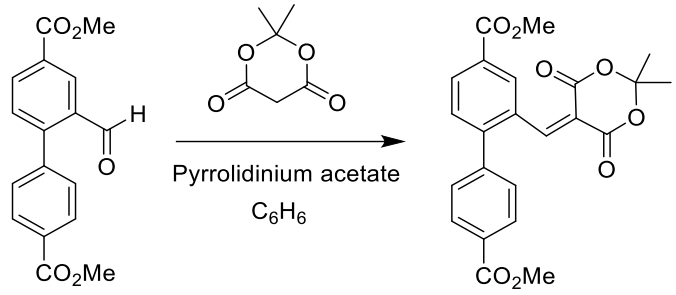

Dimethyl 2-formylbiphenyl-4,4'-dicarboxylate (1.87 g, 6.26 mmol) and 2,2-dimethyl-1,3-dioxane-4,6-dione (994 mg, 6.88 mmol) were dissolved in dry benzene (29 mL) and placed under Ar(g). Pyrrolidine (51.4 μL, 0.625 mmol) in dry benzene (1 mL) was combined with acetic acid (35.8 μL, 0.625 mmol) and stirred at room temperature for 1 min before adding to the above solution. The yellow white suspension was then stirred at room temperature overnight, forming a clear dark orange solution. The solvent was then removed *in vacuo* to yield a red oily solid which was further dried under high vacuum overnight. The crude solid was then recrystallized from boiling MeOH, giving a yellowish white powder (1.50 g, 3.53 mmol, 56%). ^{1}H NMR (500 MHz, $CDCl_3$) δ 8.33 (s, 1H), 8.32 (d, *J* = 1.5 Hz, 1H), 8.21 (dd, *J*

= 8.1, 1.5 Hz, 1H), 8.12 (d, *J* = 8.4, Hz, 2H), 7.57 (d, *J* = 8.1 Hz, 1H), 7.40 (d, *J* = 8.4 Hz, 2H), 3.96 (s, 3H), 3.95 (s, 3H), 1.75 (s, 6H) ppm.

d) 2-((2,2-Dimethyl-4,6-dioxo-1,3-dioxan-5-ylidene)methyl)biphenyl-4,4'-dicarboxylic acid

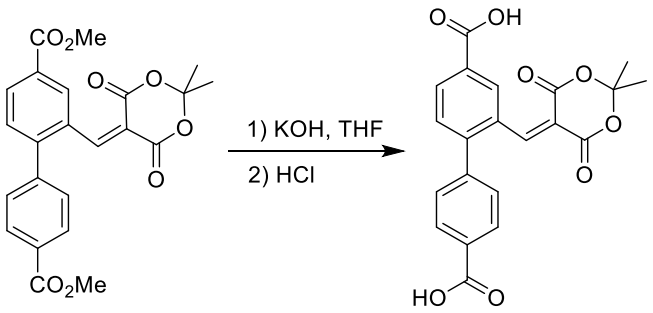

Dimethyl 2-((2,2-dimethyl-4,6-dioxo-1,3-dioxan-5-ylidene)methyl)biphenyl-4,4'-dicarboxylate (151 mg, 0.355 mmol) was dissolved in dry THF (6.75 mL), split into 3 vials and cooled on ice before the addition of 1 M KOH (1.0 mL each). The opaque suspensions were stirred on ice, allowing to gradually warm to room temperature and stirred overnight. THF was then removed *in vacuo* before cooling the clear yellow aqueous layer on ice and gradually acidifying with 1 M HCl to pH 2.0. The fine white solid was then collected via suction filtration, washing thoroughly with H_2O before drying overnight under high vacuum to yield a fine white powder. Recrystallization from hot MeOH:H_2O (5:1 v:v) gave pure product (132 mg, 0.333 mmol, 94%). ^{1}H NMR (500 MHz, DMSO-d_6) δ 13.22 (s, 2H), 8.22 (s, 1H), 8.18 (s, 1H), 8.12 (dd, *J* = 8.0, 1.5 Hz, 1H), 8.03 (d, *J* = 8.4 Hz, 2H), 7.69 (d, *J* = 8.1 Hz, 1H), 7.53 (d, *J* = 8.4 Hz, 2H), 1.69 (s, 6H) ppm.

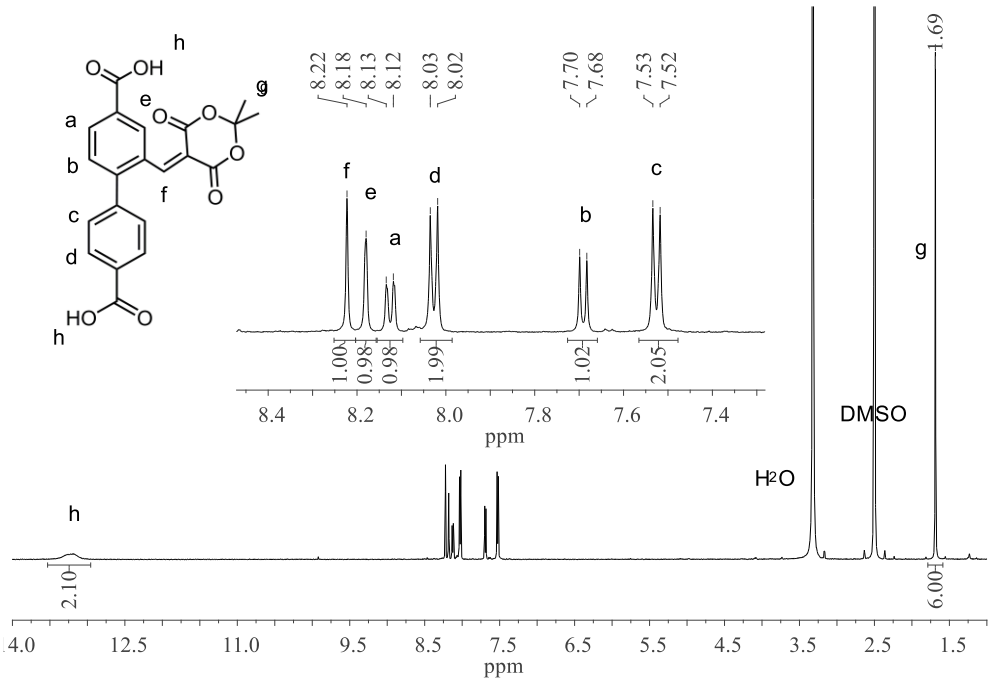

Figure 4.30: Ligand bpdc-CHMeldrums in DMSO-d_6.

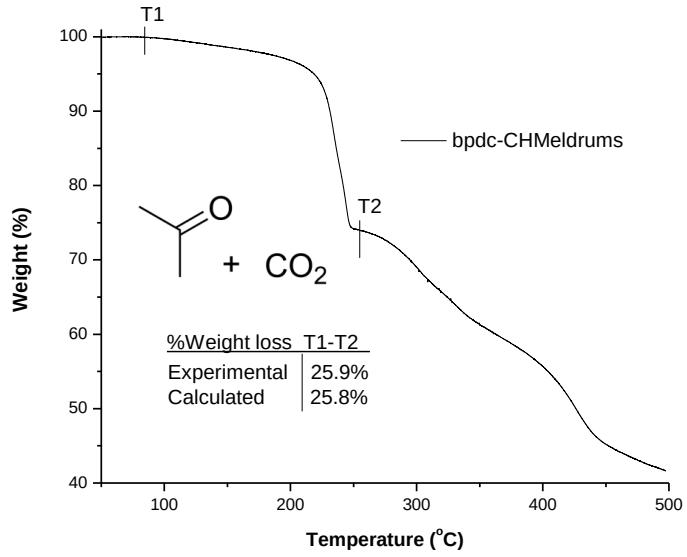

Figure 4.31: Thermogravimetric analysis (TGA) trace for bpdc-CHMeldrums.

e) Dimethyl 2-((2,2-dimethyl-4,6-dioxo-1,3-dioxan-5-yl)methyl)biphenyl-4,4'-dicarboxylate

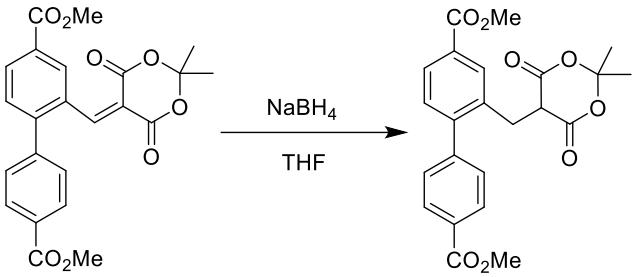

Dimethyl 2-((2,2-dimethyl-4,6-dioxo-1,3-dioxan-5-ylidene)methyl)biphenyl-4,4'-dicarboxylate (610 mg, 1.44 mmol) was dissolved in dry CH_2Cl_2 (9.26 mL), cooled on ice and acidified to pH 2.5 by acetic acid. $NaBH_4$ (136 mg, 3.54 mmol) in dry CH_2Cl_2 (8.63 mL) was then added in aliquots over 1 hr before leaving the reaction mixture to stir overnight on ice. Brine was then added and the organic layer washed twice with brine and thrice with H_2O before drying over Na_2SO_4. Solvent was removed *in vacuo* yielding a white, oily solid; this was further crystallised from MeOH (539 mg, 1.26 mmol, 88%). ^{1}H NMR (500 MHz, $CDCl_3$) δ 8.12 (d, *J* = 8.3 Hz, 2H), 8.07 (d, *J* = 1.3 Hz, 1H), 7.98 (dd, *J* = 7.9, 1.6 Hz, 1H), 7.45 (d, *J* = 8.3 Hz, 2H), 7.31 (d, *J* = 7.9 Hz, 1H), 3.95 (s, 3H), 3.94 (s, 3H), 3.58 (t, *J* = 6.1 Hz, 1H), 3.48 (d, *J* = 6.1 Hz, 2H), 1.67 (s, 3H), 1.62 (s, 3H).

f) 2-((2,2-Dimethyl-4,6-dioxo-1,3-dioxan-5-yl)methyl)biphenyl-4,4'-dicarboxylic acid

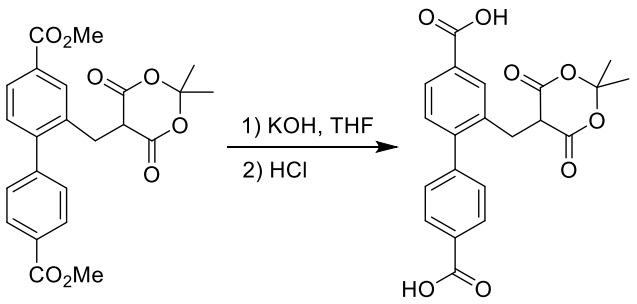

Dimethyl 2-((2,2-dimethyl-4,6-dioxo-1,3-dioxan-5-yl)methyl)biphenyl-4,4'-dicarboxylate (186 mg, 0.437 mmol) was dissolved in dry THF (8.38 mL), placed under $Ar_{(g)}$ and cooled on ice before the addition of 1 M KOH (3.86 mL). The slightly opaque yellow solution was stirred on ice overnight. THF was then removed *in vacuo* before cooling the aqueous layer on ice and gradually acidifying with 1 M HCl to pH 2.0. Product was then extracted into ethyl acetate (3 x 5 mL). Organic layers were then combined and dried over Na_2SO_4 before removing the solvent *in vacuo* and drying the fine white solid under high vacuum overnight (171 mg, 0.429 mmol, 98%). ^{1}H NMR (500 MHz, DMSO-d_6) δ 13.00 (s, 2H), 8.01 (d, *J* = 8.3 Hz, 3H), 7.85 (d, *J* = 7.8 Hz, 1H), 7.51 (d, *J* = 8.2 Hz, 2H), 7.32 (d, *J* = 7.9 Hz, 1H), 4.64 (t, *J* = 5.6 Hz, 1H), 3.28 (d, *J* = 5.5 Hz, 2H), 1.77 (s, 3H), 1.63 (s, 3H).

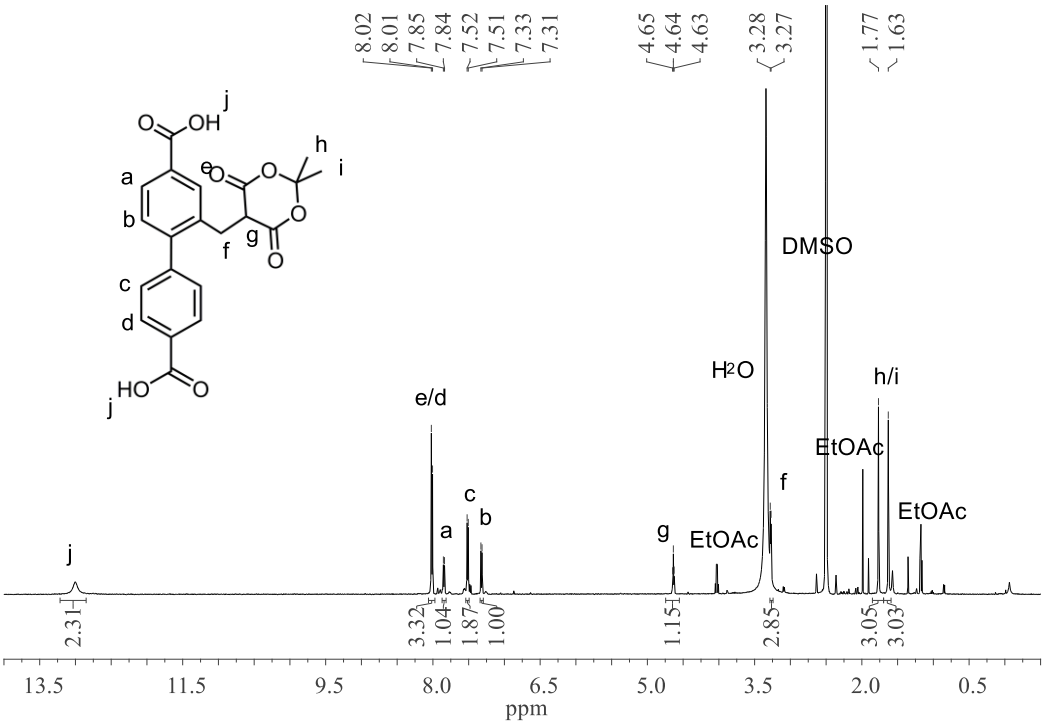

Figure 4.32: Ligand bpdc-Meldrums in DMSO-d_6.

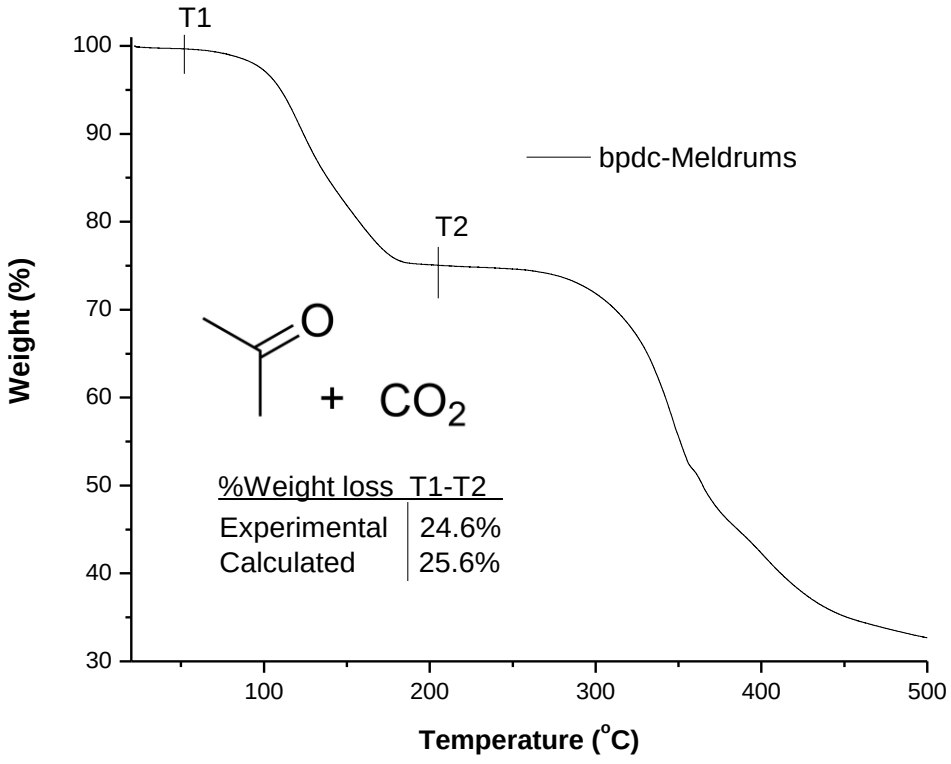

Figure 4.33: Thermogravimetric analysis (TGA) trace for bpdc-Meldrums.

Synthesis of symmetrically disubstituted Meldrum's acid ligand (bpdc-SymMeldrums)

a) *Tert*-butyl 4-bromo-3-methylbenzoate

4-Bromo-3-methylbenzoic acid (5.06 g, 23.5 mmol) was dissolved in thionyl chloride (50 mL) and a few drops of dry DMF and placed under Ar(g) with stirring before heating to 80 ^{o}C for 3 hrs. Thionyl chloride was removed *in vacuo* using solvent trap. Red solid was then further dried under high vacuum for 1 hr before dissolving in dry THF (30 mL) and placing under Ar(g) with stirring on ice. ^{t}BuOK (10.5 g, 93.3 mmol) in dry THF (93 mL) was then added dropwise to the clear orange solution before stirring overnight on ice, forming a thick tan slurry. The reaction was quenched pouring over ice/H_2O before extracting with ethyl acetate. The organic layer was dried over Na_2SO_4 and filtered before removing the solvent under low pressure and further drying the orange/tan solid under high vacuum overnight. (3.78 g, 13.9 mmol, 59%). ^{1}H NMR (500 MHz, $CDCl_3$) δ 7.83 (d, *J* = 1.3 Hz, 1H), 7.63 (dd, *J* = 8.3, 1.7 Hz, 1H), 7.56 (d, *J* = 8.3 Hz, 1H), 2.43 (s, 3H), 1.58 (s, 9H).

b) Di-*tert*-butoxycarbonyl 2,2'-dimethylbiphenyl-4,4'-dicarboxylate.

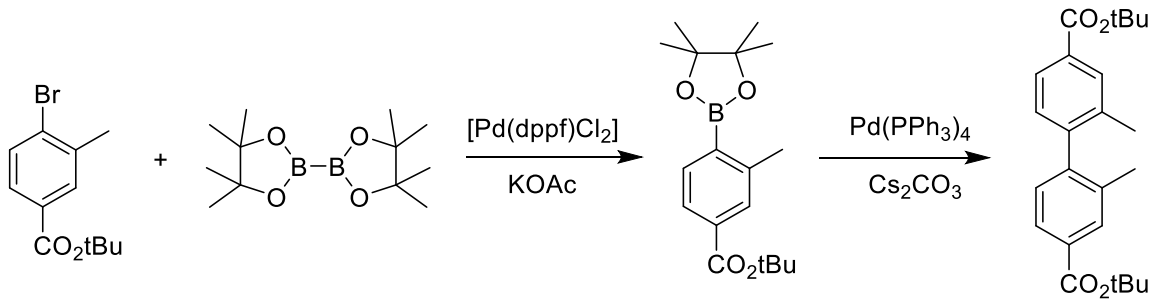

Tert-butyl 4-bromo-3-methylbenzoate (1.84 g, 6.79 mmol) was combined with boron bispinacolato (2.13 g, 8.39 mmol), potassium acetate (2.67 g, 27.2 mmol) and [Pd(dppf)Cl_2] (154 mg, 0.210 mmol) and suspended in DMSO (16.0 mL), placed under Ar(g) and heated at 80 ^{o}C for 90 min during which time the red/brown suspension turned clear. Additional boron bispinacolato (513 mg, 2.02 mmol) and [Pd(dppf)Cl_2] (151 mg, 0.206 mmol) were added and the reaction mixture returned to heat for 5 hours. After disappearance of the starting material as monitored by TLC (1:10 EtOAc:Hex, SiO_2) a second lot of *tert*-butyl 4-bromo-3-methylbenzoate acid (1.05 g, 3.87 mmol) with Pd(PPh_3)$_4$ (259 mg, 0.224 mmol) and Cs_2CO_3 (3.78 g, 11.6 mmol) were added, the reaction mixture returned under Ar(g) and heated with stirring at 81 ^{o}C for 8 hours. A final lot of *tert*-butyl 4-bromo-3-methylbenzoate acid (850

mg, 3.13 mmol), $Pd(PPh_3)_4$ (101 mg, 0.0874 mmol) and Cs_2CO_3 (3.08 g, 9.45 mmol) were added and the reaction returned to reflux for a further 7 hours. The black reaction mixture was allowed to cool to room temperature. DMSO was removed under vacuum distillation, H_2O added, the solution acidified to pH 2.0 and the product extracted with ethyl acetate. Organic layers were combined, dried over $MgSO_4$ and purified by silica flash column chromatography (hexane). Red oil obtained (930 mg, 2.43 mmol, 36%). ^{1}H NMR (500 MHz, $CDCl_3$) δ 7.91 (s, 2H), 7.86 (d, *J* = 7.9 Hz, 2H), 7.12 (d, *J* = 7.9 Hz, 2H), 2.07 (s, 6H), 1.61 (s, 18H).

c) Di-*tert*-butoxycarbonyl 2,2'-dibromomethylbiphenyl-4,4'-dicarboxylate

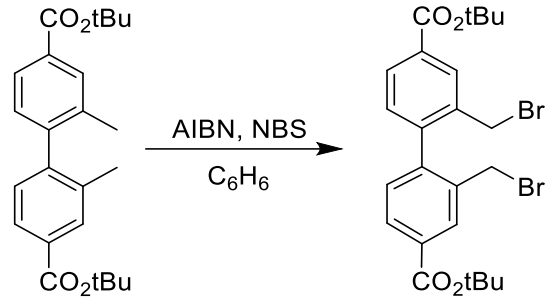

Di-*tert*-butoxycarbonyl 2,2'-dimethylbiphenyl-4,4'-dicarboxylate (930 mg, 2.43 mmol) was dissolved in dry benzene (35 mL) before the addition of *N*-bromosuccimide (908 mg, 5.10 mmol) and AIBN (39.2 mg, 0.239 mmol). The reaction mix was then heated at 80 °C under Ar(g) for 3 hours. The solvent was removed *in vacuo* and the residue purified by silica flash column chromatography (ethyl acetate/hexane) affording a light brown coloured oil, which further crystallized to give pure product as a white crystalline solid (578 mg, 1.07 mmol, 44%). ^{1}H NMR (500 MHz, $CDCl_3$) δ 8.16 (d, *J* = 1.6 Hz, 2H), 8.00 (dd, *J* = 7.9, 1.7 Hz, 2H), 7.32 (d, *J* = 7.9 Hz, 2H), 4.34 (d, *J* = 10.2 Hz, 2H), 4.17 (d, *J* = 10.2 Hz, 2H), 1.63 (s, 18H).

d) Di-*tert*-butyl 2',2'-dimethyl-4',6'-dioxo-5,7-dihydrospiro[dibenzo[a,c][7]annulene-6,5'-[1,3]dioxane]-3,9-dicarboxylate

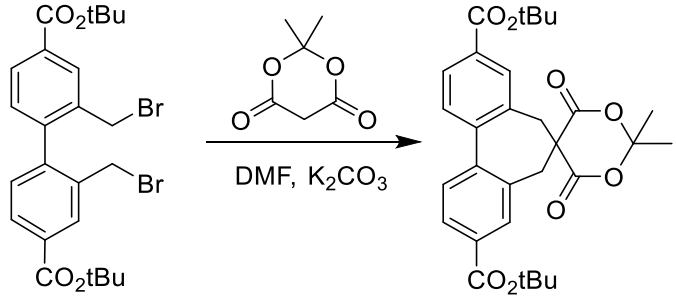

Di-*tert*-butoxycarbonyl 2,2'-dibromomethylbiphenyl-4,4'-dicarboxylate (200 mg, 0.370 mmol) was dissolved in dry DMF (5 mL) and cooled on ice for 10 min before the addition of

2,2-dimethyl-1,3-dioxane-4,6-dione (66.5 mg, 0.461 mmol) and potassium carbonate (103 mg, 0.743 mmol). The pale yellow suspension was then stirred overnight on ice. The reaction was quenched by pouring over ice/H_2O before gradually acidifying to pH 1.5 with 1 M HCl. The white solid was then collected via suction filtration, washing copiously with cold H_2O before drying under suction and further drying overnight under high vacuum. The crude product was recrystallized from hot CH_2Cl_2/hexane (1:1), filtered, washed with cold hexane (148 mg, 0.283 mmol, 77%). ^{1}H NMR (500 MHz, $CDCl_3$) δ 8.06 (d, *J* = 7.9 Hz, 2H), 7.84 (s, 2H), 7.47 (d, *J* = 8.0 Hz, 2H), 3.32 (s, 2H), 2.97 (s, 2H), 1.84 (s, 6H), 1.61 (s, 18H).

e) 2',2'-Dimethyl-4',6'-dioxo-5,7-dihydrospiro[dibenzo[a,c][7]annulene-6,5'-[1,3]dioxane]-3,9-dicarboxylic acid

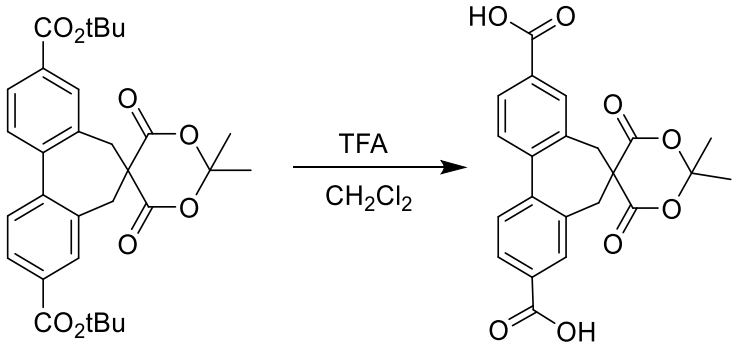

Di-*tert*-butyl 2',2'-dimethyl-4',6'-dioxo-5,7-dihydrospiro[dibenzo[a,c][7]annulene-6,5'-[1,3]dioxane]-3,9-dicarboxylate (50.2 mg, 0.0957 mmol) was dissolved in dry CH_2Cl_2 (8.33 mL) and cooled on ice before the addition of TFA (737 μL, 9.57 mmol). The reaction was then stirred on ice for 24 hours. The solvent was removed *in vacuo*, and the resulting white residue further dried under high vacuum, yielding a white solid (46.5 mg, 0.113 mmol, quant. yield). ^{1}H NMR (500 MHz, DMSO-d_6) δ 13.06 (s, 2H), 8.01 (d, *J* = 7.8 Hz, 2H), 7.87 (s, 2H), 7.60 (d, *J* = 7.8 Hz, 2H), 3.21 (s, 2H), 3.01 (s, 2H), 1.82 (s, 6H).

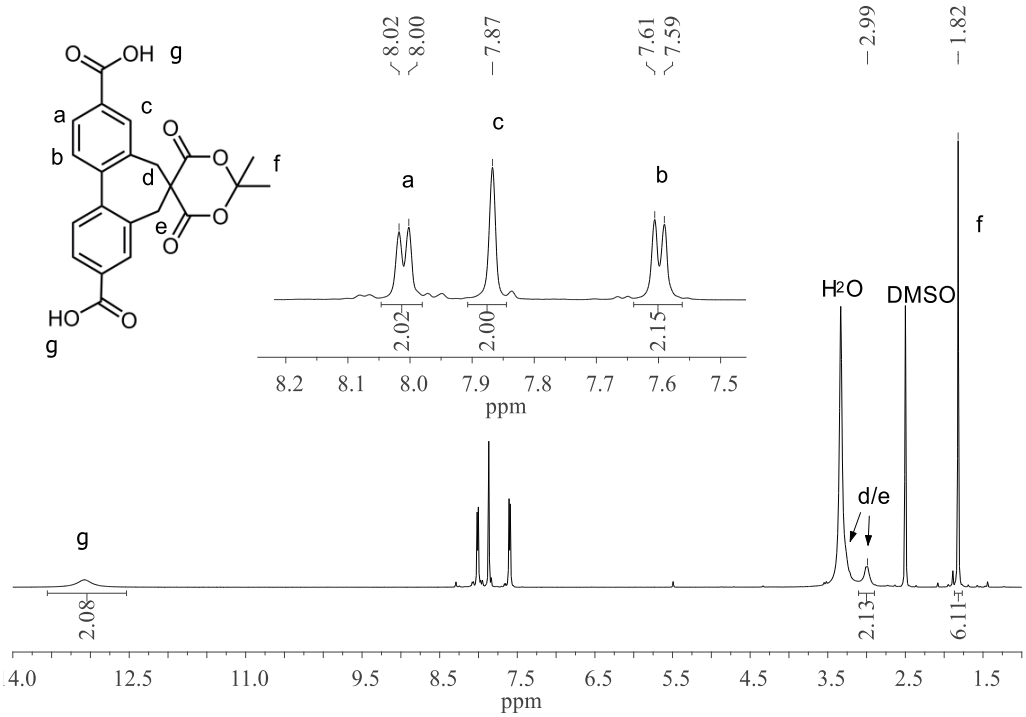

Figure 4.34: Ligand bpdc-symMeldrums in DMSO-d_6.

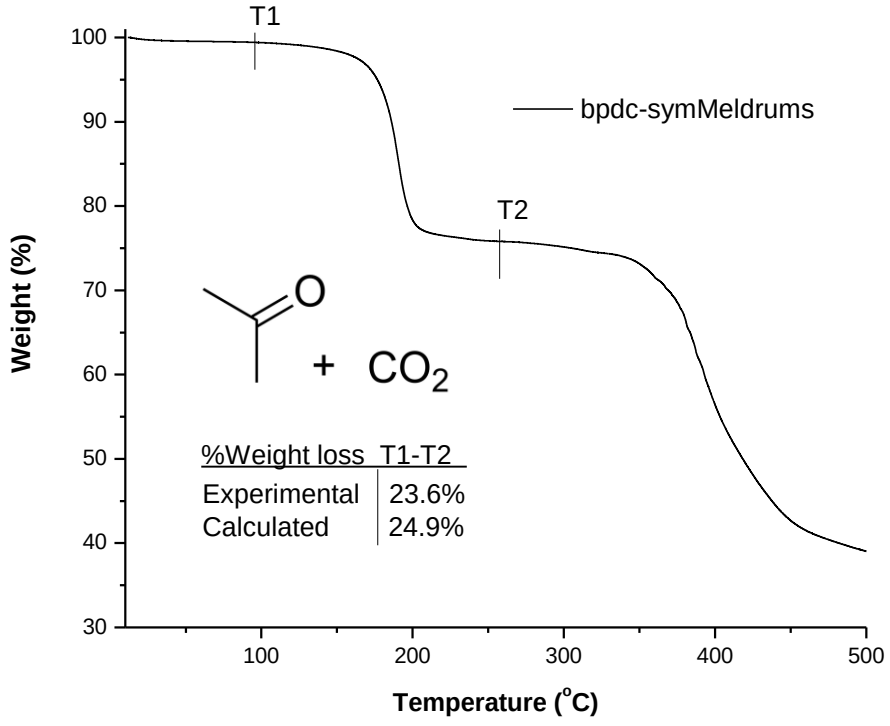

Figure 4.35: Thermogravimetric analysis (TGA) trace for bpdc-symMeldrums.

Table 4.2: Crystallography data of esterified Meldrum's acid ligands

Compound	**Bdc^{tBu}-Meldrums**	**Bpdc^{OMe}-Meldrums**	**Bpdc^{OMe}-CHMeldrums**
Formula	$C_{23}H_{30}O_8$	$C_{23}H_{22}O_8$	$C_{23}H_{20}O_8$
Formula weight	434.47	426.40	424.39
Crystal size (mm)	0.61 x 0.25 x 0.15	0.4 × 0.3 × 0.1	0.41 × 0.17 × 0.19
Temperature (K)	138.15	153	123.15
Wavelength (Å)	1.54178	1.54178	1.54178
Crystal system	Monoclinic	Triclinic	Monoclinic
Space group	$P2_1/c$	P-1	$C2/c$
Unit cell lengths (Å)	a = 15.93(2) b = 14.415(18) c = 10.579(17)	a = 8.5576(4) b = 10.7601(5) c = 12.7266(9)	a = 36.252(3) b = 6.6598(2) c = 20.4447(14)
Unit cell angles (°)	α = 90 β = 99.53(3) γ = 90	α = 69.655(5) β = 71.640(5) γ = 69.549(5)	α = 90 β = 124.290(9) γ = 90
Unit cell volume (Å^3)	2395(6)	1004.23(11)	4078.1(6)
Z	4	2	8
D_{calc} (g cm^{-3})	1.205	1.410	1.382
μ (mm^{-1})	0.755	0.899	0.885
F(000)	928.0	448.0	1776.0
Reflns coll./unique, R_{int}	21107 / 4374, 0.0408	11738 / 3700, 0.0420	23229 / 3927, 0.0304
Data range	8.0 Å > d > 0.81 Å	8.0 Å > d > 0.81 Å	8.0 Å > d > 0.81 Å
Index ranges	-19≤h≤19, -17≤k≤17, -11≤l≤12	-10≤h≤7, -13≤k≤12, -15≤l≤14	-43≤h≤43, -8≤k≤ 8, -19≤l≤24
Completeness	93.2 %	93.8 %	97.8 %
T_{min}, T_{max}	0.840, 1.000	0.786, 1.00	0.816, 1.000
R indices for data with $I>2\sigma(I)$	R_1 = 0.0680, wR_2 = 0.1877	R_1 = 0.0583, wR_2 = 0.1757	R_1 = 0.0413, wR_2 = 0.1073
R indices for all data	R_1 = 0.1093, wR_2 = 0.2464	R_1 = 0.0671, wR_2 = 0.2082	R_1 = 0.0470, wR_2 = 0.1251
Largest difference peak and hole (e Å^{-3})	0.27/ -0.25	0.44/ -0.46	0.35/ -0.25

Table 4.3: Crystallography data of esterified Meldrum's acid ligands

Compound	**Bpdc^{OMe}-symMeldrums**	**Bpdc^{OMe}-symMalonic**
Formula	$C_{101}H_{100}O_{33}$	$C_{44}D_2Cl_6H_{36}O_{16}$
Formula weight	1881.74	1037.46
Crystal size (mm)	0.61 x 0.25 x 0.15	0.32 × 0.19 × 0.20
Temperature (K)	293	123
Wavelength (Å)	1.54187	1.54187
Crystal system	Triclinic	Triclinic
Space group	*P*-1	*P*-1
Unit cell lengths (Å)	a = 10.2088(5) b = 13.3456(6) c = 18.1489(13)	a = 10.4977(3) b = 10.5460(4) c = 11.3036(8)
Unit cell angles (º)	α = 85.220(6) β = 75.080(5) γ = 70.343(5)	α = 78.435(5) β = 68.540(5) γ = 81.205(6)
Unit cell volume (Å^3)	2250.0(2)	1136.66(11)
Z	2	1
D_{calc} (g cm^{-3})	1.389	1.516
μ (mm^{-1})	0.877	4.072
F(000)	984.0	533.0
Reflns coll./unique, R_{int}	31862 / 8450, 0.0649	14034 / 4244, 0.1838
Data range	8.0 Å > *d* > 0.81 Å	8.0 Å > *d* > 1.04 Å
Index ranges	-11≤*h*≤12, -16≤*k*≤16, -21≤*l*≤21	-12≤*h*≤11, -13≤*k*≤12, -13≤*l*≤11
Completeness	95.3 %	95.3 %
T_{min}, T_{max}	0.737, 1.000	0.328, 1.000
R indices for data with *I*>2σ(*I*)	R_1 = 0.0870, wR_2 = 0.2693	R_1 = 0.1297, wR_2 = 0.3459
R indices for all data	R_1 = 0.1202, wR_2 = 0.3170	R_1 = 0.1406, wR_2 = 0.3812
Largest difference peak and hole (e Å^{-3})	0.66/ -0.61	0.67/ -0.91

Table 4.4: Crystallography data of esterified Meldrum's acid ligands

Compound	**(Bdc^{tBu})2-bisMeldrums**	**(Bpdc^{tBu})2-bisMeldrums**	**(Bpdc^{OMe})2-spiroMeldrums**
Formula	$C_{80}H_{104}O_{24}$	$C_{26}H_{30}O_6$	$C_{22}H_{21}O_7$
Formula weight	1449.63	438.71	397.39
Crystal size (mm)	0.61 x 0.25 x 0.15	0.22 × 0.34 × 0.51	0.46 × 0.18 × 0.23
Temperature (K)	140	133	123
Wavelength (Å)	1.54187	1.54187	1.54187
Crystal system	Triclinic	Monoclinic	Triclinic
Space group	*P*-1	$P2_1/c$	*P*-1
Unit cell lengths (Å)	a = 11.9777(19) b = 12.674(2) c = 13.4268(18)	a = 18.0749(18) b = 22.925(3) c = 11.6590(13)	a = 9.063(4) b = 13.896(5) c = 16.899(7)
Unit cell angles (°)	α = 90.889(10) β = 98.756(9) γ = 93.482(9)	α = 90 β = 90.092(6) γ = 90	α = 97.468(12) β = 103.572(12) γ = 101.656(12)
Unit cell volume (Å^3)	2010.1(5)	4831.0(9)	1990.6(14)
Z	2	8	4
D_{calc} (g cm^{-3})	1.198	1.206	1.326
μ (mm^{-1})	0.724	0.693	0.828
F(000)	776.0	1873.0	836.0
Reflns coll./unique, R_{int}	21537 / 6103, 0.0659	11579/ 3964, 0.0536	19741 / 3907, 0.1404
Data range	8.0 Å > *d* > 0.81 Å	8.0 Å > *d* > 1.05 Å	8.0 Å > *d* > 1.02 Å
Index ranges	-14≤*h*≤13, -13≤*k*≤15, -13≤*l*≤16	-13≤*h*≤17, -21≤*k*≤18, -11≤*l*≤8	-8≤*h*≤8, -13≤*k*≤13, -16≤*l*≤16
Completeness	77.1 %	91.1 %	99.8 %
T_{min}, T_{max}	0.651, 1.000	0.559, 1.00	0.314, 1.00
R indices for data with *I*>2σ(*I*)	R_1 = 0.0748, *wR*2 = 0.2303	R_1 = 0.0628; wR_2 = 0.1649	R_1 = 0.1135; wR_2 = 0.2968
R indices for all data	R_1 = 0.1166, *wR*2 = 0.2733	R_1 = 0.0793; wR_2 = 0.1840	R_1 = 0.1564; wR_2 = 0.3444
Largest difference peak and hole (e Å^{-3})	0.25/ -0.34	0.34 / −0.32	0.28 / −0.30

Chapter 5 – Synthesis of Meldrum's acid MOFs

5.1. Introduction

The Meldrum's acid ligands developed have good thermal stability in the solid state, as shown by thermogravimetric analysis (TGA). This lent confidence that they can be incorporated into MOFs if appropriate reaction conditions can be found.

Within the limitations of the solvent stability of the Meldrum's acid ligands developed, there are still methods for synthesizing a Meldrum's acid functionalized MOF through room temperature and PSM approaches to MOF synthesis. Keeping in mind the goal of nucleophilic reaction of the thermolyzed substrate and the lessons learnt from the work of Chapters 2 and 3 in substrate selection, the targeted framework for incorporation of the Meldrum's acid would ideally be an exceedingly robust MOF such as UiO-66/67, which would allow both for the examination of the stability of the ketene species in a confined environment as well as potential access to a range of materials with variable pore chemistries.

5.2. Results and discussion

In examining potential MOF synthesis methods the following limiting facts were considered:

1) Acetone inhibits degradation of the ligands for up to one week at room temperature
2) Water hydrolyzes the Meldrum's acid ring of the ligands
3) Base degrades the ligand (to malonic acid in bdc/bpdc-Meldrums and to an aldehyde in case of bpdc-CHMeldrums – see experimental section)
4) Temperature accelerates ligand degradation

This led to the following guiding principles in designing room temperature Meldrum's acid MOF formation:

1) Acetone as primary solvent to favour Meldrum's acid in equilibrium
2) Dry solvents and limited contact with any amide solvents to reduce hydrolysis
3) Use of the minimum volume of base for a short reaction time and ideally have base-ligand interaction concurrent with MOF formation
4) Room/low temperature only

5.2.1. Direct incorporation using room temperature synthesis

As proof of principle for direct incorporation a MOF synthesis based primarily upon dry acetone was developed utilizing the classic idea of slow vapour diffusion applied in the original synthesis of the historic MOF-5 (Figure 5.1).

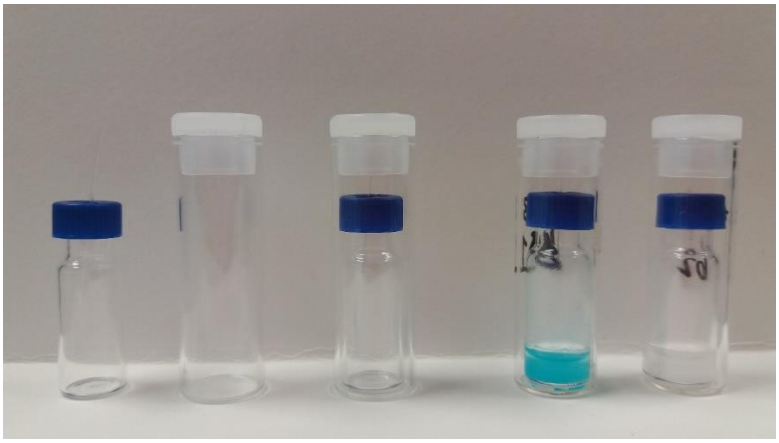

Figure 5.1: Room temperature vapour diffusion MOF synthesis experimental set up.

Using slow vapour diffusion of triethylamine (Et_3N) in n-heptane or diethyl ether into the less volatile ligand and metal solution of acetone and propan-2-ol (full details in experimental section), single crystal quality IRMOF-10-symMeldrums crystals were obtained and confirmed phase-pure by PXRD and NMR analysis (Figure 5.2-5.4 and Table 5.1).

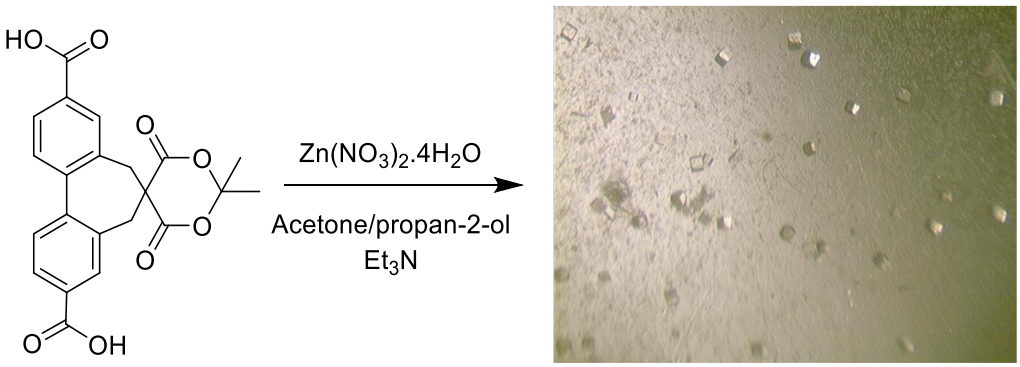

Figure 5.2: IRMOF-10-symMeldrums using room temperature vapour diffusion conditions.

5.2.2. IRMOF-10-symMeldrums

The close matching of the literature IRMOF-10 and experimental bulk sample of the above synthesis indicates that IRMOF-10-symMeldrums is the only phase present.

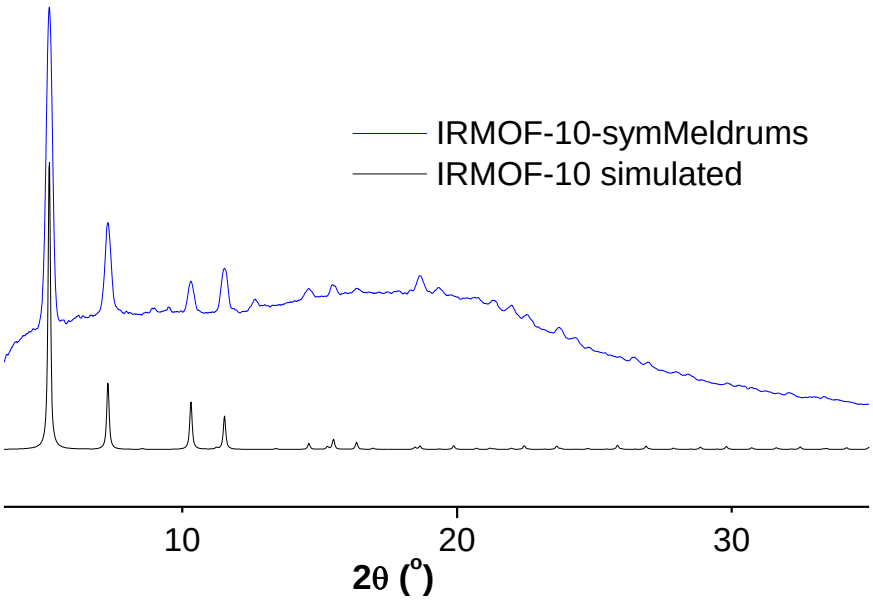

Figure 5.3: Simulated (calculated from literature[20]) for IRMOF-10 and experimental PXRD pattern for IRMOF-10-symMeldrums.

Absence of any significant aromatic impurities suggests that there is limited decomposition occurring with the integrals obtained matching well with the expected structure with Meldrum's acid intact.

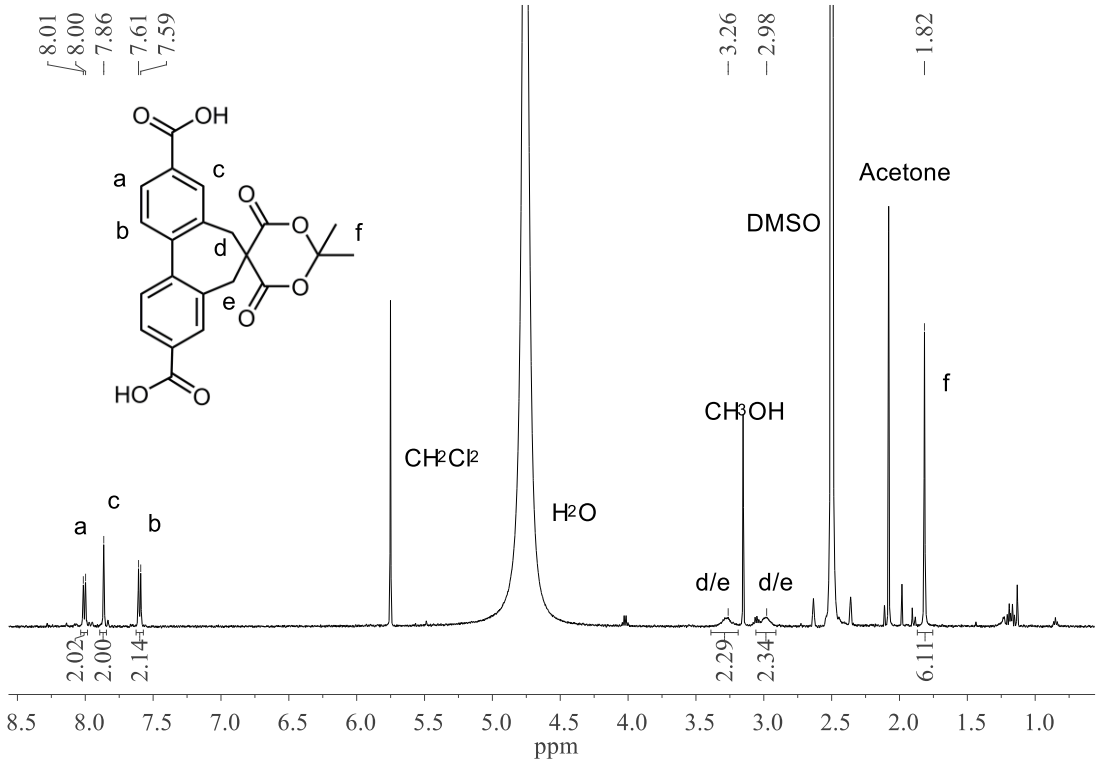

Figure 5.4: ^{1}H NMR spectroscopic analysis of digested IRMOF-10-symMeldrums in DMSO-d_6/DCl.

Table 5.1: Crystallographic data for IRMOF-10-symMeldrums

Compound	**$Zn_4O(bpdc\text{-}symMeldrums)_3$**
Formula	$C_{45}O_{13}Zn_4$
Formula weight	1010.94
Crystal size (mm)	0.12 x 0.09 x 0.11
Temperature (K)	129.15
Wavelength (Å)	1.54187
Crystal system	Cubic
Space group	*P*-43m
Unit cell lengths (Å)	a = 17.1930(15) b = 17.1930(15) c = 17.1930(15)
Unit cell angles (°)	α = 90 β = 90 γ = 90
Unit cell volume ($Å^3$)	5082.2(13)
Z	1
D_{calc} (g cm^{-3})	0.330
μ (mm^{-1})	0.652
F(000)	495.0
Reflns coll./unique, R_{int}	9389 / 1709, 0.0891
Data range	8.0 Å > d > 0.81 Å
Index ranges	$-21 \leq h \leq 18$, $-21 \leq k \leq 15$, $-8 \leq l \leq 16$
Completeness	88.8 %
T_{min}, T_{max}	0.881, 1.000
R indices for data with $I>2\sigma(I)$	R_1 = 0.1532, wR_2 = 0.3633
R indices for all data	R_1 = 0.2584, wR_2 = 0.4449
Largest difference peak and hole (e $Å^{-3}$)	0.65/ -0.43

The cubic crystal structure shows no sign of second lattice formation with the Meldrum's acid functionality crystallographically disordered over multiple locations and no electron-density visible in the pores (see Appendix). Thus, the TPG is shown to suppress

interpenetration during MOF synthesis. This is consistent with previous literature in IRMOF-10 where bulky photo or thermolabile protecting groups have suppressed or controlled interpenetration in this more rigid MOF.

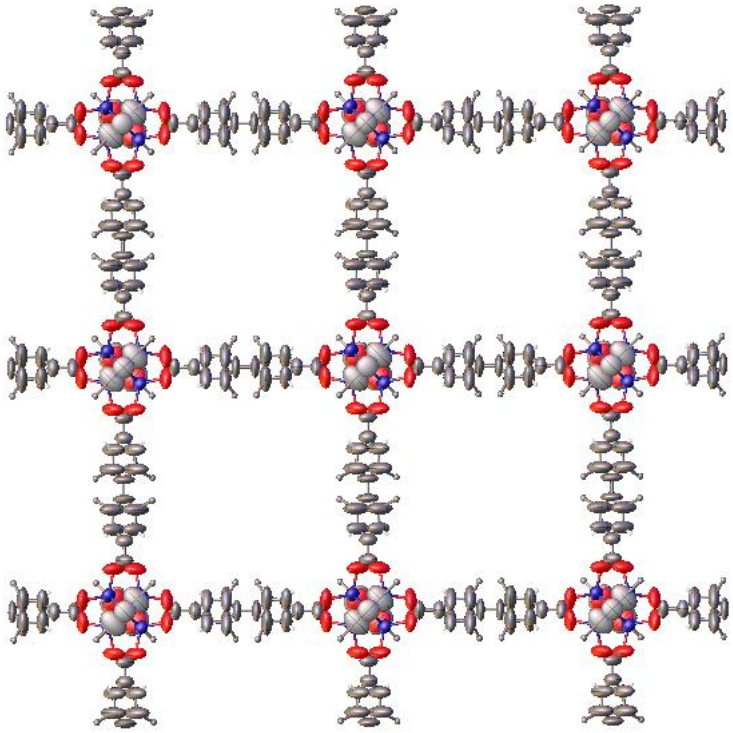

Figure 5.5: Non-interpenetrated structure of IRMOF-10-symMeldrums, ellipsoids plotted at 50% probability. The Meldrum's acid group is highly disordered in the pore so is only modelled to the first atom and refined isotropically.

This method was also trialled with the remaining Meldrum's ligands and copper salts but was unsuccessful in forming crystalline material without ligand degradation.

A solvent-based diffusion method was also developed using the alkylidene Meldrum's ligand with relatively higher solvent stability (see experimental section). This was partially successful in obtaining IRMOF-10-CHMeldrums. However, due to the sensitivity of the layering process and the requirement of limited base contact with ligand occurring concurrent with MOF formation this method was not reliably reproducible without some ligand degradation caused by layer disruption (up to 30%). Therefore, no further characterization was carried out.

Room temperature MUF-77 and other MOF synthesis

Extensive efforts were made to incorporate Meldrum's acid ligands into the multicomponent MOF, MUF-77, using an established room temperature synthesis and variations involving minor to no heating. However, all showed ligand degradation occurring

early in MOF formation, resulting in amorphous materials with total ligand degradation in the case of bdc-Meldrums and bpdc-Meldrums, marginally crystalline materials with some ligand intact or crystalline materials with total ligand degradation in the case of the alkylidene and symmetrically substituted Meldrum's acid ligands.

Synthesis of some copper-based MOFs, including pillar-layer MOFs with bipyridine, were also attempted but still showed ligand degradation occurring despite short reaction times, low room temperature, and mild base addition conditions.

Therefore, *in situ* reactions and post-synthetic routes were pursued.

Additive and inhibitive attempt with bpdc-CHO and bdc-CHMeldrums respectively

Due to the survival of the alkylidene Meldrum's acid ligand during recrystallization in boiling methanol/water and at room temperature, MOF-synthesis trials under a range of conditions were undertaken for the alkylidene Meldrum's acid. However, base-catalyzed Knoevenagel condensation is a reversible reaction (Figure 5.6) and under standard solvothermal conditions of MOF synthesis in amide-based solvents the ligand reverted back to the aldehyde species, forming highly crystalline aldehyde-functionalized MOFs (Figure 5.7). The aldehyde-functionalized MOFs formed through this decomposition process were significantly larger and clearer in appearance than those using only the bpdc-CHO (Figure 5.8), suggesting that the decomposition process of the bulkier Meldrum's acid group participated in slowing crystal formation. In this way the alkylidene Meldrum's acid group could be suggested to be a type of sacrificial modulator during MOF synthesis

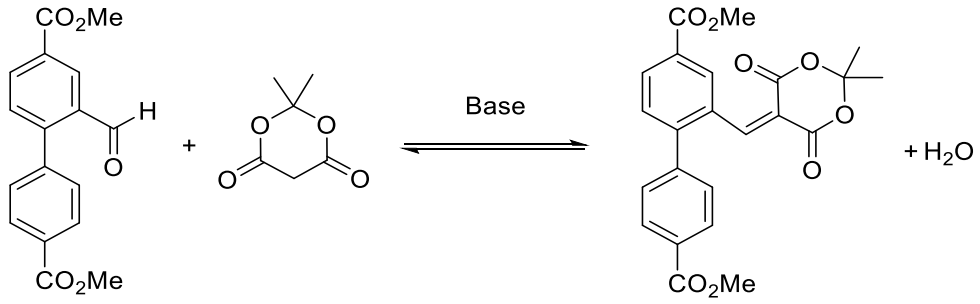

Figure 5.6: Knoevenagel condensation reaction equilibrium between formyl-substituted bpdc and the alkylidene Meldrum's acid derivative.

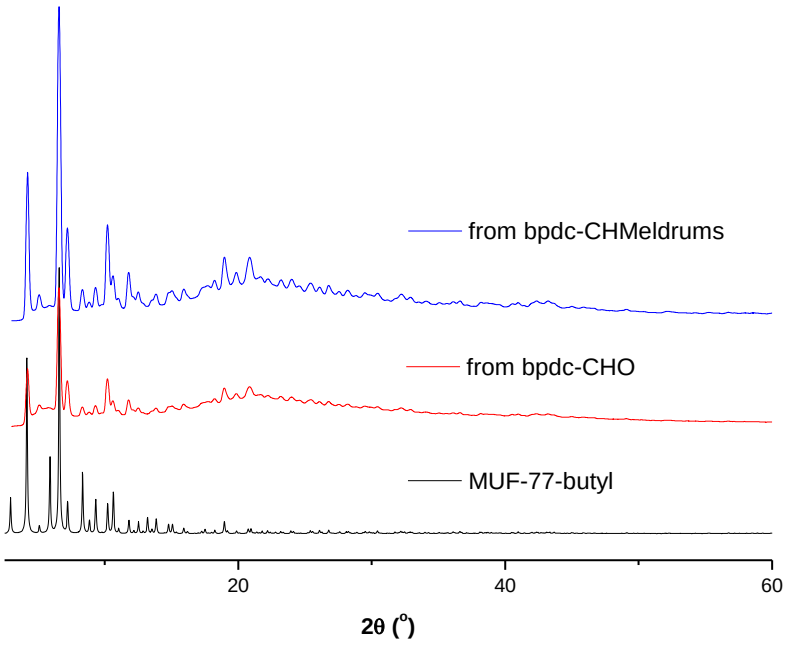

Figure 5.7: Simulated PXRD of parent MUF-77-butyl and experimental PXRD of MUF-77-bpdc-CHO synthesis from bpdc-CHO and bpdc-CHMeldrums ligands.

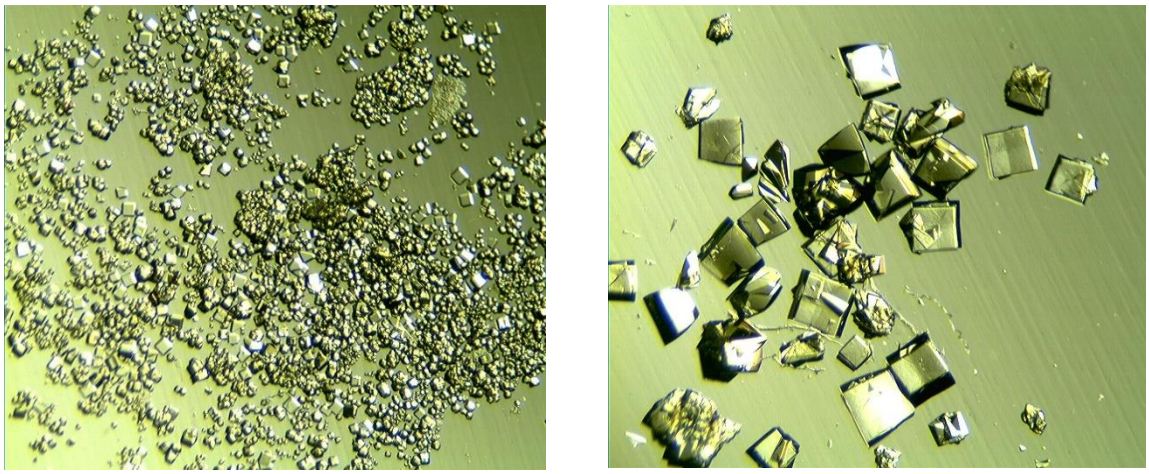

Figure 5.8: MUF-77-bpdc-CHO synthesis with H_2bpdc-CHO (left) and H_2bpdc-CHMeldrums (right).

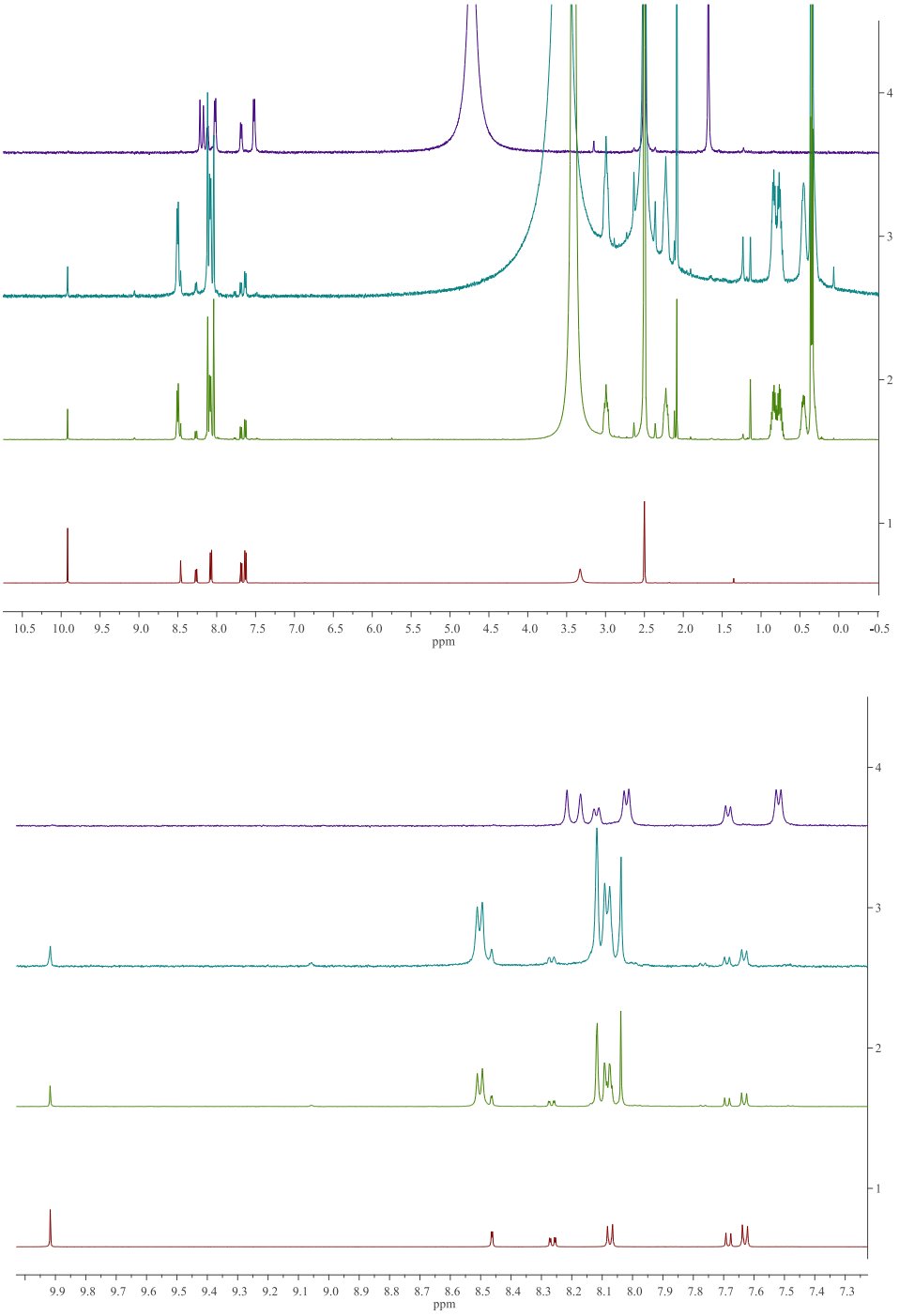

Figure 5.9: ^{1}H NMR analysis of both MOF synthesis and comparison with relevant ligands. Top and bottom spectra are bpdc-CHMeldrums and bpdc-CHO respectively. Middle blue and green spectra are from MUF-77 synthesis using bpdc-CHMeldrums and bpdc-CHO. Aromatic region clearly shows clean bpdc-CHO present in both MOF synthesis. Other peaks present in NMR correspond to the bdc and truxene ligands present in MUF-77 structure.

Significantly larger and more crystalline single crystals were observed in the synthesis of MUF-77-bpdc-CHO involving degradation of bpdc-CHMeldrums (Figures 5.7 and 5.8). This suggests that a type of modulating effect independent of the presence of free Meldrum's acid and specific to the bpdc-CHMeldrums ligand decomposition process is occurring. The presence

of the –CHMeldrums functionality during MOF synthesis may act jointly as a sacrificial modulator and chemical protecting group in the installation of an aldehyde in the MOF framework. The sacrificial modulator decomposes during MOF synthesis but alters the desired properties of the MOF material in a manner inaccessible in absence of the group.

Both the addition and inhibition MUF-77 MOF synthesis routes failed to yield a Meldrum's acid functionalized MOF. Potentially, there is a second inhibitive option for either room temperature or solvothermal MOF synthesis that involves the use of acetic anhydride, as in the original synthesis of Meldrum's acid in acid catalyzed addition of malonic acid and acetic anhydride. This could be trialled in a UiO synthesis that already relies on presence of acid for crystalline MOF formation.

In situ decomposition of alkylidene Meldrum's acid moiety to an aldehyde group is similar to the early removal of acetoxyl groups from 2,5-dihydroxybenzene-1,4-dicarboxylic acid (dhybdc) in a Zn MOF synthesis with bpy by Kitagawa et al.[232] In this latter case of [Zn(dhybdc)(bpy)].4DMF, a more significant suppression of interpenetration and installation of otherwise coordinating hydroxyl groups was achieved. Similarly, alkyl group removal during UiO MOF synthesis has been investigated.[233]

5.2.3. Synthesis of a zirconium cluster

Due to the greater observed stability of the bis-substituted Meldrum's acid side-products, a range of MOF synthesis conditions were undertaken with the ligands. In pursuit of $(bpdc)_2$-bisMeldrums at 85 ^{o}C with a zirconium source, a $ZrO_8Zr_{12}(OMe)_{36}$ cluster was obtained.

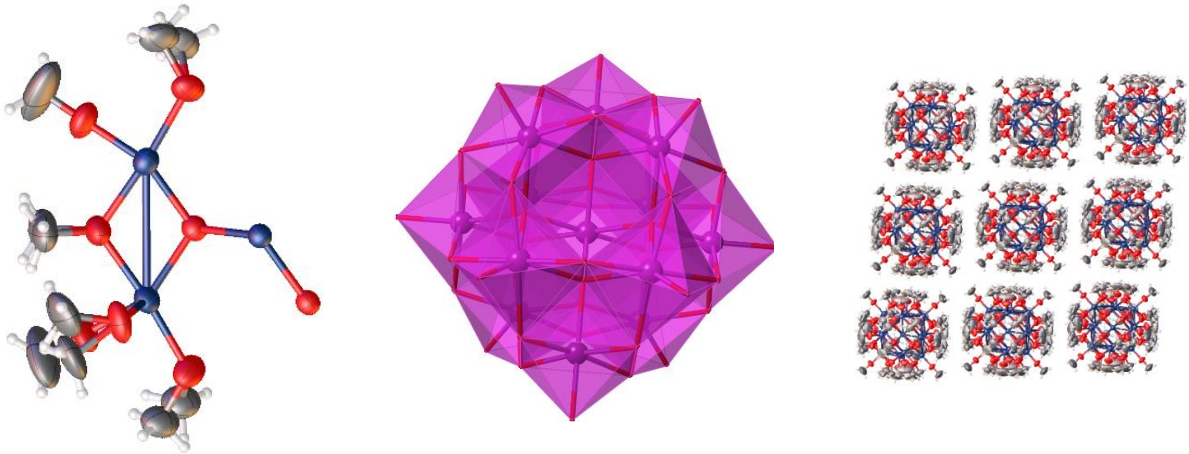

Figure 5.10: From left, the asymmetric unit cell of $ZrO_8Zr_{12}(OMe)_{36}$, $Zr_{13}O_{44}$ core of cluster (omitting capping methoxide ligands for clarity) and the square packing form of the hydrophobic cluster.

Table 5.2: Crystallographic data for zirconium cluster

Compound	**$Zr_{13}O_{44}C_{36}H_{108}$ cluster**
Formula	$C_{18}H_{64}O_{22}Zr_{6.5}$
Formula weight	1215.57
Crystal size (mm)	0.2 x 0.2 x 0.2
Temperature (K)	142.15
Wavelength (Å)	1.54178
Crystal system	Trigonal
Space group	*R*-3
Unit cell lengths (Å)	a = 17.2648(9) b = 17.2648(9) c = 27.777(2)
Unit cell angles (°)	α = 90 β = 90 γ = 120
Unit cell volume ($Å^3$)	7170.4(9)
Z	6
D_{calc} (g cm^{-3})	1.689
μ (mm^{-1})	11.738
F(000)	3589.7
Reflns coll./unique, R_{int}	29413/ 3116, 0.0835
Data range	8.0 Å > d > 0.81 Å
Index ranges	-21≤h≤17, -20≤k≤21, -30≤l≤34
Completeness	99.1 %
T_{min}, T_{max}	0.648, 1.000
R indices for data with $I>2\sigma(I)$	R_1 = 0.0521, wR_2 = 0.1365
R indices for all data	R_1 = 0.0924, wR_2 = 0.1526
Largest difference peak and hole (e $Å^{-3}$)	1.37/ -1.67

A polyoxometalate (POM) is a polyatomic ion (usually an anion) consisting of three or more transition metal oxyanions combined in a closed 3-dimensional structure through shared oxygen atoms. Corner and side-sharing of smaller zirconium-oxygen clusters into a large Zr 26 SBU has been incorporated into MOFs.[234]

The above zirconium POM consists of an 8-coordinate Zr(IV) centre surrounded by 12 7-coordinate edge-shared $Zr(OMe)_3$. This cluster is neutrally charged with the capping methoxides forming a cuboid rather than spherical shape resulting in close packing with no solvent. This cluster appears to be a novel addition to a relatively scarce set of known zirconium oxide cluster species with nuclearity between 11 and 18. Recently, a cluster[235] was isolated from a $ZrCl_4$ hydrothermal synthesis in a not dissimilar manner using formic acid as a cluster size modulator.[235]

Keggin-type polyoxometalates have been incorporated into MOFs[236] and a precursor node approach to MOF synthesis has been established.[49, 237] Additionally, this is not a known SBU in MOFs , and would therefore constitute a novel robust metal node-based MOF potentially useful for industrial applications. Therefore, a range of different ligands containing carboxylic acid, pyridine and azole coordinating moieties were trialled. However, only the cluster was reformed. Higher temperatures than those used (65-85 ^{o}C) or additives might be necessary for displacement of the capping ligands for diverging ligand coordination and MOF formation.

5.3. Postsynthetic routes towards Meldrum's acid MOFs

5.3.1. Post-synthetic ligand exchange (PSE)

Post-synthetic ligand exchange (PSE), trialled in acetone using conditions based on literature procedures,[238] was attempted to incorporate the Meldrum's acid ligand into MUF-77. While the ligand exchange could be observed qualitatively (displacement of an orange coloured azo containing bpdc ligand) and quantitatively (dissolution of the MUF-77 crystal for NMR) single crystal XRD analysis of the colourless or pale exchanged shell of the crystal indicated total amorphization. This is contrary to the bulk PXRD that showed highly crystalline parent MOF indicating that the unexchanged core of the sample crystals maintained order. ^{1}H NMR analysis showed partial ligand degradation was still occurring. Thus, no further PSE experiments with MUF-77 were trialled.

5.3.2. Post-synthetic modification (PSM) routes to UiO-Meldrum's MOFs

Post-synthetic exchange in acetone, inhibiting the formation of the malonic acid, is a potential method for incorporation of a ligand bearing a Meldrum's acid functionality into a MOF material. Alternatively, post-synthetic modification of a MOF functionalized with an appropriate precursor ligand can be pursued, obtaining Meldrum's acid through selected chemical reaction steps *in situ*.

The robust UiO-66/67 framework has already been introduced as an ideal scaffold material for covalent PSM (see Introduction). The hard-acid to hard-base pairing of the zirconium-oxygen bonds of the UiO-66/67 MOF frameworks grants them their characteristic robustness and causes them to be resistant to ligand substitution by incoming solvent molecules under mild conditions such as is observed for the hard-soft bond pairing of zinc-based MOFs. In literature, HF or strongly basic solutions are used to digest zirconium MOFs for NMR and mass spectrometry (MS) analysis. Due to the assured destruction of the Meldrum's acid group in these standard zirconium MOF digestion procedures the success of Meldrum's acid ligand incorporation can be verified using gas chromatography of the head space of a heated MOF sample (monitoring for acetone), IR spectroscopy and/or through easily visualized chemical reactions such as conjugating a fluorescent or dye moiety to the ketene-carrying linkers post MOF thermolysis. This latter option would also allow direct visualization of the extent of ligand substitution in the MOF.

Reaction with Meldrum's acid in a post-synthetic step in a supramolecular material has been observed to proceed cleanly and in higher yields than when undertaken on the ligand alone (Figure 5.11).[239]

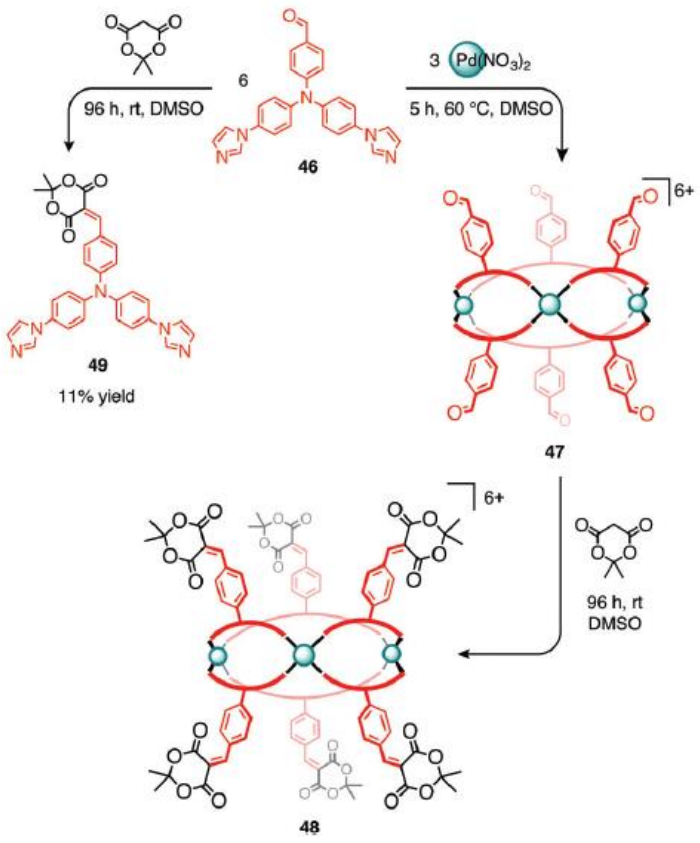

Figure 5.11: Meldrum's acid addition to supramolecular assemblies through a Knoevenagel condensation reaction, showing higher yield (quantitative) than when undertaken on the ligand alone (11%). Figure taken from reference.[239]

The covalent PSM route makes use of the well-established chemical robustness of UiO-MOFs to carry out the reaction with Meldrum's acid *in situ* using a precursor ligand of a more rudimentary functional group such as an alkylbromide or aldehyde (Figure 5.12).

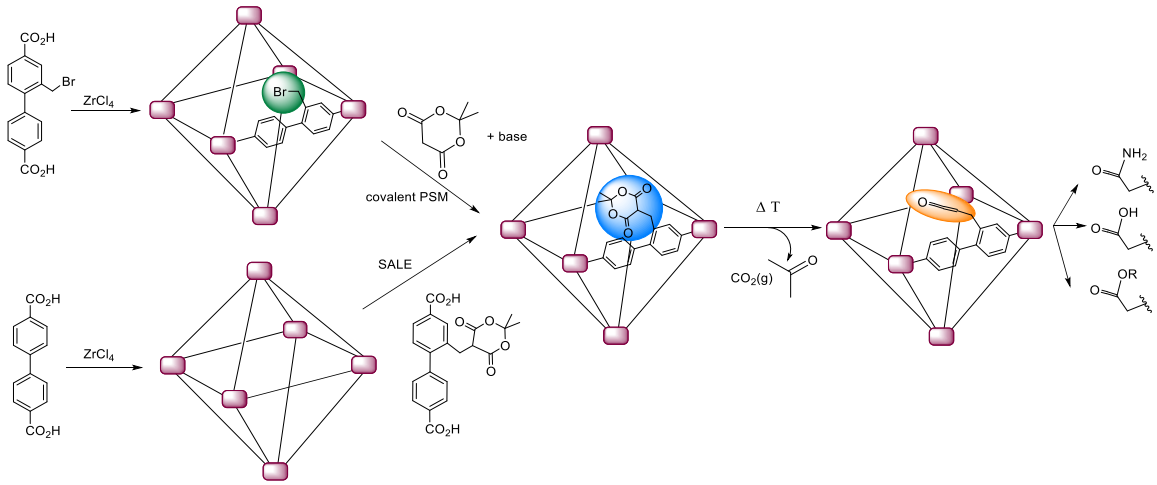

Figure 5.12: Covalent or dative PSM leading to incorporation of Meldrum's acid group into framework for subsequent thermolysis and ketene chemistry.

The above covalent and dative PSM methods suggested are most likely to lead to incompletely functionalized Meldrum's acid MOFs given the limitations of solvent diffusion-based methods as elaborated on in Chapter 1. However, when viewed in the light of practical applications, lower loadings of the functional groups in the UiO-66/67 frameworks, which are relatively strut-dense, have been found to be beneficial in literature (Figure 5.13).

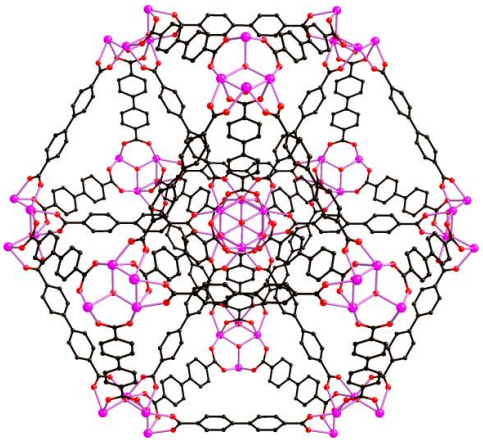

Figure 5.13: The strut-dense (and remarkably beautiful) UiO-67 framework.

For the covalent PSM method the synthesis of UiO-67-CH_2Br and UiO-67-CHO analogue MOFs were targeted. Trials using triethylamine or pyrrolidinium acetate as the requisite base would then allow Meldrum's acid formation within MOF following the Michael addition or Knoevenegal condensation pathway with the bpdc-CH_2Br and bpdc-CHO ligands respectively.

5.4.3 $[Zr_6O_6(OH)_4(bpdc\text{-}CH_2Br)_6]$ UiO67-CH_2Br

Bpdc-CH_2Br was synthesized (see Appendix) and successfully trialled in UiO-67 MOF synthesis reactions leading to two methods being developed for bulk and potentially single crystal MOF synthesis.

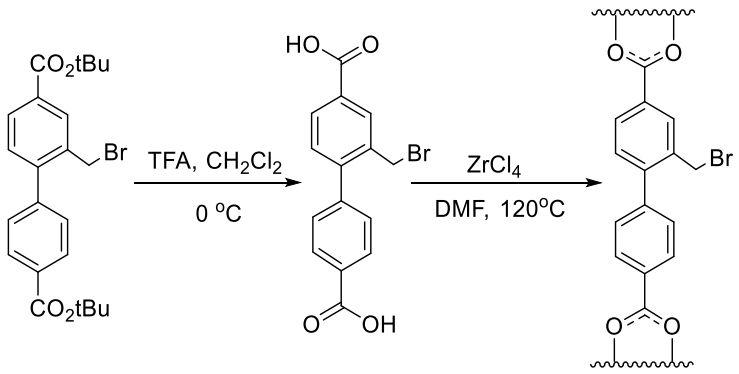

Figure 5.14: Reaction scheme for ester removal to form bpdc-CH_2Br and MOF synthesis.

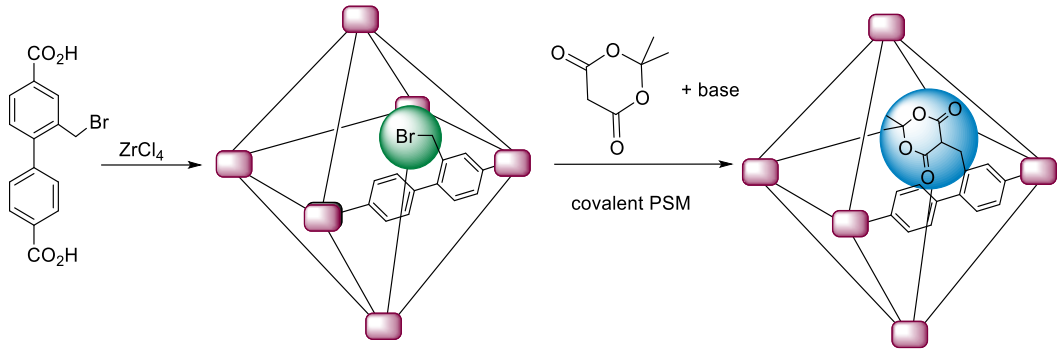

Figure 5.15: Covalent PSM scheme for incorporation of Meldrum's acid functionality into a UiO-type MOF using ligand bpdc-CH_2Br.

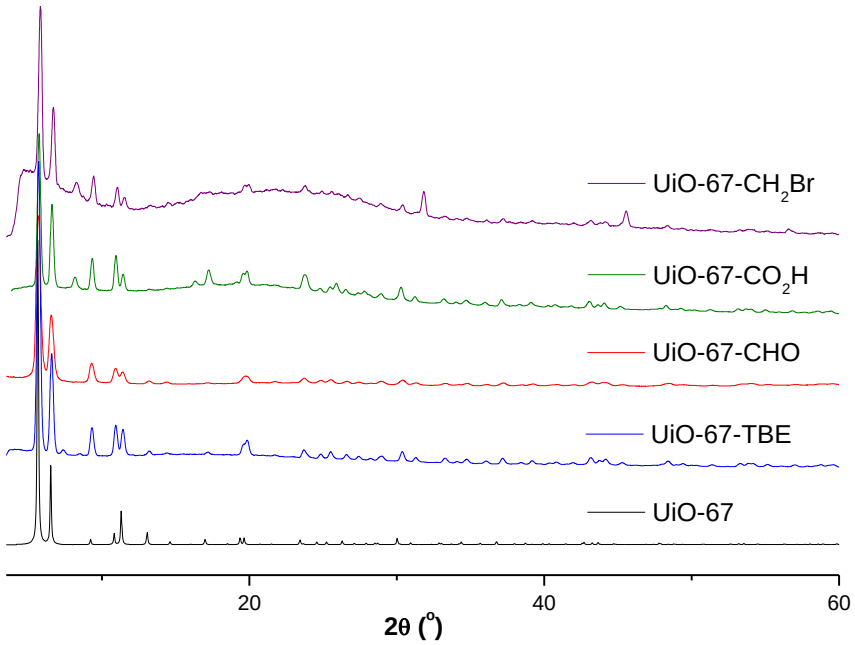

Figure 5.16: Simulated PXRD spectra of UiO-67 parent structure and experimental PXRD of analogues synthesized.

Unfortunately, an impurity (which is also incorporated into the MOF) is introduced during the removal of the *tert*-butyl ester groups, as evidenced by ^1H NMR spectroscopy of ligand and UiO-67-CH_2Br MOF.

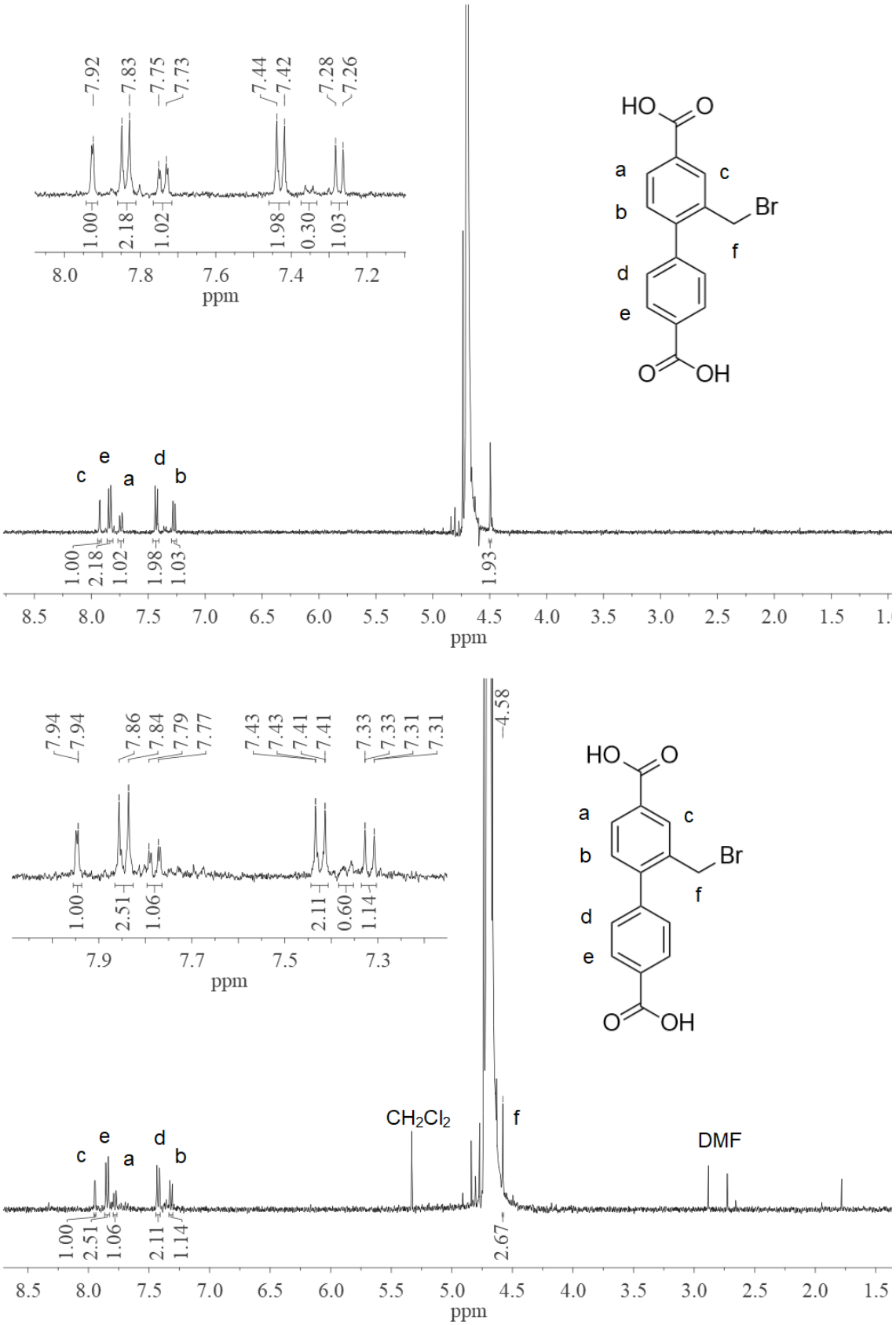

Figure 5.17: ^{1}H NMR analysis of digested UiO-67-CH_2Br (bottom) and bpdc-CH_2Br ligand (top) in D_2O/CsF. Inset shows the aromatic region where the impurity persists in a significant ratio to the desired mono-brominated ligand.

Despite further purification of the mono-brominated ligand and gentler, drier ester removal conditions trialled the same impurity was generated during *tert*-butyl ester removal and subsequent MOF synthesis.

An alternative PSM ligand, bpdc-CHO, was thus synthesized using the new bpdc-Meldrum's ligand synthesis through the alkylidine Meldrum's acid species. This aldehyde-functionalised ligand survives methyl ester removal and UiO-67 synthesis conditions cleanly (Figure 5.18). UiO67-CHO was subsequently synthesized for Knoevenagel condensation with pyrrolidinium acetate and Meldrum's acid to be carried out inside the MOF at room temperature.

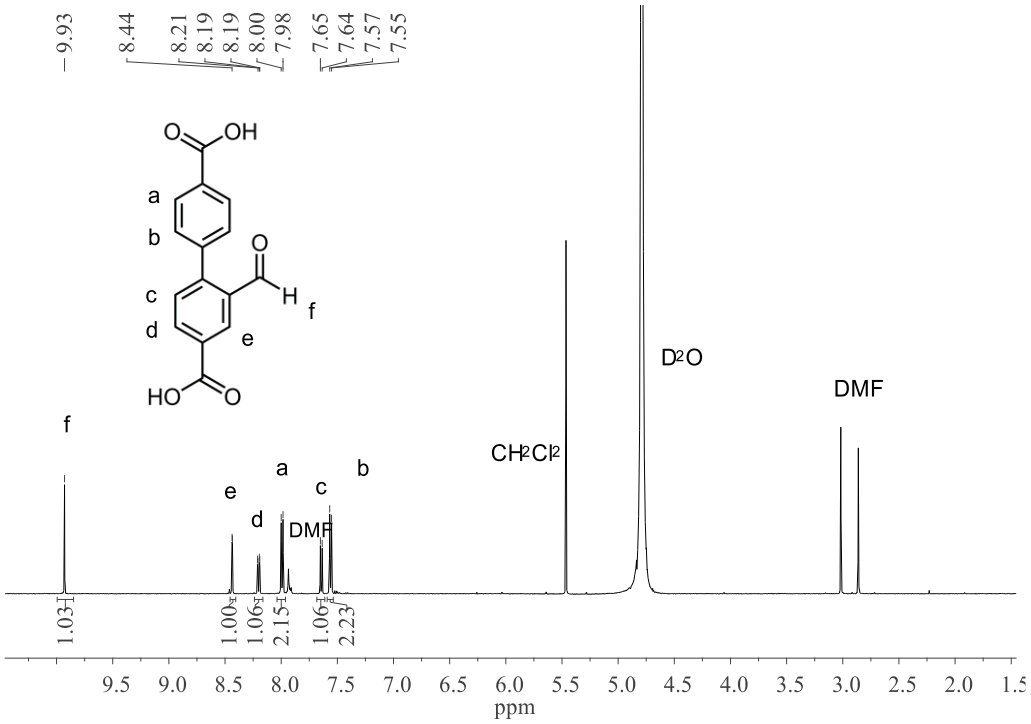

Figure 5.18: ^{1}H NMR analysis of digested UiO-67-CHO in D_2O/CsF.

Due to time constraints, the reaction of these PSM MOFs to form Meldrum's acid functionalized UiO-67 analogues has not yet been done.

Alongside pursuit of Meldrum's acid MOFs, other TPG-functionalized MOFs were formed and characterized. Both UiO-67-TBE and UiO-67-NHBoc were attempted. While the former formed cleanly and in good yield, the latter showed consistent deprotection of the bpdc-NHBoc was occurring simultaneously with MOF formation, as was previously noted in the synthesis of MUF20-Bβ pillar-layer MOF in Chapter 3.

A single crystal synthesis method with a high ratio of benzoic acid modulator gave the expected structure for UiO-67-TBE. Due to the high disorder in the MOF the sidechain is not visible but NMR analysis shows that the ligand survives intact (Figure 5.19).

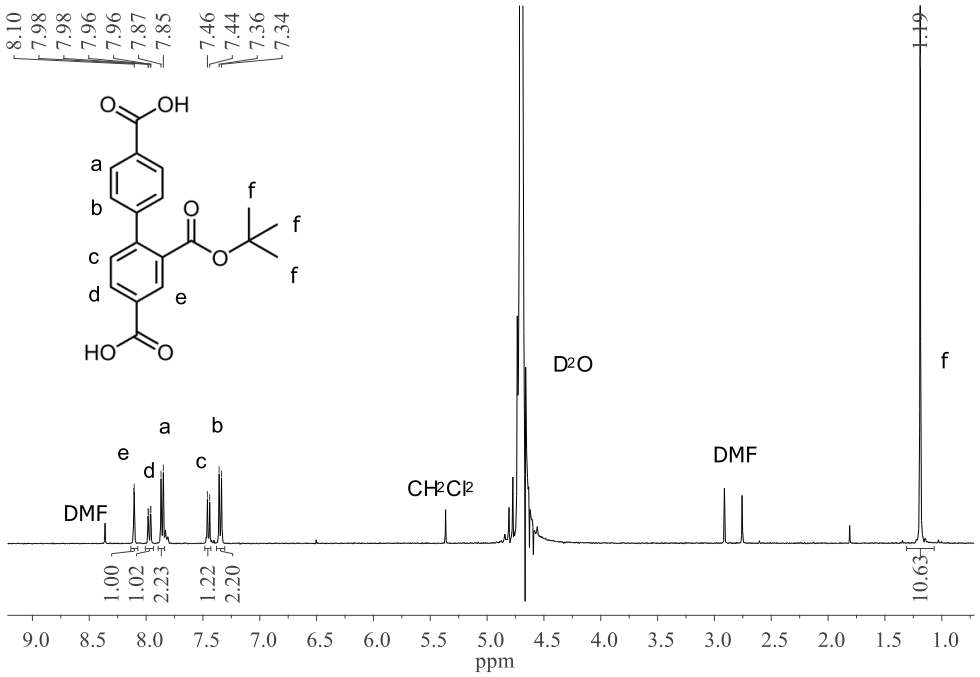

Figure 5.19: ^{1}H NMR analysis of digested UiO-67-TBE in D_2O/CsF.

This MOF was successfully thermolyzed to form the UiO67-CO_2H MOF by heating of a solvent-exchanged and dried sample of UiO-67-TBE in a microwave at 165 ^{o}C for 8 hrs or 170 ^{o}C for 6 hours.

As in Chapter 2 and 3, a synthesis of the MOF with the unprotected ligand – in this case bpdc-CO_2H – was attempted. Surprisingly, unlike with pillar-layer MOFs, UiO-67-CO_2H formed cleanly and in good yield. This could be done using single crystal conditions to obtain small cubic crystals or foregoing benzoic acid for a more rapid synthesis to obtain a white microcrystalline powder in higher yield (Appendix).

5.4.Conclusion

Due to the equilibrium favouring the formation of the malonic acid the Meldrum's acid ligands developed in Chapter 4 were found to be sensitive to traditional MOF synthesis conditions. High temperature, amide-based methods decompose the Meldrum's moiety to the malonic acids or catalyse the reverse Knoevenegal condensation reaction to the aldehyde in the

case of the alkylidene Meldrum's acid. However, in spite of this a room temperature, acetone-based synthesis was shown to successfully form a Meldrum's acid MOF.

Additionally, due to the versatility of metal-organic materials two post-synthetic routes to Meldrum's acid functionalized MOFs were identified and pursued.

The robust zirconium-based material was also shown to incorporate a *tert*-butyl ester TPG group readily which could then be formed cleanly post thermolysis. Exploratory MOF synthesis with the bis substituted Meldrum's acid ligands yielded a novel zirconium oxygen cluster. Further studies into exchange of the methoxide ions for divergently coordinating ligands to form a new zirconium MOF topology could open up another branch of robust MOF materials for applications.

5.5. Experimental section

5.5.1. General procedures

All starting compounds and solvents were used as received from commercial sources without further purification unless otherwise noted. NMR spectra were recorded at room temperature on a Bruker-500 Avance instrument, with the use of the solvent proton as an internal standard. Thermogravimetric analysis (TGA) was performed on a TA Instruments Q50 instrument.

Method A: ^{1}H NMR analysis of digested UiO MOFs

For ^{1}H NMR spectroscopy, the mother liquor of the as-synthesized MOF powders was replaced with fresh dry DMF multiple times, followed by repeated washing and subsequent soaking in dry acetone for several hours. The excess acetone was then decanted and the samples placed under vacuum overnight to remove residual solvent from the pores. The powders were then digested using the following protocol: approximately 2 mg CsF in 630 µL D_2O was mixed and added to around 5 mg of MOF, adding more CsF directly to digest sample thereafter as necessary. Spectra were acquired immediately following dissolution.

Method B: ^{1}H NMR analysis of digested IRMOF-10-Meldrums MOF samples

For ^{1}H NMR spectroscopy, the mother liquor of the as-synthesized MOF crystals was replaced with fresh dry acetone multiple times allowing soaking for several hours. The excess acetone was then decanted and the samples placed under vacuum overnight to remove residual solvent from the pores. The crystals were then digested using the following protocol: 23 µL of

a 35% DCl solution in D_2O was mixed with 1 mL of DMSO-d_6 to give a DCl/DMSO-d_6 stock solution. Around 5 mg of MOF was digested in 150 µL of this stock solution together with 480 µL of DMSO-d_6. Spectra were acquired immediately following dissolution.

Thermogravimetric Analysis (TGA)

Freshly prepared MOF samples were prepared as for NMR analysis except that samples were placed under vacuum for a minimum of 24 hours. Samples were then transferred to an aluminium sample pan and then measurements were commenced under an N_2 flow with a heating rate of 5 °C /min.

Powder X-ray diffraction patterns

All powder X-ray diffraction experiments were carried out on a Rigaku Spider X-ray diffractometer with Cu K_α radiation (Rigaku MM007 microfocus rotating-anode generator), monochromated and focused with high-flux Osmic multilayer mirror optics, and a curved image plate detector. The data were obtained from freshly prepared MOF samples that had been ground into slurry in a small amount of DMF, DEF or DBF and kept damp with solvent throughout the measurement. The two-dimensional images of the Debye rings were integrated with 2DP[194] (Version 1.0.3.4) to give 2Θ vs I diffractograms. The predicted powder patterns were generated from their single-crystal structures using Mercury v4.10.

Single crystal X-ray diffraction

Crystals were mounted on a MiTaGen mylar loop before coating in Fomblin oil and placed under cold stream at stated temperature in crystallography table. IRMOF-10-symMeldrums was collected in dry DBF in a polymer sleeve at room temperature. Diffraction data was collected on a Rigaku Spider diffractometer equipped with a MicroMax MM007 rotating-anode generator (Cu K_α radiation, 1.54180 Å), high-flux Osmic multilayer mirror optics; diffraction data were recorded on a curved image-plate detector. Data were collected at the temperatures listed in crystallography tables and were integrated, scaled, and averaged with FS_Process.[195] XPREP was used to determine the space group and the structures were solved using SHELXS or SHELXT and refined with SHELXL.[196] Platon was employed to determine the solvent accessible volume.[197] All non-hydrogen atoms were found in the electron density difference map. All hydrogen atoms were calculated using the appropriate restraints. All non-hydrogen atoms were refined anisotropically.

5.5.2. Ligand Synthesis and characterization

a) 2,2'-bis(bromomethyl)-[1,1'-biphenyl]-4,4'-dicarboxylic acid

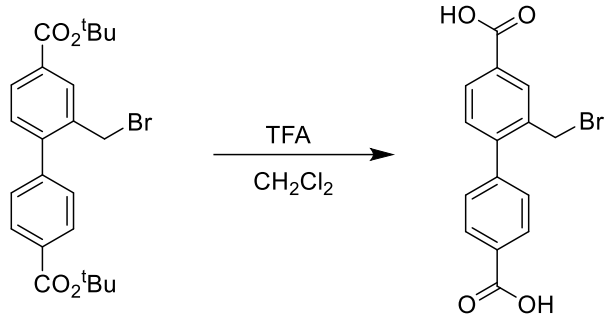

Tert-butyl 2-bromomethyl-[1,1'-biphenyl]-4,4'-dicarboxylate (139 mg, 0.311 mmol) was dissolved in dry CH_2Cl_2 (25 mL) and cooled on ice before the addition of TFA (2.10 mL). Reaction mixtures were stirred overnight, gradually warming to room temperature. Solvent was then removed under vacuum using warm water bath, dried under vacuum before further drying overnight under high vacuum to yield a white powder (~130 mg). ^{1}H NMR (400 MHz, DMSO-d_6) δ 13.12 (s, 2H), 8.19 (d, J = 1.7 Hz, 1H), 8.06 (d, J = 8.5 Hz, 2H), 7.96 (dd, J = 8.0, 1.8 Hz, 1H), 7.59 (d, J = 8.5 Hz, 2H), 7.42 (d, J = 8.0 Hz, 1H), 4.67 (s, 2H).

b) 2-formylbiphenyl-4,4'-dicarboxylic acid

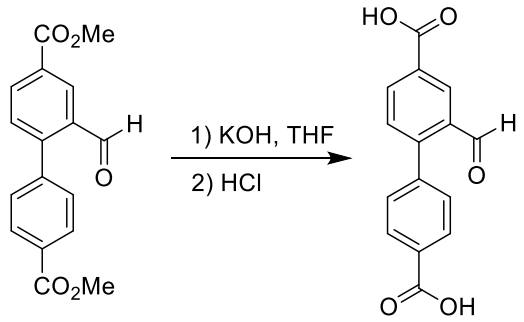

Dimethyl 2-formylbiphenyl-4,4'-dicarboxylate (151 mg, 0.517 mmol) was dissolved in dry THF (6.75 mL), split into 3 vials and cooled on ice before the addition of 1 M KOH (1.49 mL each). The opaque white suspensions were stirred on ice overnight. Reaction mixtures were combined into a RBF and THF was then removed *in vacuo* before cooling the clear yellow aqueous layer on ice and gradually acidifying with 1 M HCl to pH 2.0. The fine white solid was then collected via suction filtration, washing thoroughly with H_2O before drying overnight under high vacuum to yield a greenish white powder (136 mg, 97%). ^{1}H NMR (500 MHz, DMSO-d_6) δ 13.28 (s, 2H), 9.92 (s, 1H), 8.46 (d, J = 1.8 Hz, 1H), 8.26 (dd, J = 8.0, 1.9 Hz, 1H), 8.07 (dd, J = 8.2, 1.8 Hz, 2H), 7.68 (d, J = 8.0 Hz, 1H), 7.63 (dd, J = 8.2, 1.8 Hz, 2H) ppm.

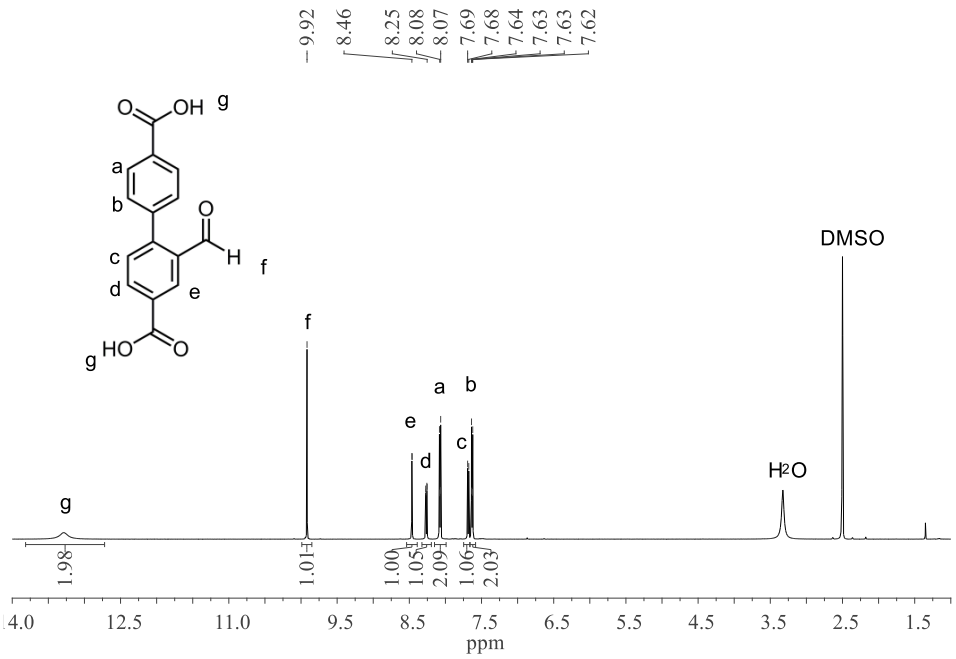

Figure 5.20: Ligand H_2bpdc-CHO in DMSO-d_6.

5.5.1. MOF synthesis and characterization

IRMOF-10-symMeldrums

3.0 mg of bpdc-symMeldrums ligand was dissolved in 1.2 mL dry acetone and 200 µL volumes aliquoted into 6 x 1 mL GC vials with septum lid. 24.1 mg of $Zn(NO_3)_2.4H_2O$ was dissolved in 300 µL propan-2-ol and 50 µL aliquoted into each of above vials. 600 µL n-heptane and 30 µL Et_3N were combined and 105 µL aliquots taken into 6 x 4 mL crystallisation vials. The septum lids of the ligand and metal salt solution vials were each pierced with a fine glass capillary and placed inside the outer vial containing the volatile base solution before lidding firmly and placing at room temperature overnight. Clear, colourless cubic crystals obtained. Yield: 1.2 mg.

UiO-67 analogues

i) Synthesis of $[Zr_6O_4(OH)_4(bpdc\text{-}TBE)_6]$ (UiO-67-TBE)

2-(*tert*-Butoxycarbonyl)-[1,1'-biphenyl]-4,4'-dicarboxylic acid (5.0 mg, 0.015 mmol), benzoic acid (167 mg, 1.37 mmol) and $ZrCl_4$ (6.9 mg, 0.030 mmol) were combined in a 5 mL scintillation vial and DMF (1.75 mL) added. The solution was briefly sonicated before placing in an oven heated to 85 ^oC for 7 days, affording small cubic single crystals. The material was

then washed with DMF and solvent-exchanged with dry CH_2Cl_2 before drying under high vacuum and storing at room temperature.

ii) Synthesis of $[Zr_6O_4(OH)_4(bpdc\text{-}CO_2H)_6]$ via PSD from UiO-67-TBE

The thermolyzed UiO-67 analogue, $[Zr_6O_4(OH)_4(bpdc\text{-}CO_2H)_6]$, was obtained by heating of a solvent-exchanged and dried sample of UiO-67-TBE in a microwave at 165 ^oC for 8 hrs or 170 ^oC for 6 hours.

iii) Synthesis of $[Zr_6O_4(OH)_4(bpdc\text{-}CO_2H)_6]$ directly (UiO-67-CO_2H)

[1,1'-Biphenyl]-2,4,4'-tricarboxylic acid (5.2 mg, 0.018 mmol), benzoic acid (179 mg, 1.47 mmol) and $ZrCl_4$ (8.5 mg, 0.036 mmol) were combined in a 5 mL scintillation vial and DMF (1.75 mL) added. The solution was briefly sonicated before placing in an oven heated to 85 ^oC for 2 days, affording very small cubic single crystals. This was then washed with DMF and solvent-exchanged with dry CH_2Cl_2 before drying under high vacuum and storing at room temperature.

Rapid synthesis method

[1,1'-Biphenyl]-2,4,4'-tricarboxylic acid (23.9 mg, 0.083 mmol) and $ZrCl_4$ (40.2 mg, 0.173 mmol) were combined in a 20 mL scintillation vial with PEG-lined lid and DMF (8.3 mL) added. The solution was briefly sonicated before placing in an oven heated to 85 ^oC for 3 days, affording white powder. This was then washed with DMF and solvent-exchanged with dry CH_2Cl_2 before drying under high vacuum and storing at room temperature.

iv) Synthesis of $[Zr_6O_4(OH)_4(bpdc\text{-}CHO)_6]$ PSM MOF (UiO-67-CHO)

2-Formyl-[1,1'-biphenyl]-4,4'-dicarboxylic acid (23.9 mg, 0.088 mmol) and $ZrCl_4$ (42.8 mg, 0.184 mmol) were combined in a 20 mL scintillation vial with PEG-lined lid and DMF (8.75 mL) added. The solution was briefly sonicated before placing in an oven heated to 85 ^oC for 3 days, affording white powder. This was then washed with DMF and solvent-exchanged with dry CH_2Cl_2 before drying under high vacuum and storing at room temperature.

v) Synthesis of $[Zr_6O_4(OH)_4(bpdc\text{-}CH_2Br)_6]$ PSM MOF (UiO-67-CH_2Br)

2-(Bromomethyl)-[1,1'-biphenyl]-4,4'-dicarboxylic acid (5.04 mg, 0.015 mmol), benzoic acid (45.7 mg, 0.374 mmol) and $ZrCl_4$ (8.6 mg, 0.036 mmol) were combined in a 20 mL scintillation vial with PEG-lined lid and DMF (1.75 mL) added. The solution was briefly sonicated before placing in an oven heated to 85 ^oC for 5 days, affording white powder. This

was then washed with DMF and solvent-exchanged with dry CH_2Cl_2 before drying under high vacuum and storing at room temperature.

Chapter 6 - Summary and perspectives

6.1. Thesis Summary

Development of MOF chemistry is still in relative infancy regarding investigation of novel chemistry within the constrained and crystallographically visible pores of metal-organic frameworks. As outlined in this thesis, decoration of these pore environments is not always straightforward. Many of the more successful literature applications of MOFs involve post-synthetic modification (PSM) of some form or another. Therefore, research undertaken to extend the current post-synthesis techniques in their variety of substrate MOF frameworks, ligands or bestowed utility will have far-reaching consequences in a range of MOF applications through improved tailoring of form to function. In this respect, the thermolabile protecting group (TPG) strategy can be seen as worthy of further research due to being a broadly applicable and effective MOF PSM technique. Additionally, a TPG PSM has advantages over current techniques such as photolabile protecting groups which require material transparency alongside retained porosity, or covalent PSM requiring full penetration of reactive agents into the core of the MOF. Synthesis of ligands that bestow novel functionality upon the MOF material, especially in a multifunctional responsive manner, is of great interest in successfully applying or discovering new applications of MOFs.

In this thesis, the incorporation of a protected carboxylic acid using the TPG strategy was further extended onto the ubiquitous 4,4`-biphenyldicarboxylic acid (bpdc) backbone and the novel bpdc-TBE ligand synthesized. In combination with the functionalized bpy ligands and bpdc-NHBoc previously formed, a family of MOFs was targeted (Chapters 2 and 3). The influence of the functional group was investigated on such material properties as inter-lattice hydrogen bonding, control of phase and degree of interpenetration as well as crystallographic and thermal stability.

In Chapter 2, analysis of the TPG-functionalized pillar-layer materials was undertaken by comparison of the mono-functionalized MOFs to those materials formed from direct synthesis using ligands carrying the bare amine (MUF20-Aβ` and MUF20-B`α) and carboxylic acid functionalities (MUF20-Aγ` and MUF20-C`α). Functionalization of the layer was clearly shown to have a non-concentration dependent influence on the MOF gas sorption properties, enhancing the gas uptake despite the decreased pore volume through a pore-filling effect that both acted as a strong gating phenomenon – as suggested through the significant hysteresis – and structural support against collapse during activation.

Consequences of both the type – carbamate versus ester - and location of the TPG - in the pillar (MUF20-Aβ and MUF20-Aγ) or layer (MUF20-Bα and MUF20-Cα) - of the MOF on MOF formation and structure was clear. Positioning of the -TBE TPG in the layer of the MUF20-Cα demonstrated that TPG inter-lattice interactions have the more significant effect over steric bulk in increasing gas uptake and suppressing unwanted phases.

MOF synthesis difficulties encountered using the unprotected amine and carboxylic acid ligands further confirmed the value of a protecting group strategy. In amine decoration of the bpdc layer, partial thermolysis of MIF20-Bα was shown to be a useful strategy in accessing an otherwise unattainable pure pillar-layer MOF phase incorporating bpdc-NH_2.

Although only marginal crystallinity upon complete thermolysis - despite a multitude of thermolysis conditions trialled – was found for the mono-functionalized MUF20-Bα and MUF20-Cα MOFs, the retained crystallinity of MUF20-Dα indicates that thermolytic deprotection is not concurrent with loss of crystallinity in the case of TPG-functionalization of pillar-layer MOFs.

The TPG strategy did allow for the formation of the materials MUF20-Aγ and MUF20-Dα with free carboxylic acid groups otherwise not obtainable through direct synthesis methods - the first instance of a carboxylic acid being incorporated into a MOF using a TPG. Additionally, as this field continues to rapidly develop novel synthesis techniques such as bdc material doping for enhanced robustness, available activation procedures such as supercritical CO_2, or simply recommendations of activation solvent (e.g. pentane) will contribute to these materials retaining porosity upon activation. Already MUF20-Dα indicates that even such dynamic materials as breathing pillar-layer MOFs can be both activated and thermolyzed with their inherent order maintained.

In Chapter 3, the TPG strategy was shown to control phase of the material formed through position and state of protection of a hydrogen donor amine moiety. The amine moiety when present on the bpdc ligand had a strongly determining effect on the final MOF formed, setting up multiple hydrogen-bonding interactions with a free-carboxylate oxygen of a second lattice forming two alternative non-MUF20-B`α competing phases and completely disfavouring formation of the parent MUF20-Aα phase. But, when present on the bpy pillar, this chemical group was shown to be inconsequential in forming the desired MOF material, indicating the directing effect of the bpdc backbone in the formation of pillar-layer MOFs. This research contributes to the body of knowledge developing on the structural import of multicomponent MOF functionalization in the choice of ligand backbone to modify as well as insights into the

interactions formed during MOF synthesis itself, which is still very much a 'black box' area in MOF chemistry. Both of these factors – the positional relevance and phase-controlling interactions of functional groups during synthesis – form an important part in designing catalytic MOF pores.

In Chapter 3, this analysis was further expanded through a full range of MOF syntheses including comparison to the directly functionalized ligand backbone analogues. This work elaborated on the directing influence of the more strongly coordinating carboxylate ligand in the formation of pillar-layer MOFs as well as the importance of the functional group utilized. Bpdc-TBE groups were shown to localise within the layers of the MOF, allowing for the steric bulk of an additional TBE or NHBoc TPG on the pillar bpy as well as readily forming the half-protected MUF20-Cβ`. The bpdc-NHBoc functionalized MOF did not allow for this. Due to the positioning of the functionality within the pores of the MOF not even the presence of an amine moiety proved compatible. In all synthesis conditions trialled, competing phases were either persistently present or dominating. In particular, an IRMOF phase, consisting of bpdc backbone ligand and Zn^{2+} only, was favoured where the steric bulk of the NHBoc group on the bpdc ligand directly prohibited inclusion of any modified bpy ligand.

The validity of controlling material properties by the TPG strategy was shown in the ability to completely reverse the directing effect of the bpdc-NH_2 ligand when combined with a specifically modified bpy ligand. Whereas bpy-NH_2 and bpy-NHBoc still favoured formation of the MUF20-B`α-dia or diamondoid topology MOF (refer to fold-out), bpy-TBE completely disfavoured these competing phases, forming the parent phase MUF20-B`γ.

General trends in literature such as the increasing of gas uptake with decoration of MOF pores by polar groups, dynamic nature of the pillar-layer MOF structure upon host-guest interactions, and the occlusion of gases from pores based on size-selectivity were expanded on.

In Chapter 4, novel TPGs incorporating a ketene or methylene ketene moiety upon thermolysis were synthesized and characterized. These ligands offer a multifunctional TPG handle for MOF materials where upon thermolysis the reactive ketene or methylene ketene moiety might be diversified to a range of different chemical moieties such as hydroxyl, amine, carboxyl, or chiral groups, through exposure to an appropriate nucleophile. Single-crystal structures collected on the esterified ligands and literature analysis indicate that proximity of the carboxylic acid groups could be activating the Meldrum's acid moiety and lowering ketene formation temperature. Synthesis of a symmetric extended Meldrum's acid ligand was attempted to increase thermal stability.

In Chapter 5, due to the inability of the ambitiously reactive Meldrum's acid TPGs to survive traditional MOF synthesis conditions, alternative synthesis conditions, postsynthetic methods such as solvent-assisted ligand exchange, and postsynthetic covalent modification were trialled resulting in the first instance of a MOF carrying the Meldrum's acid group within the widely-studied IRMOF framework. The TPG steric bulk in this more rigid MOF structure was shown to suppress interpenetration to form IRMOF-10.

Within the range of conditions trialled, reversibility of the decomposition mechanism of the alkylidene Meldrum's acid ligand to the parent aldehyde under solvothermal conditions was investigated. Routes towards Meldrum's acid functionalized UiO and MUF-77 frameworks through PSM were established through incorporation of an aldehyde ligand, bpdc-CHO. Additionally, use of the bis-substituted Meldrum's acid as a tetratopic linker with $ZrCl_4$ yielded a previously unknown zirconium oxygen cluster that was robust and reformed under different MOF synthesis conditions trialled.

6.2. Tuning of thermal stability for TPG strategy compatibility

The results of this thesis revealed that thermal stability of both MOF and ligand is a key factor in the development and application of a TPG strategy. Both of these stabilities have shown themselves amenable to controlled tuning. Use of a slow-diffusing 2-methylhexyl versus *tert*-butyl ester TPG can drastically improve thermal stability. Ligand thermolytic temperature can be customized through choice of substitution pattern, substituents, and isolation from destabilizing influences. Understanding of the dependency of thermal cyclization pathways on moiety conformation will lead the way in this direction. *In silico* studies of the proposed ligands may help to identify involvement from contributing HOMO/LUMO pairs into known decomposition pathways that favour undesirable results such as decreased stability to moisture post attachment to a ligand backbone.

Bolstering robustness of 'breathing' MOF frameworks for better working capacity and sensing applications is also a goal. To that end, pursuing MOFs with better hard/soft acid/base pairing will improve the resultant material stability. Alternatively, within the zinc-based pillar-layer MOFs of Chapter 2, incorporation of a bdc impurity also served to enhance material properties such as robustness and gas uptake.

6.3. Exploring more TPGs, functional groups, and ligand backbones

In the MUF20 MOF, since an interpenetrated structure is still formed, one additional challenge may be to tailor the steric bulk and interactions of the TPGs to inhibit interpenetration. Potential also exists for tuning of the gate-opening pressure of these materials with TPGs that could then be partially or fully removed for increased porosity.

Other targets could include synthesis of phosphate or sulfonic acid thermolabile protecting groups (TPGs) or expansion onto novel backbones such as pyrazole or imidazole-based ligands in pursuit of diversification of the pore characteristics of MOFs.

6.4. Towards catalytic pores

A more appropriate parent MOF for future TPG research may be MUF-77 which has been shown to be thermally stable, easy to handle, and compatible to both functionalization and thermolysis. Due to the precision with which the position of these functional handles installed can be orientated within the MOF pores this is a ripe chance for functionalization of the existing bpdc, bdc or truxene or related azotruxene backbone.

There are many challenges remaining in this direction. Most obviously finding a trend in fit of TPG functionality to MOF. However, a thermolabile protecting group strategy has already shown itself to be an important contributor to the MOF field. This is only likely to continue to grow as more sustainable, multifunctional materials are sought for diverse applications.

Orthogonal chemical handles in porous materials, especially in the area of polymerization, are likely to contribute to novel property control beyond triggered porosity, such as reversible sensing behaviour, self-catenation, self-healing and synergistic effects from dual-functionalized MOFs.

6.5. Directions towards reversibly thermoresponsive polymers

Applications of thermolabile groups explored in this thesis have been irreversible transformations, like most postsynthetic deprotection reactions. However, in polymer chemistry, reversibility of a transformation is key in imbuing such properties as self-healing and an extended lifespan to a material. Within the MOF field, self-healing photocatalysts[240] and defect-healing materials have been established. In the latter case, healing mainly occurs through heating in ligand mixtures in a PSE manner[142] or exposure to synthesis solvent

enabling structural rearrangement.[241]. As early as 2013, a self-healing copper MOF 'membrane' has been established in this way.[242]

Within the MOF field, notably among soft porous crystal research, MOF-based self-healing membranes has been highlighted as a target.[243] Self-healing properties in membranes can be from layering of active components such as through distributed reversible chemical bonding and rearrangements such as component exchange (passive healing) or controlled release of healing agents from embedded microcapsules. Humidity, photo and thermal triggers are some of the few established stimuli for triggering self-healing. All have existing parallels within MOF research. Indeed, flexible/breathing MOF systems are already highly reversible materials capable of self-healing post deformation, as in the case of methanol-loss in MUF20-Aγ.

Already ZIF MOF-based self-repairing membranes are finding application in superhydrophobic membranes for waste water treatment,[244] and as self-lubricating membranes.[245]. In the latter case, the advantage of MOFs over traditional nanocontainers is clear as understanding of the kinetic and structural properties of these capsules determines diffusion to the released active material inside the coating matrix. [246]

Example of a microcapsules have applications in Nafion fuel cell membranes,[247] and passive healing reversible Diels-Alder based self-repairing automobile coatings.[248] Applications of reversible chemistries in MOF materials are a more efficient use of energy as dedicated materials need only be partly replaced or become entirely self-repairing.

Examples of reversible chemistries (Figure 6.1) show that hetero-Diels-Alder systems have debonding on demand (DoD) or self-healing due to their dynamic exchange between closed cross-link and open structure.[249]

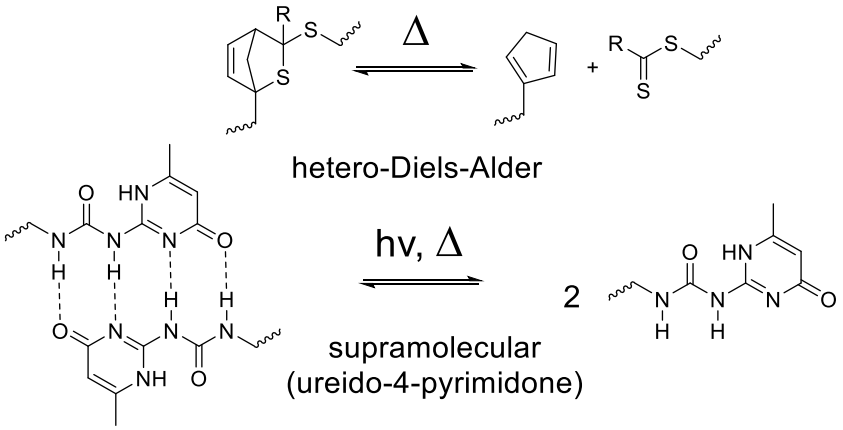

Figure 6.1: Two existing reversible chemistry examples in polymer systems illustrating dynamic covalent bonding (top) and supramolecular assembly (bottom).

The former moieties have already been introduced into MIL-88-Fe as a chemically 'reprogrammable' MOF.[250] The latter supramolecular interaction through urea functionalities has been introduced into MOFs and a urea-based UiO-66-polymer hybrid systems developed.[251] Within polymer systems, dynamic urea reversible –bonding is underway,[252-253] and shows excellent tuning of thermal stability (Figure 6.2) in both MOF[254] and traditional polymer.[255] In a zinc acetate, isocyanate, and urea hybrid system, zinc ions were shown to speed up the reaction of urea dissociation by two orders of magnitude via the formation of bound Zn complexes, imbuing self-healing.[253]

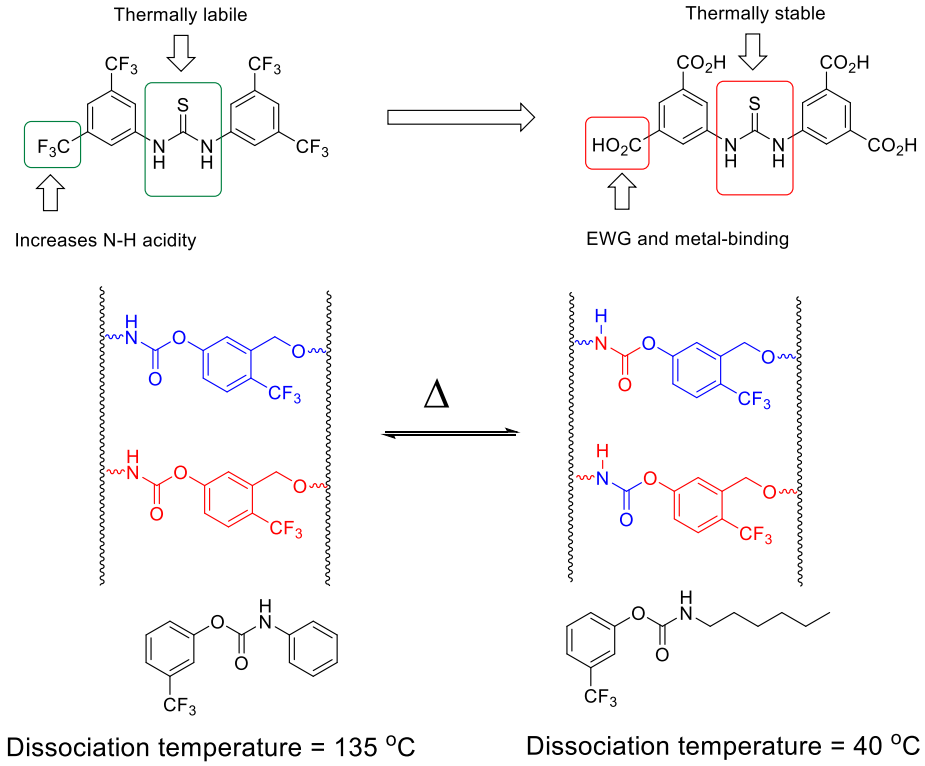

Figure 6.2: (Top) Thermal stability of urea moieties can be tuned to be more stable for incorporation into MOFs. (Middle and bottom) Dissociation temperature of urethanes in polymers can be reduced by the introduction of electron-withdrawing groups providing the required mobility for the healing exchange process.

Meldrum's acid is already known as a permanent cross-linking agent through ketene formation. However, reversible 'click' chemistry of thiols with Meldrum's acid was recently established [256] and a related reversible conjugate addition-elimination reaction of Meldrum's acid has already been incorporated into silicone networks for elastomeric vitrimer synthesis that can be recycled up to 10 times without degradation of material properties.[257] This disubstuted sulfur-bearing Meldrum's acid derivative was exceedingly stable, undergoing heating to 110 °C in C_6D_6 in a J-Young tube sealed under ambient conditions with little change by NMR integration after 16 h of heating (5% change, using 1,4-cyclooctadiene as an internal standard) and no observed new products. Only upon reaching 178 °C was mass loss

accompanied by evolution of volatile compounds with masses corresponding to carbon dioxide and acetone observed.

Meldrum's acid can also be utilized in a Donor-Acceptor Stenhouse Adduct (DASA) system which allows for reversible and selective photo switching (Figure 6.3).[258]

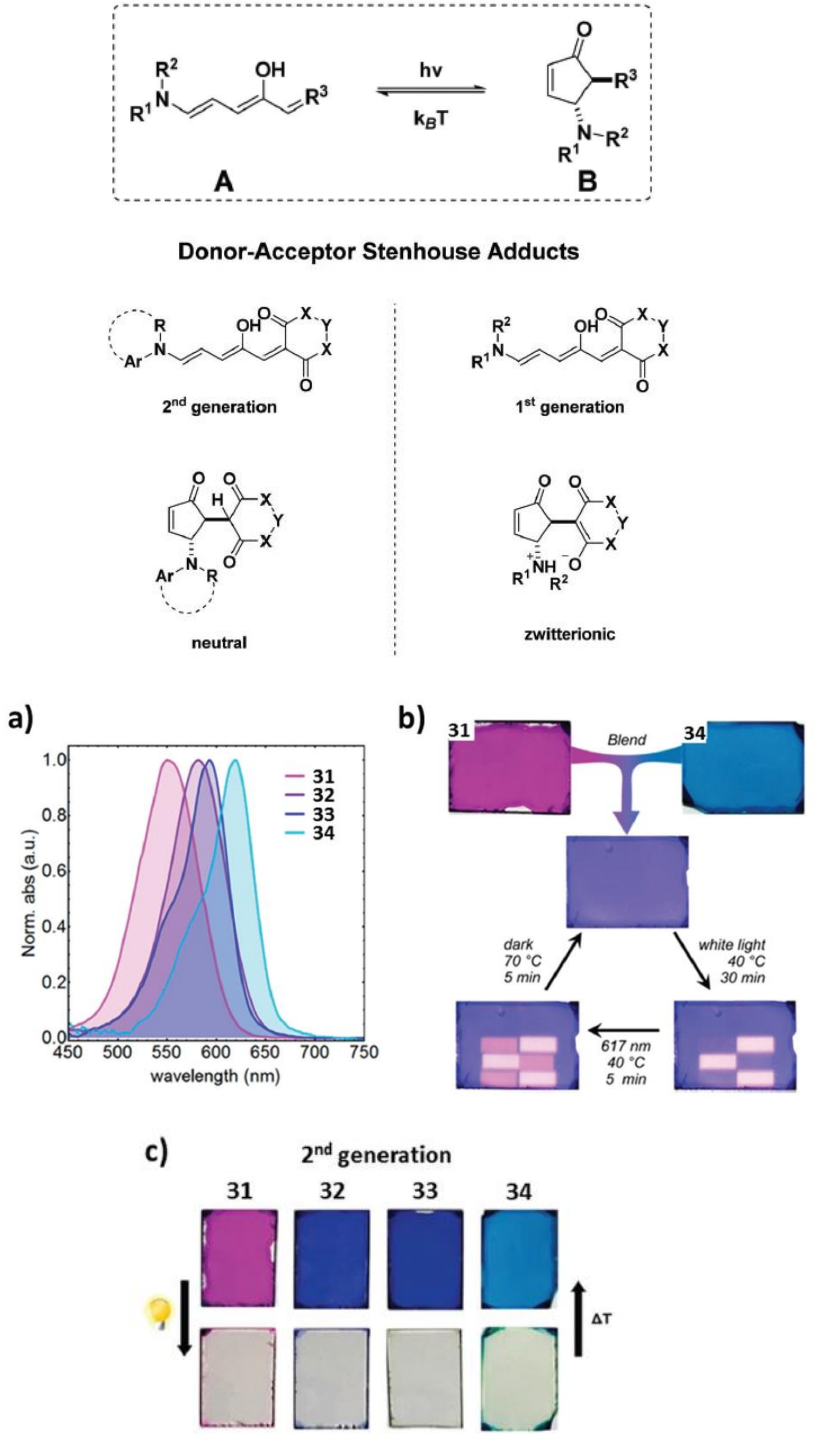

Figure 6.3: (Top) Reversible mechanism of DASA system. First and second generation DASAs. (Bottom) Wavelength selective photoswitching of DASA-polymer conjugates. Figure adapted from reference.[259]

DASA systems show great promise in sensing applications. Use of the Meldrum's acid moiety in this system allows both thermally reversible photoswitching (Figure 6.3 top) and ketene formation as elaborated on in Chapter 4. Tuning of the thermal generation of both the photoswitching cyclization and ketene formation are areas of great interest.[162, 225, 259] and would add to the existing toolkit of thermal/photo reversible systems such as in the photodimerization of 1,4-bis[2-(4-pyridyl)ethenyl]benzene (1,4-bpeb) ligand undertaken for *in situ* and reversible solid state polymerization in a MOF.[260]

Deliberate use of MOF flexibility could be useful in solving long-standing hurdles in other areas, such as in silica cracking through drastic volume change upon de(lithiation). This field is increasingly turning towards flexible polymer bindings that show reversible (or self-healing) properties,[261] of which promising candidates incorporate strong supramolecular interactions. In-depth understanding of the bonding interactions that influence MOF structure and flexibility could then be used to pair optimally with polymer chemistry and applications just as structural knowledge of MOFs is enabling pairing of hybrid crystals.[262]

References

1. Batten, S. R.; Champness, N. R.; Chen, X.-M.; Garcia-Martinez, J.; Kitagawa, S.; Öhrström, L.; O'Keeffe, M.; Paik Suh, M.; Reedijk, J., Terminology of metal–organic frameworks and coordination polymers (IUPAC Recommendations 2013). *Pure Appl. Chem.* **2013,** *85* (8), 1715-1724.
2. Lian, X.; Erazo-Oliveras, A.; Pellois, J. P.; Zhou, H. C., High efficiency and long-term intracellular activity of an enzymatic nanofactory based on metal-organic frameworks. *Nat Commun* **2017,** *8* (1), 2075.
3. Liao, P. Q.; Huang, N. Y.; Zhang, W. X.; Zhang, J. P.; Chen, X. M., Controlling guest conformation for efficient purification of butadiene. *Science* **2017,** *356* (6343), 1193-1196.
4. Mondloch, J. E.; Katz, M. J.; Isley Iii, W. C.; Ghosh, P.; Liao, P.; Bury, W.; Wagner, G. W.; Hall, M. G.; DeCoste, J. B.; Peterson, G. W.; Snurr, R. Q.; Cramer, C. J.; Hupp, J. T.; Farha, O. K., Destruction of chemical warfare agents using metal–organic frameworks. *Nat Mater* **2015,** *14*, 512.
5. Howarth, A.; Liu, Y.; Li, P.; Li, Z.; Wang, T.; Hupp, J.; Farha, O., *Chemical, thermal and mechanical stabilities of metal–organic frameworks*. 2016; Vol. 1, p 15018.
6. Farha, O. K.; Eryazici, I.; Jeong, N. C.; Hauser, B. G.; Wilmer, C. E.; Sarjeant, A. A.; Snurr, R. Q.; Nguyen, S. T.; Yazaydın, A. Ö.; Hupp, J. T., Metal–Organic Framework Materials with Ultrahigh Surface Areas: Is the Sky the Limit? *J Am Chem Soc* **2012,** *134* (36), 15016-15021.
7. Hoskins, B. F.; Robson, R., Infinite polymeric frameworks consisting of three dimensionally linked rod-like segments. *J Am Chem Soc* **1989,** *111* (15), 5962-5964.
8. Hoskins, B. F.; Robson, R., Design and construction of a new class of scaffolding-like materials comprising infinite polymeric frameworks of 3D-linked molecular rods. A reappraisal of the zinc cyanide and cadmium cyanide structures and the synthesis and structure of the diamond-related frameworks $[N(CH_3)_4][CuIZnII(CN)_4]$ and CuI[4,4',4'',4'''-tetracyanotetraphenylmethane]$BF_4.xC_6H_5NO_2$. *J Am Chem Soc* **1990,** *112* (4), 1546-1554.
9. Corporation, M. I., Using Metal-Organic Frameworks (MOFs) to Store, Separate and Transport Gases. AZoM.
10. Cavka, J. H.; Jakobsen, S.; Olsbye, U.; Guillou, N.; Lamberti, C.; Bordiga, S.; Lillerud, K. P., A new zirconium inorganic building brick forming metal organic frameworks with exceptional stability. *J Am Chem Soc* **2008,** *130* (42), 13850-1.
11. Rosi, N. L.; Kim, J.; Eddaoudi, M.; Chen, B.; O'Keeffe, M.; Yaghi, O. M., Rod packings and metal-organic frameworks constructed from rod-shaped secondary building units. *J Am Chem Soc* **2005,** *127* (5), 1504-18.
12. Deng, H.; Grunder, S.; Cordova, K. E.; Valente, C.; Furukawa, H.; Hmadeh, M.; Gandara, F.; Whalley, A. C.; Liu, Z.; Asahina, S.; Kazumori, H.; O'Keeffe, M.; Terasaki, O.; Stoddart, J. F.; Yaghi, O. M., Large-pore apertures in a series of metal-organic frameworks. *Science* **2012,** *336* (6084), 1018-23.
13. Pachfule, P.; Garai, B.; Banerjee, R., Functionalization and Isoreticulation in a Series of Metal-Organic Frameworks Derived from Pyridinecarboxylates. *Inorg Chem* **2016,** *55* (15), 7200-5.
14. Dybtsev, D. N.; Nuzhdin, A. L.; Chun, H.; Bryliakov, K. P.; Talsi, E. P.; Fedin, V. P.; Kim, K., A homochiral metal-organic material with permanent porosity, enantioselective sorption properties, and catalytic activity. *Angew. Chem. Int. Ed. Engl.* **2006,** *45* (6), 916-20.
15. Kitagawa, S.; Kitaura, R.; Noro, S., Functional porous coordination polymers. *Angew. Chem. Int. Ed. Engl.* **2004,** *43* (18), 2334-75.
16. Haneda, T.; Kawano, M.; Kojima, T.; Fujita, M., Thermo-to-photo-switching of the chromic behavior of salicylideneanilines by inclusion in a porous coordination network. *Angew. Chem. Int. Ed. Engl.* **2007,** *46* (35), 6643-5.
17. Yaghi, O. M.; O'Keeffe, M.; Ockwig, N. W.; Chae, H. K.; Eddaoudi, M.; Kim, J., Reticular synthesis and the design of new materials. *Nature* **2003,** *423* (6941), 705-14.
18. Chui, S. S. Y.; Lo, S. M. F.; Charmant, J. P. H.; Orpen, A. G.; Williams, I. D., A Chemically Functionalizable Nanoporous Material $[Cu_3(TMA)_2(H_2O)_3]$n. *Science* **1999,** *283* (5405), 1148-1150.

19. Barthelet, K.; Marrot, J.; Riou, D.; Férey, G., A Breathing Hybrid Organic-Inorganic Solid with Very Large Pores and High Magnetic Characteristics. *Angew. Chem.* **2002,** *114* (2), 291-294.
20. Eddaoudi, M.; Kim, J.; Rosi, N.; Vodak, D.; Wachter, J.; O'Keeffe, M.; Yaghi, O. M., Systematic design of pore size and functionality in isoreticular MOFs and their application in methane storage. *Science* **2002,** *295* (5554), 469-72.
21. Huang, X. C.; Lin, Y. Y.; Zhang, J. P.; Chen, X. M., Ligand-directed strategy for zeolite-type metal-organic frameworks: zinc(II) imidazolates with unusual zeolitic topologies. *Angew. Chem. Int. Ed. Engl.* **2006,** *45* (10), 1557-9.
22. Park, K. S.; Ni, Z.; Côté, A. P.; Choi, J. Y.; Huang, R.; Uribe-Romo, F. J.; Chae, H. K.; O'Keeffe, M.; Yaghi, O. M., Exceptional chemical and thermal stability of zeolitic imidazolate frameworks. *Proc Natl Acad Sci U S A* **2006,** *103* (27), 10186-10191.
23. Prussian Blue. In *Wikipedia*. Retrieved June 23, from https://en.wikipedia.org/wiki/Prussian_blue.
24. Fujita, M.; Kwon, Y. J.; Washizu, S.; Ogura, K., Preparation, Clathration Ability, and Catalysis of a Two-Dimensional Square Network Material Composed of Cadmium(II) and 4,4'-Bipyridine. *J Am Chem Soc* **1994,** *116* (3), 1151-1152.
25. Li, H.; Eddaoudi, M.; O'Keeffe, M.; Yaghi, O. M., Design and synthesis of an exceptionally stable and highly porous metal-organic framework. *Nature* **1999,** *402* (6759), 276-279.
26. Kawata, S.; Kitagawa, S.; Kumagai, H.; Kudo, C.; Kamesaki, H.; Ishiyama, T.; Suzuki, R.; Kondo, M.; Katada, M., Rational Design of a Novel Intercalation System. Layer-Gap Control of Crystalline Coordination Polymers, {[Cu(CA)(H(2)O)(m)()](G)}(n)() (m = 2, G = 2,5-Dimethylpyrazine and Phenazine; m = 1, G = 1,2,3,4,6,7,8,9-Octahydrophenazine). *Inorg Chem* **1996,** *35* (15), 4449-4461.
27. Kondo, M.; Yoshitomi, T.; Matsuzaka, H.; Kitagawa, S.; Seki, K., Three-Dimensional Framework with Channeling Cavities for Small Molecules:{[M2(4, 4'-bpy)3(NO3)4]·xH2O}n(M□ Co, Ni, Zn). *Angew. Chem. Int. Ed.* **1997,** *36* (16), 1725-1727.
28. Yaghi, O. M.; Li, G.; Li, H., Selective binding and removal of guests in a microporous metal-organic framework. *Nature* **1995,** *378* (6558), 703-706.
29. Furukawa, H.; Cordova, K. E.; O'Keeffe, M.; Yaghi, O. M., The chemistry and applications of metal-organic frameworks. *Science* **2013,** *341* (6149), 1230444.
30. Furukawa, H.; Yaghi, O. M., Storage of hydrogen, methane, and carbon dioxide in highly porous covalent organic frameworks for clean energy applications. *J Am Chem Soc* **2009,** *131* (25), 8875-83.
31. Deng, H.; Doonan, C. J.; Furukawa, H.; Ferreira, R. B.; Towne, J.; Knobler, C. B.; Wang, B.; Yaghi, O. M., Multiple functional groups of varying ratios in metal-organic frameworks. *Science* **2010,** *327* (5967), 846-50.
32. Park, K. S.; Ni, Z.; Cote, A. P.; Choi, J. Y.; Huang, R.; Uribe-Romo, F. J.; Chae, H. K.; O'Keeffe, M.; Yaghi, O. M., Exceptional chemical and thermal stability of zeolitic imidazolate frameworks. *Proc Natl Acad Sci U S A* **2006,** *103* (27), 10186-10191.
33. Cychosz, K. A.; Matzger, A. J., Water stability of microporous coordination polymers and the adsorption of pharmaceuticals from water. *Langmuir* **2010,** *26* (22), 17198-202.
34. Küsgens, P.; Rose, M.; Senkovska, I.; Fröde, H.; Henschel, A.; Siegle, S.; Kaskel, S., Characterization of metal-organic frameworks by water adsorption. *Microporous Mesoporous Mater.* **2009,** *120* (3), 325-330.
35. Seo, Y.-K.; Yoon, J. W.; Lee, J. S.; Hwang, Y. K.; Jun, C.-H.; Chang, J.-S.; Wuttke, S.; Bazin, P.; Vimont, A.; Daturi, M.; Bourrelly, S.; Llewellyn, P. L.; Horcajada, P.; Serre, C.; Férey, G., Porous Materials: Energy-Efficient Dehumidification over Hierachically Porous Metal-Organic Frameworks as Advanced Water Adsorbents (Adv. Mater. 6/2012). *Adv. Mater.* **2012,** *24* (6), 710-710.
36. Bromberg, L.; Diao, Y.; Wu, H.; Speakman, S. A.; Hatton, T. A., Chromium(III) Terephthalate Metal Organic Framework (MIL-101): HF-Free Synthesis, Structure, Polyoxometalate Composites, and Catalytic Properties. *Chem. Mater.* **2012,** *24* (9), 1664-1675.

37. Férey, G.; Mellot-Draznieks, C.; Serre, C.; Millange, F.; Dutour, J.; Surblé, S.; Margiolaki, I., A Chromium Terephthalate-Based Solid with Unusually Large Pore Volumes and Surface Area. *Science* **2005,** *309* (5743), 2040-2042.
38. Wu, H.; Chua, Y. S.; Krungleviciute, V.; Tyagi, M.; Chen, P.; Yildirim, T.; Zhou, W., Unusual and highly tunable missing-linker defects in zirconium metal-organic framework UiO-66 and their important effects on gas adsorption. *J Am Chem Soc* **2013,** *135* (28), 10525-32.
39. Fang, Z.; Bueken, B.; De Vos, D. E.; Fischer, R. A., Defect-Engineered Metal–Organic Frameworks. *Angew. Chem. Int. Ed.* **2015,** *54*, 7234.
40. Bennett, T. D.; Cheetham, A. K.; Fuchs, A. H.; Coudert, F. X., Interplay between defects, disorder and flexibility in metal-organic frameworks. *Nat Chem* **2016,** *9* (1), 11-16.
41. Mondloch, J. E.; Katz, M. J.; Planas, N.; Semrouni, D.; Gagliardi, L.; Hupp, J. T.; Farha, O. K., Are Zr(6)-based MOFs water stable? Linker hydrolysis vs. capillary-force-driven channel collapse. *Chem Commun (Camb)* **2014,** *50* (64), 8944-6.
42. Wang, T. C.; Bury, W.; Gomez-Gualdron, D. A.; Vermeulen, N. A.; Mondloch, J. E.; Deria, P.; Zhang, K.; Moghadam, P. Z.; Sarjeant, A. A.; Snurr, R. Q.; Stoddart, J. F.; Hupp, J. T.; Farha, O. K., Ultrahigh surface area zirconium MOFs and insights into the applicability of the BET theory. *J Am Chem Soc* **2015,** *137* (10), 3585-91.
43. Park, J.; Feng, D.; Zhou, H. C., Structure-assisted functional anchor implantation in robust metal-organic frameworks with ultralarge pores. *J Am Chem Soc* **2015,** *137* (4), 1663-72.
44. Chen, Z.; Hanna, S. L.; Redfern, L. R.; Alezi, D.; Islamoglu, T.; Farha, O. K., Reticular chemistry in the rational synthesis of functional zirconium cluster-based MOFs. *Coord. Chem. Rev.* **2019,** *386*, 32-49.
45. Farha, O. K.; Yazaydin, A. O.; Eryazici, I.; Malliakas, C. D.; Hauser, B. G.; Kanatzidis, M. G.; Nguyen, S. T.; Snurr, R. Q.; Hupp, J. T., De novo synthesis of a metal-organic framework material featuring ultrahigh surface area and gas storage capacities. *Nat Chem* **2010,** *2* (11), 944-8.
46. Mondloch, J. E.; Bury, W.; Fairen-Jimenez, D.; Kwon, S.; DeMarco, E. J.; Weston, M. H.; Sarjeant, A. A.; Nguyen, S. T.; Stair, P. C.; Snurr, R. Q.; Farha, O. K.; Hupp, J. T., Vapor-phase metalation by atomic layer deposition in a metal-organic framework. *J Am Chem Soc* **2013,** *135* (28), 10294-7.
47. Ahn, S.; Nauert, S. L.; Buru, C. T.; Rimoldi, M.; Choi, H.; Schweitzer, N. M.; Hupp, J. T.; Farha, O. K.; Notestein, J. M., Pushing the Limits on Metal-Organic Frameworks as a Catalyst Support: NU-1000 Supported Tungsten Catalysts for o-Xylene Isomerization and Disproportionation. *J Am Chem Soc* **2018,** *140* (27), 8535-8543.
48. Yabushita, M.; Li, P.; Kobayashi, H.; Fukuoka, A.; Farha, O. K.; Katz, A., Complete furanics-sugar separations with metal-organic framework NU-1000. *Chem Commun (Camb)* **2016,** *52* (79), 11791-11794.
49. Honicke, I. M.; Senkovska, I.; Bon, V.; Baburin, I. A.; Bonisch, N.; Raschke, S.; Evans, J. D.; Kaskel, S., Balancing Mechanical Stability and Ultrahigh Porosity in Crystalline Framework Materials. *Angew. Chem. Int. Ed. Engl.* **2018,** *57* (42), 13780-13783.
50. Stoeck, U.; Krause, S.; Bon, V.; Senkovska, I.; Kaskel, S., A highly porous metal-organic framework, constructed from a cuboctahedral super-molecular building block, with exceptionally high methane uptake. *Chem Commun (Camb)* **2012,** *48* (88), 10841-3.
51. Krause, S.; Bon, V.; Senkovska, I.; Stoeck, U.; Wallacher, D.; Tobbens, D. M.; Zander, S.; Pillai, R. S.; Maurin, G.; Coudert, F. X.; Kaskel, S., A pressure-amplifying framework material with negative gas adsorption transitions. *Nature* **2016,** *532* (7599), 348-52.
52. Mason, J. A.; Veenstra, M.; Long, J. R., Evaluating metal–organic frameworks for natural gas storage. *Chem. Sci.* **2014,** *5* (1), 32-51.
53. Peng, Y.; Krungleviciute, V.; Eryazici, I.; Hupp, J. T.; Farha, O. K.; Yildirim, T., Methane storage in metal-organic frameworks: current records, surprise findings, and challenges. *J Am Chem Soc* **2013,** *135* (32), 11887-94.

54. Shekhah, O.; Wang, H.; Paradinas, M.; Ocal, C.; Schupbach, B.; Terfort, A.; Zacher, D.; Fischer, R. A.; Woll, C., Controlling interpenetration in metal-organic frameworks by liquid-phase epitaxy. *Nat Mater* **2009,** *8* (6), 481-4.
55. Farrusseng, D.; Aguado, S.; Pinel, C., Metal-organic frameworks: opportunities for catalysis. *Angew. Chem. Int. Ed. Engl.* **2009,** *48* (41), 7502-13.
56. Lee, J.; Farha, O. K.; Roberts, J.; Scheidt, K. A.; Nguyen, S. T.; Hupp, J. T., Metal-organic framework materials as catalysts. *Chem Soc Rev* **2009,** *38* (5), 1450-9.
57. Ma, L.; Abney, C.; Lin, W., Enantioselective catalysis with homochiral metal-organic frameworks. *Chem Soc Rev* **2009,** *38* (5), 1248-56.
58. Dhakshinamoorthy, A.; Opanasenko, M.; Čejka, J.; Garcia, H., Metal organic frameworks as heterogeneous catalysts for the production of fine chemicals. *Cat. Sci. & Tech.* **2013,** *3* (10), 2509.
59. Chen, L.; Zheng, H.; Zhu, X.; Lin, Z.; Guo, L.; Qiu, B.; Chen, G.; Chen, Z. N., Metal-organic frameworks-based biosensor for sequence-specific recognition of double-stranded DNA. *Analyst* **2013,** *138* (12), 3490-3.
60. Kreno, L. E.; Leong, K.; Farha, O. K.; Allendorf, M.; Van Duyne, R. P.; Hupp, J. T., Metal-organic framework materials as chemical sensors. *Chem Rev* **2012,** *112* (2), 1105-25.
61. Cui, Y.; Yue, Y.; Qian, G.; Chen, B., Luminescent functional metal-organic frameworks. *Chem Rev* **2012,** *112* (2), 1126-62.
62. Zhang, J. W.; Zhang, H. T.; Du, Z. Y.; Wang, X.; Yu, S. H.; Jiang, H. L., Water-stable metal-organic frameworks with intrinsic peroxidase-like catalytic activity as a colorimetric biosensing platform. *Chem Commun (Camb)* **2014,** *50* (9), 1092-4.
63. Yoon, M.; Suh, K.; Natarajan, S.; Kim, K., Proton conduction in metal-organic frameworks and related modularly built porous solids. *Angew. Chem. Int. Ed. Engl.* **2013,** *52* (10), 2688-700.
64. Shimizu, G. K.; Taylor, J. M.; Kim, S., Chemistry. Proton conduction with metal-organic frameworks. *Science* **2013,** *341* (6144), 354-5.
65. Horike, S.; Umeyama, D.; Kitagawa, S., Ion conductivity and transport by porous coordination polymers and metal-organic frameworks. *Acc Chem Res* **2013,** *46* (11), 2376-84.
66. Duan, J.; Higuchi, M.; Krishna, R.; Kiyonaga, T.; Tsutsumi, Y.; Sato, Y.; Kubota, Y.; Takata, M.; Kitagawa, S., High CO2/N2/O2/CO separation in a chemically robust porous coordination polymer with low binding energy. *Chem. Sci.* **2014,** *5* (2), 660-666.
67. Mercedes-Benz. Mercedes-Benz F125 2011. www.emercedesbenz.com/autos/mercedes-benz/concept-vehicles/mercedes-benz-f125-research-vehicle-technology.
68. BASF. BASF's Metal Organic Frameworks (MOFs) increase fuel storage capacity in Natural Gas Vehicles 2013. http://www.youtube.com/watch?v=LCX-sYZ0ImE.
69. Li, P.; Vermeulen, N. A.; Malliakas, C. D.; Gómez-Gualdrón, D. A.; Howarth, A. J.; Mehdi, B. L.; Dohnalkova, A.; Browning, N. D.; O'Keeffe, M.; Farha, O. K., Bottom-up construction of a superstructure in a porous uranium-organic crystal. *Science* **2017,** *356* (6338), 624-627.
70. Ahmed, A.; Seth, S.; Purewal, J.; Wong-Foy, A. G.; Veenstra, M.; Matzger, A. J.; Siegel, D. J., Exceptional hydrogen storage achieved by screening nearly half a million metal-organic frameworks. *Nat Commun* **2019,** *10* (1), 1568.
71. Ma, S.; Sun, D.; Simmons, J. M.; Collier, C. D.; Yuan, D.; Zhou, H.-C., Metal-Organic Framework from an Anthracene Derivative Containing Nanoscopic Cages Exhibiting High Methane Uptake. *J Am Chem Soc* **2008,** *130* (3), 1012-1016.
72. Furukawa, H.; Ko, N.; Go, Y. B.; Aratani, N.; Choi, S. B.; Choi, E.; Yazaydin, A. O.; Snurr, R. Q.; O'Keeffe, M.; Kim, J.; Yaghi, O. M., Ultrahigh porosity in metal-organic frameworks. *Science* **2010,** *329* (5990), 424-8.
73. Chung, Y. G.; Bai, P.; Haranczyk, M.; Leperi, K. T.; Li, P.; Zhang, H.; Wang, T. C.; Duerinck, T.; You, F.; Hupp, J. T.; Farha, O. K.; Siepmann, J. I.; Snurr, R. Q., Computational Screening of Nanoporous Materials for Hexane and Heptane Isomer Separation. *Chem. Mater.* **2017,** *29* (15), 6315-6328.

74. Arnó, J.; Farha, O. K.; Morris, W.; Siu, P. W.; Tom, G. M.; Weston, M. H.; Fuller, P. E. In *ION-X Dopant Gas Delivery System Performance Characterization at Axcelis*, 2018 22nd International Conference on Ion Implantation Technology (IIT), 16-21 Sept. 2018; 2018; pp 227-230.
75. Rieth, A. J.; Dinca, M., Controlled Gas Uptake in Metal-Organic Frameworks with Record Ammonia Sorption. *J Am Chem Soc* **2018,** *140* (9), 3461-3466.
76. Jenks, J. J.; Motkuri, R. K.; TeGrotenhuis, W.; Paul, B. K.; McGrail, B. P., Simulation and Experimental Study of Metal Organic Frameworks Used in Adsorption Cooling. *Heat Transfer Engineering* **2016,** *38* (14-15), 1305-1315.
77. Cui, S.; Qin, M.; Marandi, A.; Steggles, V.; Wang, S.; Feng, X.; Nouar, F.; Serre, C., Metal-Organic Frameworks as advanced moisture sorbents for energy-efficient high temperature cooling. *Sci Rep* **2018,** *8* (1), 15284.
78. Wang, S.; Lee, J. S.; Wahiduzzaman, M.; Park, J.; Muschi, M.; Martineau-Corcos, C.; Tissot, A.; Cho, K. H.; Marrot, J.; Shepard, W.; Maurin, G.; Chang, J.-S.; Serre, C., A robust large-pore zirconium carboxylate metal–organic framework for energy-efficient water-sorption-driven refrigeration. *Nat Energy* **2018,** *3* (11), 985-993.
79. Wang, S.; Wang, Q.; Feng, X.; Wang, B.; Yang, L., Explosives in the Cage: Metal-Organic Frameworks for High-Energy Materials Sensing and Desensitization. *Adv. Mater.* **2017,** *29* (36), 1701898.
80. Luz, I.; Llabrés i Xamena, F. X.; Corma, A., Bridging homogeneous and heterogeneous catalysis with MOFs: "Click" reactions with Cu-MOF catalysts. *J Catal* **2010,** *276* (1), 134-140.
81. Srirambalaji, R.; Hong, S.; Natarajan, R.; Yoon, M.; Hota, R.; Kim, Y.; Ho Ko, Y.; Kim, K., Tandem catalysis with a bifunctional site-isolated Lewis acid-Bronsted base metal-organic framework, NH2-MIL-101(Al). *Chem Commun (Camb)* **2012,** *48* (95), 11650-2.
82. Skobelev, I. Y.; Sorokin, A. B.; Kovalenko, K. A.; Fedin, V. P.; Kholdeeva, O. A., Solvent-free allylic oxidation of alkenes with O2 mediated by Fe- and Cr-MIL-101. *J Catal* **2013,** *298* (0), 61-69.
83. Valvekens, P.; Vermoortele, F.; De Vos, D., Metal–organic frameworks as catalysts: the role of metal active sites. *Catal. Sci. Tech.* **2013,** *3* (6), 1435.
84. Garibay, S. J.; Cohen, S. M., Isoreticular synthesis and modification of frameworks with the UiO-66 topology. *Chem Commun (Camb)* **2010,** *46* (41), 7700-2.
85. Kandiah, M.; Nilsen, M. H.; Usseglio, S.; Jakobsen, S.; Olsbye, U.; Tilset, M.; Larabi, C.; Quadrelli, E. A.; Bonino, F.; Lillerud, K. P., Synthesis and Stability of Tagged UiO-66 Zr-MOFs. *Chem. Mater.* **2010,** *22* (24), 6632-6640.
86. Kim, M.; Cohen, S. M., Discovery, development, and functionalization of Zr(iv)-based metal–organic frameworks. *CrystEngComm* **2012,** *14* (12), 4096-4104.
87. Kandiah, M.; Usseglio, S.; Svelle, S.; Olsbye, U.; Lillerud, K. P.; Tilset, M., Post-synthetic modification of the metal–organic framework compound UiO-66. *J Mat Chem* **2010,** *20* (44), 9848.
88. Wang, C.; Xie, Z.; deKrafft, K. E.; Lin, W., Doping metal-organic frameworks for water oxidation, carbon dioxide reduction, and organic photocatalysis. *J Am Chem Soc* **2011,** *133* (34), 13445-54.
89. Kim, J.; Kim, S.-N.; Jang, H.-G.; Seo, G.; Ahn, W.-S., CO_2 cycloaddition of styrene oxide over MOF catalysts. *Appl. Catal. A* **2013,** *453* (0), 175-180.
90. Liu, L.; Zhou, T. Y.; Telfer, S. G., Modulating the Performance of an Asymmetric Organocatalyst by Tuning Its Spatial Environment in a Metal-Organic Framework. *J Am Chem Soc* **2017,** *139* (39), 13936-13943.
91. Moghadam, P. Z.; Li, A.; Wiggin, S. B.; Tao, A.; Maloney, A. G. P.; Wood, P. A.; Ward, S. C.; Fairen-Jimenez, D., Development of a Cambridge Structural Database Subset: A Collection of Metal–Organic Frameworks for Past, Present, and Future. *Chem. Mater.* **2017,** *29* (7), 2618-2625.
92. Barthel, S.; Alexandrov, E. V.; Proserpio, D. M.; Smit, B., Distinguishing Metal-Organic Frameworks. *Cryst. Growth Des.* **2018,** *18* (3), 1738-1747.
93. Hausdorf, S.; Baitalow, F.; Seidel, J.; Mertens, F. O., Gaseous species as reaction tracers in the solvothermal synthesis of the zinc oxide terephthalate MOF-5. *J Phys Chem A* **2007,** *111* (20), 4259-66.

94. Hausdorf, S.; Wagler, J.; Mossig, R.; Mertens, F. O., Proton and water activity-controlled structure formation in zinc carboxylate-based metal organic frameworks. *J Phys Chem A* **2008,** *112* (33), 7567-76.
95. Dutta, A.; Koh, K.; Wong-Foy, A. G.; Matzger, A. J., Porous solids arising from synergistic and competing modes of assembly: combining coordination chemistry and covalent bond formation. *Angew. Chem. Int. Ed. Engl.* **2015,** *54* (13), 3983-7.
96. Sun, J.; Zhou, Y.; Chen, Z.; Tu, B.; Weng, L.; Zhao, D., Synthesis and Structure of a New Open Metal-organic-inorganic Hybrid Framework [$Sn(SO_4)(BDC)(H_2O)$](BDC=Terephthalic acid). *Chem. J. Chin. Uni.* **2003,** *24* (9), 1555-1557.
97. Yaghi, O. M.; Davis, C. E.; Li, G.; Li, H., Selective Guest Binding by Tailored Channels in a 3-D Porous Zinc(II)−Benzenetricarboxylate Network. *J Am Chem Soc* **1997,** *119* (12), 2861-2868.
98. Li, H.; Davis, C. E.; Groy, T. L.; Kelley, D. G.; Yaghi, O. M., Coordinatively Unsaturated Metal Centers in the Extended Porous Framework of $Zn_3(BDC)_3{\cdot}6CH_3OH$ (BDC = 1,4-Benzenedicarboxylate). *J Am Chem Soc* **998,** *120* (9), 2186-2187.
99. Liu, L.; Konstas, K.; Hill, M. R.; Telfer, S. G., Programmed Pore Architectures in Modular Quaternary Metal–Organic Frameworks. *J Am Chem Soc* **2013,** *135*, 17731.
100. Muller, K.; Singh Malhi, J.; Wohlgemuth, J.; Fischer, R. A.; Woll, C.; Gliemann, H.; Heinke, L., Water as a modulator in the synthesis of surface-mounted metal-organic framework films of type HKUST-1. *Dalton Trans* **2018,** *47* (46), 16474-16479.
101. Gutov, O. V.; Molina, S.; Escudero-Adan, E. C.; Shafir, A., Modulation by Amino Acids: Toward Superior Control in the Synthesis of Zirconium Metal-Organic Frameworks. *Chemistry* **2016,** *22* (38), 13582-7.
102. Marshall, R. J.; Hobday, C. L.; Murphie, C. F.; Griffin, S. L.; Morrison, C. A.; Moggach, S. A.; Forgan, R. S., Amino acids as highly efficient modulators for single crystals of zirconium and hafnium metal–organic frameworks. *J Mat Chem A* **2016,** *4* (18), 6955-6963.
103. Bumstead, A. M.; Cordes, D. B.; Dawson, D. M.; Chakarova, K. K.; Mihaylov, M. Y.; Hobday, C. L.; Duren, T.; Hadjiivanov, K. I.; Slawin, A. M. Z.; Ashbrook, S. E.; Prasad, R. R. R.; Wright, P. A., Modulator-Controlled Synthesis of Microporous STA-26, an Interpenetrated 8,3-Connected Zirconium MOF with the the-i Topology, and its Reversible Lattice Shift. *Chemistry* **2018,** *24* (23), 6115-6126.
104. Vermoortele, F.; Bueken, B.; Le Bars, G.; Van de Voorde, B.; Vandichel, M.; Houthoofd, K.; Vimont, A.; Daturi, M.; Waroquier, M.; Van Speybroeck, V.; Kirschhock, C.; De Vos, D. E., Synthesis Modulation as a Tool to Increase the Catalytic Activity of Metal-Organic Frameworks: The Unique Case of UiO-66(Zr). *J Am Chem Soc* **2013,** *135*, 11465.
105. Ghorbanloo, M.; Safarifard, V.; Morsali, A., Heterogeneous catalysis with a coordination modulation synthesized MOF: morphology-dependent catalytic activity. *New J. Chem.* **2017,** *41* (10), 3957-3965.
106. Bosch, M.; Yuan, S.; Zhou, H.-C., Group 4 Metals as Secondary Building Units: Ti, Zr, and Hf-based MOFs. In *The Chemistry of Metal–Organic Frameworks*, Wiley-VCH Verlag GmbH & Co. KGaA: 2016; pp 137-170.
107. Muthu Prabhu, S.; Kancharla, S.; Park, C. M.; Sasaki, K., Synthesis of modulator-driven highly stable zirconium-fumarate frameworks and mechanistic investigations of their arsenite and arsenate adsorption from aqueous solutions. *CrystEngComm* **2019,** *21* (14), 2320-2332.
108. Ni, Z.; Masel, R. I., Rapid production of metal-organic frameworks via microwave-assisted solvothermal synthesis. *J Am Chem Soc* **2006,** *128* (38), 12394-5.
109. Liang, W.; D'Alessandro, D. M., Microwave-assisted solvothermal synthesis of zirconium oxide based metal-organic frameworks. *Chem Commun (Camb)* **2013,** *49* (35), 3706-8.
110. Son, W. J.; Kim, J.; Kim, J.; Ahn, W. S., Sonochemical synthesis of MOF-5. *Chem Commun (Camb)* **2008,** (47), 6336-8.
111. Jung, D. W.; Yang, D. A.; Kim, J.; Kim, J.; Ahn, W. S., Facile synthesis of MOF-177 by a sonochemical method using 1-methyl-2-pyrrolidinone as a solvent. *Dalton Trans* **2010,** *39* (11), 2883-7.

112. Ameloot, R.; Stappers, L.; Fransaer, J.; Alaerts, L.; Sels, B. F.; De Vos, D. E., Patterned Growth of Metal-Organic Framework Coatings by Electrochemical Synthesis. *Chem. Mater.* **2009,** *21* (13), 2580-2582.
113. Friščić, T.; Fábián, L., Mechanochemical conversion of a metal oxide into coordination polymers and porous frameworks using liquid-assisted grinding (LAG). *CrystEngComm* **2009,** *11* (5), 743.
114. Friščić, T.; Reid, D. G.; Halasz, I.; Stein, R. S.; Dinnebier, R. E.; Duer, M. J., Ion- and Liquid-Assisted Grinding: Improved Mechanochemical Synthesis of Metal-Organic Frameworks Reveals Salt Inclusion and Anion Templating. *Angew. Chem.* **2010,** *122* (4), 724-727.
115. Baeg, J. Y.; Lee, S. W., A porous, two-dimensional copper coordination-polymer containing guest molecules: hydrothermal synthesis, structure, and thermal property of [Cu(BDC)(bipy)](BDCH 2) (BDC=1,4-benzenedicarboxylate; bipy=4,4 ′ -bipyridine). *Inorg Chem Comm* **2003,** *6* (3), 313-316.
116. Choi, E. Y.; Park, K.; Yang, C. M.; Kim, H.; Son, J. H.; Lee, S. W.; Lee, Y. H.; Min, D.; Kwon, Y. U., Benzene-templated hydrothermal synthesis of metal-organic frameworks with selective sorption properties. *Chemistry* **2004,** *10* (21), 5535-40.
117. Yang, E.-C.; Zhao, H.-K.; Ding, B.; Wang, X.-G.; Zhao, X.-J., Four Novel Three-Dimensional Triazole-Based Zinc(II) Metal−Organic Frameworks Controlled by the Spacers of Dicarboxylate Ligands: Hydrothermal Synthesis, Crystal Structure, and Luminescence Properties. *Cryst. Growth Des.* **2007,** *7* (10), 2009-2015.
118. Yi, F. Y.; Chen, D.; Wu, M. K.; Han, L.; Jiang, H. L., Chemical Sensors Based on Metal-Organic Frameworks. *Chempluschem* **2016,** *81* (8), 675-690.
119. Kreno, L. E.; Leong, K.; Farha, O. K.; Allendorf, M.; Van Duyne, R. P.; Hupp, J. T., Metal–Organic Framework Materials as Chemical Sensors. *Chem Rev* **2012,** *112* (2), 1105-1125.
120. Huang, Y. B.; Liang, J.; Wang, X. S.; Cao, R., Multifunctional metal-organic framework catalysts: synergistic catalysis and tandem reactions. *Chem Soc Rev* **2017,** *46* (1), 126-157.
121. Azarifar, D.; Ghorbani-Vaghei, R.; Daliran, S.; Oveisi, A. R., A Multifunctional Zirconium-Based Metal-Organic Framework for the One-Pot Tandem Photooxidative Passerini Three-Component Reaction of Alcohols. *ChemCatChem* **2017,** *9* (11), 1992-2000.
122. Yang, X.; Xu, Q., Bimetallic Metal–Organic Frameworks for Gas Storage and Separation. *Crys. Growth. Des.* **2017,** *17* (4), 1450-1455.
123. Bae, Y. S.; Snurr, R. Q., Development and evaluation of porous materials for carbon dioxide separation and capture. *Angew. Chem. Int. Ed. Engl.* **2011,** *50* (49), 11586-96.
124. Li, J. R.; Kuppler, R. J.; Zhou, H. C., Selective gas adsorption and separation in metal-organic frameworks. *Chem Soc Rev* **2009,** *38* (5), 1477-504.
125. Schoenecker, P. M.; Carson, C. G.; Jasuja, H.; Flemming, C. J. J.; Walton, K. S., Effect of Water Adsorption on Retention of Structure and Surface Area of Metal–Organic Frameworks. *Ind Eng Chem Res* **2012,** *51* (18), 6513-6519.
126. Kaye, S. S.; Dailly, A.; Yaghi, O. M.; Long, J. R., Impact of preparation and handling on the hydrogen storage properties of Zn4O(1,4-benzenedicarboxylate)3 (MOF-5). *J Am Chem Soc* **2007,** *129* (46), 14176-7.
127. Han, S.; Huang, Y.; Watanabe, T.; Nair, S.; Walton, K. S.; Sholl, D. S.; Carson Meredith, J., MOF stability and gas adsorption as a function of exposure to water, humid air, SO2, and NO2. *Microporous Mesoporous Mater.* **2013,** *173* (0), 86-91.
128. Rowsell, J. L. C.; Yaghi, O. M., Metal–organic frameworks: a new class of porous materials. *Microporous Mesoporous Mater.* **2004,** *73* (1-2), 3-14.
129. Jiang, H.-L.; Makal, T. A.; Zhou, H.-C., Interpenetration control in metal–organic frameworks for functional applications. *Coord. Chem. Rev.* **2013,** *257* (15-16), 2232-2249.
130. Cohen, S. M., The Postsynthetic Renaissance in Porous Solids. *J Am Chem Soc* **2017,** *139* (8), 2855-2863.
131. Jiang, J.; Zhao, Y.; Yaghi, O. M., Covalent Chemistry beyond Molecules. *J Am Chem Soc* **2016,** *138* (10), 3255-65.

132. Jameson, H., Postsynthetic methods in metal-organic framework (MOF) chemistry. *Chem NZ* **2017,** *81*, 112-114.
133. Cohen, S. M., Postsynthetic methods for the functionalization of metal-organic frameworks. *Chem Rev* **2012,** *112* (2), 970-1000.
134. Kim, M.; Cahill, J. F.; Prather, K. A.; Cohen, S. M., Postsynthetic modification at orthogonal reactive sites on mixed, bifunctional metal-organic frameworks. *Chem Commun (Camb)* **2011,** *47* (27), 7629-31.
135. Marshall, R. J.; Forgan, R. S., Postsynthetic Modification of Zirconium Metal-Organic Frameworks. *Eur. J. Inorg. Chem.* **2016,** *2016* (27), 4310-4331.
136. Fracaroli, A. M.; Siman, P.; Nagib, D. A.; Suzuki, M.; Furukawa, H.; Toste, F. D.; Yaghi, O. M., Seven Post-synthetic Covalent Reactions in Tandem Leading to Enzyme-like Complexity within Metal-Organic Framework Crystals. *J Am Chem Soc* **2016,** *138* (27), 8352-5.
137. Denny, M. S.; Moreton, J. C.; Benz, L.; Cohen, S. M., Metal–organic frameworks for membrane-based separations. *Nat Rev Mat* **2016,** *1* (12), 16078.
138. Kokado, K., Network polymers derived from the integration of flexible organic polymers and rigid metal–organic frameworks. *Polym. J.* **2017,** *49* (4), 345-353.
139. Zhang, Y.; Feng, X.; Li, H.; Chen, Y.; Zhao, J.; Wang, S.; Wang, L.; Wang, B., Photoinduced Postsynthetic Polymerization of a Metal–Organic Framework toward a Flexible Stand-Alone Membrane. *Angew. Chem. Int. Ed.* **2015,** *54* (14), 4259-4263.
140. Lee, W. R.; Hwang, S. Y.; Ryu, D. W.; Lim, K. S.; Han, S. S.; Moon, D.; Choi, J.; Hong, C. S., Diamine-functionalized metal–organic framework: exceptionally high CO2capacities from ambient air and flue gas, ultrafast CO2uptake rate, and adsorption mechanism. *Energy Environ. Sci.* **2014,** *7* (2), 744-751.
141. Wickenheisser, M.; Jeremias, F.; Henninger, S. K.; Janiak, C., Grafting of hydrophilic ethylene glycols or ethylenediamine on coordinatively unsaturated metal sites in MIL-100(Cr) for improved water adsorption characteristics. *Inorg. Chim. Acta* **2013,** *407* (0), 145-152.
142. Lee, S. J.; Doussot, C.; Baux, A.; Liu, L.; Jameson, G. B.; Richardson, C.; Pak, J. J.; Trousselet, F.; Coudert, F.-X.; Telfer, S. G., Multicomponent Metal–Organic Frameworks as Defect-Tolerant Materials. *Chem. Mater.* **2015,** *28* (1), 368-375.
143. Szilágyi, P. Á.; Serra-Crespo, P.; Gascon, J.; Geerlings, H.; Dam, B., The Impact of Post-Synthetic Linker Functionalization of MOFs on Methane Storage: The Role of Defects. *Front. Energy Res.* **2016,** *4* (9).
144. De Vos, A.; Hendrickx, K.; Van Der Voort, P.; Van Speybroeck, V.; Lejaeghere, K., Missing Linkers: An Alternative Pathway to UiO-66 Electronic Structure Engineering. *Chem Mater* **2017,** *29* (7), 3006-3019.
145. Fei, H.; Shin, J.; Meng, Y. S.; Adelhardt, M.; Sutter, J.; Meyer, K.; Cohen, S. M., Reusable oxidation catalysis using metal-monocatecholato species in a robust metal-organic framework. *J Am Chem Soc* **2014,** *136* (13), 4965-73.
146. Fei, H.; Cahill, J. F.; Prather, K. A.; Cohen, S. M., Tandem postsynthetic metal ion and ligand exchange in zeolitic imidazolate frameworks. *Inorg Chem* **2013,** *52* (7), 4011-6.
147. Kitaura, R.; Iwahori, F.; Matsuda, R.; Kitagawa, S.; Kubota, Y.; Takata, M.; Kobayashi, T. C., Rational design and crystal structure determination of a 3-D metal-organic jungle-gym-like open framework. *Inorg Chem* **2004,** *43* (21), 6522-4.
148. Li, T.; Kozlowski, M. T.; Doud, E. A.; Blakely, M. N.; Rosi, N. L., Stepwise ligand exchange for the preparation of a family of mesoporous MOFs. *J Am Chem Soc* **2013,** *135* (32), 11688-91.
149. Liu, C.; Zeng, C.; Luo, T. Y.; Merg, A. D.; Jin, R.; Rosi, N. L., Establishing Porosity Gradients within Metal-Organic Frameworks Using Partial Postsynthetic Ligand Exchange. *J Am Chem Soc* **2016,** *138* (37), 12045-8.
150. Gonzalez Miera, G.; Bermejo Gomez, A.; Chupas, P. J.; Martin-Matute, B.; Chapman, K. W.; Platero-Prats, A. E., Topological Transformation of a Metal-Organic Framework Triggered by Ligand Exchange. *Inorg Chem* **2017,** *56* (8), 4577-4584.

151. Liu, T. F.; Zou, L.; Feng, D.; Chen, Y. P.; Fordham, S.; Wang, X.; Liu, Y.; Zhou, H. C., Stepwise synthesis of robust metal-organic frameworks via postsynthetic metathesis and oxidation of metal nodes in a single-crystal to single-crystal transformation. *J Am Chem Soc* **2014,** *136* (22), 7813-6.
152. Deshpande, R. K.; Waterhouse, G. I.; Jameson, G. B.; Telfer, S. G., Photolabile protecting groups in metal-organic frameworks: preventing interpenetration and masking functional groups. *Chem Commun (Camb)* **2012,** *48* (10), 1574-6.
153. Lun, D. J.; Waterhouse, G. I.; Telfer, S. G., A general thermolabile protecting group strategy for organocatalytic metal-organic frameworks. *J Am Chem Soc* **2011,** *133* (15), 5806-9.
154. Ablott, T. A.; Turzer, M.; Telfer, S. G.; Richardson, C., High Temperature Postsynthetic Rearrangement of Dimethylthiocarbamate-Functionalized Metal–Organic Frameworks. *Cryst. Growth. Des.* **2016,** *16* (12), 7067-7073.
155. Lipson, V. V.; Gorobets, N. Y., One hundred years of Meldrum's acid: advances in the synthesis of pyridine and pyrimidine derivatives. *Mol Divers* **2009,** *13* (4), 399-419.
156. Ivanov, A. S., Meldrum's acid and related compounds in the synthesis of natural products and analogs. *Chem Soc Rev* **2008,** *37* (4), 789-811.
157. Janikowska, K.; Rachoń, J.; Makowiec, S., Acyl Meldrum's acid derivatives: application in organic synthesis. *Russ. Chem. Rev.* **2014,** *83* (7), 620-637.
158. Leibfarth, F. A.; Wolffs, M.; Campos, L. M.; Delany, K.; Treat, N.; Kade, M. J.; Moon, B.; Hawker, C. J., Low-temperature ketene formation in materials chemistry through molecular engineering. *Chem. Sci.* **2012,** *3* (3), 766-771.
159. Koukhareva, I.; Lebedev, A., 3'-Protected 2'-deoxynucleoside 5'-triphosphates as a tool for heat-triggered activation of polymerase chain reaction. *Anal. Chem.* **2009,** *81* (12), 4955-62.
160. Chmielewski, M. K.; Tykarska, E.; Markiewicz, W. T.; Rypniewski, W., Engineering N-(2-pyridyl)aminoethyl alcohols as potential precursors of thermolabile protecting groups. *New J. Chem.* **2012,** *36* (3), 603-612.
161. Leibfarth, F. A.; Kang, M.; Ham, M.; Kim, J.; Campos, L. M.; Gupta, N.; Moon, B.; Hawker, C. J., A facile route to ketene-functionalized polymers for general materials applications. *Nat Chem* **2010,** *2* (3), 207-12.
162. Kwon, T.-w.; Jeong, Y. K.; Lee, I.; Kim, T.-S.; Choi, J. W.; Coskun, A., Systematic Molecular-Level Design of Binders Incorporating Meldrum's Acid for Silicon Anodes in Lithium Rechargeable Batteries. *Adv Mater.* **2014,** *26* (47), 7979-7985.
163. Weidong He, W. L., James Dickerson, *Gas Transport in Solid Oxide Fuel Cells*. 1 ed.; Springer International Publishing: 2014; p XIV, 75.
164. Thommes, M.; Kaneko, K.; Neimark Alexander, V.; Olivier James, P.; Rodriguez-Reinoso, F.; Rouquerol, J.; Sing Kenneth, S. W., Physisorption of gases, with special reference to the evaluation of surface area and pore size distribution (IUPAC Technical Report). In *Pure Appl. Chem.*, 2015; Vol. 87, p 1051.
165. Park, J.; Howe, J. D.; Sholl, D. S., How Reproducible Are Isotherm Measurements in Metal–Organic Frameworks? *Chem. Mater.* **2017,** *29* (24), 10487-10495.
166. Lueking, A. D.; Wang, C. Y.; Sircar, S.; Malencia, C.; Wang, H.; Li, J., A generalized adsorption-phase transition model to describe adsorption rates in flexible metal organic framework RPM3-Zn. *Dalton Trans* **2016,** *45* (10), 4242-57.
167. Demuynck, R.; Rogge, S. M. J.; Vanduyfhuys, L.; Wieme, J.; Waroquier, M.; Van Speybroeck, V., Efficient Construction of Free Energy Profiles of Breathing Metal-Organic Frameworks Using Advanced Molecular Dynamics Simulations. *J Chem Theory Comput* **2017,** *13* (12), 5861-5873.
168. Walton, K. S.; Snurr, R. Q., Applicability of the BET method for determining surface areas of microporous metal-organic frameworks. *J Am Chem Soc* **2007,** *129* (27), 8552-6.
169. Lee, J. H.; Jeoung, S.; Chung, Y. G.; Moon, H. R., Elucidation of flexible metal-organic frameworks: Research progresses and recent developments. *Coord. Chem. Rev.* **2019,** *389*, 161-188.
170. Blackwood, S. Thermolabile Protecting Groups in Metal-Organic Frameworks Massey University, 2016.

171. Dau, P. V.; Kim, M.; Garibay, S. J.; Munch, F. H.; Moore, C. E.; Cohen, S. M., Single-atom ligand changes affect breathing in an extended metal-organic framework. *Inorg Chem* **2012,** *51* (10), 5671-6.
172. Ferguson, A.; Liu, L.; Tapperwijn, S. J.; Perl, D.; Coudert, F.-X.; Van Cleuvenbergen, S.; Verbiest, T.; van der Veen, M. A.; Telfer, S. G., Controlled partial interpenetration in metal–organic frameworks. *Nat Chem* **2016,** *8* (3), 250-257.
173. Liu, L.; Telfer, S. G., Systematic ligand modulation enhances the moisture stability and gas sorption characteristics of quaternary metal-organic frameworks. *J Am Chem Soc* **2015,** *137* (11), 3901-9.
174. Dau, P. V.; Cohen, S. M., The influence of nitro groups on the topology and gas sorption property of extended Zn(ii)-paddlewheel MOFs. *CrystEngComm* **2013,** *15* (45), 9304.
175. Bryant, M. R.; Ablott, T. A.; Telfer, S. G.; Liu, L.; Richardson, C., High temperature expulsion of thermolabile groups for pore-space expansion in metal–organic frameworks. *CrystEngComm* **2019,** *21* (1), 60-64.
176. Jasuja, H.; Walton, K. S., Effect of catenation and basicity of pillared ligands on the water stability of MOFs. *Dalton Trans* **2013,** *42* (43), 15421-6.
177. Henke, S.; Schneemann, A.; Wutscher, A.; Fischer, R. A., Directing the breathing behavior of pillared-layered metal-organic frameworks via a systematic library of functionalized linkers bearing flexible substituents. *J Am Chem Soc* **2012,** *134* (22), 9464-74.
178. Witkowska, A.; Krygier, D.; Brzezinska, J.; Chmielewski, M. K., Modulating the Stability of 2-Pyridinyl Thermolabile Hydroxyl Protecting Groups via the "Chemical Switch" Approach. *J Org Chem* **2015,** *80* (24), 12129-36.
179. Aggarwal, H.; Das, R. K.; Bhatt, P. M.; Barbour, L. J., Isolation of a structural intermediate during switching of degree of interpenetration in a metal-organic framework. *Chem Sci* **2015,** *6* (8), 4986-4992.
180. Shivanna, M.; Yang, Q. Y.; Bajpai, A.; Sen, S.; Hosono, N.; Kusaka, S.; Pham, T.; Forrest, K. A.; Space, B.; Kitagawa, S.; Zaworotko, M. J., Readily accessible shape-memory effect in a porous interpenetrated coordination network. *Sci Adv* **2018,** *4* (4), eaaq1636.
181. Ardila-Suárez, C.; Perez-Beltran, S.; Ramírez-Caballero, G. E.; Balbuena, P. B., Enhanced acidity of defective MOF-808: effects of the activation process and missing linker defects. *Catal Sci Tech* **2018,** *8* (3), 847-857.
182. Ma, J.; Kalenak, A. P.; Wong-Foy, A. G.; Matzger, A. J., Rapid Guest Exchange and Ultra-Low Surface Tension Solvents Optimize Metal–Organic Framework Activation. *Angew Chem* **2017**.
183. Howarth, A. J.; Peters, A. W.; Vermeulen, N. A.; Wang, T. C.; Hupp, J. T.; Farha, O. K., Best Practices for the Synthesis, Activation, and Characterization of Metal–Organic Frameworks. *Chem. Mater.* **2016,** *29* (1), 26-39.
184. Sircar, S.; Wu, H.; Li, J.; Lueking, A. D., Effect of time, temperature, and kinetics on the hysteretic adsorption-desorption of H2, Ar, and N2 in the metal-organic framework Zn2(bpdc)2(bpee). *Langmuir* **2011,** *27* (23), 14169-79.
185. Park, I., Adsorption Hysteresis Dynamics. In *Seventh International Conference on Fundamentals of Adsorption*, Nagasaki, Japan, 2001.
186. Zhang, X.; Chen, W.; Shi, W.; Cheng, P., Highly selective sorption of CO2 and N2O and strong gas-framework interactions in a nickel(ii) organic material. *J Mat Chem A* **2016,** *4* (41), 16198-16204.
187. Bhattacharya, B.; Haldar, R.; Maity, D. K.; Maji, T. K.; Ghoshal, D., Pillared-bilayer porous coordination polymers of Zn(ii): enhanced hydrophobicity of pore surface by changing the pillar functionality. *CrystEngComm* **2015,** *17* (18), 3478-3486.
188. Bury, W.; Fairen-Jimenez, D.; Lalonde, M. B.; Snurr, R. Q.; Farha, O. K.; Hupp, J. T., Control over Catenation in Pillared Paddlewheel Metal–Organic Framework Materials via Solvent-Assisted Linker Exchange. *Chem. Mater.* **2013,** *25* (5), 739-744.
189. Lalonde, M.; Bury, W.; Karagiaridi, O.; Brown, Z.; Hupp, J. T.; Farha, O. K., Transmetalation: routes to metal exchange within metal–organic frameworks. *J Mat Chem A* **2013,** *1* (18), 5453.

190. Ortiz, A. U.; Boutin, A.; Fuchs, A. H.; Coudert, F. X., Metal–Organic Frameworks with Wine-Rack Motif: What Determines Their Flexibility and Elastic Properties? *J. Chem. Phys.* **2013,** *138*, 174703.
191. Kim, K. C.; Yoon, T.-U.; Bae, Y.-S., Applicability of using CO2 adsorption isotherms to determine BET surface areas of microporous materials. *Microporous Mesoporous Mater.* **2016,** *224*, 294-301.
192. Dybtsev, D. N.; Chun, H.; Kim, K., Rigid and flexible: a highly porous metal-organic framework with unusual guest-dependent dynamic behavior. *Angew. Chem. Int. Ed. Engl.* **2004,** *43* (38), 5033-6.
193. Lama, P.; Das, R. K.; Smith, V. J.; Barbour, L. J., A combined stretching-tilting mechanism produces negative, zero and positive linear thermal expansion in a semi-flexible Cd(II)-MOF. *Chem Commun (Camb)* **2014,** *50* (49), 6464-7.
194. Rigaku *2DP*, Rigaku: 2011.
195. Yang, D.; Odoh, S. O.; Wang, T. C.; Farha, O. K.; Hupp, J. T.; Cramer, C. J.; Gagliardi, L.; Gates, B. C., *J. Am. Chem. Soc.* **2015,** *137*, 7391.
196. Sheldrick, G. M., A short history of SHELX. *Acta Crystallogr A* **2008,** *64* (Pt 1), 112-22.
197. A.L.Spek, *Acta Cryst.* **2009,** *D65*.
198. Wannapaiboon, S.; Schneemann, A.; Hante, I.; Tu, M.; Epp, K.; Semrau, A. L.; Sternemann, C.; Paulus, M.; Baxter, S. J.; Kieslich, G.; Fischer, R. A., Control of structural flexibility of layered-pillared metal-organic frameworks anchored at surfaces. *Nat Commun* **2019,** *10* (1), 346.
199. Bhattacharya, B.; Saha, D.; Maity, D. K.; Dey, R.; Ghoshal, D., Syntheses, X-ray structures, gas adsorption and luminescent properties of three coordination polymers of Zn(ii) dicarboxylates mixed with a linear, neutral, and rigid N,N′-donor ligand. *CrystEngComm* **2014,** *16* (22), 4783-4795.
200. Ferguson, A.; Liu, L.; Tapperwijn, S. J.; Perl, D.; Coudert, F. X.; Van Cleuvenbergen, S.; Verbiest, T.; van der Veen, M. A.; Telfer, S. G., *Nat. Chem.* **2016,** *8*, 250.
201. Yang, H.; Guo, F.; Lama, P.; Gao, W. Y.; Wu, H.; Barbour, L. J.; Zhou, W.; Zhang, J.; Aguila, B.; Ma, S., Visualizing Structural Transformation and Guest Binding in a Flexible Metal-Organic Framework under High Pressure and Room Temperature. *ACS Cent Sci* **2018,** *4* (9), 1194-1200.
202. Tseng, T.-W.; Luo, T.-T.; Tsai, C.-C.; Lu, K.-L., A huge diamondoid metal–organic framework with a neo-mode of tenfold interpenetration. *CrystEngComm* **2015,** *17* (15), 2935-2939.
203. Chen, Y.; Wang, X.-C.; Yang, Q.; Xu, Y.-C.; Tong, J.-T.; Yuan, H.; Xiao, D.-R., Four novel coordination frameworks with high degree of diamondoid interpenetration containing scarce quadruple-stranded homo-axis helices and quintuple-stranded molecular braids. *Inorg Chim Acta* **2016,** *448*, 42-50.
204. Guo, X.-M.; Yan, Y.-N.; Guo, H.-d.; Wang, N., The construction of two novel interpenetrating diamondoid networks presenting unusual [3 + 2] and [4 + 4] modes. *Inorg Chem Comm* **2015,** *61*, 105-108.
205. Aggarwal, H.; Das, R. K.; Engel, E. R.; Barbour, L. J., A five-fold interpenetrated metal-organic framework showing a large variation in thermal expansion behaviour owing to dramatic structural transformation upon dehydration-rehydration. *Chem Commun (Camb)* **2017,** *53* (5), 861-864.
206. Xiong, S.; Liu, Q.; Wang, Q.; Li, W.; Tang, Y.; Wang, X.; Hu, S.; Chen, B., A flexible zinc tetrazolate framework exhibiting breathing behaviour on xenon adsorption and selective adsorption of xenon over other noble gases. *J Mat Chem A* **2015,** *3* (20), 10747-10752.
207. Yang, Q. Y.; Lama, P.; Sen, S.; Lusi, M.; Chen, K. J.; Gao, W. Y.; Shivanna, M.; Pham, T.; Hosono, N.; Kusaka, S.; Perry, J. J. t.; Ma, S.; Space, B.; Barbour, L. J.; Kitagawa, S.; Zaworotko, M. J., Reversible Switching between Highly Porous and Nonporous Phases of an Interpenetrated Diamondoid Coordination Network That Exhibits Gate-Opening at Methane Storage Pressures. *Angew Chem Int Ed Engl* **2018,** *57* (20), 5684-5689.
208. Aggarwal, H.; Lama, P.; Barbour, L. J., Transformation from non- to double-interpenetration in robust Cd(II) doubly-pillared-layered metal-organic frameworks. *Chem Commun (Camb)* **2014,** *50* (93), 14543-6.
209. Aggarwal, H.; Bhatt, P. M.; Bezuidenhout, C. X.; Barbour, L. J., *J Am Chem Soc* **2014,** *136*, 3776.

210. Lama, P.; Barbour, L. J., Distinctive Three-Step Hysteretic Sorption of Ethane with In Situ Crystallographic Visualization of the Pore Forms in a Soft Porous Crystal. *J Am Chem Soc* **2018,** *140* (6), 2145-2150.
211. Calle, M.; Lee, Y. M., Thermally Rearranged (TR) Poly(ether−benzoxazole) Membranes for Gas Separation. *Macromolecules* **2011,** *44* (5), 1156-1165.
212. Pourkhosravani, M.; Dehghanpour, S.; Farzaneh, F.; Sohrabi, S., Designing new catalytic nanoreactors for the regioselective epoxidation of geraniol by the post-synthetic immobilization of oxovanadium(IV) complexes on a ZrIV-based metal–organic framework. *React Kinet, Mech Cat* **2017,** *122* (2), 961-981.
213. Bauer, G.; Ongari, D.; Xu, X.; Tiana, D.; Smit, B.; Ranocchiari, M., Metal-Organic Frameworks Invert Molecular Reactivity: Lewis Acidic Phosphonium Zwitterions Catalyze the Aldol-Tishchenko Reaction. *J Am Chem Soc* **2017,** *139* (50), 18166-18169.
214. Bhattacharjee, S.; Khan, M.; Li, X.; Zhu, Q.-L.; Wu, X.-T., *Recent Progress in Asymmetric Catalysis and Chromatographic Separation by Chiral Metal–Organic Frameworks*. 2018; Vol. 8, p 120.
215. Gotthardt, M. A.; Grosjean, S.; Brunner, T. S.; Kotzel, J.; Ganzler, A. M.; Wolf, S.; Brase, S.; Kleist, W., Synthesis and post-synthetic modification of amine-, alkyne-, azide- and nitro-functionalized metal-organic frameworks based on DUT-5. *Dalton Trans* **2015,** *44* (38), 16802-9.
216. Bryant, M. R.; Burrows, A. D.; Kepert, C. J.; Southon, P. D.; Qazvini, O. T.; Telfer, S. G.; Richardson, C., Mixed-Component Sulfone–Sulfoxide Tagged Zinc IRMOFs: In Situ Ligand Oxidation, Carbon Dioxide, and Water Sorption Studies. *Cryst Growth Des* **2017,** *17* (4), 2016-2023.
217. Leus, K.; Perez, J. P. H.; Folens, K.; Meledina, M.; Van Tendeloo, G.; Du Laing, G.; Van Der Voort, P., UiO-66-(SH)2 as stable, selective and regenerable adsorbent for the removal of mercury from water under environmentally-relevant conditions. *Faraday Discuss.* **2017,** *201* (0), 145-161.
218. Johnson, J. A.; Chen, S.; Reeson, T. C.; Chen, Y. S.; Zeng, X. C.; Zhang, J., Direct X-Ray Observation of Trapped Co2 in a Predesigned Porphyrinic Metal–Organic Framework. *Chem. - Eur. J.* **2014,** *20*, 7632.
219. Zhang, Z.; Zhang, L.; Wojtas, L.; Nugent, P.; Eddaoudi, M.; Zaworotko, M. J., Templated synthesis, postsynthetic metal exchange, and properties of a porphyrin-encapsulating metal-organic material. *J Am Chem Soc* **2012,** *134* (2), 924-7.
220. De, D.; Pal, T. K.; Bharadwaj, P. K., A Porous Cu(II)-MOF with Proline Embellished Cavity: Cooperative Catalysis for the Baylis-Hillman Reaction. *Inorg Chem* **2016,** *55* (14), 6842-4.
221. Gui, B.; Meng, X.; Xu, H.; Wang, C., Postsynthetic Modification of Metal-Organic Frameworks through Click Chemistry. *Chin. J. Chem .* **2016,** *34* (2), 186-190.
222. Tuci, G.; Rossin, A.; Xu, X.; Ranocchiari, M.; van Bokhoven, J. A.; Luconi, L.; Manet, I.; Melucci, M.; Giambastiani, G., "Click" on MOFs: A Versatile Tool for the Multimodal Derivatization of N3-Decorated Metal Organic Frameworks. *Chem. Mater.* **2013,** *25* (11), 2297-2308.
223. Seth, S.; Savitha, G.; Moorthy, J. N., Diverse isostructural MOFs by postsynthetic metal node metathesis: anionic-to-cationic framework conversion, luminescence and separation of dyes. *J Mat Chem A* **2015,** *3* (45), 22915-22922.
224. Noori, Y.; Akhbari, K., Post-synthetic ion-exchange process in nanoporous metal–organic frameworks; an effective way for modulating their structures and properties. *RSC Advances* **2017,** *7* (4), 1782-1808.
225. Allen, A. D.; Tidwell, T. T., New Directions in Ketene Chemistry: The Land of Opportunity. *Eur. J. Org. Chem.* **2012,** *2012* (6), 1081-1096.
226. Allen, A. D.; Tidwell, T. T., Ketenes and other cumulenes as reactive intermediates. *Chem Rev* **2013,** *113* (9), 7287-342.
227. George, L.; Wong, M. W.; Wentrup, C., Carboxyketenes, methyleneketenes, vinylketenes, oxetanediones, ynols, and ylidic ketenes from Meldrum's acid derivatives. *Org Biomol Chem* **2007,** *5* (9), 1437-41.
228. Fillion, E.; Fishlock, D., Scandium triflate-catalyzed intramolecular Friedel–Crafts acylation with Meldrum's acids: insight into the mechanism. *Tetrahedron* **2009,** *65* (33), 6682-6695.

229. Maraval, V.; Chauvin, R., Carbo-mers: from skeleton to function. *New J. Chem.* **2007,** *31* (11), 1853.
230. Fillion, E.; Wilsily, A.; Fishlock, D., Probing persistent intramolecular C-H...X (X = O, S, Br, Cl, and F) bonding in solution using benzyl Meldrum's acid derivatives. *J Org Chem* **2009,** *74* (3), 1259-67.
231. Ramachary, D. B.; Chowdari, N. S.; Barbas, C. F., 3rd, Organocatalytic asymmetric domino knoevenagel/diels-alder reactions: a bioorganic approach to the diastereospecific and enantioselective construction of highly substituted spiro[5,5]undecane-1,5,9-triones. *Angew. Chem. Int. Ed. Engl.* **2003,** *42* (35), 4233-7.
232. Yamada, T.; Kitagawa, H., Protection and deprotection approach for the introduction of functional groups into metal-organic frameworks. *J Am Chem Soc* **2009,** *131* (18), 6312-3.
233. Hahm, H.; Ha, H.; Kim, S.; Jung, B.; Park, M. H.; Kim, Y.; Heo, J.; Kim, M., Synthesis of secondary and tertiary amine-containing MOFs: C–N bond cleavage during MOF synthesis. *CrystEngComm* **2015,** *17* (30), 5644-5650.
234. Nateghi, B.; Boldog, I.; Domasevitch, K. V.; Janiak, C., More versatility than thought: large {Zr26} oxocarboxylate cluster by corner-sharing of standard octahedral subunits. *CrystEngComm* **2018,** *20* (35), 5132-5136.
235. Sun, Q.; Liu, C.; Zhang, G.; Zhang, J.; Tung, C. H.; Wang, Y., Aqueous Isolation of 17-Nuclear Zr/Hf Oxide Clusters during the Hydrothermal Synthesis of ZrO2 /HfO2. *Chemistry* **2018,** *24* (55), 14701-14706.
236. Cheng, W.; Shen, F.-C.; Xue, Y.-s.; Luo, X.; Fang, M.; Lan, Y.-Q.; Xu, Y., A Pair of Rare Three-Dimensional Chiral Polyoxometalate-Based Metal–Organic Framework Enantiomers Featuring Superior Performance as the Anode of Lithium-Ion Battery. *ACS Applied Energy Materials* **2018,** *1* (9), 4931-4938.
237. Sapianik, A. A.; Zorina-Tikhonova, E. N.; Kiskin, M. A.; Samsonenko, D. G.; Kovalenko, K. A.; Sidorov, A. A.; Eremenko, I. L.; Dybtsev, D. N.; Blake, A. J.; Argent, S. P.; Schroder, M.; Fedin, V. P., Rational Synthesis and Investigation of Porous Metal-Organic Framework Materials from a Preorganized Heterometallic Carboxylate Building Block. *Inorg Chem* **2017,** *56* (3), 1599-1608.
238. Karagiaridi, O.; Bury, W.; Mondloch, J. E.; Hupp, J. T.; Farha, O. K., Solvent-assisted linker exchange: an alternative to the de novo synthesis of unattainable metal-organic frameworks. *Angew. Chem. Int. Ed. Engl.* **2014,** *53* (18), 4530-40.
239. Samanta, D.; Chowdhury, A.; Mukherjee, P. S., Covalent Postassembly Modification and Water Adsorption of Pd3 Self-Assembled Trinuclear Barrels. *Inorg Chem* **2016,** *55* (4), 1562-8.
240. Kim, D.; Whang, D. R.; Park, S. Y., Self-Healing of Molecular Catalyst and Photosensitizer on Metal-Organic Framework: Robust Molecular System for Photocatalytic H2 Evolution from Water. *J Am Chem Soc* **2016,** *138* (28), 8698-701.
241. Muller, K.; Vankova, N.; Schottner, L.; Heine, T.; Heinke, L., Dissolving uptake-hindering surface defects in metal-organic frameworks. *Chem Sci* **2019,** *10* (1), 153-160.
242. Chen, Z.; Wang, G.; Xu, Z.; Li, H.; Dhotel, A.; Zeng, X. C.; Chen, B.; Saiter, J. M.; Tan, L., Metal-organic frameworks capable of healing at low temperatures. *Adv. Mater.* **2013,** *25* (42), 6106-11.
243. Hosono, N.; Kitagawa, S., Modular Design of Porous Soft Materials via Self-Organization of Metal-Organic Cages. *Acc Chem Res* **2018,** *51* (10), 2437-2446.
244. Cai, Y.; Chen, D.; Li, N.; Xu, Q.; Li, H.; He, J.; Lu, J., Superhydrophobic Metal–Organic Framework Membrane with Self-Repairing for High-Efficiency Oil/Water Emulsion Separation. *ACS Sust Chem Eng* **2018,** *7* (2), 2709-2717.
245. Zhang, G.; Xie, G.; Si, L.; Wen, S.; Guo, D., Ultralow Friction Self-Lubricating Nanocomposites with Mesoporous Metal-Organic Frameworks as Smart Nanocontainers for Lubricants. *ACS Appl Mater Interfaces* **2017,** *9* (43), 38146-38152.
246. Shchukin, D. G.; Mohwald, H., Self-repairing coatings containing active nanoreservoirs. *Small* **2007,** *3* (6), 926-43.
247. Wang, L.; Advani, S. G.; Prasad, A. K., Self-Healing Composite Membrane for Proton Electrolyte Membrane Fuel Cell Applications. *J Electrochem Soc* **2016,** *163* (10), F1267-F1271.

248. Sung, S.; Kim, S. Y.; Lee, T. H.; Favaro, G.; Park, Y. I.; Lee, S.-H.; Ahn, J. B.; Noh, S. M.; Kim, J. C., Thermally reversible polymer networks for scratch resistance and scratch healing in automotive clear coats. *Prog. Org. Coat.* **2019,** *127*, 37-44.
249. Gorsche, C.; Schnoell, C.; Koch, T.; Moszner, N.; Liska, R., Debonding on Demand with Highly Cross-Linked Photopolymers: A Combination of Network Regulation and Thermally Induced Gas Formation. *Macromolecules* **2018,** *51* (3), 660-669.
250. Nayab, S.; Trouillet, V.; Gliemann, H.; Hurrle, S.; Weidler, P. G.; Rashid Tariq, S.; Goldmann, A. S.; Barner-Kowollik, C.; Yameen, B., Chemically reprogrammable metal organic frameworks (MOFs) based on Diels-Alder chemistry. *Chem Commun (Camb)* **2017,** *53* (83), 11461-11464.
251. Yao, B. J.; Jiang, W. L.; Dong, Y.; Liu, Z. X.; Dong, Y. B., Post-Synthetic Polymerization of UiO-66-NH2 Nanoparticles and Polyurethane Oligomer toward Stand-Alone Membranes for Dye Removal and Separation. *Chemistry* **2016,** *22* (30), 10565-71.
252. Zechel, S.; Geitner, R.; Abend, M.; Siegmann, M.; Enke, M.; Kuhl, N.; Klein, M.; Vitz, J.; Gräfe, S.; Dietzek, B.; Schmitt, M.; Popp, J.; Schubert, U. S.; Hager, M. D., Intrinsic self-healing polymers with a high E-modulus based on dynamic reversible urea bonds. *Npg Asia Materials* **2017,** *9*, e420.
253. Wang, Z.; Gangarapu, S.; Escorihuela, J.; Fei, G.; Zuilhof, H.; Xia, H., Dynamic covalent urea bonds and their potential for development of self-healing polymer materials. *J Mat Chem A* **2019,** *7* (26), 15933-15943.
254. Alegre-Requena, J. V.; Marqués-López, E.; Herrera, R. P.; Díaz, D. D., Metal–organic frameworks (MOFs) bring new life to hydrogen-bonding organocatalysts in confined spaces. *CrystEngComm* **2016,** *18* (22), 3985-3995.
255. Kuhl, N.; Abend, M.; Geitner, R.; Vitz, J.; Zechel, S.; Schmitt, M.; Popp, J.; Schubert, U. S.; Hager, M. D., Urethanes as reversible covalent moieties in self-healing polymers. *Eur. Polym. J.* **2018,** *104*, 45-50.
256. Fulton, D. A., Synthesis: Click chemistry gets reversible. *Nat Chem* **2016,** *8* (10), 899-900.
257. Ishibashi, J. S. A.; Kalow, J. A., Vitrimeric Silicone Elastomers Enabled by Dynamic Meldrum's Acid-Derived Cross-Links. *ACS Macro Letters* **2018,** *7* (4), 482-486.
258. Ulrich, S.; Hemmer, J. R.; Page, Z. A.; Dolinski, N. D.; Rifaie-Graham, O.; Bruns, N.; Hawker, C. J.; Boesel, L. F.; Read de Alaniz, J., Visible Light-Responsive DASA-Polymer Conjugates. *ACS Macro Letters* **2017,** *6* (7), 738-742.
259. Lerch, M. M.; Szymanski, W.; Feringa, B. L., The (photo)chemistry of Stenhouse photoswitches: guiding principles and system design. *Chem Soc Rev* **2018,** *47* (6), 1910-1937.
260. Medishetty, R.; Park, I. H.; Lee, S. S.; Vittal, J. J., Solid-state polymerisation via [2+2] cycloaddition reaction involving coordination polymers. *Chem Commun (Camb)* **2016,** *52* (21), 3989-4001.
261. Kwon, T. W.; Choi, J. W.; Coskun, A., The emerging era of supramolecular polymeric binders in silicon anodes. *Chem Soc Rev* **2018,** *47* (6), 2145-2164.
262. Kwon, O.; Kim, J. Y.; Park, S.; Lee, J. H.; Ha, J.; Park, H.; Moon, H. R.; Kim, J., Computer-aided discovery of connected metal-organic frameworks. *Nat Commun* **2019,** *10* (1), 3620.

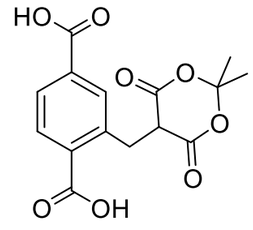

bdc-Meldrums

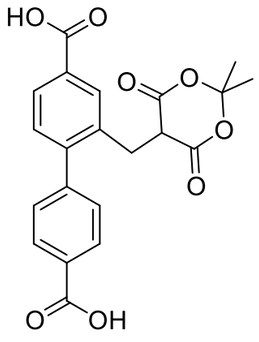

bpdc-Meldrums

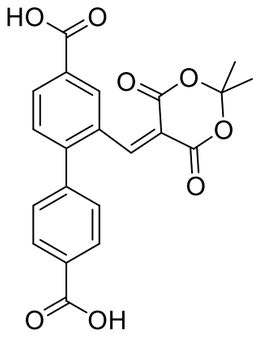

bpdc-CHMeldrums

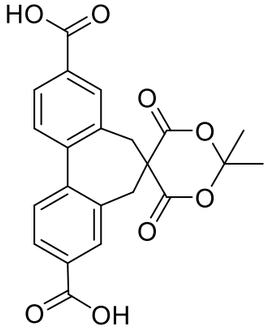

bpdc-symMeldrums

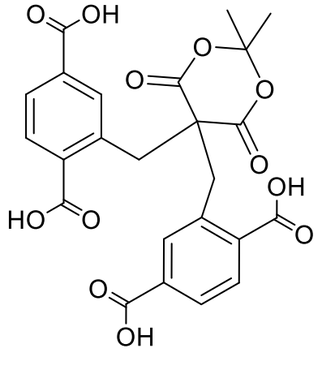

$(bdc)_2$-bisMeldrums

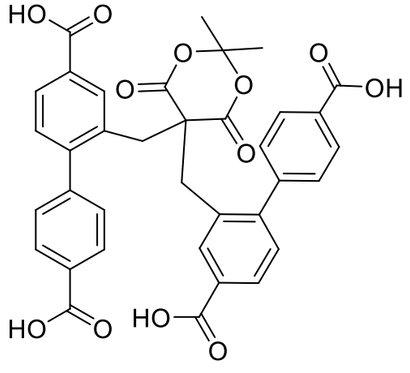

$(bpdc)_2$-bisMeldrums

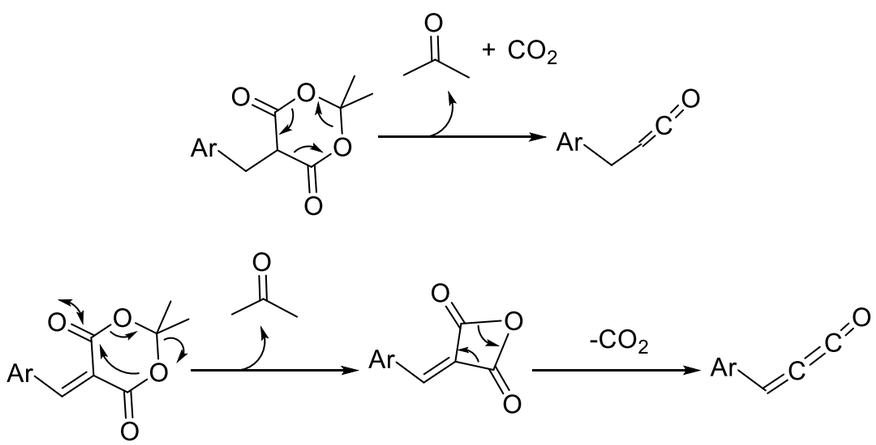

Malonic anhydride/oxetanedione

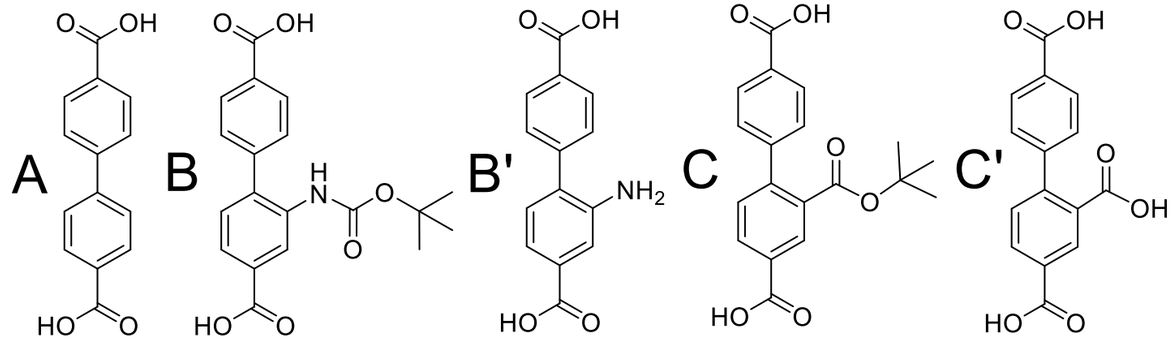

bpdc | bpdc-NHBoc | bpdc-NH_2 | bpdc-TBE | bpdc-CO_2H

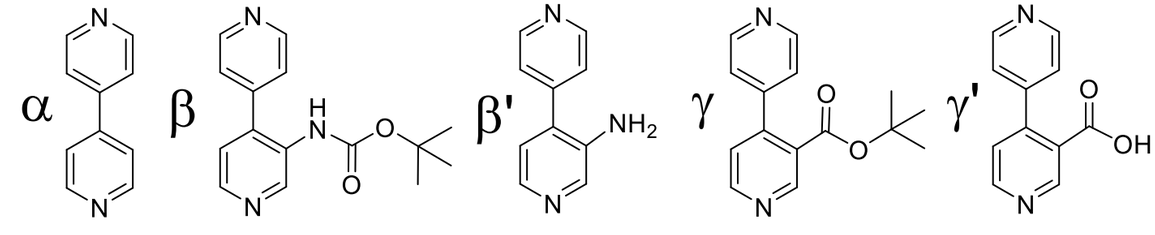

bpy | bpy-NHBoc | bpy-NH_2 | bpy-TBE | bpy-CO_2H

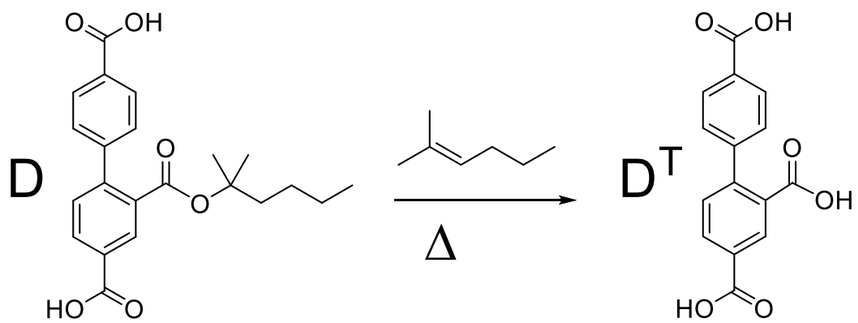

bpdc-2mh | bpdc-CO_2H

MOF	Bpdc	Bpy	Space group	$\Delta T_{1/2}$ (°C)	Cell Vol. (Å^3)	density
MUF20-Aα			*P*-1	*NA*	3159.2	0.805
MUF20-Aα-dia			*Cc*	*NA*	2428.3	1.263
MUF20-Aβ			*P*-1	140	3152.5	0.93
MUF20-Aβ^T			*NA*	*NA*	*NA*	*NA*
MUF20-Aβ`			*P*-1	*NA*	3165.9	0.821
MUF20-Aγ			*P*-1	150	3185.1	0.905
MUF20-Aγ^T			*NA*	*NA*	*NA*	*NA*
MUF20-Aγ (MeOH-loss)			*P2$_1$/c*	-	6318.7	0.912
MUF20-Bα			*P*-1	180	3137.5	0.912
MUF20-B^{T}α			*NA*	*NA*	*NA*	*NA*
MUF20-B`α-dis			*P*-1	*NA*	3232.1	1.335
MUF20-B`α-dia			*P*-1	*NA*	6570.0	0.964
MUF20-B`β			*Pbca*	145	6514.7	1.207
MUF20-B`β`			*C 2/c*	*NA*	13529	1.027
MUF20-B`γ			*P*-1	145	3196.6	0.932
MUF20-Cα			*P*-1	160	3112.2	1.004
MUF20-Cβ			*P 2$_1$/c*	145, 225	6293.7	1.143
MUF20-Cβ`			*P*-1	155	3132.8	0.935
MUF20-Cγ			*P 2$_1$/c*	170, 225	6274.3	1.024
MUF20-Dα			*P*-1	165	3168.9	1.102
MUF20-D^{T}α			*P*-1	*NA*	2648.8	1.072
MUF20-Dβ			*C 2/c*	195	12938.1	1.198

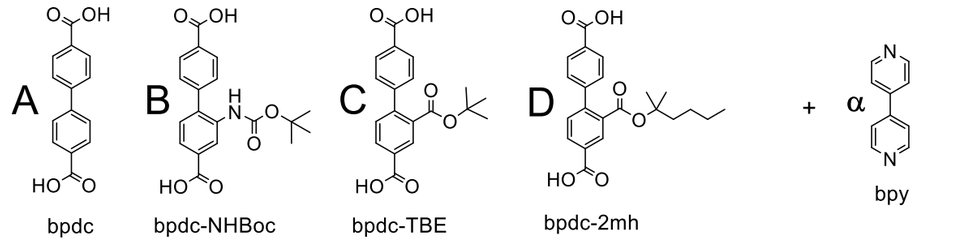

A 2-fold interpenetrated pillar-layer MOF is formed by:
Ligands A, B, C, or D combined with α, as well as by B` and γ

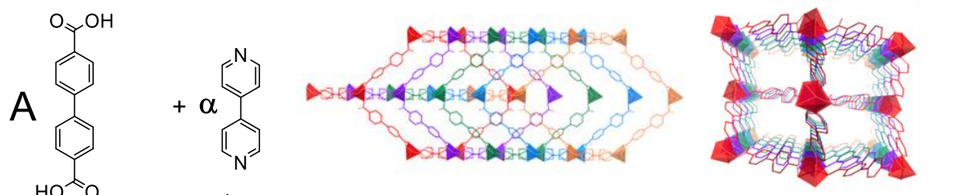

Ligands A and α also form a 5-fold interpenetrated diamondoid MOF with 1D pores

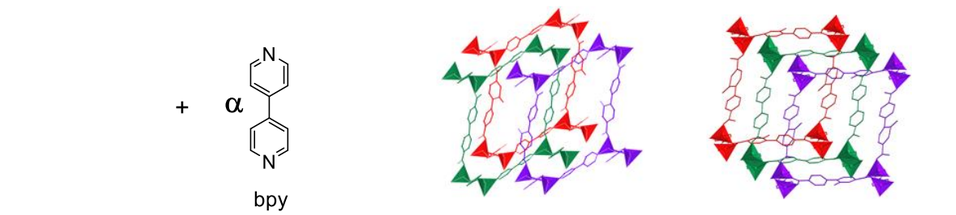

Ligands B` and α form a 3-fold interpenetrated pillar-layer type MOF with distorted SBU

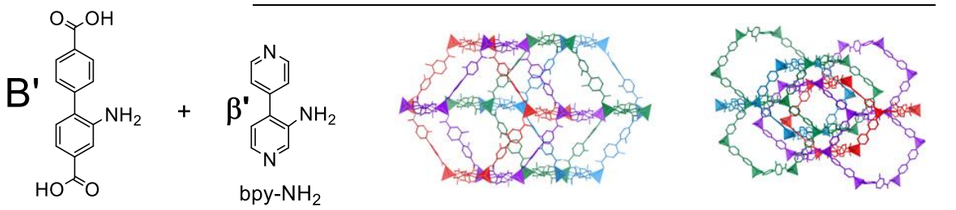

Ligands B` and β` form a 4-fold interpenetrated diamondoid MOF

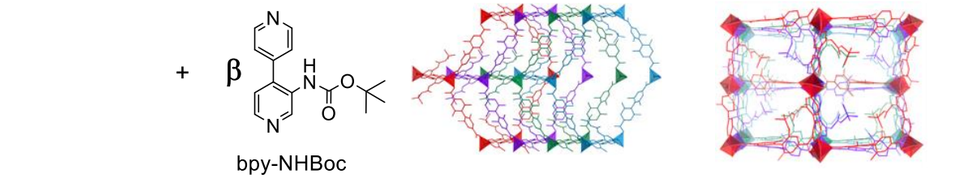

Ligands B` and β form a 4-fold interpenetrated diamondoid MOF with 1D pores

Appendix for:

Interior Decoration of Metal-Organic Frameworks through a Thermolabile Protecting Group Strategy

Heather Taylor Jameson[a]

a) MacDiarmid Institute for Advanced Materials and Nanotechnology, Institute of Fundamental Sciences, Massey University, Palmerston North, New Zealand.

Table of Contents

1. Selection of MUF20 MOF thermolysis trials Chapters 2 and 3

1.1. Trials towards *in situ* thermolysis on gas sorption activation port

Table 1.1: Solvent-free thermolysis conditions explored

Method	MOF	Temp. (°C)	Time (hrs)	PXRD	^{1}H NMR
Under Atmosphere on TGA	Aβ	150	170 min	Crystalline	0.17 : 1, TBE:CO_2H
	Aβ*	160	3	Marginal	Bpy-NH_2
	Aγ*	160	3	Marginal	Bpy-CO_2H
	Cα	115	20	Crystalline	Bpdc-TBE
	Cα	125	20	Crystalline	Bpdc -TBE
	Cα	135	20	Mostly Crystalline	1 : 0.6, TBE :CO_2H
	Cα	140	10	Mostly Crystalline	1 : 1, TBE : CO_2H
	Cα	140	20	Marginal	0.25 : 1, TBE : CO_2H
	Cα	143	15	Crystalline	0.33 : 1, TBE : CO_2H
	Cα	145	20	Amorphous	0.04 : 1, TBE : CO_2H
	Cα	150	5	Crystalline	0.9 : 1, TBE : CO_2H
	Cα	160	1.25	Crystalline	1 : 0.4, TBE : CO_2H
	Cα	160	3	Marginal	0.18 : 1, TBE:CO_2H
	Cα	230	Ramp	Amorphous	Bpdc -CO_2H
	Cβ	230	Ramp	Amorphous	Bpdc -CO_2H
	Cγ	208	Ramp	Amorphous	Bpdc -CO_2H
	Bα	256	Ramp	Diffuse scattering	Bpdc-NH_2(2%Boc)
	Bα	200	70 min	Amorphous	0.27 : 1, Boc : NH_2
	B'γ	205	Ramp	Marginal	Bpy-CO_2H
In oil bath under vacuum	Cα	80	10	Crystalline	Bpdc-TBE
	Cα	160	3	Crystalline	1 : 0.12, TBE:CO_2H
	Cα	160	6	Crystalline	1 : 0.23, TBE:CO_2H
	Cα	160	14	Crystalline	0.55 : 1, TBE:CO_2H
	Cα	175	12	Marginal	0.27 : 1, TBE : CO_2H
	Cα	180	10	Amorphous	BPDC-CO_2H
In oil bath under Argon	Cα	160	8	Crystalline	1 : 0.34, TBE : CO_2H
	Cα	160	16	Crystalline	0.33 : 1, TBE : CO_2H
	Cα	175	14	Marginal	0.13 : 1, TBE : CO_2H

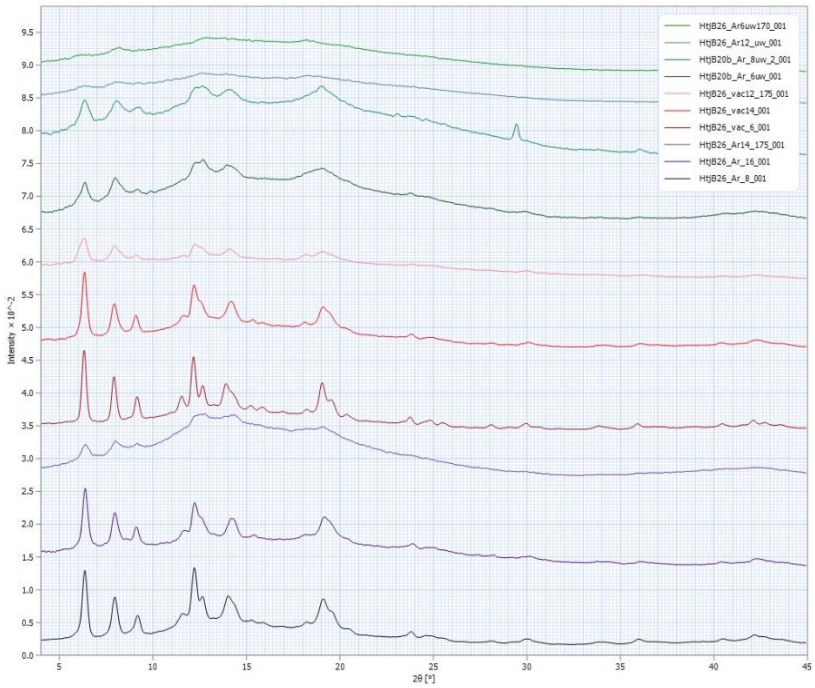

Figure 1.1: PXRD analysis of relevant thermolysis trials.

1.2. Trials towards separate thermolysis

In 15 mL microwave vessel using approx. 2 mg material, dry, under argon or in 1 mL listed solvent.

Table 1.2: Separate thermolysis conditions explored

Framework Used	Temperature (°C)	Time (hrs)	Solvent	PXRD	^{1}H NMR
Cα	160	3	DBF	Marginal	0.07:1,TBE:CO_2H
Cα	160	3.5	DBF	Marginal	BPDC-CO_2H
Cα	160	3	Dioxane	Marginal	1 : 1, TBE : CO_2H
Cα	160	3	Toluene	Crystalline	1 : 0.3,TBE:CO_2H
Cα	165	6	Toluene	Marginal	1 : 1, TBE : CO_2H
Cα	160	3	Argon	Crystalline	1 : 0.4,TBE:CO_2H
Cα	160	6	Argon	Marginal	0.16:1,TBE:CO_2H
Cα	160	8	Argon	Marginal	0.17:1,TBE:CO_2H
Cα	160	12	Argon	Amorphous	0.14:1,TBE:CO_2H
Cα	170	6	Argon	Amorphous	0.16:1,TBE:CO_2H
Cα	160	3	Atmosphere	Amorphous	BPDC-CO_2H
Cβ	160	3	EG	Amorphous	BPDC-CO_2H
Cβ	160	3	DMF	Amorphous	BPDC-CO_2H*
Cγ	160	3	DMF	Amorphous	BPDC-CO_2H*
Cβ	135	3	Atmosphere	MostlyCrystalline	1 : 0.2,TBE:CO_2H
Cβ	150	3	Atmosphere	MostlyCrystalline	1 : 0.5,TBE:CO_2H
Cβ	155	3	Atmosphere	Amorphous	0.1 : 1,TBE:CO_2H
Cβ	155	6	Atmosphere	Amorphous	0.1 : 1,TBE:CO_2H
Cβ	157	3	Atmosphere	Amorphous	BPDC-CO_2H

*MUF20-Cβ and MUF20-Cγ sensitive selectively to DMF over DBF for bpy removal

During thermolysis trials almost complete removal of bpy from the framework during heating with DMF occurred for the MIF20-Cβ and MUF20-Cγ frameworks. Bpy loss did not occur in DBF trials, possibly due to steric bulk of the solvent hindering diffusion and coordination to zinc.

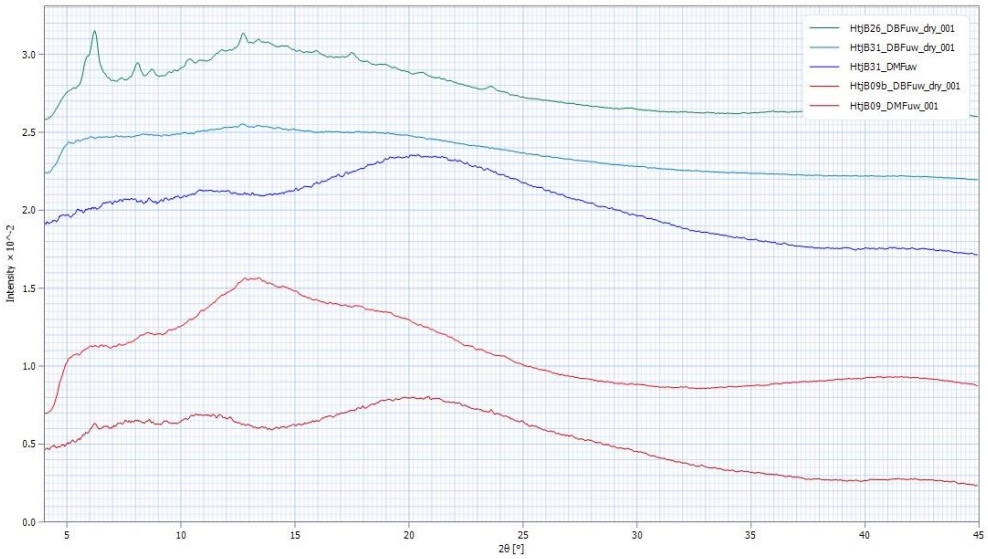

Figure 1.2: PXRD analysis of relevant thermolysis trials.

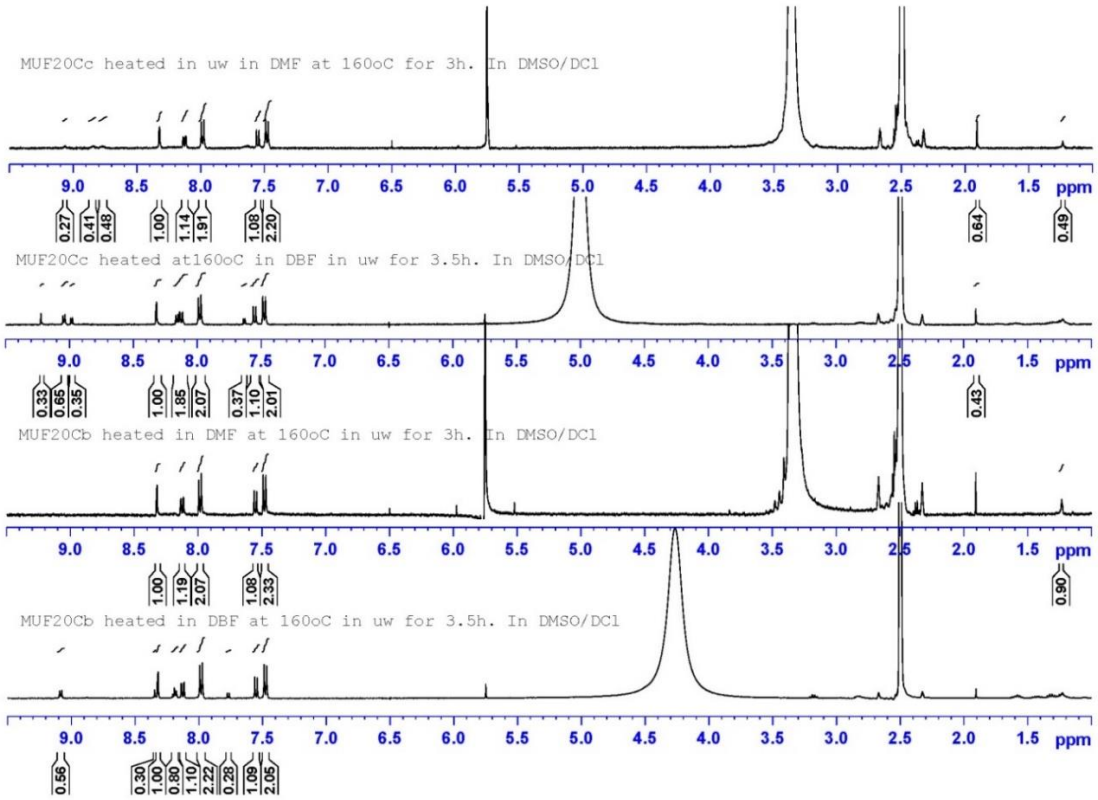

Figure 1.3: NMR analysis of relevant thermolysis trials.

1.3. Best thermolysis conditions for MUF20-Cα

Table 1.3: Separate thermolysis conditions explored

Temperature (°C)	Time (hrs)	Solvent	PXRD	^{1}H NMR
160	14	Vacuum	Crystalline	0.55 : 1, TBE : CO_2H
175	12	Vacuum	Marginally Crystalline	0.27 : 1, TBE : CO_2H
160	3	DBF	Marginally Crystalline	0.07 : 1, TBE : CO_2H
160	3.5	DBF	Marginally Crystalline	BPDC-CO_2H
160	3	Toluene	Crystalline	1 : 0.3, TBE : CO_2H
165	6	Toluene	Marginally Crystalline	1 : 1, TBE : CO_2H

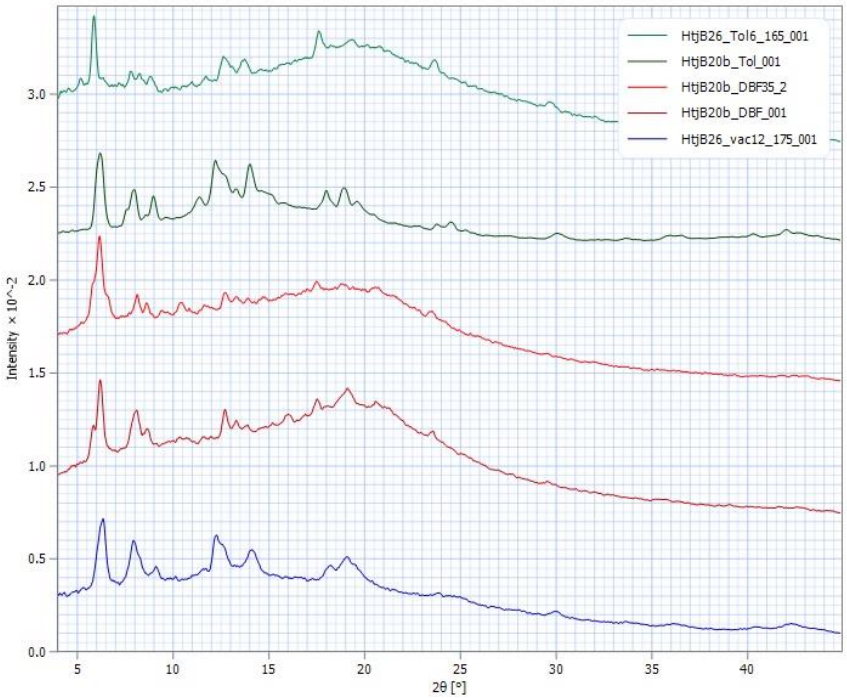

Figure 1.4: PXRD analysis of relevant thermolysis trials.

Attempts to apply the DBF thermolysis procedure to MUF20-Cβ and MUF20-Cγ failed, while the TPG is completely gone so is any crystallinity – see above for DMF vs DBF thermolysis of MUF20-Cβ and MUF20-Cγ.

2. Chapter 2 –Mono-functionalized pillar-layer (PLMOFs) SI

2.1. Ligand synthesis and characterization

General procedures

All starting compounds and solvents were used as received from commercial sources of reagent grade or higher and deionised water used in all cases unless otherwise noted. Column chromatography was carried out on silica gel (grade 60, mesh size 230-400, Scharlau). Unless specified otherwise, all NMR spectra were recorded at room temperature. NMR analysis was performed on Bruker-400 and Bruker-500 Avance instruments, with the use of the solvent proton as an internal standard. IR spectra were collected on a Thermo Scientific Nicolet 5700 FT-IR spectrophotometer equipped with an attenuated total reflection (ATR) module (Smart Omni sampler, Ge crystal). Spectra were measured at a resolution of 4 cm^{-1}. Elemental analyses were performed by the Campbell Microanalytical Laboratory at the University of Otago, New Zealand. Thermogravimetric analysis (TGA) was performed on a TA Instruments Q50 instrument.

2.1.1. Initial synthesis steps to bpdc-TBE and synthesis of bpdc-2mh

a) 2-Methylbiphenyl-4,4`-dicarboxylic acid

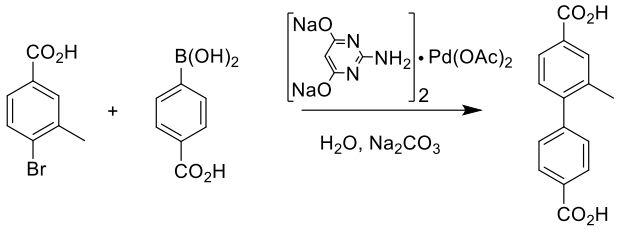

Pd Catalyst Solution (0.25 mM)

Palladium(II) acetate (5.7 mg, 25 μmol) and 2-amino-4,6-dihydroxypyrimidine (6.4 mg, 50 μmol) were combined in a 50 mL conical flask. 4.02 mL of a solution of NaOH (0.0995 g, 2.49 mmol in 100 mL MQ H_2O) was then added and the mixture stirred at 60 ^oC until a clear, dark yellow solution formed. The solution was then allowed to cool to room temperature before transferring, with washing, into a 100 mL volumetric flask and made up with MQ H_2O.

2-Methylbiphenyl-4,4`-dicarboxylic acid synthesis (optimised from literature procedure)

Commercially available 4-carboxyphenylboronic acid (500 mg, 3.01 mmol) and 4-bromo-3-methylbenzoic acid (454 mg, 2.11 mmol) were combined in a conical flask. A solution of Na_2CO_3 (860 mg, 8.11 mmol) in MQ H_2O (16.25 mL) was added and the mixture heated with vigorous stirring to 70 ^oC, forming a clear yellow solution. 1.075 mL of the 0.25 mM Pd^{II} catalyst solution above was added at this temperature and the reaction

stirred under atmosphere for 2 hrs. After significant precipitation the reaction was quenched by placing on ice, acidified to pH 2.0 with 1 M HCl and the pink solid collected via suction filtration, washing thoroughly with H_2O, before drying under high vacuum overnight (540 mg, quant. yield). ^{1}H NMR (500 MHz, DMSO-d_6) δ 8.02 (d, *J* = 8.3 Hz, 2H), 7.89 (s, 1H), 7.83 (dd, *J* = 7.9, 1.3 Hz, 1H), 7.50 (d, *J* = 8.3 Hz, 2H), 7.35 (d, *J* = 7.9 Hz, 1H), 2.28 (s, 3H) ppm.

b) Dimethyl 2-methylbiphenyl-4,4`-dicarboxylate

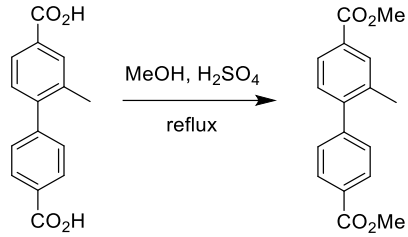

2-Methylbiphenyl-4,4`-dicarboxylic acid (5.66 g, 22.1 mmol) was suspended in CH_3OH (540 mL) and conc. H_2SO_4 (4.03 mL) added. The reaction mix was then heated at 82 ^{o}C overnight. The clear, orange solution was concentrated *in vacuo* at 40 ^{o}C until precipitation occurred before cooling in a -20 ^{o}C freezer for 30 min. Cold H_2O was added until no further precipitation was observed and the pink/orange solid was collected by suction filtration, washed with cold H_2O, and further dried under high vacuum overnight to afford a fine pink/white powder (6.28 g, 95%). ^{1}H NMR (500 MHz, $CDCl_3$) δ 8.11 (d, *J* = 8.2 Hz, 2H), 7.97 (s, 1H), 7.91 (d, *J* = 8.0 Hz, 1H), 7.40 (d, *J* = 8.2 Hz, 2H), 7.29 (d, *J* = 7.9 Hz, 1H), 3.96 (s, 3H), 3.94 (s, 3H)), 2.30 (s, 3H) ppm.

c) Dimethyl 2-(dibromomethyl)biphenyl-4,4`-dicarboxylate

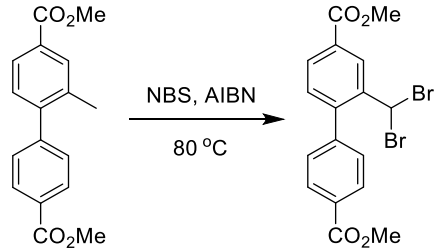

Dimethyl 2-methylbiphenyl-4,4`-dicarboxylate (6.27 g, 22.1 mmol) was dissolved in dry benzene (375 mL) before the addition of *N*-bromosuccinimide (NBS) (9.84 g, 55.3 mmol) and azobisisobutyronitrile (AIBN) (1.49 g, 9.08 mmol). The stirring white suspension was then placed under Ar(g) and heated at 82 °C for 12 hrs. Additional *N*-bromosuccinimide (2.52 g, 14.1 mmol) and AIBN (372 mg, 2.27 mmol) were added, and the reaction stirred at 85 °C for 5 hours before the final addition of *N*-bromosuccinimide (2.43 g, 13.6 mmol) and AIBN (307 mg, 1.87 mmol) and stirring overnight at 85 ^{o}C. Solvent was removed *in vacuo* and the orange white solid was recrystallized from boiling ethyl acetate or CH_2Cl_2. Yellow crystals were collected *via* decanting, rinsing with crystallization solvent. Sequential recrystallizations of decanted solvent yielded further product (8.76 g, 90-98%). ^{1}H NMR (500 MHz, $CDCl_3$) δ 8.76 (d, *J* = 1.6 Hz, 1H), 8.17 (dd, *J* = 8.3, 1.7 Hz, 2H), 8.01

(dd, *J* = 8.0, 1.7 Hz, 1H), 7.46 (dd, *J* = 8.4, 1.8 Hz, 2H), 7.24 (d, *J* = 8.0 Hz, 1H), 6.56 (s, 1H), 3.99 (s, 3H), 3.97 (s, 3H) ppm.

d) Dimethyl 2-formylbiphenyl-4,4`-dicarboxylate

– Central starting material for ligands bpdc-2mh, bpdc-TBE, bpdc-CHMeldrums, and bpdc-Meldrums

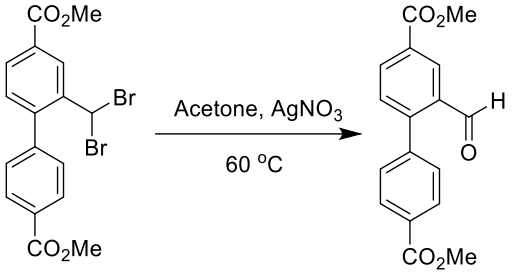

Dimethyl 2-(dibromomethyl)biphenyl-4,4`-dicarboxylate (3.76 g, 8.50 mmol) was dissolved in acetone (150 mL) and heated to 70 °C with stirring. Next, $AgNO_3$ (3.61 g, 21.3 mmol) in H_2O (35 mL) was heated to 70 °C and added dropwise over 20 min, giving a milky reaction mix. After stirring for 2 hours, the solid was removed by hot filtration, and the filtrate concentrated in volume to ~80 mL. 50 mL of H_2O was added to the filtrate and the product extracted with ethyl acetate (3 x 70 mL), dried over Na_2SO_4, filtered, and the solvent removed *in vacuo* to afford a white solid (2.70 g, 106%). Highly pure product could be obtained by recrystallization from boiling ethyl acetate (81%). ^{1}H NMR (500 MHz, $CDCl_3$) δ 9.98 (s, 1H), 8.69 (s, 1H), 8.32 (d, *J* = 8.0 Hz, 1H), 8.17 (d, *J* = 8.1 Hz, 2H), 7.55 (d, *J* = 8.0 Hz, 1H), 7.48 (d, *J* = 8.1 Hz, 2H), 3.99 (s, 3H), 3.97 (s, 3H) ppm.

e) Dimethyl 2-carboxylic acid biphenyl-4,4`-dicarboxylate

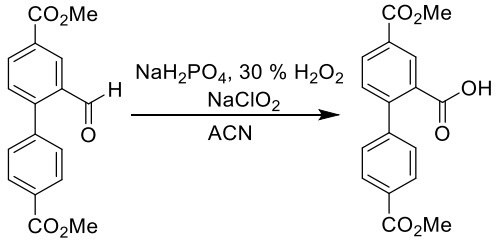

Dimethyl 2-formylbiphenyl-4,4`-dicarboxylate (4.30 g, 14.4 mmol) was semi-suspended in ACN (140 mL) before the addition of NaH_2PO_4 (870 mg, 7.25 mmol) in H_2O (15 mL) and 30% H_2O_2 (2.42 mL). After cooling on ice, 80% $NaClO_2$ (2.28 g, 25.2 mmol) in H_2O (60 mL) was added dropwise over 20 minutes with vigorous stirring. The reaction mix was then stirred at room temperature for 9 hours, then at 30 °C overnight. After cooling on ice, the reaction was quenched with $Na_2S_2O_3.5H_2O$, then acidified with 3 M HCl to pH ~2.0. The product was then extracted with ethyl acetate (4 x 60 mL), dried over Na_2SO_4, filtered, and the solvent removed

in vacuo to afford an off-white solid. This was then suspended in MQ H_2O and sonicated for 30 min. Off-white solid was then collected, washed with H_2O and dried under high vacuum (4.20 g, 92%). ^{1}H NMR (500 MHz, $CDCl_3$) δ 8.63 (d, *J* = 1.6 Hz, 1H), 8.22 (dd, *J* = 8.0, 1.8 Hz, 1H), 8.07 (dd, *J* = 8.5, 1.8 Hz, 2H), 7.43 (d, *J* = 8.0 Hz, 1H), 7.40 (dd, *J* = 8.4, 1.8 Hz, 2H), 3.96 (s, 3H), 3.94 (s, 3H) ppm.

f) Dimethyl 2-((2-methylhexan-2-yloxy)carbonyl)biphenyl-4,4'-dicarboxylate

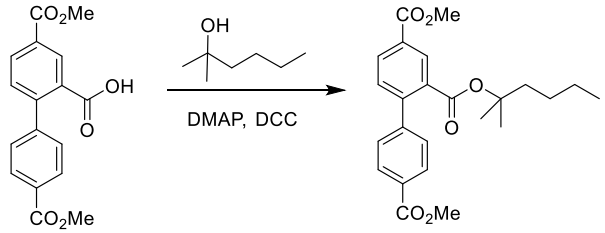

Dimethyl 2-carboxylic acid biphenyl-4,4'-dicarboxylate (1.08 g, 3.44 mmol) was suspended in dry CH_2Cl_2 (20 mL) and DMF (1 mL) added to solubilise. DMAP (504 mg, 4.12 mmol) and 2-methyl-2-hexanol (1.23 mL, 8.59 mmol) was added and the reaction mix cooled on ice with stirring. Next, DCC (851 mg, 4.12 mmol) was added and the reaction mix stirred on ice for 10 minutes, then at room temperature over 2 days. The solid was removed by filtering through a celite pad rinsing with CH_2Cl_2, and the filtrate was concentred *in vacuo*. The residue was then purified by silica flash chromatography (CH_2Cl_2/hexane), affording a pale yellow oil (1.08 g, 76%). ^{1}H NMR: (500Mz, $CDCl_3$): δ 0.84 (t, *J* = 7.4 Hz, 3H), 1.03 (m, 2H), 1.18 (m, 2H), 1.31 (s, 6H), 1.51 (m, 2H), 3.95 (s, 3H), 3.96 (s, 3H), 7.40 (dd, *J* = 8.2, 2.3 Hz, 2H), 7.56 (d, *J* = 8.1 Hz, 1H), 8.08 (dt, *J* = 8.4, 1.9 Hz, 2H), 8.15 (dd, *J* = 8.2, 1.8 Hz, 1H), 8.45 (d, *J* = 1.8 Hz, 1H), ppm.

g) 2-((2-methylhexan-2-yloxy)carbonyl)biphenyl-4,4'-dicarboxylic acid

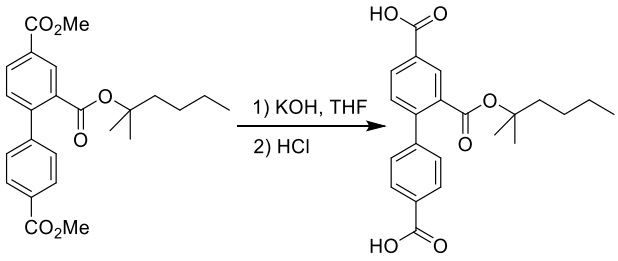

Dimethyl 2-((2-methylhexan-2-yloxy)carbonyl)biphenyl-4,4'-dicarboxylate (1.07 g, 2.59 mmol) was dissolved in THF (15 mL) with stirring before the addition of 1 M NaOH (23 mL), and the 2-phase reaction mix was then stirred at room temperature for 18 hours. The THF was removed *in vacuo*, and the aqueous reaction mix cooled on ice and acidified with 1 M HCl to pH 2.0. The resulting white precipitate was collected by filtration, washed with H_2O, and then dried under vacuum to afford a white powder (926 mg, 93%). ^{1}H NMR: (500 MHz, DMSO-d_6): δ 0.77 (t, *J* = 7.3 Hz, 3H), 0.90 (m, 2H), 1.10 (m, 2H), 1.27 (s, 6H), 1.4 (m, 2H), 7.46 (dd, *J* = 6.5, 2.0 Hz, 2H), 7.55 (d, *J* = 8.0 Hz, 1H), 8.01 (dd, 6.5, 2.0 Hz, 2H), 8.13 (dd, *J* = 8.0, 1.8 Hz, 1H), 8.24 (d, *J* = 1.8 Hz, 1H).

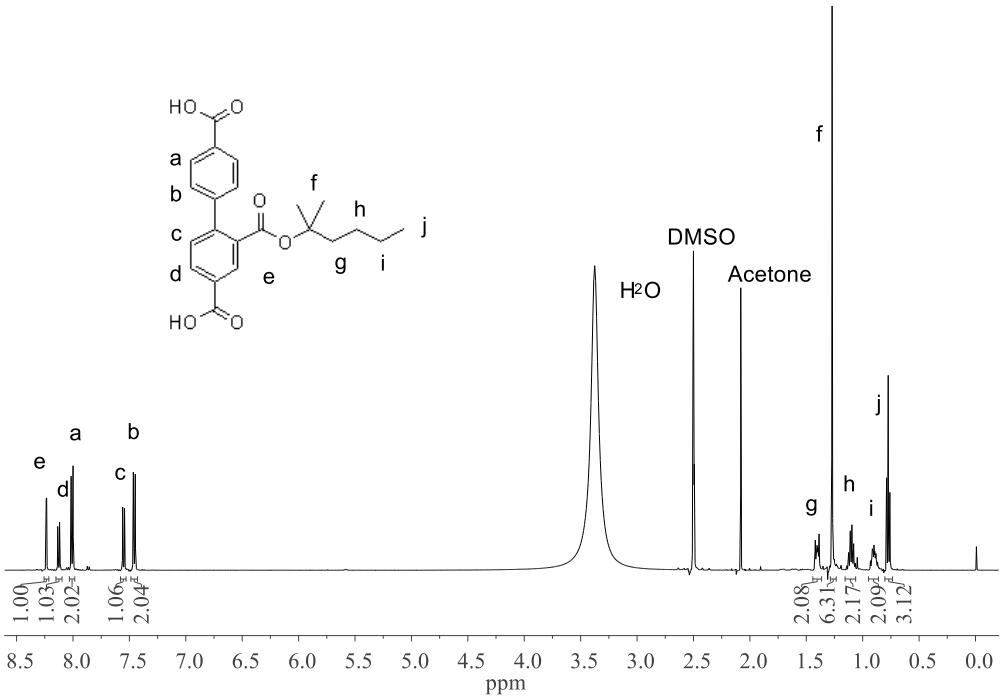

Figure 2.1: ^{1}H NMR spectrum of bpdc-2mh in DMSO-d_6.

2.1.2. TGA percentage weight loss coordinates for MUF20 TPG ligands

Table 2.1: TGA coordinates used for MUF20 TPG ligands (temperature, weight loss (%))

Bpy-NHBoc (β)		
Point	T1	T2
Coordinates	95.7, 96.5	171.1, 62.8
Bpy-TBE (γ)		
Point	T1	T2
Coordinates	67.4, 100.0	210.5, 34.1
Bpdc-NHBoc (B)		
Point	T1	T2
Coordinates	55.4, 99.8	245.3, 70.8
Bpdc-TBE (C)		
Point	T1	T2
Coordinates	99.9, 99.5	232.3, 81.7
Bpdc-2mh (D)		
Point	Point	Point
Coordinates	107.3, 99.5	214.7, 72.1

2.2. MOF synthesis and characterization

General procedures

All starting compounds and solvents were used as received from commercial sources of reagent grade or higher and MilliQ water used in all cases unless otherwise noted. Unless specified otherwise, all NMR spectra were recorded at room temperature. NMR analysis was performed on Bruker-400 and Bruker-500 Avance instruments, with the use of the solvent proton as an internal standard. Elemental analyses were performed by the Campbell Microanalytical Laboratory at the University of Otago, New Zealand. Thermogravimetric analysis (TGA) was performed on a TA Q50 instrument.

^{1}H NMR analysis of digested MUF20 and MUF-77 MOF samples

For ^{1}H NMR spectroscopy, the mother liquor of the as-synthesized MOF crystals was replaced with fresh dry DMF multiple times, followed by repeated washing and subsequent soaking in dry CH_2Cl_2 for several hours. The excess CH_2Cl_2 was then decanted and the samples placed under vacuum overnight to remove residual solvent from the pores. The crystals were then digested using the following protocol: 23 µL of a 35% DCl solution in D_2O was mixed with 1 mL of DMSO-d_6 to give a DCl/DMSO-d_6 stock solution. Around 5 mg of MOF was digested in 150 µL of this stock solution together with 480 µL of DMSO-d_6. Spectra were acquired immediately following dissolution.

Thermogravimetric Analysis (TGA)

Thermogravimetric analyses were performed on a TA Instruments Q50 instrument. Freshly prepared MOF samples were prepared as for gas sorption except that the CH_2Cl_2 was removed using a benchtop vacuum pump and were placed under vacuum for 4- 12 hours. Samples were then transferred to an aluminium sample pan and then measurements were commenced under an N_2 flow with a heating rate of 5 °C /min.

Powder X-ray diffraction patterns

All powder X-ray diffraction experiments were carried out on a Rigaku Spider X-ray diffractometer with Cu K_α radiation (Rigaku MM007 microfocus rotating-anode generator), monochromated and focused with high-flux Osmic multilayer mirror optics, and a curved image plate detector. The data were obtained from freshly prepared MOF samples that had been ground into slurry in a small amount of DMF, DEF or DBF and kept damp with solvent throughout the measurement. The two-dimensional images of the Debye rings were integrated with 2DP[1] (Version 1.0.3.4) to give 2θ vs I diffractograms. The predicted powder patterns were generated from their single-crystal structures using Mercury v4.10.

Gas adsorption measurements

Low pressure adsorption isotherms were measured by a volumetric method using a Quantachrome Autosorb-iQ instrument. Freshly prepared MOF samples were washed with DMF and then activated by repeated washing and subsequent soaking in CH_2Cl_2 for several hours over the course of several days. The samples were then transferred to a pre-dried and weighed analysis tube, still covered with CH_2Cl_2. The sample tube was then heated at 1 ºC per minute to 30 ºC under vacuum then held under a dynamic vacuum at 10^{-6} Torr for 12 h. Accurate sample masses were calculated using degassed samples. All adsorption measurements used ultra-high purity gases.

2.2.1. MUF20 and direct analogues MOF synthesis

Non-isolatable or amorphous direct synthesis MUF20 MOFs

a) MUF20-Aγ`

Single crystal quality crystals were absent in all synthesis trialed.

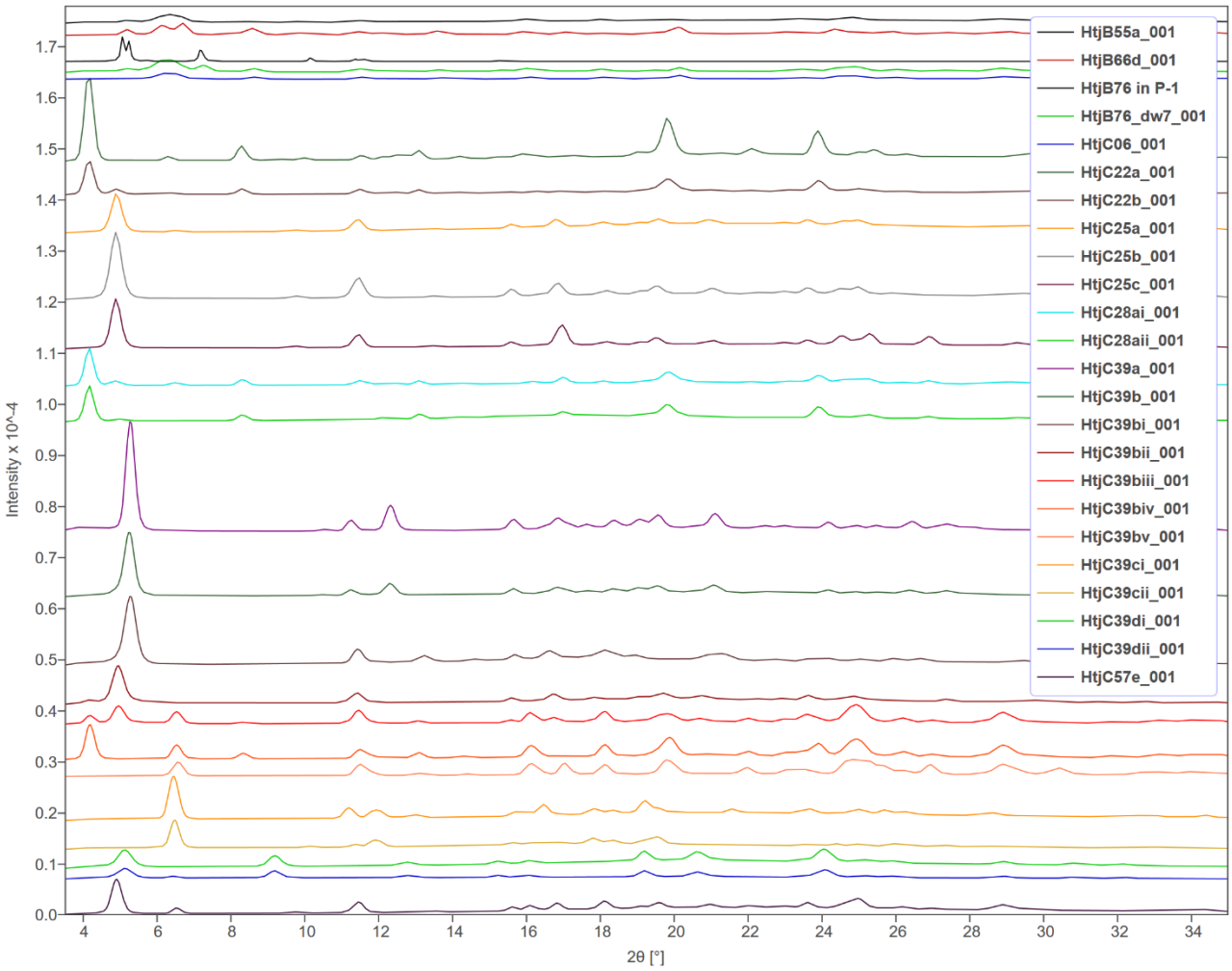

Figure 2.2: Experimental PXRD of attempted MUF20-Aγ` synthesis.

Phase-pure PXRD synthesis conditions yielded varying NMR ratios despite consistent washing.

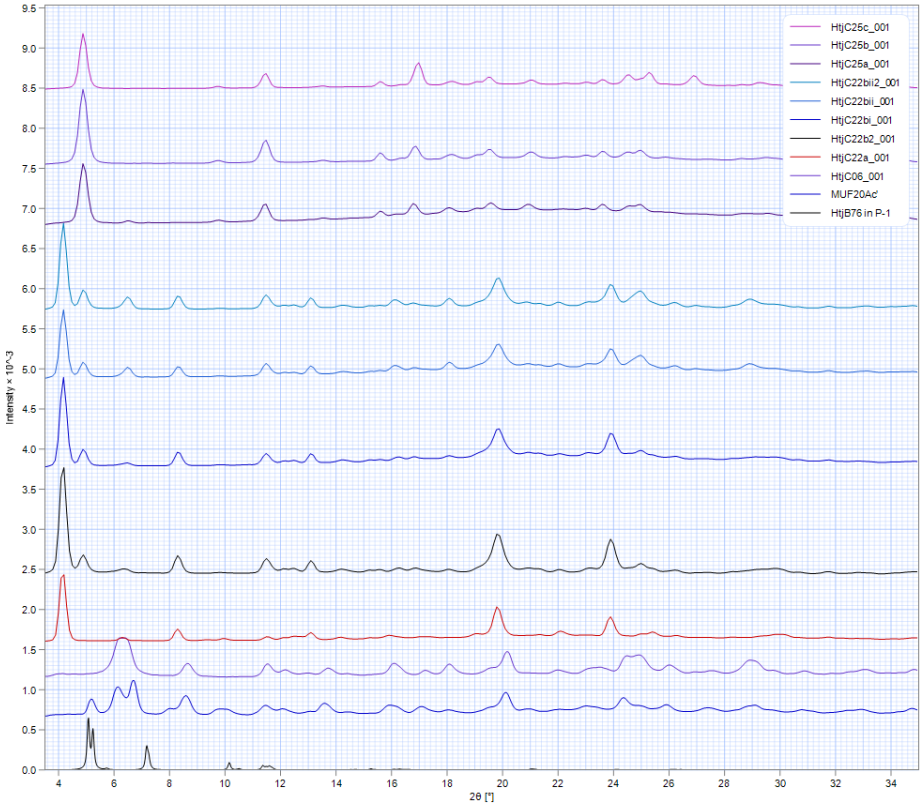

Figure 2.3: Experimental PXRD of phase-pure MUF20-Aγ` synthesis.

When the NMR are normalized by bpy-CO_2H ligand content, the change in relative ligand ratios for the same PXRD is easily visualized. This suggests either a material resistant to washing (microcrystalline microporous powders) or a materials tolerant of potential defect sites. There was no clear trend on what causes the ligand ratio to change.

NMR analysis:

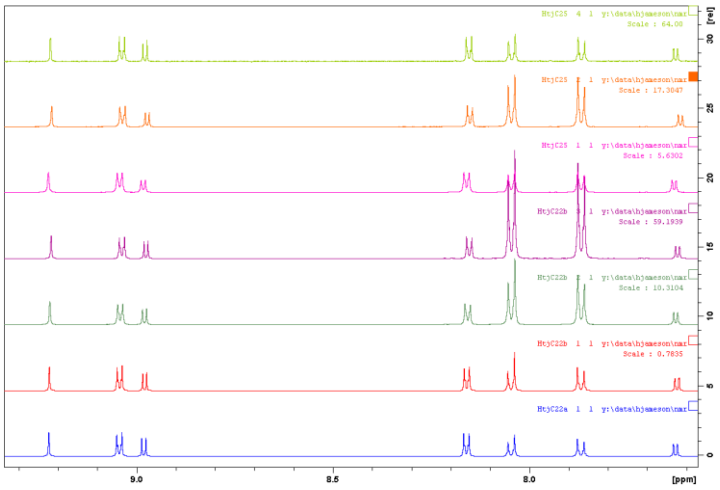

Figure 2.4: ^{1}H NMR analysis of phase-pure MUF20-Aγ` synthesis.

b) MUF20-C`α

Single crystal could not be obtained. Phase-pure PXRD synthesis samples had varying NMR ratios despite consistent washing.

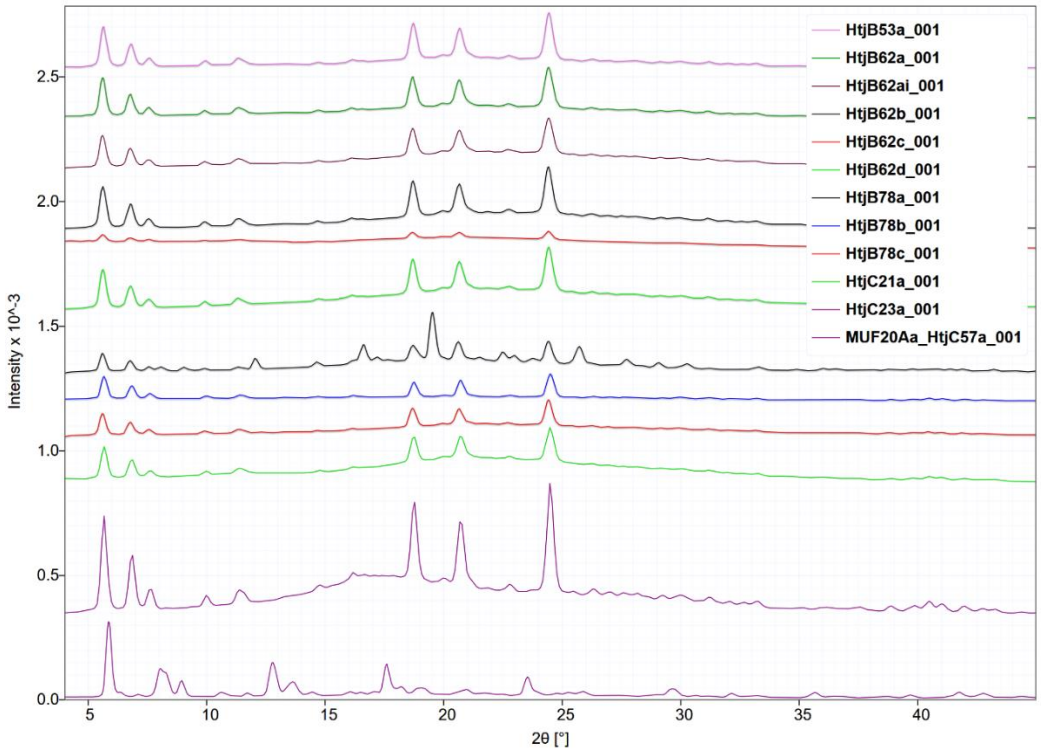

Figure 2.5: Experimental PXRD of MUF20-Aα and attempted MUF20-C`α synthesis.

2.3. TGA percentage weight loss coordinates for MUF20 MOFs Chapters 2

Table 2.2: Loop TGA coordinates (temperature, weight (%))

MUF20-Bα (Experimental 21.2%)			
Point	T1	T2	T3
Coordinates	104.8, 99.4	251.4, 78.1	N/A
MUF20-Cα (Experimental 12.3%)			
Point	T1	T2	T3
Coordinates	92.5, 97.8	232.9, 85.4	N/A
MUF20-Aγ (Experimental 7 %)			
Point	T1	T2	T3
Coordinates	84.5, 99.0	210.7, 87.8	N/A

Table 2.3: TGA coordinates (temperature, weight (%))

MUF20-Aβ (Experimental 12.0%)		
Point	T1	T2
Coordinates	82.3, 99.2	199.5, 87.2
MUF20-Dα (Experimental 17.4 %)		
Point	T1	T2
Coordinates	78.7, 97.9	251.7, 80.5

2.4. Gas sorption characterization

2.4.1. Gas sorption isotherm trials

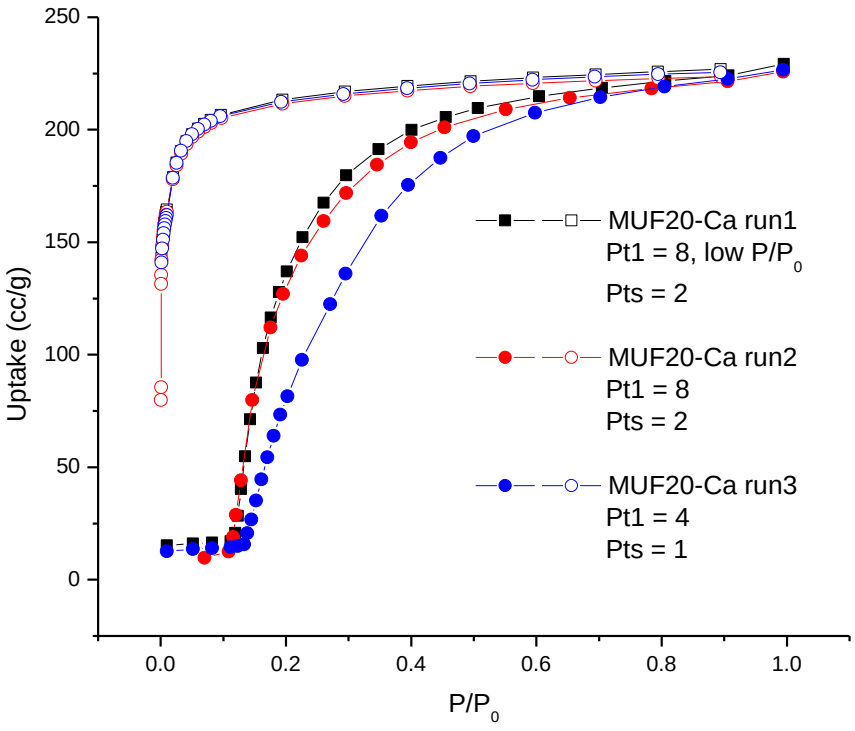

Figure 2.6: Volumetric N_2 adsorption (filled) and desorption (open) isotherms measured at 77 K.

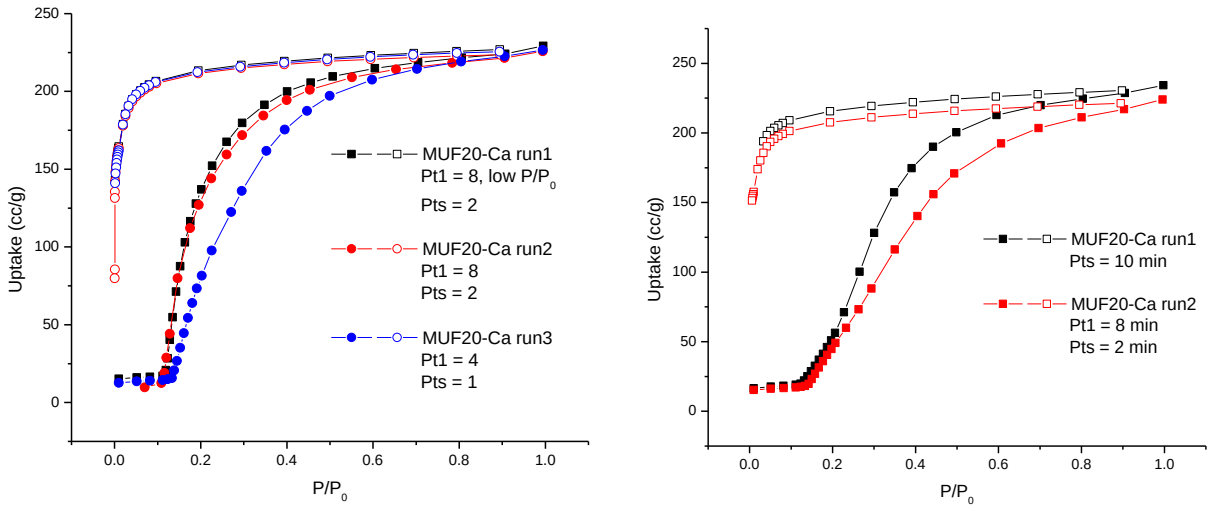

Figure 2.7: Volumetric N_2 adsorption (filled) and desorption (open) isotherms measured at 77 K.

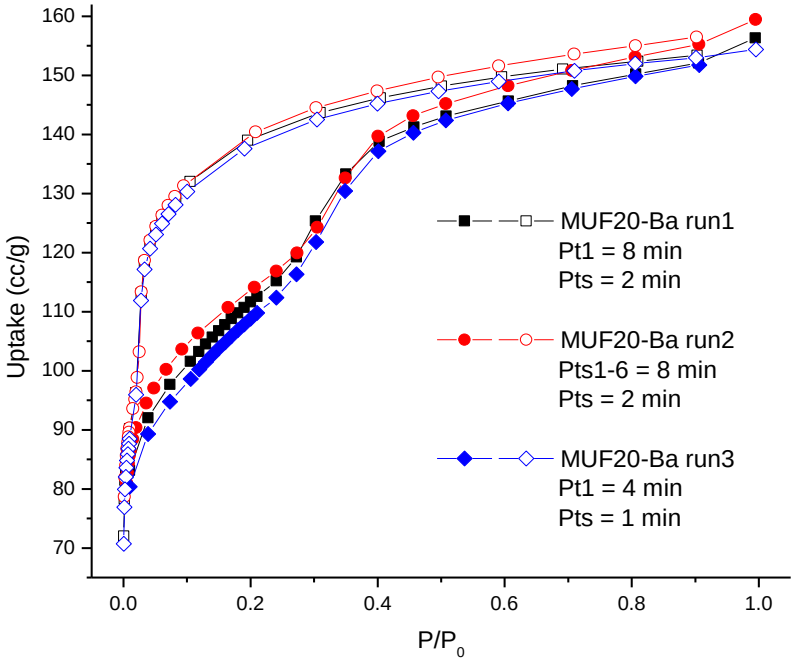

Figure 2.8: Volumetric N_2 adsorption (filled) and desorption (open) isotherms measured at 77 K.

2.4.2. BET calculations from N_2 isotherms at 77 K

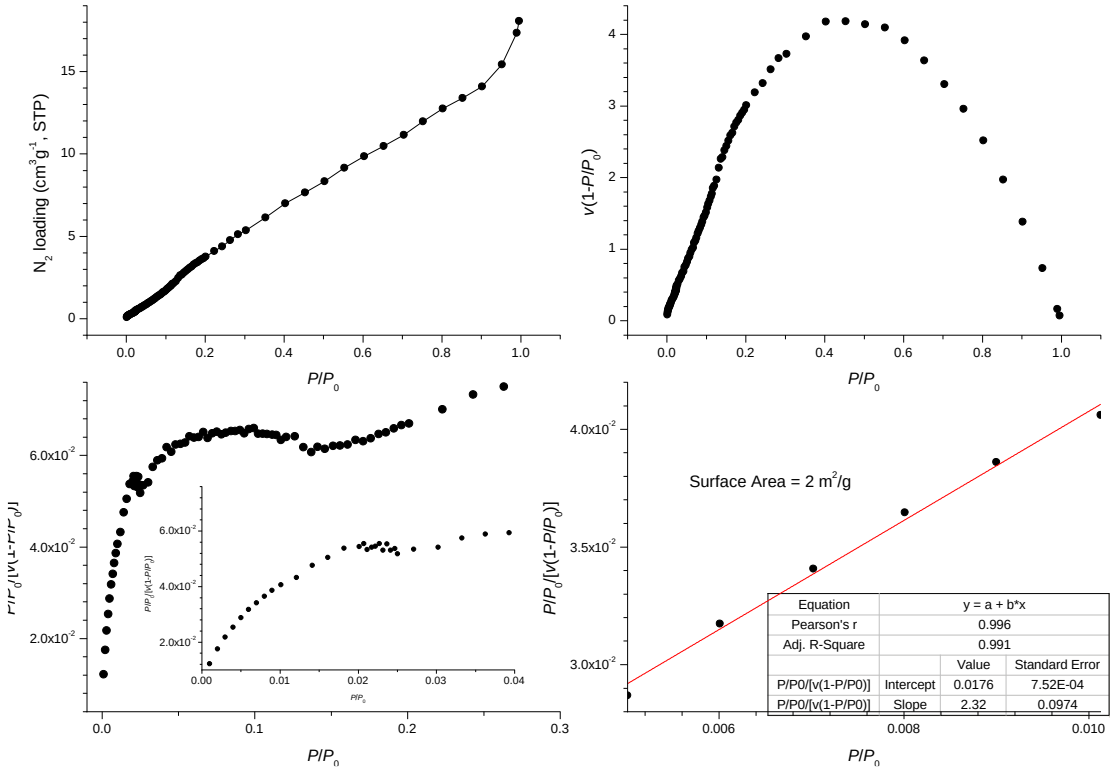

Figure 2.9: BET calculation for MUF20-Aβ[T].

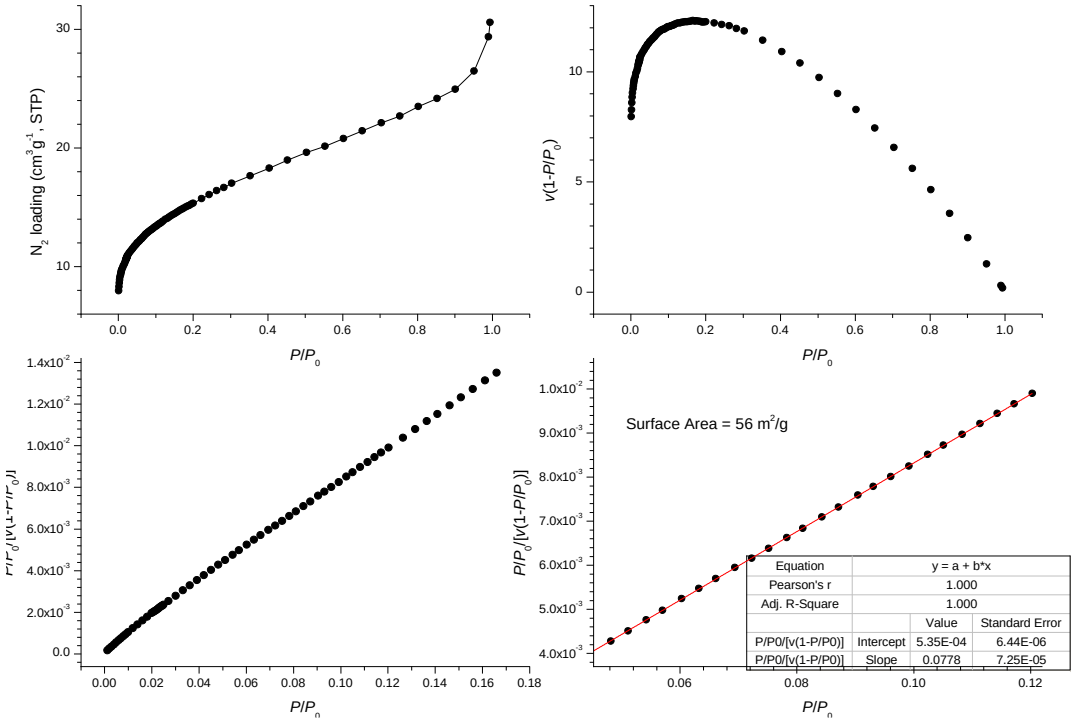

Figure 2.10: BET calculation for MUF20-Aγ from the N_2 isotherms at 77 K.

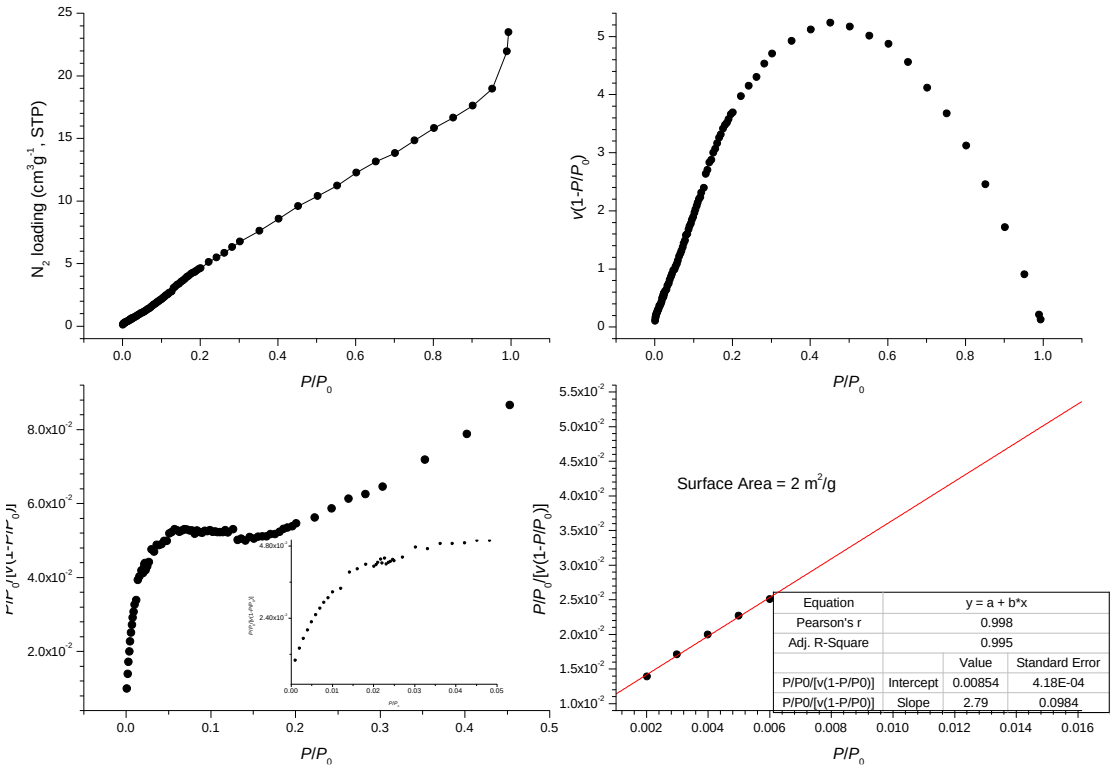

Figure 2.11: BET calculation for MUF20-Aγ^{T}.

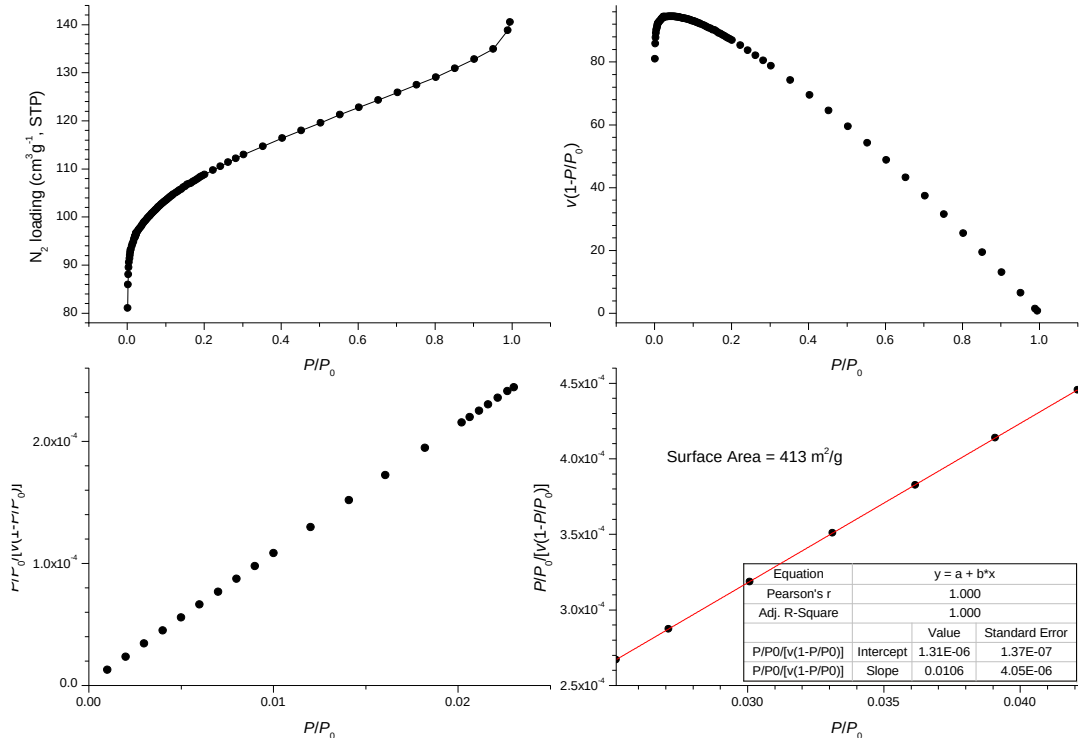

Figure 2.12: BET calculation for MUF20-Aβ` from the N_2 isotherms at 77 K.

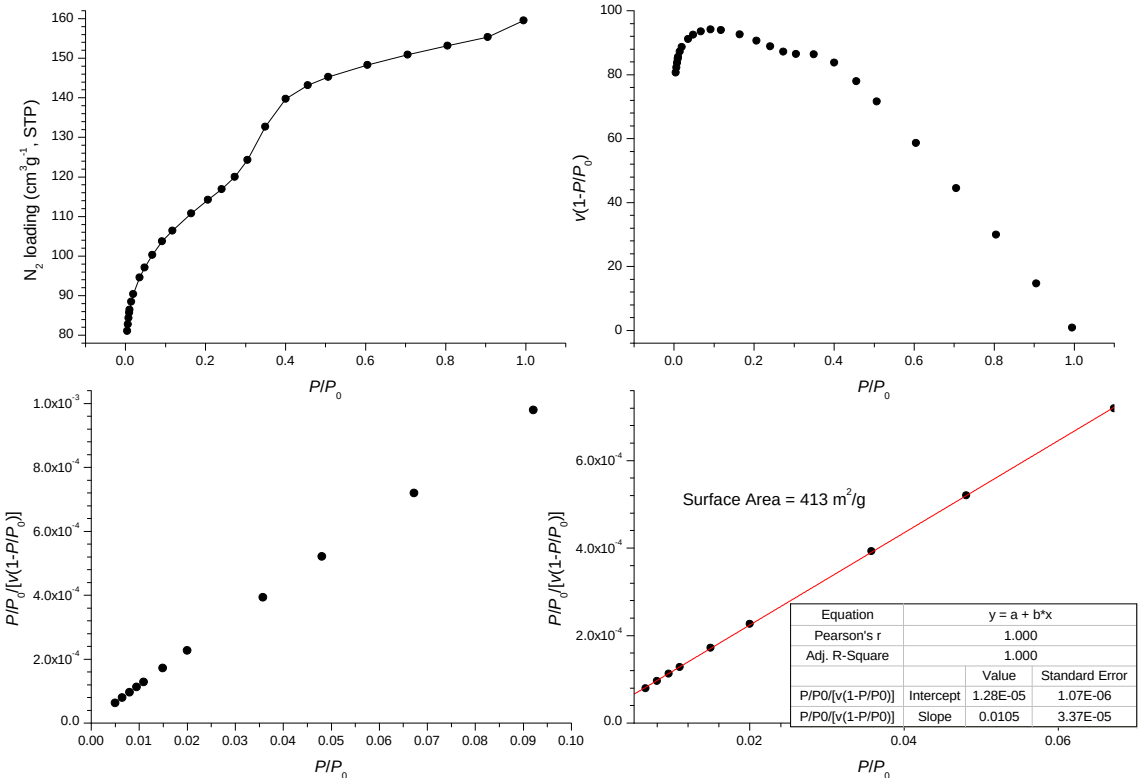

Figure 2.13: BET calculation for MUF20-Bα from the N_2 isotherms at 77 K.

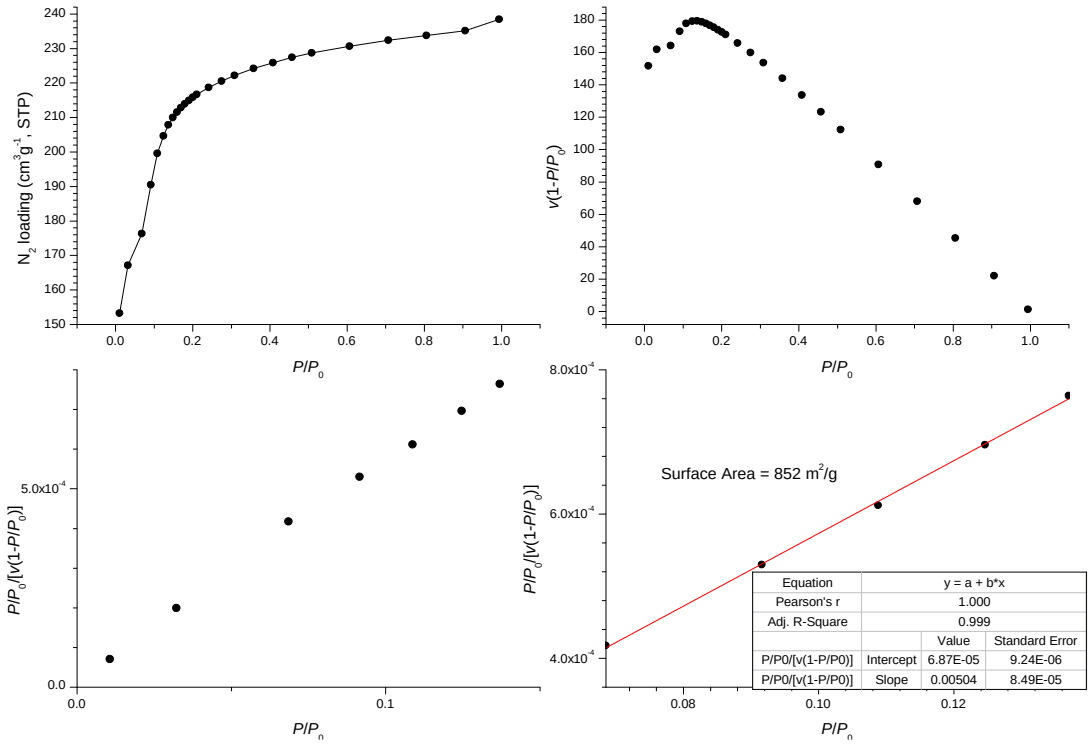

Figure 2.14: BET calculation for MUF20-B^{T}α from the N_2 isotherms at 77 K.

2.4.3. BET calculations from CO_2 isotherms at 273 K

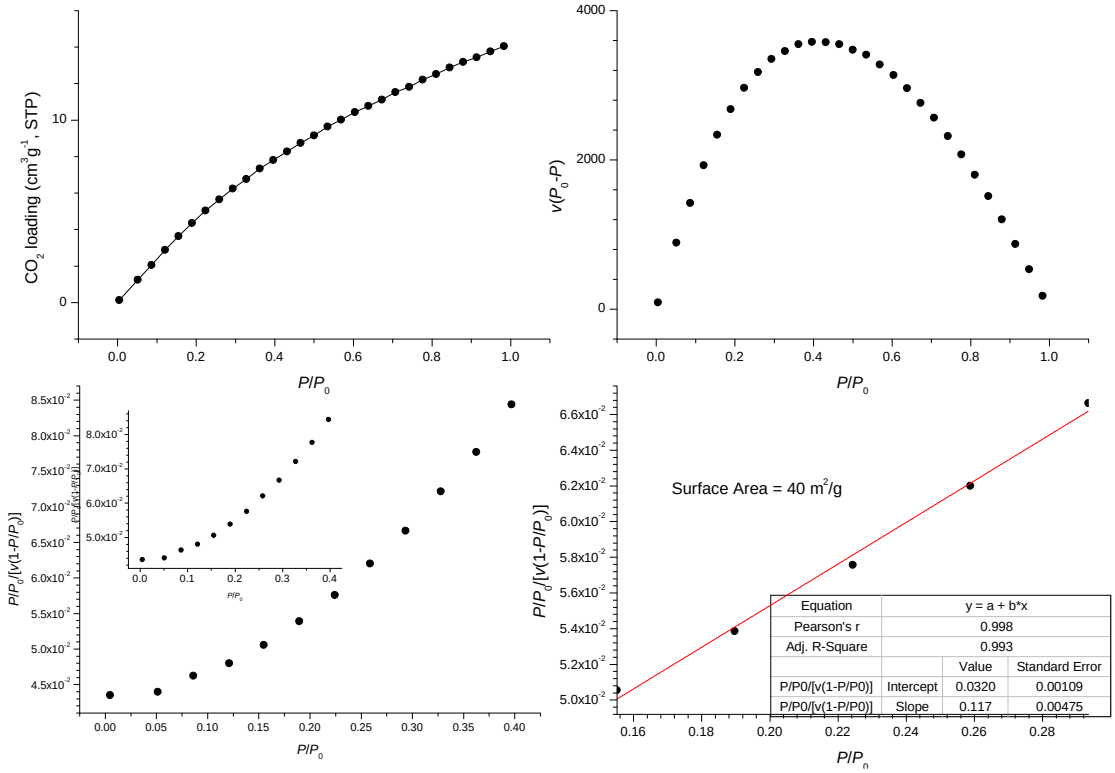

Figure 2.15: BET calculation for MUF20-Aβ.

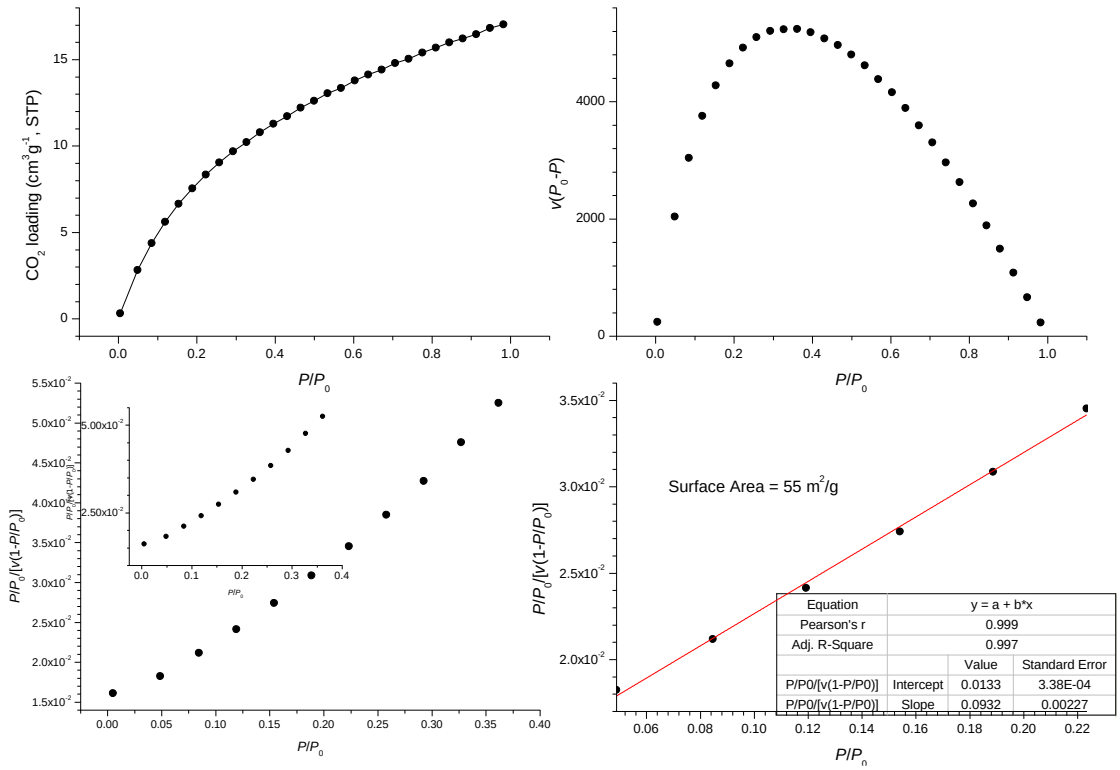

Figure 2.16: BET calculation for MUF20-Aγ.

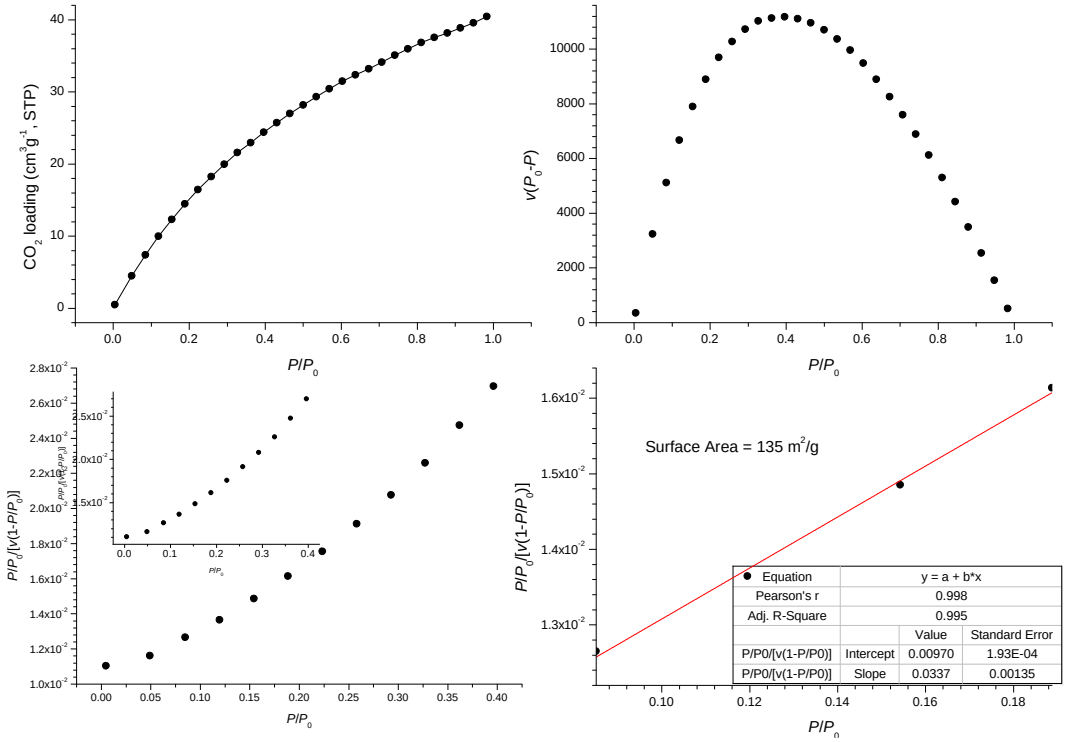

Figure 2.17: BET calculation for MUF20-Aβ`.

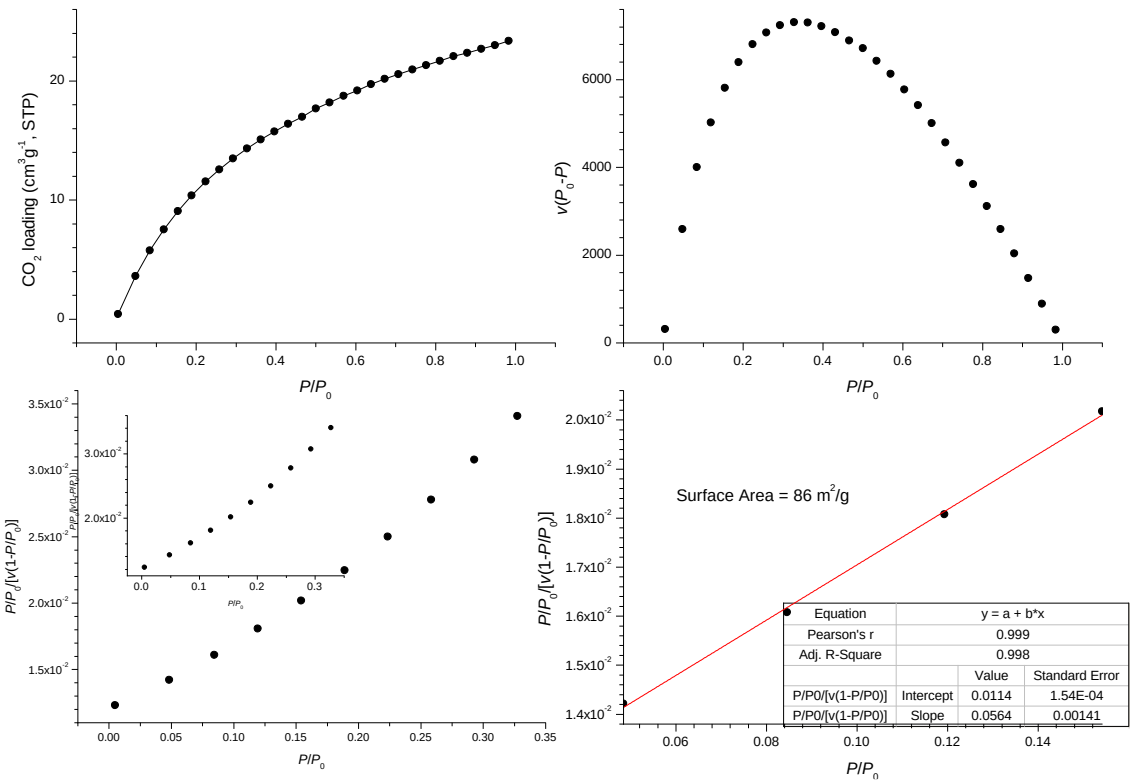

Figure 2.18: BET calculation for MUF20-Aβ^{T}.

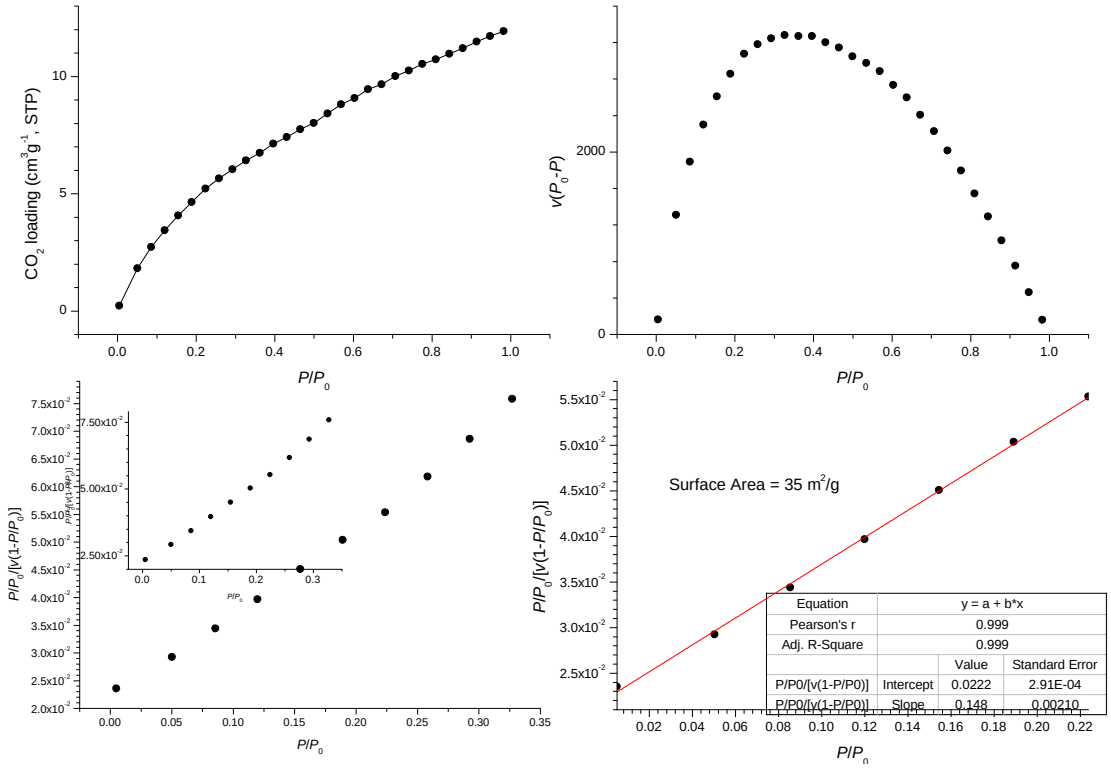

Figure 2.19: BET calculation for MUF20-Aγ[T].

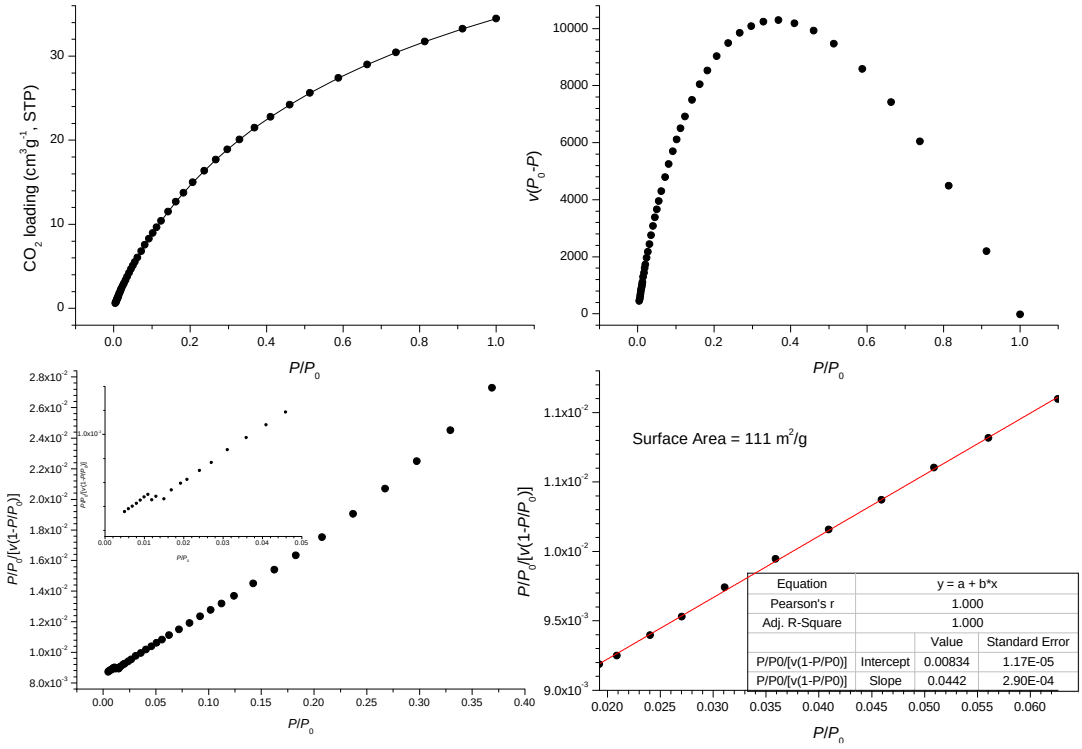

Figure 2.20: BET calculation for MUF20-Bα.

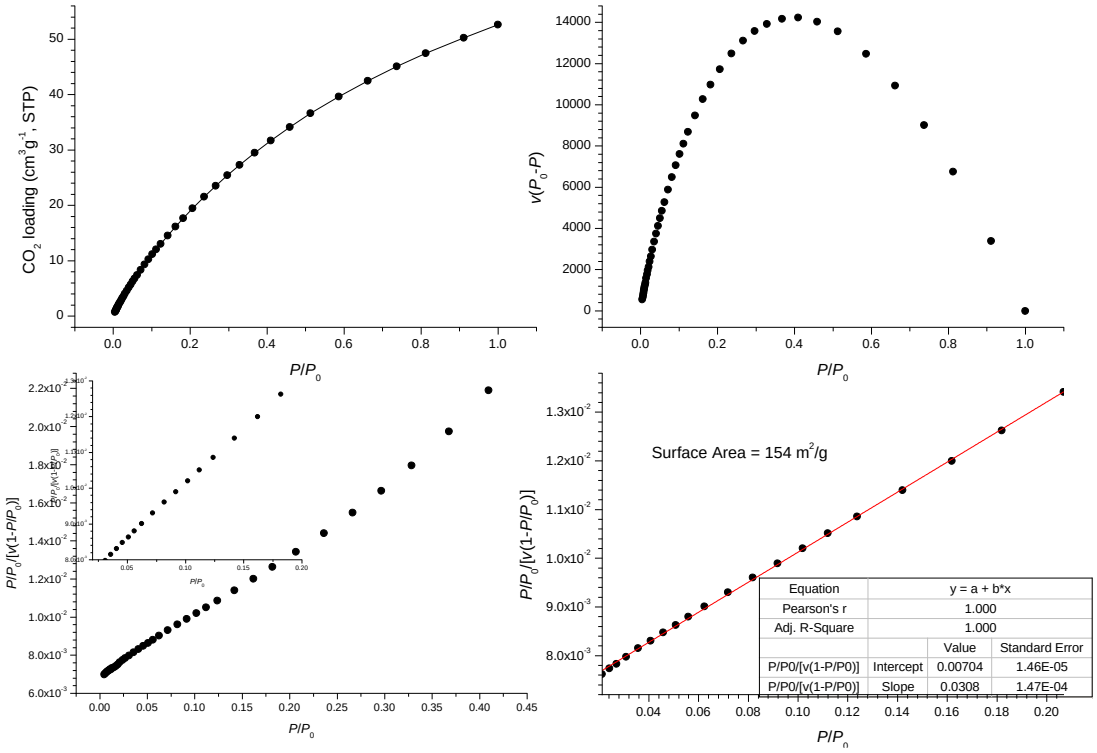

Figure 2.21: BET calculation for MUF20-B^{T}α.

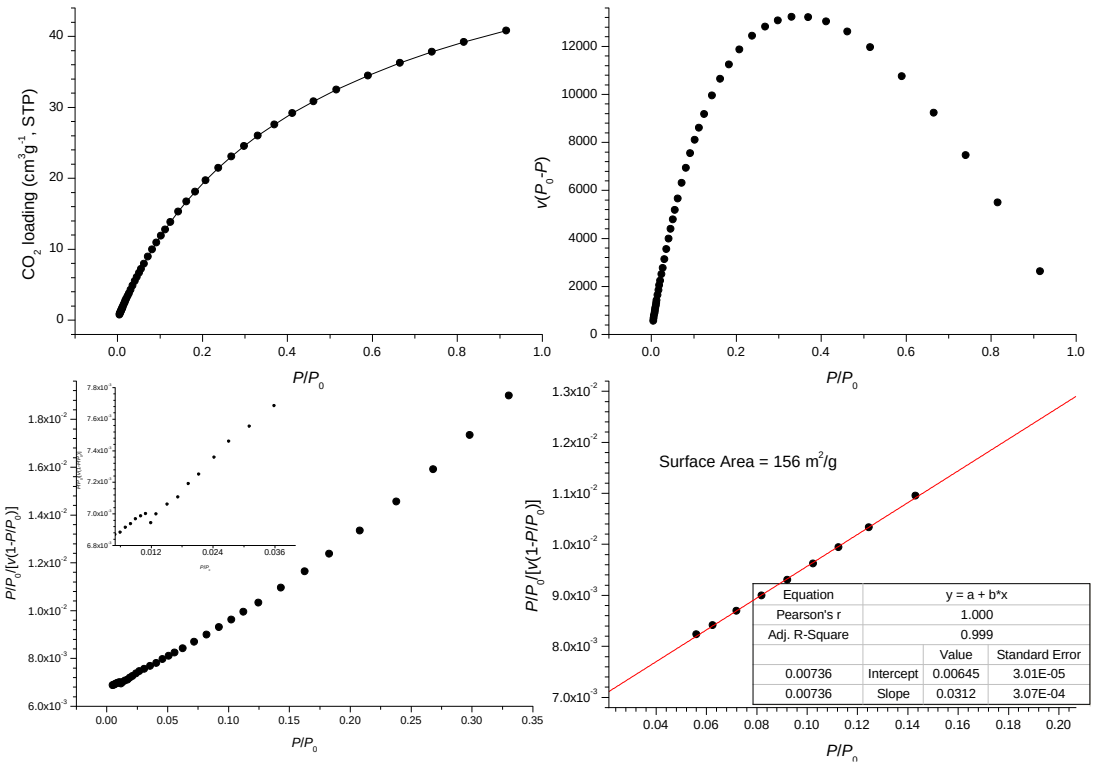

Figure 2.22: BET calculation for MUF20-Cα.

2.4.4. Geometric surface area calculation

Geometric surface area was calculated along literature guidelines.[2] In brief, the desolvated and disorder free CIFs of MOFs were loaded in Mercury v3.8. The solvent accessible void was then investigated, using as molecular probe distance the kinetic radius of N_2 (1.82 Å) at 77 K and CO_2 (1.65 Å) at 273 K.

The geometric surface area (SA) was then calculated as follows:

- Solvent accessible void was converted from $Å^3$/unit cell to cm^3/unit cell.
- Volume was converted to SA/unit cell in cm^2 using assumption of a simple sphere.
- Number of unit cells/cm^3 calculated from conversion of cell volume ($Å^3$ to cm^3) and division of 1 cm^3 by unit cell volume.
- 1/crystal density gives cm^3/g

$$SA\left(\frac{m^2}{g}\right) = [\frac{SA}{unit\ cell} \times \frac{\#unit\ cells}{cm^3} \times \frac{1}{density}(\frac{cm^3}{g})] \times \frac{1}{10{,}000}$$

This calculated accessible surface area serves as a theoretical upper limit for a perfect crystal.

2.4.5. Assorted gas sorption isotherms

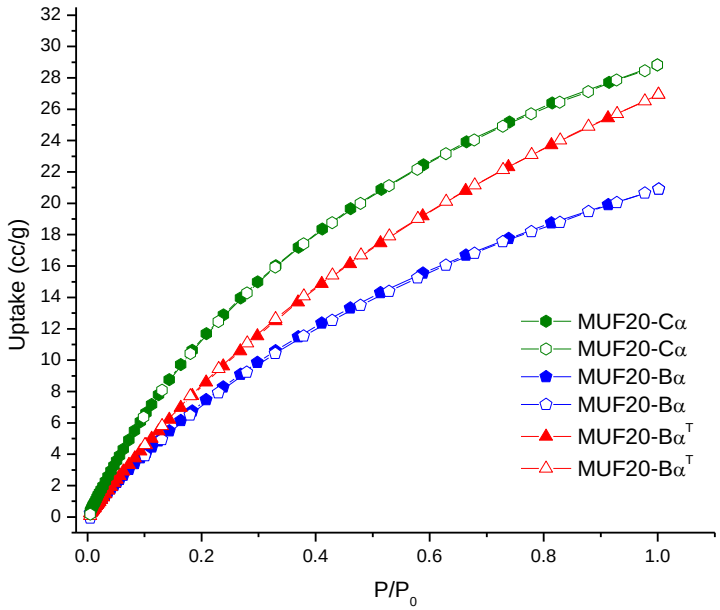

Figure 2.23: Volumetric N_2 adsorption (filled) and desorption (open) isotherms measured at 195 K.

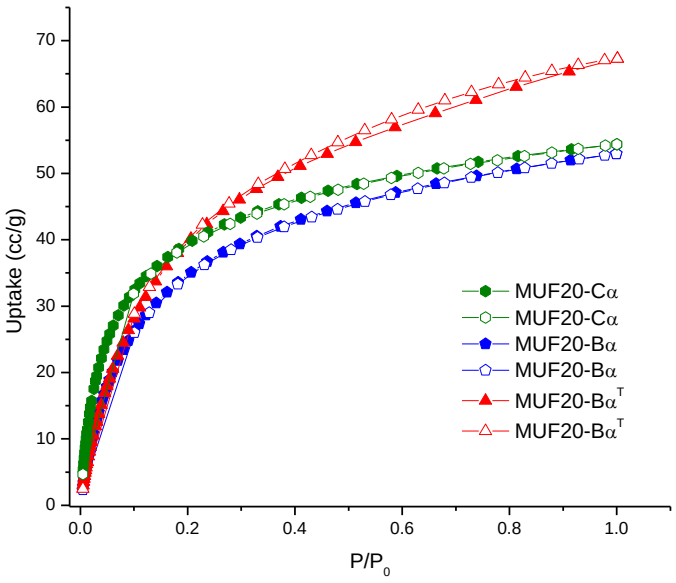

Figure 2.24: Volumetric CH_4 adsorption (filled) and desorption (open) isotherms measured at 195 K.

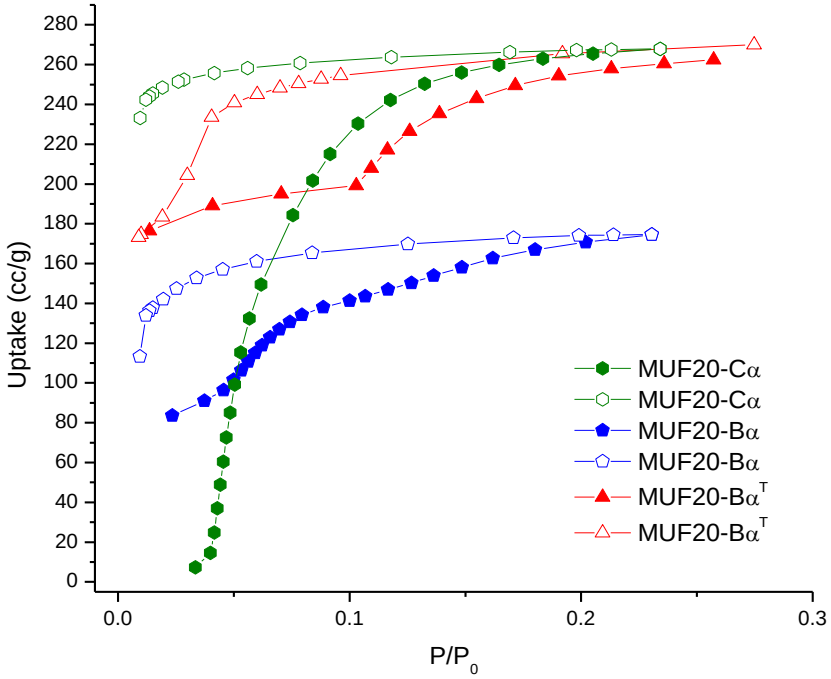

Figure 2.25: Volumetric Ar adsorption (filled) and desorption (open) isotherms measured at 77 K.

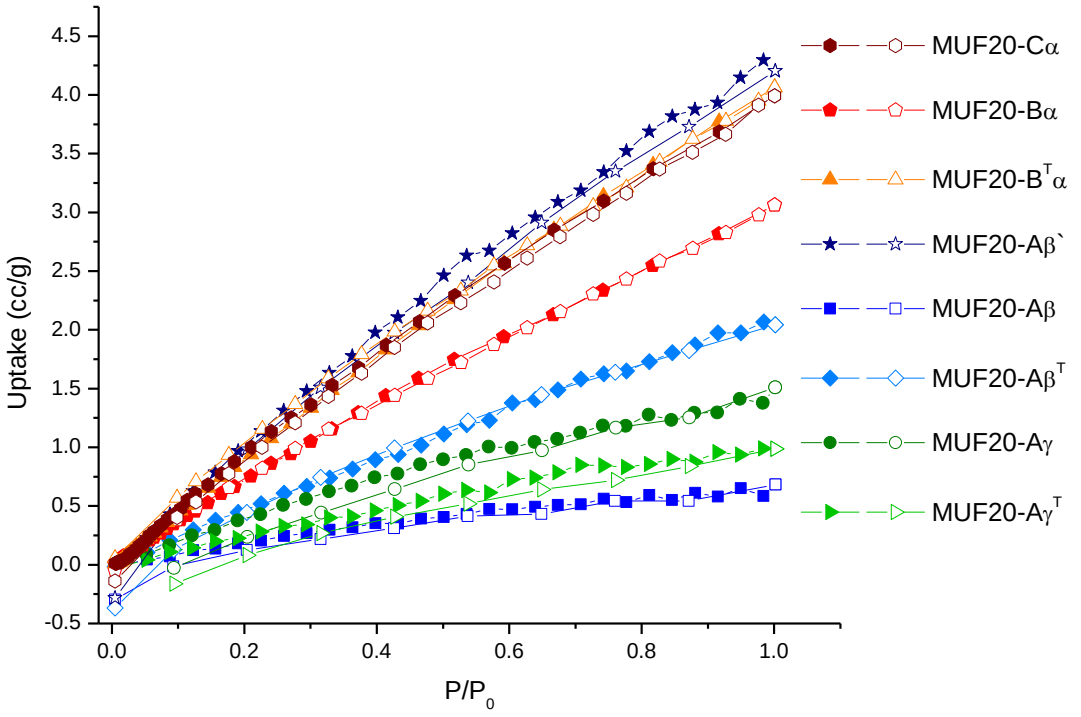

Figure 2.26: Volumetric N_2 adsorption (filled) and desorption (open) isotherms measured at 273 K. Lines are a guide to the eye only.

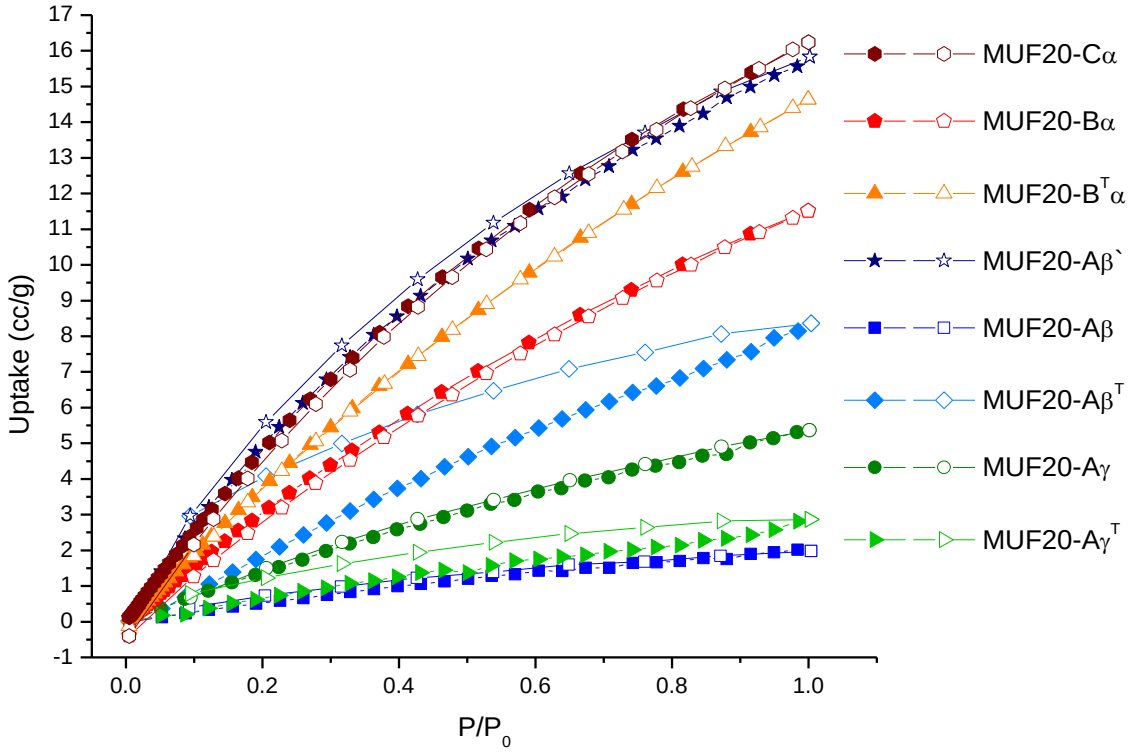

Figure 2.27: Volumetric CH_4 adsorption (filled) and desorption (open) isotherms measured at 273 K. Lines are a guide to the eye only.

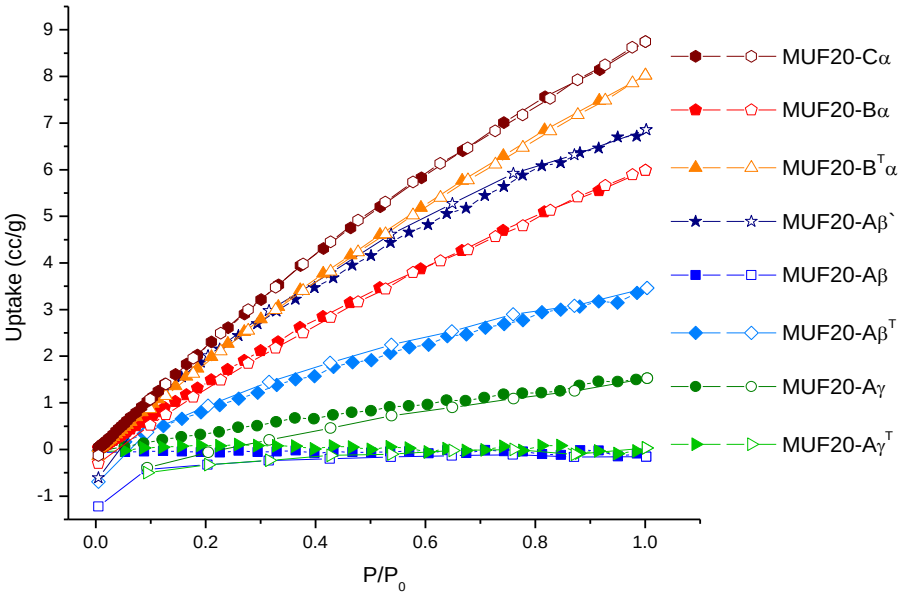

Figure 2.28: Volumetric CH_4 adsorption (filled) and desorption (open) isotherms measured at 298 K. Lines are a guide to the eye only.

2.4.6. Bdc impurity sample characterization

a) PXRD analysis

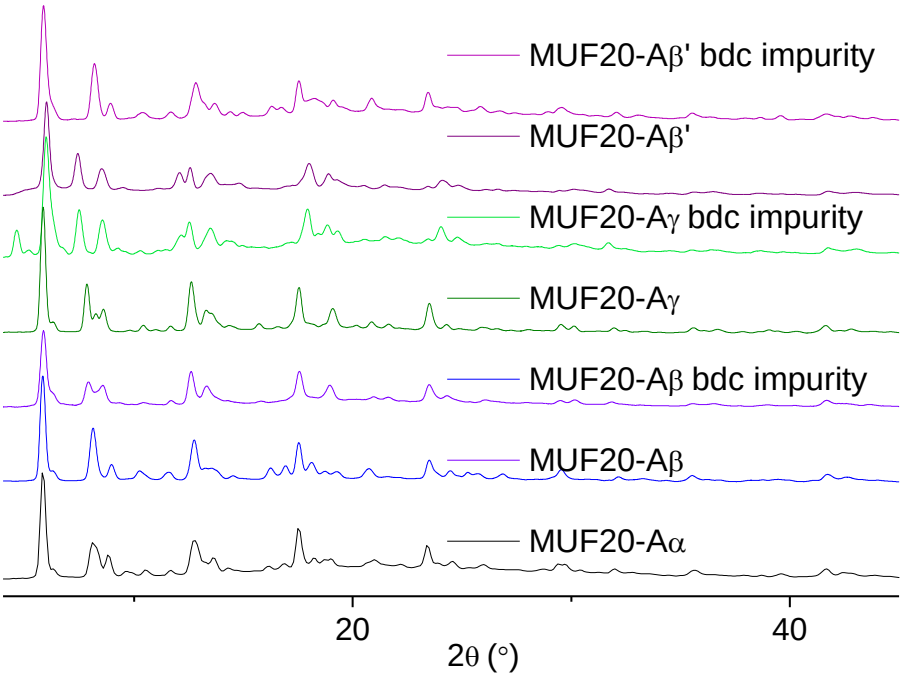

Figure 2.29: PXRD analysis of MUF20 bdc impurity samples compared to pure analogues and experimental parent MOF PXRD, MUF20-Aα.

b) ^{1}H NMR analysis

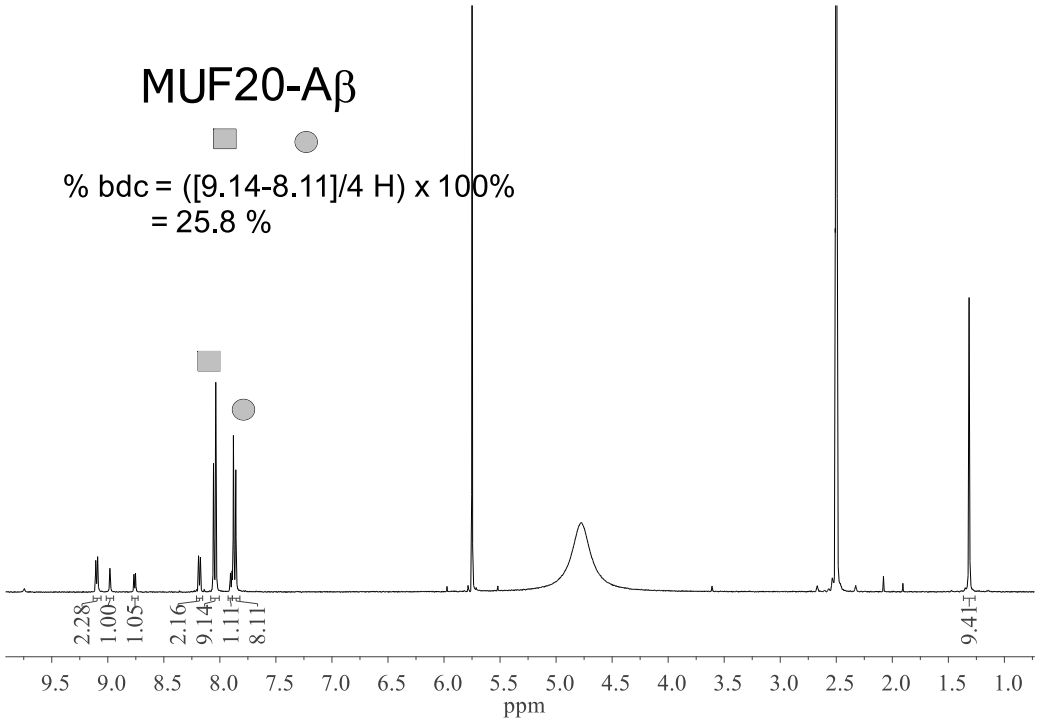

Figure 2.30: ^{1}H NMR analysis of MUF20-Aγ bdc impurity sample post solvent-exchange in DMSO-δ6/DCl.

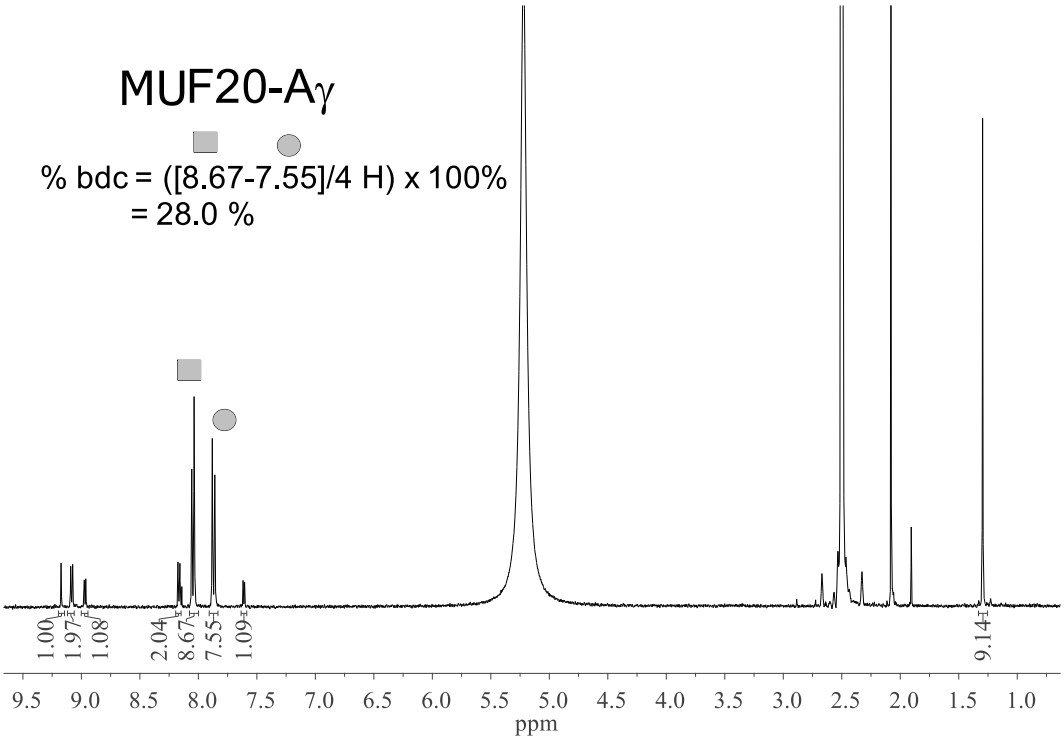

Figure 2.31: ^{1}H NMR analysis of MUF20-Aβ bdc impurity sample post solvent-exchange in DMSO-δ6/DCl.

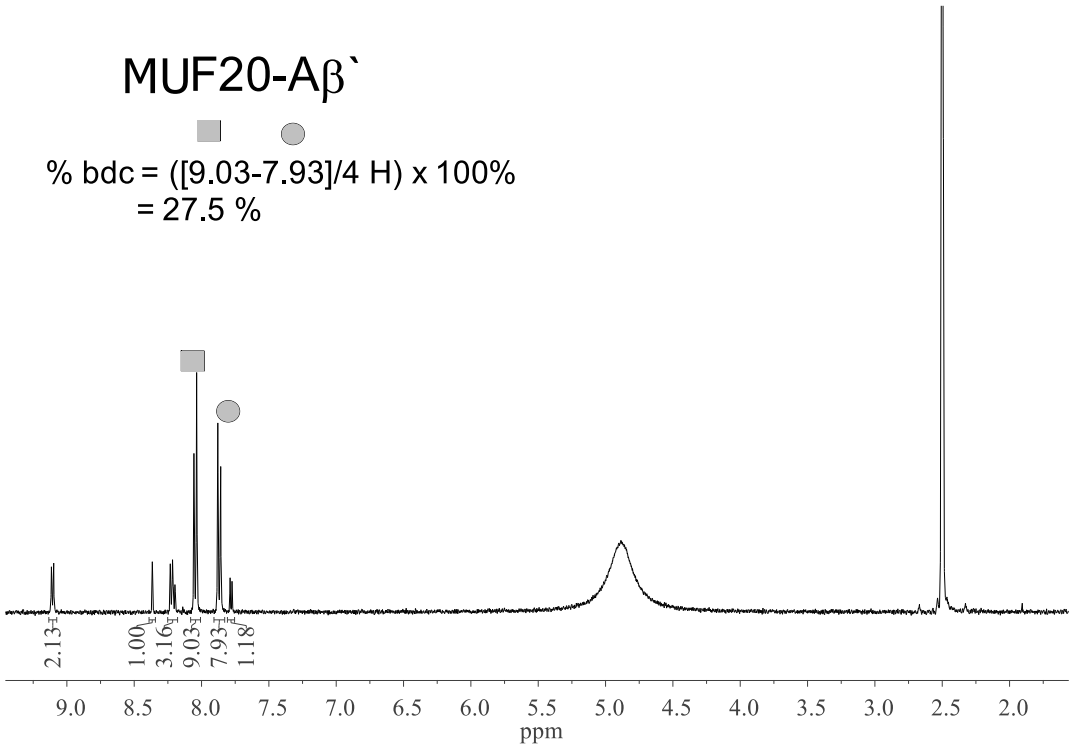

Figure 2.32: ^{1}H NMR analysis of MUF20-Aβ` bdc impurity sample post solvent-exchange in DMSO-δ6/DCl.

c) Gas sorption isotherms

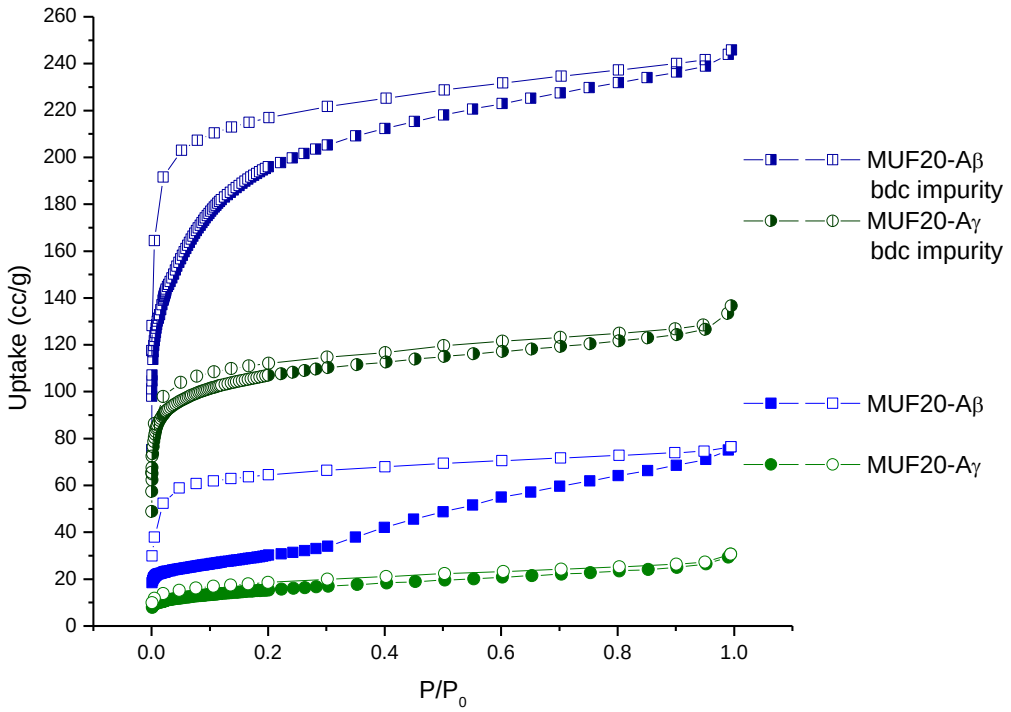

Figure 2.33: Volumetric N_2 adsorption (filled) and desorption (open) isotherms measured at 77 K.

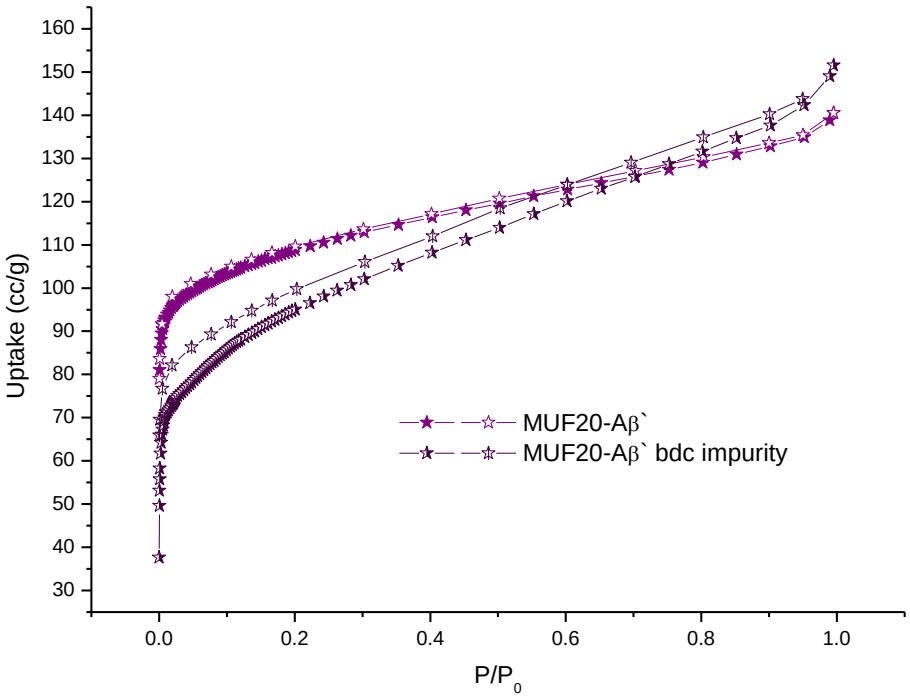

Figure 2.34: Volumetric N_2 adsorption (filled) and desorption (open) isotherms measured at 77 K.

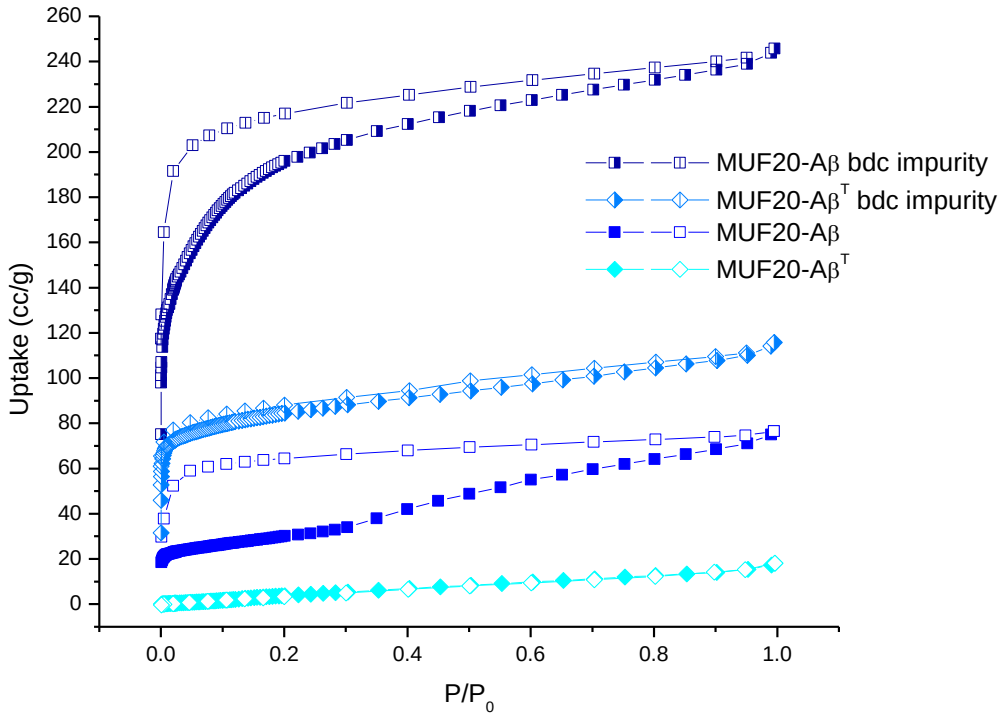

Figure 2.35: Volumetric N_2 adsorption (filled) and desorption (open) isotherms measured at 77 K.

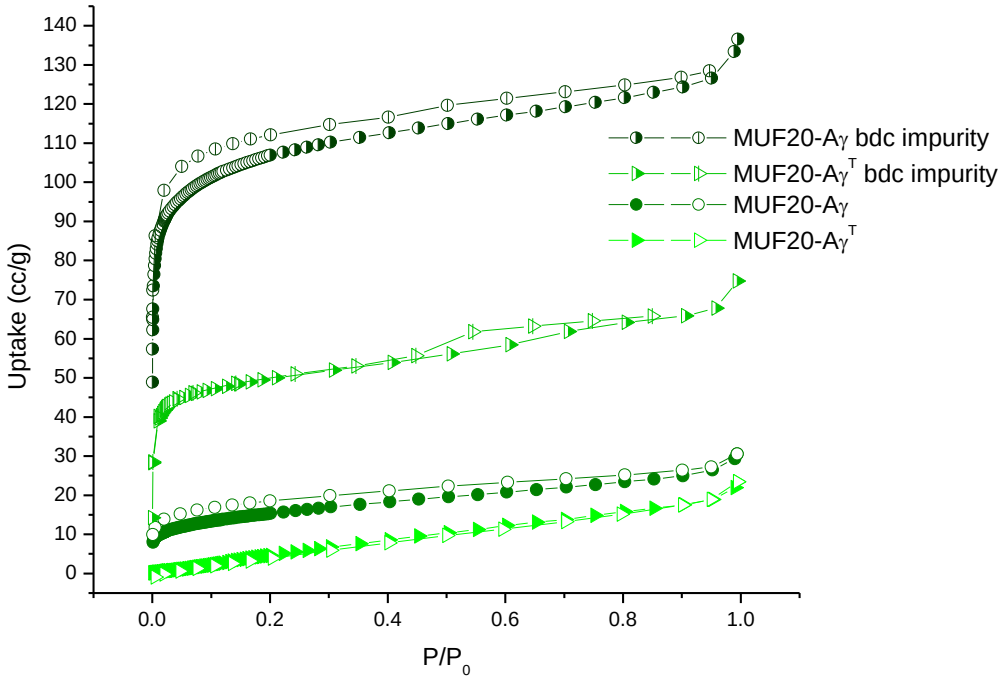

Figure 2.36: Volumetric N_2 adsorption (filled) and desorption (open) isotherms measured at 77 K.

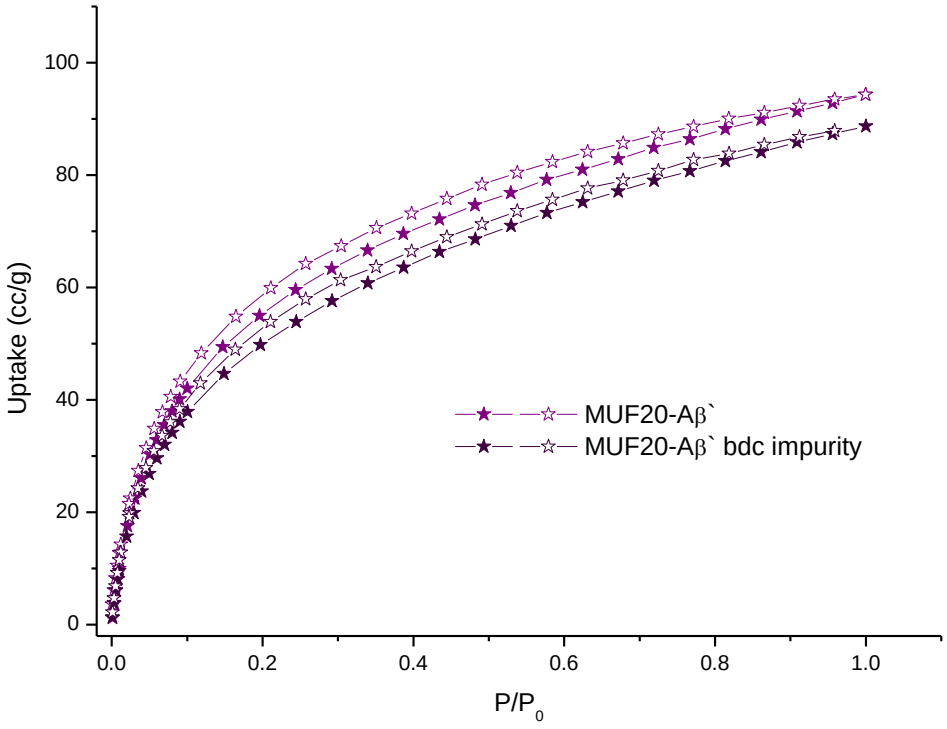

Figure 2.37: Volumetric H_2 adsorption (filled) and desorption (open) isotherms measured at 77 K.

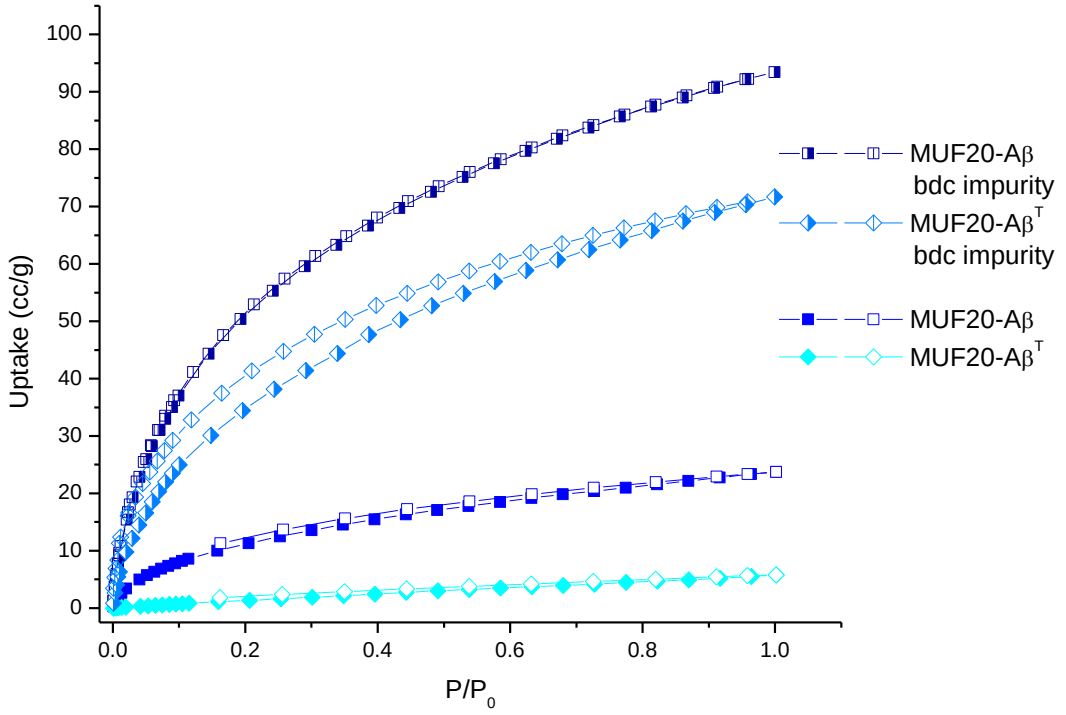

Figure 2.38: Volumetric H_2 adsorption (filled) and desorption (open) isotherms measured at 77 K.

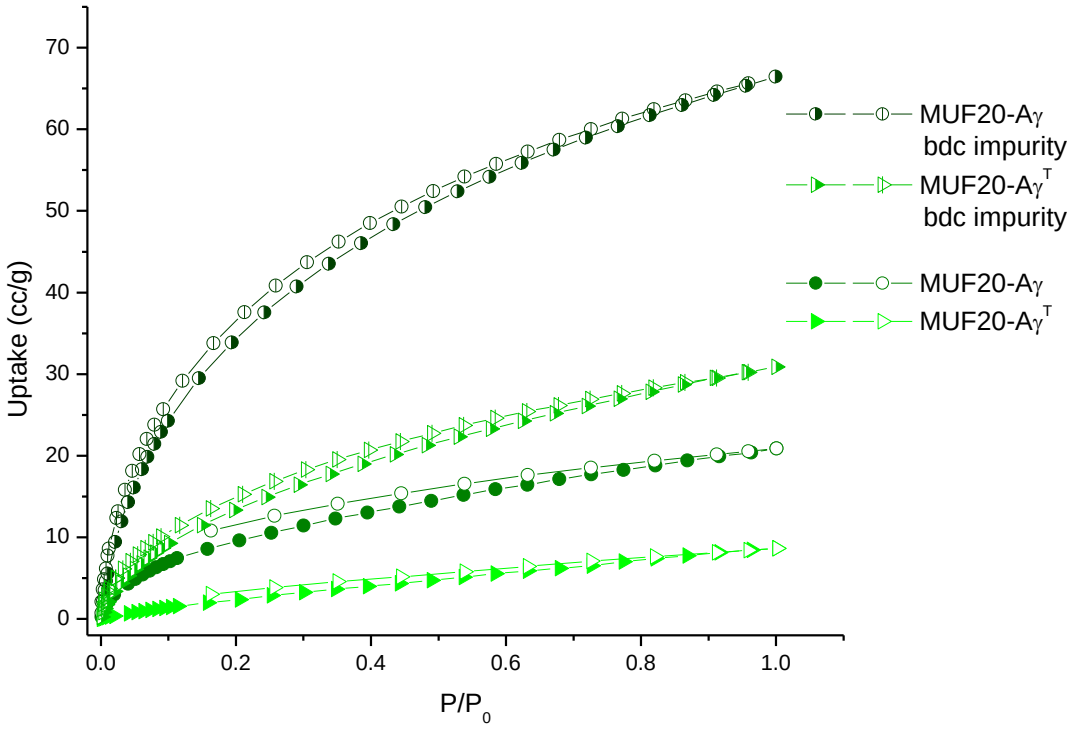

Figure 2.39: Volumetric H_2 adsorption (filled) and desorption (open) isotherms measured at 77 K.

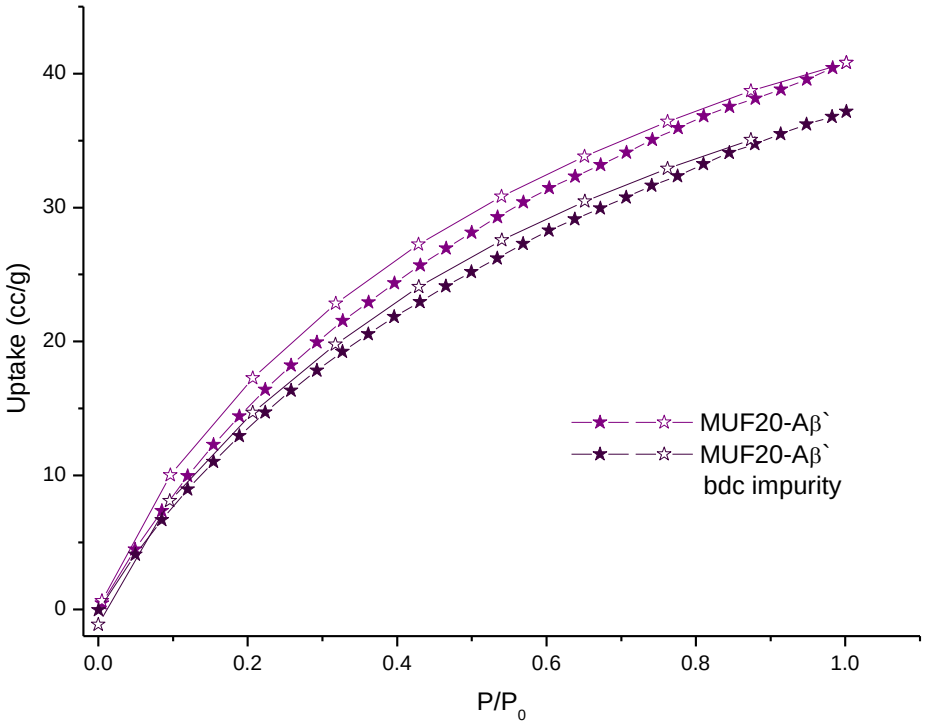

Figure 2.40: Volumetric CO_2 adsorption (filled) and desorption (open) isotherms measured at 273 K.

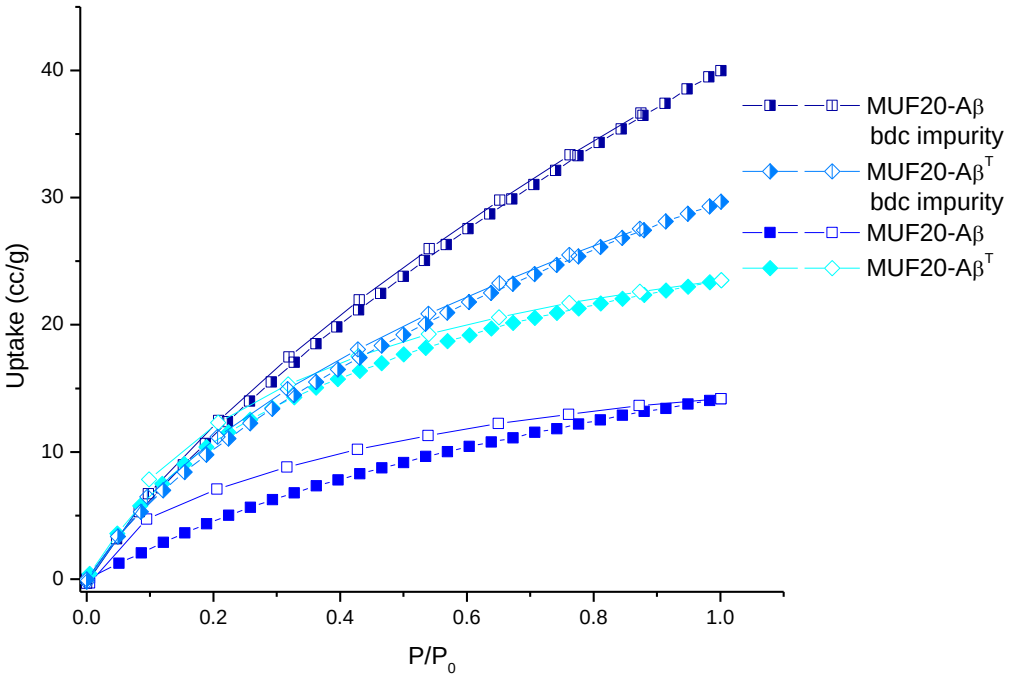

Figure 2.41: Volumetric CO_2 adsorption (filled) and desorption (open) isotherms measured at 273 K.

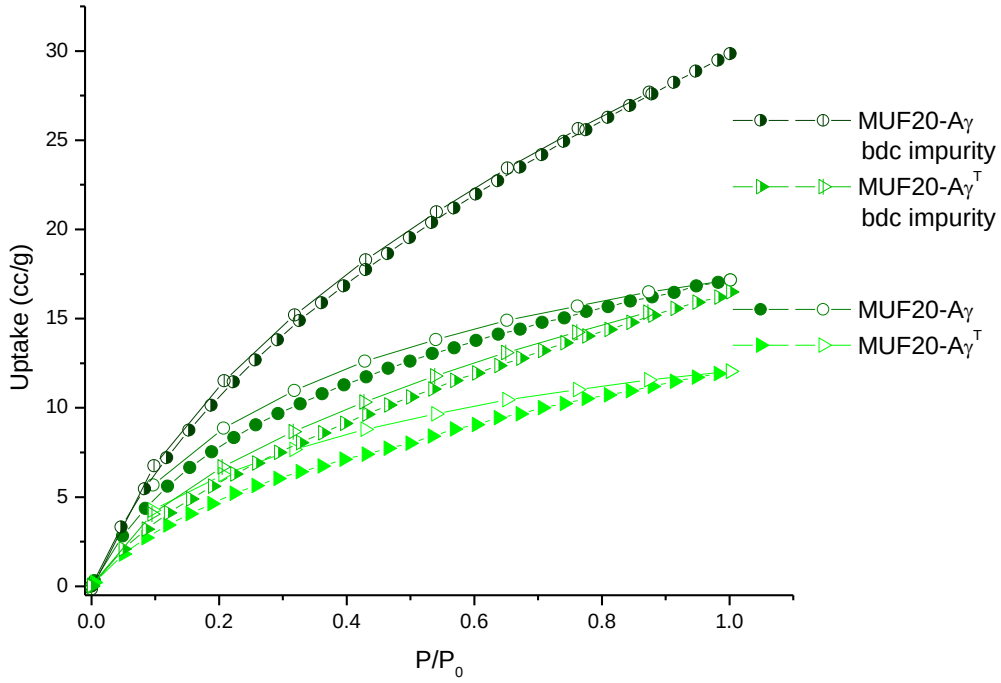

Figure 2.42: Volumetric CO_2 adsorption (filled) and desorption (open) isotherms measured at 273 K.

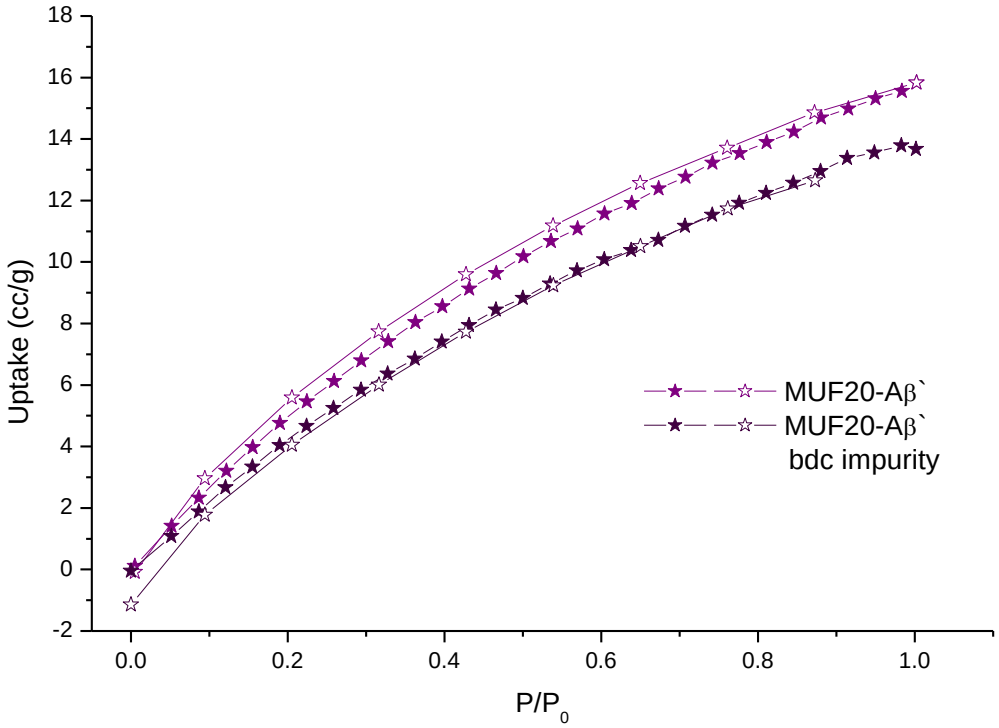

Figure 2.43: Volumetric CH_4 adsorption (filled) and desorption (open) isotherms measured at 273 K.

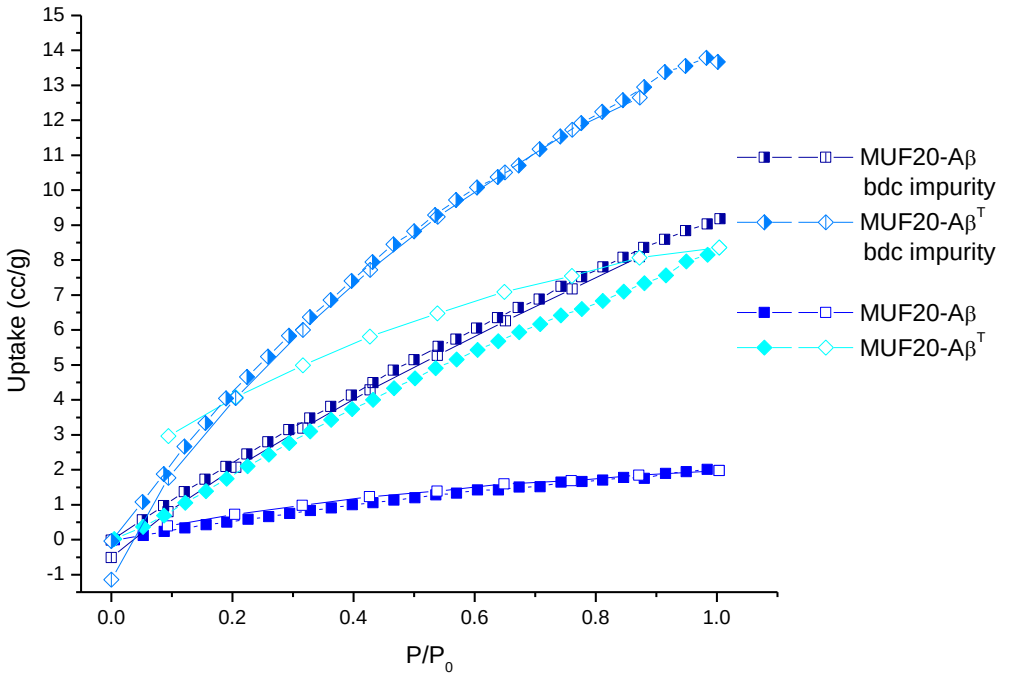

Figure 2.44: Volumetric CH_4 adsorption (filled) and desorption (open) isotherms measured at 273 K.

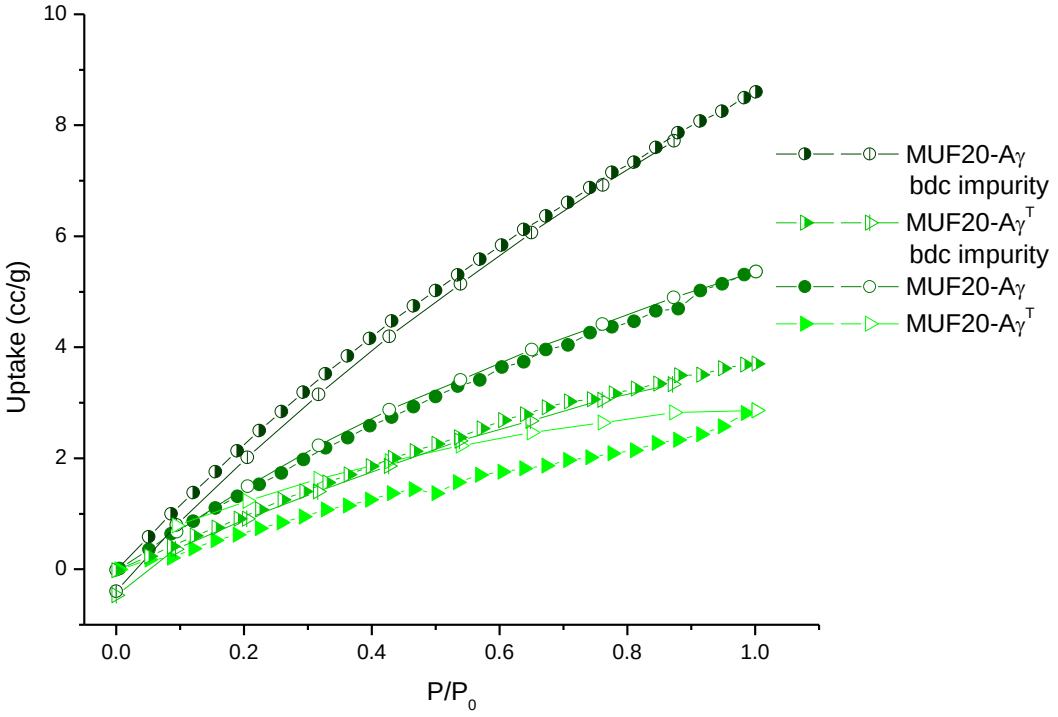

Figure 2.45: Volumetric CH_4 adsorption (filled) and desorption (open) isotherms measured at 273 K.

2.5. XRD characterization

2.5.1. Single crystallography of bpyCO_2K

Table 2.4: Crystallography details for bpy-CO_2K coordination polymer

Compound	**Bpy-CO_2K**
Formula	$C_{11}H_7KN_2O_2$
Formula weight	238.29
Crystal size (mm)	0.18 × 0.25 × 0.29
Temperature (K)	93
Wavelength (Å)	1.54187
Crystal system	Monoclinic
Space group	$P2_1/c$
Unit cell lengths (Å)	a = 12.0851(16) b = 12.0080(16) c = 7.1371(10)
Unit cell angles (°)	α = 90 β = 101.819(7) γ = 90
Unit cell volume (Å^3)	1013.8(2)
Z	4
D_{calc} (g cm^{-3})	1.561
μ (mm^{-1})	4.477
F(000)	488.0
Reflns coll./unique, R_{int}	12518 / 1964, 0.1381
Data range	8.0 Å > d > 0.81 Å
Index ranges	$-12 \leq h \leq 14$, $-14 \leq k \leq 14$, $-8 \leq l \leq 8$
Completeness	98.6 %
T_{min}, T_{max}	0.695, 1.000
R indices for data with $I>2\sigma(I)$	R_1 = 0.0752, wR_2 = 0.2011
R indices for all data	R_1 = 0.0783, wR_2 = 0.2084
Largest difference peak and hole (e Å^{-3})	0.75/ -0.64

3. Chapter 3 –Dual-functionalized pillar-layer (PLMOFs) SI

3.1. MOF synthesis and characterization

General procedures

All starting compounds and solvents were used as received from commercial sources of reagent grade or higher and MilliQ water used in all cases unless otherwise noted. Unless specified otherwise, all NMR spectra were recorded at room temperature. NMR analysis was performed on Bruker-400 and Bruker-500 Avance instruments, with the use of the solvent proton as an internal standard. Elemental analyses were performed by the Campbell Microanalytical Laboratory at the University of Otago, New Zealand. Thermogravimetric analysis (TGA) was performed on a TA Q50 instrument.

^{1}H NMR analysis of digested MUF20 and MUF-77 MOF samples

For ^{1}H NMR spectroscopy, the mother liquor of the as-synthesized MOF crystals was replaced with fresh dry DMF multiple times, followed by repeated washing and subsequent soaking in dry CH_2Cl_2 for several hours. The excess CH_2Cl_2 was then decanted and the samples placed under vacuum overnight to remove residual solvent from the pores. The crystals were then digested using the following protocol: 23 µL of a 35% DCl solution in D_2O was mixed with 1 mL of DMSO-d_6 to give a DCl/DMSO-d_6 stock solution. Around 5 mg of MOF was digested in 150 µL of this stock solution together with 480 µL of DMSO-d_6. Spectra were acquired immediately following dissolution.

Thermogravimetric Analysis (TGA)

Thermogravimetric analyses were performed on a TA Instruments Q50 instrument. Freshly prepared MOF samples were prepared as for gas sorption except that the CH_2Cl_2 was removed using a benchtop vacuum pump and were placed under vacuum for 4- 12 hours. Samples were then transferred to an aluminium sample pan and then measurements were commenced under an N_2 flow with a heating rate of 5 °C /min.

Powder X-ray diffraction patterns

All powder X-ray diffraction experiments were carried out on a Rigaku Spider X-ray diffractometer with Cu K_α radiation (Rigaku MM007 microfocus rotating-anode generator), monochromated and focused with high-flux Osmic multilayer mirror optics, and a curved image plate detector. The data were obtained from freshly prepared MOF samples that had been ground into slurry in a small amount of DMF, DEF or DBF and kept damp with solvent throughout the measurement. The two-dimensional images of the Debye rings were integrated with 2DP[1] (Version 1.0.3.4) to give 2θ vs I diffractograms. The predicted powder patterns were generated from their single-crystal structures using Mercury v4.10.

3.1.1. TGA percentage weight loss coordinates for MUF20 MOFs Chapter 3

Table 3.1: Loop TGA coordinates (temperature, weight (%))

MUF20-Cβ` (Experimental 11.5%)			
Point	T1	T2	T3
Coordinates	97.8, 98.2	213.7, 87.2	N/A
MUF20-B`β (Experimental 17.2 %)			
Point	T1	T2	T3
Coordinates	52.9, 97.9	236.5, 80.7	N/A
MUF20-B`γ (Experimental 5.5 %)			
Point	T1	T2	T3
Coordinates	69.6, 98.1	216.3, 92.4	N/A
MUF20-Cβ (Experimental 21.3 %)			
Point	T1	T2	T3
Coordinates	85.8, 99.6	201.6, 83.8	281.6, 77.4
MUF20-Cγ (Experimental 15.7 %)			
Point	T1	T2	T3
Coordinates	138.9, 100.4	198.4, 89.9	253.7, 84.7

Table 3.2: TGA coordinates (temperature, weight (%))

MUF20-Dβ (Experimental 21.0 %)		
Point	T1	T2
Coordinates	107.8, 100.6	281.6, 79.6

Despite absence of DMF (as shown by NMR) MUF20-B`β` similarly shows low termperature weight loss indicating that this loss may be associated with the free amine content of the material (Figure 3.49). Further studies into this were not undertaken since outside the focus of this thesis.

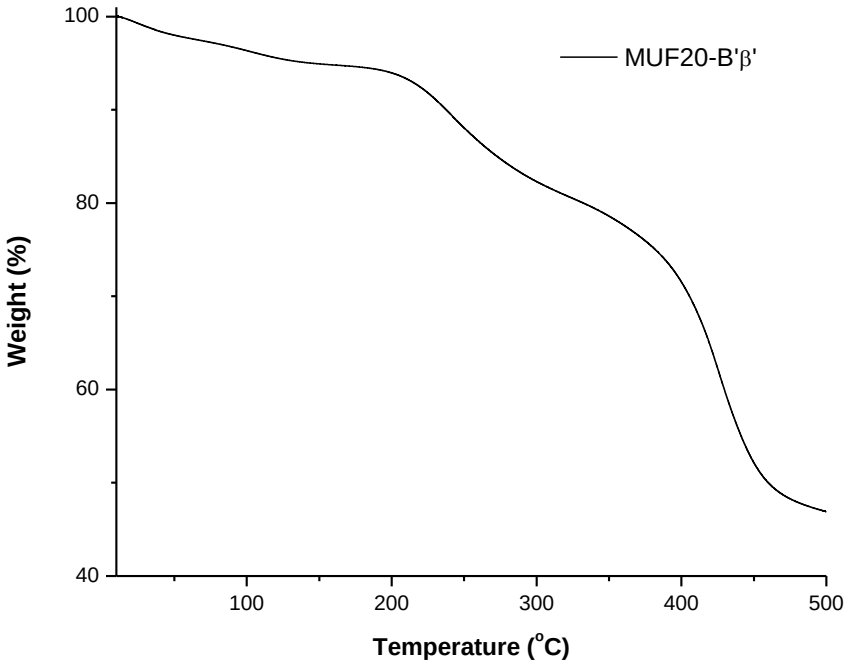

Figure 3.1: Thermogravimetric analysis (TGA) trace for MUF20-B`β`.

3.1.2. MUF20 MOF synthesis and characterization

a) MUF20-Bβ [Zn_2(bpdc-NHBoc)$_2$(bpy-NHBoc)]

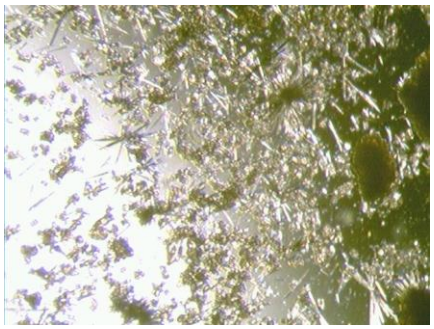

Bpdc-NHBoc (2.4 mg, 0.0067 mmol), bpy-NHBoc (3.3 mg, 0.012 mmol), and $Zn(NO_3)_2.4H_2O$ (1.6 mg, 0.61 μmol) were combined in a 4 mL scintillation vial. MeOH (1.125 mL) was then added and the mixture briefly sonicated before addition of DEF (0.125 mL). After sonicating a second time the vial was placed in an oven at 85 °C for 2 days. After 10 min in the oven, the lid of the vial was re-tightened and Teflon tape placed around the join of the lid. Pale yellow needle clusters and chunks formed.

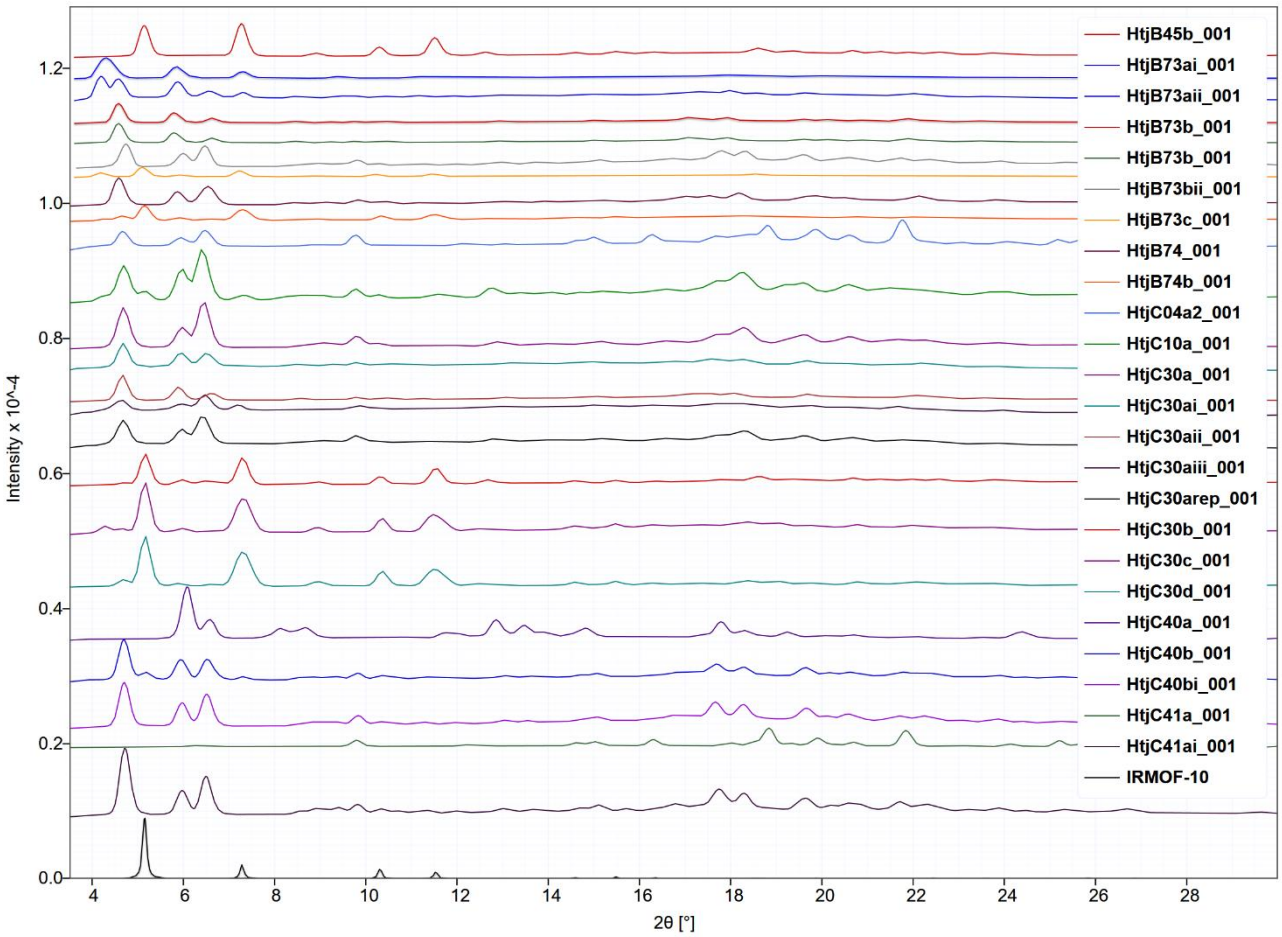

Figure 3.2: Simulated PXRD of IMROF-10 and experimental PXRD of attempted MUF20-Bβ synthesis.

NMR analysis:

^{1}H NMR indicates partial de-protection occurs during MOF synthesis (between 11 and 30 %), even at low concentrations (1.25 mg into 1.25 mL (C30ai sample in Figure 2.2)). This deprotection yields a mixture of 1:2 bpy-NHBoc:bpdc-NHBoc and 1:2 bpy-NH_2:bpdc-NH_2 - showing that de-protection of the bpy and bpdc TPG ligands was simultaneous. However, doubling the reaction mixture concentration results in bpdc-NHBoc deprotection at around twice the rate of the bpy-NHBoc ligand.

From top of NMR spectra to bottom: MUF20-Aβ`, MUF20-Aβ, bpdc-NH_2, MUF20-Bα. The bottom four NMR from MUF20-Bβ synthesis trials indicate the crystalline MOF obtained contains a mixture of all four ligands: bpdc-NHBoc, bpdc-NH_2, bpy-NHBoc, and bpy-NH_2.

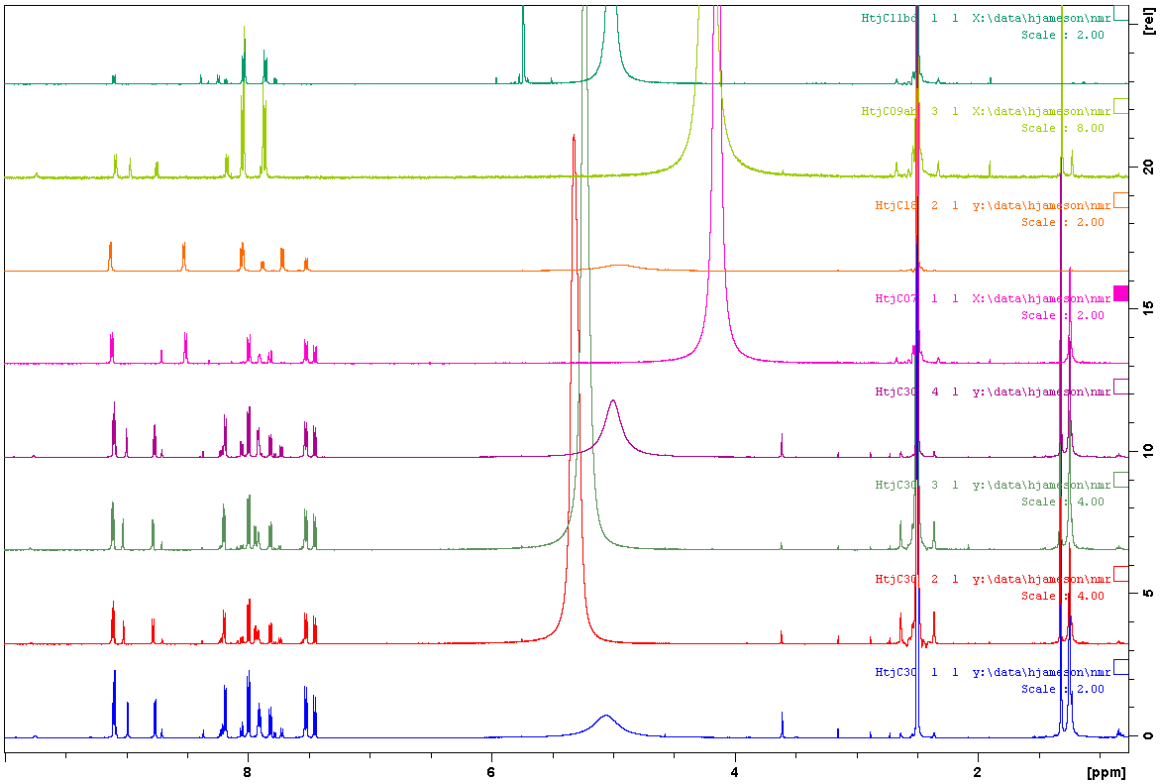

Figure 3.3: ^{1}H NMR analysis of attempted MUF20-Bβ synthesis.

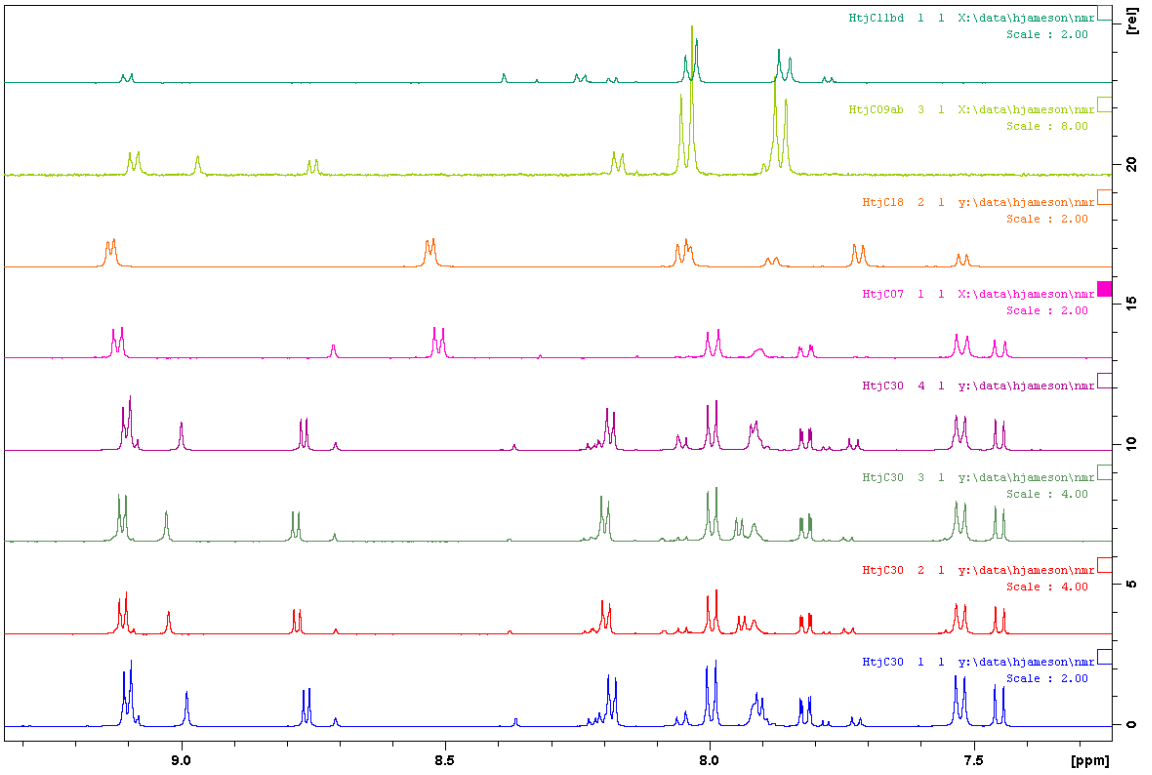

Figure 3.4: ^{1}H NMR analysis of aromatic region of attempted MUF20-Bβ synthesis.

b) MUF20-Bγ

Bpdc-NHBoc (1.8 mg, 7.0 μmol), bpy-TBE (2.2 mg, 8.6 μmol), and $Zn(NO_3)_2.4H_2O$ (1.4 mg, 5.4 μmol) were combined in a 4 mL scintillation vial. 2:1 MeOH:DEF (1.25 mL) was then added and the mixture briefly sonicated before placing in an oven at 85 °C for 24 hours. Slight film with blockish crystals formed. 1:1 ratio of IRMOF to a new unknown phase was encountered.

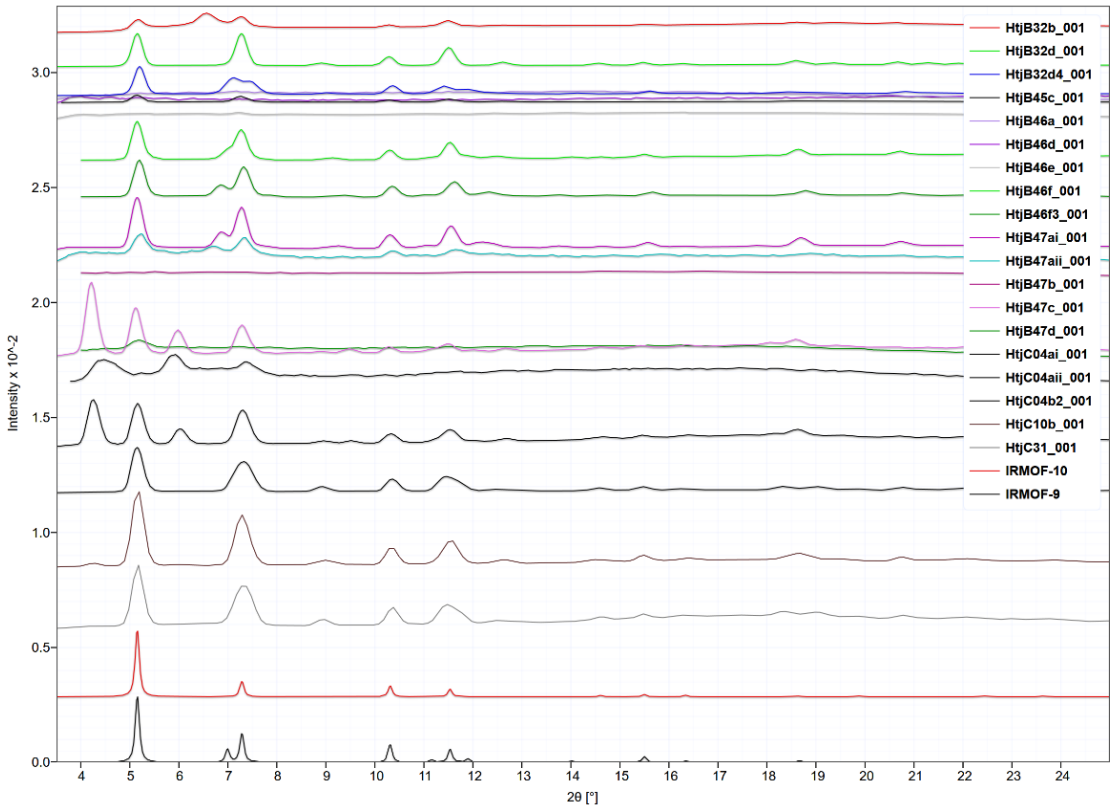

Figure 3.5: Simulated PXRD of IRMOF-9 and IRMOF-10 and experimental PXRD of attempted MUF20-Bγ synthesis.

3.1.3. Non-isolatable or amorphous direct synthesis MUF20 MOFs

a) MUF20-Bβ`

Mixed phases only were obtained and could not be synthesized phase-pure. Single crystal collected on did not resolve.

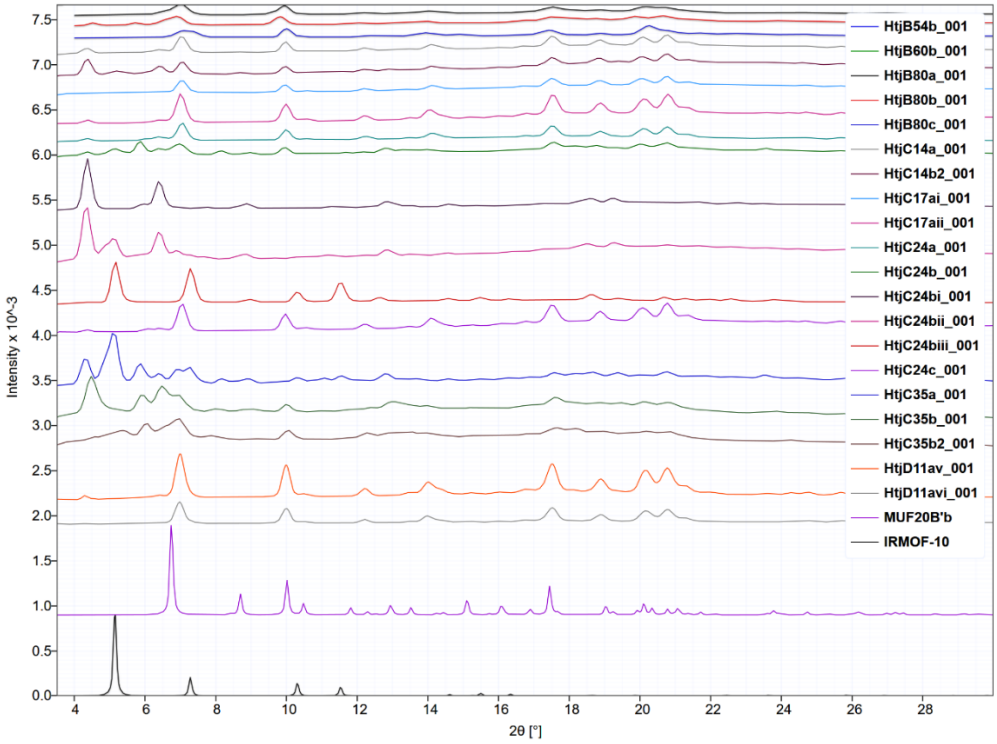

Figure 3.6: Simulated PXRD of IRMOF-10 and MUF20-B`β and experimental PXRD of attempted MUF20-Bβ` synthesis.

Mixtures of phases including ones previously encountered in MUF20-Aγ` and MUF20-B`β synthesis, otherwise IRMOF phases mostly commonly obtained.

b) MUF20-Bγ`

Could not be synthesized phase-pure with single-crystal quality. Unknown phase.

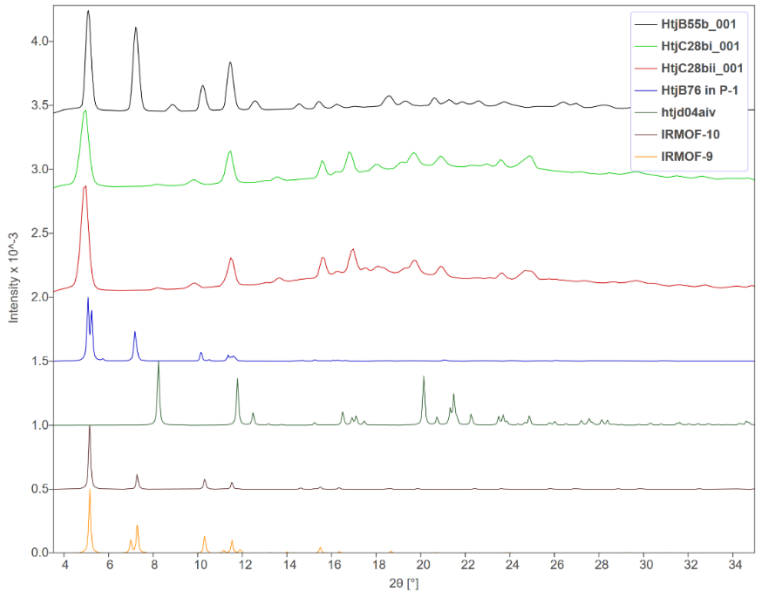

Figure 3.7: Simulated PXRD of IRMOF-9,-10, MUF20-Aα-dia, and bpy-CO_2K, and experimental PXRD of attempted MUF20-Bβ` synthesis.

c) MUF20-B`γ`

Mixed phases, could not be synthesized phase-pure. Similar phases encountered in bpy-CO_2K synthesis and MUF20-Bγ` as well as MUF20-Aγ`.

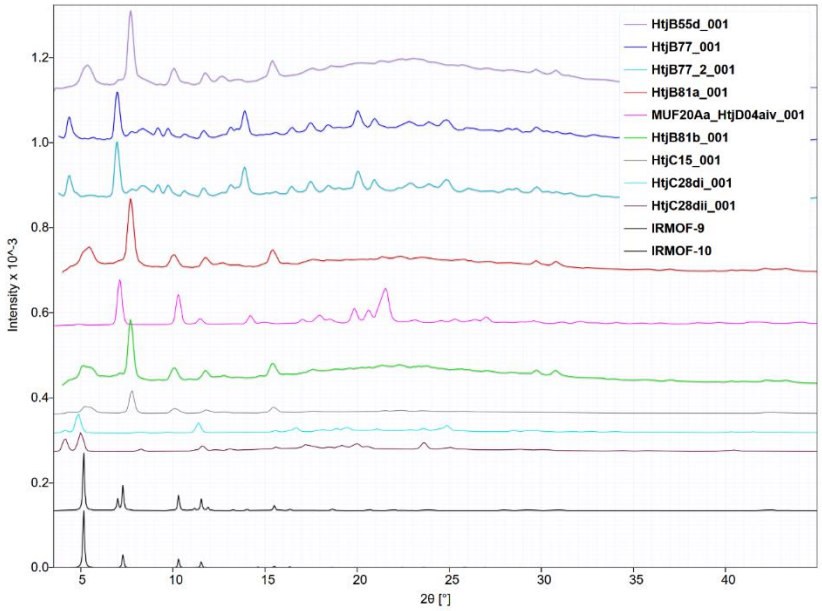

Figure 3.8: Simulated PXRD of IRMOF-9 and IRMOF-10 and experimental PXRD of attempted MUF20-Bβ` synthesis.

d) MUF20-Cγ`

Single crystal could not be obtained. Phase-pure PXRD synthesis samples had varying NMR ratios despite consistent washing.

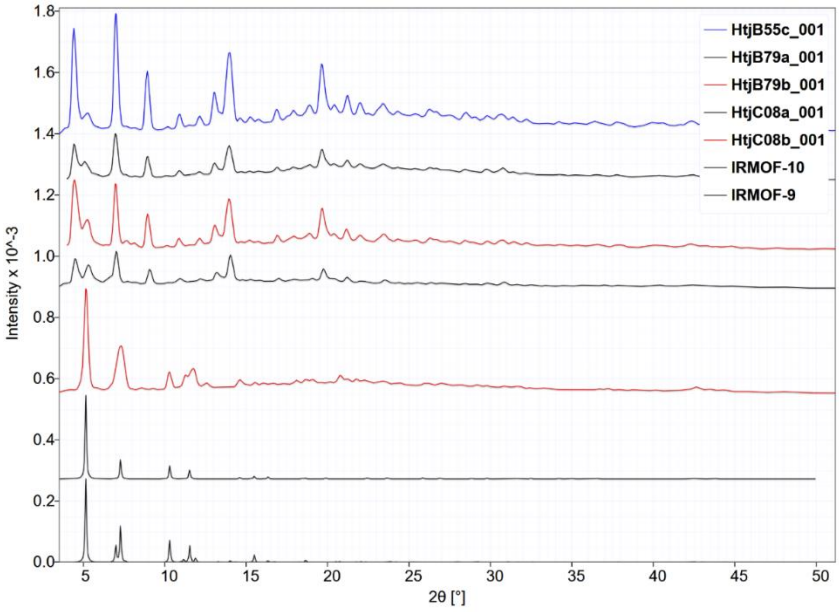

Figure 3.9: Simulated PXRD of IRMOF-9 and IRMOF-10 and experimental PXRD of attempted MUF20-Cγ` synthesis.

e) MUF20-C`β

MUF20-C`β formed amorphous phase only under conditions trialled.

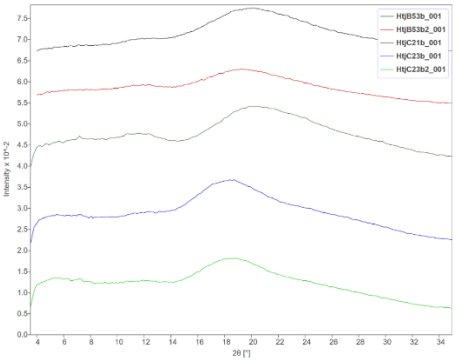

Figure 3.10: Experimental PXRD of attempted MUF20-C`β synthesis.

f) MUF20-C`β`

Despite multiple conditions trialed a single crystal could not be obtained. Phase-pure PXRD synthesis samples had varying NMR ratios despite consistent washing.

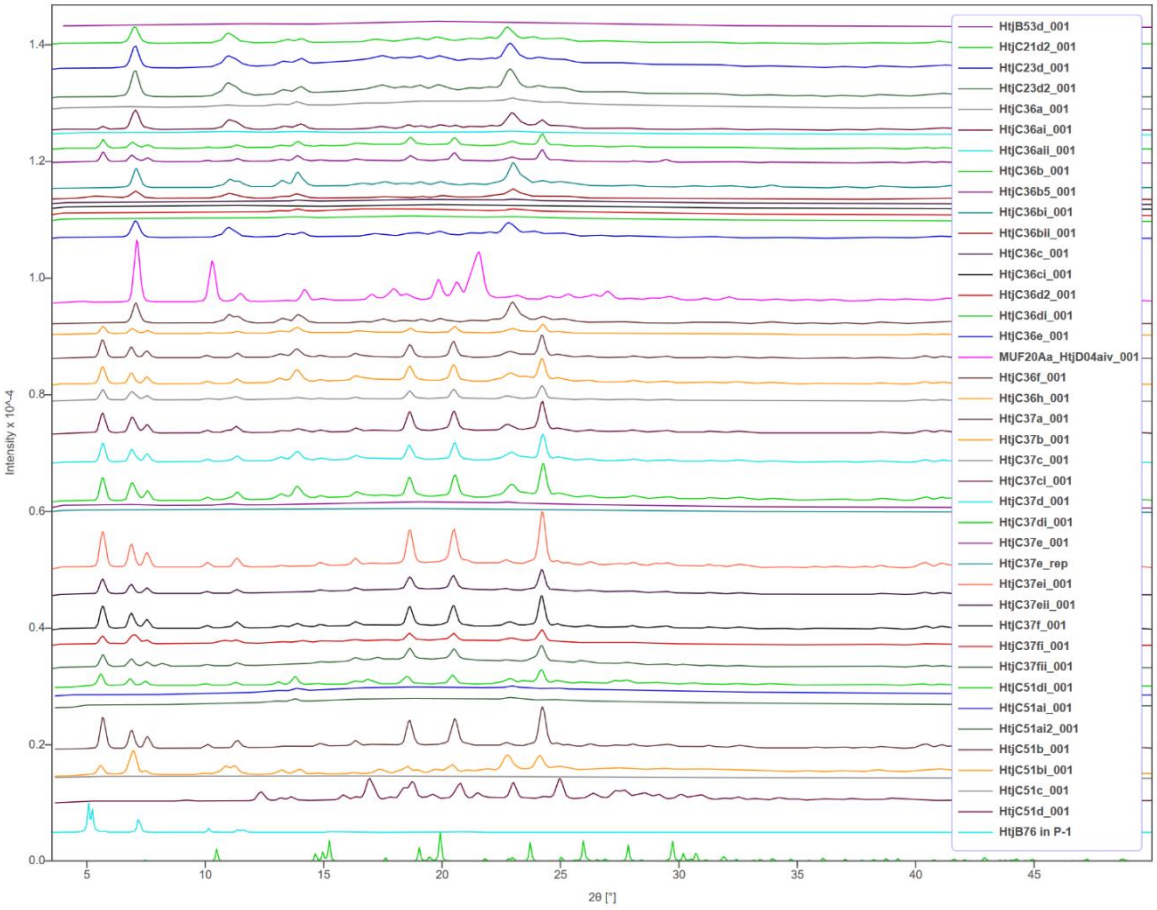

Figure 3.11: Simulated bpy-CO_2K PXRD and experimental PXRD of attempted MUF20-C`β` synthesis.

g) MUF20-C`γ

Amorphous only phase obtained.

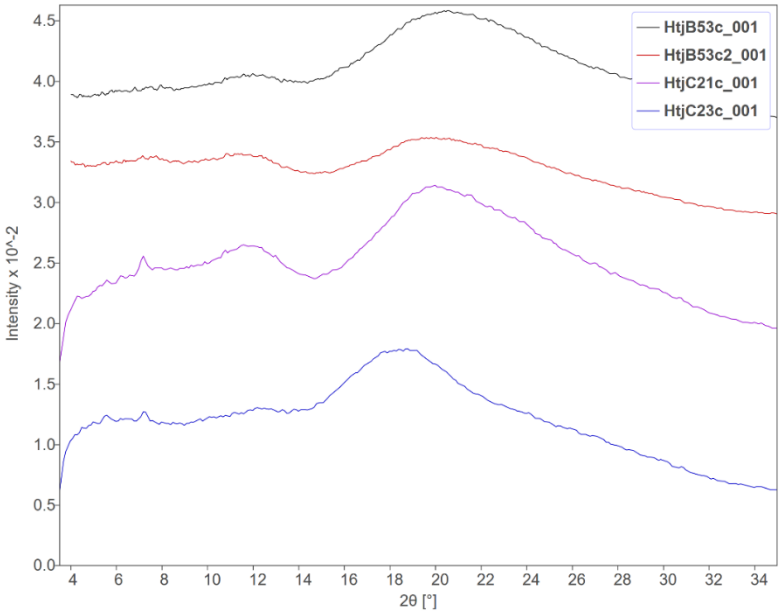

Figure 3.12: Experimental PXRD of attempted MUF20-C`γ synthesis.

h) MUF20-C`γ`

Single crystal could not be obtained.

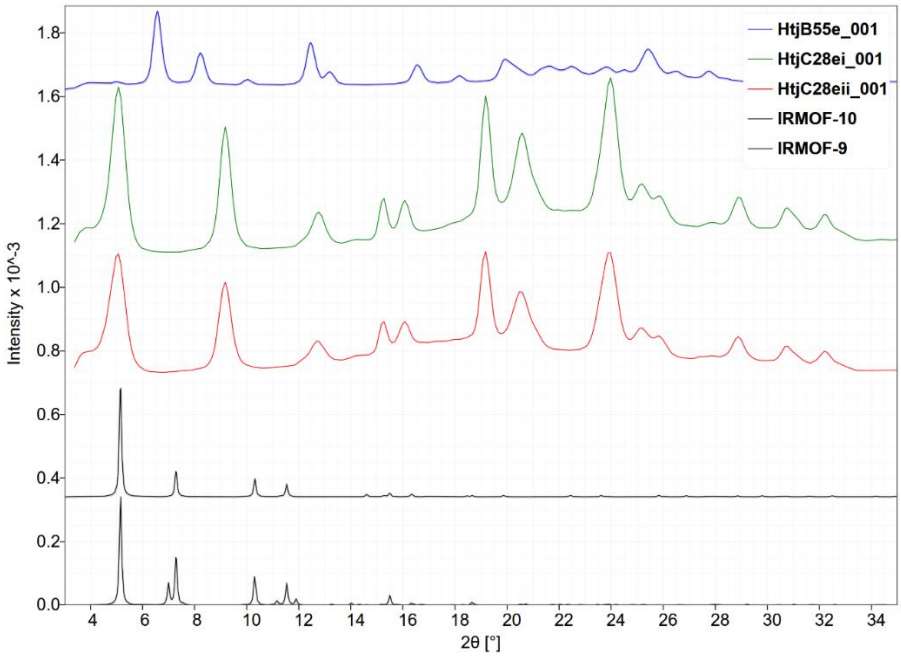

Figure 3.13: Simulated PXRD of IRMOF-9 and IRMOF-10 and experimental PXRD of attempted MUF20-C`γ` synthesis.

4. Chapter 4 –Meldrum's acid ligands; synthesis of a ketene TPG SI

4.1. Ligand synthesis and characterization

General procedures

All starting compounds and solvents were used as received from commercial sources of reagent grade or higher and deionised water used in all cases unless otherwise noted. Column chromatography was carried out on silica gel (grade 60, mesh size 230-400, Scharlau). Unless specified otherwise, all NMR spectra were recorded at room temperature. NMR analysis was performed on Bruker-400 and Bruker-500 Avance instruments, with the use of the solvent proton as an internal standard. IR spectra were collected on a Thermo Scientific Nicolet 5700 FT-IR spectrophotometer equipped with an attenuated total reflection (ATR) module (Smart Omni sampler, Ge crystal). Spectra were measured at a resolution of 4 cm^{-1}. Elemental analyses were performed by the Campbell Microanalytical Laboratory at the University of Otago, New Zealand. Thermogravimetric analysis (TGA) was performed on a TA Instruments Q50 instrument.

Ligands targeted

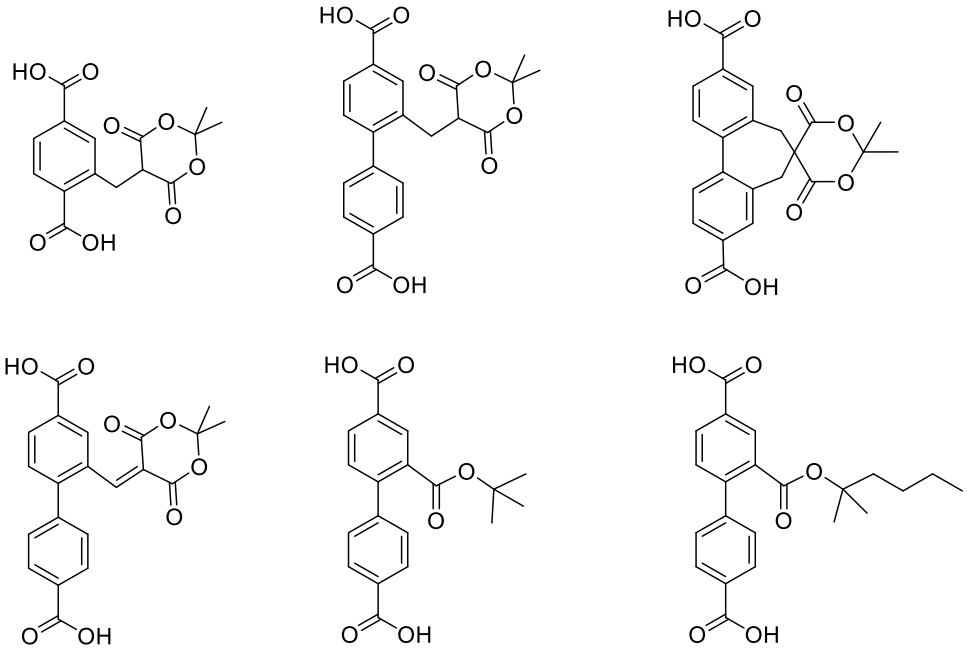

Final synthesis scheme:

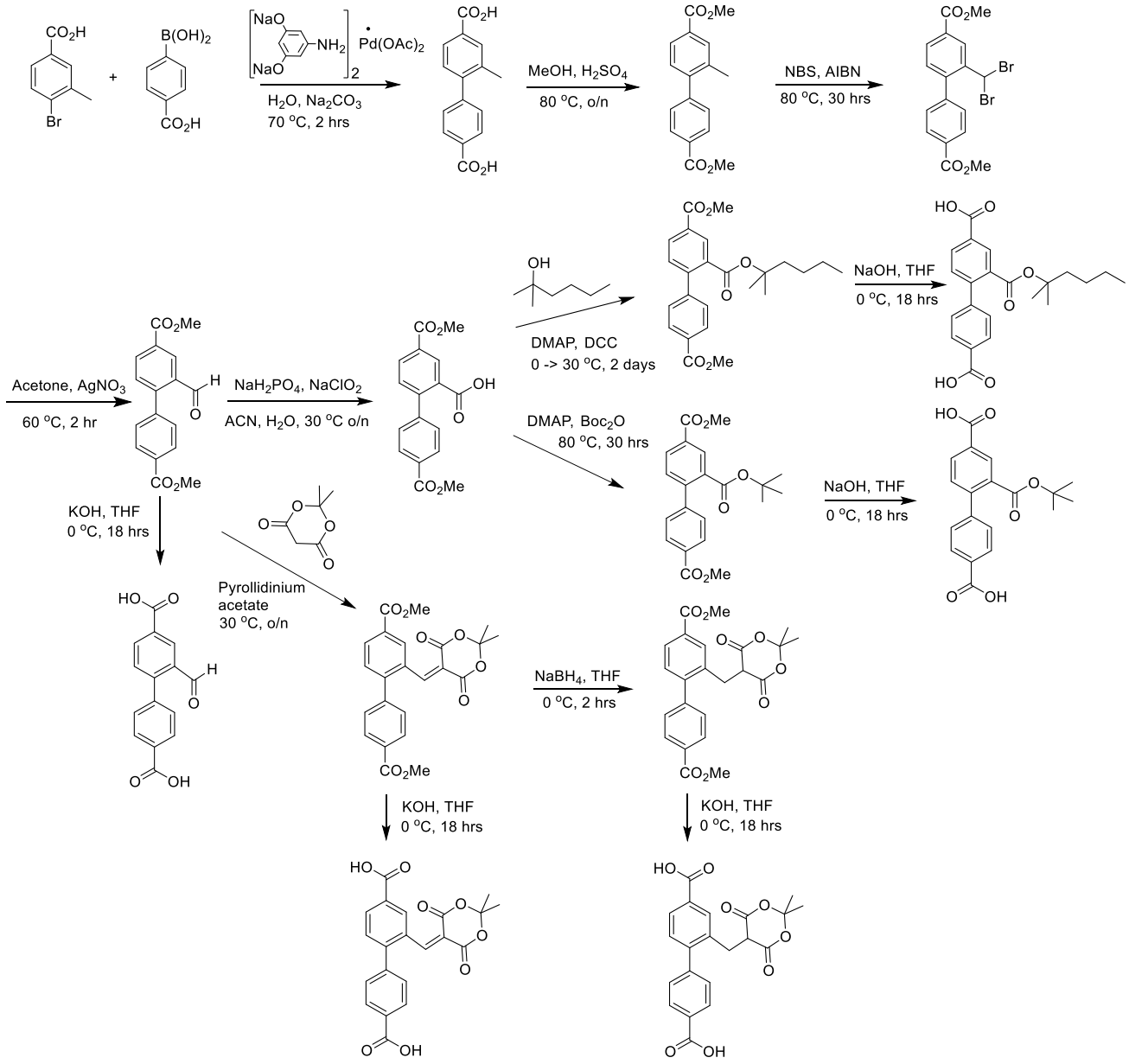

4.1.1. Synthesis of bpdc-CHO, bpdc-CO_2H, and spirocyclic Meldrums ligands

2-formylbiphenyl-4,4'-dicarboxylic acid

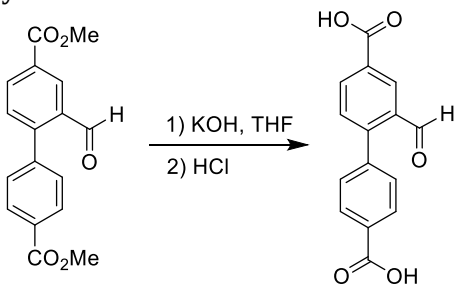

Dimethyl 2-formylbiphenyl-4,4'-dicarboxylate (151 mg, 0.517 mmol) was dissolved in dry THF (6.75 mL), split into 3 vials and cooled on ice before the addition of 1 M KOH (1.49 mL each). The opaque white

suspensions were stirred on ice overnight. Reaction mixtures were combined into a RBF and THF was then removed *in vacuo* before cooling the clear yellow aqueous layer on ice and gradually acidifying with 1 M HCl to pH 2.0. The fine white solid was then collected via suction filtration, washing thoroughly with H_2O before drying overnight under high vacuum to yield a greenish white powder (136 mg, 97%). ^{1}H NMR (500 MHz, DMSO-d_6) δ 13.28 (s, 2H), 9.92 (s, 1H), 8.46 (d, *J* = 1.8 Hz, 1H), 8.26 (dd, *J* = 8.0, 1.9 Hz, 1H), 8.07 (dd, *J* = 8.2, 1.8 Hz, 2H), 7.68 (d, *J* = 8.0 Hz, 1H), 7.63 (dd, *J* = 8.2, 1.8 Hz, 2H) ppm.

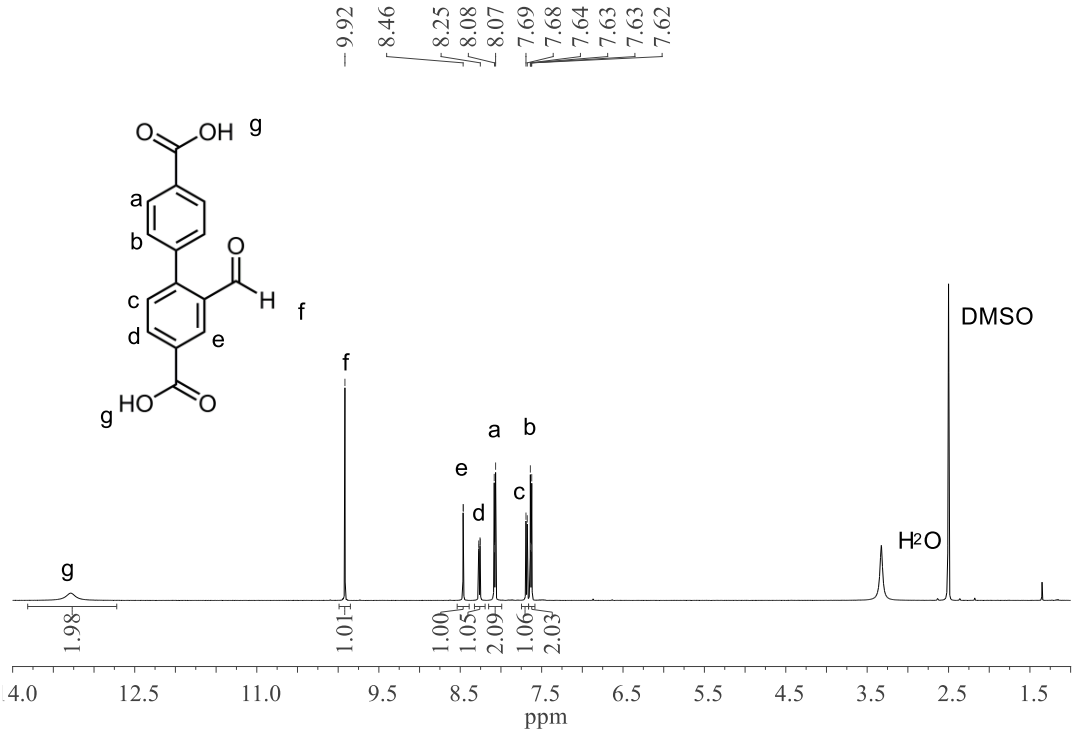

Figure 4.1: ^{1}H NMR spectrum of bpdc-CHO in DMSO-d_6.

[1,1'-biphenyl]-2,4,4'-tricarboxylic acid

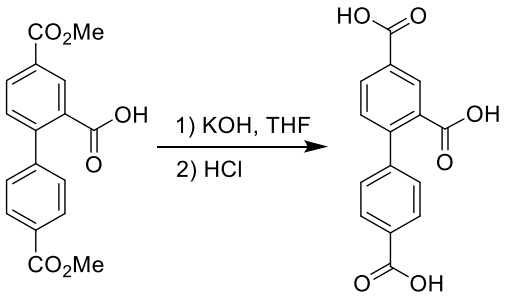

4,4'-bis(methoxycarbonyl)-[1,1'-biphenyl]-2-carboxylic acid (303.5 mg, 0.966 mmol) was dissolved in dry THF (4.5 mL) and cooled on ice before the addition of 1 M KOH (7.14 mL each). The opaque white suspension was stirred overnight, allowing to gradually warm to room temperature. THF was then removed *in vacuo* before cooling the clear yellow aqueous layer on ice and gradually acidifying with 1 M HCl to pH 1.0. The fine white solid was then collected via suction filtration, washing thoroughly with H_2O before drying overnight under high

vacuum to yield a white powder (249.5 mg, 90%). ^{1}H NMR (400 MHz, DMSO-d_6) δ 13.15 (s, 3H), 8.32 (d, J = 1.7 Hz, 1H), 8.12 (dd, J = 8.0, 1.8 Hz, 1H), 7.98 (d, J = 8.5 Hz, 2H), 7.54 (d, J = 8.0 Hz, 1H), 7.48 (d, J = 8.5 Hz, 2H).

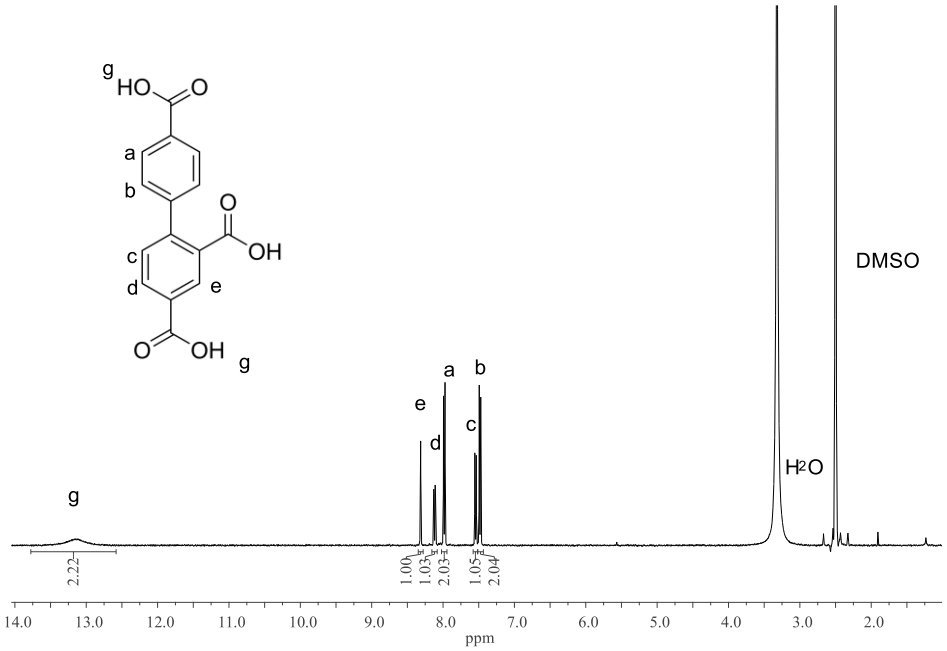

Figure 4.2: ^{1}H NMR spectrum bpdc-CO_2H in DMSO-d_6.

a) [1,1'-biphenyl]-2,4,4'-tricarboxylic acid

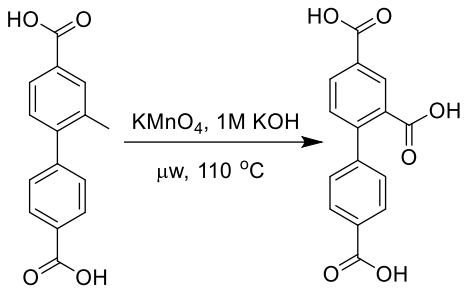

2-methyl-[1,1'-biphenyl]-4,4'-dicarboxylic acid (105.4 mg, 0.411 mmol) and $KMnO_4$ (137.7 mg, 0.871 mmol) and 1M $KOH_{(aq)}$ were combined in a 15 mL microwave vessel. The reaction mixture was then irradiated for 10 min at 110 °C. This was then filtered through celite, washing with H_2O five times. The filtrate was cooled on ice before acidification to pH~2.5 with 3M HCl. The fine white solid was then collected via suction filtration, washing thoroughly with H_2O before drying overnight under high vacuum to yield a shiny flaky white solid that was further recrystallized from acetic acid/H_2O (69.6 mg, 59%). ^{1}H NMR (500 MHz, DMSO-d_6) δ 13.09 (s, 3H), 8.32 (d, J = 1.5 Hz, 1H), 8.12 (dd, J = 8.0, 1.6 Hz, 1H), 7.98 (d, J = 8.2 Hz, 2H), 7.55 (d, J = 8.0 Hz, 1H), 7.48 (d, J = 8.2 Hz, 2H).

b) Tetramethyl 2,2''-(9-hydroxy-9-methoxy-3,3-dimethyl-1,5-dioxo-2,4-dioxaspiro[5.5]undecane-7,11-diyl)bis([1,1'-biphenyl]-4,4'-dicarboxylate)

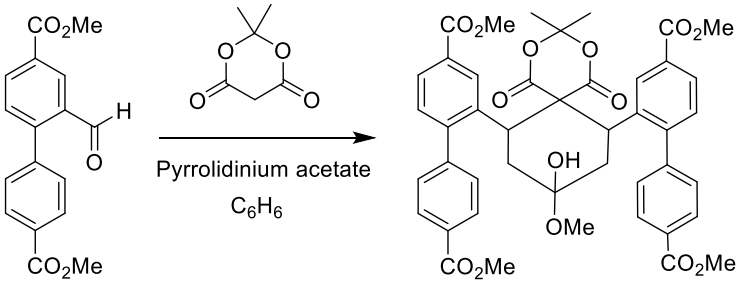

In the presence of trace amounts of methanol and pyrrolidinium acetate the methylated bpdc-CHMeldrum's ligand undergoes double Michael addition reaction at room temperature to form the spirocyclic product.

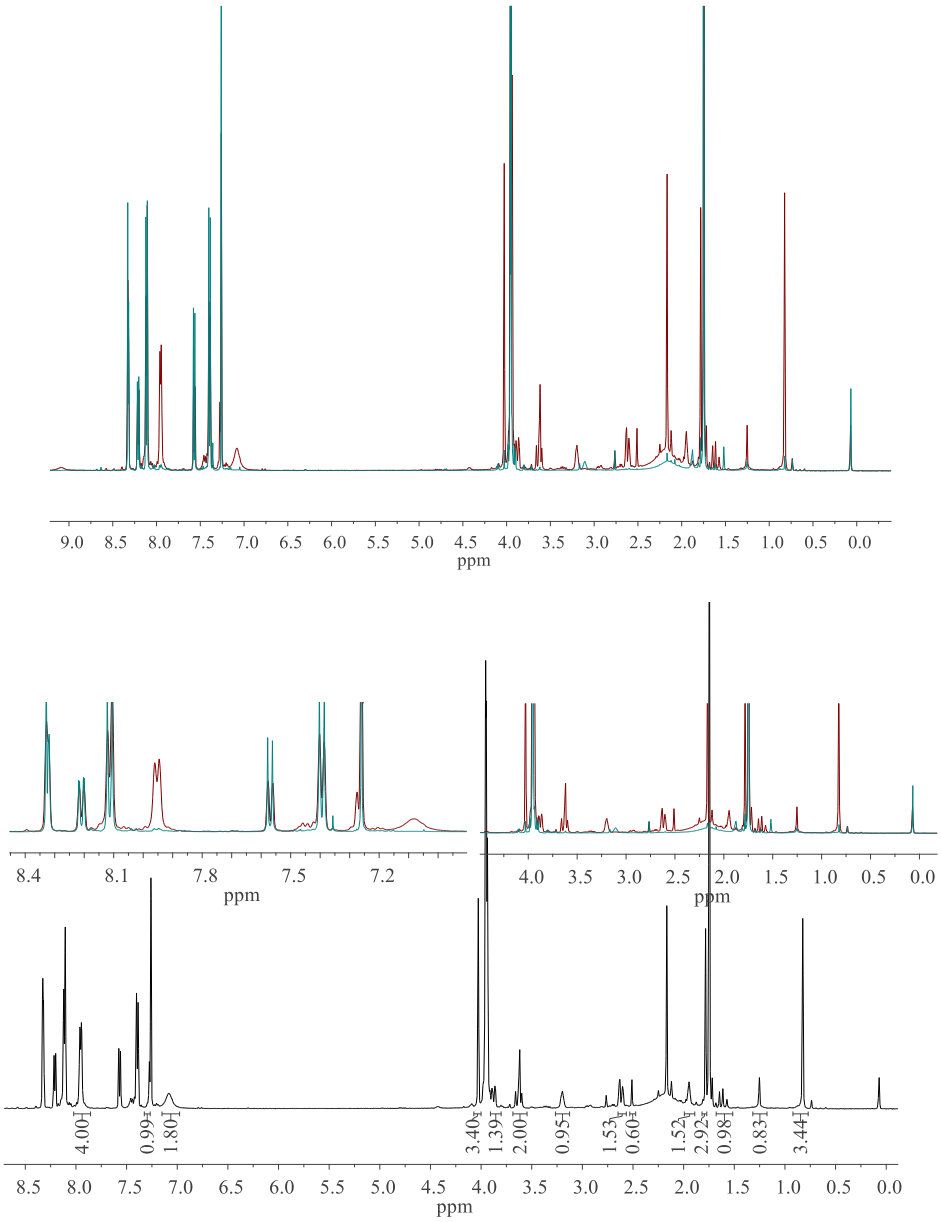

Figure 4.3: ^{1}H NMR spectrum of digested spirocyclic Meldrum's acid ligand in $CDCl_3$ mixed with the starting material, methyl-esterified bpdc-CHMeldrums. Appearance of methyl

and alkyl protons at low ppm associated with cyclohexane moiety. Also separation of methyl ester peaks of ligand backbone at ~4.0 ppm as well as differentiation of Meldrum's acid methyl proton peak at 1.8 ppm.

4.1.2. Synthesis of bpdc-Meldrums, $(bpdc)_2$-bisMeldrums and bpdc-CH_2Br

Tert-butyl ester route:

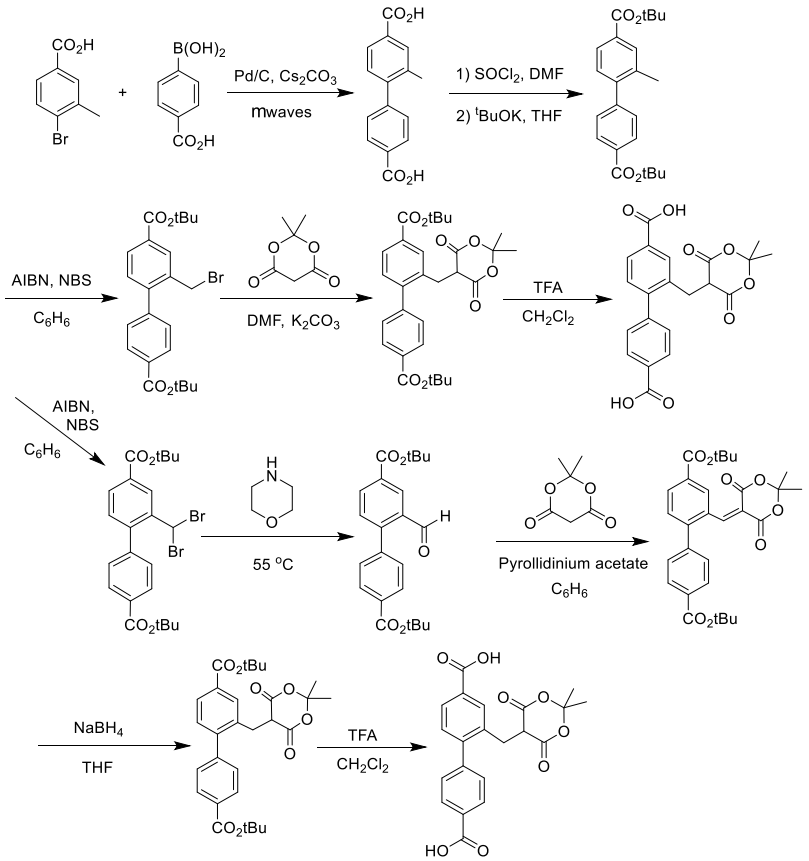

First step utilises microwave method detailed in first reaction scheme.

Dibrominated side product could be recovered into ligand synthesis through conversion into an aldehyde using morpholine after the conditions used for synthesis of the methyl ester biphenyl formyl dicarboxylate were found to be incompatible with the *tert*-butyl ester group.

(a) Di-*tert*-butyl 2-methylbiphenyl-4,4'-dicarboxylate

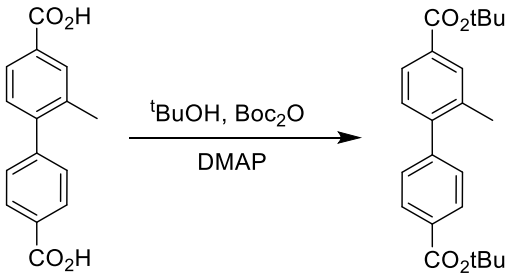

Crude 2,2'-dimethylbiphenyl-4,4'-dicarboxylic acid (1.56 g, 6.09 mmol) was dissolved in a mixture of *tert*-butanol/THF (1:1, 40 mL), then di-*tert*-butyl dicarbonate (5.60 mL, 24.4 mmol) and 4-dimethylaminopyridine (893 mg, 7.31 mmol) were added. The clear dark red solution was then stirred at 40 °C under $Ar_{(g)}$ overnight. More di-*tert*-butyl dicarbonate (2.80 mL, 12.2 mmol) and 4-dimethylaminopyridine (446 mg, 3.65 mmol) was added, and then stirred at 40 °C under $Ar_{(g)}$ overnight. The solvent was then removed *in vacuo* and an orange/pink suspension formed in CH_2Cl_2 which was filtered through a sintered glass funnel, rinsing with CH_2Cl_2 until orange colour leached from solid grey impurities. The filtrate was then concentrated *in vacuo* to 1-2 mL before purifying by silica flash column chromatography (10% CH_2Cl_2:hexane) affording a clear red oil which gradually crystallizes as an orange solid. (1.46 g, 65%). ^{1}H NMR (400 MHz, $CDCl_3$) δ 8.05 (d, *J* = 8.5 Hz, 2H), 7.90 (s, 1H), 7.86 (dd, *J* = 7.9, 1.7 Hz, 1H), 7.36 (d, *J* = 8.5 Hz, 2H), 7.26 (d, *J* = 7.9 Hz, 1H), 2.29 (s, 3H), 1.62 (s, 9H), 1.61 (s, 9H).

Alternatively:

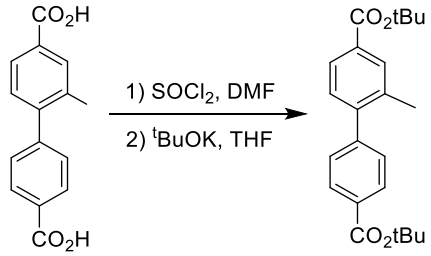

Crude 2,2'-dimethylbiphenyl-4,4'-dicarboxylic acid (1.56 g, 6.09 mmol) 4-bromo-3-methylbenzoic acid (5.06 g, 23.5 mmol), was dissolved in thionyl chloride (50 mL) and a few drops of dry DMF and placed under $Ar_{(g)}$ with stirring before heating to 80 ^{o}C for 3 hrs. Thionyl chloride removed *in vacuo* using solvent trap. Red solid further dried under high vacuum for 1 hr before dissolving in dry THF (30 mL) and placing under $Ar_{(g)}$ with stirring on ice. ^{t}BuOK (10.5 g, 93.3 mmol) in dry THF (93 mL) was then added dropwise to the clear orange solution before stirring overnight on ice, forming a thick tan slurry. The reaction was quenched pouring over ice/H_2O before extracting with ethyl acetate. The organic layer was dried over Na_2SO_4 before removing the solvent under low pressure and further drying the orange/tan solid under high vacuum overnight. (3.78 g, 59%).

(b) Di-*tert*-butyl 2-(bromomethyl)biphenyl-4,4'-dicarboxylate

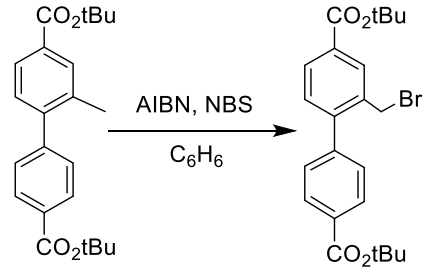

Di-*tert*-butyl 2-methylbiphenyl-4,4'-dicarboxylate (902 mg, 2.45 mmol) was dissolved in dry benzene (30 mL) before the addition of N-bromosuccinimide (523 mg, 2.94 mmol) and AIBN (160 mg, 0.977 mmol). The reaction mix was then heated at 70 °C under $Ar_{(g)}$ for 18 hours. TLC analysis (3:1 CH_2Cl_2/hexane) indicated a mixture of the starting material, mono-brominated compound, and other compounds. However, ^{1}H NMR analysis of the crude reaction mixture showed the product to be relatively pure. The solvent was removed *in vacuo* and the residue purified by silica flash column chromatography (10% CH_2Cl_2/hexane) affording a clear oil (0.25 g, 21%, completely clean product or 1.14 g all up, 94%, of tolerable purity). ^{1}H NMR: (400 MHz, $CDCl_3$) δ 8.14 (d, *J* = 1.6 Hz, 1H), 8.09 (d, *J* = 8.5 Hz, 2H), 7.96 (dd, *J* = 8.0, 1.7 Hz, 1H), 7.49 (d, *J* = 8.5 Hz, 2H), 7.29 (d, *J* = 8.0 Hz, 1H), 4.42 (s, 2H), 1.62 (s, 9H), 1.61 (s, 9H).

(c) Di-*tert*-butyl 2 –((2,2-dimethyl-4,6-dioxo-1,3-dioxan-5-yl)methyl)-4,4'-dicarboxylate

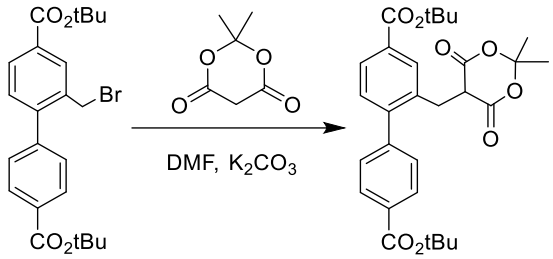

Di-*tert*-butyl-2-(bromomethyl)biphenyl-4,4'-dicarboxylate (502 mg, 1.12 mmol) was dissolved in dry DMF (2.85 mL) and cooled on ice for 10 min before the addition of 2,2-dimethyl-1,3-dioxane-4,6-dione (179 mg, 1.24 mmol), and potassium carbonate (171 mg, 1.24 mmol). The pale yellow suspension was then stirred on ice for 12 hours. The reaction was quenched by pouring over ice/H_2O before gradually acidifying to ~pH 1.5 with 1M HCl. The white solid was then collected via suction filtration, washing copiously with cold H_2O before drying under suction and further drying overnight under high vacuum. The crude product was recrystallized from hot CH_2Cl_2/hexane (1:1), filtered, washing with cold hexane. (177 mg, 31%).

ci) Tetra-*tert*-butyl 2,2''-((2,2-dimethyl-4,6-dioxo-1,3-dioxane-5,5-diyl)bis(methylene))bis([1,1'-biphenyl]-4,4'-dicarboxylate)

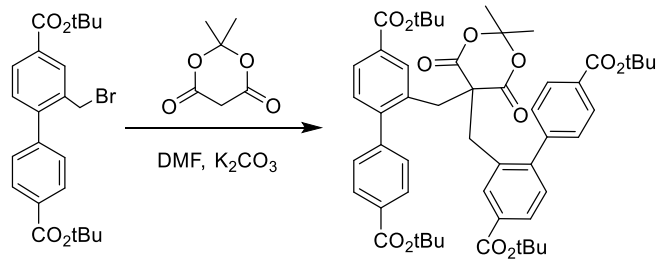

The monosubstituted species was recrystallized from hot CH_2Cl_2/hexane (1:1), filtered, washing with cold hexane. The collected filtrate crystallizes as the bis species, white crystalline solid (275 mg, 56%). ^{1}H NMR (500 MHz, $CDCl_3$) δ 8.01 (d, *J* = 8.3 Hz, 4H), 7.82 (dd, *J* = 8.0, 1.6 Hz, 2H), 7.78 (d, *J* = 1.5 Hz, 2H), 7.24 (d, *J* = 8.3 Hz, 4H), 7.18 (d, *J* = 8.0 Hz, 2H), 3.37 (s, 4H), 1.62 (s, 18H), 1.54 (s, 18H), 1.03 (s, 6H).

(d) 2-((2,2-dimethyl-4,6-dioxo-1,3-dioxan-5-yl)methyl)biphenyl-4,4'-dicarboxylic acid.

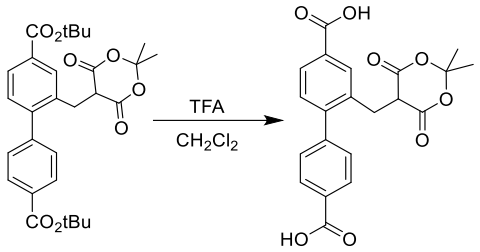

Di-*tert*-butyl 2–((2,2-dimethyl-4,6-dioxo-1,3-dioxan-5-yl)methyl)-4,4'-dicarboxylate (141 mg, 0.276 mmol) was dissolved in dry CH_2Cl_2 (25 mL) and cooled on ice to 0 °C before the addition of TFA (2.12 mL, 27.6 mmol). The reaction was then left to warm to room temperature under continuous stirring for 3 hours 50 min. The solvent was removed *in vacuo* and the solid dried overnight before sonicating/rinsing briefly in $CHCl_3$ and filtering off the white solid (82 mg, 74%). ^{1}H NMR (500 MHz, DMSO-d_6) δ 13.03 (s, 2H), 8.03 (d, J = 8.2 Hz, 2H), 7.93 (s, 1H), 7.86 (dd, *J* = 7.9, 1.6 Hz, 1H), 7.48 (d, *J* = 8.2 Hz, 2H), 7.32 (d, *J* = 7.9 Hz, 1H), 4.64 (t, *J* = 5.4 Hz, 1H), 3.09 (d, *J* = 7.7 Hz, 2H), 1.77 (s, 3H), 1.63 (s, 3H).

di) 2,2''-((2,2-dimethyl-4,6-dioxo-1,3-dioxane-5,5-diyl)bis(methylene))bis([1,1'-biphenyl]-4,4'-dicarboxylic acid)

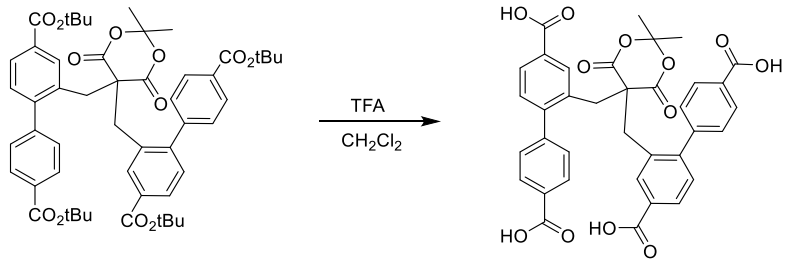

Tetra-*tert*-butyl 2,2''-((2,2-dimethyl-4,6-dioxo-1,3-dioxane-5,5-diyl)bis(methylene))bis([1,1'-biphenyl]-4,4'-dicarboxylate) (30.5 mg, 0.0348 mmol) was dissolved in dry CH_2Cl_2 (2.98 mL) and cooled on ice to 0 °C before the addition of TFA (264 μL, 3.43 mmol). The reaction was then stirred on ice for 12 hours. Additional TFA (132 μL, 1.71 mmol) was added and the clear, colourless solution stirred for a further 12 hours. The solvent was removed *in vacuo* and the solid dried overnight under high vacuum to yield a white powder (23.6 mg,

quant. yield). ^{1}H NMR (500 MHz, DMSO-d_6) δ 13.06 (s, 4H), 7.99 (d, J = 8.2 Hz, 4H), 7.85 (d, J = 8.0 Hz, 2H), 7.68 (s, 2H), 7.32 (d, J = 8.1 Hz, 4H), 7.29 (d, J = 8.0 Hz, 2H), 1.04 (s, 6H).

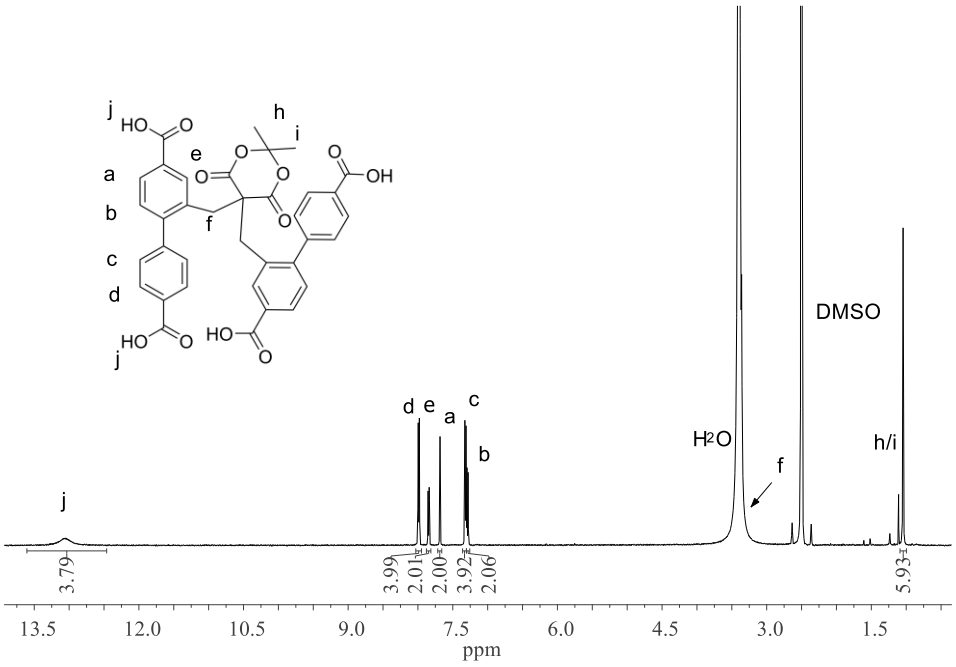

Figure 4.4: ^{1}H NMR spectrum of $(bpdc)_2$-bisMeldrums in DMSO-d_6.

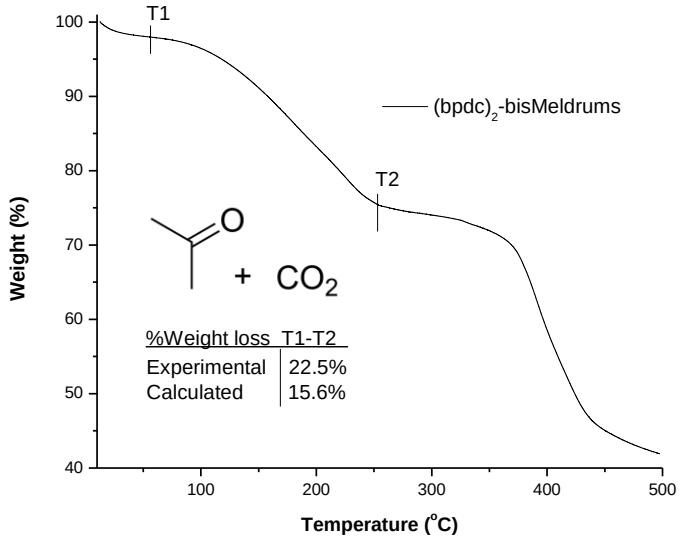

Figure 4.5: Thermogravimetric analysis (TGA) trace for $(bpdc)_2$-bisMeldrums.

The syntheses of copper(II), manganese(II), chromium(III), cobalt(II) and nickel(II) MOFs[3] were attempted with the bis ligands at 85 °C in various solvents without success. Despite multiple different solvothermal MOF synthesis conditions trialled, neither of the two bis species isolated has formed MOFs as yet. The lack of success to date with solvothermal synthesis involving the bis-substituted Meldrum's acid

ligands may be attributed to the restricted coordination modes with the four carboxylates lying somewhat parallel rather than being completely divergent to each other as in porphyrin and other literature tetratopic ligands.

e) 2,2'-bis(bromomethyl)-[1,1'-biphenyl]-4,4'-dicarboxylic acid

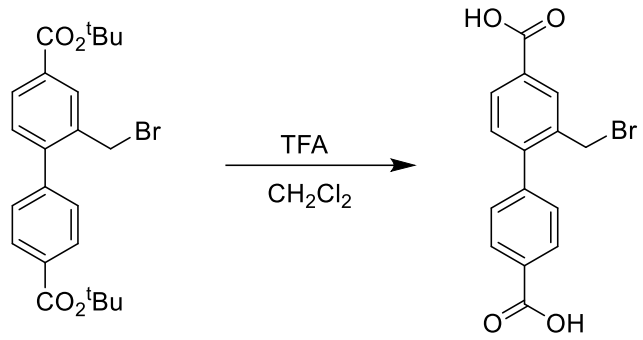

Tert-butyl 2-bromomethyl-[1,1'-biphenyl]-4,4'-dicarboxylate (139 mg, 0.311 mmol) was dissolved in dry CH_2Cl_2 (25 mL), and cooled on ice before the addition of TFA (2.10 mL). Reaction mixtures were stirred overnight, gradually warming to room temperature. Solvent was then removed under vacuum using warm water bath, dried under vacuum before further drying overnight under high vacuum to yield a white powder (~130 mg). ^{1}H NMR (400 MHz, DMSO-d_6) δ 13.12 (s, 2H), 8.19 (d, J = 1.7 Hz, 1H), 8.06 (d, J = 8.5 Hz, 2H), 7.96 (dd, J = 8.0, 1.8 Hz, 1H), 7.59 (d, J = 8.5 Hz, 2H), 7.42 (d, J = 8.0 Hz, 1H), 4.67 (s, 2H).

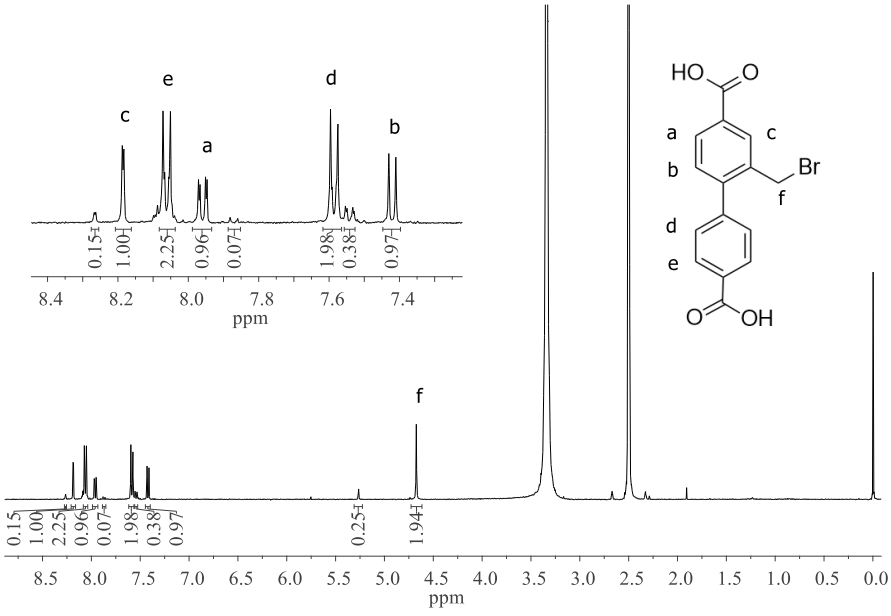

Figure 4.6: ^{1}H NMR spectrum of bpdc-CH_2Br in DMSO-d_6.

f) Di-*tert*-butyl 2-formyl-[1,1'-biphenyl]-4,4'-dicarboxylate

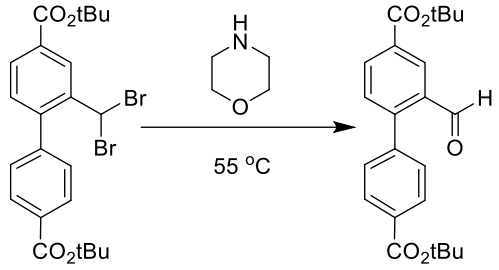

Di-*tert*-butyl 2-(dibromomethyl)-[1,1'-biphenyl]-4,4'-dicarboxylate (1.55 g, 2.94 mmol) was dissolved in morpholine (4.18 mL) and flushed with $Ar_{(g)}$ before heating to 59 °C for 18 hours. The reaction mixture was monitored by TLC (4:1 CH_2Cl_2: Hexane) and a further 25 mL morpholine added, stirred for an hour, 3.5 mL morpholine added and stirred overnight at 62 °C. A final 5 mL morpholine was added and the reaction mixture stirred for 3 hours before cooling to room temperature. An equivalent volume of ethyl acetate was then added and the suspension stirred at room temperature for 25 minutes before filtering the white solid. The filtrate was concentrated and washed with 5% citric acid before removing the solvent *in vacuo*, yielding a reddish solid (1.12 g, 66%). ^{1}H NMR (500 MHz, $CDCl_3$) δ 9.97 (s, 1H), 8.59 (d, *J* = 1.7 Hz, 1H), 8.25 (dd, *J* = 8.0, 1.8 Hz, 1H), 8.10 (d, *J* = 8.3 Hz, 2H), 7.50 (d, *J* = 8.0 Hz, 1H), 7.43 (d, *J* = 8.3 Hz, 2H), 1.63 (s, 9H), 1.62 (s, 9H).

g) Di-*tert*-butyl 2-((2,2-dimethyl-4,6-dioxo-1,3-dioxan-5-ylidene)methyl)-[1,1'-biphenyl]-4,4'-dicarboxylate

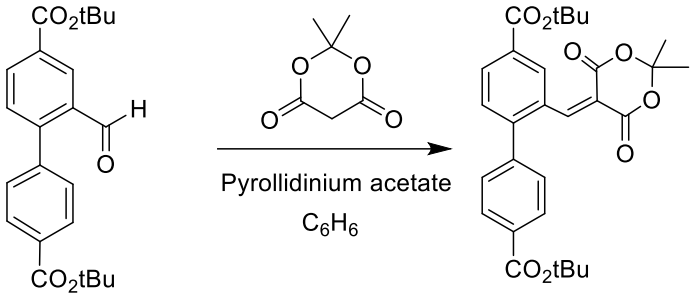

Di-*tert*-butyl 2-formyl-[1,1'-biphenyl]-4,4'-dicarboxylate (743 mg, 1.94 mmol) and 2,2-dimethyl-1,3-dioxane-4,6-dione (308 mg, 2.14 mmol) were dissolved in dry benzene (9.0 mL) and placed under $Ar_{(g)}$. Pyrrolidine (16.0 μL, 0.194 mmol) in dry benzene (320 μL) was combined with acetic acid (11.1 μL, 0.194 mmol) and stirred at room temperature for 1 min before adding to the above solution. The slightly pink suspension was then stirred at room temperature for 22 hours. The solvent was then concentrated *in vacuo*, cooled to room temperature and a crystalline pale yellow solid obtained (455 mg, 46%). The crude decant could be further recrystallized from boiling MeOH. ^{1}NMR (500 MHz, $CDCl_3$) δ 8.33 (s, 1H), 8.28 (d, *J* = 1.5 Hz, 1H), 8.14 (dd, *J* = 8.0, 1.5 Hz, 1H), 8.05 (d, *J* = 8.4 Hz, 2H), 7.53 (d, *J* = 8.1 Hz, 1H), 7.36 (d, *J* = 8.4 Hz, 2H), 1.74 (s, 6H), 1.61 (s, 19H).

h) Di-*tert*-butyl 2–((2,2-dimethyl-4,6-dioxo-1,3-dioxan-5-yl)methyl)-4,4'-dicarboxylate

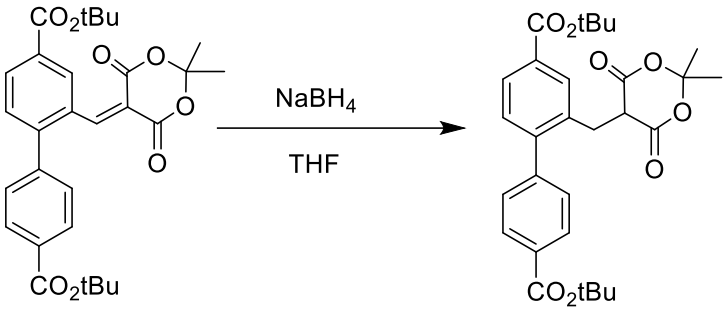

Di-*tert*-butyl 2-((2,2-dimethyl-4,6-dioxo-1,3-dioxan-5-ylidene)methyl)-[1,1'-biphenyl]-4,4'-dicarboxylate (455.3 mg, 0.895 mmol) was dissolved in dry CH_2Cl_2 (5.87 mL), cooled on ice and acidified to pH 2.5 by acetic acid. $NaBH_4$ (86.5 mg, 2.24 mmol) in dry CH_2Cl_2 (5.47 mL) was then added in aliquots over 1 hr before leaving the reaction mixture to stir overnight on ice. Brine was then added and the organic layer washed twice with Brine and thrice with H_2O before drying over Na_2SO_4. Solvent was removed *in vacuo* yielding a white, oily solid (381.7 mg, 84%). ^{1}H NMR (500 MHz, $CDCl_3$) δ 8.06 (d, *J* = 8.3 Hz, 2H), 8.01 (d, *J* = 1.3 Hz, 1H), 7.91 (dd, *J* = 7.9, 1.6 Hz, 1H), 7.40 (d, *J* = 8.4 Hz, 2H), 7.26 (d, *J* = 7.9 Hz, 1H), 3.61 (t, *J* = 6.2 Hz, 1H), 3.46 (d, *J* = 6.2 Hz, 2H), 1.67 (s, 3H), 1.63 (s, 3H), 1.61 (s, 9H), 1.61 (s, 9H).

4.1.3. Synthesis of bdc-Meldrums and (bdc)$_2$-bisMeldrums

Reaction Scheme

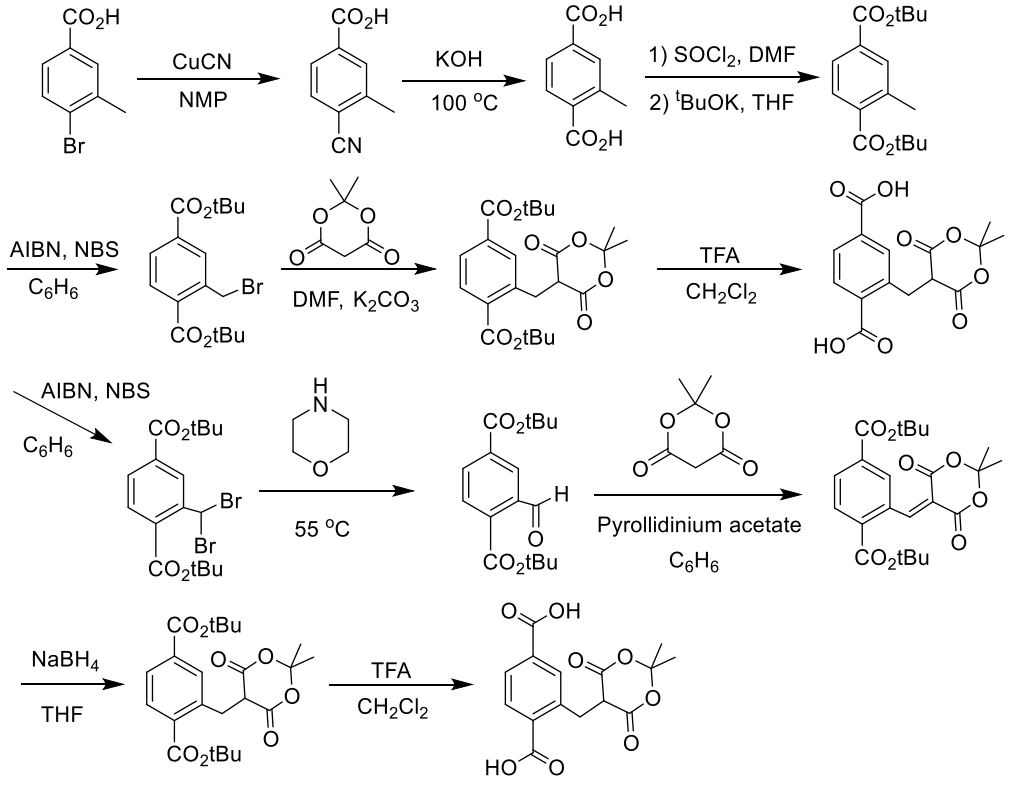

a) 4-cyano-3-methylbenzoic acid

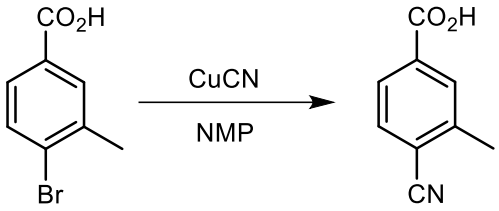

4-bromo-3-methyl benzoic acid (2.50 g, 11.5 mmol), CuCN (4.15g, 49.3 mmol) were combined in a 35 mL μw vessel, NMP (15 mL) was added, flushed with $Ar_{(g)}$ and thoroughly mixed before heating without stirring at 155 °C for 3 days. The reaction mixture was cooled to room temperature and 1 M KOH (30 mL) added before filtering. The filtrate was cooled on ice and gradually acidified to pH 2.0 before extracting with ethyl actetate, initially filtering both organic and aqueous to remove solid impurities. The organic layers were combined, dried over Na_2SO_4, filtered and solvent removed *in vacuo* to yield a moist red brown solid. Carried forward without thorough drying. ^{1}H NMR (500 MHz, DMSO-d_6) δ 13.40 (s, 1H), 7.98 (s, 1H), 7.88 (s, 1H), 7.87 (s, 1H), 2.54 (s, 3H).

b) 2-methylterephthalic acid

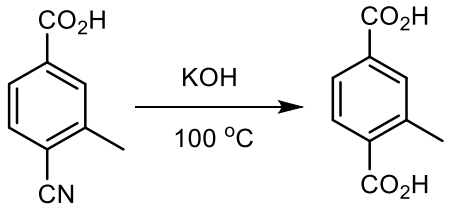

4-cyano-3-methylbenzoic acid (9.39 g, 58.3 mmol) was dissolved in 1 M KOH (213 mL) and the dark red solution placed under $Ar_{(g)}$ and stirred at 97 °C for 7 days, monitoring reaction progress through ^{1}H NMR. The clear yellow reaction mixture was then filtered and the filtrate cooled on ice before acidifying to pH 1.5 with 3 M HCl. The off-white precipitate was collected via Buchner filtration, washing thrice with H_2O and drying under suction before further drying under high vacuum overnight to give an off-white powder (9.74 g, 93%). ^{1}H NMR (500 MHz, DMSO-d_6) δ 7.53 (s, 1H), 7.50 (d, J = 7.8 Hz, 1H), 7.26 (d, J = 7.8 Hz, 1H), 2.16 (s, 3H).

c) Di-*tert*-butyl 2-methylterephthalate

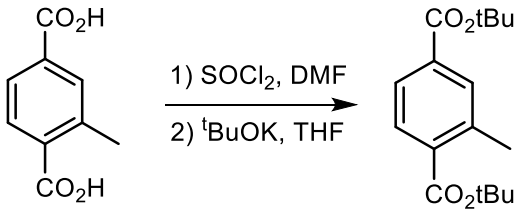

2-methylterephthalic acid (9.74 g, 0.0541 mol) was dissolved in thionyl chloride (118 mL, 1.62 mol) and 10 drops dry DMF before placing under $Ar_{(g)}$ and heating to 76 ^{o}C and stirring for 2 hours. Thionyl chloride removed *in vacuo* using solvent trap. Red solid further dried under high vacuum for 90 min before dissolving in dry THF (96 mL) and placing under $Ar_{(g)}$ with stirring on ice. ^{t}BuOK (30.1 g, 0.270 mol) in dry THF (270 mL) was then added dropwise to the clear brownish orange solution before stirring the black/brown reaction mixture for 3 hours on ice. The reaction was quenched pouring over ice/H_2O before extracting with ethyl acetate. The organic layer was dried over Na_2SO_4 and filtered before removing the solvent under low pressure and further drying the black oil under high vacuum overnight (13.6 g, 86%). The crude product was then purified by flash silica column chromatography (CH_2Cl_2:hexane) to yield crystalline white solid (9.96 g, 63%). ^{1}H NMR (400 MHz, $CDCl_3$) δ 7.81 (m, 3H), 2.58 (s, 3H), 1.60 (s, 9H), 1.59 (s, 9H).

d) Di-*tert*-butyl 2-(bromomethyl)terephthalate

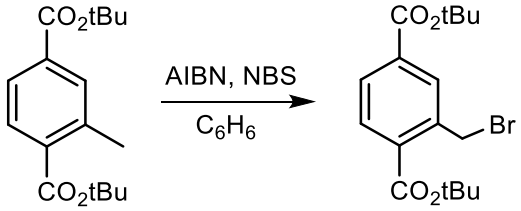

e) Tetra-*tert*-butyl-2,2'-((2,2-dimethyl-4,6-dioxo-1,3-dioxane-5,5-diyl)bis(methylene))diterephthalate

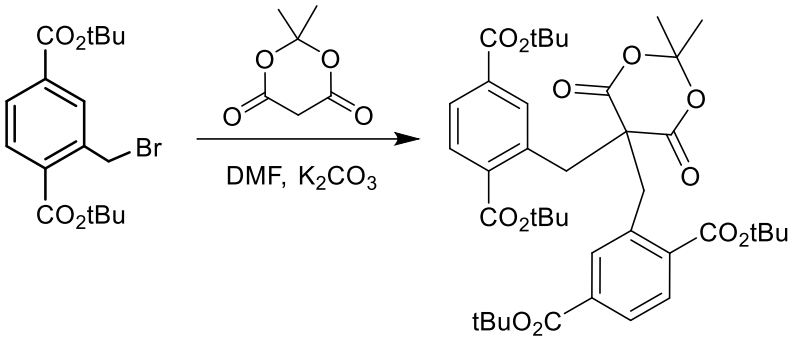

Di-*tert*-butyl 2-(bromomethyl)terephthalate (501 mg, 1.35 mmol) was dissolved in dry DMF (2.85 mL) and cooled on ice for 10 min before the addition of 2,2-dimethyl-1,3-dioxane-4,6-dione (213 mg, 1.47 mmol), and potassium carbonate (205 mg, 1.48 mmol). The pale yellow suspension was then stirred overnight on ice. The reaction was quenched by pouring over ice/H_2O before gradually acidifying to pH 1.5 with 1M HCl. The white solid was then collected via suction filtration, washing copiously with cold H_2O before drying under suction and further drying overnight under high vacuum. The monosubstituted species was recrystallized from minimum hot CH_2Cl_2 and hexane. The collected decant crystallises as the bis, slightly beige crystalline solid

(189 mg, 39%). ^{1}H NMR (500 MHz, $CDCl_3$) δ 7.91 (s, 2H), 7.85 (d, *J* = 8.1 Hz, 2H), 7.78 (d, *J* = 8.1 Hz, 2H), 1.58 (s, 18H), 1.56 (s, 18H), 1.15 (s, 6H).

f) 2,2'-((2,2-dimethyl-4,6-dioxo-1,3-dioxane-5,5-diyl)bis(methylene))diterephthalic acid

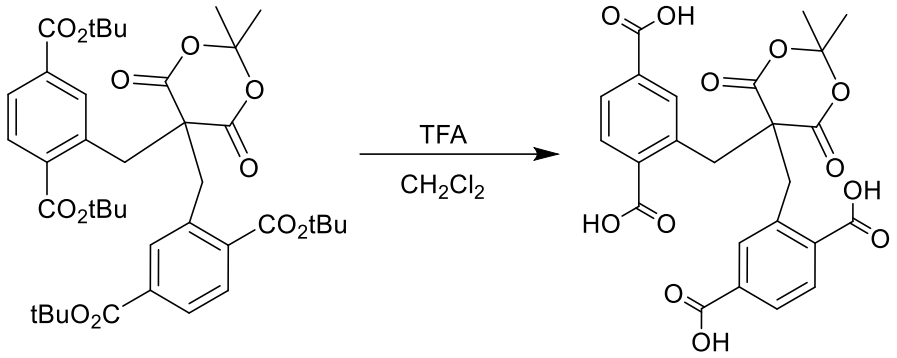

Tetra-*tert*-butyl 2,2'-((2,2-dimethyl-4,6-dioxo-1,3-dioxane-5,5-diyl)bis(methylene))diterephthalate (50.6 mg, 0.0698 mmol) was dissolved in dry CH_2Cl_2 (6.0 mL) and cooled on ice to 0 °C before the addition of TFA (532 µL, 6.91 mmol). The reaction was then stirred on ice for 16 hours. Additional TFA (50 µL, 0.649 mmol) was added and the clear, colourless solution stirred for 4 hours on ice before a final lot of TFA (85 µL, 1.10 mmol). Stirred on ice for 16 hours. The solvent was removed *in vacuo* and the solid dried overnight under high vacuum yielding a white powder (23.6 mg, quant. yield). ^{1}H NMR (500 MHz, DMSO-d_6) δ 13.31 (s, 4H), 7.90 (dd, *J* = 8.1, 1.6 Hz, 2H), 7.85 (d, *J* = 8.1 Hz, 2H), 7.82 (d, *J* = 1.3 Hz, 2H), 3.94 (s, 4H), 1.06 (s, 6H).

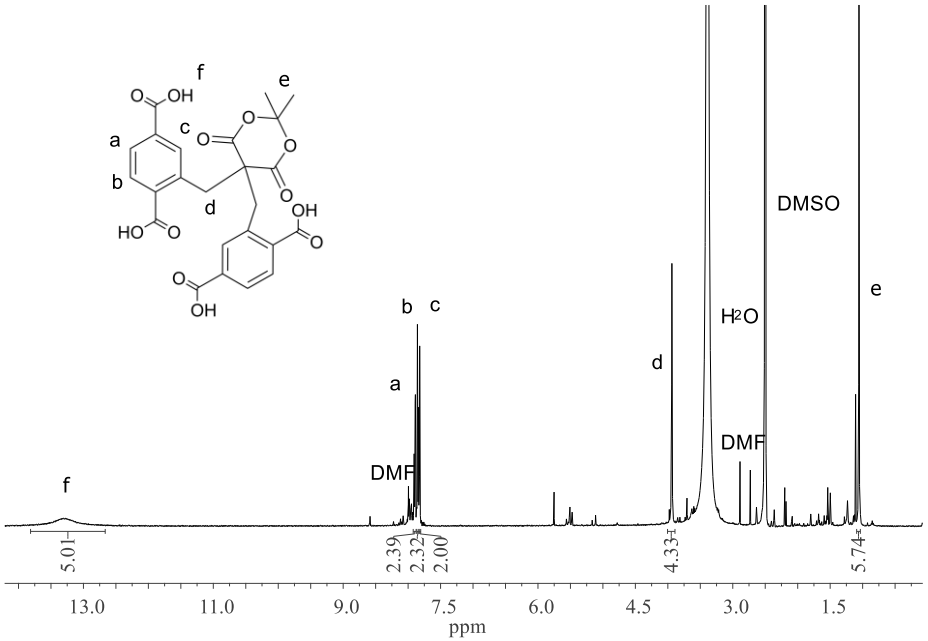

Figure 4.7: ^{1}H NMR spectrum of $(bdc)_2$-bisMeldrums in DMSO-d_6.

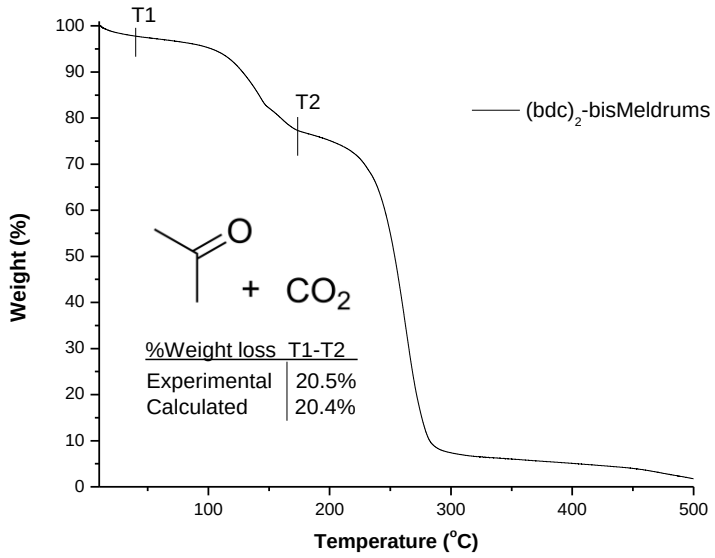

Figure 4.8: Thermogravimetric analysis (TGA) trace for $(bdc)_2$-bisMeldrums.

g) Di-*tert*-butyl 2-formylterephthalate

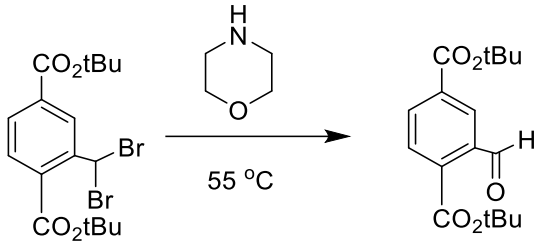

Di-*tert*-butyl 2-(dibromomethyl)terephthalate (138 mg, 0.307 mmol) was dissolved in morpholine (523 µL) and the clear yellow solution placed under $Ar_{(g)}$ before heating to 55 °C for 5 hours. The opaque white suspension was cooled to room temperature and diluted with an equal volume of ethyl acetate and stirred for 10 min. The solid was then filtered, washing thrice with ethyl acetate. The combined organic layer was then washed thrice with 5% citric acid solution before drying over Na_2SO_4, filtering and removing the solvent *in vacuo*, yielding a yellow crystalline solid (77 mg, 82%). ^{1}H NMR (500 MHz, $CDCl_3$) δ 10.56 (s, 1H), 8.43 (d, *J* = 1.5 Hz, 1H), 8.20 (dd, *J* = 8.0, 1.6 Hz, 1H), 7.91 (d, *J* = 8.0 Hz, 1H), 1.63 (s, 9H), 1.61 (s, 9H).

h) Di-*tert*-butyl 2-((2,2-dimethyl-4,6-dioxo-1,3-dioxan-5-ylidene)methyl)terephthalate

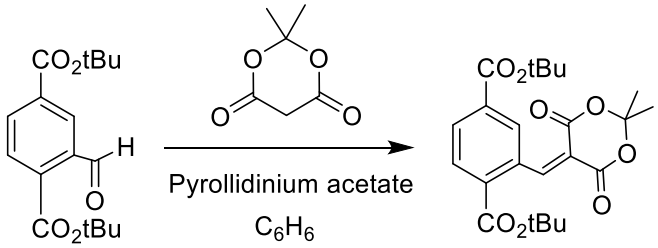

Di-*tert*-butyl 2-formylterephthalate (19.1 mg, 0.0624 mmol) and 2,2-dimethyl-1,3-dioxane-4,6-dione (9.9 mg, 0.069 mmol) were dissolved in dry benzene (320 μL) and placed under $Ar_{(g)}$. Pyrrolidine (5.5 μL, 0.0062 mmol) in dry benzene (90.7 μL) was combined with acetic acid (3.8 μL, 0.0062 mmol) and stirred at room temperature for 1 min before adding to the above solution. The clear, yellow solution was then stirred at room temperature overnight. The solvent was then removed *in vacuo* to yield an off-white powder (carried into next step without further purification). ^{1}H NMR (500 MHz, $CDCl_3$) δ 8.81 (s, 1H), 7.97 (s, 2H), 7.82 (s, 1H), 1.72 (s, 6H), 1.49 (s, 9H), 1.47 (s, 9H).

i) Di-*tert*-butyl 2-((2,2-dimethyl-4,6-dioxo-1,3-dioxan-5-yl)methyl)terephthalate

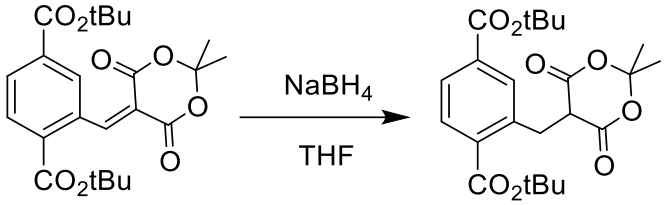

Di-*tert*-butyl 2-((2,2-dimethyl-4,6-dioxo-1,3-dioxan-5-ylidene)methyl)terephthalate (27.0 mg, 0.0624 mmol (assuming quant. Yield prev.step) was dissolved in dry CH_2Cl_2 (0.4 mL), cooled on ice and acidified to pH 2.5 by acetic acid. $NaBH_4$ (7.0 mg, 0.185 mmol) in dry CH_2Cl_2 (0.4 mL) was then added in aliquots over 1 hr before leaving the reaction mixture to stir overnight on ice. Brine was then added and the organic layer washed twice with Brine and thrice with H_2O before drying over Na_2SO_4. Solvent was removed *in vacuo* yielding a white, oily solid (13.5 mg, 50% over 2 steps). ^{1}H NMR (500 MHz, $CDCl_3$) δ 8.16 (s, 1H), 7.88 (dd, *J* = 8.1, 1.4 Hz, 1H), 7.79 (d, *J* = 8.1 Hz, 1H), 4.39 (t, *J* = 6.2 Hz, 1H), 3.63 (d, *J* = 6.2 Hz, 2H), 1.80 (s, 3H), 1.77 (s, 3H), 1.60 (s, 9H), 1.58 (s, 9H).

4.2. TGA percentage weight loss coordinates for Meldrum's acid TPG ligands

Table 4.1: Meldrum's acid ligands TGA coordinates (temperature, weight (%))

Bdc-Meldrums (Experimental 32.6%)		
Point	T1	T2
Coordinates	87.2, 99.8	160.4, 67.2
Bpdc-Meldrums (Experimental 24.6%)		
Point	T1	T2
Coordinates	51.9, 99.7	205.5, 75.1

Bpdc-CHMeldrums (Experimental 25.9%)		
Point	T1	T2
Coordinates	84.6, 99.9	254.9, 74.0
Bpdc-symMeldrums (Experimental 23.6%)		
Point	T1	T2
Coordinates	96.0, 99.4	257.5, 75.8
$(Bpdc)_2$-bisMeldrums (Experimental 22.5%)		
Point	T1	T2
Coordinates	56.2, 97.9	253.1, 75.4
$(Bdc)_2$-bisMeldrums (Experimental 20.5%)		
Point	T1	T2
Coordinates	39.5, 97.8	173.7, 77.3

4.3. Establishing malonic acid decomposition product

a) 2-((2,2-dimethyl-4,6-dioxo-1,3-dioxan-5-yl)methyl)-[1,1'-biphenyl]-4,4'-dicarboxylic acid

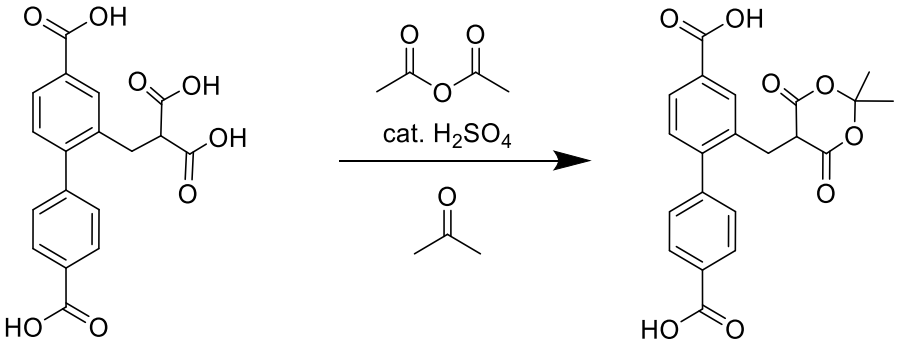

2-(2,2-dicarboxyethyl)-[1,1'-biphenyl]-4,4'-dicarboxylic acid (10 mg, 0.0279 mmol) was suspended in dry acetone (150 µL) and cooled on ice prior to the addition of 98% conc. H_2SO_4 (50 µL). Acetic anhydride (150 µL) was then added dropwise over 10 min. The white slurry gradually formed a clear yellow solution, which darkened to orange over time. Upon observation of precipitation from the orange solution the reaction mixture was diluted with Hex:EtOac (200 µL 3:1) and quenched on ice/H_2O slurry. H_2O was added until pH 2.5 and the white precipitate was collected via suction filtration and further dried overnight under high vacuum.

b) 2-((2,2-dimethyl-4,6-dioxo-1,3-dioxan-5-yl)methyl)terephthalic acid

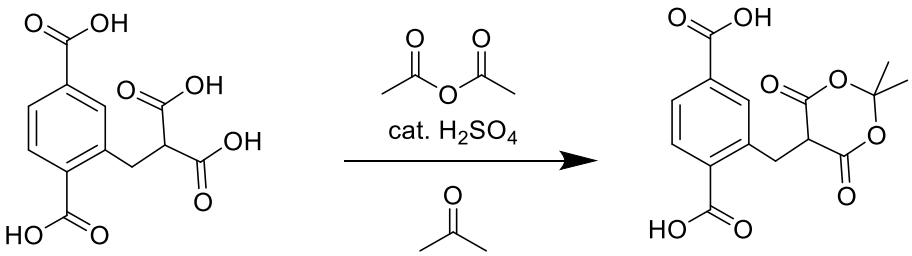

2-(2,2-dicarboxyethyl)terephthalic acid (20 mg, 0.0709 mmol) was suspended in dry acetone (300 µL) and cooled on ice prior to the addition of 98% conc. H_2SO_4 (100 µL). Acetic anhydride (300 µL) was then added dropwise over 15 min. The white slurry gradually formed a dark orange suspension whereupon an adiditonal 50 µL Acetic anhydride was added. The reaction mixture was diluted with Hex/EtOAc (800 µL 3:1) and quenched on ice/H_2O slurry. H_2O was added until pH 2.5 and the white precipitate was collected via suction filtration and further dried overnight under high vacuum.

4.4. Synthesis of extended Meldrum's acid ligands

Reactions scheme

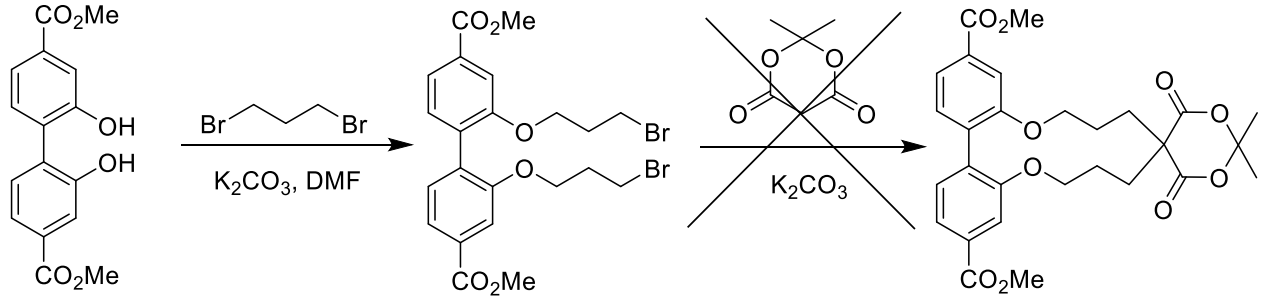

c) Dimethyl 2,2'-bis(3-bromopropoxy)biphenyl-4,4'-dicarboxylate

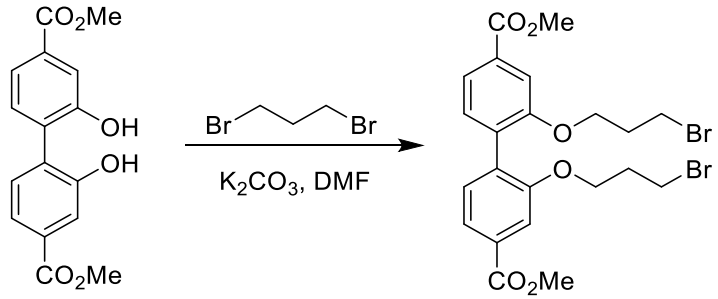

Dimethyl 2,2'-dihydroxybiphenyl-4,4'-dicarboxylate (100 mg, 0.331 mmol) was combined with K_2CO_3 (300 mg, 2.17 mmol), 1,3-dibromopropane (400 µL, 3.92 mmol) and 2 drops DMF (anhydrous). The gray white slurry was then placed under $Ar_{(g)}$ and stirred overnight at 100 °C. Following the reaction progress by TLC (1%

MeOH/CH_2Cl_2) a second addition of 1,3-dibromopropane (300 µL, 2.94 mmol) and K_2CO_3 (17 mg, 0.123 mmol) was added and the reaction mixture again stirred overnight at 100 °C. After cooling to room temperature, cold distilled H_2O was added (20 mL) and the crude product was extracted with CH_2Cl_2 (4 x 20 mL). The organic layers were combined, dried over Na_2SO_4, solvent removed *in vacuo* and the yellow oil further dried under high vacuum. The product was purified by silica flash column chromatography (CH_2Cl_2/hexane) to yield a slightly yellow oil that slowly crystallises to a white solid at room temperature (44 mg, 24%). ^{1}H NMR (500 MHz, $CDCl_3$) δ 7.70 (dd, *J* = 7.8, 1.4 Hz, 2H), 7.63 (d, *J* = 1.3 Hz, 2H), 7.30 (d, *J* = 7.8 Hz, 2H), 4.12 (t, *J* = 5.7 Hz, 4H), 3.94 (s, 6H), 3.32 (t, *J* = 6.3 Hz, 4H), 2.15 (q, *J* = 6.0 Hz, 4H).

ai) Dimethyl 7,8-dihydro-6H-dibenzo[f,h][1,5]dioxonine-3,11-dicarboxylate

Trailing second spot on TLC. Appears simultaneously during reaction with leading product spot.

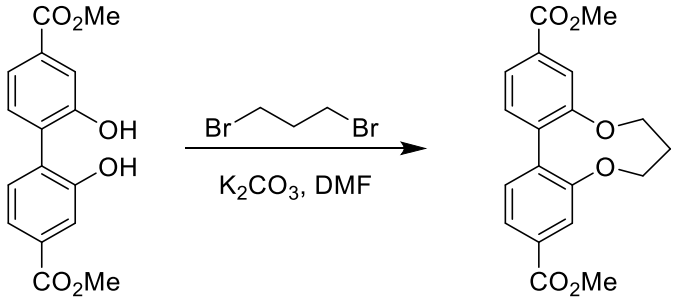

^{1}H NMR (500 MHz, $CDCl_3$) δ 7.81 (dd, *J* = 7.8, 1.5 Hz, 2H), 7.78 (d, *J* = 1.4 Hz, 2H), 7.34 (d, *J* = 7.8 Hz, 2H), 4.43 (d, *J* = 4.9 Hz, 2H), 3.94 (s, 6H), 2.04 (q, *J* = 5.2 Hz, 2H), 0.88 (t, *J* = 7.0 Hz, 2H).

d) 2,2'-bis(3-bromopropoxy)-[1,1'-biphenyl]-4,4'-dicarboxylic acid

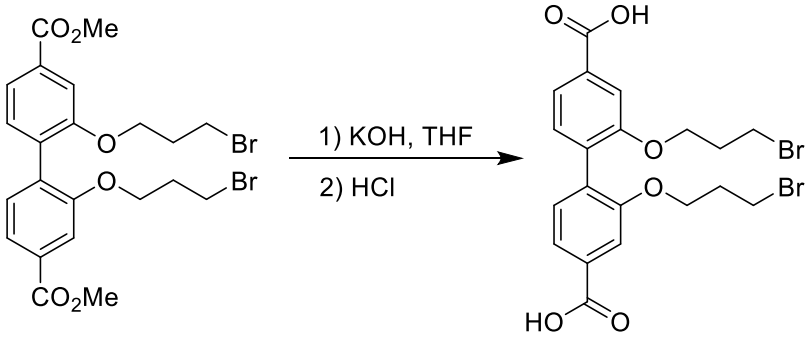

Dimethyl 2-((2,2-dimethyl-4,6-dioxo-1,3-dioxan-5-ylidene)methyl)biphenyl-4,4'-dicarboxylate (10.1 mg, 0.0186 mmol) was dissolved in dry THF (0.4 mL), and cooled on ice before the addition of 1 M KOH (163 µL each). The slightly opaque suspension was stirred on ice, allowing to gradually warm to room temperature and stirred overnight. Reaction was monitored by TLC (1% MeOH/CH_2Cl_2) and a additional 1 M KOH (163 µL)

added. After stirring for a further 3 hours, THF was then removed *in vacuo* before cooling the clear yellow aqueous layer on ice and gradually acidifying with 1 M HCl to pH 2.0. The fine white solid was then collected via suction filtration, washing thoroughly with H_2O before drying overnight under high vacuum to yield a fine white powder. ^{1}H NMR (500 MHz, DMSO-d_6) δ 13.06 (s, 2H), 7.60 (d, J = 8.0 Hz, 2H), 7.58 (s, 2H), 7.32 (d, J = 7.7 Hz, 2H), 4.10 (t, J = 5.8 Hz, 4H), 3.42 (t, J = 6.4 Hz, 4H), 2.10 (q, J = 6.0 Hz, 4H).

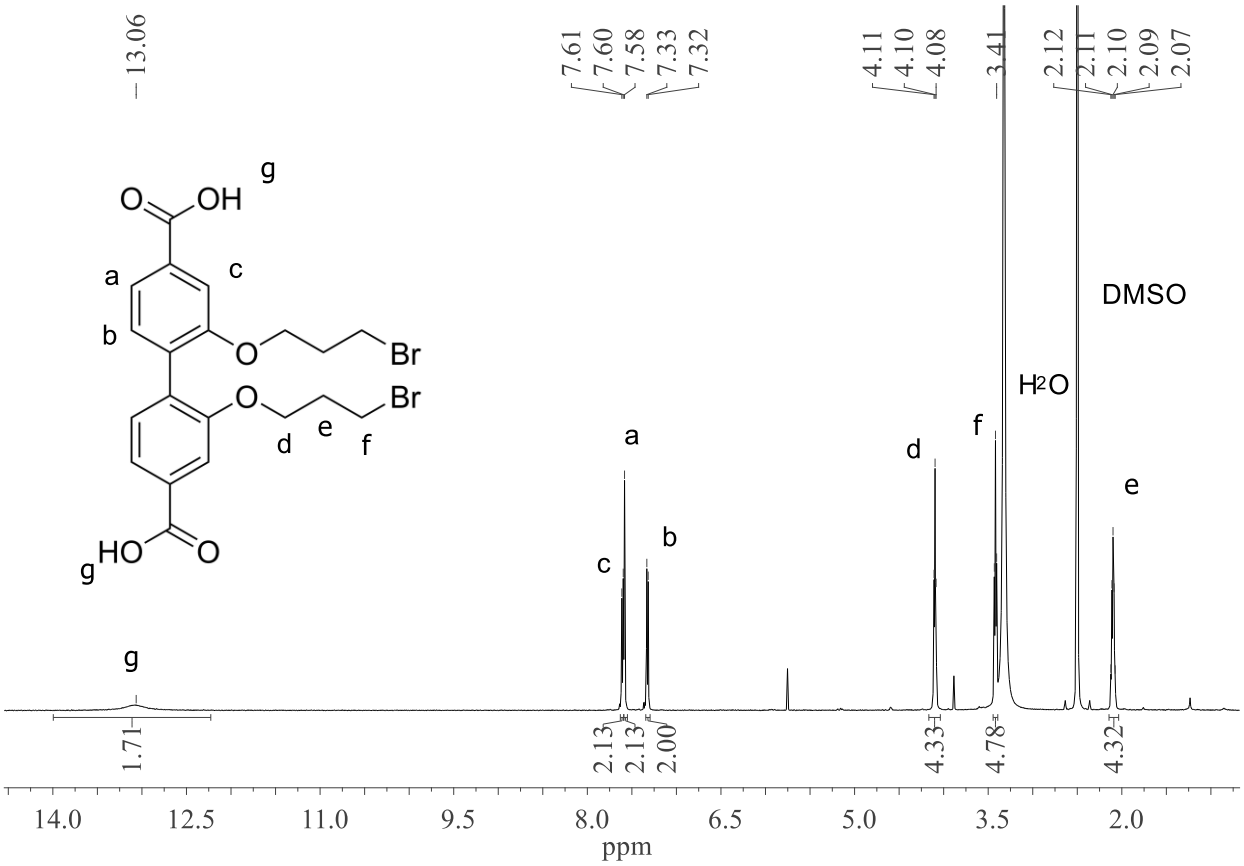

Figure 4.9: ^{1}H NMR spectrum of bpdc-$(O(CH_2)_3Br)_2$ in DMSO-d_6.

4.4.1. Crystallography data for extended ligand synthesis

Table 4.2: Crystallography data for esterified extended ligands.

Compound	**Bpdc-$(OCH_2)_2$**	**Bpdc-$(OCH_2CH_2CH_2Br)_2$**
Formula	$C_{76}H_{72}O_{24}$	$C_{88}H_{96}Br_8O_{24}$
Formula weight	1369.33	2176.92
Crystal size (mm)	0.31 x 0.4 x 0.29	0.25 x 0.24 x 0.32
Temperature (K)	188.15	93.15
Wavelength (Å)	1.54187	1.54187
Crystal system	Monoclinic	Orthorhombic
Space group	$P2_1/c$	*Pbcn*
Unit cell lengths (Å)	a = 10.4537(7) b = 17.7625(8) c = 9.1241(5)	a = 7.6853(11) b = 17.315(3) c = 16.9602(17)
Unit cell angles (°)	α = 90 β = 97.206(7) γ = 90	α = 90 β = 90 γ = 90
Unit cell volume ($Å^3$)	1680.82(17)	2256.9(5)
Z	1	1
D_{calc} (g cm^{-3})	1.353	1.602
μ (mm^{-1})	0.843	4.859
F(000)	720.0	1096.0
Reflns coll./unique, R_{int}	23972 / 3181, 0.0632	9253 / 1006, 0.1448
Data range	8.0 Å > *d* > 0.81 Å	8.0 Å > *d* > 1.05 Å
Index ranges	$-12 \leq h \leq 12$, $-21 \leq k \leq 21$, $-8 \leq l \leq 10$	$-7 \leq h \leq 7$, $-15 \leq k \leq 15$, $-16 \leq l \leq 16$
Completeness	96.4 %	98.2 %
T_{min}, T_{max}	0.774, 1.000	0.630, 1.000
R indices for data with $I>2\sigma(I)$	R_1 = 0.0559, wR_2 = 0.1623	R_1 = 0.0502, wR_2 = 0.1115
R indices for all data	R_1 = 0.0701, wR_2 = 0.1929	R_1 = 0.1393, wR_2 = 0.1224
Largest difference peak and hole (e $Å^{-3}$)	0.22/ -0.2	0.430/ -0.45

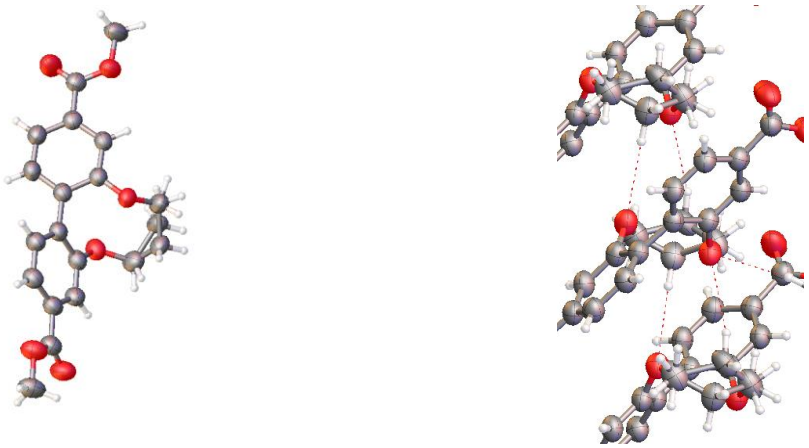

Figure 4.10: Single crystal structure of esterified bpdc-$O_2(CH_2)_3$ showing intermolecular hydrogen-bonding.

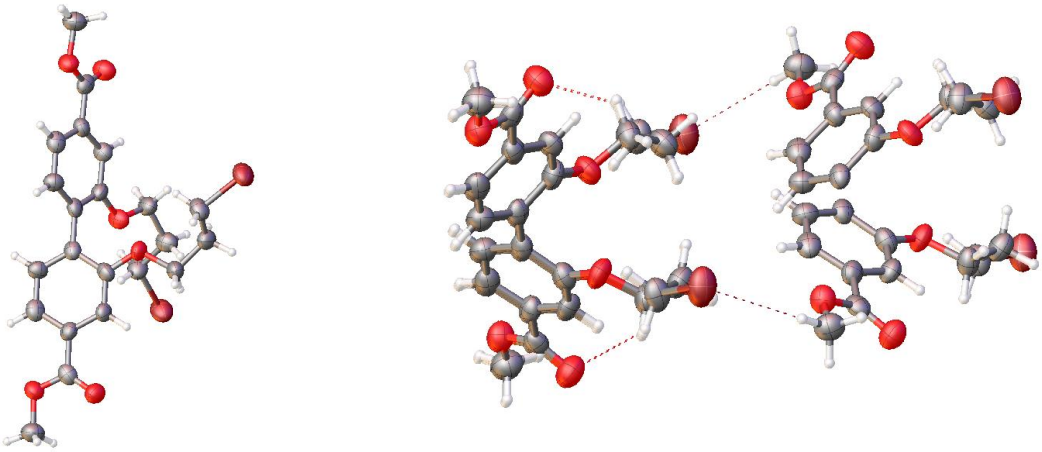

Figure 4.11: Single crystal structure of esterified bpdc-$(O(CH_2)_3Br)_2$ showing non-classical intermolecular hydrogen-bonding.

5. Chapter 5 –Synthesis of Meldrum's acid MOFs SI

5.1. MOF synthesis and characterization

General procedures

XRD Analysis

All powder X-ray diffraction experiments were carried out on a Rigaku Spider X-ray diffractometer with Cu K_α radiation (Rigaku MM007 microfocus rotating-anode generator), monochromated and focused with high-flux Osmic multilayer mirror optics, and a curved image plate detector. The data were obtained from freshly prepared MOF samples that had been very gently ground in a small amount of DBF and kept damp in a polymer sleeve throughout the measurement. The two-dimensional images of the Debye rings were integrated with

2DP[1] (Version 1.0.3.4) to give 2θ vs I diffractograms. The predicted powder patterns were generated from their single-crystal structures using Mercury v4.10.

Single crystal XRD analysis involved mounting selected crystal on a MiTeGen mylar loop in DBF at room temperature in a polymer sleeve.

5.2. IRMOF-10-symMeldrums

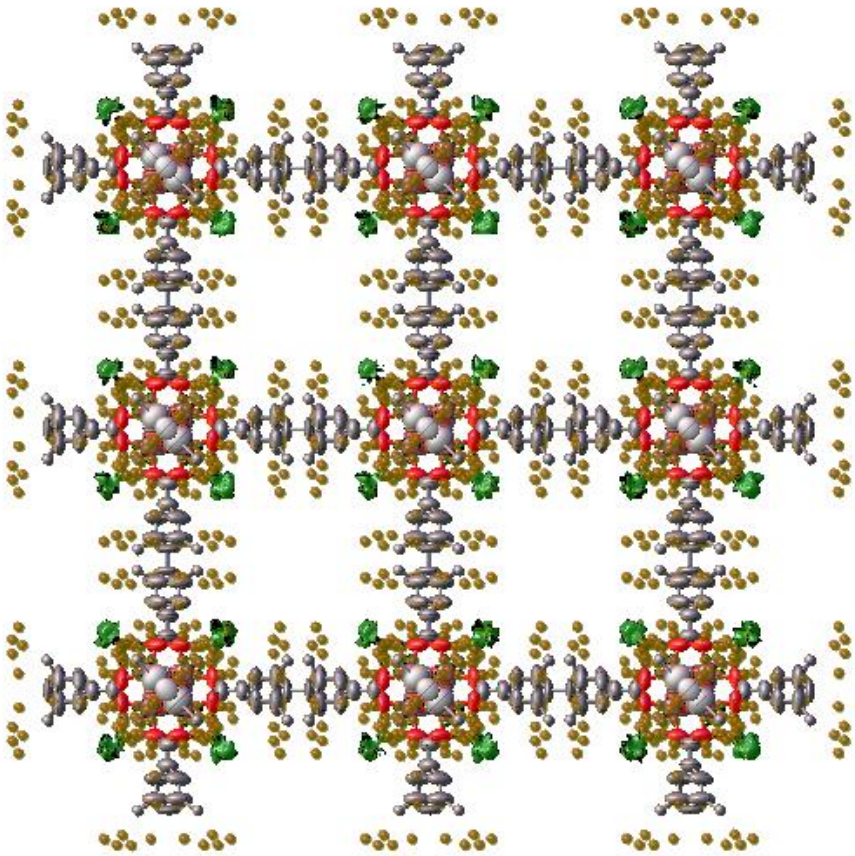

Figure 5.1: Single crystal structure of IRMOF-10-symMeldrums showing absence of significant electron density in pores.

6. References

[1] Rigaku, Rigaku, **2011**.

[2] T. Düren, F. Millange, G. Férey, K. S. Walton, R. Q. Snurr, *The Journal of Physical Chemistry C* **2007**, *111*, 15350-15356.

[3] aN. Stock, S. Biswas, *Chem Rev* **2012**, *112*, 933-969; bC. Janiak, J. K. Vieth, *New J. Chem.* **2010**, *34*, 2366.